Hypervelocity impacts and the evolution of planetary surfaces and interiors

by

Wesley Andrés Watters

B.Sc., Mathematics, Massachusetts Institute of Technology (1999)
B.Sc., Physics, Massachusetts Institute of Technology (2000)
M.Sc., Earth and Planetary Science, Massachusetts Institute of Technology (2000)

Submitted to the Department of Earth, Atmospheric, and Planetary Sciences
in partial fulfillment of the requirements for the degree of

Doctor of Philosophy
in Planetary Science and Planetary Geophysics

at the

MASSACHUSETTS INSTITUTE OF TECHNOLOGY

February 2009

Author .....
Department of Earth, Atmospheric, and Planetary Sciences
December 11, 2008

Certified by .....
Maria T. Zuber
Department Head
E.A. Griswold Professor of Geophysics and Planetary Science
Massachusetts Institute of Technology
Thesis Supervisor

Certified by .....
John P. Grotzinger
Fletcher Jones Professor of Geology
California Institute of Technology
Thesis Supervisor

Accepted by .....
Prof. Daniel Rothman
Professor of Geophysics
Chair, EAPS Graduate Committee

Hypervelocity impacts and the evolution of planetary surfaces and interiors

by

Wesley Andrés Watters

Submitted to the Department of Earth, Atmospheric, and Planetary Sciences
on December 11, 2008, in partial fulfillment of the
requirements for the degree of
Doctor of Philosophy
in Planetary Science and Planetary Geophysics

Abstract

The thesis consists of five studies relating impact processes to the evolution of planetary interiors as well as impact structures on planetary surfaces. Chapter 2 is concerned with developing methods for estimating the amount of heat deposited deep in terrestrial mantles by large impacts. Chapter 3 makes use of these results to compute the consequences of impact-related thermal buoyancy perturbations in numerical models of subsolidus convection. Among the important results of this work is a relation for the time-scale on which a buoyancy anomaly flattens and spreads before it is halted by convective downflows, as well as a condition that indicates for what perturbation magnitudes and Rayleigh numbers the flow is significantly slowed at a global scale. Chapter 4 describes a structural model of Endurance Crater in Meridiani Planum on Mars, which is constrained by observations gathered by the MER-B Opportunity rover. These results reveal new insights about the planform shape of the crater excavation flow, as well as the connection between crater shape and pre-existing structures in target materials. The study presented in chapter 5 relates the planimetric shape of simple impact craters on Mars ($D < 5$ km) to the geological targets in which they form, as well as rim diameter. Planform crater shape is characterized by a suite of morphometric parameters, including Fourier harmonic amplitudes and phase angles, as well as measures of deviation from radial symmetry and convexity. In addition to finding the morphometric dependence on target properties, this work has illuminated prominent transitions between different cratering regimes, and contains a measure of the global distribution of planform elongation azimuths – which may relate to impact azimuth and provide an estimate of Mars' past obliquity variations. Finally, Chapter 6 describes a stochastic-kinematic model of the interaction between the excavation front and fractures in the target, which replicates many of the observations obtained in Chapter 5.

Thesis Supervisor: Maria T. Zuber
Title: Department Head
E.A. Griswold Professor of Geophysics and Planetary Science
Massachusetts Institute of Technology

Thesis Supervisor: John P. Grotzinger
Title: Fletcher Jones Professor of Geology
California Institute of Technology

Acknowledgments

It has been my immense pleasure and privilege to pursue graduate studies in the EAPS department at MIT. During my time here, I've had the good fortune to meet, befriend, as well as work together with and alongside many extraordinary people. It is impossible to overstate how much I am grateful to my academic advisors, Maria T. Zuber and John P. Grotzinger. Both as scientific mentors and as friends they have spared no effort or expense to give me the guidance, support, and resources needed to pursue my research. Working with Maria and John through the years has been enormously stimulating and rewarding in ways too varied and numerous to recount here – I am forever in their debt. I also want to highlight the hugely stimulating friendships that I have enjoyed with fellow graduate students Kristen Cook, David Fike, Ian Garrick-Bethell, Douglas Jerolmack, Sarah Stewart Johnson, and Erwan Mazarico. My time at MIT would have been greatly impoverished also without the friendship and scientific counsel of professors Bradford H. Hager, Richard P. Binzel, Benjamin Weiss and Samuel Bowring, as well as post-doctoral fellows Laurent Husson and Jeffrey Andrews-Hanna.

The EAPS community is blessed to have so many exceptionally warm and gifted people working in the administrative staff, who have been an indispensible and enriching part of my graduate school experience. In particular I would like to thank Roberta Allard, Joe Hankins, Dr. Vicki McKenna, Linda Meinke, Mark Pendleton, Carol Sprague, Jacqueline Taylor, Patricia Walsh, and Kerin Willis. I would also like to extend thanks to Prof. Steve Squyres of Cornell University for inviting me to participate in the Mars Exploration Rover mission, which was among the highlights of my graduate career. I want to thank my close friend Prof. Anthony Coleman of the Department of Philosophy at Willamette University for convincing me that Cartesian skepticism is untenable, sparing me further embarrassment as a *scientist* who finds it compelling. I would like to thank Ying Zhang for her friendship and generous help on many occasions. I am grateful to all of the friends who have been close companions throughout this period, without whom the journey would not have been nearly so abundant with meaning and adventure, as well as huge amounts of fun.

This thesis is dedicated to three people in particular. First, I want to recall the memory of Roberta Bennett-Calorio, who worked in EAPS as an administrative assistant for more than ten years. She was a dear friend and confidant, as well as one of the most compassionate, good-humored, buoyant, and courageous people whom I have ever known. This work is also dedicated to my parents, Allan Eugene Watters and Cecilia Farfán Verse. Throughout my childhood and to the present day, they have encouraged me to pursue my passions and have helped me and guided me at every chance and by every means at their disposal. It is largely thanks to their love and encouragement, their breadth of mind and spirit, their curiosity and wise counsel and the exercise of their uncommon talents, that I have had the chance to pursue and ultimately to fulfill many childhood dreams.

Professional acknowledgments

I would like to acknowledge the use of (a) Mars Orbiter Camera (MOC) images processed by Malin Space Science Systems that are available at `http://www.msss.com/moc_gallery/`, as well as (b) High Resolution Imaging Science Experiment (HiRISE) images processed by the HiRISE Operations Center at the University of Arizona and available at `http://hirise.lpl.arizona.edu/katalogos.php`, and (c) Mars Exploration Rover images processed by the Multimission Image Processing Laboratory (MIPL) at the Jet Propulsion Laboratory in Pasadena, CA. The data used in the last three chapters of this thesis is a product of the genius and hard work of countless engineers and scientists who envisaged, constructed, and deployed

the Mars Global Surveyor (MGS), Mars Reconnaisance Orbiter (MRO), and Mars Exploration Rover (MER) spacecraft and their instrument payloads (especially MOC, HiRISE, and PANCAM (MER)). I would like to thank Drew Barringer for allowing myself and colleagues access to the rim trails around Barringer Crater near Winslow, AZ, for five days in late January of 2008. I would also like to acknowledge John Abelson and Mel Simon and the Agouron Institute for their generous support.

Contents

1 Introduction **9**

2 Estimation of heat deposited in terrestrial mantles by large impacts **15**
2.1 Shock-heating of terrestrial mantles: an overview 15
2.2 Estimates of shock heating 18
2.3 Reference models for pressure and density 21
2.4 Impedance match solution 24
2.5 Effects of ambient pressure and density 25
2.6 Consequences of an upper mantle layer 32

3 Geodynamical consequences of large thermal perturbations for convecting mantles **35**
3.1 Overview 35
3.2 Convection-model perturbations I 36
3.3 Evolution of the shock-heated region 38
3.4 Convection-model perturbations II 47
3.5 Time-scale of spreading 47
3.6 Global stagnation criterion 53
3.7 Alternative convection models 58
3.8 Geological implications 59
3.9 Current-downflow collisions 61
3.10 Conclusions 66

4 Geological structure of Endurance Crater, Meridiani Planum, Mars **69**
4.1 Overview 69
4.2 Bedding orientations and layer thicknesses 70
4.3 Layer surface model 75
4.4 Styles of crater excavation 79

5 Fourier analysis of impact crater morphology: relating target properties and planimetric shape **95**
5.1 MOC Crater-Target Survey . . . 95
5.2 Crater/Target Attributes: MOC-FCC & HiRISE-FCC . . . 104
5.3 HiRISE Fresh Crater Catalog: Analyses . . . 113
5.4 Harmonic phase angles and the obliquity of Mars . . . 144
5.5 MOC Fresh Crater Catalog: Analyses . . . 155
5.6 Conclusions . . . 170

6 Stochastic-kinematic model of crater excavation in fractured targets **175**
6.1 Model requirements . . . 175
6.2 Model description . . . 176
6.3 SKEM Simulated Crater Catalogue (SKEM-SCC) . . . 181
6.4 D^*-dependence of radial deviation . . . 182
6.5 Distributions of morphometric quantites . . . 185
6.6 Dominant harmonics . . . 190
6.7 Acceleration function $G(\psi)$ . . . 194
6.8 Outstanding questions . . . 195

A Auxiliary Material for Chapter 3 **199**
A.1 Spreading time-scale relation: estimated parameter values . . . 199
A.2 Type I perturbations and global stagnation . . . 199

B Auxiliary Material for Chapter 5: HiRISE-FCC **205**

C Auxiliary Material for Chapter 5: MOC-FCC **219**

Chapter 1

Introduction

Impacts and planetary interiors:
Shock-heating of terrestrial mantles and consequences for mantle convection

The first half of the thesis concerns the effects of very large impacts upon the evolution of planetary interiors. In Chapter 2 we propose several methods for estimating the heat deposited deep in planetary interiors by large impacts, and in Chapter 3 we explore the geodynamical consequences of impact-related buoyancy perturbations in numerical models of mantle convection. One of the interesting questions addressed by this work concerns the pattern and timing of volcanism related to large impact events.

Collisions of large planetary bodies are thought to have played a central role in the formation and thermal evolution of the terrestrial planets and moons. Apart from their role in planetary accretion (Wetherill [1990]), the largest collisions might have caused resurfacing on a global scale (Tonks and Melosh [1993]). Long after the formation of the terrestrial planets, smaller collisions had a major influence on the evolution of planetary interiors.

Much recent attention has focused on the possibility that impacts initiate volcanism, and several mechanisms have been offered. A handful of studies have tried to relate impacts to volcanism occurring at large distances. It was suggested by Schultz and Gault [1975] that the focusing of seismic waves following an impact can cause disruption of antipodal terrains, and Williams and Greeley [1994] proposed that fractures formed in this manner can serve as conduits for magmas.

Most work has focused on volcanism in the immediate vicinity of impacts. It was long ago suggested that the collapse of large complex craters can cause uplift of upper-mantle rocks that melt upon decompression (Green [1972]). The distances involved in this uplift are possibly too small, however, to provoke widespread melting (Ivanov and Melosh [2003]). A related mechanism emphasizes the overburdern pressure drop caused by crater excavation, expected to initiate instantaneous decompression-melting of a small volume in the upper mantle (comparable to the excavation volume) beneath a thin lithosphere (Green [1972], Jones et al. [2002], Elkins-Tanton and Hager [2005]). Subsequent relaxation of the lithosphere and the anomalous partial melt buoyancies can lead to upwelling of additional material that melts upon decompression, forming a long-lived shallow mantle plume.

A few studies have suggested that impacts can initiate *deep* mantle plumes. Abbott and Isley [2002] finds a correlation between the ages of major impacts and episodes of plume-initiated volcanism in the terrestrial geologic record. A causal mechanism was suggested by Muller [2002], in which avalanches at the core-mantle boundary (CMB) are triggered by the high shear stresses imparted in highly oblique impacts, exposing insulated regions of the D'' layer to core heating. Leaving aside the formidable problem of relating deep mantle plumes to a Chicxulub-scale event, time-scales for plume ascent are too long to reconcile this impact with the flood basalts of the Deccan Traps (Loper [1991]).

The evolution of large partial- and total melt volumes generated by giant impacts was addressed more recently in Reese et al. [2004] and Reese and Solomatov [2006]. The former study

estimates the volume of magmatic construction that results from a long-lived shallow mantle plume initiated by a large impact on Mars, obtaining volumes comparable to the total volume of the Tharsis rise. The latter study (Reese and Solomatov [2006]) employs a suite of analytical models and scaling arguments to estimate the time-scales associated with different stages of the evolution, such as differentiation, crystallization, dynamic adjustment and lateral spreading of the melt volume. The authors find that giant impacts can form extensive magma oceans which upon cooling exhibit crustal thickness variations similar to what is observed for the hemispheric dichotomy on Mars. Still more recently, a cooling viscous drop model was used by Monteux et al. [2007] to obtain the time- and length-scaling for the dynamic adjustment of impact-related thermal anomalies in the absence of ambient fluid motion, for the case of large impacts on bodies ranging in size beween the Moon and Mars.

A number of studies have addressed a possible link between impacts and the mare basalts that flooded large basins on the moon. Manga and Arkani-Hamed [1991] proposed that high-porosity ejecta blankets, by insulating the radiogenic KREEP layer, can trap enough heat to generate the lunar mare. To explain the absence of mare in the large South Pole-Aitken (SPA) basin, Arkani-Hamed and Pentecost [2001] examined the flattening and spreading of an impact-heating anomaly associated with basins of Imbrium and SPA size. In their numerical simulations, the KREEP layer was completely swept away by the spreading motion for SPA-sized impacts and not for those Imbrium-sized. With the aim of explaining the volume, late onset, and longevity of mare basalt volcanism, Ghods and Arkani-Hamed [2007] added impact-heating perturbations to a model lunar mantle – an unstable layer that was initially not convecting – and claimed that whole-mantle convection and its consequences were an outcome of the perturbations. It should be noted that impacts could not have induced whole-mantle convection in young terrestrial mantles that were already convecting, and neither will buoyancy perturbations have this consequence in numerical models of a convecting layer.

In Chapter 2, we describe a method for calculating the heat deposited by shock-waves at great depths in terrestrial mantles, which takes into account the increase in density and pressure. Later, these estimates are matched to a characteristic [and dimensionless] perturbation temperature and size, for projectile radii in range $R = 200$ km to 900 km and vertical incident velocities in the range $v_i = 7$ to 20 km/s. In Chapter 3 we examine how thermal buoyancy perturbations can disrupt and reorganize circulation in a convecting layer, as well as obtain the time-scaling of this interaction.

Impacts and planetary surfaces: Structure of simple impact craters

The science of impact crater geology began with the investigations of D. M. Barringer in the first years of the 20th century, when he correctly identified several salient features of simple impact craters at the famous impact structure that now bears his name (Barringer [1905]): (a) an inverted stratigraphic sequence in the upper rim walls above the pre-impact horizon, (b) the uplift of strata that are flat-lying in the far-field, and (c) materials of meteoritic origin having a concentric distribution with respect to the crater. This initial work began a decades-long debate about the origins of Barringer Crater (also called "Meteor Crater" in this thesis), which was resolved in favor of an impact genesis by Gene Shoemaker's landmark detailed geologic analyses. Shoemaker [1960] presented a careful geological description and comparison of nuclear explosion craters and Barringer Crater, noting several features in common: (a) overturned synclinal folds (the "overturned flap"), (b) debris that preserves an inverted stratigraphic sequence in the upper fold limb, (c) crater floors covered with allocthonous debris (known as a breccia lens). Subsequent investigations of other simple impact craters such as the very young Henbury craters in central Australia (Milton and Michel [1965], Milton [1968]), and the Odessa Crater in west Texas (Shoemaker and Eggleton [1961],

Evans [1961]) identified similar structural features. Although our focus in the present study is the structure of simple impact craters, it should be noted that the study of shock-metamorphosed rocks became an important feature of field investigations at Barringer Crater from the beginning (Barringer [1905]), and was eventually regarded as the most compelling signature of an impact origin. For example, shock metamorphism was ultimately described at Lonar Crater in India (Nayak [1972]), and was then recognized – along with Barringer and the Henbury craters – as one of the best-preserved simple impact structures on Earth. Later investigators have described an overturned syncline and inverted stratigraphy at Lonar as well (e.g.,Maloof et al. [2007]).

The core-drilling investigation of Roddy et al. [1975] at Barringer Crater measured the amount of rim uplift and variation in thickness of inverted strata with distance from the crater rim. Core-drilling at the Brent crater in Ontario, Canada (Dence [1968]) was used to resolve an outstanding paradox also addressed in the present thesis. Small-scale laboratory experiments in sand and low-strength targets (e.g., Gault et al. [1968], Stoeffler et al. [1975], Piekutowski [1977]) reveal the overturned synclinal fold and an inverted stratigraphy on crater flanks, but not the breccia lens on the crater floor which in large craters significantly lowers the ratio of depth to diameter. Dence [1968] found that the allochthonous debris in the breccia lens did not exhibit the high degree of shock metamorphism found in ejected materials, and for this reason was not fallout material, and must instead have been sourced from the crater walls. The authors proposed the notion of a "transient crater," opened by the excavation flow and preserved in small-scale experiments, but which in large-scale craters is modified as the unstable upper-rim walls collapse and slump into the crater floor, forming a breccia lens. Left unresolved was the size-scale at which this transition occurs, and in Chapter 5 we present observations that constrain this transition diameter for simple craters on Mars. Returning to our chronology, ground-penetrating radar was later used at Barringer Crater to resolve the shape of the breccia lens (Pilon et al. [1991]).

Some of the subsequent geological analysis of simple craters has focused on the description offaulting and fracturing caused by the cratering flow and subsequent, early-stage modification. Faults occur in four main types: (a) shallow-to-steeply dipping overthrusts, dipping craterward, in which the upper block moves away from the crater (e.g., at the Henbury Craters (Milton [1968]), Odessa Crater (Shoemaker and Eggleton [1961], Evans [1961]), and observed in laboratory experiments (Gault et al. [1968])), (b) rotated faults (thrusts, normal, and reverse) associated with crater wall uplift, dipping $\leq 45^{\circ}$ away from the crater, in which the upper block is displaced craterward with respect to the lower block (e.g., at Barringer (Shoemaker and Eggleton [1961]) and Lonar (Maloof et al. [2007])); (c) steeply-dipping to listric normal faults in which the upper block moves craterward, associated with early-modification and slumping of the transient crater (e.g., at Lonar (Maloof et al. [2007])); (d) "tear-faults" formed when adjacent blocks are uplifted different amounts by the excavation flow (e.g., at Barringer (Shoemaker [1960], Roddy [1978])).

Impacts also cause widespread fracturing of target materials as well as re-activation of preexisting fractures. Fracturing has been studied in detail at Lonar Crater by Kumar [2005], who described three sets of impact-induced fracture systems: conical, concentric, and radial (N.B. Maloof et al. [2007] found no evidence for conical and crater-radial fracturing at Lonar). Kumar and Kring [2008] reports the same fracture systems at Barringer crater. It should be noted that although fractures having these geometries have been observed in laboratory experiments, recent work has shown that this is a consequence of wave reflections from the edges of the target blocks (Senft and Stewart [2007]) and are not anticipated for simple craters forming in an effectively infinite half-space.

Of special importance to this thesis is the effect of pre-existing faults and fractures upon the planform cratering flow and final planimetric crater shape. It was first suggested by Shoemaker [1960] that crater excavation is more effi-

cient along pre-existing planes-of-weakness, and that this accounts for the highly quadratic shape of Barringer crater, which formed in sedimentary rocks having a regionally extensive conjugate set of orthogonal joints which bisect the crater corners. This suggestion was seemingly confirmed by a small number of preliminary laboratory experiments (Gault et al. [1968]) although these results were never followed up with a systematic study. The conclusions of Shoemaker [1960] were later supported by the observations of Roddy [1978], but directly contradicted by the detailed survey of fracture azimuths reported in Kumar and Kring [2008]. In this latter study, the Kaibab carbonate unit (in which most of the crater was excavated) exhibits conjugate-orthogonal joints which are aligned with the straight crater walls. The observations of Fulmer and Roberts [1963] based upon a large number of explosion crater observations confirmed that small craters with highly polygonal shapes formed in comparatively indurated targets with well-developed fracture systems, while highly circular craters formed in unconsolidated sediments or weekly indurated rocks.

Other studies addressing the consequences of target properties for crater shape have focused upon the effects of layering. The case of weak-over-strong layering has received the most attention in laboratory experiments (e.g., Quaide and Oberbeck [1968], Piekutowski [1977]) and more recently in a modeling study (Senft and Stewart [2007]). These efforts have successfully reproduced a wide range of features well-known from planetary surface observations, including terraces and flat-bottoms as well as central mounds. Studies of explosion cratering on a large-scale in many kinds of geological materials have also been used to determine how depth and diameter depend upon target properties as well as depth of charge (e.g., Vortman [1969]).

In Chapter 4 we describe the study of Endurance Crater in Meridiani Planum on Mars, which is based primarily upon the observations of the MER-B Opportunity rover. In several regards, the Endurance Crater data-set presents an ideal and unprecedented chance to study the structure of simple impact craters. First, Endurance formed in banded or layered sedimentary rocks that were initially flat-lying, where the bands and layers are easily traced around the crater wall. Second, Endurance is extremely fresh by terrestrial standards, and belongs to a size range (D = 150 m) that is rarely or never so well preserved on Earth, since craters of this size are quickly eroded and buried. Third, Endurance formed in rocks exhibiting a conjugate-orthogonal set of joints that can be easily measured and compared with the crater planform. Fourth, because of the abundance of orbiter imagery, we can compare and apply what is learned at Endurance to the structure of other impact craters forming in the same target materials, elsewhere in Meridiani Planum. As we shall see, the study presented in Chapter 4 yields new insights into the formation of small impact craters that were not possible before this data set was assembled by the MGS, MRO, and MER-B spacecraft.

Impacts and planetary surfaces:
Impact crater morphometry

The discipline of crater morphometry blossomed with the study of lunar impact craters in Apollo imagery. The most important early results identified the simple-to-complex transition, which occurs on the Moon for diameters in the range D = 15 km to D = 25 km, and which is expressed in numerous morphological metrics, including rim-crest diameter versus depth, rim height, flank width, rimwall slope, floor diameter, circularity, and rim-crest evenness (Pike [1977]). In Chapter 5 we shall focus exclusively upon properties of the planimetric shape of impact craters, such as the deviation from planform radial symmetry as a function of crater diameter. Most early studies found no dependence of planform circularity upon crater diameter (e.g., Ronca and Salisbury [1966] and Murray and Guest [1970]), but the most comprehensive of these (Pike [1977]) found that radial symmetry increased with diameter up to the simple-complex transition and then decreased with increasing diameter above this transition.

Measures of radial symmetry can be useful

but fail to capture much information about the planform shape. Eppler et al. [1977] proposed using a Fourier decomposition of the [planimetric] rim crest outline into harmonic amplitudes and phase angles to more completely describe crater morphology, and this has been adapted for use in the present study in Chapter 5. This approach was used in Eppler et al. [1983] to study the effects of varying geological targets (e.g., lunar highlands versus lowlands and mare), presence of topography, and extent of modification upon the planform shape of lunar complex craters, and more generally to characterize the whole range of variations in complex crater morphology. Other early studies demonstrated that the straight segments of complex crater walls tend to align with ambient tectonic stress fields indicated by faults (Schultz [1976], Scott and Watkins [1997]), where this was more recently confirmed for populations of complex craters in the Martian highlands (Ohman et al. [2005]).

Studies of Martian crater morphometry and morphology based upon Mariner- and Viking-era datasets largely focused upon crater depth-diameter ratios and the shapes of apparently lobate or fluidized ejecta deposits in attempts to correlate these with concentrations of subsurface volatiles (e.g., Mouginis-Mark [1978], Cintala and Mouginis-Mark [1980], Barlow and Bradley [1990]). The global surface topography supplied by the Mars Orbiter Laser Altimeter (MOLA) instrument on board the Mars Global Surveyor spacecraft sparked a flurry of new morphometric analyses addressing the three-dimensional shape of large simple craters and complex craters (e.g., Garvin and Frawley [1998], Garvin et al. [2000]). Among the most interesting outcomes was that craters in northern lowland populations were markedly deeper than their highland counterparts, and that the simple-to-complex transition occurs at a larger diameter in the northern lowlands (Boyce et al. [2006], Stewart and Valiant [2006]), suggesting they formed in stronger target materials.

Crater morphometers have also trained their sights on the comparatively small population of highly elliptical craters, or craters believed to have formed in highly oblique impacts. Classic experimental studies in quartz sand and granite (Gault and Wedekind [1978], Fechtig et al. [1972]) showed that small craters that are significantly elongated along the impact azimuth only when the incidence angle (i.e., measured with respect to the normal) was greater than 75 to 80 degrees. Recent experiments (Wallis et al. [2005]) for strength-dominated mm-scale craters (nylon projectile into aluminum) have shown that the impact azimuth is preserved in the crater shape for incidence angles of as small as 10° and can be recovered using an eigenfunction expansion of the high-resolution topography (Wallis and McBride [2002]). It is unclear from this work, however, whether the results can be applied to planetary-scale impacts where slumping is important, where strength effects are less important, or indeed whether this information is contained in the planimetric rim trace alone. The population of large elliptical craters have received numerous interpretations, and have been used in a few studies to estimate the positions of Martian paleo-poles in the time when large impacts formed on the surface of Mars (e.g., Schultz and Lutz-Garihan [1982], Boutin and Arkani-Hamed [2007]).

The foregoing morphometric observations and analyses were concerned primarily with large simple craters as well as complex craters on the Moon, and Mars (e.g., $D \geq 3$ km in the case of Mars). With the arrival of the High Resolution Imaging Science Experiment (HiRISE) on board MRO, a new range of crater sizes have been captured at high resolution (0.25 m/pixel). The HiRISE instrument has already acquired many images of small, fresh impact craters (from $D = 20$ m to $D = 4$ km) that formed in a wide variety of geological targets – at higher resolution and over a larger portion (of a geologically far more diverse planet) than what was acquired by the Apollo missions for the Moon. Unlike the lunar data set, the HiRISE images of the Martian surface are illumined by light scattered from an atmosphere, so that shading alone (which can introduce significant biases) is not required to indicate morphology. In Chapter 5, the new HiRISE data are used to find as-yet undiscovered morphometric transitions and relations

between small crater shape and geologic target properties, as well as the distribution of small crater elongation azimuths at a global scale.

Impacts and planetary surfaces:
Models of the cratering flow

Among the earliest efforts to build realistic models of the cratering flow (in the (r, z) plane) were the semi-analytic kinematic "Z models" of Maxwell [1977], which derive from the condition of incompressible flow, and assuming that the radial velocity has the the functional form $u = \alpha(t)/R^Z$ (for a time-dependence $\alpha(t)$ and positive value of $Z \approx 3$), observed in experiments. The very simple solution for the streamlines is a highly realistic excavation flow field, and the model has been refined and adapted in numerous ways (e.g., Croft [1980], Grieve and Garvin [1984]) to study crater excavation. A majority of modeling efforts up to now have used Eulerian hydrocodes to solve the fundamental equations of motion and equations of state, to study the cratering flow and transient cavity formation (e.g., Thompson [1988], McGlaun et al. [1990]). Owing to the expense of computational resources for such models, only very recently have these become fully three-dimensional as well as capable of treating strength properties and damage in a realistic fashion (Senft and Stewart [2007]). Modeling the effects of realistic strength *heterogeneities* in a fully three-dimensional domain remains largely outside the reach of current capabilities.

We attempt to bridge this gap with a simple model that makes an *ansatz* about the effect of target structures upon the crating flow, which is (in reality) the outcome of a very complex physical process. In the final chapter of this thesis (Chapter 6) we present a 2-D Monte Carlo kinematic model of the *planform* of cratering flow that makes a simple assumption regarding the interaction of the excavation front with fractures in the target. The purpose of this simple model is to illuminate how heterogeneities in the target may translate to asymmetries in the cratering flow, which can reproduce the spectrum of crater planforms observed on planetary surfaces.

Chapter 2

Estimation of heat deposited in terrestrial mantles by large impacts

Abstract: In this chapter we describe several related methods for calculating the heat deposited by shock-waves at the increased temperatures and pressures of terrestrial mantles, and supply estimates of shock-heating caused by projectiles with radii in the range 200 to 900 km and vertical incident velocities in the range 7 to 20 km/s. These estimates are derived using basic thermodynamic relations as well as the Hugoniot equations-of-state (EOS) that have been measured for terrestrial mantle materials. In order to account for the effects of increasing density and pressure with depth, we have divided the mantle into thin layers whose densities and bounding pressures increase with depth, where these are based upon Hugoniot-referenced models of the terrestrial and Martian interiors. For each layer we compute a new Hugoniot-EOS centered upon the unshocked density and pressure, and use the planar impact approximation to calculate the transmitted peak shock pressures. Estimates based upon this method are also compared with those computed using simpler approximations. The thermal perturbations derived in this chapter are used in Chapter 3 to investigate the long-term consequences for convection in terrestrial mantles of thermal perturbations caused by large impacts.

2.1 Shock-heating of terrestrial mantles: an overview

A projectile incident at velocities typical of planetary collisions will cause a supersonic stress wave (a shock wave) to propagate through the target and projectile. A shock accelerates the material through which it passes to the particle velocity, u, while the shock front travels at a speed U. The pressure P, specific volume V, specific internal energy E, of the compressed material are related to uncompressed values (E_0, V_0, P_0) and the particle- and front velocities in the Hugoniot equations (Melosh [1989]):

$$\rho(U-u) = \rho_0 U \quad (2.1)$$

$$P - P_0 = \rho_0 u U \quad (2.2)$$

$$E - E_0 = (P+P_0)(V_0 - V)/2 \quad (2.3)$$

where $\rho_0 = 1/V_0$ and $\rho = 1/V$. (N.B. An index of symbols used in this chapter and the next is supplied at the end of Chapter 3.) For mantle rocks, the experimentally-determined Hugoniot curve (shock equation-of-state) in U-u space is well-described by a linear relationship between shock and particle velocities:

$$U = C + Su \quad (2.4)$$

where C is roughly the speed of sound at STP.

Target materials are shocked to an approximately uniform peak shock pressure P_c within the isobaric core (IC) radius, r_c. Outside of this region, peak shock pressure P_s decays as an in-

verse power law of the radial distance r from the site of impact (Ahrens and O'Keefe [1977]):

$$P_s = P_c(r_c/r)^n \tag{2.5}$$

Using the Sandia 2D axisymmetric hydrocode CSQ, Pierazzo et al. [1997] found good agreement among decay law exponents for a wide range of materials. Fitting to results for iron, granite and dunite (among others), Pierazzo et al. [1997] measured for n:

$$n = (-1.84 \pm 0.17) + (2.61 \pm 0.14) \log v_i, \tag{2.6}$$

where v_i is the vertical incident velocity in km/s. We designate the exponents for the steepest, average, and most-gradual decay-laws as follows:

$$n_+ \equiv (-1.84 + 0.17) + ... \quad (2.61 + 0.14) \log v_i \tag{2.7}$$

$$n_0 \equiv -1.84 + (2.61) \log v_i \tag{2.8}$$

$$n_- \equiv (-1.84 - 0.17) + ... \quad (2.61 - 0.14) \log v_i \tag{2.9}$$

In addition to the decay laws in Pierazzo et al. [1997], a steeper decay law was obtained from the attenuation measured for particle velocities away from underground nuclear explosions. A compilation of these observations finds that particle velocity decays as $r^{-1.87}$ (Perret and Bass [1975]). Substituting this law for particle velocity into the second Hugoniot equation (2.2) and also substituting the shock EOS (eq. (2.4)) for U, one obtains an alternative peak-pressure decay law from the Perret and Bass estimate (Melosh [1989]):

$$P_s = \rho_0[C + Su_c(r_c/r)^{1.87}]u_c(r_c/r)^{1.87} \tag{2.10}$$

where ρ_0 is the uncompressed density, and u_c is the particle velocity in the IC. Three additional results from Pierazzo et al. [1997] are used in the present study. First, the radius r_c of the IC (fitted to results obtained for many materials and impact velocities) is given by $r_c = R(10^{a_1})v_i^{b_1}$ where $a_1 = -0.346 \pm 0.034$ and $b_1 = 0.211 \pm 0.022$, and where R is the projectile radius and v_i is in km/s. Second, the depth d_c of the IC center is given by $d_c = R(10^{a_2})v_i^{b_2}$ where $a_2 = -0.516 \pm 0.060$ and $b_2 = 0.361 \pm 0.038$. The decay of particle velocity was reported as follows: $u = u_c(r_c/r)^m$ for $m = a + b\log(v_i)$ where $a = -0.31 \pm 0.09$, $b = 1.15 \pm 0.06$. In our calculations, we shall assume mean values for the exponents in these scaling relations.

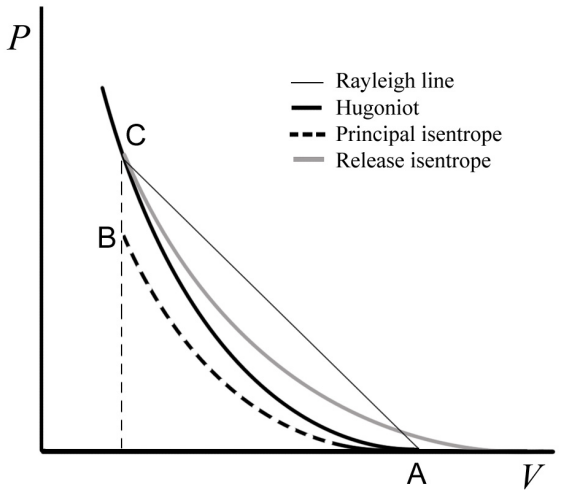

Figure 2-1: P-V space representation of a Hugoniot centered at state `A`, the Hugoniot-referenced principal isentrope, and the release isentrope from state `C`.

A typical Hugoniot curve along with release and compression isentropes are illustrated in Figure 2-1. The uncompressed state at STP is labeled `A`. The target material is shocked to state `C` on the Hugoniot curve indicated by the dark solid line. Decompression occurs along a release isentrope (gray solid line), resulting in a lower density at STP (due to thermal expansion of the hotter, uncompressed material). The principle isentrope (dashed line) illustrates the path taken if the material were compressed adiabatically to the density of states B and C.

The internal energy of the shock state can be calculated using equation (2.3). If $E_0 \approx 0$, this is equivalent to the area beneath the Rayleigh line drawn in Figure 2-1. Decompression converts much of the internal energy of the shocked state into mechanical energy. The waste heat (irreversible work) is given by the area between the Rayleigh line and the release isentrope. Using

elementary thermodynamic relations we can estimate the waste heat assuming that the decompression follows the release isentrope, and these methods are described in Section 2.2. This involves first calculating the temperature of a given shock state along the Hugoniot, and then the decompressed temperature along the release isentrope.

Gault and Heitowit [1963] derived a simple estimate of the waste heat ΔE_w, in which the shocked material is assumed to unload along a thermodynamic path that is approximated by the Hugoniot. This relation is derived by integrating the Hugoniot from the shock state to the release state in P-V space, and subtracting this from the shock state energy (eq. (2.3)). (Assuming a linear shock EOS (eq. (2.4)) and using the first two Hugoniot equations (2.1) - (2.2), one readily obtains the Hugoniot in P-V space.) This waste heat estimate is divided by the specific heat at constant pressure C_p to estimate the temperature increase ΔT_s caused by the shock. In Gault and Heitowit [1963], ΔE_w is written in terms of the particle velocity u. We derive an alternative form in terms of the shock-increased pressure $P_\delta = P_s - P_0$ (for peak shock pressure P_s):

$$\begin{aligned} \Delta T_s(P_\delta) &= \frac{P_\delta}{2\rho_0 S}(1 - f^{-1}) \\ &- (C/S)^2[f - \ln f - 1] \quad (2.11) \\ \text{where} \quad f(P_\delta) &\equiv -\frac{P_\delta}{\beta}\left(1 - \sqrt{\frac{2P_\delta}{\beta} + 1}\right)^{-1} \\ \text{and} \quad \beta &\equiv \frac{C^2\rho_0}{2S} \end{aligned}$$

where $\rho_0 = 1/V_0$ is the density prior to shock compression, corresponding to P_0. The principal advantage of this method is expedience, since we can avoid the numerical integrations required for the isentrope-release methods. The amount of shock heating as a function of peak shock pressure is shown in Figure 2-2 for three methods described in Section 2.2, where the subscripts i1 and i2 refer to isentrope-release and h2 refers to the result from equation (2.11) (i.e., "Hugoniot-release"). Equation (2.11) overestimates the amount of shock heating by roughly 20% at 125 GPa (1000 K), and 10% at 50 GPa ($\sim$ 100 K). The thermal perturbations that we construct in section 3.2 of the next chapter are limited by the solidus temperature, which is not estimated ever to exceed mantle geotherms by much more than 1000 K. Because shock heating decays rapidly with depth in the mantle (for large shock pressures), the net effect of this error is to overestimate the characteristic size of our perturbations by at most 200 km.

As a shock wave propagates into the mantle of a terrestrial planet, the density and pressure of the unshocked target material increase with depth. Moreover, a Hugoniot centered at higher densities and pressures is different from one centered at STP for the same material. In order to estimate the shock heating, therefore, we require reference models of pressure and density for the two cases considered in this study: the Earth and Mars. For both planets we assume a single chemically homogeneous layer with mantle properties (the consequences of adding an upper-mantle layer are considered in Section 2.6). The reference model for pressure is constructed from a Hugoniot-referenced compression isentrope, using the shock equation of state (EOS) obtained by McQueen [1991] for lower-mantle rocks (for Earth models), and dunite and peridotite (for Mars models). The reference models for density are given by the adiabatic compression. A detailed account of how these models were assembled is supplied in Section 2.3.

A simple approach for estimating shock temperature with depth is to calculate the shock heating from equation (2.11), while substituting for P_δ the difference between expected peak shock pressures from equation (2.5) and the ambient lithostatic pressure (from reference models). This approach is somewhat simplistic, however, since we have not totally accounted for the effect of increasing density. That is, the starting density ρ_0 in equation (2.11) is a function of depth. Even once this correction is made, we must account for changes in the Hugoniot as the starting pressure and density increase.

As mentioned, the Hugoniot of a material shocked from a state (ρ_0, P_0) is not the same as

the Hugoniot of the same material when shocked from (ρ_1, P_1) where $P_1 > P_0$ and $\rho_1 > \rho_0$. This problem is addressed in detail in Section 2.5. In outline, our approach is to divide the mantle into a stack of thin layers of increasing density, whose interfacial pressures also increase with depth. For each layer we obtain a Hugoniot centered upon its density. We invoke the planar impact approximation (see Section 2.4) and calculate the impedance match solution for the peak pressure of shocks transmitted through each layer. Within each layer, peak shock pressure is assumed to decay according to equation (2.5). In this way, we obtain the shock pressure and shock heating with depth. (Because the Hugoniot climbs the compression isentrope with increasing depth, these are called "climbing shocks," whereas estimates obtained by simply substituting the difference between P_s (from equation (2.5)) and lithostatic pressure for P_δ and reference model densities (Section 2.3) for ρ_0 in equation (2.11), are called "foundering shocks". Finally, estimates using equation (2.11) with equation (2.5) substituted for P_s without accounting for lithostatic pressure are called "ordinary shocks.")

Shock heating estimates obtained by these methods are plotted in Figure 2-3. From this it is clear that the effect of lithostatic pressure is very important, while the difference between climbing- and foundering shock estimates is negligible. A detailed discussion of the methods used to obtain these estimates for ΔT_s is contained in Section 2.5. One of the principal conclusions of this work is that the range in shock-pressure decay exponents computed by Pierazzo et al. [1997] accounts for a range of shock-heating estimates that exceeds the errors associated with using the Hugoniot-release or foundering-shock approximations discussed above.

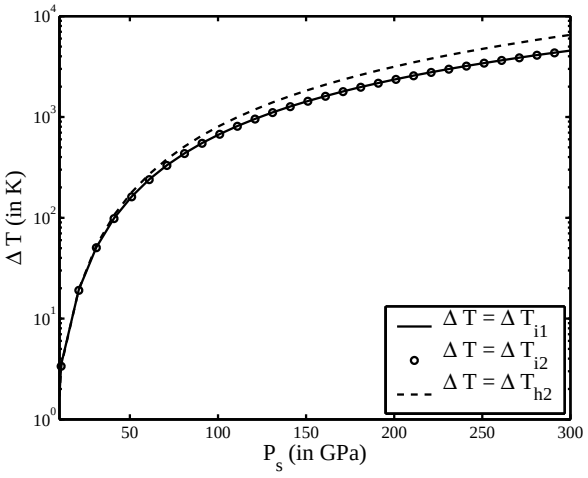

Figure 2-2: Shock heating calculated using three methods described in Section 2.2, versus peak shock pressure P_s. (Assuming lower-mantle properties: e.g., $S = 1.25$, $C = 7.4$ km/s; see Section 2.3.) The subscripts i1 and i2 refer to "isentrope-release" methods (adiabatic decompression) and h2 refers to the "Hugoniot-release" method, summarized in Section 2.1 and detailed in Section 2.2.

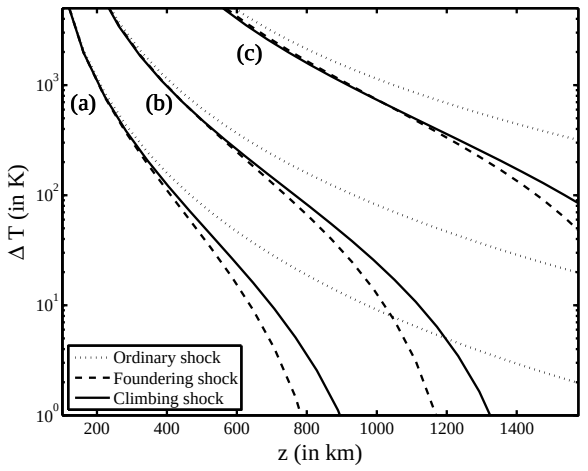

Figure 2-3: Shock heating as a function of depth for projectiles with a range of sizes, vertically incident at 15 km/s, for the case of the Mars-C reference model (see Sections 2.3 through 2.5). The shock pressure decay law exponent is $n = n_0$. From left to right: (a) $R = 50$ km, (b) $R = 100$ km, (c) $R = 250$ km.

2.2 Estimates of shock heating

There are several ways to calculate the temperature upon release. In this section we discuss two methods that assume release occurs along an isentrope ("isentrope-release methods" I and

II), and compare these results to the Hugoniot-release method outlined above. Both methods involve first calculating the temperatures of shock states along the Hugoniot. Then, for a given shock state, we can calculate the final temperature along the release isentrope. These methods (I and II) differ in the manner that shock state temperatures are calculated. In one case we require knowledge of the principal isentrope (indicated by a dashed line in Figure 2-1). Since isentropes are used also in other parts of this study, we first demonstrate how to calculate isentropes referenced to known Hugoniots (i.e., "Hugoniot-referenced isentropes"). For this and other derivations in this study, we shall make use of the Grüneisen parameter, whose value γ_0 at STP is given by:

$$\gamma_0 = V_0 \left(\frac{dP}{dE}\right)_V \tag{2.12}$$

There is considerable uncertainty about the behavior of γ at very high pressures, but evidence from high-pressure diamond-anvil and shock experiments indicates that $\gamma\rho \approx \gamma_0\rho_0$: i.e., $(dP/dE)_V$ is approximately constant.[1] We shall assume that $\rho\gamma$ is constant throughout these calculations and later estimate the manner in which modifying γ alters slightly our results.

In what follows, the symbol E_j represents the difference between the specific internal energy of state j along the principal isentrope (i.e., the state with specific volume V_j) and the internal energy of the unshocked material E_0. The subscript "Hj" will refer to the state with specific volume V_j along the *Hugoniot*. Using the assumption of constant $\rho\gamma$ and equation (2.12) we can write the Grüneisen EOS, in this case relating states between the Hugoniot and Hugoniot-referenced isentrope:

$$P_{Hj} - P_j = \rho\gamma(E_{Hj} - E_j) \tag{2.13}$$

It follows from the first and second laws of thermodynamics that:

$$dE = TdS - PdV \tag{2.14}$$

[1] Alternatively, $(\gamma/\gamma_0) = (\rho_0/\rho)^n$ for some n in the range from 0.5 to 1. (Schubert et al. [2001])

Along an isentrope, $dS = 0$, so that $dE = -PdV$. Using the index j to indicate states in an increasing or decreasing sequence, we may write this as a difference relation:

$$E_j - E_{j-1} = -(P_j + P_{j-1})\Delta V/2 \tag{2.15}$$

where $\Delta V = V_j - V_{j-1}$. Combining equations (2.13) and (2.15) and solving for P_j, we obtain equation (3.5) in McQueen [1991]:

$$P_j = \frac{P_{Hj} - \rho\gamma(P_{j-1}\Delta V/2 + E_{Hj} - E_{j-1})}{1 + \rho\gamma\Delta V/2} \tag{2.16}$$

Internal energies along the Hugoniot E_{Hj} are easily calculated using equation (2.3). For any state (P_{Hj}, V_{Hj}) along the Hugoniot, we can use equation (2.16) to obtain a release isentrope, or we can obtain a principal (compression) isentrope starting with the state (P_{H0}, V_{H0}) at which the Hugoniot is centered.

We turn now to calculating temperatures along an isentropic path. We begin with the following thermodynamic relation (see Meyers [1994] for a derivation):

$$TdS = C_v dT + T\rho\gamma C_v dV \tag{2.17}$$

where C_v is the specific heat at constant volume. For an isentropic path, $dS = 0$. Solving for dT/T and integrating as in Meyers [1994], gives:

$$T_2 = T_1 \exp\left(-\int_{V_1}^{V_2} \frac{\gamma}{V} dV\right) \tag{2.18}$$

Using equation (2.18) we can calculate the temperature of any state along an isentrope, given that we know the temperature T_j of some state (P_j, V_j) along this path.

It remains for us to calculate the temperatures of states along the Hugoniot curve. According to "method I" (using results from McQueen [1967] and Meyers [1994]), we combine equations (2.14) and (2.17) by eliminating TdS, and then substitute the Hugoniot shock-augmented energy for dE (eq. (2.3)). This leads to the following dif-

ferential equation (McQueen [1967]):

$$dT = \frac{(V_0 - V)}{2C_v} dP + \left(\frac{P - P_0}{2C_v} - T\rho\gamma \right) dV \tag{2.19}$$

The solution can be written as a centered-difference relation that supplies the temperatures T_j for a sequence of states along an adiabatic path (McQueen [1991]):

$$\begin{aligned} T_j &= (1 + \rho\gamma\Delta V/2)^{-1}(T_{j-1}[1 - \rho\gamma\Delta V/2] + ... \\ &\quad ... + [(V_0 - \bar{V})\Delta P + (\bar{P} - P_0)\Delta V]/2C_v) \end{aligned} \tag{2.20}$$

where $\bar{V} = (V_j + V_{j+1})/2$, $\bar{P} = (P_j + P_{j-1})/2$, $\Delta P = P_j - P_{j-1}$ and $\Delta V = V_j - V_{j-1}$. Alternatively, by method II (Stewart-Mukhopadhyay [2002]) we invoke a simple energy balance. The internal energy of state C in Figure 2-1 is equal to the energy acquired along the path $AB + BC$:

$$E_C = E_{AB} + E_{BC} = \int_{V_A}^{V_B} P_I dV + \int_{T_B}^{T_C} C_v dT \tag{2.21}$$

where P_I is pressure along the principal isentrope. The first integral on the rhs is integrated numerically, once we have obtained P_I using equation (2.16). We can calculate E_C using equation (2.3) for the shock energy, and T_B using equation (2.18). It is then a simple matter to solve the resulting equation for T_C. The process is repeated for all states of interest along the Hugoniot.

Having used method I or II to obtain the along-Hugoniot temperatures, we can use equation (2.18) to calculate the release temperatures. A third method (III) involves integrating the release isentrope obtained using (2.16) in P-V space, and subtracting this *energy* from the shock energy in equation (2.3). In order to calculate the temperature difference between the final and initial state at STP, one can divide this result by the specific heat at constant pressure C_p. This approach requires many more calculations than I or II. If the range in specific volume or density is divided into N states, then to calculate the shock-heating for the corresponding range in pressures requires just N difference iterations using equation (2.16) or (2.20), whereas by method III, a total of N^2 iterations are required since a new release isentrope must be calculated using equation (2.16) for each state.

We turn now to the Hugoniot-release method outlined earlier. In Gault and Heitowit [1963], ΔE_w is written in terms of the particle velocity u. Dividing by C_p, the shock-heating is given by:

$$\Delta T_s(u) = \frac{u^2}{2C_p}(1 - 2[\xi - \xi^2 \ln(1 + 1/\xi)]) \tag{2.22}$$

where $\xi \equiv (C/Su)$. The principal advantage of using this equation (in terms of u) or equation (2.11) is that we avoid the numerical integrations described in the foregoing discussion of the "isentrope-release" methods. In the isentrope-release case, when shocking from a single pressure and using a single Hugoniot, it is possible to construct a look-up table (using the numerical integrations) that would supply ΔT_s as a function of P_s. When shocking from different initial pressures and using a Hugoniot that changes with increasing depth in the mantle, repeating these integrations becomes rather cumbersome. (We shall discuss the effects of lithostatic pressure upon shock heating in Section 2.5 – for now, we assume that $P_0 \approx 0$).

Note that these "Hugoniot-release" equations and the numerical "isentrope-release" methods rely upon estimates of the specific heat at constant pressure and volume. This quantity is a strong function of temperature below the Debye temperature T_D. At temperatures above T_D, C_v approaches a limiting value of 25.1 J mol^{-1}K^{-1} (i.e., roughly 1250 J kg^{-1}K^{-1} for mantle compounds, for which the molecular weight is roughly 21; C_p is a few percent larger (Schubert et al. [2001])). Thankfully, $T_D < 1100$ K for all mantle silicates. Mantle temperatures in terrestrial planets exceed this upper bound on T_D, and therefore we may assume that C_p and C_v are approximately constant (and close to the limiting value) when calculating shock-augmented temperatures in terrestrial mantles.

We can now calculate the shock-heating as a function of distance according to the several methods so far discussed, by assuming a decay

law for P_s (see equation (2.5)) or u. In what follows, $\Delta T_{h1} \equiv \Delta T_s(u)$ (i.e., equation (2.22)), $\Delta T_{h2} \equiv \Delta T_s(P_\delta)$ (i.e., equation(2.11)), ΔT_{i1} is the shock-promoted temperature calculated with "isentrope-release" method I and ΔT_{i2} is the shock-augmented temperature calculated with method II (i.e., the subscript h is for "Hugoniot-release" and i is for "isentrope-release"). Figure 2-4 is a plot of the shock heating calculated with all four methods, as a function of distance r from the center of the IC (for projectile radius $R = 250$ km incident at $v_i = 15$ km/s, decay exponent $n = n_0$ in (2.5), and $S = 1.25$, $C = 7.4$ km/s for projectile and target (see Section 2.3)). For the starting pressure we assume $P_0 = 0$ so that $P_\delta = P_s$ in equation (2.11). In order to calculate $\Delta T_{h1}(r)$ (i.e., $\Delta T_s(u(r))$) we use the mean decay law for u in Pierazzo et al. [1997], which accounts for the marked difference between the results for this and the other methods. Figure 2-2 is a plot of the shock heating as a function of peak shock pressure P_s for the methods in which peak shock-pressure is used (instead of u). In Figure 2-5 we show the fractional difference between the shock heating calculated for each method as a function of distance r, and in Figure 2-6 we do the same for P_s.

The isentrope-release methods produce estimates of shock-heating that are effectively equivalent. It is clear that equation (2.11) is a good estimate of shock heating for low shock pressures. That is, for $P_s < 50$ GPa the discrepancy is less than 10%, reaching 30% for $P_s > 300$ GPa (N.B. the IC pressure for a $v_i = 15$ km/s impact is roughly 400 GPa). For the example shown in Figure 2-5, the 10% margin is reached at roughly 1/3 the depth of Earth's mantle.

2.3 Reference models for pressure and density

As a shock wave propagates into the mantle of a terrestrial planet, the density and pressure of the uncompressed target material increase with depth. Moreover, the Hugoniot curve centered at higher densities and pressures will be different from that centered at STP for the same mate-

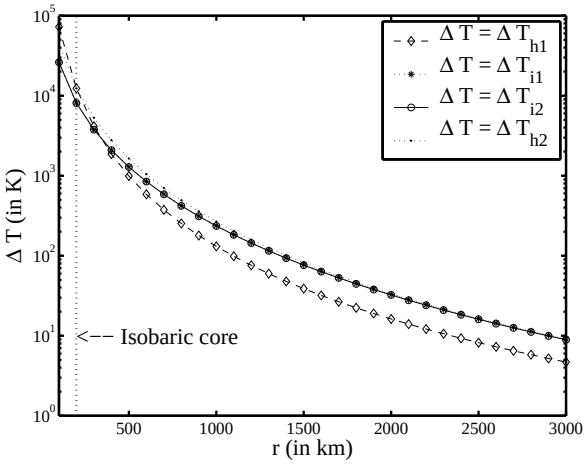

Figure 2-4: Shock heating as a function of distance r from the center of the isobaric core, calculated using four methods in a chemically homogeneous medium and assuming an STP-centered Hugoniot, for the case of a projectile with $R = 250$ km and $v_i = 15$ km/s. ΔT_{h1} refers to the shock heating calculated with equation (2.22). ΔT_{h2} refers to shock-heating calculated with equation (2.11): i.e., Hugoniot-release method II. ΔT_{i1} and ΔT_{i2} were calculated using the isentrope-release methods I and II described in the text. We have assumed the mean decay law, $n = n_0$.

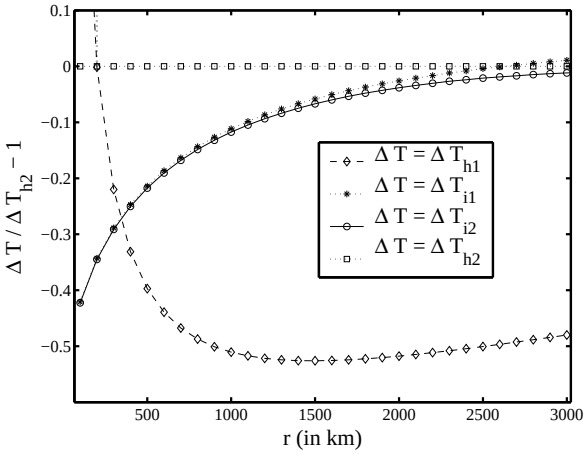

Figure 2-5: Fractional difference in the shock heating calculated according to four methods described in the text, as a function of distance r from the isobaric core. ($R = 250$ km and $v_i = 15$ km/s, $n = n_0$.)

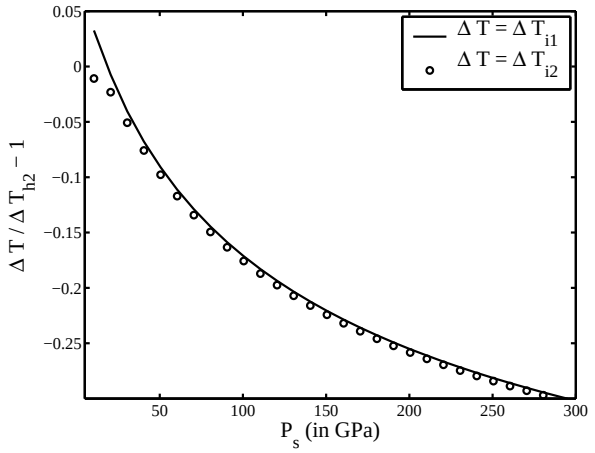

Figure 2-6: Fractional difference in shock heating calculated according to three methods described in the text, as a function of peak shock pressure P_s. ($R = 250$ km and $v_i = 15$ km/s, $n = n_0$.)

rial. In this section and the next one, we examine the consequences of these effects upon estimates of shock-heating. Even before we address these consequences, it is necessary to construct reasonable reference models of pressure with depth for Earth- and Mars-like planets.

In our calculations we assume the target is a single chemically homogeneous layer. In the case of the Earth, our single-layer model resembles the lower mantle, although "extended" to the surface – i.e., with a surface density of slightly more than 4.00 g/cm^3. There are several reasons for this choice. First, the ICs of the largest impacts that we consider are expected to penetrate the lower mantle, so that it is not unrealistic to solve the impedance-matching for lower-mantle properties. Second, heating of the lithosphere and near-surface is very complex because of layered compositions and the interference of decompression waves. That is, we cannot hope to calculate accurately the near-surface heating, and we are mainly interested in heat deposited at great depths where large thermal anomalies will affect the mantle circulation. Third, it is far easier to calculate the shock heating for a chemically-homogeneous layer, and then to calculate a correction that results from adding a small upper-layer with a lower density (i.e., the upper mantle). This correction is estimated in Section 2.6.

For the case of Earth our reference model is largely determined by the shock EOS chosen for lower-mantle materials. That is, we assume values for S and C obtained in McQueen [1991] for the lower mantle (i.e., $S = 1.25$, $C = 7.4$ km/s). In that study, a shock-EOS was fitted (in an iterative fashion) to the seismically-derived density profile and corresponding lithostatic pressure, where adjustments to initial densities were made to agree with the Earth's moment-of-inertia. (McQueen [1991] assumes that $\gamma = 1.25$ and we shall do likewise, and later estimate the consequences of this assumption as a source of error.[2]) We have used this lower-mantle shock EOS to construct a principal [compression] isentrope, according to equation (2.16). In McQueen [1991] the mantle Hugoniot is centered at $\rho_0 = 4.09$ g/cm^3. The density with depth in our reference model is obtained by assuming that density changes result from adiabatic compression in a chemically homogeneous layer loaded by gravity (Schubert et al. [2001]):

$$\rho(z) = \rho_0/(1 - \rho_0 g z \beta_a), \qquad (2.23)$$

where g is assumed to be constant across the mantle, and where β_a is the adiabatic compressibility. In choosing β_a and ρ_0 we seek a density model that satisfies the following conditions: (i) it should make a reasonable fit to the seismically-derived PREM density profile of Dziewonski and Anderson [1981]; (ii) the pressure range obtained using equation (2.16) for the corresponding range in mantle densities should be consistent with that derived in the PREM model (i.e., roughly 140 GPa). We are able to satisfy these requirements by choosing $\beta_a = 2.5 \times 10^{-12}$ Pa^{-1} and $\rho_0 = 4.05$ g/cm^3. It should be noted that β_a is thought to range across the mantle from 8.7×10^{-12} Pa^{-1} in the upper mantle to 1.5×10^{-12} Pa^{-1} at the core-mantle boundary. The [constant] value that we have chosen is consistent with values estimated to occur at mid-

[2] A 10% change in this value accounts for a $< 1\%$ change in the estimates of S and C (McQueen [1991]).

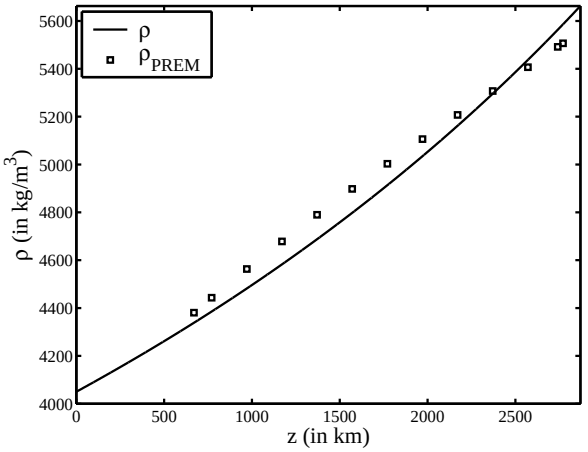

Figure 2-7: Model of density as a function of depth in the Earth used in our calculations. This profile is obtained assuming adiabatic compression from a STP density of 4,050 kg/m^3, the density at which the reference Hugoniot is centered. The adiabatic compressibility is assumed constant across the layer, and chosen so that the density range matches that of the PREM model (Dziewonski and Anderson [1981]).

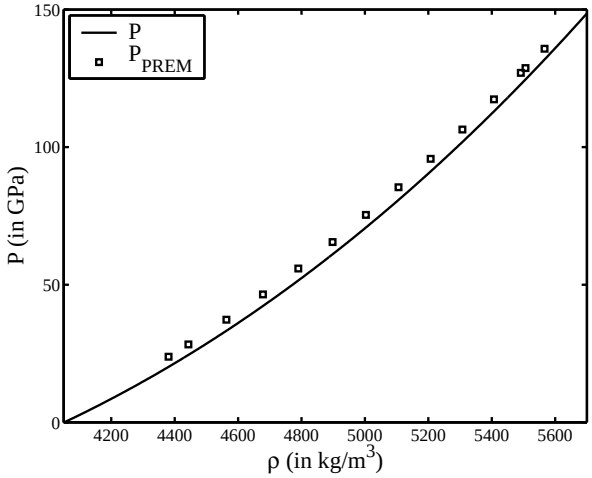

Figure 2-8: Compression isentrope for the chemically homogeneous "extended" lower-mantle layer of an Earth-like planet. The plot shows the ambient (lithostatic) pressure P as a function of density ρ based upon the fitted shock EOS in McQueen [1991], as well as the PREM model of Dziewonski and Anderson [1981].

dle depths in the lower mantle (Schubert et al. [2001]). The density profile obtained from (2.23) is plotted in Figure 2-7 along with PREM values. We have plotted the Hugoniot-referenced compression isentrope as well as pressure versus density of the PREM model in Figure 2-8.

In addition to the Earth, we address the case of planets with proportions comparable to those of Mars. The internal structure of Mars is constrained by several observations, including geochemical analysis of the SNC meteorites, the moment of inertia factor (Folkner et al. [1997]), estimates of crustal thickness from gravity and topography measurements (Zuber et al. [2000]), and the planet's total size and mass. Attempts have been made to construct density profiles of the Martian mantle that are informed by SNC compositions at expected mantle temperatures and pressures for a range of core sizes and compositions (Bertka and Fei [1998]), while maintaining agreement with the moment-of-inertia factor (Spohn et al. [1998], Spohn et al. [2001]). These studies obtain a density range across the mantle of roughly 3.5 g/cm^3 to 4.3 g/cm^3 that is robust with respect to marked changes in core radius. Occurring in this range are several density steps associated with phase transformations from olivine to β-spinel and then β-spinel to γ-spinel. As in the case of our Earth model, we shall assume a chemically homogeneous layer with no phase transformations, and fit an adiabatic profile to the overall expected range in densities. Assuming that $\rho_0 = 3.5$ g/cm^3, a good approximation is achieved by setting $\beta_a = 6.5 \times 10^{-12}$ Pa^{-1} in equation (2.23), where $g \approx 3.7$ m/s^2 across the Martian mantle.

It remains for us to propose a reasonable compression isentrope and shock EOS for the Martian mantle. Assuming mantle compositions can be approximated by dunite or peridotite, we can use shock EOS parameters for these materials, measured for the low-pressure phase in shock experiments. For peridotite with density 3.2 g/cm^3; $S = 0.93$ and $C = 5.78$ km/s (Ahrens and Johnson [1995]). For dunite with a STP density of 3.26 g/cm^3; $S = 0.86$ and $C = 6.6$ km/s (McQueen et al. [1967]). Experiments with dunite at higher initial densities are inconclusive

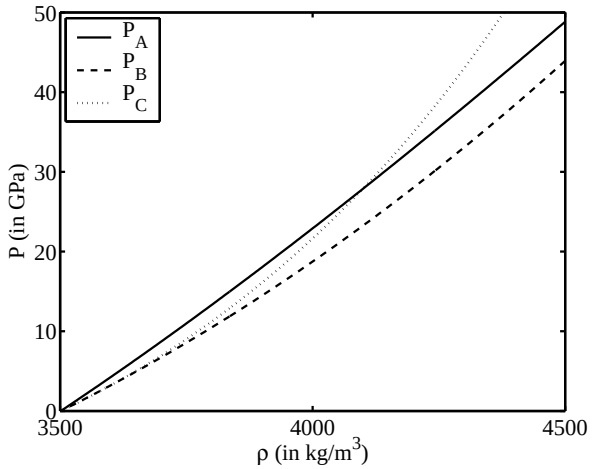

Figure 2-9: Principal isentrope assumed for the chemically-homogeneous mantle of a Mars-like planet. Shown is the ambient (lithostatic) pressure P as a function of density ρ based upon three proposed shock EOS for dunite in the low-pressure phase of shock experiments. The subscripts A, B and C correspond to the reference models Mars-A, Mars-B, and Mars-C, as described in the text.

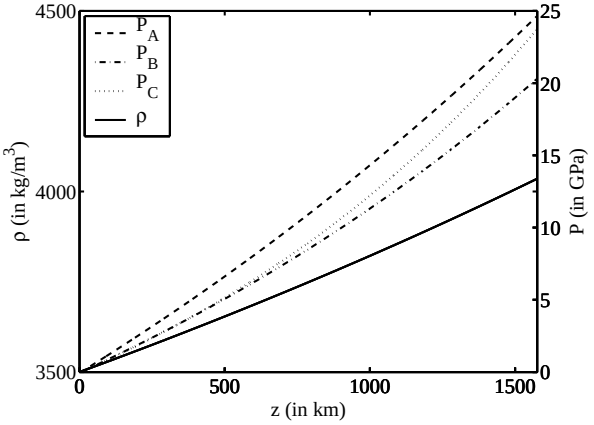

Figure 2-10: Density as a function of depth (solid line) in the Mars model. This profile is obtained assuming adiabatic compression from a STP density of 3,500 kg/m^3, the density at which the reference Hugoniot is centered. The adiabatic compressibility is assumed constant across the layer, and chosen so that the density range matches that of reference models for Mars suggested by Bertka and Fei [1998] as well as Spohn et al. [1998]. Pressure with depth is also shown, calculated from the assumed density profile as well as the principal isentropes shown in Figure 2-9. The subscripts A, B and C correspond to the reference models Mars-A, Mars-B, and Mars-C, as described in the text.

for the low-pressure phase (below 45 GPa) owing to large scatter in the results from shock experiments. McQueen et al. [1967] report $S = 0.86$ and $C = 6.0$ km/s, while admitting that an alternative fit nearer to the phase transformation gives $S = 1.20$ and $C = 5.6$ km/s. Another estimate is reported in Ahrens and Johnson [1995]: $S = 1.8$ and $C = 5.5$ km/s. We have opted to base our calculations upon three reference models that assume values for S and C that are consistent with the range of values reported in the literature for dunite. Note that the values for peridotite are intermediate. Table 2.1 is a list of S and C for reference models "Mars-A", "Mars-B", and "Mars-C". The resulting isentropes are shown in Figure 2-9, and the pressure and density profiles are shown in Figure 2-10.

2.4 Impedance match solution

We shall briefly review the concept of impedance matching because it is used in several parts of this study. It follows from mass conservation that particle velocity does not change across an interface between materials in contact. Accordingly, so long as these materials are not interpenetrating, pressures at their common boundary must be equal. The volume between shocks propagating into the target and projectile must therefore attain the same pressure and particle velocity at the interface. It is easy to apply this principal if we assume the planar impact approximation (PIA). In the PIA we treat the case of an infinite sheet of projectile material impinging a flat half-space of target material. (In this way, we avoid the complications introduced by the curvature of planetary and projectile surfaces.)

Suppose the projectile is incident at a velocity v. Using the Hugoniot equations we can write the projectile shock pressure as a function $P_A(u_A)$ of the particle velocity u_A in the rest frame of the projectile, and we can write

Table 2.1: Shock EOS parameters for Martian reference models

Model	S	C (in km/s)
Mars-A	0.86	6.6
Mars-B	1.20	5.6
Mars-C	1.80	5.5

the target's shock pressure as a function $P_B(u)$ of the particle velocity u in the rest frame of the target. In the rest frame of the target, the particle velocity in the *projectile* is $u_A = v - u$. Since the pressures must match, we can solve $P_B(u) = P_A(v-u)$ to obtain the post-impact particle velocity u in the rest frame of the target. For the case of a linear shock EOS, the functions $P_A(v-u)$ and $P_B(u)$ can be obtained from the second Hugoniot equation (2.2) after substituting equation (2.4) for U (Ahrens [1987]):

$$\begin{aligned} P_A(v-u) &= P_{0A} + ... \qquad (2.24) \\ &\quad \rho_{0A}(v-u)[C_A + S_A(v-u)] \\ P_B(u) &= P_{0B} + ... \qquad (2.25) \\ &\quad \rho_{0B}u(C_B + S_B u) \end{aligned}$$

where the subscript "$0A$" indicates uncompressed quantities in the projectile and "$0B$" in the target, and where S_A and S_B are the slopes and C_A and C_B the intercepts of equation (2.4) for projectile and target, respectively. The solution to $P_B(u) = P_A(v-u)$ is just:

$$\begin{aligned} u &= (-b - \sqrt{b^2 - 4ac})/2a \qquad (2.26) \\ \text{where} \quad a &= \rho_{0A}S_A - \rho_{0B}S_B \\ b &= -(\rho_{0A}C_A + 2\rho_{0A}S_A v + \rho_{0B}C_B) \\ c &= (P_{0A} - P_{0B}) + ... \\ &\quad v(\rho_{0A}C_A + \rho_{0A}S_A v) \end{aligned}$$

The impedance-match solution for the particle velocity u can then be substituted into equation (2.24) or (2.25) to obtain the interface shock pressure. We can use this procedure to calculate the isobaric core pressure for the decay law in equation (2.5). In the special case where the projectile and target materials are identical (i.e., the same S, C, and ρ), equation (2.26) yields $u_c = (1/2)v$ for the IC particle velocity. We shall make this assumption in most of our calculations and later estimate its consequences as a source of error (see Section 2.6).

2.5 Effects of ambient pressure and density

In this section we estimate the consequences of adiabatic compression and increasing ambient pressure with depth upon estimates of shock-heating in terrestrial mantles. A simple approach is to begin by calculating, for a given depth z, the difference between the peak shock pressure P_s obtained from equation (2.5) and the ambient pressure $P_{ls}(z)$ obtained using equations (2.16) and (2.23). For the three values of the decay law exponent (eqs. (2.7) - (2.9)), P_s and $P_s - P_{ls}$ are plotted in Figure 2-11 for the Earth and Figure 2-12 for Mars-B ($R = 500$ km, $v_i = 15$ km/s). A simple estimate of the shock heating is accomplished by comparing these plots with Figure 2-2. In the case of an Earth-like planet (Figure 2-11), while the range in decay exponents accounts for a range from 20 to 700 K of shock-heating at the core-mantle boundary (CMB), the effect of ambient pressure is to prevent any direct heating of the CMB. In the case of Mars-B, heating of the CMB occurs only for $n = n_-$ if ambient pressure is taken into consideration. This way of estimating the consequences of ambient pressure is somewhat simplistic, since we have not totally accounted for the effect of the increasing density. That is, the uncompressed density ρ_0 in equation (2.11) is now a function of depth according to equation (2.23). Even once this correction is made, we must still account for changes in the Hugoniot as the starting pressure and density increase. That is, the Hugoniot of a material shocked from a state (ρ_0, P_0) is not the same as the Hugoniot of the same material when shocked from (ρ_1, P_1) where $P_1 > P_0$ and $\rho_1 > \rho_0$. In this section we propose a method for estimating the magnitude of this effect.

In overview, our approach shall be to divide the mantle into a stack of thin layers of increas-

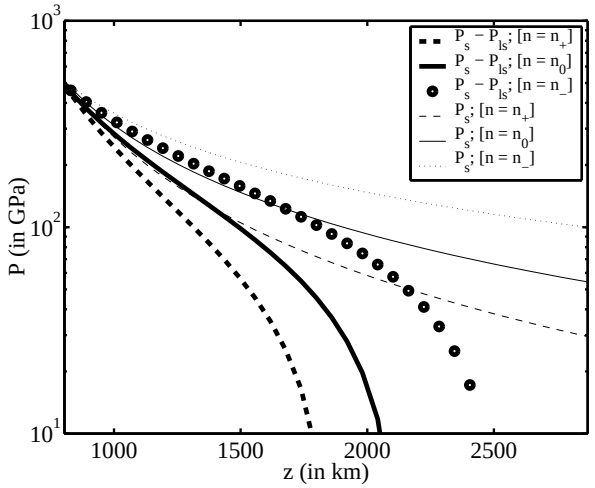

Figure 2-11: Peak shock pressure decay with depth (outside of the IC) in the Earth for three decay laws. This plot shows P_s and $P_s - P_{ls}$ for a projectile with $R = 500$ km incident at 15 km/s.

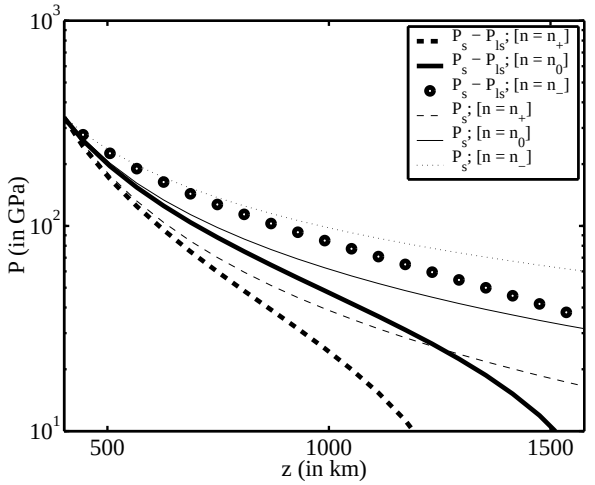

Figure 2-12: Peak shock pressure decay with depth (outside of the IC) in the case of Mars-B and three decay laws. This plot shows P_s and $P_s - P_{ls}$, assuming a projectile with $R = 500$ km incident at 15 km/s.

ing density, whose interfacial pressures also increase with depth. For each layer we obtain a Hugoniot centered upon its density. We invoke the planar impact approximation (PIA) and calculate the impedance match solution for the peak pressure of shocks transmitted through each layer. As we'll discuss later, *within* each layer the peak shock pressure is assumed to decay in accordance with equation (2.5), and in this way we obtain the peak shock pressure with depth. We begin by calculating a recentered Hugoniot in P-V space. For this purpose, we derive a slightly more general form of equation (3.3) in McQueen [1991] (the latter addresses the special case of reflected shocks).

We begin with a Hugoniot that is centered at a state (V_0, P_0) along the principal isentrope (Figure 2-13). We wish to calculate the Hugoniot centered at a state (V_1, P_1). The original Hugoniot is the loci of states P_2 and the recentered Hugoniot is the loci of states P_2'. The internal energies E_0 and E_1 of the starting states can be calculated by integrating the principal isentrope from STP. We start by writing the difference of the shock-state energies (where primed quantities refer to the recentered Hugoniot) using equation (2.3):

$$\begin{aligned} E_2 - E_2' &= [(P_2 + P_0)(V_0 - V_2)/2 + E_0] \\ &- [(P_2' + P_1)(V_1 - V_2)/2 + E_1] \end{aligned} \tag{2.27}$$

We invoke the Grüneisen EOS (eqs. (2.12) and (2.13)) to relate internal energies for states at the same specific volume, in order to obtain an alternative expression for the same quantity:

$$E_2 - E_2' = (P_2 - P_2')/\rho\gamma \tag{2.28}$$

By eliminating $E_2 - E_2'$ between equations (2.27) and (2.28) and solving for P_2', we obtain the following expression for the recentered Hugoniot:

$$\begin{aligned} P_2' &= (1 - (\rho\gamma/2)(V_1 - V_2))^{-1}(P_2 - \\ &- (\rho\gamma/2)[(P_2 + P_0)(V_0 - V_2) - P_1(V_1 - V_2) \\ &+ 2(E_0 - E_1)]) \end{aligned} \tag{2.29}$$

In part of what follows we shall have to cal-

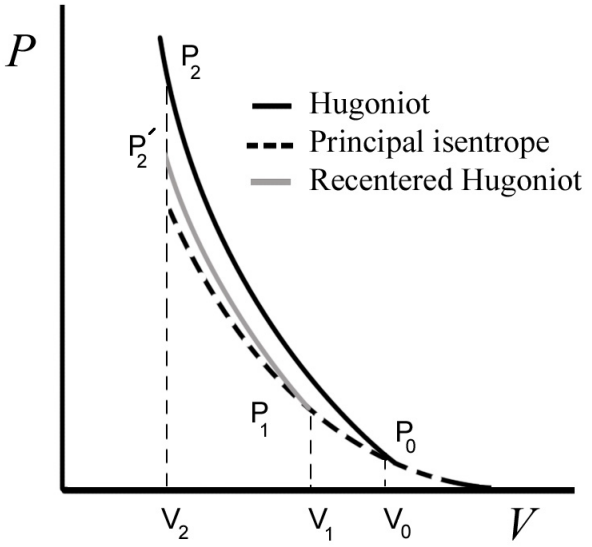

Figure 2-13: P-V space representation of a Hugoniot centered at a state (V_0, P_0) along the principal isentrope and a recentered Hugoniot, centered at a state (V_1, P_1) further displaced along the isentrope.

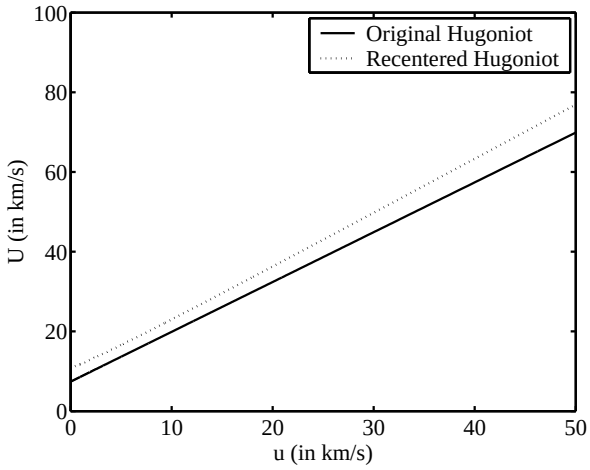

Figure 2-14: Original and recentered Hugoniots in U-u space (i.e., shock-velocity U versus particle velocity u).

culate Hugoniots that are recentered at states that occur along the original Hugoniot (centered at (V_0, P_0)), in which case E_1 is calculated using equation (2.3). Note that if equation (2.29) alone were used to obtain a new Hugoniot at each layer, then each new Hugoniot would be expressed in terms of the Hugoniot of the previous layer. After 50 layers, this process leads to a 50-fold nested expression in terms of the Hugoniot of the first layer. Since this is woefully impractical, our solution is to transform each recentered Hugoniot into U-u space and then to fit a line to obtain new values of S and C, which can be used in the next iteration to construct a Hugoniot in P-V space. The transformation to U-u space is obtained from the first and second Hugoniot equations (2.1) and (2.2) (Melosh [1989]):

$$u = \sqrt{(P - P_0)(V_0 - V)} \quad (2.30)$$

$$U = V_0\sqrt{(P - P_0)/(V_0 - V)} \quad (2.31)$$

Figure 2-14 is the plot of a recentered Hugoniot (recentered to $1/V_1 = 5,300$ kg/m^3 along the original Hugoniot from STP) that has been

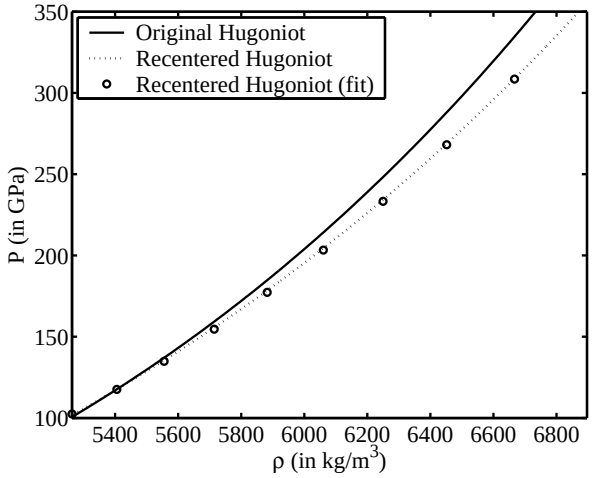

Figure 2-15: Original and recentered Hugoniots in P-ρ space, and the U-u space fit to the recentered Hugoniot.

transformed into U-u space in the manner described. We notice immediately that the result is not a perfectly straight line. In the range of interest (particle velocities of roughly 1/2 the impact velocity: i.e., up to 10 km/s for $v_i = 20$ km/s), this curve is reasonably straight and we fit a line across this domain. Figure 2-15 shows a plot of the recentered Hugoniot obtained using (2.29) as well as the fit to this Hugoniot in U-u space, which has been transformed back to P-ρ space. In the range of pressures of interest in this study, the comparison is excellent. The "compression offset" used in this example (i.e., $(V_1/V_0 - 1)$) is far greater than what is needed for the transition between adjacent layers. We shall nevertheless require recentered Hugoniots to be accurate for such large compressions, since we must calculate the recentered Hugoniot for *reflected* shocks, as described in what follows.

Suppose a shock wave travels through layer k with shock EOS parameters S_k and C_k. When it arrives at the interface between layers k and $k+1$ with some peak shock pressure P_s, part of its energy shall be transmitted and some reflected. This situation is equivalent to a planar impact between layer k and $k+1$, where the incident velocity of the "projectile" is the particle velocity u_k to which material in layer k has been accelerated by the shock (Ahrens [1987]). The reflected shock is akin to the shock that travels through the incident projectile following impact. We may therefore solve for the pressure of the transmitted shock (the interface pressure) by means of the impedance match method described in Section 2.4, where $v = u_k$ and the subscript A refers to the properties of layer k *in the shocked state* and B to layer $k+1$ in the unshocked state. That is, the values of S and C for layer k are those for the Hugoniot recentered at the shock-compressed density in layer k.

In order to complete this picture, we must stipulate what happens to the peak pressure of a shock *within* a given layer on its downward traverse. We assume that shock pressure decays at the rate implied by equation (2.5) within a given layer. That is, we assume this decay-law holds for a homogeneous medium at any uniform starting pressure. The reasons for this choice are two-fold. First, as mentioned earlier, the decay in shock pressure is largely a geometrical effect, caused by the distribution of shock wave energy over an expanding shell (Melosh [1989]). Second, the decay in shock energy is due also to the deposition of waste heat, which as we saw depends upon the size of the thermodynamic path bounded by the release isentrope (Gault and Heitowit [1963]). Since this path is *smaller* at higher initial pressures, we might expect this component of the decay to be smaller. That is, assuming the law in equation (2.5) holds for the decay within layers probably amounts to an overestimate of shock pressure decay.

As described in the overview, we designate peak shock pressures calculated by this method as "climbing shocks". Peak shock pressures calculated using equation (2.5) alone are called "ordinary shocks". An example of the difference between these is plotted in Figure 2-16. Using more than 30 layers will change by less than 1% the depth at which the climbing shock pressure (above the ambient pressure) reaches zero. Finally, peak pressures calculated using equation (2.5) with the ambient [lithostatic] pressure P_{ls} subtracted (as indicated by the bold lines and points in Figures 2-11 and 2-12) are called "foundering shocks" in the following discussion.

We can now use foundering-shock and climbing-shock estimates of peak pressure to estimate shock-heating in terrestrial mantles. This is accomplished by substituting these estimates for P_s in equation (2.11) (where $P_\delta = P_s - P_0$ and values of P_0 are calculated from the isentrope (2.16)), as well as substituting (2.23) for ρ_0 in this expression. Examples for impacts on Mars and the Earth are plotted in Figures 2-3 and 2-17, respectively. We note immediately that the correction to foundering-shocks is slight when compared with the contrast between these and "ordinary shocks". A clearer sense for this correction is illustrated in plots such as those shown in Figures 2-18 and 2-19 (Earth and Mars-B, respectively), where the shock-heating ΔT_f for foundering shocks is subtracted from that obtained for climbing shocks (ΔT_c), for each of three decay laws. Foundering shock pressures are seen to overestimate the shock-heating

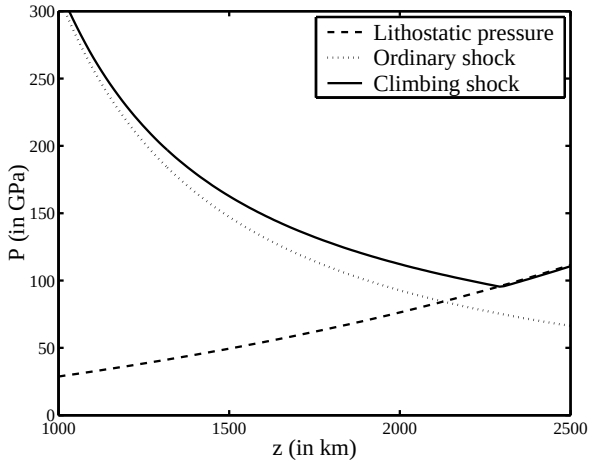

Figure 2-16: Peak shock pressure decay profile for an ordinary and climbing shock, and lithostatic pressure as a function of depth in the Earth, where $n = n_0$ (for a projectile with $R = 500$ km incident at $v_i = 15$ km/s).

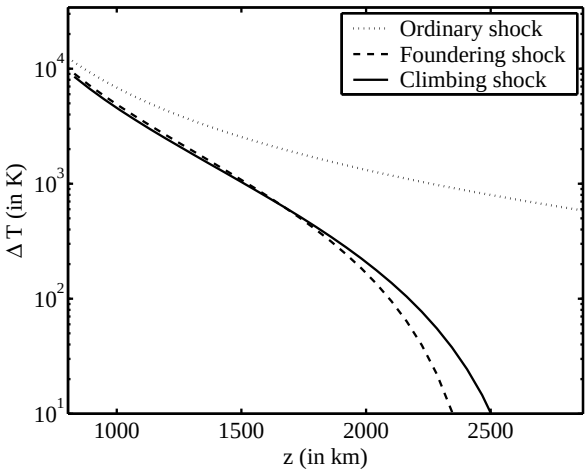

Figure 2-17: Shock heating as a function of depth (outside of the IC) for an ordinary shock, as well as foundering and climbing shocks ($R = 500$ km, $v_i = 15$ km/s). Our reference model in this case is that for the Earth, and the decay law exponent for P_s is $n = n_-$.

by as much as hundreds of degrees for high shock pressures, and to underestimate by far smaller amounts (up to 100 K) at low pressures. The shock-heating calculated for climbing- and foundering-shocks for a range of shock-pressure decay exponents, impact energies, and reference models, are plotted in Figure 2-3, and Figures 2-20 through 2-24. Estimates of shock-heating at the core-mantle boundary (CMB) are listed in Table 2.2 for foundering shocks and a range of impact energies and decay exponents, in the case of Martian reference models (N.B. numbers following "+" or "-" indicate the correction for climbing shocks). Some of these estimates for CMB heating amount to a considerable fraction of the largest temperature gradients that can be expected across a thermal boundary layer above the CMB of Mars. As can be seen in Figure 2-22, only the largest impacts ($R = 1000$ km, $v_i = 15$ km/s) will heat the CMB of the Earth (assuming $n = n_0$), and only by tens of degrees.

We now consider briefly to what extent these results are sensitive to changes in the value of γ used to calculate the principal isentrope. In reference models for Mars and Earth we assumed $\gamma = 1.25$ (assumed in McQueen [1991] to obtain

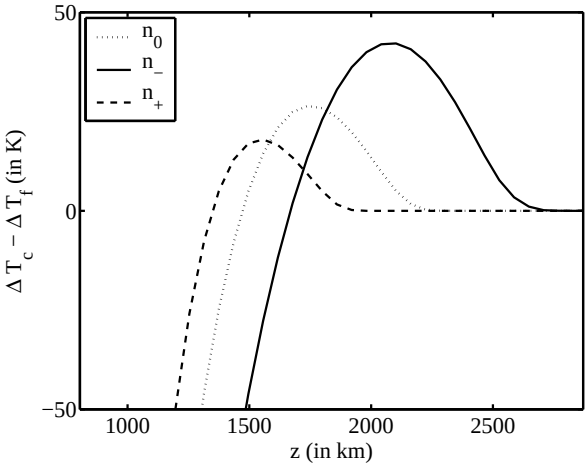

Figure 2-18: Difference in estimates of shock heating for foundering shocks ΔT_f and climbing shocks ΔT_c as a function of depth in the Earth for three shock pressure decay exponents and a projectile with R = 500 km incident at 15 km/s.

Table 2.2: Shock-heating of the CMB, calculated for foundering and climbing shocks (temperatures in K). Numbers indicate the temperature increase at the CMB estimated for foundering shocks. Numbers following "+" or "-" indicate the correction for climbing shocks.

v_i (km/s)	n	$R = 50$ km	100 km	250 km	500 km
Mars-A reference model					
10	n_+	0	0	0	$29 + 3$
	n_0	0	0	$6 + 3$	$145 + 3$
	n_-	$2 + 1$	$18 + 5$	$142 + 8$	$494 - 5$
15	n_+	0	0	0	$76 + 10$
	n_0	0	0	$1 + 2$	$283 + 14$
	n_-	0	0	$63 + 14$	$818 + 10$
20	n_+	0	0	0	$205 + 28$
	n_0	0	0	$0 + 2$	$596 + 40$
	n_-	0	0	$48 + 19$	$1473 + 46$
Mars-B reference model					
10	n_+	0	0	$0 + 1$	$108 + 3$
	n_0	0	0	$36 + 7$	$367 - 15$
	n_-	$16 + 6$	$77 + 8$	$360 - 8$	$979 - 63$
15	n_+	0	0	0	$259 + 18$
	n_0	0	0	$15 + 12$	$708 + 2$
	n_-	0	$2 + 5$	$226 + 28$	$1653 - 46$
20	n_+	0	0	$0 + 1$	$601 + 61$
	n_0	0	0	$12 + 19$	$1382 + 50$
	n_-	0	$0 + 1$	$206 + 61$	$2866 + 7$
Mars-C reference model					
10	n_+	0	0	$1 + 4$	$221 - 9$
	n_0	0	$0 + 2$	$86 + 10$	$633 - 70$
	n_-	$43 + 11$	$166 - 1$	$623 - 65$	$1489 - 201$
15	n_+	0	0	$0 + 5$	$521 + 13$
	n_0	0	0	$49 + 36$	$1226 - 60$
	n_-	0	$11 + 20$	$464 + 31$	$2547 - 214$
20	n_+	0	0	$0 + 11$	$1127 + 87$
	n_0	0	0	$47 + 70$	$2292 + 3$
	n_-	0	$0 + 12$	$461 + 122$	$4307 - 173$

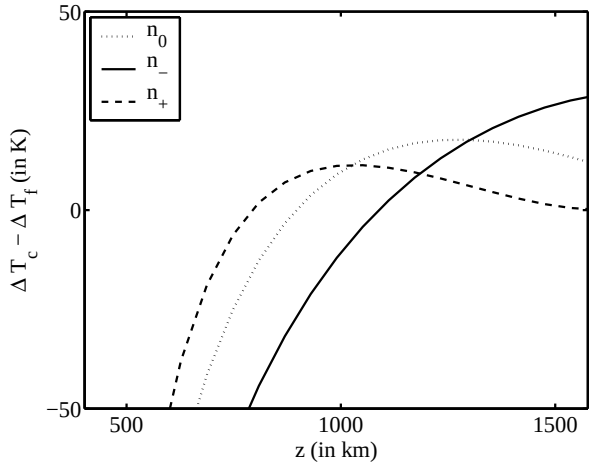

Figure 2-19: Difference in estimates of shock heating for foundering shocks ΔT_f and climbing shocks ΔT_c as a function of depth in the case of Mars-B for three shock pressure decay exponents and a projectile with R = 250 km incident at 15 km/s.

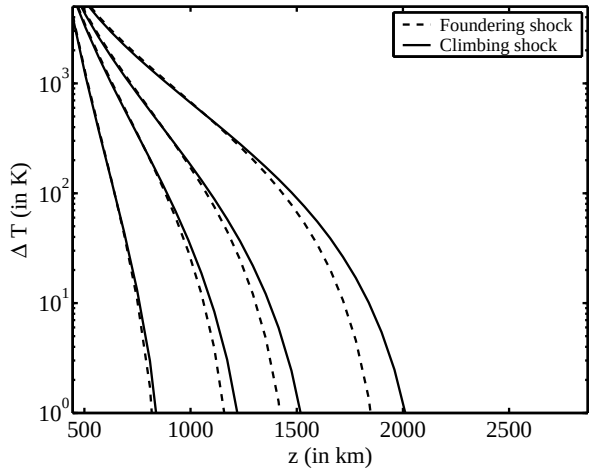

Figure 2-20: Shock heating for four peak shock pressure decay laws as a function of depth (outside of the IC) in the Earth, for foundering and climbing shocks. From left to right: Perret-Bass law (eq. (2.10) (Perret and Bass [1975])), and Pierazzo laws $n = n_+$, $n = n_0$, $n = n_-$ (Pierazzo et al. [1997]). In this case, $R = 250$ km, $v_i = 15$ km/s.

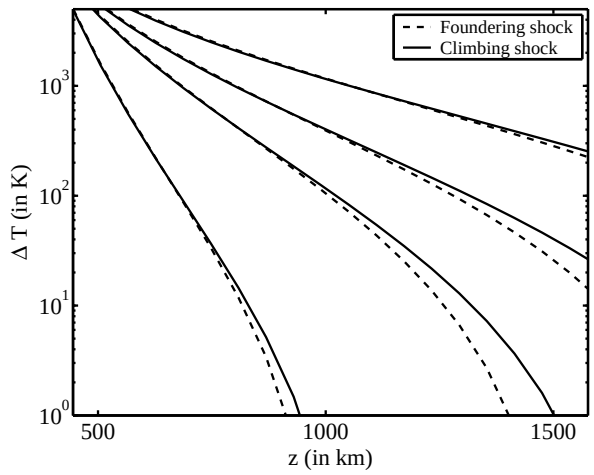

Figure 2-21: Shock heating for four peak shock pressure decay laws as a function of depth (outside of the IC), for foundering and climbing shocks in the case of Mars-B. From left to right: Perret-Bass law, Pierazzo laws $n = n_+$, $n = n_0$, $n = n_-$. In this case, $R = 250$ km, $v_i = 15$ km/s.

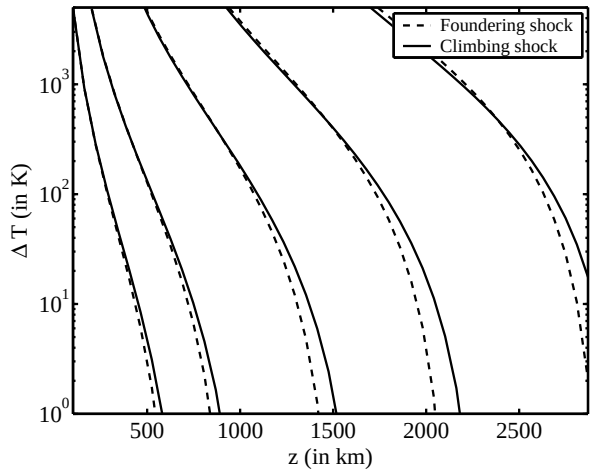

Figure 2-22: Shock heating as a function of depth (outside of the IC) in the Earth for projectiles with a range of sizes incident at 15 km/s. The shock pressure decay law exponent is $n = n_0$. From left to right: $R = 50, 100, 250, 500, 1000$ km.

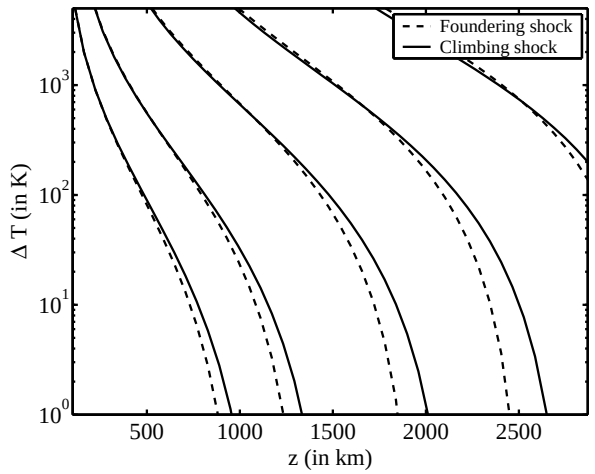

Figure 2-23: Shock heating as a function of depth (outside of the IC) in the Earth for projectiles with a range of sizes incident at 15 km/s. The shock pressure decay law exponent is $n = n_{-}$. From left to right: $R = 50, 100, 250, 500, 1000$ km.

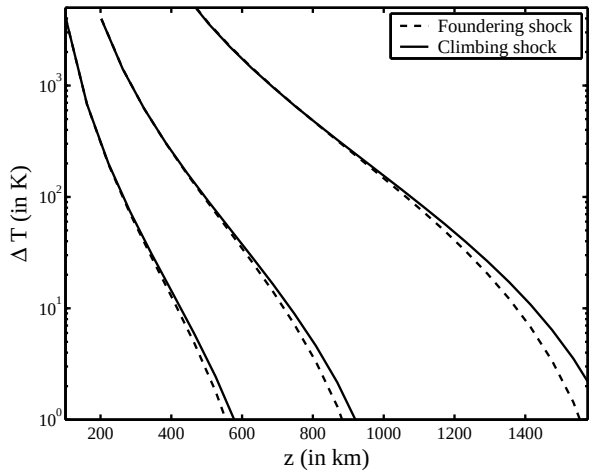

Figure 2-24: Shock heating as a function of depth (outside of the IC) for projectiles with a range of sizes incident at 15 km/s, for the case of Mars-A. The shock pressure decay law exponent is $n = n_0$. From left to right: $R = 50, 100, 250$ km.

the shock EOS fit to lower-mantle values). Values for the lower mantle are thought to reside within the range $1.2 \leq \gamma \leq 1.5$ (Schubert et al. [2001]). Using $\gamma = 0.70$ causes the estimates for $v_i = 15$ km/s, $R = 500$ km, $n = n_0$ in Table 2.2 to diminish by at most 7%. Setting $\gamma = 1.50$ causes the estimates for this case to increase by at most 5%.

2.6 Consequences of an upper mantle layer

We briefly consider the consequences of adding an upper mantle layer with a different shock EOS and STP density. In particular, we consider a layer of uniform density ρ_0' and thickness d that overlies the lower mantle, and we obtain the impedance match solution for the IC pressure using the properties for this layer. The resulting shock pressure then decays according to equation (2.5) until the shock reaches the top of the upper mantle. Another impedance matching (using the lower-mantle Hugoniot and a recentered Hugoniot for the reflected shock in the upper mantle) is used to calculate the shock pressure at the upper/lower mantle interface. Equation (2.5) is then used to estimate the IC pressure that would produce the same shock pressure at depth d in the one-layer model. In this way, the addition of an upper mantle layer with a given set of properties can be matched to an equivalent change in the impact energy for the one-layer model.

Let us suppose that we add a 660 km layer that has density $\rho_0' = 3.4$ g/cm^3 and the shock EOS values $S = 1.46$ and $C = 6$ km/s fitted by McQueen [1991] to the upper mantle. For a projectile with $R = 250$ km and $v_i = 15$ km/s, the equivalent IC pressure P_c for the one-layer model is 15% smaller. This is roughly equivalent to the impact of a projectile with the same radius, except with velocity 13.5 km/s. (Recall from Section 2.4 that the IC pressure P_c is a function of the impact velocity alone if the projectile has the same material properties as the target.) To estimate the consequences for shock heating at low shock pressures for ordinary shocks ($P_0 = 0$ for all z and constant ρ_0), we substitute equa-

tion (2.5) for P_δ in equation (2.11) and write the result to first non-vanishing order in $1/r$:

$$\Delta T_s(r) \approx \frac{S}{3C}\left(\frac{P_c r_c^n}{\rho_0 C r^n}\right)^3 \tag{2.32}$$

If P_c is reduced by 15%, then the shock-induced heating (ΔT_s) for large r is diminished by 40% in the case of ordinary shocks. The consequences for climbing and foundering shocks of course depend also upon the ambient pressure.

We characterize the upper-mantle layer using the low-pressure phase shock EOS for peridotite that was quoted earlier, the equivalent IC pressure P_c for the one-layer case is 35% less, corresponding to the impact of a projectile with the same radius incident at 11.5 km/s instead of 15 km/s (this means a reduction of 70% for shock-heating at large r in the case of ordinary shocks).

Using the mean law from Pierazzo et al. [1997] for the IC depth d_c and radius r_c, for the Earth we calculate that the IC of impacts with $R = 400$ km projectiles incident at $v_i = 15$ km/s will overlap the lower mantle. The center of the IC of impacts with $R = 750$ km projectiles incident at $v_i = 15$ km/s will penetrate the lower mantle. Thus, for impacts in this energy range, the foregoing corrections are not important.

Finally, note that we have assumed that the projectile has the same material properties as the target. Changes to the projectile-target density ratio also result in changes to the isobaric core pressure that can be matched to a different impact energy in the case of identical projectile-target materials. These corrections are easily calculated using the impedance match method. For example, if the projectile has half of the target's density, this lowers the IC pressure P_c by 30% (for $v_i = 15$ km/s). If the projectile has 3/4 of the target density, the IC pressure is lowered by 15%. In this study, we have assumed that target and projectile densities are equivalent.

Conclusions

The simple "foundering shock" method outlined in Section 2.1 and forumulated in Section 2.5 (where other methods are also discussed) provides an effective estimate of the shock heating that results from vertical hypervelocity impacts at great depths in terrestrial mantles. This is accomplished by: (a) assuming that release occurs along the Hugoniot; (b) expressing the amount of shock heating in terms of the peak shock pressure (equation (2.11)); (c) substituting for peak shock pressure the difference between a power-law shock pressure decay and lithostatic pressure (as a function of depth), and substituting for ρ_0 the mantle reference model density (as a fuction of depth). The errors in this approach do not exceed the uncertainties associated with peak shock pressure decay law exponents for the range of material properties reported in Pierazzo et al. [1997]. For estimating the characteristic perturbation temperature ΔT_p (the difference between solidus and geotherm) and size (the depth at which shock heating decays to a value below ΔT_p), the error associated with the aforesaid approximation accounts for a slight over-estimation of the characteristic perturbation size.

Chapter 3

Geodynamical consequences of large thermal perturbations for convecting mantles

Abstract: In this chapter we examine the effects of thermal perturbations on a convecting layer of incompressible fluid with uniform viscosity in the limit of infinite Prandtl number and the Boussinesq approximation, for two upper boundary conditions (free- and no-slip) and heat sources (100% volumetric heating and 100% bottom heating), in 2D Cartesian finite-element simulations. Small, low-temperature perturbations are swept into nearby downflows and have almost no effect on the ambient flow field. Large, high-temperature perturbations are rapidly buoyed and flattened, and spread along the layer's upper boundary as a viscous gravity current. The spreading flow severs and displaces downwellings in its path, and also thins and stabilizes the upper thermal boundary layer (TBL), preventing new instabilities from growing until the spreading motion stops. A return flow driven by the spreading current displaces the roots of plumes toward the center of the spreading region, and inhibits nascent plumes in the basal TBL. When spreading halts, the flow field is reorganized as convection re-initiates. We obtain an expression for the spreading timescale, t_s, in terms of the Rayleigh number (Ra) and the dimensionless perturbation temperature (Θ) and size (Λ), as well as a condition that indicates for what values of these parameters (Θ, Λ, and Ra, in combination) is convection is slowed at a system-wide scale. Moreover, we examine in detail the interaction between the spreading front and convective downflows to illuminate the source of this behavior. The results of Chapter 2 are used to relate perturbations having a characteristic magnitude and size to perturbations produced by projectiles with radii in the range 200 to 900 km and vertical incident velocities in the range 7 to 20 km/s.

In our model mantles, the perturbations corresponding to very large impacts cause two episodes of magmatism with different source regions. The first occurs over a broad spatial scale and comparitively long time-scale, deriving material from the shock-heated region (caused by the flattening- and spreading flow). The second is scattered across the spreading region in localized zones, deriving material from unshocked mantle as well as from the basal thermal boundary layer, and which results from the broad-scale reorganization of the convection pattern after spreading halts. Finally, we consider potential applications of this work for understanding the history of early Mars.

3.1 Overview

In Sections 3.2 and 3.4 we use the results from the previous chapter and the estimated thermal structure of terrestrial mantles to construct thermal perturbations for use in our convection simulations. Perturbations of type I (Section 3.2) are formed by truncating the shock-heating

profile at a model solidus, and perturbations of type II (Section 3.4) are formed by raising temperatures uniformly by a constant amount over a semi-circular region. Section 3.3 contains a qualitative description of general features of the post-impact-heating evolution following perturbations of type I, based on time-lapse snapshots of the temperature and velocity fields. In Section 3.5 we discuss the results of a large number of simulations with perturbations of type II, used to obtain an expression for the time-scale of dynamic adjustment: the "spreading timescale," t_s. In Section 3.6 we supply the conditions under which convection is dramatically slowed and the circulation pattern reorganized at a global scale. Section 3.7 contains a discussion of the implications of these results for alternative convection models, including other rheologies and three-dimensional model domains. In Section 3.8 we consider potential applications of our work for understanding the history of early Mars. Finally, in Section 3.9 we examine the interaction between viscous spreading currents and localized convective downflows, to shed light on the source of scaling relationships measured from global system properties in Sections 3.5 and 3.6.

3.2 Convection-model perturbations I

We turn now to constructing thermal perturbations caused by shock-heating for use in 2D finite-element simulations of mantle convection. We consider two kinds of perturbations. In the first case (type I perturbations), the anomaly is constructed according to the shock-heating vs. depth profiles calculated in the previous section, where temperatures are set equal to the solidus temperature wherever this value is exceeded. This requires a model of the thermal structure of the mantle, which is discussed later in this section. We use this kind of perturbation, which has a realistic shape, to probe general features of the perturbation-driven flow in Section 3.3. In the second case (type II perturbations, discussed in Section 3.4), we raise mantle temperatures by a uniform amount throughout a semicircular region (with no imposed solidus ceiling). For that case we quantify the time-scales of dynamic adjustment (Section 3.5) in terms of the characteristic perturbation temperature and size. The simpler type II anomaly was used so that our results can be generalized more easily. Later, in Sections 3.4 and 3.6, we make explicit the relationship between these types.

In order to construct type I perturbations, we calculate the shock heating as a function of distance r from the IC center along rays oriented at an angle ϕ from the vertical. The IC is centered at a depth, d_c, according to the law supplied in Pierazzo et al. [1997] (see Section 2.1). We calculate shock heating along the rays for $\phi > 0$ by replacing z in the density profile (equation (2.23), Section 2.3) with $(d_c + r\cos\phi)$. In this way, the density profile (and the corresponding pressure profile) is "stretched" as a fuction of r as the angle ϕ increases. In calculating the climbing shock estimates for ΔT_s, we therefore obtain a 2D function $\Delta T_s = f(r, \phi)$. A 2D linear interpolation is used to construct the perturbation for regularly-spaced cells in a rectilinear coordinate system $\Delta T_s = g(x, z)$. Shock heating in the near-surface region is complicated by the interference of decompression waves – we do not expect our estimates to be realistic in this zone.

Melt volume and model assumptions

Temperatures at the highest shock pressures considered in this study reach upwards of 10^4 K, exceeding the temperatures at which vaporization is expected. Vaporization, crater excavation and crater collapse dominate the evolution at short times near the planet surface and are not addressed in this study. We do not address the contribution of melt generated by the release of overburden pressure during and following the excavation process (Jones et al. [2002]). Neither do we consider the processes associated with melt extraction or the decompression melting of shock-heated, upwelling mantle rocks. The dynamical consequences of differentiation are also ignored. The anomalous density of type I perturbations is due entirely to thermal expansion from shock-deposited heat. The shock-augmented tempera-

ture is set equal to the local solidus temperature, T_m, wherever this value is exceeded.

Some of the reasons for this choice are physical and some are practical in nature. First, regions that are raised to the liquidus temperature are apt to dissipate heat by convection and cool rapidly into partial melts on time-scales that are short when compared with the time-scales of subsolidus convection. Reese and Solomatov [2006] estimated that the time-scale associated with crystallization of a total-melt volume (spanning the mantle depth) down to a 40% melt fraction (the transition from crystal-suspension to partially-molten solid) would take a mere 300 to 1000 yrs. Cooling to solidus would require an additional 100 to 300 Myr if surface recycling occurs (Newtonian rheology), and much longer (up to 1 Gyr) if a stagnant lid forms over the melt volume (Reese and Solomatov [2006]). The former time-scale (100-300 Myr) is comparable to the shortest time-scales of dynamic adjustment calculated in this study (i.e., for the largest Rayleigh numbers).

Moreover, partial melts have a strongly temperature-dependent rheology. The convection models that we consider in this study are isoviscous and ammenable to fast computation, so that we cannot treat in a realistic fashion viscosity of the partial melt. The time-scales of initial dynamic adjustment and subsequent spreading of the viscous gravity current are mainly determined by the subsolidus rheology outside of the partial melt volume, as well as the anomalous buoyancy of the partial melt. The time- and length- scaling that characterizes a spreading, cooling viscous drop are barely altered by strongly temperature-dependent viscosity with large viscosity contrasts (Monteux et al. [2007]).

Our calculations of shock-heating anticipate that temperatures reaching the solidus will span much of the mantle for large impacts. The perturbations considered in this study correspond to the smallest melt volumes addressed in Reese and Solomatov [2006], and for which the time-scales of dynamic adjustment are large compared with the crystallization times, precluding the formation of large magma oceans.

In reality, on time-scales associated with melt percolation and differentiation, a large quantity of melt is extracted while the density of the mantle residuum is diminished. Reese et al. [2004] considered the effects of melt extraction by comparing the time-scales associated with convection and melt percolation. The authors estimated that a characteristic density contrast of 2% is associated with 15 % melt extraction and 3% melt retention (assumed for the impact-related buoyancy anomalies in their models). A two percent drop in density corresponds to a 1000 K temperature anomaly in our models (assuming an expansivity of 2×10^{-5} K^{-1}).

An anomalous buoyancy that derives from a partial melt is likely to dissipate far less rapidly than an equivalent thermal buoyancy. In our models, the anomalous buoyancy of thermal perturbations rapidly diminishes while very hot materials are brought close to the upper boundary, whose temperature is fixed. The resulting high thermal gradients cause rapid heat loss through the upper boundary, so that much of the remaining flow is driven by a smaller anomalous buoyancy. Therefore, translating between partial melt buoyancies and equivalent thermal buoyancies is only approximately valid for the rapid "flattening" stage (rapid viscous relaxation), and not for the "spreading" stage (spreading viscous gravity current) of the post-impact evolution (see Section 3.3).

Thermal reference models

In Section 3.3 we describe the numerical models used to solve for the evolution of temperature and velocity. The starting temperature field (before perturbations are added) is obtained by running our models until a statistical steady state is reached: i.e., a solution in which the averaged mantle velocity through time has a constant distribution. The dimensionless geotherm (horizontally-averaged temperature profile) obtained from this solution is used to construct type I perturbations, as described below.

In order to enforce the upper-bound on shock-heating we require a model solidus $T_m(z)$. For the Earth, we use a solidus that is consistent with the upper-bound reported in Zerr et al. [1998]

for a pyrolitic lower mantle (Stacey [1992]). For the relatively shallow Martian mantle we use the pressure-parameterization by Reese and Solomatov [1999] of the peridotite solidus. It was demonstrated by Schmerr et al. [2001] that an iron-enriched Martian mantle solidus lies, on average, roughly 200 K below the peridotite solidus. It should be noted, however, that the uncertainty in Martian mantle geotherms is greater than 200 K.

Heating associated with adiabatic compression does not occur in our convection models. We therefore subtract from $T_m(z)$ (the solidus) the additional temperature ΔT_{ad} contributed by the adiabatic gradient. This correction is applied from the base of the upper thermal boundary layer to the base of the mantle. The adiabatic gradient is obtained using equation (2.23) in Section 2.3, along the principal isentrope. We chose an interior temperature for Earth's mantle such that the maximum horizontally-averaged temperature in the upper thermal boundary layer of our model lies just below the solidus ($\approx$ 1700 K). In the case of Mars, we have chosen 1700 K for the base of the thermal boundary layer, consistent with the basal lithosphere temperature of model geotherms reported in Spohn et al. [1998].

Figure 3-1 contains two diagrams showing the horizontally-averaged model geotherm $\langle T \rangle$, the solidus T_m and the solidus with the adiabatic gradient subtracted ($T_m - \Delta T_{ad}$), for the case of (a) Earth and (b) Mars. In the plots of Figure 3-2 we show the difference between this adjusted solidus T'_m and the geotherm $\langle T \rangle$, as well as the shock heating with depth calculated for an impact on (a) the Earth and (b) Mars (see caption for details of the projectile parameters). In Figure 3-3 we illustrate each step in the construction of a type I perturbation, where the top frame corresponds to a time-independent steady-state temperature field. The middle frame shows the shock heating caused by an impact. The last frame shows the sum of the top and middle frames, where T = T'_m wherever this value was exceeded in the sum.

3.3 Evolution of the shock-heated region

In this section we supply a qualitative description of the post-impact evolution based on time-lapse snapshots of the temperature and velocity fields following the insertion of type I perturbations. Solutions for temperature and velocity were obtained using finite-element simulations of mantle convection for the case of an incompressible fluid in the limit of infinite Prandtl number. These were carried-out using the 2D cartesian version of CONMAN King et al. [1990]. We have assumed a uniform viscosity in order to efficiently model the evolution for a large number of perturbation sizes, for different initial- and boundary conditions and a range of Rayleigh numbers on large meshes.

The aspect ratio of our mesh and domain is 1x6 for the calculations discussed in this section only, and 1x10 for the 8,000 calculations of Section 3.5, where this is consistent with the estimated proportions of terrestrial mantles. The number of cells used in the vertical dimension was chosen so that thermal boundary layers were spanned by at least five cells in all cases. That is, for a calculation with $Ra = 1.0 \times 10^6$ we used a rectilinear mesh spanned by 120 elements in the vertical dimension, and 120 $\times$ 6 (this section) or 120 $\times$ 10 (Section 3.5) elements in the horizontal dimension, all of them evenly spaced. Wrap-around boundary conditions were imposed at the vertical bounding walls. By "100% bottom heating" we refer to models in which the temperatures of the upper and lower boundaries were fixed at constant values (i.e., not a lower-boundary heat flux condition). Only the upper boundary temperature was fixed for calculations with 100% volumetric heating. Both upper and lower boundaries are impermeable. The dynamic Courant time-step depends on the largest velocities in a given state of the system. The most important time-scale in the perturbation-driven evolution, the spreading time-scale (t_s), is typically spanned by 750 to 1500 program time-steps.

We begin with several caveats before describ-

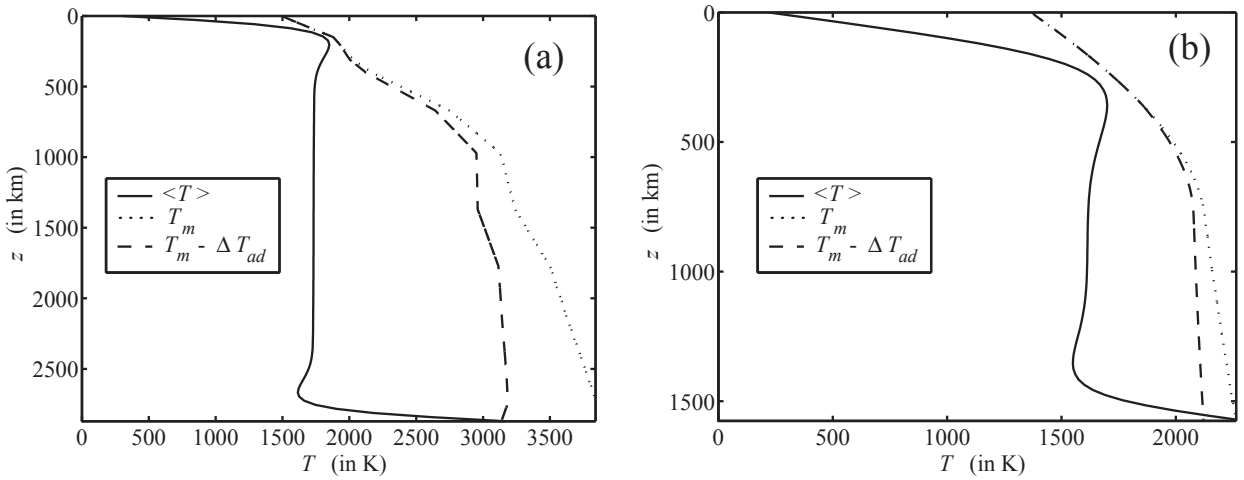

Figure 3-1: Thermal structure of (a) an Earth-like planet and (b) a Mars-like planet, assumed for constructing type I perturbations. The solid line indicates horizontally-averaged mantle temperature $\langle T \rangle$ of a convection model calculation carried to quasi-steady-state ((a) $Ra = 7.5 \times 10^5$, stress-free upper boundary, fixed lower boundary temperature with no internal heating, (b) $Ra = 1.5 \times 10^5$, no-slip upper boundary, fixed lower boundary temperature with no internal heating). Also plotted is the solidus temperature T_m and "corrected" solidus temperature with the adiabatic gradient ΔT_{ad} subtracted. See text for discussion.

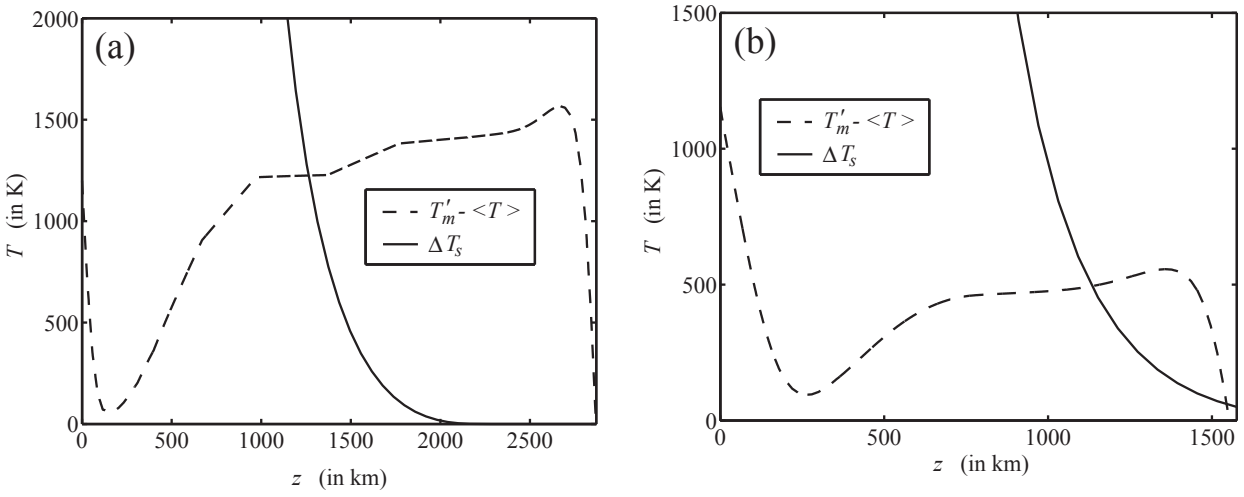

Figure 3-2: Shock heating ΔT_s with depth in the mantle of (a) an Earth-like planet caused by a projectile with radius $R = 600$ km and incident velocity 15 km/s and (b) a Mars-like planet (Mars-A; see Section 2.3) caused by a projectile with radius $R = 375$ km and incident velocity 15 km/s. Peak shock pressure decays with exponent $n = n_0$. The adjusted solidus temperature T'_m minus the model geotherm $\langle T \rangle$ is plotted also. The perturbation temperature with depth directly beneath the impact is given by $T'_m - \langle T \rangle$ until it is crossed by ΔT_s, and by ΔT_s below this depth.

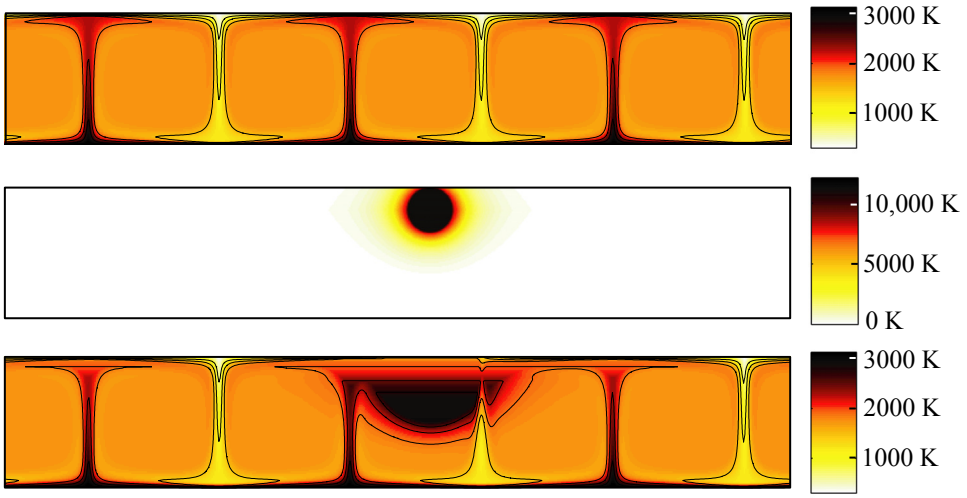

Figure 3-3: Construction of type I perturbations in two dimensions. The top frame shows a portion of the pre-impact temperature field $T_0(x, z)$. The middle frame illustrates the temperature field calculated for shock-heating ($\Delta T_s(x, z)$). The bottom frame shows the sum of these, where the temperature is set to $T'_m(z)$ (the local solidus temperature) at all points where $T_0 + \Delta T_s \geq T'_m$.

ing the model results in detail. First, it should be emphasized that our calculations are carried-out in two-dimensions, so that instabilities which grow and detach from the basal thermal boundary layer (TBL) are neither plumes or the margins of rolls, where these latter structures are defined in terms of a three-dimensional geometry. Our convention is to refer to narrow upwellings as "plumes", and in Section 3.7 we consider to what extent our results apply to the three-dimensional case.

Second, the Rayleigh numbers for Earth-like models in this section are smaller than the Rayleigh number of whole-mantle convection in the modern Earth, which is estimated to exceed 10^7 (i.e., an internal heating Rayleigh number). The value of Ra for the Earth's early mantle was larger still. In Sections 3.5 and 3.6 we report on results for internal heating Rayleigh numbers comparable to modern values. We then assume these results hold for even larger values in order to estimate the consequences of large impacts for model mantles with values of Ra appropriate for the early solar system. Accurate calculations of convection on high aspect-ratio meshes for very high Rayleigh numbers are outside the reach of our computational and temporal resources, since more mesh elements are required to resolve adequately the evolution of thermal boundary layers.

For the simulations described in this section, the temperature of the lower boundary is fixed and there is no internal heating. This ensures a large temperature contrast for the basal TBL and a markedly unstable source layer for deep mantle plumes. Except for the interaction with plumes, general features of the evolution are very similar for the case of 100% volumetric heating, and for this reason we focus here on the bottom-heating case. The basal TBL for models in this section are spanned by a larger temperature contrast (as a fraction of the whole-mantle convective driving temperature) than is considered realistic for the Earth's CMB.

Numerous time-lapse snapshots of the temperature and velocity fields have been used to confirm that the fundamental processes described in this section for low-Ra models operate in an identical fashion at higher Ra, although across different temporal and spatial scales. Convection models with 100% bottom heating at low Rayleigh numbers have the advantage that ini-

tial conditions are time-independent solutions of the governing equations. Changes in the temperature and velocity fields are therefore readily visible and can be assigned directly to the influence of the perturbation, which is less easily separated from the evolution of a time-dependent solution in which plumes and downwellings are constantly emerging and vanishing. The results in Sections 3.5 and 3.6 are derived from a larger range in Rayleigh numbers, with internal heating and time-dependent initial conditions. We find that quantifiable properties of the evolution do not significantly depend upon whether the initial condition was time-dependent.

The Martian mantle is thinner than Earth's mantle, so that impacts of the same energy will produce perturbations on a different scale with respect to layer thickness, in some cases heating the CMB directly. We do not consider the effects of solid-state phase transformations, which occur within Mars at great depths and have been shown to diminish the number of large plumes in convection models (Harder and Christensen [1996], Breuer et al. [1998]). For the results reported in this section only, we enforce a stress-free upper boundary condition in the case of Earth-like models, and no-slip upper boundaries in the case of Mars-like models. The latter is an attempt to mimic the conditions of a stagnant lid, below which viscosity is approximately uniform (Solomatov [1995]).

Stages of the post-impact evolution

The post-impact evolution for large-magnitude perturbations (i.e., large size and high-temperature) observed in our models is summarized in Figure 3-4, and for a sample model calculation in Figure 3-5 ($R = 600$ km, $v_i = 15$ km/s, $n = n_0$; $Ra = 7.5 \times 10^5$, terrestrial mantle properties, and a stress-free upper boundary).

(a) **Flattening stage**: First, the buoyant region rises and flattens on the comparatively short time-scale of viscous relaxation (Figure 3-4, frame B; Figure 3-5, $t_1 < t < t_2$). The dynamics of the flattening stage are largely indifferent to the pre-impact convection pattern.

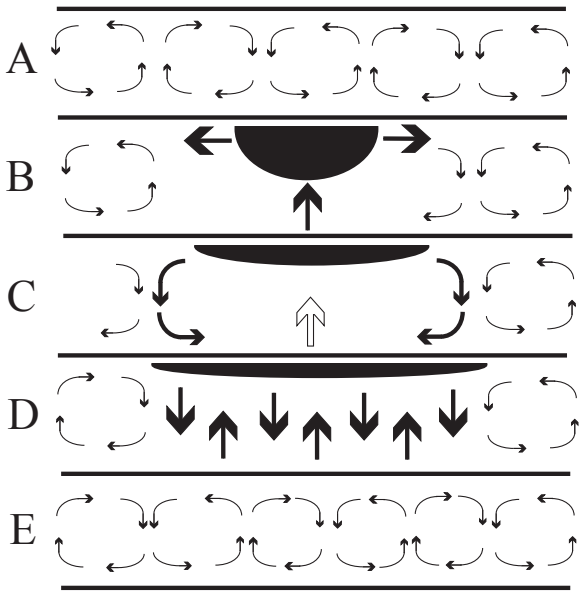

Figure 3-4: Principal stages in the evolution of the flow field following the insertion of large perturbations. A: Pre-impact convection pattern. B: Flattening stage: vigorous buoyant ascent of the perturbation as it flattens on the time-scale of viscous relaxation. C: Spreading stage: the perturbation spreads along the top of the layer as a viscous gravity current, stabilizing the upper boundary. This motion drives a large-scale circulation pattern that also stabilizes the basal TBL and focuses flow below the center of the spreading region. In some cases this causes plume roots to coalesce into a megaplume. The flow decelerates throughout the spreading region as convection is stopped. D: Recovery stage: the double-roll circulation pattern is maintained but stops expanding as the spreading current is halted by downwellings. Plumes and downwellings emerge in basal and upper TBLs as convection resumes and reorganizes the flow field (E).

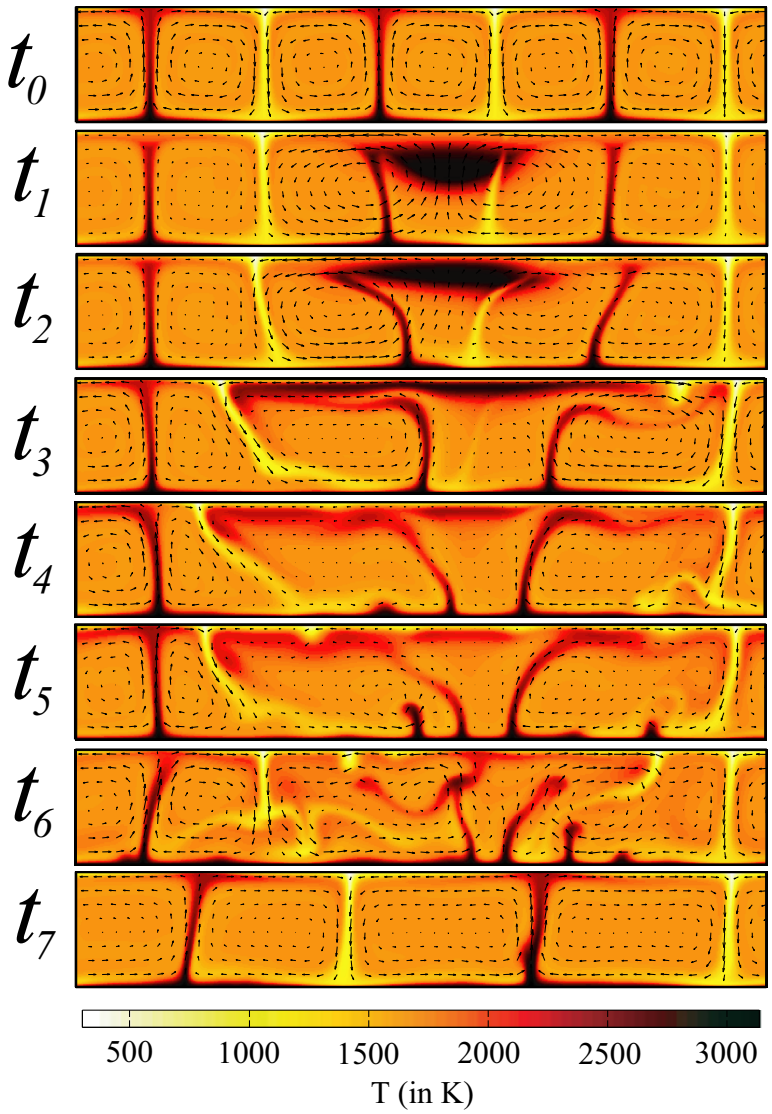

Figure 3-5: Evolution of the temperature and velocity fields for an Earth-like model (terrestrial mantle properties, stress-free upper boundary) and $Ra = 7.5 \times 10^5$ following insertion of a large-magnitude perturbation ($R = 600$ km, $v_i = 15$ km/s, $n = n_0$). Part (a) of Figure 3-2 shows the shock-heating profile for this case. The important features of the evolution are, frame-by-frame: $t_0 = 0$ Myr: Pre-impact, steady-state solution. $t_1 = 8$ Myr: Flattening stage: double-roll pattern emerges as the perturbation flattens rapidly. $t_2 = 50$ Myr: The perturbation begins to spread as a viscous gravity current along the upper boundary. Plumes and downwellings are deflected. $t_3 = 225$ Myr: The leftward-spreading flow encounters a downwelling and displaces it a long distance (intact). The excess buoyancy driving the front is drained by the downwelling flow, and the spreading motion slows. The rightward flow has severed a downwelling, and displaces its root a long-distance. The return flow along the bottom of the layer pushes the roots of plumes toward the center of the spreading region. $t_4 = 550$ Myr: The hot spreading current and its return flow, by stabilizing both boundary layers, has caused large nearly-stagnant zones to form in the spreading region. Plumes formerly deflected now right themselves, eroding the current and reducing further its driving buoyancy. The spreading motion slows down, and the basal return flow now fails to stabilize the basal TBL. Instabilities emerge and inflate. $t_5 = 730$ Myr: Downwellings and plumes emerge as the recovery stage begins. $t_6 = 1.6$ Gyr: Vigorous flow of the recovery stage as convection reorganizes. Note the high concentration of plumes near the center of the [former] spreading region. $t_7 = 10$ Gyr: The reorganized convection pattern.

The flow brings high-temperature materials to the cold upper boundary in a relatively short time. The resulting large vertical temperature gradients, spanning a broad region of the upper boundary, cause rapid heat escape.

(b) **Spreading stage:** The substantially cooler anomaly then spreads along the upper boundary as a viscous gravity current (Figure 3-4, frame C; Figure 3-5, $t_2 < t < t_4$). The spreading flow drives circulation in the layer over an expanding region, spanning the entire layer depth. This circulation creates a double-roll pattern with a weak central upwelling and marginal downwellings. (In three dimensions, this flow field would assume an annular shape.) Downwellings are destroyed when their source roots are sheared off by the spreading motion. Alternatively, the spreading current can displace an intact downwelling long distances, while its excess buoyancy is drained by the downwelling flow (Figure 3-5, leftward spreading current, frames t_3 and t_4), causing the current to slow down. The spreading motion, and simultaneous thinning of the upper thermal boundary layer (TBL) by the influx of hot material, stabilize the upper boundary against the formation of new instabilities and downwellings. This stabilizing effect and the destruction of downwellings stops convection and forms large zones of nearly stagnant flow (Figure 3-5, frame t_4).

The spreading current also deflects plumes in its path, bending them in some cases parallel to the spreading motion. The upward flow in plumes that normally drains the basal thermal boundary layer is interrupted and slowed as a result. Meanwhile, the centrally-directed return flow along the bottom of the mantle initially stabilizes the basal thermal boundary layer, which thickens while it is not being drained. The return flow along the base of the layer also pushes the roots of plumes close together, in some cases causing these to coalesce near the center of the spreading region. Shortly before the spreading motion halts, deflected plumes begin to right themselves and sometimes erode the spreading current, subtracting from the anomalous buoyancy driving its motion. New instabilities form in the basal TBL, inflate, and eventually detach as plumes.

(c) **Recovery stage:** Finally, the spreading motion is halted and the flow field is reorganized (Figure 3-4, frame D; Figure 3-5, $t_4 < t < t_7$). The fronts of the spreading current are stopped by downwellings, even while the pattern of motion (the double roll) remains largely intact. New downwellings emerge in the spreading region. A high concentration of plumes form in the spreading region also, where new plumes detach from inflating instabilities, and where the roots of old plumes have been pushed by the return flow. Convection has fully re-initiated and the flow pattern reorganizes.

In the case of 100% bottom heating just described, the emergence of new downwellings in the spreading region can sometimes happen before the spreading motion halts. These downwellings emerge in zones of stagnating flow and where righted plumes have eroded through the blanket of hot material left behind by the spreading current. This enables the upper thermal boundary to recover locally, so that instabilities can emerge and inflate. The case of 100% volumetric heating differs in this regard, since the absence of plumes precludes them disrupting the spreading current. In all the cases that we have studied so far with 100% volumetric heating, downwellings in the spreading region do not emerge until after the spreading motion halts. Also, because of the spoke-like shape of plumes in three dimensions, this effect is unlikely to have the same importance for that geometry.

The evolution of the temperature and velocity fields just described indicates two major episodes of magmatism characterized by very different source regions, spatial distributions, and timescales. The first has a highly uniform spatial distribution and broad extent, and occurs during the flattening and spreading stages. All of the material for this magmatic episode is derived from the perturbation itself: i.e., from shock-heated mantle rocks brought to the solidus by the flattening flow and distributed broadly by the spreading flow. The second episode occurs in the recovery stage, as new downwellings and plumes emerge. In this stage, hot material deriving either from the basal TBL or the un-

shocked mantle are carried to the upper boundary by the vigorous motions of the reorganizing flow field. The magmatism associated with this event is likely to be localized spatially in pockets throughout the spreading region, occurring as sporadic episodes lasting for short times.

For the calculation shown in Figure 3-5, the pre-impact convection pattern is significantly reorganized by a pertubation with $R = 600$ km incident at $v_i = 15$ km/s (decay law exponent $n = n_0$). For the same incident velocity, perturbations resulting from projectile radii $R = 500$ km and $R = 400$ km also considerably alter the pattern by significantly displacing or breaching nearby downwellings. The case for $R = 300$ km (Figure 3-6), with the same convection model and incident velocity, fails to reorganize the pre-impact flow field at long times, and the spreading flow is halted and drained by the nearest downwelling. The spreading time-scale (the duration of the spreading stage) is noticeably shorter. Globally-averaged mantle velocities are barely depressed in this case because no downwellings are destroyed. Still smaller perturbations make the transition from an advective mode of spreading to a diffusive mode before they are swept into nearby downflows.

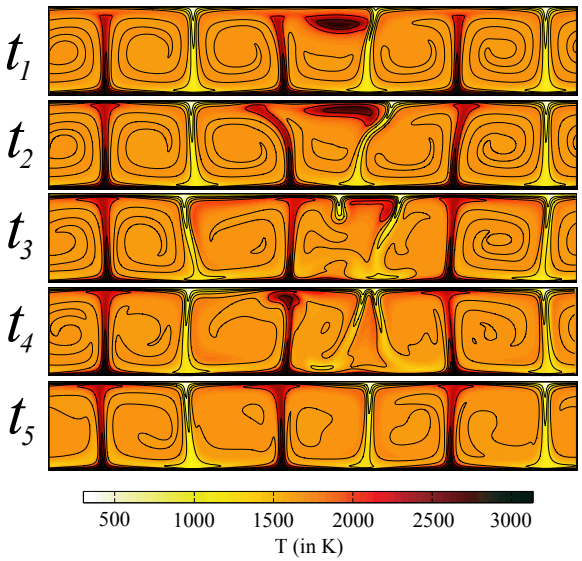

Figure 3-6: Evolution of the temperature field for the same convection model as shown in Figure 3-5, following an impact perturbation with the same incident velocity and $R = 300$ km (i.e., stress-free upper boundary, terrestrial mantle dimensions and properties, $Ra = 7.5 \times 10^5$, $v_i = 15$ km/s, $n = n_0$.) In this case, the perturbation-driven flow fails to reorganize the pattern, and is quickly halted and drained by nearby downwellings. The times corresponding to each frame are: $t_1 = 15$ Myr, $t_2 = 160$ Myr, $t_3 = 490$ Myr, $t_4 = 810$ Myr, $t_5 = 3.8$ Gyr. The spreading stage ended well before $t = 490$ Myr.

For a separate series of simulations the anomaly was centered on a downwelling, in a model mantle with Martian dimensions and a no-slip upper boundary, where $Ra = 10^5$. For incident velocity $v_i = 15$ km/s ($n = n_0$), only perturbations with $R > 250$ km succeeded in reorganizing the pattern. In Section 3.6 we derive a condition, expressed in terms of perturbation magnitude, which indicates whether the flow-field is significantly altered at a global scale, by predicting whether globally-averaged mantle velocities will be depressed significantly.

Finally, we explored the case of a marginally-unstable layer, where $Ra = 5 \times 10^3$ for a mantle with Martian dimensions and a no-slip upper boundary. In this scenario, even very large impacts (e.g., $R = 500$ km, $v_i = 15$ km/s) fail to reorganize the circulation pattern. This is consistent with the condition that we derive in Section 3.6, according to which the tendency for any convecting system to slow down at a global scale decreases with decreasing Ra for perturbations of a given magnitude. That is, the dissipative structures of low-Ra convection are comparatively robust with respect to spatially-localized perturbations. Note, however, that the change in Ra for this case is in effect due entirely to an increase in viscosity, while the applied driving temperature is held constant. Moreover, changes in projectile radius R for a constant incident velocity v_i mostly affect the size and not the temperature of the resulting perturbation. That is, for a constant characteristic perturbation temperature, expressed as a fraction of the whole-mantle convective driving temperature, even the largest projectile radii (largest perturbations) which reorganized the pattern for high Ra, fail to do this

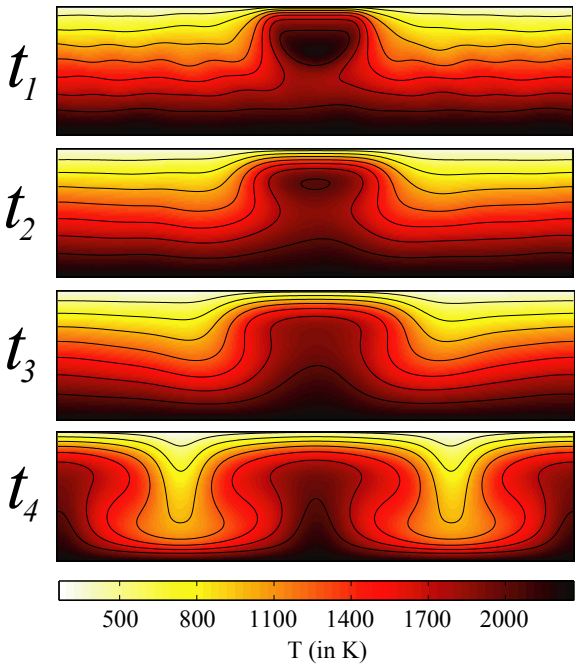

Figure 3-7: Evolution of a marginally-unstable layer ($Ra = 5{,}000$, no-slip upper boundary, Martian mantle properties) with weak spatially-periodic thermal perturbations and a single impact perturbation ($R = 250$ km, $v_i = 15$ km/s, $n = n_0$). Adjustment of the perturbation establishes a long-lived plume, on which the long-term pattern is centered. Times corresponding to each frame are: $t_1 = 110$ Myr, $t_2 = 550$ Myr, $t_3 = 1.1$ Gyr, $t_4 = 27.5$ Gyr.

for low-Ra convection.

Since convection is slow to begin from slight density heterogeneities in a marginally-unstable layer, larger thermal perturbations control the long-term circulation pattern by fixing the location of long-lived plumes. In Figure 3-7 we show the results of a calculation in which a thermal anomaly was added to a marginally-unstable layer with a conductive thermal profile, upon which weak, spatially-periodic perturbations were also superposed. Unsurprisingly, the large perturbation organizes the flow field at long times.

Consequences for deep mantle plumes

There are several ways in which a thermal perturbation may directly or indirectly initiate, amplify, disrupt or suppress mantle plumes. Deep mantle plumes are focused upwellings of hot material that form within the unstable thermal boundary layer (TBL) at the base of terrestrial mantles. The discussion for the remainder of this section is informed by the results of numerical and laboratory studies of plume initiation (Whitehead [1975], Olson et al. [1987], Bercovici and Kelly [1997], Schubert et al. [2001]). The basal TBL is a hot, low density layer overlain by a cool, higher density mantle. A small local increase in thickness of the TBL results in a local decrease in density that drives upward flow. This upward flow increases the thickness of the TBL still further, resulting in a positive feedback, and therefore an instability: a proto-plume. The proto-plume grows in size as it is filled from below and as the TBL is drained, and can merge with other instabilities of similar size as they drift toward common density lows. The proto-plume detaches if its Stokes ascent velocity exceeds the rate at which it is inflating.

Linear stability analysis indicates that thermal boundary layers are stable with respect to small-amplitude perturbations if the local Rayleigh number Ra_δ does not exceed a critical value Ra_{cr} (Howard [1966]). That is, the condition for stability is given by:

$$Ra_\delta \equiv \frac{\alpha g \Delta T \delta^3}{\kappa \nu} \leq Ra_{cr} \qquad (3.1)$$

where α is the thermal expansivity, g is the gravitational acceleration, δ is the local TBL thickness, κ is the thermal diffusivity, ΔT is the temperature contrast across the layer, and ν is the kinematic viscosity of the overlying mantle. This inequality does not, however, supply a complete picture of the conditions for plume formation, since it does not reflect the interaction with large-scale coherent motions in the mantle, which can tend to stabilize the upper and basal TBLs against the emergence and growth of Rayleigh-Taylor instabilities.

From these considerations we can start to

imagine how large thermal perturbations in the overlying mantle could suppress or initiate deep mantle plumes: (i) The shock waves can raise temperatures in the basal TBL or the lower-most mantle directly. This would lift TBL isotherms beneath the site of impact, with the potential of initiating buoyant perturbations in the layer (i.e., causing δ to increase locally, increasing Ra_δ). Moreover, heating of the lower mantle can lower the mantle viscosity ν (also increasing Ra_δ, and not addressed in our models). (ii) In at least two ways, the perturbation-driven flow, directed away from the basal TBL (upward), might initiate a buoyancy perturbation in this layer. First, the ascending motion could lift isotherms and form a region of low density in the layer. Second, the ascending motion could directly entrain portions of the basal TBL. In this case, the rate of growth of a proto-plume is driven by upward flow in the overlying mantle, and is faster than the relatively slow process of diapir inflation. (iii) The large-scale anomaly-driven circulation can increase the number and concentration of plumes by either one of two mechanisms. First, the return flow pushes the roots of plumes and nascent diapirs toward the center of the spreading region (i.e., toward a position beneath the site of impact). Second, the ascending motion above the basal TBL, by lifting basal isotherms, could create a local density low into which plumes and buoyant instabilities drift. (iv) Finally, the large-scale anomaly-driven circulation can suppress the formation of instabilities in two ways. First, the double-roll flow pattern set up by the flattening and spreading flow initially accelerates horizonal motions in the basal TBL, thereby shortening the mean residence time of the material in this layer. As this motion stalls when the spreading current is halted, the mean residence time increases, allowing instabilities to grow larger and detach as plumes. Second, the general circulation can impart a shearing flow at the boundaries, which can also suppress the emergence of Rayleigh-Taylor instabilties (Richter [1973]).

By far the most important mechanisms observed in our simulations are (iii) and (iv) as we have already seen in Figure 3-5, with some evidence for (i) and (ii). In Figure 3-8 we show a magnified view of the temperature field at three time steps for a mantle with Martian dimensions and a no-slip upper boundary, where the CMB is heated by hundreds of degrees K (R = 500 km, v_i = 15 km/s, $n = n_0$). In this case, two roots of pre-existing plumes are pushed center-ward by the return spreading flow, and coalesce. The triple-hump structure that occurs in a basal isotherm (visible at $t = t_2$) suggests that a proto-diapir may have formed directly under the perturbation before merging with adjacent plumes. It is possible this was caused by the mechanisms described in (i) and (ii) above: i.e., direct heating by the perturbation, or a local buoyancy anomaly formed by the ascending motions. In the last frame ($t = t_3$) a "megaplume" has formed from the merging of plume roots with the proto-diapir in the basal TBL.

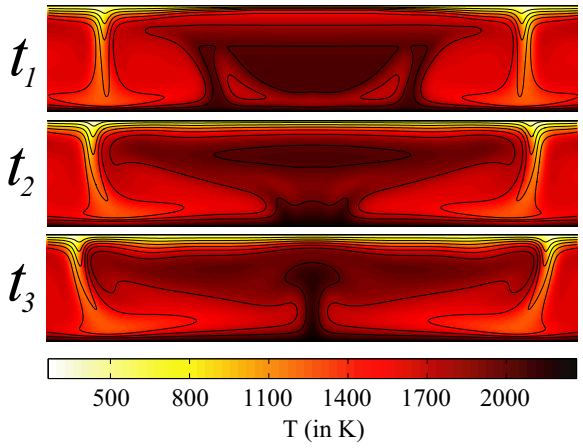

Figure 3-8: Evolution of the temperature field (magnified view) following the insertion of a thermal perturbation (R = 500 km, v_i = 15 km/s, $n = n_0$; $Ra = 10^5$, rigid upper boundary, Martian mantle properties). In this case the CMB is heated directly, and shock-heating raises CMB temperatures by hundreds of degrees. The anomaly-driven circulation focuses flow in the basal TBL directly under the anomaly, causing instabilities and plumes to coalesce. A giant pulse of hot material sourced from the basal TBL occurs by $t = t_3$. The times corresponding to each frame are: t_1 = 25 Myr, t_2 = 275 Myr, t_3 = 560 Myr.

3.4 Convection-model perturbations II

Type I perturbations exhibit a characteristic size and temperature. The characteristic temperature increase ΔT_p is given by the average difference between the geotherm and solidus. A characteristic size scale λ_p is given by the depth at which shock heating drops below ΔT_p. For the case depicted in part (b) of Figure 3-2, these values can be read from the abscissa and ordinate where the plotted curves intersect (e.g., $\lambda_p \approx$ 1100 km and $\Delta T_p \approx 500$ K). Insofar as a thermal perturbation can be described by a characteristic magnitude and length scale, quantifiable properties of the subsequent evolution may be simple functions of dimensionless groups comprising these quantities. In addition to the Rayleigh number, the relevant dimensionless groups are:

$$\Lambda \equiv \lambda_p/\lambda_m \tag{3.2}$$

$$\Theta \equiv \Delta T_p/\Delta T_c \tag{3.3}$$

where λ_m is the thickness of the convecting layer and ΔT_c is the temperature contrast driving mantle convection (i.e., the applied temperature contrast for 100% bottom heating, and the temperature contrast spanning a conductive geotherm in the absence of convection for the case of 100% volumetric heating).

Type II perturbations are constructed by raising mantle temperatures across a semicircular region of radius λ_p by the amount ΔT_p (with no imposed solidus ceiling). At the end of Section 3.6 we relate the parameters Θ and Λ of type II perturbations to the characteristic size and magnitude of type I perturbations resulting from impacts with a range of projectile radii and velocities, and model mantles with terrestrial and Martian properties. Note that according to our definition of type I perturbations, the corresponding value of Θ is mostly determined by the planet's thermal structure (i.e., the mean difference between solidus and geotherm, and the convective driving temperature) in the case of impacts large enough to significantly heat the lower mantle. In time-lapse movies of the temperature and velocity fields, all features of the post-heating evolution described in Section 3.3 for type I perturbations are also observed for perturbations of type II.

3.5 Time-scale of spreading

We turn now to quantifying the effects of impact heating for a thermal perturbation that can be described by a characteristic temperature and size (type II). Our goals in this section are to quantify properties of the qualitative description in Section 3.3, and especially the spreading time t_s at which the spreading stage ends, for a range of conditions. Above all, we seek an expression for t_s.

Scaling arguments

As mentioned in the previous section, the relevant dimensionless groups are the Rayleigh number Ra and two dimensionless numbers that characterize the magnitude and size of the perturbation, Θ and Λ, defined in equations (3.2) and (3.3). We start by posing an *ansatz* for the spreading time, as a scaling relation that comprises all of the relevant dimensionless groups:

$$t_s/t_m = f(\Lambda, \Theta, Ra_{(H)}) \tag{3.4}$$

$$t_s = K_0 \Theta^\alpha \Lambda^\beta Ra_{(H)}^\gamma \tag{3.5}$$

where t_m is a characteristic time-scale associated with convection and K_0 is a dimensional coefficient. ($Ra_{(H)}$ represents the volumetric- or bottom-heating Rayleigh number – whichever applies.) This general form can be motivated by considering the competition between the spreading motion of a viscous gravity current and convection in the ambient fluid. For example, a simple boundary layer theory supplies a characteristic velocity for 2D convection in the case of 100% bottom heating and a stress-free upper boundary (Schubert et al. [2001]):

$$v_{\text{conv}} = (1/3)(\kappa/\lambda_m) Ra^{2/3} \tag{3.6}$$

where κ is thermal diffusivity and λ_m is the convecting layer thickness. Assuming that motions in the ambient fluid can be ignored, the front-

velocity for a viscous gravity current that spreads along a stress-free boundary in two dimensions with an ambient density contrast $\Delta\rho_p$, constant cross-sectional area λ_p^2, and viscosity μ (for the current and ambient fluid), exhibits the following scaling with time t (Lister and Kerr [1989]):

$$v_{\text{grav}} \sim \left(\frac{\Delta\rho_p g \lambda_p^4}{\mu} \right)^{1/3} t^{-2/3}. \qquad (3.7)$$

To estimate the spreading time-scale, we can solve for the time when these two velocities become roughly equal. Because we are considering only temperature-related density contrasts, we may set $\Theta = \Delta\rho_p/\Delta\rho_m$ where $\Delta\rho_m$ is the density contrast driving mantle convection. Setting $\Lambda \equiv \lambda_p/\lambda_m$, we obtain by equating (3.6) and (3.7) and solving for t:

$$t_s \sim \frac{\lambda_m^2}{\kappa} \Theta^{1/2} \Lambda^2 Ra^{-1/2} \qquad (3.8)$$

In the case where equation (3.7) is replaced with the appropriate scaling relation for a viscous gravity current that spreads along a rigid boundary (Huppert [1982]), we instead find that $\alpha = 1/4$, $\beta = 3/2$, and $\gamma = -1/2$ in equation (3.5), where the Rayleigh number exponent is assumed to be 3/5 in equation 3.6 for this case. For a stress-free upper boundary and 100% volumetric heating, $\alpha = 1/2$, $\beta = 2$, $\gamma = -1/4$. As we will see later in this section, this simple scaling analysis gives a reasonable estimate for the values of α and γ, as well as the relative magnitude and sign of all the parameters in equation (3.5). In what follows, we derive empirically the values of these parameters using a large set of numerical calculations.

Numerical models and measured quantities

As before (Section 3.3), for each boundary condition and set of input parameters we obtained quasi-steady-state solutions of the governing equations (i.e., where the globally-averaged velocity is unchanging or fluctuates about a stable mean). We added perturbations of type II to these temperature field solutions and then computed the subsequent evolution until $t > t_s$.

Our calculations can be grouped into four sets, designated A, B, C, and D, according to upper boundary condition (no-slip or stress-free) and heat source (100% bottom- or volumetric heating). Each set is made up of five subsets, one for each of five Rayleigh numbers, where these are $Ra/10^5 = \{0.75, 2.50, 7.50, 10.0, 25.0\}$ for bottom heating and $Ra_H/10^5 = \{9.45, 23.6, 104, 154, 533\}$ for volumetric heating (as summarized in Table 3.1). For each Rayleigh number (i.e., in each subset) we performed 400 simulations, for every combination of 20 values of Θ and Λ, for a grand total of $4 \times 5 \times 400 = 8,000$ simulations. The values of Λ are $\{0.05, 0.10, 0.15..., 1.00\}$ for all subsets, and the range in Θ depends on the amount of internal heating (since this determines the convective driving temperature ΔT_c). Among the cases with bottom heating, many of the initial conditions (the starting solutions) are time-independent (see Table 3.1). See Section 3.3 for additional details regarding mesh dimensions and boundary conditions. Perturbations were emplaced between downwellings and plumes: i.e., centered on rolls.

At regular time intervals, we recorded the temperature and velocity at each row of nodes, averaged across the entire mantle width, as well as over one quarter of the width, centered on the perturbation ("quarter frame"). A time-series of the mantle velocity v averaged over the quarter frame is shown in the top panel of Figure 3-9 for one of the smallest and weakest perturbations, in a calculation belonging to set A ($Ra/10^5 = 7.5$, 100% bottom heating, stress-free upper B.C.). In the case of time-independent initial conditions like this one, even a weak perturbation has a noticeable effect. In this case, the mean flow velocity is not initially accelerated above the starting value of 7 mm/yr. Instead it drops to a minimum value which determines the "stagnation time," t_{stag} (dashed line). Movies of the temperature field for this case reveal that the perturbation hardly flattens or spreads at all (except by diffusion). Instead, the anomaly drifts into the nearest downwelling and is drained into it. The minimum velocity in the time-series of

Table 3.1: Estimated value of the parameter ξ for the impact magnitude $\Upsilon \equiv \Theta\Lambda^{\xi}$, obtained by minimizing the sum of standard deviations about a running average in plots of v_{stag} vs. $\Theta\Lambda^{\xi}$, to achieve an optimal collapse. Confidence limits (68.5%, 95.4%, 99.7%) were obtained from a bootstrap using $N = 1000$ random samplings with replacement. The abbreviations and labels signify the following: "set" identifies the calculation set; $Ra_{(H)}$ = the Rayleigh number; BC = upper boundary condition (where "f" = stress-free and "r" = rigid (i.e., no-slip)); "IC" = initial condition (where "t.i." = time-independent and "t.d." = time-dependent). "Ht" = heat source (where "b" = 100% bottom heating, "v" = 100% volumetric heating). Each subset (each line of the table) represents 400 calculations, and all were used to obtain estimates of ξ and the confidence limits. The unweighted average of ξ (for the entire table) is 3.02, with a standard deviation of 0.66.

set	$Ra_{(H)}/10^5$	BC	IC	Ht	ξ	68.3%	95.4%	99.7%
A	0.75	f	t.i.	b	2.1	± 0.03	± 0.17	± 0.27
A	2.50	f	t.i.	b	2.4	± 0.08	± 0.13	± 0.23
A	7.50	f	t.i.	b	2.8	± 0.02	± 0.12	± 0.18
A	10.0	f	t.i.	b	2.9	± 0.10	± 0.11	± 0.21
A	25.0	f	t.d.	b	3.0	± 0.06	± 0.16	± 0.46
B	0.75	r	t.i.	b	2.1	± 0.09	± 0.19	± 0.22
B	2.50	r	t.i.	b	2.5	± 0.06	± 0.16	± 0.24
B	7.50	r	t.d.	b	3.0	± 0.16	± 0.36	± 0.56
B	10.0	r	t.d.	b	2.6	± 0.12	± 0.28	± 0.38
B	25.0	r	t.d.	b	2.9	± 0.19	± 0.58	± 0.98
C	9.45	f	t.d.	v	2.0	± 0.47	± 0.97	± 1.13
C	23.6	f	t.d.	v	3.1	± 0.26	± 0.66	± 0.86
C	104	f	t.d.	v	4.3	± 0.37	± 0.94	± 1.34
C	154	f	t.d.	v	3.7	± 0.22	± 0.42	± 0.68
C	533	f	t.d.	v	2.9	± 0.13	± 0.27	± 0.37
D	9.45	r	t.d.	v	3.7	± 0.33	± 0.57	± 0.83
D	23.6	r	t.d.	v	2.9	± 0.55	± 1.25	± 1.75
D	104	r	t.d.	v	3.8	± 0.25	± 0.45	± 0.75
D	154	r	t.d.	v	3.6	± 0.27	± 0.37	± 0.53
D	533	r	t.d.	v	4.1	± 0.17	± 0.27	± 0.57

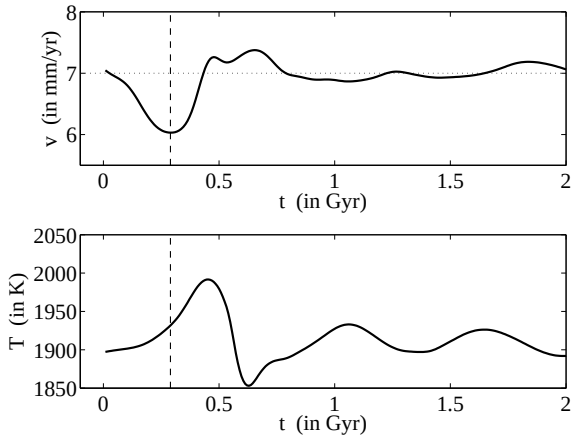

Figure 3-9: TOP: Plot of mean flow velocity for one-quarter slice of the mantle (centered on the perturbation), where the minimum value indicates the stagnation time $t_{\rm stag}$, marked with a dashed line ($Ra = 7.5 \times 10^5$, stress-free upper boundary, 100% bottom heating, $\Lambda = 0.25$, $\Theta = 0.11$). Although the perturbation in this case was small and low-temperature, its effects are noticeable in this initially time-independent solution. BOTTOM: For the same calculation, a plot of mean temperature of nodes at a fixed depth inside the basal TBL. Steadily increasing or decreasing temperature indicates a steadily thickening or thinning basal TBL, respectively. The global maximum indicates t_b, the time until maximum size and draining of the basal TBL, which is normally $\approx 1.5 t_{\rm stag}$.

Figure 3-9 occurs when the perturbation reaches the fastest portion of the downflow (i.e., when it interferes with the fastest region of the convective flow-field, at roughly 1/2 the mantle depth). Throughout the remainder of this report, "stagnation" refers to flow in the layer (or a portion of it) reaching a minimum averaged velocity, and does not mean that flow has halted. As we saw in Section 3.3, larger perturbations can create large zones that are virtually stagnant, and the name derives from this observation.

While the flow slows, the basal TBL thickens, and is drained shortly afterward at time t_b. This lapse ($t_b - t_{\rm stag}$) is illustrated in the time-series at the bottom of Figure 3-9, which shows the temperature at a fixed depth within the basal TBL. As the TBL thickens, this temperature increases, and decreases when the layer is drained while instabilities grow and detach, or become swept into adjacent plumes.

The corresponding time series are shown in Figure 3-10 for the same convection model and starting condition although with a stronger perturbation, where $\Lambda = 0.5$ and $\Theta = 0.59$. In this case, the quarter-frame averaged velocity is accelerated to nearly three times its pre-perturbation value (v_0) and plummets during the short-lived flattening stage. The temporal minimum of velocity averaged over a quarter slice of the mantle is less than half of v_0. The thickening and draining of the basal TBL is readily noticeable in the corresponding time series for temperature at a fixed depth in this layer (bottom panel, Figure 3-10). By recording the times of the velocity minimum ($t_{\rm stag}$) and temperature maximum (t_b) in these time-series for all calculations, we find that a value $t_b/t_{\rm stag} \approx 1.5$ occurs with the greatest frequency.

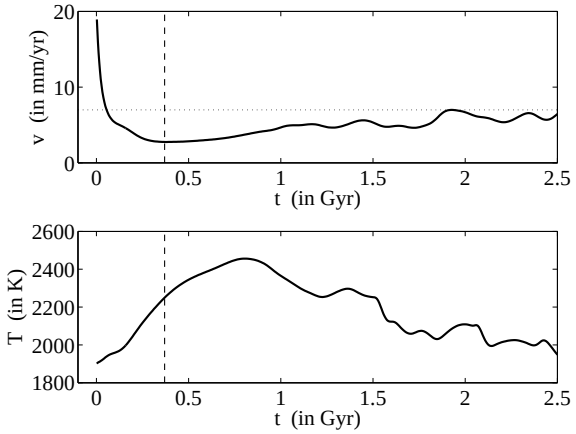

Figure 3-10: The same quantities as plotted in Figure 3-9 from an identical starting condition, although with a stronger perturbation ($\Lambda = 0.50$, $\Theta = 0.59$). The quarter-frame averaged velocity is initially accelerated well above the pre-perturbation value of 7 mm/yr (dotted line), and drops to less than half this value at the stagnation time (dashed line).

We have estimated the spreading time t_s indirectly, by measuring two timescales which are

coupled to the spreading time for a range of conditions. These are the stagnation time, $t_{\rm stag}$, and the "leveling time," $t_{\rm lev}$. This correspondence was noted in time-lapse movies of the temperature field, generated for a subset of all calculations. The stagnation time is reached when the mean mantle velocity in the quarter frame (one-quarter slice of the mantle centered on the perturbation), averaged over long time intervals, reaches its minimum value. This occurs after spreading has ceased, and remnants of the perturbation sink into nearby downwellings, causing the fastest regions of the velocity field to slow down. For a range of conditions, the spreading timescale is therefore approximately equal to the stagnation time-scale minus the time required for perturbation remnants to sink into nearby downwellings, $t_{\rm sink}$. This latter time is a function of the Rayleigh number only. Defining t_{s1} to be an estimate of the spreading time t_s derived from the stagnation time-scale, we can write:

$$t_{\rm stag} = t_{\rm sink} + t_{s1} \Longrightarrow t_{s1} = t_{\rm stag} - g_1(Ra_{(H)}) \tag{3.9}$$

where g_1 is some function of $Ra_{(H)}$.

For each calculation we have stored at regular time intervals the horizontal temperature profile at the base of the pre-impact upper TBL. The quantity σ_T is the standard deviation of this domain-spanning temperature profile. The "leveling timescale" $t_{\rm lev}$ is defined as the time when σ_T reaches its minimum value. This corresponds to a time when the spreading flow has slowed or halted, so that no additional downwellings are destroyed or fused (which causes σ_T to decrease) and before new ones emerge (which causes σ_T to increase). Therefore, for a range of conditions, $t_{\rm lev}$ approximately corresponds to the end of spreading. The leveling time is offset from the spreading time estimate t_{s2} by a quantity that depends on $Ra_{(H)}$ in the case of sets B and C, and Ra in addition to Θ in the case of set A:

$$t_{s2} = t_{\rm lev} - g_2(\Theta, Ra_{(H)}) \tag{3.10}$$

Figure 3-11 depicts the approximately linear trend of both timescales as a function of Λ for a subset of calculations in set A (i.e., stress-free upper boundary, 100% bottom heating, and $Ra = 10^6$, $\Theta = 0.32$). The functions g_1 and g_2 in equations (3.9) and (3.10) were estimated by fitting a line to plots of $t_{\rm lev}$ and $t_{\rm stag}$ versus Λ to obtain the intercept values. These results are supplied in Table 3.2.

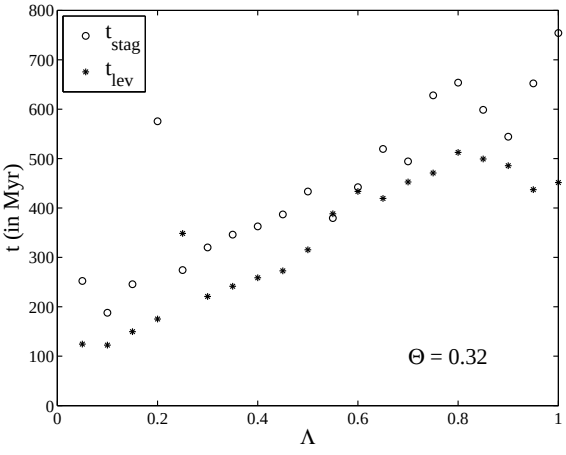

Figure 3-11: Stagnation and Leveling time-scales ($t_{\rm stag}$ and $t_{\rm lev}$, respectively) versus dimensionless perturbation size Λ, for dimensionless perturbation temperature $\Theta = 0.32$ (Set A; $Ra = 10^6$, stress-free upper boundary, 100% bottom heating). Both are approximately linear functions of Λ up to $\Lambda = 0.8$, where the spreading anomaly reaches a global extent. Subtracting the y-axis intercepts, both quantities are estimates of the spreading time (t_{s1} and t_{s2}, respectively).

We have said that equations (3.9) and (3.10) are valid for a range of conditions, and we turn now to describing these. These conditions have been determined from close examination of movies generated for the evolution of the temperature and velocity fields for a subset of the calculations in each of the sets A, B, and C.

The rollover in $t_{\rm lev}$ that occurs at $\Lambda = 0.8$ in Figure 3-11 is a common feature of such curves. This corresponds to a configuration of the temperature field in which nearly all downwellings have been swept together or destroyed. Larger perturbation sizes only cause the system to achieve this configuration sooner (i.e., $t_{\rm lev}$ decreases with larger Λ). In the case of large Θ, this corresponds to the spreading-flow reaching

Table 3.2: Estimated parameter values for expressions relating the Stagnation and Leveling time-scales to perturbation size, perturbation temperature, and Rayleigh number. In general, $\{t_{\rm stag}, t_{\rm lev}\} = f(\Theta, \Lambda, Ra_{(H)})$, where f is a nontrivial function of these variables. For a range of conditions, $\{t_{\rm stag}, t_{\rm lev}\} \approx \{t_{s1}, t_{s2}\} + K_1 \Theta^{\zeta} Ra_{(H)}^{\eta}$, where the relation for spreading time-scale has the form $\{t_{s1}, t_{s2}\} = K_0 \Theta^{\alpha} \Lambda^{\beta} Ra_{(H)}^{\gamma}$ (see Table 3.3). Estimates of ζ and η are supplied in the table below for $t_{\rm stag}$ and $t_{\rm lev}$ in sets A-C. Only in the case of set A and the quantity $t_{\rm lev}$ is ζ nonzero. In this case, $\zeta = 0.40$ (68.3% confidence limit: ± 0.07; 95.4% confidence limit: ± 0.17), and $\eta = -0.50$ (68.3% confidence limit: ± 0.06; 95.4% confidence limit: ± 0.10). Confidence limits were obtained from a bootstrap using $N = 1000$ random samplings with replacement. Since these correspond to the values of α and γ, respectively, $t_{\rm lev} \approx (K_0 \Lambda^{\alpha} + K_1) \Theta^{\beta} Ra_{(H)}^{\gamma}$ for this case only. The abbreviations and labels signify the following: "set ID: t" identifies the calculation set and the time-scale; $Ra_{(H)}$ = range in Rayleigh numbers; BC = upper boundary condition (where "f" = stress-free and "r" = rigid (i.e., no-slip)); "IC" = initial condition (where "t.i." = time-independent and "t.d." = time-dependent); "Ht" = heat source (where "b" = 100% bottom heating, "v" = 100% volumetric heating).

set ID: t	$Ra_{(H)}/10^5$	BC	IC	Ht	$K_1/10^5$	ζ	η
$A : t_{\rm stag}$	$[0.75, 10]$	f	t.i.	b	5.33	0.00	-0.59
$B : t_{\rm stag}$	$[0.75, 2.5]$	r	t.i.	b	1.97	0.00	-0.44
$A : t_{\rm lev}$	$[0.75, 10]$	f	t.i.	b	1.29	0.40	-0.50
$B : t_{\rm lev}$	$[0.75, 7.5]$	r	t.i.	b	0.331	0.00	-0.31
$C : t_{\rm lev}$	$[100, 530]$	f	t.d.	v	1810	0.00	-0.99

a global extent. This feature of $t_{\rm lev}$is therefore a consequence of the system's finite size.

Rollovers and plateaus of this sort also occur in plots of $t_{\rm stag}$ versus Λ, at values of Λ above which the perturbation destroys nearby downwellings, causing the flow in this region (the quarter-slice centered on the perturbation) virtually to stagnate. In these cases, the quarter-sample averaged velocity is not sensitive to (decouples from) the large-scale spreading flow, so that $t_{\rm stag}$ does not reflect t_s.

It should be noted also that t_{s1} and t_{s2} are estimates of the time when the spreading flow is slowed and then halted by downwellings on one of the two spreading fronts (e.g., see frames t_3 through t_5 in Figure 3-5: leftward spreading current). In those cases where the spreading flow is greatly slowed by a downwelling that is ultimately breached (i.e., severed and bypassed), the spreading time can greatly exceed the trend shown in Figure 3-11. Examples of these obvious outliers are represented by the points $\Lambda = 0.2$ and $\Lambda = 0.25$. For this reason, t_{s1} and t_{s2} should be considered to represent a lower bound for the absolute spreading time-scale t_s.

Finally, there are numerous cases for which either $t_{\rm stag}$ or $t_{\rm lev}$ (or both) are completely decoupled from the spreading timescale, for most or all perturbation magnitudes. This is often the case for time-dependent initial conditions, where the spontaneous emergence and disappearance of downwellings, near and far away from the spreading region, plays a large role in determining $t_{\rm stag}$ and $t_{\rm lev}$. For example, none of the calculations in set D (100% volumetric heating with a no-slip upper boundary) could be used for this part of the analysis. The stagnation time was only coupled to the spreading time for the initially time-independent solutions in the case of 100% bottom heating. Significantly, however, the leveling timescale was strongly coupled to the spreading timescale for three Rayleigh numbers in set C, all with strongly time-dependent initial conditions (100% volumetric heating, stress-free upper boundary).

Estimated parameter values

We have estimated the values of the exponents in equation (3.5) for t_{s1} and t_{s2} by means of a simple parameter search, minimizing the norm of residuals from a least-squares linear regression in log-log space. Only those calculations satisfying the aforementioned conditions were used in the inversion. For each set of calculations (A, B, and C), the inversion was first performed for each Rayleigh number separately. This revealed a significant crossover transition from a distinct behavior at very small perturbation magnitudes. We performed the inversion twice for each Rayleigh number, in one case keeping and in the other excluding perturbation magnitudes below the crossover transition. The inversion was also performed for calculations derived from each set as a whole (multiple Rayleigh numbers), as shown in Figure 3-12 for calculations in sets A and B. The estimated exponent values for this global inversion are supplied in Table 3.3. We have reported also the 95.4% confidence limits obtained from a bootstrap analysis, using $N = 1000$ random samplings with replacement (Press et al. [1988]). The results from the inversions performed separately for each Rayleigh number are printed in Appendix A, in Tables A.1 and A.2 along with the crossover transition for each case. There was no crossover transition noted for t_{s2} in set C, and therefore no threshold was applied.

According to the results in Table 3.3, estimates of α, β, and γ for t_{s1} are essentially identical for free and rigid upper boundaries in the case of bottom heating ($\alpha \approx 0.3$, $\beta \approx 1.0$, $\gamma \approx -0.5$), where the crossover threshold has been applied. For the case of t_{s2}, the estimates of β concur for both boundary conditions and for bottom- as well as volumetric heating ($\beta \approx 1.0$). The estimates of γ (for t_{s1} and t_{s2}) agree for the case of bottom heating, and are very different (as expected) for volumetric heating. The most significant difference occurs in the estimates of α for t_{s2}. In particular, α is larger than corresponding estimates for t_{s1}, and its value for the case of a no-slip upper boundary ($\alpha = 0.62$) is significantly greater than its value for the case of a stress-free upper boundary ($\alpha = 0.40$). Finally, note that the estimated values of α and β for t_{s2} in set C (free upper boundary, 100% volumetric heating) are essentially indistinguishable from the estimates of α and β for t_{s1} in set A (free upper boundary, 100% bottom heating).

In summary, the results in Table 3.3 suggest that $\beta \approx 1$ for both boundary conditions and heat sources, $\gamma \approx -0.5$ for bottom heating (both boundary conditions) and $\gamma \approx -0.13$ for volumetric heating and a free upper boundary. Estimates of the exponent α range from 0.3 to 0.4 for the case of a stress-free upper boundary, and from 0.33 to 0.62 for the case of a rigid upper boundary. It is worth noting that the simple estimates obtained by deriving equation (3.8) were not far from the mark in the case of α and γ, and predicted correctly that $\beta > \alpha > \gamma$.

3.6 Global stagnation criterion

We turn now to finding those values of Θ and Λ which guarantee that a perturbation reorganizes the circulation in model mantles at a global scale. As already mentioned, one of the most significant consequences of the perturbation-driven flow is that mantle velocities are greatly depressed. To begin, we define the "stagnation velocity" v_{stag} as the minimum (in time) of the globally-averaged mantle velocity. We find that v_{stag} is a nontrivial function of the quantity $\Theta\Lambda^{\xi}$, which therefore provides a convenient measure of the perturbation magnitude in terms of its effect on the mantle as a whole. The value of the exponent ξ was estimated by means of a simple parameter search, minimizing the sum of standard deviations about a running average of v_{stag} in order of increasing $\Theta\Lambda^{\xi}$. The estimated values of ξ are reported in Table 3.1, along with confidence limits derived from a bootstrap analysis. It is worth noting a possible trend in ξ with increasing Rayleigh number, although an exact relationship is hard to establish based on these results. The mean value of ξ, when averaging over all subsets in Table 3.1, is 3.02. In what follows, the "perturbation magnitude" refers to the quantity $\Upsilon \equiv \Theta\Lambda^3$.

Table 3.3: Estimated parameter values for spreading time-scale relations, $\{t_{s1}, t_{s2}\} = K_0 \Theta^\alpha \Lambda^\beta Ra^\gamma$, obtained by means of a simple parameter search, minimizing the norm of residuals from a least-squares linear regression in log-log space. Also given are 95.4% confidence limits obtained from a bootstrap ($N = 1000$ random samplings with replacement), where: "set ID: t" identifies the calculation set and the time-scale; $Ra_{(H)}$ = range in Rayleigh numbers; BC = upper boundary condition (where "f" = stress-free and "r" = rigid (i.e., no-slip)); "IC" = initial condition (where "t.i." = time-independent and "t.d." = time-dependent); "Ht" = heat source (where "b" = 100% bottom heating, "v" = 100% volumetric heating); "c.c." indicates whether a threshold was applied to remove perturbations below the crossover transition; n indicates the number of simulations used in the inversion (i.e., model results for a given perturbation size and temperature). Estimated parameter values for individual subsets (for individual Rayleigh numbers) are supplied in Tables A.1 and A.2 of Appendix A, along with the crossover condition for each case.

set ID:t	$Ra_{(H)}/10^5$	BC	IC	Ht	c.c.	n	$K_0/10^5$	α	β	γ
$A : t_{s1}$	$[0.75, 10]$	f	t.i.	b	N	767	6.97	0.30 ± 0.03	0.92 ± 0.02	-0.50 ± 0.01
$A : t_{s1}$	$[0.75, 10]$	f	t.i.	b	Y	552	6.97	0.29 ± 0.02	1.01 ± 0.02	-0.49 ± 0.01
$B : t_{s1}$	$[0.75, 2.5]$	r	t.i.	b	N	185	12.2	0.42 ± 0.09	1.07 ± 0.04	-0.50 ± 0.03
$B : t_{s1}$	$[0.75, 2.5]$	r	t.i.	b	Y	119	9.84	0.33 ± 0.06	1.03 ± 0.06	-0.53 ± 0.02
$A : t_{s2}$	$[0.75, 10]$	f	t.i.	b	N	911	10.4	0.37 ± 0.02	1.07 ± 0.05	-0.51 ± 0.02
$A : t_{s2}$	$[0.75, 10]$	f	t.i.	b	Y	747	10.3	0.40 ± 0.03	0.96 ± 0.03	-0.52 ± 0.01
$B : t_{s2}$	$[0.75, 7.5]$	r	t.i.	b	N	418	12.5	0.65 ± 0.06	1.05 ± 0.05	-0.48 ± 0.02
$B : t_{s2}$	$[0.75, 7.5]$	r	t.i.	b	Y	381	14.4	0.62 ± 0.05	0.96 ± 0.04	-0.50 ± 0.02
$C : t_{s2}$	$[104, 533]$	f	t.d.	v	N	309	0.147	0.30 ± 0.03	1.03 ± 0.04	-0.13 ± 0.04

We define "global stagnation" as an event in which the globally-averaged mantle flow velocity is depressed three standard deviations below its temporal mean, $\bar{v}$: i.e., $v < \bar{v} - 3\sigma_v$ where σ_v is the temporal standard deviation about $\bar{v}$ prior to insertion of the anomaly. The critical perturbation magnitude Υ_{crit} is that value of Υ above which all perturbations cause global stagnation. Figure 3-13 shows v_{stag} as a function of the perturbation magnitude for the case of 100% bottom heating, a stress-free upper boundary, and $Ra = 2.5 \times 10^6$ (a time-dependent initial condition). The value of $\bar{v} - 3\sigma_v$ has been labeled, along with Υ_{crit}. First, it is worth noting that this curve has a nontrivial shape. The shape of $v_{\text{stag}} = f(\Upsilon)$ is different for each set in Table 3.1, often differing among subsets (i.e., different Rayleigh numbers). Second, it should be emphasized that while global stagnation occurs in many calculations for which $\Upsilon < \Upsilon_{\text{crit}}$, this quantity ($\Upsilon_{\text{crit}}$) has been defined as the perturbation magnitude above which all perturbations cause global stagnation. In this way, the condition guarantees that global stagnation is a direct consequence of the spreading flow, and not of an interaction between the spreading flow and a fortuitous configuration of the pre-existing convection pattern. Note that for those subsets with a time-independent initial condition, the measured value of σ_v is vanishingly small. For those cases, we set $\sigma_v \equiv 0.12\bar{v}$, which is typically observed for time-dependent solutions.

In Figure 3-14 we show the dependence of Υ_{crit} upon the Rayleigh number, where the explicit relation is supplied in the box at right for each of the sets A, B, C, and D. For all cases, we find that $\Upsilon_{\text{crit}} = f(Ra)$ has the form: $\Upsilon_{\text{crit}} = C_0 Ra^{-q}$, where $0 < q < 1$. Significantly, the critical perturbation magnitude decreases as an inverse power law of the Rayleigh number. As the Rayleigh number increases, the perturbation magnitude required for global stagnation decreases most rapidly for volumetric heating and a stress-free upper boundary ($\Upsilon_{\text{crit}} \sim Ra^{-0.83}$) and most gradually for volumetric heating and a no-slip upper boundary ($\Upsilon_{\text{crit}} \sim Ra^{-0.48}$). It

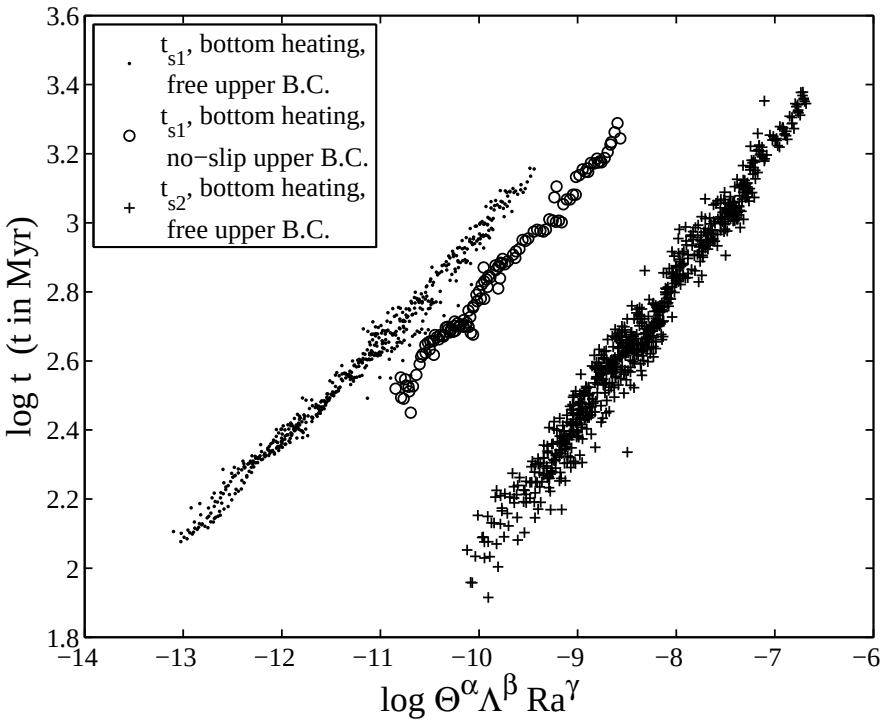

Figure 3-12: Spreading time-scales t_{s1} and t_{s2} plotted as a function of $\Theta^{\alpha}\Lambda^{\beta}Ra^{\gamma}$, where the exponents have been estimated using a simple parameter search, minimizing the norm of residuals from a least-squares linear regression in log-log space. Note that each data cloud corresponds to a different set of estimated parameter values (for α, β, and γ) where these are listed in Table 3.3 along with 95.4% confidence limits and the range in Rayleigh number. Points below the crossover limit were excluded (see text for discussion).

should be remembered, however, that Ra and Θ are not independent, since $Ra \sim \Delta T_c$ and $\Theta \equiv \Delta T_p / \Delta T_c$. For a given dimensionless perturbation size Λ, the critical perturbation temperature $(\Delta T_p)_{\rm crit}$ therefore scales with Ra as $(\Delta T_p)_{\rm crit} \sim Ra^{1-q}$.

Figure 3-15 can be used to relate perturbations of type I to perturbations of type II and the critical perturbation magnitude, $\Upsilon_{\rm crit}$, assuming that the relations in Figure 3-14 are valid for (can be extended to) the large internal-heating Rayleigh numbers of early terrestrial mantles (10^9 to 10^{10}). We have plotted $\Upsilon_{\rm crit}$ for 100% volumetric heating, for both free- and no-slip upper boundaries. Each point represents a different projectile radius R and vertical incident velocity v_i indicated by the marker symbol and size. These can be translated to corresponding values of Θ and Λ, and compared with $\Upsilon_{\rm crit}$. Points lying above the curves of constant $\Upsilon_{\rm crit}$ represent perturbations that would cause global stagnation for model mantles with terrestrial and Martian properties (e.g., shock EOS, mantle thickness with respect to depth of impact heating, and convective driving temperature).

For both cases we have chosen a convective driving temperature ΔT_c appropriate for the early solar system. The convective driving temperature for the case of volumetric heating – the temperature contrast spanning a conductive profile in the absence of convection – is given by: $\Delta T_c = \rho H \lambda_m^2 / 2k$, where ρ is a characteristic density, H is the internal heating, λ_m is the mantle thickness, and k is thermal conductivity. For the Earth we have assumed: $\rho = 4,000$ kg/m^3, $\lambda_m = 2,870$ km, and $k = 10$ W/K-m. (The value of thermal conductivity in the Earth's lower mantle is a matter of controversy;

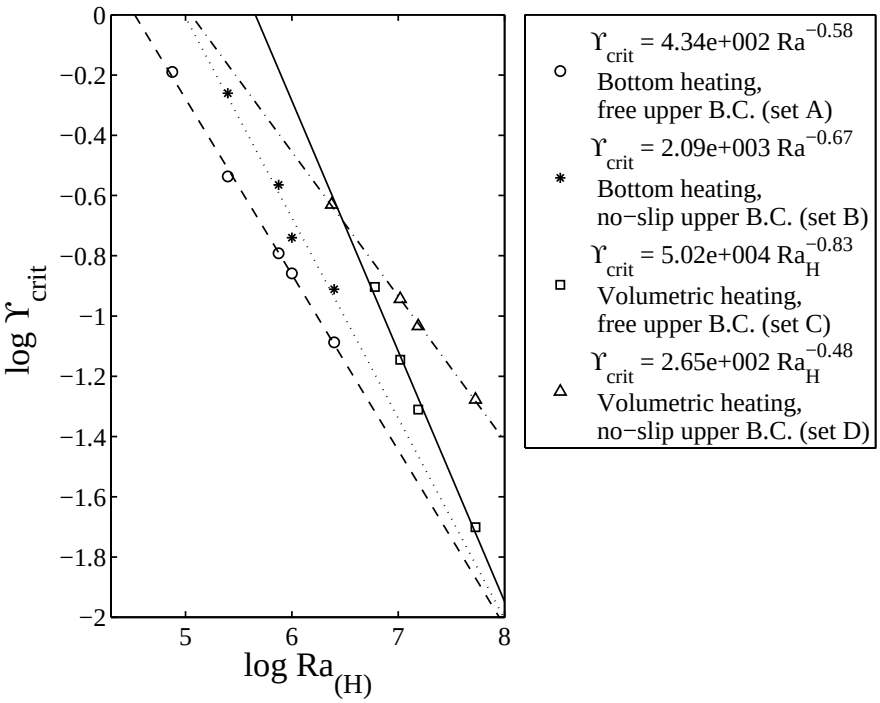

Figure 3-14: Critical perturbation magnitude $\Upsilon_{\rm crit}$ versus Rayleigh number, and linear fits used to obtain the global stagnation criterion for the following conditions: 100% bottom heating with free- and no-slip upper boundaries; 100% volumetric heating with free and no-slip upper boundaries. Note that an internal heating Rayleigh number is used for the latter two cases. For all values of the perturbation magnitude $\Upsilon \equiv \Theta\Lambda^3 > \Upsilon_{\rm crit}$, the globally-averaged mantle flow velocity is depressed 3σ below its temporal mean prior to anomaly insertion, $\bar{v}$. Note that not all subsets in Table 3.1 were used; for some of the low-Ra subsets, $\bar{v} - 3\sigma_v$ was not reached for any of the impact magnitudes considered.

the value we have chosen lies at the middle of the range of reported estimates (Schubert et al. [2001]).) For the case of Mars we have assumed: $\rho = 3,400$ kg/m^3, $\lambda_m = 1,700$ km, and $k = 4$ W/K-m (Schubert and Spohn [1990], Yoder et al. [2003]). The value of H depends on the density of radiogenic heat production in the mantle. We assume the same value for Earth and Mars, based upon a modern estimate for the terrestrial mantle projected backwards in time using known decay constants, as commonly used in thermal history models:

$$H = \frac{1}{\rho}(1.7 \times 10^{-7}\ \mathrm{Wm}^{-3}) \exp(-1.38 \times 10^{-17} t) \tag{3.11}$$

where t is the time since planet formation in seconds (Stevenson et al. [1983], Schubert et al. [2001]). Assuming a time that corresponds to the Late Heavy Bombardment (~ 500 Myr), we obtain $\Delta T_c = 5.5 \times 10^4$ K for the Earth and $\Delta T_c = 4.2 \times 10^4$ K for Mars. We have reproduced the plots in Figure 3-15 for modern and intermediate values of the driving temperature in Appendix A, Figures A-1 and A-2.

Finally, the perturbation temperature ΔT_p, which represents the separation between geotherm and solidus, is plotted in Figure 3-15 for $\Delta T_p = \{1000, 650, 400, 250, 150, 100\}$ K (from top to bottom). It should be remembered that higher Rayleigh numbers imply a hotter mantle, so that geotherms approach the solidus, limiting the size of ΔT_p and therefore of $\Theta \equiv \Delta T_p / \Delta T_c$. As Figure 3-15 shows for the terrestrial case, global stagnation in model mantles can be expected for $R \geq 600$ km at

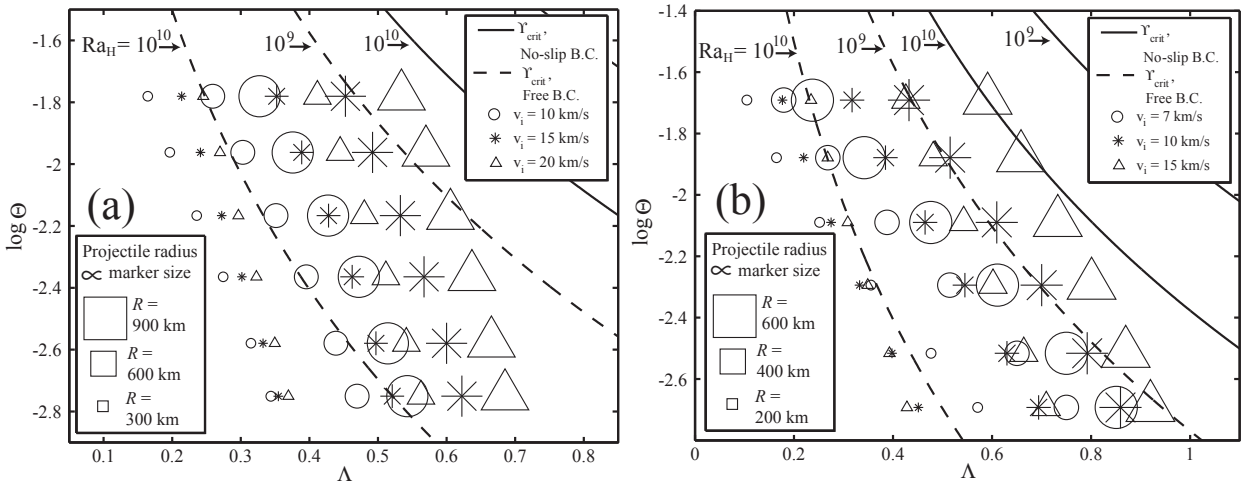

Figure 3-15: Diagrams relating perturbations of type I to perturbations of type II and the global stagnation criterion, $\Upsilon \equiv \Theta\Lambda^3 > \Upsilon_{\rm crit}$ for internal-heating Rayleigh numbers 10^9 and 10^{10} in the case of a rigid- (solid lines) and stress-free upper boundary (dashed lines), for a model mantle with (a) terrestrial and (b) Martian dimensions and material properties (i.e., used to calculate shock-heating). In each case we have chosen an effective driving temperature ΔT_c appropriate for the early solar system (i.e., the temperature contrast spanning a conductive geotherm in the absence of convection for 100% volumetric heating; see text for discussion). In the case of Earth (a), $\Delta T_c = 5.5 \times 10^4$ K; and in the case of Mars (b), $\Delta T_c = 4.2 \times 10^4$ K. Each point represents a projectile radius, R, and incident velocity, v_i, which can be related to the dimensionless perturbation temperature and size, Θ and Λ, respectively (where the peak shock pressure decays with exponent $n = n_0$ and the "climbing-shock" method was used to calculate the amount of heating). Points that lie above a given solid or dashed curve satisfy the global stagnation criterion for the corresponding Rayleigh number and upper boundary condition, and therefore will depress the globally-averaged mantle flow velocity to 3σ below its temporal mean value prior to anomaly insertion. The perturbation temperature, which respresents the separation between geotherm and solidus is, from top to bottom, $\Delta T_p = \{1000, 650, 400, 250, 150, 100\}$ K (where $\Theta = \Delta T_p / \Delta T_c$). Note that Λ corresponds to the dimensionless mantle depth at which the shock-heating curve crosses the solidus. See text for a discussion of values assumed for other mantle properties, and Section A.2 of Appendix A for the same diagrams with different values assumed for ΔT_c.

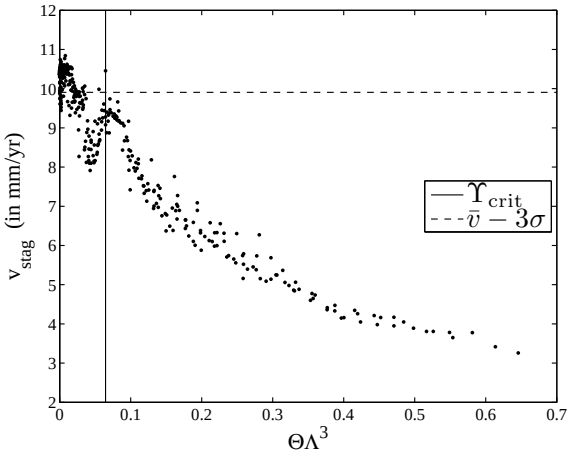

Figure 3-13: Stagnation velocity $v_{\rm stag}$ (i.e., temporal minimum of the globally-averaged velocity following anomaly insertion) versus perturbation magnitude $\Upsilon = \Theta\Lambda^3$ for $Ra = 2.5 \times 10^6$ in the case of 100% bottom heating and a stress-free upper boundary (N.B., a time-dependent initial condition). The critical perturbation magnitude ($\Upsilon_{\rm crit}$) corresponds to that value of $\Theta\Lambda^3$ above which all perturbations depress the globally-averaged mantle velocity to 3σ below its mean value.

incident velocities in the range 15-20 km/s only for the extremely high internal heating Rayleigh number $Ra_H = 10^{10}$ and a stress-free upper boundary. For the Martian case, projectiles with $R \geq 600$ km and incident velocity $v_i \geq 7$ km/s will cause global stagnation for $Ra_H = 10^{10}$ and a stress-free upper boundary; $v_i \geq 15$ km/s and the same radius assures the condition is met for $Ra_H = 10^9$. Perturbations in the range considered are not guarenteed to cause global stagnation for either model if the upper boundary is rigid (no-slip).

3.7 Alternative convection models

Convection models with temperature-dependent viscosity are likely to respond in different ways to thermal perturbations, where this will depend heavily on the the resulting viscosity contrasts. As mentioned, the time-scale of viscous relaxation in the flattening stage is controlled by the ambient viscosity (outside of the perturbation) and the anomalous buoyancy of the perturbation itself, so that temperature-dependent viscosity is unlikely to have a significant effect in this stage. Monteux et al. [2007] found that the time- and length- scaling for viscous-drop spreading in the transition from the advective- to the diffusive- regime is mostly unchanged by a strongly temperature-dependent viscosity. Nonetheless, because the interaction with downwellings is what mostly controls the duration of the spreading stage in our models, significant changes to their mechanical properties will likely affect the nature of this interaction and therefore also the spatial and temporal extent of the perturbation-driven flow.

In general, convection models with a small viscosity contrast – a maximum/minimum viscosity ratio of less than 100 – will resemble the isoviscous case, since the mechanical properties of the thermal boundary layer are similar to those of the mantle as a whole (Solomatov [1995]). For higher viscosity ratios, convection is largely controlled by the sluggish motions of a thick and highly viscous upper boundary layer (Solomatov [1995]). Thick and slow-moving downflows firmly rooted in the sluggish lid may halt the motions of the low-viscosity spreading current upon collision. Alternatively, foundering slabs that are sufficiently thin may be weakened by the high-temperatures of the anomaly and severed by the spreading motion.

For thick stagnant lids, all but very large perturbations will reside mostly in the immobile upper boundary layer, and will have essentially no dynamical consequence for convection in the mantle. Nonetheless, convection in the approximately isothermal regions beneath a stagnant lid and between broadly-spaced sluggish downflows may respond to the largest thermal anomalies in a way that is similar to what occurs in our simulations. Since the convective driving temperature is largely determined by the overall viscosity contrast, this quantity will be significantly smaller than what has been assumed in our isoviscous models. Insofar as plumes control the location of magmatic centers in a stagnant-lid

mantle, the most significant consequence of the perturbation-driven flow might be the tendency for plumes to become concentrated near the center of the spreading region.

Our simulations were conducted using a two-dimensional geometry, and the dynamics in three dimensions are likely to be different in important respects. The tendency of a vertical shearing flow to suppress Rayleigh-Taylor instabilities at the upper and lower boundary layers will have the greatest effect upon convective motions that are transverse to this flow (Richter [1973]): i.e., transverse to radial spreading. Time- and length- scaling with respect to perturbation magnitude will change because the flattening and spreading of the perturbation reaches a smaller spatio-temporal extent as its volume is spread out (and driving buoyancy exhausted) over three dimensions rather than two. In 3D, upward flows in high-Ra convection assume a wide range of shapes depending on the amount of internal heating, from cylindrical plumes to diffuse and broad-scale upwellings. The scale of spreading may be limited less by three-dimensional structures: e.g., plumes in 2D can significantly erode and even "behead" the spreading front, while a three-dimensional spreading flow can partially circumvent these structures. Downwellings are barriers to lateral flow in two dimensions, whereas in 3D only very long sheet-like downflows will retard the motion completely in one of multiple directions.

Going forward, this work can be extended in several ways. As mentioned, it is worthwhile repeating this exercise for more realistic temperature- and stress-dependent rheologies and geometries in order to obtain the scaling in these cases for the spreading time and global stagnation criterion. In addition to the important differences mentioned above, since the growth rate of proto-diapirs depends inversely upon the ambient viscosity, the effects of direct heating of the CMB will be more pronounced, since even temperature changes of hundreds of degrees will modify mantle viscosities above the basal TBL by orders of magnitude. It will be important also to use realistic estimates of the buoyancy associated with retained melts in the shock-heated volume. For this purpose, the same experiments can be conducted with perturbations having a material instead of thermal buoyancy.

3.8 Geological implications

Owing to significant simplifications in our models, as well as our limited knowledge of the thermal state and structure of young planetary interiors, it is not possible to draw firm conclusions from our work regarding the evolution of early terrestrial mantles, or to apply directly the scaling relationships obtained above. Nonetheless, some of the processes that occur in our simulations may have played an important role in the early solar system, and we turn now to consider these in the context of early Mars as a way of highlighting significant questions for further study.

Recent work has demonstrated the plausibility of a giant-impact origin for the crustal dichotomy (Marinova et al. [2008], Nimmo et al. [2008]). Andrews-Hanna et al. [2008] extended the dichotomy boundary beneath Tharsis, completing the circumference of an immense, elliptical impact basin. Mars' internal magnetic field possibly survived dichotomy formation, since small magnetic anomalies occur in the northern lowlands that were not erased by subsequent magmatism (Acuna et al. [1999]). If mantle convection had not already reached the highly sluggish or stagnant lid regime by the the time of the dichotomy-forming impact, then the resulting buoyancy perturbation might have had profound consequences for convection in the mantle. Assuming that the "stagnation" effect illustrated in our models occurs also in three-dimensional spreading flows for relevant rheologies, this current might well have suppressed convection throughout portions of the Martian mantle. Processes which tend to diminish the efficiency of mantle convection prevent efficient cooling of the core-mantle boundary and therefore tend to suppress convection in the outer core as well (Stevenson [2001]). The spreading stage that followed a Borealis impact (and

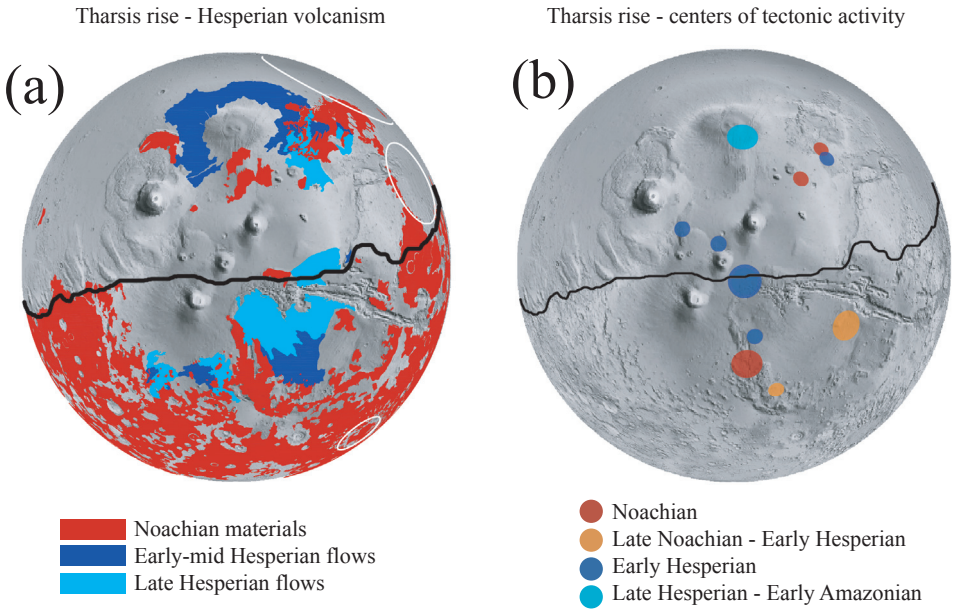

Figure 3-16: (a) Amalgamated geologic units for Noachian-aged materials and Hesperian lava flows on the Tharsis rise mapped in Scott and Tanaka [1986]. (b) Primary and secondary centers of tectonic activity reported in Anderson et al. [2001] obtained from great-circle intersections of stress-field directions derived from the orientations of tectonic structures. The dichotomy boundary from Andrews-Hanna et al. [2008] is plotted in black.

possibly subsequent large impacts) might have hastened the extinction of the Martian dynamo and internal magnetic field. This mechanism would not permanently suppress the dynamo, however, since mantle convection resumes when the spreading stage has ended. A significant interruption of convection in the mantle, depending on the time-scale of its duration, is an important consideration for thermal history models as well.

It is not known when Tharsis volcanism began, but many lines of evidence suggest that a significant proportion of this immense crustal load was in place by the late Noachian (Banerdt and Golombek [2000], Anderson et al. [2001], Phillips et al. [2001]), and that volcanism on Tharsis waned through the Hesperian but continued to recent times (Anderson et al. [2001], Hartmann and Neukum [2001]). It has been suggested that most of Tharsis volcanism was caused by a shallow-mantle upwelling induced by an impact-related buoyancy perturbation (Reese et al. [2004]) associated with the dynamic adjustment that occurs during the "flattening stage" (see Section 3.3). However, a recent inversion of gravity and topography used to reconstruct the isostatic crustal root that formed prior to volcanic loading does not reveal an impact basin beneath Tharsis (Andrews-Hanna et al. [2008]). Numerous studies have suggested that a long-lived deep mantle plume or plumes constructed the bulk of this province (e.g., Harder and Christensen [1996], Kiefer [2003]).

One of the interesting applications of our work concerns the interaction between deep mantle plumes (constructing Tharsis) and a spreading current (from a Borealis impact), and which is based upon the description in Section 3.3, illustrated in Figure 3-5. First, if the plume has reached the lithosphere before the spreading current arrives, then it is deflected southward by the spreading flow. This will cause the locus of magmatism to migrate southward until flux in the plume is suppressed and magmatism is halted

for some time. As the intensity of the spreading flow diminishes, the plume begins to right itself, so that magmatism resumes and its locus migrates northward towards the [planimetric] position of its root. Meanwhile, if the return flow is significant (along the base of the mantle), the root will have been displaced northward as well. When the plume has straightened completely, its flux is greatest and magmatism is most intense. If instead the plume emerges while the spreading flow is underway, then the first step in this process does not occur (i.e., magmatism begins in the south and intensifies while the plume is righted and the locus of magmatism migrates north). Anderson et al. [2001] observed a migration northward from the Noachian to the late Hesperian of primary centers of tectonic activity on the Tharsis rise, where these have been plotted for reference in Figure 3-16. In that study, the density function from which primary and secondary centers were derived has a marked north-south elongation during the Noachian. These observations, in light of the foregoing discussion, at least recommend the possibility that construction at Tharsis was influenced by a southward spreading flow. As the spatial-temporal development of the Tharsis rise is illuminated by future work, it may be useful to consider this hypothesis alongside others.

Bearing in mind the difficulties of applying our results to the case of three-dimensional spreading flows, our models at least suggest that spreading currents associated with very large perturbations can cause magmatism far outside the boundaries of an impact basin. In Figure 3-17 we have plotted the positions of all major impact basins as well as geological units mapped in Scott and Tanaka [1986] and Greeley and Guest [1987] and interpreted as effusive, plains-forming lava flows which occur in the southern highlands. Three of the largest regions mapped as flows are adjacent to two of three major impact basins in the southern highlands. Hellas is bordered by the early-Hesperian ridged plains unit (Hr) and its correlates (the Amphitrites Formation (Had) and ridged plains floor unit (Hh2)) to the southwest and northeast, while Isidis is adjacent to the late-Hesperian flows of Syrtis Major. Since Hellas formed at the beginning of the Noachian, if the adjacent igneous provinces are related to the flattening and spreading of an impact-induced buoyancy perturbation, this would require long time-scales of dynamic adjustment and spreading. The Argyre basin, while not adjacent to any large igneous provinces, contains extensive outcroppings of the "smooth unit" (Hpl3), also associated with lava flows.

The distribution of early-Hesperian plains-forming flows in the southern highlands indicates the global extent of early-Hesperian volcanism, which possibly also resurfaced the northern lowlands at the same time (Frey et al. [2002], Head et al. [2002]). Volcanism associated with the spreading stage might express a clear chronological progression, since the youngest magmatism occurs in the farthest reaches of the spreading flow. By contrast, recovery-stage magmatism onsets in patches throughout the spreading region at approximately the same time, as mantle convection resumes and the large-scale circulation pattern is reorganized. Going forward, as a more detailed chronology for early Mars is sorted out, it may be useful to consider whether early-Hesperian resurfacing might be related to the recovery stage magmatism of a spreading current with global reach. If related to the Borealis impact of the pre-Noachian, this would require low Rayleigh number convection for this period in Mars' history.

3.9 Current-downflow collisions

We close this chapter by examining the interaction between a spreading viscous gravity current and localized convective downwellings, and obtain from this both the Λ^3 dependence of the Global Stagnation Criterion, as well as the approximately linear dependence on Λ of the spreading timescale. By examining sequential snapshots of the temperature field, we find that there are three types of interaction, where these are illustrated schematically in Figure 3-18 and for a sample calculation in Figure 3-19. (a) In a "breaching collision," the positive buoyancy of

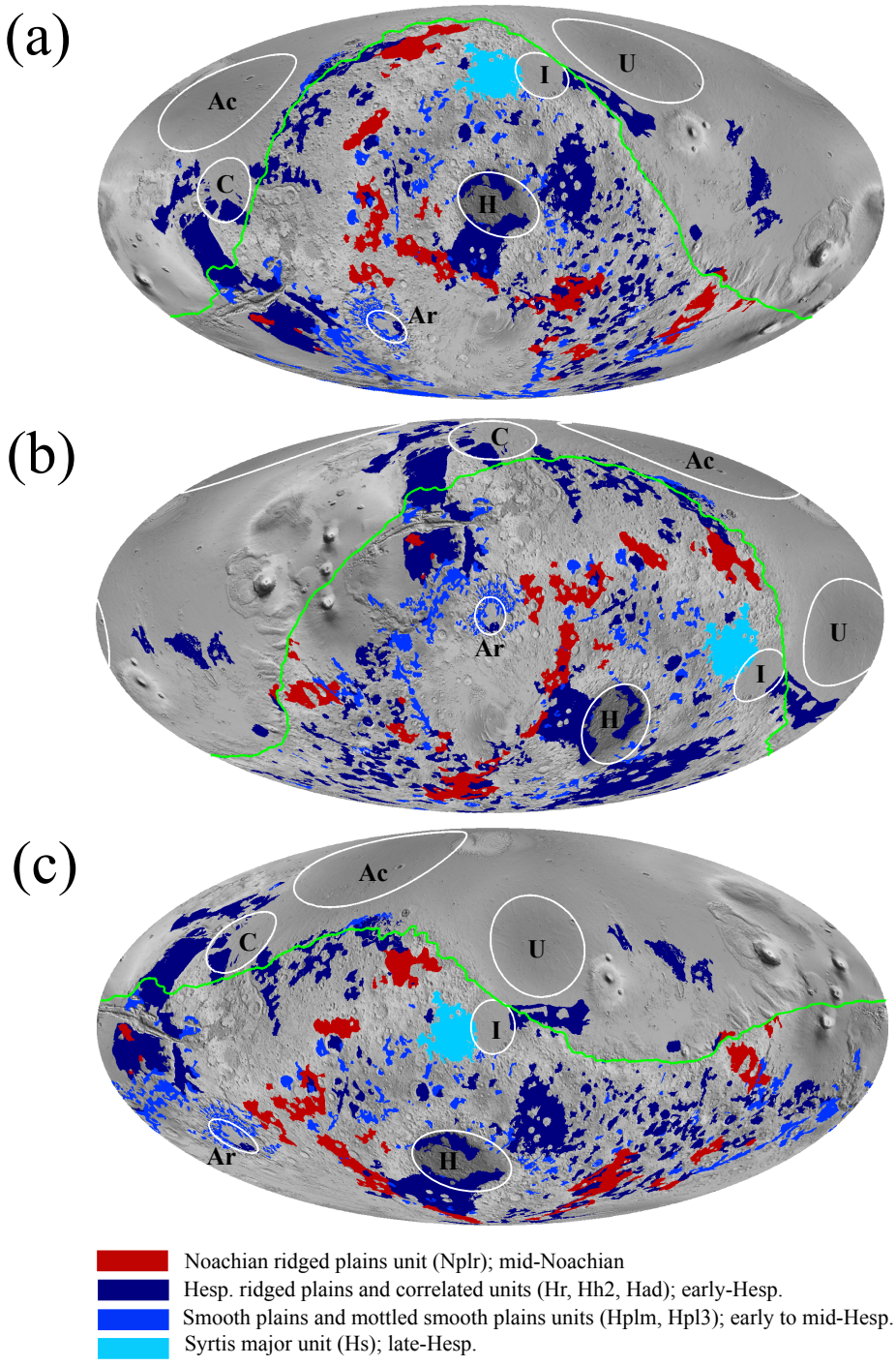

Figure 3-17: Mollweide-projected MOLA topography (grayscale) with amalgamated geologic units of effusive, plains-forming lavas mapped in Greeley and Guest [1987] and Scott and Tanaka [1986], centered on (a) Hellas, (b) Argyre, and (c) Isidis. Prominent impact basins are outlined in white: Ac = Acidalia, Ar = Argyre, C = Chryse, H = Hellas, I = Isidis, U = Utopia. The dichotomy boundary from Andrews-Hanna et al. [2008] is shown in green. Three of the largest igneous provinces are adjacent to two of three major impact basins in the southern highlands: Hellas and Isidis. The early-Hesperian ridged plains unit and its correlates in the highlands (plotted) and lowlands (not plotted) have a global distribution.

the gravity current exceeds the negative buoyancy of the downwelling. In this case, the current severs the downflow (often destroying it completely) and continues on its path. The root of the downflow is pushed in front of the current, in many cases causing the front to lose buoyancy and become unstable (see below). (b) In "halting collisions," the positive buoyancy of the gravity current only slightly exceeds the negative buoyancy of the downwelling. Heat is transferred into the downwelling through direct contact (rapidly, across a very sharp thermal gradient), and material is also drained from the current into the downflow. Both effects tend to lower the driving buoyancy of the current, causing it to slow and eventually to halt. (c) In "plunging collisions," the front of the spreading current becomes unstable and begins to founder. The positive buoyancy at the front does not exceed the negative buoyancy of the downflow, and the current is halted almost immediately upon contact.

In order to determine under what conditions "breaching" collisions occur, we require knowledge of the spreading front position as a function of time. We have obtained these data by differencing horizontal temperature profiles sampled in the upper TBL of sequential time-steps. Since the hot spreading current displaces colder ambient fluid in each time step, its motion produces a tall peak in the differenced profile that advances in the spreading direction over time. The front position (in either of two directions) is recorded by simply tracking the initially-largest peak in the differenced profile throughout the simulation. This is accomplished in two ways: (A) "Neighbor-tracking" involves finding the nearest peak in the direction of spreading. For example, in the first differenced profile (i.e., time steps t_0 and t_1) we find the tallest peak to the right of the perturbation center. In the next differenced profile (time steps t_1 and t_2), we find the peak that is nearest to the position just measured, in the direction of spreading. Provided the time-step is small enough, this method accurately tracks the front position. The tracking is stopped (and the spreading is considered to have ceased) when this peak has been displaced below a specified amount over the duration of one timestep. The "deceleration time" is defined in this way (t_{dec}), as the time at which this occurs. (B) "Height-tracking", by contrast, simply records the tallest peak in sequential differenced profiles, in the direction of spreading. Cessation of spreading is noted when a displacement is measured that exceeds a specified length. This corresponds to the moment when the front has has slowed and cooled enough that its displacements no longer produce the largest peaks in the differenced profile (i.e., the roots of downflows displaced by the spreading flow produce larger peaks). The tracking mechanism jumps to another peak, normally caused by a downwelling pushed by the spreading flow, and usually at a considerable distance in advance of the front. Each jump is recorded until the tracking eventually reaches the walls of the box. In this way, we can measure not only the positions of the advancing front through time, but also the positions of downwellings in front of the spreading current. An example is shown in Figure 3-20, where $L_{\max}$ is the maximum spreading length in grid nodes (i.e., measured before the tracking mechanism jumps to another peak). Contrasting symbols in this plot correspond to multiple peaks detected and tracked by the "height-tracking" method.

In Figure 3-20, horizontal lines correspond to the positions of nearly-stationary downwellings, slightly pushed by the spreading motion as the current displaces material in front of it. Sloped curves correspond to halting collisions that displace the obstacle (the downwelling) somewhat further with increasing perturbation size Λ (i.e., larger buoyancies). Discontinuities in these sloped curves correspond to intial perturbation sizes (Λ) at which the spreading current barely breaches a downwelling. A corresponding pattern is observed in the deceleration time scale t_{dec} measured by the "neighbor-tracking" method described above, and shown in Figure 3-21. A transitional breaching (i.e., where a downwelling barely fails to halt the spreading current) subtracts so much buoyancy from the spreading current that its front velocity is greatly diminished. As a result, it requires longer times to reach the next downwelling. As the initial buoyancy increases (i.e., increasing Λ), the current

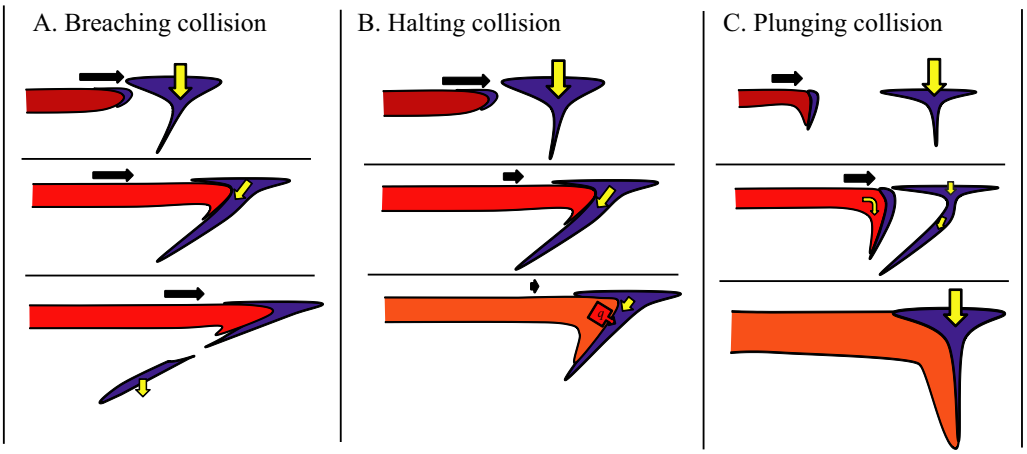

Figure 3-18: Illustration of the interaction between a spreading viscous gravity current and stationary downwelling. A) Breaching collision: the positive buoyancy of the gravity current exceeds the negative buoyancy of the downwelling. The current severs the downflow and continues on its path. B) Halting collision: the positive buoyancy of the gravity current only slightly exceeds the negative buoyancy of the downwelling. Heat is transferred into the downwelling during the interaction, and material is drained from the front. Both effects tend to lower the driving buoyancy, causing the current to slow and eventually halt. C) Plunging collision: the front of the spreading gravity current becomes unstable and begins to founder. The positive buoyancy at the front does not exceed the negative buoyancy of the downflow, and the current is halted on contact.

is less affected by the breaching collision, and reaches the next downwelling in shorter times. This behavior accounts for the pattern of stacked arcs seen in Figure 3-21. That is, long transit-times follow transitional breachings (i.e., currents are weakened by heat-transfer and draining into downflows during long interactions), and short transit times follow rapid breachings (i.e., interaction is brief and the current retains most of its driving buoyancy). We find that the local minima in this curve (for many conditons) have an approximately linear dependence on Λ, and correspond to the minimum spreading time-scale t_s and correlated stagnation and leveling time-scales shown in Figure 3-11.

The breaching and destruction of downwellings creates large zones of stagnating flow, as illustrated in Figure 3-22 for three time-steps of a sample calculation. In order to understand the origin of the Global Stagnation Criterion, we must find the exact conditions under which breaches occur. To this end, we have noted the initial sizes and temperatures, and final spreading length-scale of perturbations that are barely halted by downwellings (Λ_B,Θ_B, and L_B, respectively). These are simply the coordinates of the discontinuities noted in Figure 3-20, for all Θ. We have plotted these for the case $Ra = 10^6$ with a free-slip upper boundary in Figure 3-23, as L_B^c/Θ_B versus Λ_B in log-log space. The collapse was achieved in this case for a value of $c = 1.75$. A linear regression obtains the following relationship between these quantities:

$$L_B^c \sim \Theta_B \Lambda_B^b \tag{3.12}$$

where $b \approx 2.86$. A similar result is obtained for the case $Ra = 7.5 \times 10^5$. This value is consistent with the mean of exponents of Λ for the Global Stagnation Criterion, listed in Table 3.1.

This result also provides a key to the scaling of spreading time as a function of perturbation magnitude. Integrating equation (3.7) for the velocity of a viscous gravity current, we obtain the scaling of time t_{grav} required for a spreading gravity current to reach length L, expressed in terms of the perturbation size and temperature,

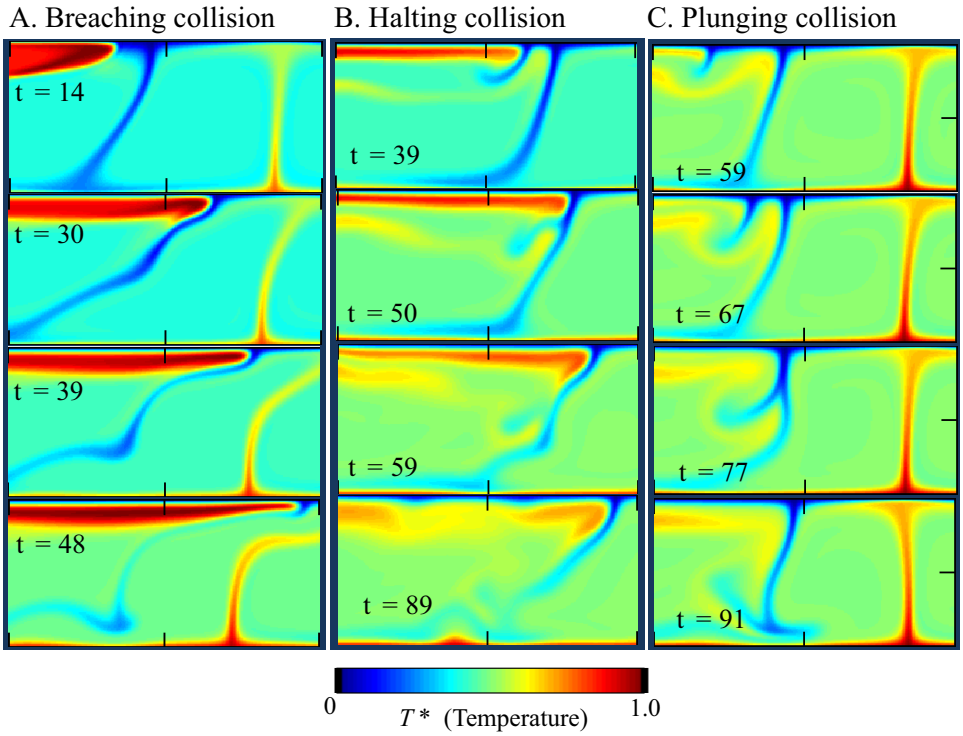

Figure 3-19: Time lapse of temperature field illustrating the interaction between the spreading gravity current and stationary downwellings: A) Breaching collision; B) Halting collision; and C) Plunging collision. See text and the caption to Figure 3-18 for discussion. (N.B. time and temperature are displayed in dimensionless [code] units.) For this case, $Ra = 10^6$, the upper boundary is free-slip, and heating is from below. The initial condition is time-independent.

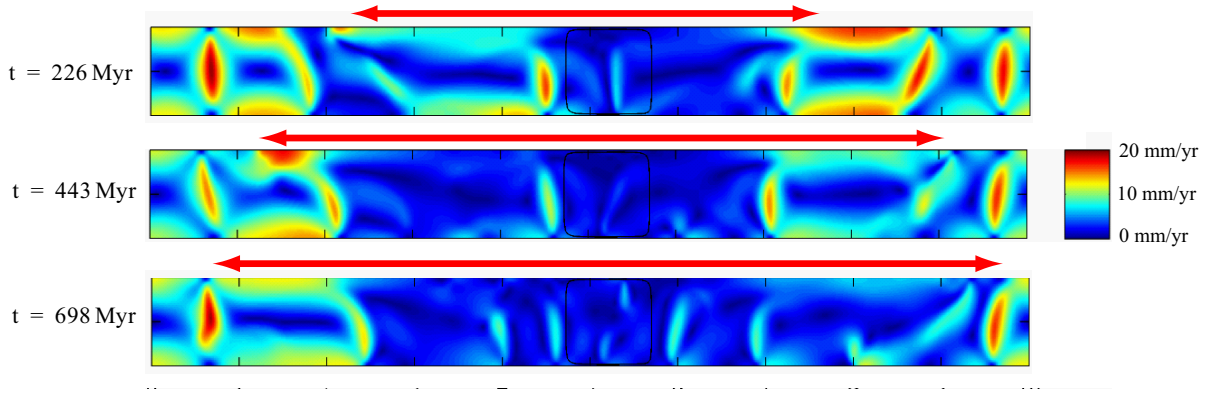

Figure 3-22: Absolute velocity field where red arrows indicate the extent of the spreading current. Large zones of stagnating flow emerge as the current destroys downwellings that drive the convection pattern. In this case, $Ra = 10^6$, the upper boundary is free-slip, and heating is from below. The initial condition is time-independent.

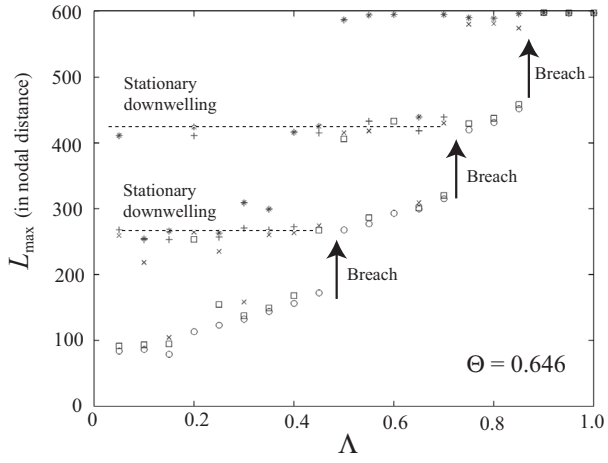

Figure 3-20: Nodal position (out of 600 nodes) of the maximum extent of the spreading current when it is halted (i.e., with respect to starting position at 0) as a function of Λ (for $\Theta = 0.646$). Contrasting symbols correspond to multiple peaks detected by the "height-tracking" mechanism described in the text. Flat lines correspond to the positions of stationary downwellings. Sloped curves correspond to halting collisions that displace the obstacle (the downwelling) somewhat further with larger perturbation size Λ (i.e., larger buoyancies). Discontinuities correspond to breaching collisions. See Figure 3-21 for the deceleration timescale $t_{\rm dec}$ measured for this set of calculations. In this case, $Ra = 10^6$, the upper boundary is rigid, and heating is from below. The initial condition is time-dependent.

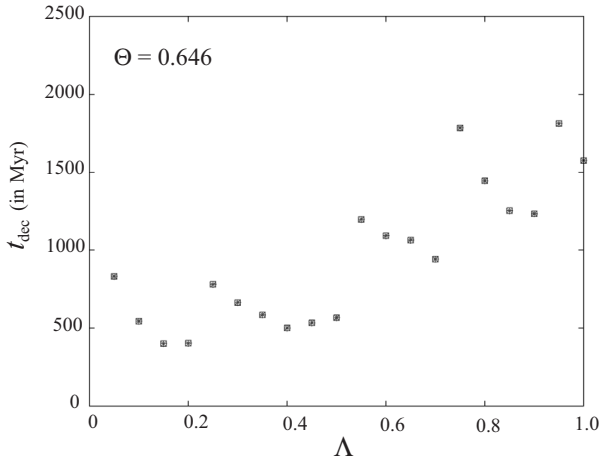

Figure 3-21: Deceleration timescale ($t_{\rm dec}$) versus Λ for a spreading gravity current ($\Theta = 0.646$) measured using the "neighbor-tracking" method. The pattern of stacked arcs (discontinuities) reflect the breaching collisions that occur as the driving buoyancy increases (i.e., as size Λ increases). See Figure 3-20 for the corresponding pattern in maximum lateral extent $L_{\rm max}$ of the same current as a function of Λ. In this case, $Ra = 10^6$, the upper boundary is rigid, and heating is from below. The initial condition is time-dependent.

and the Rayleigh number Ra:

$$t_{\rm grav} \sim \frac{b^2}{\kappa}\left(\frac{L}{b}\right)^3 Ra^{-1}\Theta^{-1}\Lambda^{-4}. \qquad (3.13)$$

We have just determined that the critical spreading length L_B for the halting/breaching transition is given by:

$$L_B^{7/4} \sim \Theta_B \Lambda_B^3 \qquad (3.14)$$

Substituting L_B for L (from equation (3.14)), Λ_B for Λ and Θ_B for Θ in equation (3.13), we find that:

$$t_{\rm sprd} \sim \Theta_B^{5/7}\Lambda_B^{8/7}. \qquad (3.15)$$

In this way, we have recovered the approximately linear dependence upon Λ of the minimum spreading time-scale (t_s). It is important to bear in mind that equation (3.13) is not strictly correct for our case because Θ decreases dramatically over time. This may account for the reason that α (in equation (3.5)) is over-estimated by equation 3.15.

3.10 Conclusions

The following results apply to the evolution of temperature- and velocity-field solutions of the equations of motion for a convecting layer of incompressible fluid with uniform viscosity in the limit of infinite Prandtl number and the Boussinesq approximation following the insertion of thermal perturbations, and obtained using a finite-element numerical calculation that assumes a 2D Cartesian geometry. The case of two upper boundary conditions (stress-free and no-slip) and heat sources (100% volumetric heat-

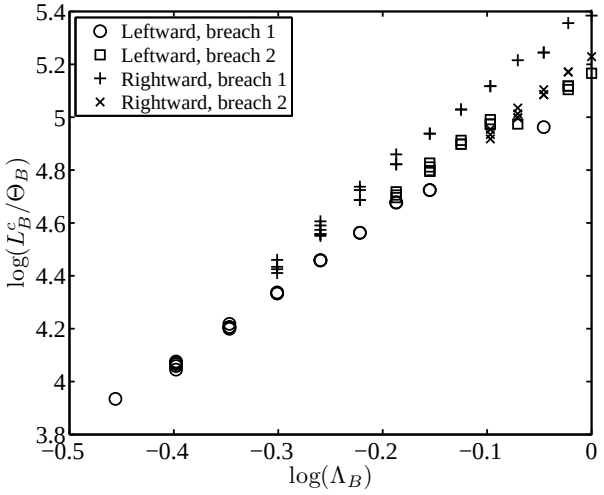

Figure 3-23: A plot of $\log L_B^c/\Theta_B$ versus $\log \Lambda_B$ for perturbation sizes Λ_B and temperatures Θ_B and maximum spreading length L_B at which spreading currents are barely halted by four downwellings in the same starting temperature field. This collapse is achieved with $c = 1.75$. In this case, $Ra = 10^6$, the upper boundary is free-slip, and heating is from below. The initial condition is time-independent.

ing and 100% bottom heating) were examined.

- Small, low-temperature perturbations are promptly halted and swept into nearby downflows, and have almost no effect on the ambient flow field. Large, high-temperature perturbations rapidly flatten and cool, and then spread along the upper boundary as a viscous gravity current. This spreading motion drives a large-scale double-roll flow pattern which has the following properties and consequences: (a) Downwellings are swept away or destroyed. (b) The upper and lower boundaries are stabilized so that new downwellings and plumes do not form, which along with (a) cause convection to cease locally. (c) Plumes are pushed to the center of the spreading region where they sometimes coalesce. The spreading flow is eventually halted by downwellings, at which time new instabilities emerge in both thermal boundary layers and convection resumes, reorganizing the flow field. The post-impact evolution implies two magmatic episodes with distinct temporal and spatial distributions, and with different source regions in the mantle (see Section 3.3).

- The timescale t_s in which the perturbation spreads along the upper boundary until it is slowed down and halted by a convective downwelling, can be expressed as a function of the Rayleigh number $Ra_{(H)}$, the dimensionless perturbation size ($\Lambda \equiv \lambda_p/\lambda_m$) and temperature ($\Theta \equiv \Delta T_p/\Delta T_c$):

$$t_s = K_0 \Theta^\alpha \Lambda^\beta Ra_{(H)}^\gamma \qquad (3.16)$$

  where $\beta \approx 1$ for both boundary conditions and heat sources, $\gamma \approx -0.5$ for bottom heating (both boundary conditions) and $\gamma \approx -0.13$ for volumetric heating (internal-heating Rayleigh number) and a stress-free upper boundary. Estimates of the exponent α range from 0.3 to 0.4 for the case of a stress-free upper boundary, and from 0.33 to 0.62 for the case of a no-slip upper boundary.

- The globally-averaged mantle velocity is depressed three standard deviations below its temporal mean value (prior to anomaly insertion) for all perturbations $\Theta\Lambda^3 \geq \Upsilon_{\rm crit}$, where $\Upsilon_{\rm crit} = C_0 Ra^{-q}$ for $0 < q < 1$. The values of C_0 and q have been determined for both upper boundary conditions and heat sources considered in this study (see Figure 3-14). This condition implies that low-Ra convection is relatively robust with respect to spatially localized thermal perturbations of a given magnitude, also confirmed in time-lapse snapshots of the temperature and velocity field for low-Ra convection. For perturbations of a given size, and assuming ΔT_c increases linearly with Ra, the perturbation temperature ΔT_p must increase only as a fractional power of the convective driving temperature ΔT_c to have the same effect on the globally-averaged velocity: i.e., $(\Delta T_p)_{\rm crit} \sim \Delta T_c^{(1-q)}$.

- The linear dependence of t_s upon Λ as well

as the Λ^3 dependence of the Global Stagnation Criterion follows from the condition for critical breaching collisions between the spreading gravity current and convective downflows (Section 3.9).

Table 3.4: Symbols (part 1)

α	Exponent of Θ in eq. (3.5).
β	Exponent of Λ in eq. (3.5).
γ	Grüneisen parameter (in Chapter 2).
γ	Exponent of Ra in eq. (3.5).
λ_p	Characteristic length scale of type II perturbation.
λ_m	Thickness of convecting layer (mantle).
Λ	λ_p/λ_m.
Θ	$\Delta T_p/\Delta T_c$.
ρ	Mantle density.
σ_v	Pre-impact temporal standard dev. about $\bar{v}$.
Υ	Perturbation magnitude: $\Upsilon \equiv \Theta\Lambda^3$.
Υ_{crit}	Critical perturbation magnitude for global stagnation.
C	Intercept of linear shock EOS in U-u space.
C_p	Specific heat at constant pressure.
C_v	Specific heat at constant volume.
d_c	Depth of center of isobaric core.
E_j	Specific internal energy of state j.
n	Shock-pressure decay exponent (eq. 2.5).
n_-	Most-gradual decay-law exponent for P_s (eq. 2.9).
n_+	Steepest decay-law exponent for P_s (eq. 2.7).
n_0	Mean decay-law exponent for P_s (eq. 2.8).
P_c	Isobaric core pressure.
P_{ls}	Lithostatic (ambient) pressure.
P_s	Peak shock pressure.
R	Projectile radius.
Ra	Bottom-heating Rayleigh number.
Ra_H	Internal-heating Rayleigh number.
$Ra_{(H)}$	Rayleigh number (internal-heating or bottom-heating).
r_c	Isobaric core radius.

Table 3.5: Symbols (part 2), and acronyms

S	Slope of linear shock EOS in U-u space.
t_{lev}	Leveling time-scale.
t_s	Spreading time-scale.
t_{s1}	Spreading time-scale estimate derived from t_{stag}.
t_{s2}	Spreading time-scale estimate derived from t_{lev}.
t_{stag}	Stagnation time-scale.
T_m	Solidus temperature.
ΔT_s	Shock-induced temperature increase.
ΔT_{ad}	Adiabatic contribution to geotherm.
ΔT_c	Convective driving temperature.
ΔT_p	Characteristic temperature of type II perturbation.
u	Particle velocity.
U	Shock front velocity.
v	Globally-averaged mantle velocity.
v_i	Projectile vertical incident velocity.
v_{stag}	Stagnation velocity.
$\bar{v}$	Pre-perturbation temporal average of v.
CMB	Core-mantle boundary.
EOS	Equation of state.
IC	Isobaric core.
PIA	Planar impact approximation.
STP	Standard temperature and pressure.
TBL	Thermal boundary layer.

Chapter 4

Geological structure of Endurance Crater, Meridiani Planum, Mars

Abstract: In this chapter we present a structural model of Endurance Crater in Meridiani Planum on Mars ($D \approx 150$ m), which formed in flat-lying layers of diagenetically banded sedimentary rocks, and was visited by the MER-B Opportunity rover in 2004. The model is constrained by four kinds of measurements derived from MER-B observations: (a) bedding orientations along the rover traverse, (b) layer thicknesses, (c) a global DEM of the entire crater at ~ 0.3 m resolution, and (d) color image panoramas of the upper crater walls acquired from two positions on the crater rim. The structural model reveals that the present planimetric shape of Endurance was mostly determined by a highly asymmetric excavation flow which produced a transient crater with significant concavities (in planform). Modal azimuths measured for the conjugate-orthogonal set of fractures in the surrounding target rocks are found to align to within five degrees of the quadratic component of the crater's planimetric outline, strongly suggesting a genetic relationship between preexisting planes of weakness in the target rocks and the crater's final shape.

4.1 Overview

Observations made by the MER-B rover in and around Endurance Crater at Meridiani Planum provide an almost unique opportunity to gain new insights regarding the formation and structure of small impact craters. Endurance is especially amenable to structural analysis because it was formed in flat-lying layers of diagenetically banded sedimentary rocks, where these exhibit marked color contrasts. As a result, layering and banding can be easily traced around the entire circumference of the crater rim wall and significant structural features are more easily interpreted. Ample context imagery supplies numerous examples of other impact craters at Meridiani Planum which exhibit similar features, and makes possible the statistical analysis of structural features in the target which, as we will see later, can be related to the planimetric shape of Endurance crater. Combining the ground truth of MER-B with the context available from the MRO/HiRISE and MGS/MOC cameras together with the unique properties of target materials at Meridiani provide an unparalleled chance to make new discoveries about the processes influencing the formation of small impact craters on Mars.

Throughout this chapter we will refer to length-scales and other properties of three-dimensional structures measured from digital elevation models (DEMs) constructed using stereo images acquired from MER-B and assembled by the Multimission Image Processing Laboratory (MIPL) at JPL. We have used these models to estimate the thickness of layers in the walls of Endurance Crater, and in this way to measure a stratigraphic section (shown in Plate L), as described in Section 4.2. We have used these measurements, and measurements of the strike and dip of bedding planes, to constrain a three-

dimensional structural model of Endurance that is informed by classic studies of terrestrial impact craters and laboratory experiments (Section 4.3). We have also used a DEM of Endurance Crater[1] as a whole (based on wide-baseline stereo observations), along with PANCAM image panoramas, to further constrain the model. The outcome of these models and observations are new insights into the processes which influence the formation of small impact craters, described in Section 4.4. The chapter closes with a brief comparison of structures observed at Meteor Crater near Winslow, Arizona, USA.

4.2 Bedding orientations and layer thicknesses

Topographic models generated using the VICAR/MIPS[2] correlator from PANCAM and NAVCAM stereo image pairs were sampled densely along laminations in rock outcrops at Endurance Crater (see Figure 4-1). Where laminations have significant relief, planes were fitted to the traced curves in a least-squares sense (an orthogonal distance regression) to measure the orientation of bedding planes.[3] Although nearly 200 traces of laminations were acquired, in only a few cases was it possible to make reliable measurements. We report only those measurements for which the along-plane measure of relief is several times greater than off-plane scatter, as described below. Sources of error include: (1) Stereo range information used to generate terrain models may have poor resolution or precision for several reasons: poor image contrast, a baseline that is too short for the measured range, or the presence of image compression artifacts that may confuse the correlation algorithm. The consequence for terrain models is an artificial increase in the roughness of model surfaces, and therefore of the sampled lamination curves. This increase in roughness leads in turn to a lack of precision in the resulting planar fits to these data. (A measure of this precision is discussed below.) Also important is (2) the manner in which points are traced from camera images (images whose pixels are co-registered with points in the terrain model topography). These points are selected manually and so their placement will of course depend upon the user's interpretation of what counts as a lamination, as well as where individual laminations reside. (3) Discrepancies in the orientation of the reference coordinate frame between different rover positions are relatively insignificant. Tests using imagery from several positions to measure the same bedding orientations, as well as repeated measurements of individual laminations indicate that the sources of error in (1) are most important.

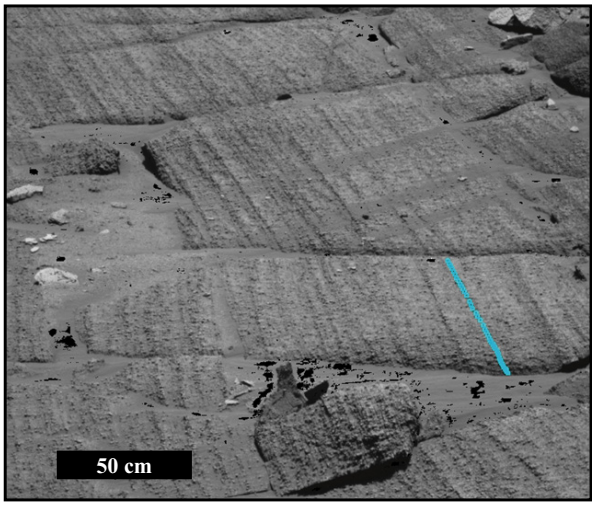

Figure 4-1: Example of a MER-B PANCAM image used to query a local digital elevation model. Sampled points correspond to the trace in three-dimensions of a lamination in sedimentary rocks at Burns Cliff on the upper rim-wall of Endurance Crater.

Points in the trace of a lamination of truly planar beds describe a roughly two-dimensional curve in three dimensional space. The point clouds (lamination traces) that we have measured describe three-dimensional curves that are

[1]The author participated in organizing the observations used to produce this digital elevation model while working as a member of the MER Athena Science Team.

[2]Developed by MIPL at the Jet Propulsion Laboratory.

[3]A common reference frame is established from solar position, time-of-measurement, and the ambient gravity field orientation at each new rover position.

only approximately coplanar in the best case. The departure from planarity and the uniqueness of the fitted plane can be estimated by the ratio of the standard deviation of distances from the fitted plane (σ_3) to the standard deviation of within-plane distances from the first principal axis of the point cloud (σ_2). We can express this as an angle $\Delta\varphi = \arctan(\sigma_3/\sigma_2)$ which indicates the shape of the point cloud when viewed along its first principal axis. Large values indicate a large departure from planarity and non-uniqueness for the fit in question. Small values indicate a planar shape and a relatively unique fit. The angle $\Delta\varphi$ is also an informal upper-bound estimate of the error in dip measurements (N.B. not the actual error because the first principal axis may not align with strike).

We have also computed the value of a metric γ equal to the mean of fluctuations between adjacent points in the point cloud in the direction of the second principal axis, expressed as a fraction of the overall standard deviation of point positions along this direction. In this way, we can confirm that we have not fitted a plane spanned by random fluctuations (errors) in the stereo range estimate. That is, γ allows us to distinguish between point clouds that resemble a smooth curve in space (normally an arc along a rock's surface or else a corner), and ones that are spanned by the scatter of erroneous range estimates (a ragged curve).

We find that a collection of rocks whose laminations exhibit consistent orientations (by informal inspection of image data) are measured to have consistent dip and strike angles provided measurements with $\gamma \geq 0.6$ or $\Delta\varphi \geq 20^\circ$ are discarded. We have listed the strike azimuths and dip angles for numerous rocks at Karatepe, Waypoint,[4] and Burns Cliff (see Plate K) in Tables 4.1 through 4.3 along with values of $\Delta\varphi$ and γ for each estimate and the position of each rock. These results are also shown in Plates H and K, where in the former case individual rocks are number-labeled and color-coded to indicate the dip angle.

[4] "Waypoint" is the only place-name in this chapter not originally used by the MER Athena Science Team.

In this way we have identified (at Karatepe West, see far right of Plate H) a transition from gently-dipping beds (dipping into the crater wall) at lower wall positions to vertical and then overturned bedding higher on the rim wall. We interpret this to be an expression of the classical overturned flap structure identified in several terrestrial impact craters (e.g., Shoemaker [1960]). This sequence is observed in cases where the flap hinge is buried in the crater wall, and will supply an important constraint upon our structural model for this region. Measurements at Karatepe East as well as Burns Cliff also indicate gently dipping beds (into the crater walls), whereas at Waypoint beds exhibit zero inclination or dip craterward. This latter result may indicate the rotation of a large volume associated with slumping, or as we will see later, possibly a tear fault in this corner of Endurance.

We have used the same data products and tools to measure the thickness of stratigraphic layers in multiple locations, where these results are listed in Table 4.4 as well as plotted in a stratigraphic column in Plate L. The sequence of primary and inverted stratigraphy can be seen in Figure 4-2. The pre-impact target surface occurs in the sand layer sandwiched between primary and inverted strata. This interpretation is partly based upon the recognition of inverted strata occurring above the sand layer in many locations around the crater rim wall, as well as noting that this layer everywhere exhibits a smooth surface, which may be contrasted with the rough surface apparent wherever sand covers rocks. Rocks occurring above the sand layer in the inverted stratigraphic sequence exhibit random orientations – i.e., the bedding geometry is not preserved in these layers of ejected debris.

The uppermost layer in the stratigraphic column below the sand is a light-toned rock (I) just 25 cm thick and which can readily located and traced on the crater walls. Beneath this are two diagenetic horizons (II and III) that are markedly darker, and which have been interpreted as diaganetic fronts associated with a fluctuating water table, marked by significant recrystallization (Grotzinger et al. [2005]). As we shall see later, perhaps because of cement-

Table 4.1: Bedding orientations for Karatepe West and East. Strike and dip are supplied in degrees. "Rock" is the rock ID that can be matched to labels in Plate H. The values of "Img" are image IDs, the values of "λ" are lamination IDs for a given rock (i.e., used to distinguish multiple laminations in the same rock). The (x, y) positions are supplied in meters and plotted in Plate K. Also listed is the goodness-of-fit $\Delta\phi$ and the metric γ used to rule-out planar fits to erroneous range estimates. We have included only measurements for which $\Delta\phi \leq 20^\circ$ and $\gamma \leq 0.6$. See text for discussion.

Rock	λ	Img	Strike	Dip	x	y	$\Delta\phi$	γ
3	1	7	315.9	66.2	683.4	-159.3	14.6	0.43
3	3	26	317.3	66.2	683.4	-159.3	14.8	0.26
6	1	19	308.9	78.1	683.4	-158.7	9.1	0.58
8	1	22	317.5	35.6	683.3	-162.1	19.8	0.49
9	3	22	19.9	34.1	683.5	-163.2	6.4	0.57
10	1	22	292.3	1.8	683.8	-163.7	4.5	0.42
10	3	22	142.3	10.5	683.8	-163.7	5.5	0.29
12	3	22	22.2	23.8	683.4	-162.4	5.2	0.39
13	1	27	119.8	64.5	684.2	-157.6	11.0	0.38
14	1	27	120.4	65.9	684.0	-157.7	14.0	0.55
16	1	30	112.3	66.4	686.8	-160.3	7.6	0.57
23	1	41	169.2	29.0	684.9	-154.3	5.3	0.25
23	1	47	171.0	27.0	684.9	-154.3	11.7	0.55
23	2	41	188.3	23.8	684.9	-154.3	6.4	0.23
23	6	46	197.4	23.1	684.9	-154.3	9.7	0.60
23	7	46	180.4	27.4	684.9	-154.3	11.2	0.58
116	1	96	113.3	60.0	698.1	-173.8	19.2	0.16
117	1	102	136.7	35.7	698.6	-174.1	8.0	0.53
117	1	103	123.9	68.2	698.6	-174.1	15.1	0.55
117	3	102	133.6	46.5	698.6	-174.1	6.2	0.41
120	1	105	91.9	22.1	692.8	-171.0	19.4	0.35
125	1	104	177.0	33.7	694.9	-173.1	16.7	0.52

Table 4.2: Bedding orientations for Waypoint location. See the caption to Table 4.1 for an explanation of contents.

Rock	λ	Img	Strike	Dip	x	y	$\Delta\phi$	γ
25	2	50	176.6	3.9	718.4	-186.1	6.7	0.30
26	1	49	260.7	11.7	714.2	-190.2	11.8	0.35
26	2	90	264.8	21.5	714.2	-190.2	12.5	0.59
26	3	90	245.7	17.6	714.2	-190.2	8.1	0.58
28	1	49	240.0	17.2	715.4	-190.4	5.2	0.55
80	3	89	292.4	24.0	717.2	-188.7	15.2	0.39
80	7	89	303.1	27.3	717.2	-188.7	18.9	0.32
81	1	86	300.5	25.0	718.6	-188.2	18.4	0.35
81	3	87	95.0	2.0	718.6	-188.2	10.5	0.29
83	1	86	295.7	27.6	717.9	-187.7	16.0	0.27
83	1	87	294.6	20.0	717.9	-187.7	14.2	0.23
85	2	86	257.5	15.2	718.3	-189.5	5.8	0.42
85	3	89	228.0	10.4	718.3	-189.5	14.5	0.25
85	4	89	269.7	15.7	718.3	-189.5	10.5	0.30
85	5	89	208.0	10.4	718.3	-189.5	18.0	0.51
85	6	89	276.3	11.2	718.3	-189.5	8.0	0.27
86	1	86	248.9	1.1	716.5	-188.8	5.5	0.28
87	3	89	315.3	17.9	716.0	-188.3	7.4	0.31
91	1	90	345.2	26.6	713.5	-189.7	3.1	0.56
92	1	90	292.5	16.1	714.0	-190.2	4.7	0.55
95	1	90	273.6	4.4	713.7	-189.1	5.6	0.30
98	4	91	356.0	13.4	712.7	-188.8	8.8	0.54
109	1	93	6.4	10.7	706.2	-184.4	12.6	0.47

Table 4.3: Bedding orientations for Burns Cliff. See the caption to Table 4.1 for an explanation of contents.

Rock	Img	λ	Strike	Dip	x	y	$\Delta\phi$	γ
35	1	74	127.3	25.6	741.9	-200.2	15.1	0.29
35	1	54	124.3	28.4	741.9	-200.2	5.5	0.53
35	1	63	116.1	40.7	741.9	-200.2	6.9	0.41
35	1	74	128.1	25.6	741.9	-200.2	11.0	0.28
35	2	66	133.2	18.6	741.9	-200.2	13.7	0.58
35	2	63	121.6	32.6	741.9	-200.2	7.5	0.30
35	2	63	118.1	35.8	741.9	-200.2	14.5	0.47
35	2	74	124.5	27.7	741.9	-200.2	13.5	0.22
35	2	74	124.5	27.2	741.9	-200.2	13.2	0.23
37	1	63	109.5	33.5	743.6	-200.6	18.1	0.37
37	1	70	105.4	36.3	743.6	-200.6	18.3	0.35
41	2	56	93.0	20.8	739.6	-199.7	14.0	0.55
42	1	57	101.3	19.5	737.5	-199.5	7.0	0.31
42	2	57	96.0	24.4	737.5	-199.5	8.2	0.31
44	1	60	113.4	38.3	730.9	-197.7	15.3	0.46
50	1	65	93.6	24.5	743.9	-204.1	15.0	0.55
50	1	73	90.7	22.1	743.9	-204.1	17.4	0.39
50	2	73	122.7	10.5	743.9	-204.1	16.6	0.54
52	1	64	124.2	15.3	740.2	-202.2	5.7	0.54
52	1	65	115.3	19.9	740.2	-202.2	7.3	0.60
53	2	73	113.7	26.2	743.5	-204.7	17.8	0.27
53	2	73	118.9	25.9	743.5	-204.7	15.1	0.27
53	2	64	121.5	37.4	743.5	-204.7	14.6	0.38
53	3	64	122.1	38.8	743.5	-204.7	10.8	0.38
53	3	73	113.7	38.2	743.5	-204.7	16.1	0.28
53	4	66	145.4	24.2	743.5	-204.7	15.7	0.51
54	1	72	242.1	29.2	742.6	-204.0	9.7	0.41
54	8	72	218.3	7.5	742.6	-204.0	5.5	0.18
56	1	65	117.7	27.1	745.3	-204.7	9.9	0.56
56	2	65	100.8	35.9	745.3	-204.7	18.7	0.45
58	1	69	119.2	31.9	741.5	-199.3	14.1	0.57
59	2	71	117.8	27.7	746.6	-202.7	8.7	0.36
62	1	75	197.7	31.4	739.5	-202.1	8.6	0.33
63	1	75	340.2	14.5	738.5	-201.8	8.7	0.55
63	1	76	342.9	16.3	738.5	-201.8	9.3	0.55
64	1	76	252.6	38.2	738.2	-201.9	16.8	0.54
70	1	80	76.1	14.7	735.1	-202.3	16.0	0.56
72	1	82	93.6	14.6	735.6	-197.9	14.4	0.59
73	1	84	76.3	21.3	731.2	-198.2	10.3	0.50

ing minerals, rocks belonging to II and III are more resistant to erosion than layers above or below. Although these horizons do not mark the boundary of a sedimentary rock layer (i.e., these were not created by depositional or erosional processes), we shall refer to these as a "layers" in the following discussion of the structural models. The rocks in I, II, and III have low-angle to flat bedding, and all of our strike and dip measurements were made from these layers only. What might be a third diagenetic band (relatively ill-defined) appears to occur in III in some locations (see Plate L). At the base of the diagenetic interval is an erosional surface which marks the upper-bound of an aeolian unit with high-angle crossbeds (Ibid.).

Throughout the remainder of this chapter we will refer to positions in the crater using an angular coordinate (an aziumth) measured clockwise with respect to north (the "azimuthal position") from the crater center.[5] Prominent corners in the rim trace have been labeled with the prefix C followed by the azimuthal position (see Plate J). In Plates A-D we have traced the boundaries between the layers just described in a panorama assembled from PANCAM images acquired at an azimuthal position of approximately 260° ("Pan position 1"). This was repeated for a panorama acquired from an azimuthal position of $\sim 100°$ in Plates E-G ("Pan position 2"). In addition to marking the inferred boundaries between layers we have also indicated the locations of likely faults. Nowhere are these more numerous and densely clustered than the west wall, which has the lowest rim and, as we shall see later, the shallowest slope.

By tracing the upper and lower bounds of II and III, we find a sequence of probable imbricated thrust faults whose precise configuration cannot be established because the rover did not visit this portion of the crater wall. These may corresponds to the shallow outwardly-dipping rotated faults or the steeper inward-dipping overthrusts, described at numerous terrestrial impact craters (e.g., Shoemaker and Eggleton [1961], Kring [2007], Maloof et al. [2007], see Chapter 1) and associated with uplift of the crater wall in the late-stage cratering flow. It may also be noteworthy that these structures are concentrated in the west wall of the crater, where the rim has been almost completely removed.

[5]The center is the deviation centroid of the crater's planimetric rim outline, as described in Chapter 5.

Table 4.4: Stratigraphic layer thicknesses: true layer thickness is given by $h = |L\sin(\phi+\theta)|$, where ϕ is the local slope, θ is dip of bedding (negative if not dipping into the crater wall), and L is the measured apparent thickness (in the plane of the crater wall). Locations are: Ke = Karatepe-East, Kw = Karatepe-West, Bu = Burns Cliff. N.B. The result for III is taken directly from Grotzinger et al. [2005]. Note also that the thickness of the sand layer is estimated for three angles of stratigraphic uplift, since the true dip could not be measured (i.e., no bedding).

Lyr	h	L	ϕ	θ	Loc.
S	1.94 m	4.0 m	23.9°	5.0°	Ke
	2.24 m	4.0 m	23.9°	10.0°	Ke
	2.52 m	4.0 m	23.9°	15.0°	Ke
I	0.24 m	0.28 m	23.9°	33.7°	Ke
II	1.06 m	1.21 m	35.0°	26.2°	Bu
	0.85 m	1.25 m	29.0°	−72.0°	Kw
	1.10 m	1.21 m	23.9°	41.0°	Ke
III	3.00 m				Bu

4.3 Layer surface model

The geology of the MER-B landing site at Meridiani Planum has been described in detail elsewhere (e.g., Grotzinger et al. [2005], McLennan et al. [2005]) and a detailed analysis of crater morphometry and assessment of the processes which have modified Endurance are reported[6] in Grant et al. [2006]. Rather than provide minute descriptions of geological structures at

[6]N.B. In this chapter we will not address the question of whether Endurance is a primary or secondary crater. Grant et al. [2006] concludes it is of primary origin, based on estimates of backwasting of the walls and the crater's present depth-diameter ratio (≈ 0.14). We note moreover that Endurance is not obviously part of an ejecta ray or cluster of small craters, and does not have a flat-bottom morphology like many secondaries in Meridiani Planum.

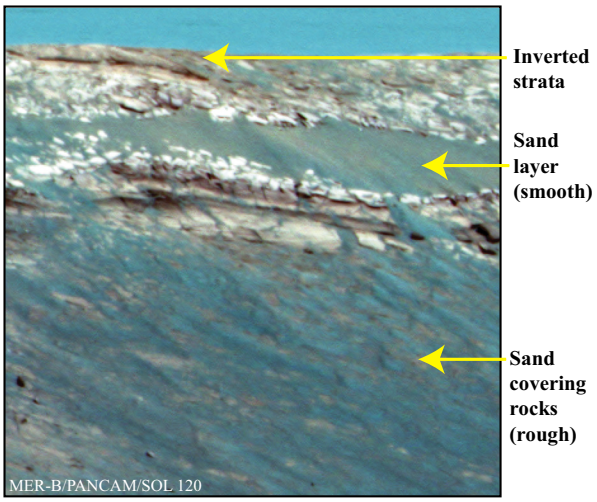

Figure 4-2: A false-color MER-B PANCAM image of "Karatepe East" taken from Pan Position 2 (azimuthal position $\sim 100°$). Clearly visible is an example of inverted stratigraphy, and a marked contrast between the pure-sand layer (smooth; in which the flap hinge resides), and rocks on the lower wall covered by sand.

Endurance Crater, our focus in this chapter will be to construct a global structural model of the deformation of layering (or diagenetic banding) in the crater walls. In this section we describe a computer-generated structural model that is based upon four types of constraints: (a) the thickness of layers measured using local DEMs based on stereo imagery; (b) the orientation of bedding planes measured along the south wall of Endurance Crater (also from local DEMs); (c) a digital elevation model of the entire crater with ≈ 0.3 m resolution (hereafter the "crater DEM" or "Endurance DEM"); and (d) false-color panoramas assembled from MER-B PANCAM images of the crater rim walls. Measurements in (a) and (b) were obtained only where the MER-B rover was able to traverse inside of Endurance Crater, along the southern wall. These measurements have informed an interpretation of the southern wall that has been used to interpret the expression of layering in other regions of the crater. For example, we assume that the stratigraphic column measured in the south reflects the stratigraphy everywhere else (i.e., that layers have a constant thickness and were flat-lying). We will use these constraints to build a model that estimates the trace, in three dimensions, of the flap hinge (i.e., the "axis" of the overturned flap "fold"). Since the flap hinge formed before slumping began, this curve is a reflection of the transient crater shape: i.e., from this we can expect to learn something about the relationship between the shape of the transient crater (the excavated shape) and the present (modified) shape of Endurance Crater.

The Endurance Crater DEM is based upon wide-baseline (5 m) stereo image panoramas acquired at two locations on the crater rim as well as one position inside the crater. This DEM, as well as a detailed description of the observations and the methods used to construct it, can be found in Li et al. [2007]. Because image coverage was not sufficient in the northwest corner, we will discard results that rely upon the crater DEM between azimuthal positions 270° and 360°.

Our geological model is called a Layer Surface Model (LSM) because it is based upon a mathematical description of the surfaces bounding the layers (or diagenetic bands) in our stratigraphic column (Plate L). These surfaces are built from a two-dimensional description of radial curves[7] that bound stratigraphic layers, where the shape of these curves are assumed not to change with azimuthal position. These cross-sectional models (model cross-sections 1 and 2) are shown in Figure 4-3, where layers[8] are labeled, along with the overturned flap and flap hinge (located at the origin in these plots). The expected thickness of the inverted layers is poorly constrained by laboratory experiments or field observations (Roddy et al. [1975]). This is not very important for our purposes because we have not tried to match model thicknesses with observed thicknesses in the overturned flap. In any case, the inverted stratigraphy is not well preserved in most locations on the walls of Endurance Crater. We have assumed that the thickness of inverted layers decays as $\sim r^{-3}$, in accordance with the

[7] i.e., in cylindrical coordinates, this is a curve in the (r, z) plane for a constant θ.

[8] Layers have been color-coded using colors sampled from the PANCAM panoramas in Plates A-D, E-G.

observations of McGetchin et al. [1973] for the radial thickness-decay of continuous ejecta as a whole (beyond the crater radius). We have approximated the radial stratigraphic uplift as a straight line oriented at just 3.5° with respect to the horizontal. This is based upon estimates of the hinge elevation at Karatepe West, the elevation change measured along the traverse from Eagle crater (Arvidson et al. [2004]) to the west rim, and that stratigraphic uplift typically persists to a distance $0.6R$ beyond the crater radius R (Roddy et al. [1975]).

As mentioned, the shape of radial bounding curves (Figure 4-3) are constant with respect to azimuth. This is a very significant simplifying assumption that is undoubtedly not realistic. That is, the cross-sectional shape shown in Figure 4-3 is an idealization unlikely to reflect the geological structure of layers in the crater wall at all azimuthal positions. Our purpose in this exercise, however, is to estimate the trace of the flap hinge in three dimensions, so that wherever we can identify patterns of layering on crater walls that are consistent with these idealized models, we are likely to obtain a reasonable estimate of the hinge position. That is, although the shape of the flap "fold" undoubtedly differs from place to place, by conservation of volume (and assuming the thickness of stratigraphic layers is constant everywhere) we can expect to locate the hinge with a precision of 1-2 meters where interpretations are confident.

We have experimented with numerous shapes for the "nose" of the fold shown in Figure 4-3. The one which most readily reproduces the patterns expressed in the walls of Endurance is more pointed than commonly depicted in classic geological cross-sections of Meteor Crater and others (i.e., model cross-section 1 in part A of Figure 4-3; cf. Shoemaker [1960], Shoemaker and Eggleton [1961], Roddy [1978], Maloof et al. [2007]). We have assigned two interpretations to the pattern of layering in the southeast wall. Cross-section model 1 makes a poor fit to one of these, so that an alternate model is used (model cross-section 2, in part B of Figure 4-3). In these model cross-sections, the thickness of layers exactly matches that in our stratigraphic model at the elevation of the flap hinge, as well as at the point directly below the hinge where the transition to the 3.5° uplift occurs. This is not exactly consistent with observations made in the course of field studies and laboratory experiments, where some amount of bulking (thickening) of upturned layers is noted in the fold itself. In the absence of good estimates of the expected change in volume, we have simply assumed that layer thicknesses are consistent with their horizontal (i.e., unmodified) counterparts. It should also be noted that this bulking may to some extent have affected the estimates of thicknesses measured for our stratigraphic column, in which case it does not make sense to compensate for this effect.

We estimate the flap hinge trace as follows. First, candidate positions for the flap hinge at all azimuths are described using a piecewise curve assembled from straight line segments and circular arcs, and specified in cylindrical coordinates (r, θ, z). The 3D layer bounding surfaces are then interpolated between the radial bounding curves, and are in turn used to assign all positions on the crater DEM to one of the layers in our model. The resulting color-coded pattern of layer expression is compared with the aforementioned PANCAM panoramas (as well as PANCAM images that have been draped on the DEM), and this process is repeated until model layer expression matches what is observed in image data. (i.e., the hinge trace is manually adjusted, the layer-expression recalculated, and so on.) The calculation of layer dip angles in all positions on the crater walls are used as an additional constraint for those locations where this quantity was measured on the south wall. The resulting hinge trace is shown in Figures 4-4 and 4-5. Trace A assumes cross-section model 1 (Figure 4-3, part A) for the entire crater, and trace B applies only to an alternate interpretation obtained only for the southeast wall (cross-section model 2). It is worth noting here that the different interpretation and shape of the model cross-section resulted in a very minute adjustment of the hinge trace (see southeast corner of Figure 4-4).

Trace C illustrates the uncertainty regarding the hinge position with respect to the west wall,

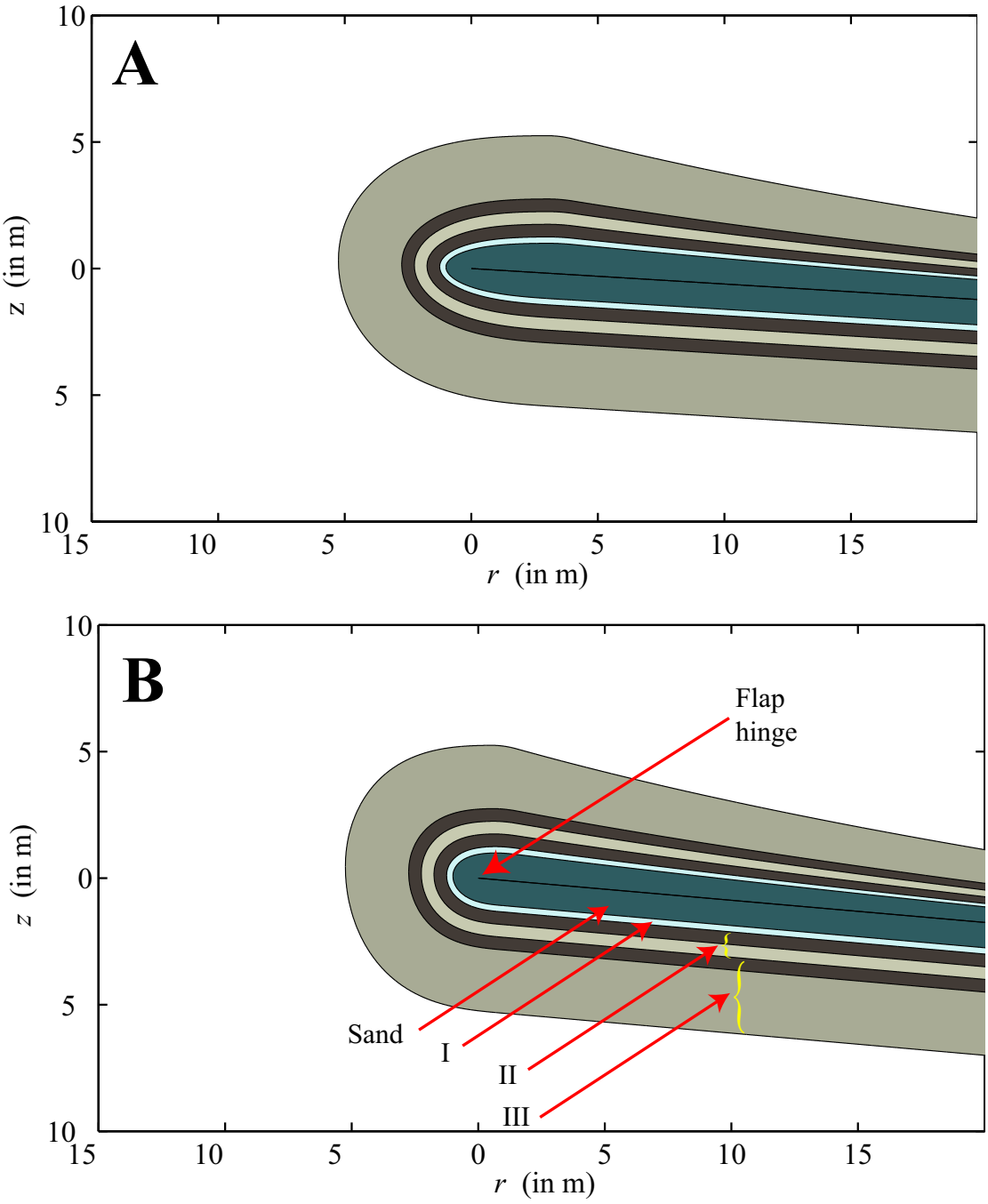

Figure 4-3: A) Cross-section model 1, where position is measured with respect to the flap hinge. B) Cross-section model 2. Important structures and stratigraphic layers are labeled.

where a low rim elevation and low wall slope – and a very thin sand layer – indicate that the wall surface lies well behind the hinge position (i.e., the hinge is not preserved), although it is impossible to estimate by what distance. Significant discontinuities observed in the plot of hinge elevation as a function of azimuthal position may be a reflection of significant faults or block rotations and slumps. The largest of these, which occurs at an azimuthal position of approximately 205° may correspond to a tear fault (it occurs near the corner C212; cf. Shoemaker [1960], Roddy [1978] for a description of tear faults in the corners of Meteor Crater) or else a rotated block. The difference between the hinge trace and the crater wall position (at the hinge's local elevation) is plotted in Figure 4-6. This is consistent with the long-term wind direction estimates measured by the author and reported in Sullivan et al. [2005], who found that rocks are preferentially abraded with sand blown from the southeast (i.e., the hinge is preserved in the southeast and has been destroyed in the west and northwest).

Layer expression on crater walls resulting from hinge trace A (Figure 4-4 and 4-5) is depicted in plan view in Figure 4-7. A map of computed dip angle for modeled layering on the crater walls is shown in Figure 4-8. Example cross-sections (with topographic profiles) are shown in Figure 4-9. Detailed 3D views of selected portions of the rim wall for hinges A, B, and C are shown in Figures 4-10, 4-11, and 4-12 (N.B. the dip angles have been color-coded in the case of Figure 4-10 for the purpose of comparing these results with measurements made in several locations on the south wall shown in Plate H). Example cross-section and topographic profiles are shown for an alternate model of the southeast wall (using model cross-section 2) in Figure 4-13.

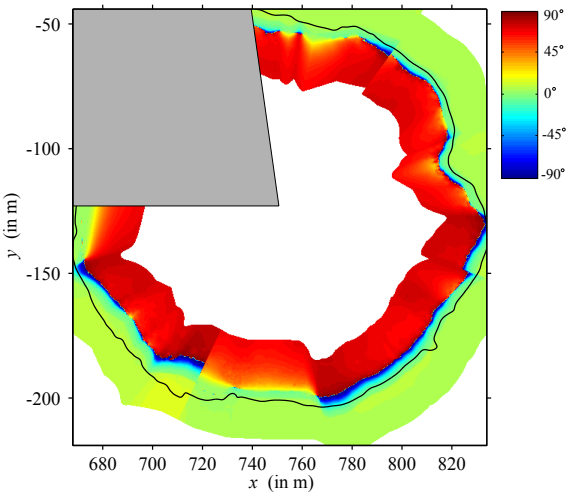

Figure 4-8: Map of dip angle (i.e., orientation with respect to the horizontal plane) of layering in the LSM. Positive values indicate that layers are locally dipped toward (into) the crater wall (and negative values, toward/into the crater).

4.4 Styles of crater excavation

The results just presented point to useful insights about the processes that influence the formation of small impact craters. For example, the hinge traces shown in Figure 4-4 are very closely related to the present-day planimetric shape of Endurance crater. In general, the flap hinge is a reflection of the transient crater shape except where it has been preserved in a rotated block or slump. Observing that the hinge trace (inferred from the LSM) closely mimics the present-day crater shape is a strong indication that this shape was mostly determined by excavation rather than significant modification. Moreover, the flap hinge in many places exhibits significant concavities. In one location, this concavity was preserved in a promontory that has been dubbed "Kalahari", located at an azimuthal position of roughly 70°. (Models of layer-expression surrounding Kalahari are shown in Figure 4-11.) We have found as part of the crater survey conducted in Chapter 5 that it is uncommon for impact craters on the surface of Mars to exhibit very marked concavities and promontories of this type. Therefore, the reasons for the preservation of this feature merit some attention.

Although without in situ observations we cannot be certain, we have interpreted the expres-

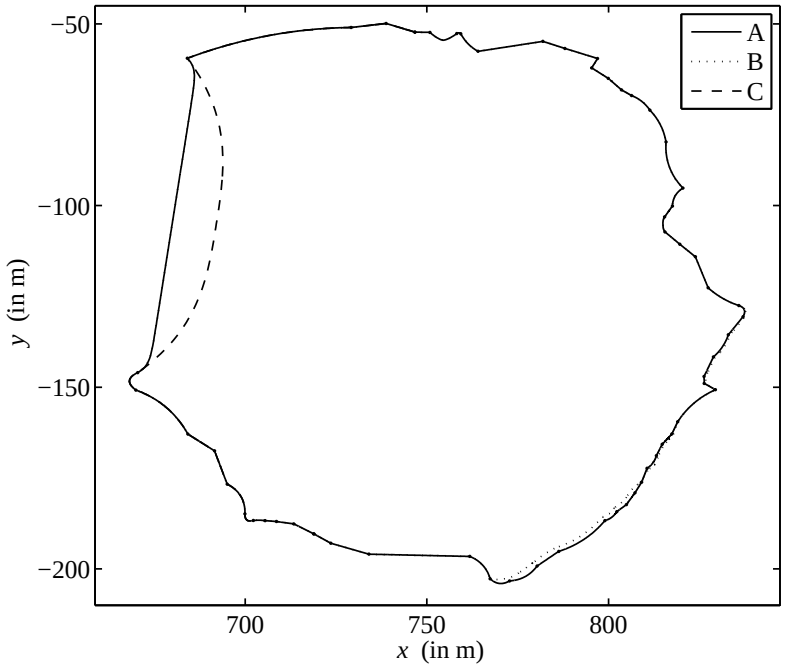

Figure 4-4: Flap hinge trace A and alternates B and C in the horizontal plane obtained from the Layer Surface Model (LSM) for A) cross-section 1; B) cross-section 2 (in the south east corner only); C) cross-section 1 (everywhere the same except the west wall). The trace is not expected to be accurate in the northwest corner, where the DEM is not reliable.

sion of layering at Kalahari and the very steep slopes just below it to coincide with vertically-oriented beds of the resistant (dark, cemented) upper portions of layers I or II (i.e., the diagenetic bands). A diagram illustrating this concept is shown in Figure 4-14. It is worth noting, moreover, that three of four locations on the upper rim wall where slopes exceed the angle of repose ($\approx 30°$ to $35°$) correspond to outcroppings, expected to be very steep or vertically oriented, of the dark resistant layers. This can be seen in a slope map derived from the crater DEM, shown in Figure 4-15. The exception is Burns Cliff, where the rocky slope on the lower wall exceeds the angle of repose, and the sand layer has evidently collapsed above it (i.e., sand cannot support slopes exceeding the angle of repose). In the north wall (in the vicinity of azimuthal position $0°$) we find what is likely the remnant of a promontory that has collapsed (see rightmost portion of Plate G). The tallest portion of the rim wall (that has survived modification) also corresponds to one of the steepest wall slopes and an outcropping of the dark resistant layer (in the southwest, see Figure 4-15). On the basis of these observations, we propose that promontories are preserved at Endurance and (as we shall see in a moment) other impact craters at Meridiani Planum because the structure of the flap "nose" has been protected from erosion by a resistant cemented layer.

The concave shape of the hinge trace that we have obtained through these modeling efforts has important implications for understanding the crater formation process. Three very simple models are illustrated in Figure 4-16 alongside the expected consequences for the expression of layering in the crater walls. In the case labeled A, the final polygonal shape is assumed to occur as a result of wall slumping that modifies a radially-symmetric transient crater. Assuming that the flap hinge reflects the planimetric

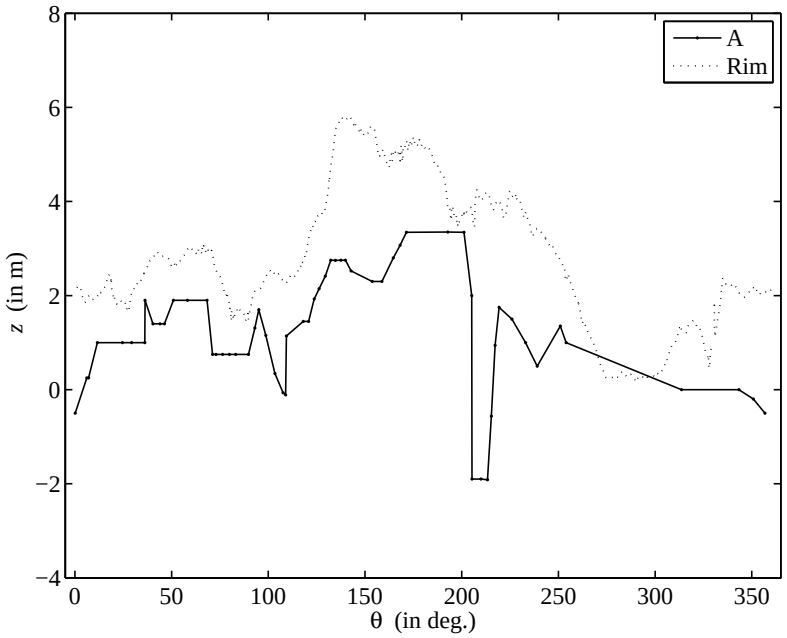

Figure 4-5: Rim crest and flap hinge trace A in the vertical dimension, obtained from the LSM, as a function of azimuthal position (in degrees from north). The dramatic minimum that occurs at approximately 205° may correspond to a rotated block, a slump, or a tear fault. This coincides with one of the corners of the crater.

shape of transient craters, this implies a pattern of lozenges that occur in the corners of a polygonal cavity. According to model B, the transient crater exhibits a polygonal (or non-circular) shape and maintains this shape after slumping. In this case, layering appears uniformly flat. In model C, the transient crater exhibits a "stellar" or concave/cuspate shape, and the unstable walls between vertices collapse. The outcome is a pattern of smiles or festoons between corners of the polygon. (N.B. depending on the cross-section model, this can also produce almond-shaped patterns between vertices.) The evidence from Endurance appears to suggest a combination of models B and C. That is, the inter-vertex festoon or lens pattern occurs on portions of the west, south, and north walls, while layering appears flat in the northwest.

Another consequence of the model concerns the expression of layering in ejecta on the crater flanks. If excavation was carried farther in the corners of the polygon, then the corresponding ejecta will be displaced to proportionally larger distances. This leads to the "coronal" pattern of ejecta-layering shown in Figure 4-17. All of the features that we have so-far described (promontories, intervertex festoons, and coronal ejecta) are expressed in other impact craters captured by orbiter cameras at Meridiani Planum, and some of these are shown in Figure 4-18.

Important questions remain, however, about what may cause these polygonal and "stellar" modes of excavation to occur, over what range in crater diameter they occur, as well as what properties of target materials may influence the excavation flow and final crater shape. A very significant piece of evidence comes from the pervasive fracture network observed at Meridiani Planum in the vicinity of Endurance and other impact craters, and observed by orbiting spacecraft as well as the MER-B rover (Figure 4-19). In Figure 4-20 we have compared a length-weighted histogram of the azimuthal orientations of these fractures to the planimetric shape of En-

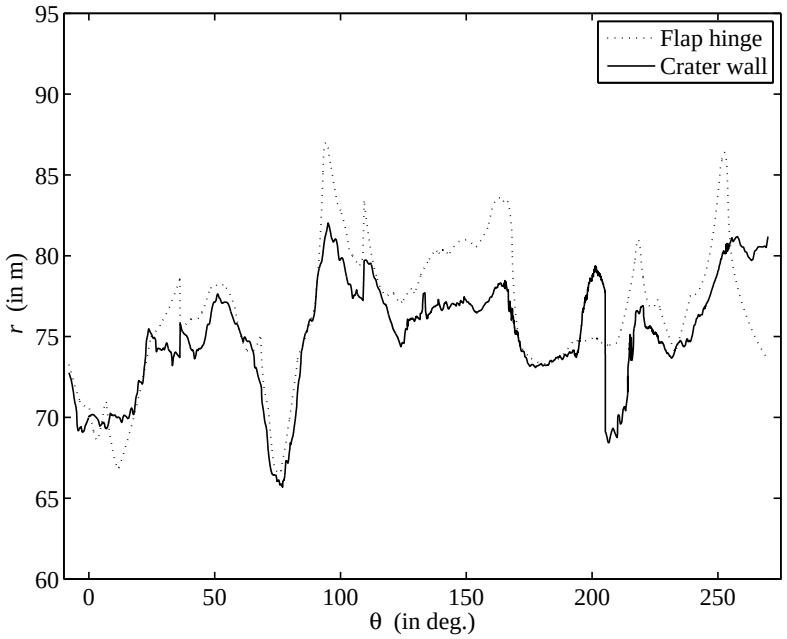

Figure 4-6: Radial position of hinge trace A (as a function of azimuth in degrees from north) and crater wall at the same elevation. That the hinge trace is behind the wall in the southeast and in front of the wall in the west (and northwest: i.e., not shown because the DEM is unreliable in this region) is consistent with the long-term wind direction estimates reported in Sullivan et al. [2005], who found that rocks are preferentially abraded with sand blown from the southeast. (N.B. This is based on the orientation of abrasion shadows behind concretions in the rocks at Eagle and Endurance craters. The author conducted the observations and analyses which support this result, reported in said reference.)

durance crater. Plotted on this histogram is the folded radius (R_f) (i.e., the radius of the estimated rim crest outline flattened onto the domain $(-180°, 180°]$ and normalized by the maximum radial deviation) as well as the orientation of the fourth harmonic amplitude (A_4) (of the rim crest outline; see Section 5.2 for a discussion of how this quantity is estimated). We find that peaks in the fracture azimuth distribution are aligned to within 5° of peaks in the folded radius or the fourth harmonic amplitude. That is, modal fracture azimuths align with the diagonals of the square component of the planimetric shape of Endurance crater. It is natural to suggest, therefore, that crater excavation is significantly enhanced in the direction of fractures or planes-of-weakness in the target, consistent with the laboratory results of Gault et al. [1968] and the observations of Shoemaker [1960] and Roddy [1978] at Meteor Crater.

We close this chapter with a brief comparison of results from Meridiani Planum with observations made at a much larger crater also formed in flat-lying sedimentary rocks (with marked color contrasts) that are also host to two sets of orthogonal systematic joints. Figure 4-21 contains photographs[9] of bedding exposed in the walls of Meteor Crater near Winslow, Arizona, USA. Parts A and B show two of only three locations in the walls of this crater where bedding exhibits near-vertical dips, where these are marked in the aerial photo of Figure 4-22. These belong to the Kaibab carbonate unit and conceal the overlying Moenkopi where the flap hinge resides (Shoemaker [1960], Kring [2007]). These three locations occur near the corners of the quadratic

[9] Acquired by the author and colleagues Ian-Garrick Bethell, Erwan Mazarico, and Jeffrey Andrews-Hanna.

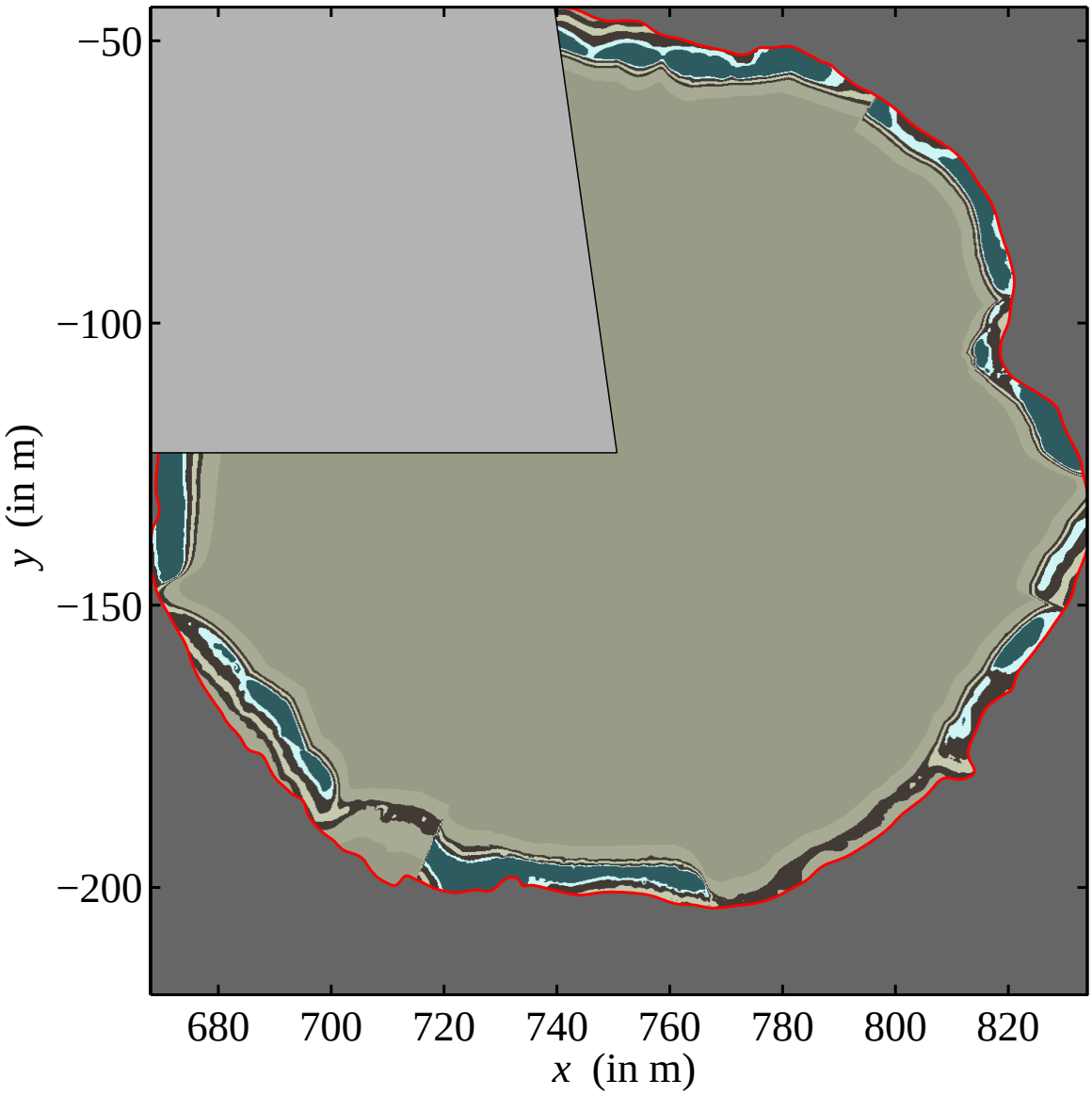

Figure 4-7: Plan view of the LSM for hinge trace A and cross-section 1. The northwest corner has been covered because the DEM in this region is not reliable.

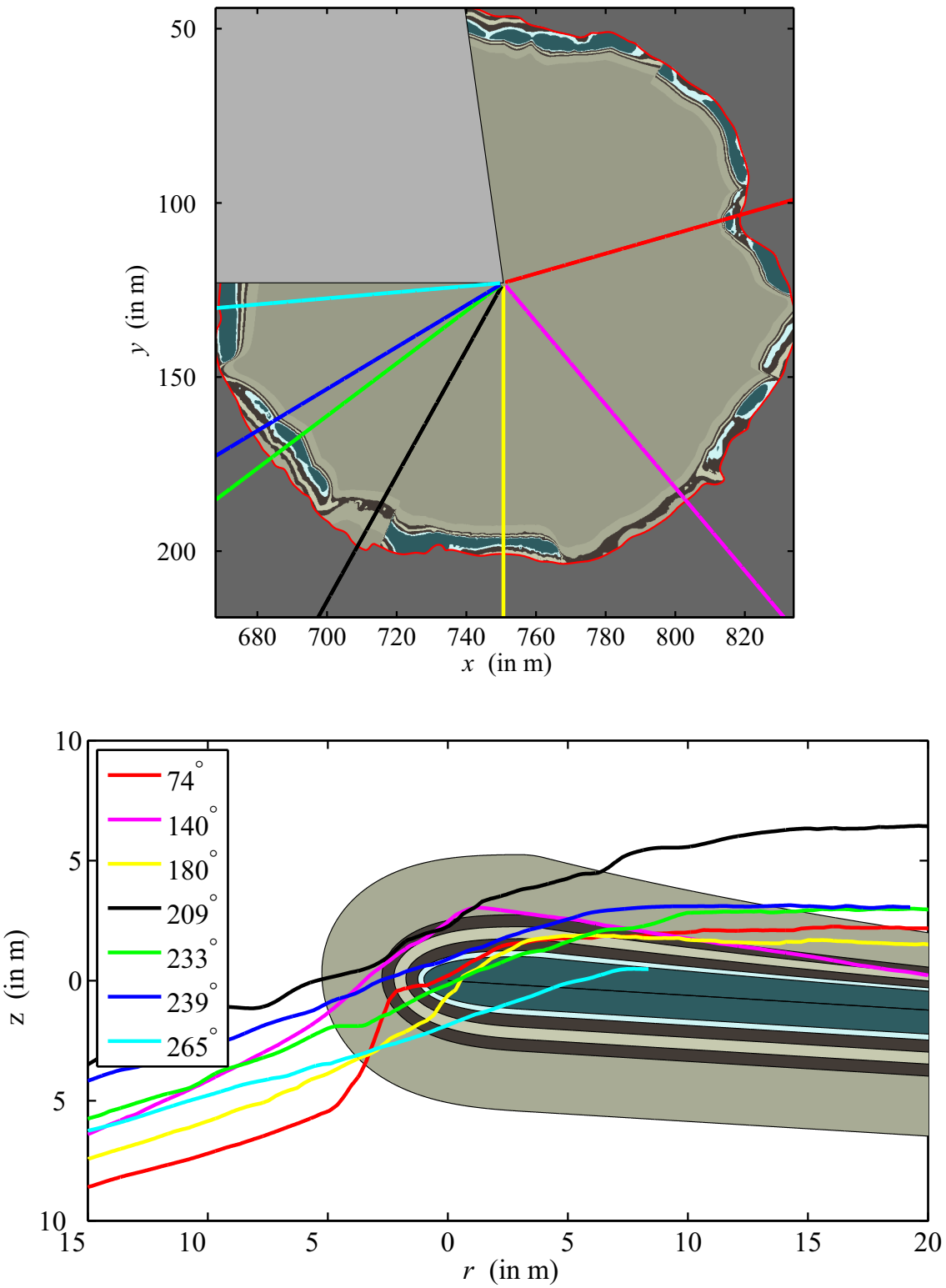

Figure 4-9: Cross-section model 1 with select radial topographic profiles of the Endurance DEM. The distances reported in the bottom frame are measured with respect to the flap hinge, and not the coordinate frame of the DEM.

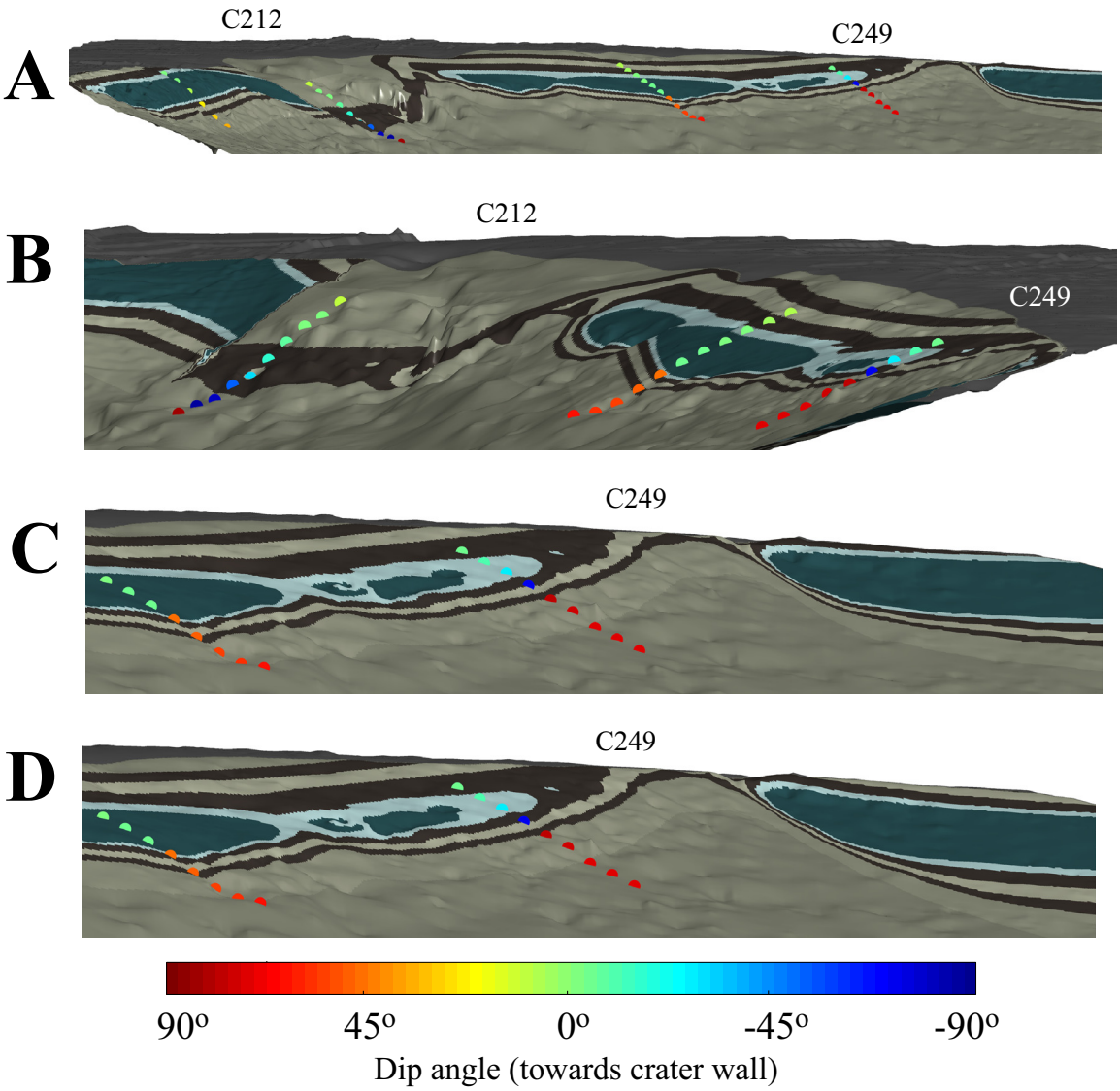

Figure 4-10: A-C) LSM representation of layer expression as well as dip angle in key locations (cf. Plate H, where measurements of dip angle measured on the south wall are indicated). Positive dip angles indicate dip is into the crater wall, while negative dip angles indicate that dip is craterward. A-C were generated using hinge trace A and cross section model 1, whereas D was produced using hinge trace C and the same cross section model. (This modification has the effect of exaggerating the corner-smile that rises to C249 from the right (cf. Plate F)). Corner positions are labeled.

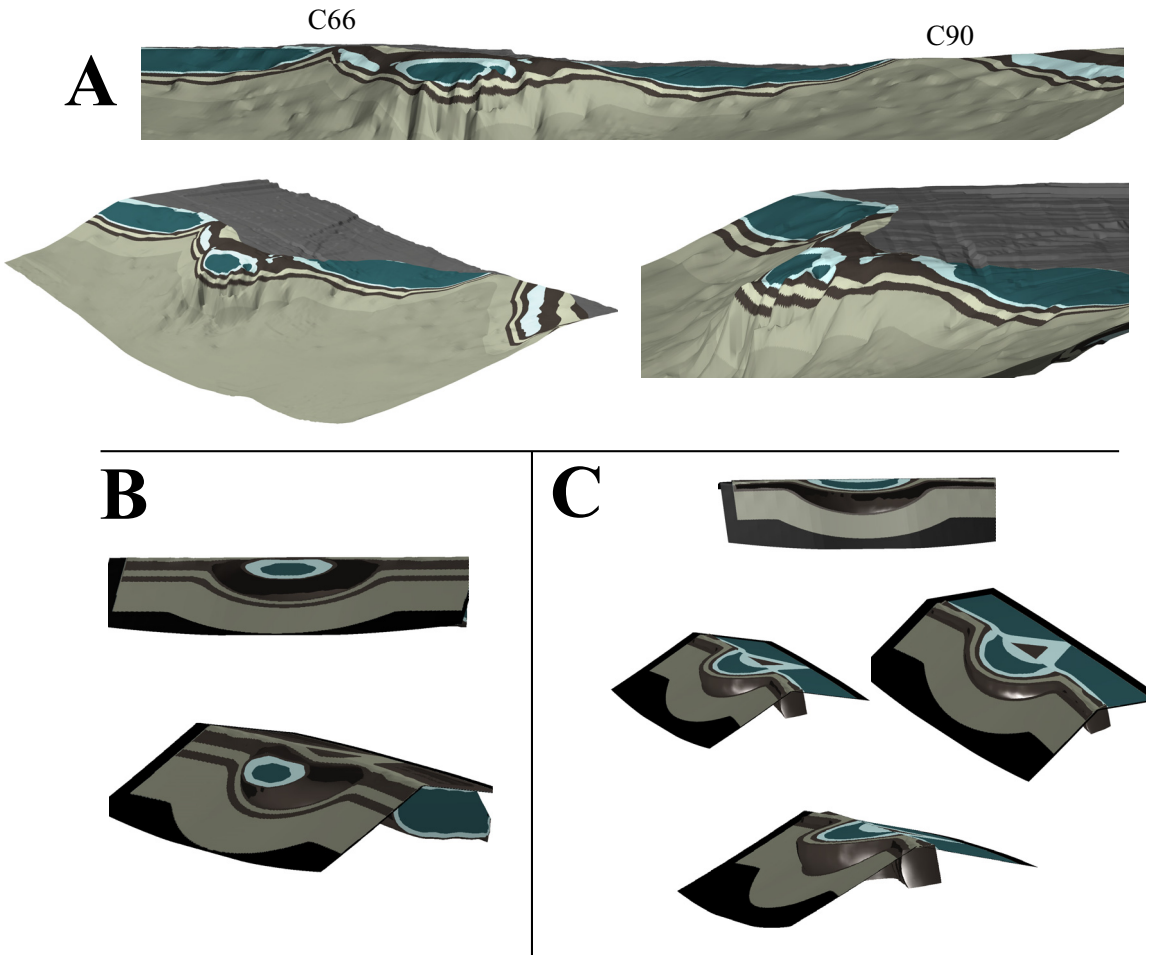

Figure 4-11: A) LSM representation of layer expression in the east wall of Endurance, including the Kalahari promontory (hinge trace A, cross-section model 1). B-C) Alternate models of Kalahari, in which the vertical beds of the resistant (dark) layers protrude from the crater wall. Corner positions are labeled.

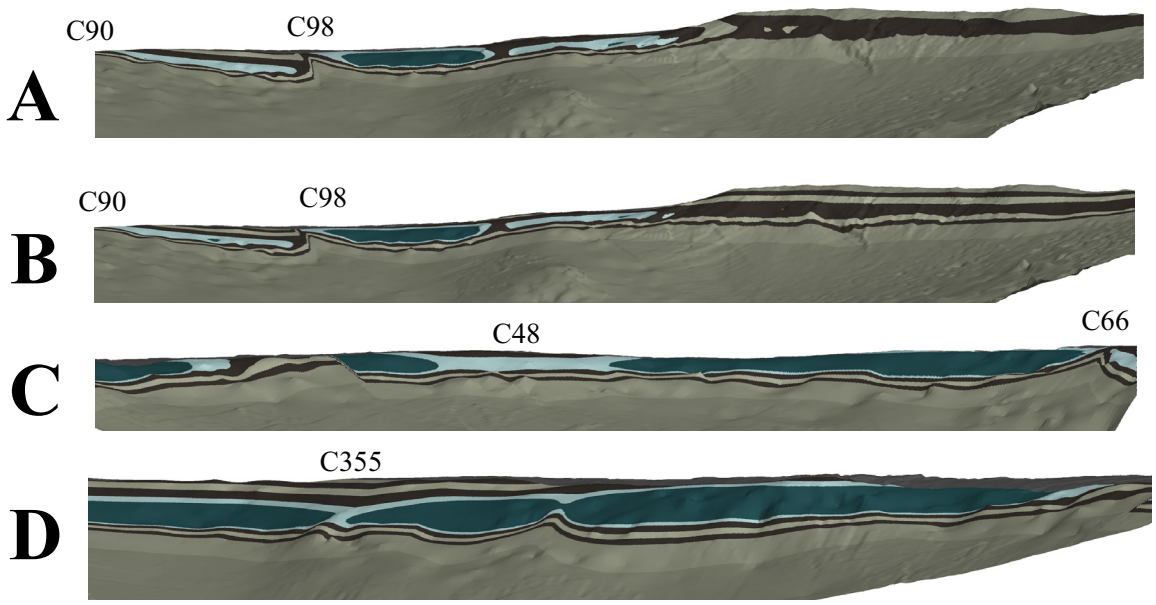

Figure 4-12: LSM representation of layer expression in A) the southeast wall (trace A, cross-section 1); B) the southeast wall (trace B, cross-section 2); C) the northeast wall (trace A, cross-section 1); D) the north wall (trace A, cross-section 1). Corner positions are labeled.

outline of Meteor Crater (i.e., the third occurs in the northeast corner). Parts C and D of Figure 4-21 illustrate the common occurrence of gently-dipping beds of the Moenkopi and Kaibab that occur along the walls *between* corners of the crater. That vertical dips only occur in the corners of Meteor Crater is a very strong indication that Meteor's shape, too, was primarily influenced by excavation rather than early modification. That is, Meteor Crater was also likely excavated in a "stellar" or at least "polygonal" mode. A very recent field study (Kumar and Kring [2008]) has shown that modal fracture azimuths align in this case with the crater *walls* rather than its diagonals. At first blush, this would appear to be at odds with the observations at Endurance, but it is important to bear in mind that Meteor is much larger and that different processes may be more important in this size regime. In Chapter 6, we present a model of crater excavation in fractured targets that provides a very natural means of reconciling the observations just described.

Captions for color plates in fold-out supplement: A) Annotated MER-B Endurance Pan Position 1 panorama (i.e., azumuthal position near 260°) marking the boundaries between layers indicated by the stratigraphic column in Plate L. Depicted here is the north wall; B) annotations for the northeast wall; C) annotations for the southeast wall; D) annotations for the southwest wall. E) Annotated MER-B Endurance Pan Position 2 panorama (i.e., azumuthal position near 100°) marking the boundaries between layers indicated by the stratigraphic column in Plate L. Depicted here is the south wall; F) annotations for the west wall; G) annotations for the north wall. H) Average dip angles of laminations in specific rocks, listed in Tables 4.1 through 4.3; I) LSM model with hinge trace A and cross-section 1 as viewed from the northwest, with corners labeled. J) Context image with corner positions labeled. K) Strike and dip directions of rocks whose dip angles are shown in Plate H and Tables 4.1 through 4.3;

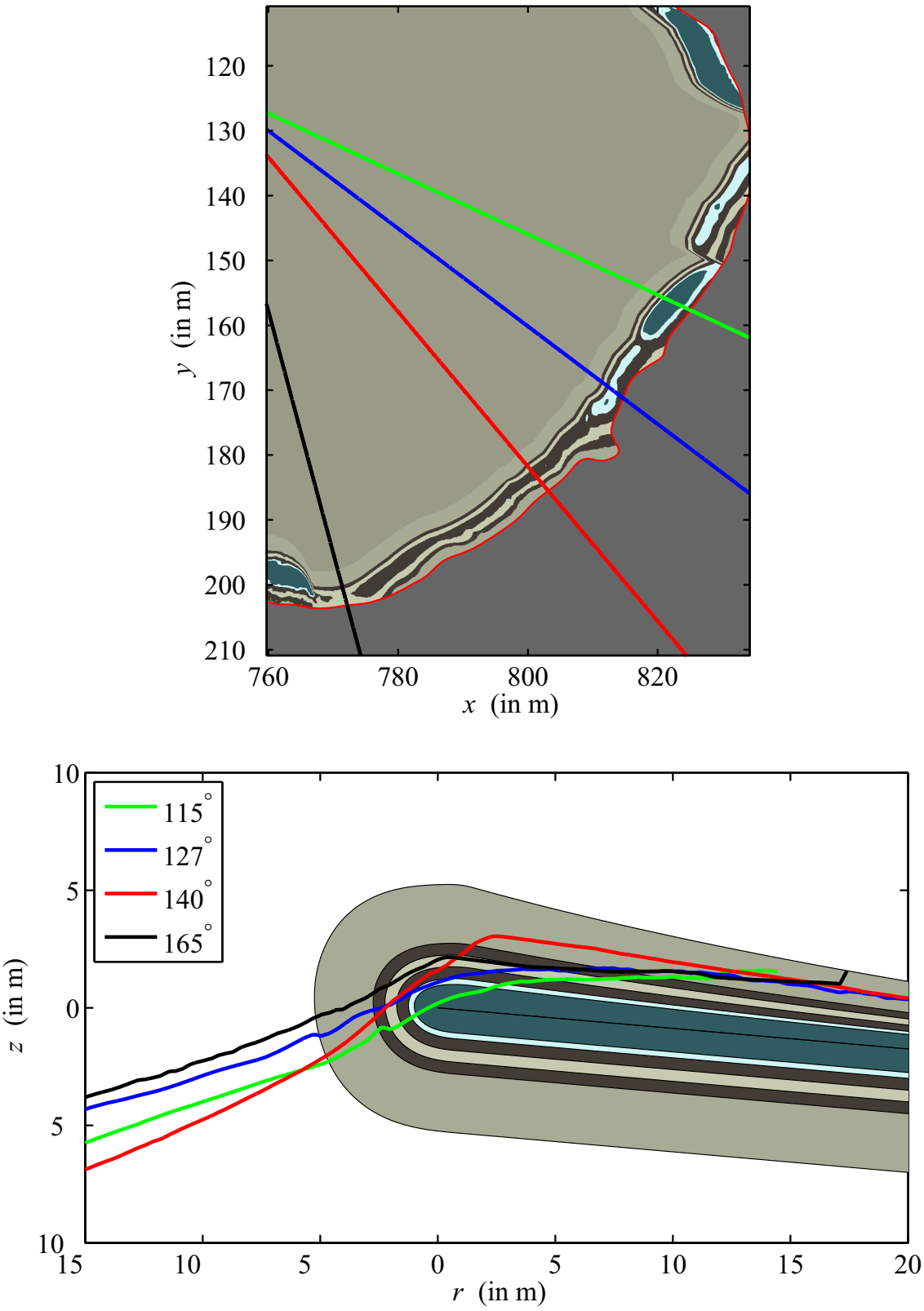

Figure 4-13: Cross-section model 2 with select radial topographic profiles of the Endurance DEM used to construct an alternate model for the southeast corner. The distances reported in the bottom frame are measured with respect to the flap hinge, and not the coordinate frame of the DEM.

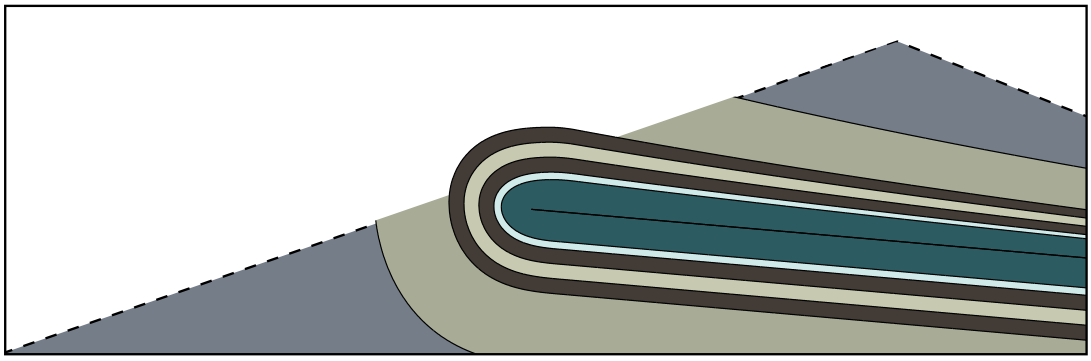

Figure 4-14: A schematic of cross-section model 2 illustrating a possible origin for the correlation of steep wall slopes with outcroppings of the dark resistant layers, as shown in Figure 4-15: i.e., the dark layers preferentially resist erosion, so that overturned or vertical beds remain in tact (e.g., Kalahari, east wall), in some cases becoming undermined and collapsing (e.g., Namib, north wall).

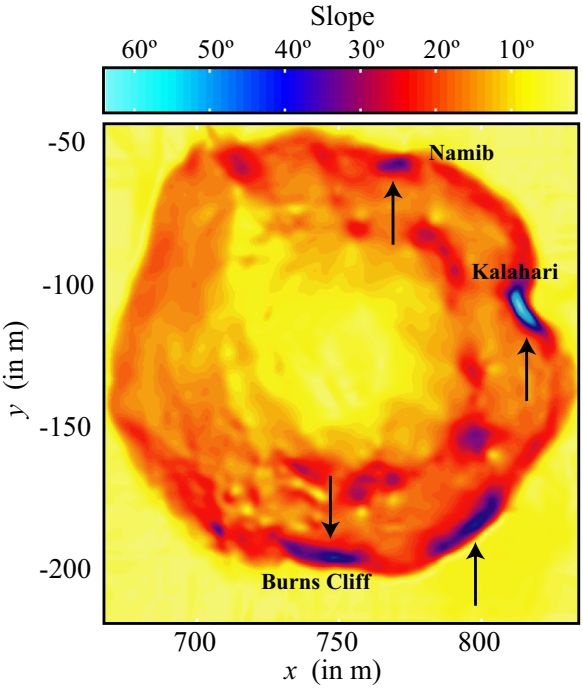

Figure 4-15: Slope map for the Endurance DEM, where three of four locations along the rim wall where steep slopes occur (i.e., all but Burns Cliff) correspond to outcroppings of steeply-dipping resistant (dark) layers. The slopes at Burns Cliff exceed the angle of repose for sand, and likely caused the collapse of the sand layer in which the hinge resides.

Figure 4-17: The stellar mode of excavation (see Figure 4-16) is reflected also in the inverted stratigraphy on the crater flanks, and produces a "coronal" pattern of layering in the continuous ejecta.

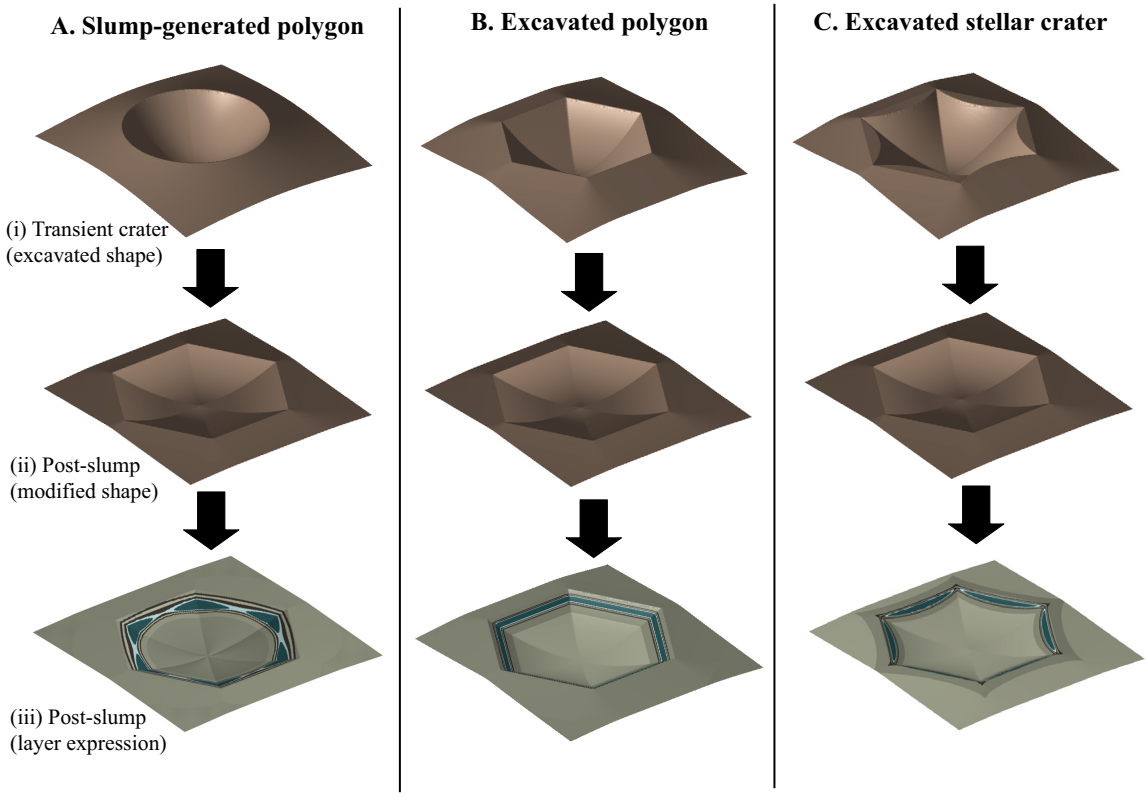

Figure 4-16: Three candidate models for the formation of simple polygonal impact craters, and resultant expression of layering in crater walls. A) A radially-symmetric transient crater is excavated, and then wall-slumping creates the polygonal shape. This is expected to produce a pattern of lozenges-in-corners. B) The transient crater exhibits a polygonal (or non-circular) shape and maintains this shape after slumping. In this case, layering appears uniformly flat. C) The transient crater exhibits a "stellar" or concave/cuspate shape, and the unstable walls between vertices collapse. The outcome is a pattern of smiles or festoons between corners of the polygon.

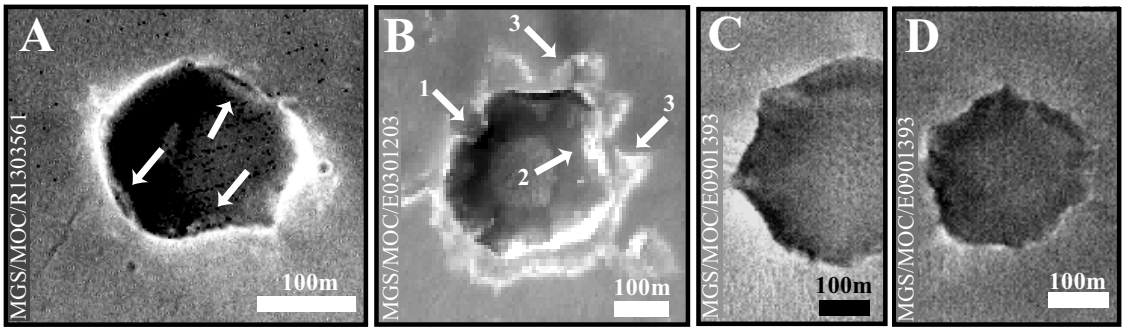

Figure 4-18: MGS/MOC images of impact craters at Meridiani Planum exhibiting features consistent with a stellar mode of excavation: A) Impact crater comparable in size to Endurance (and located just several kilometers away) with clearly-expressed festoons between corners of the polygonal rim trace; B) impact crater exhibiting "coronal" ejecta: (1) promontory, (2) possible festoon, (3) coronal ejecta pattern. That the coronal pattern is not expressed on all sides of this impact crater suggests that a polygonal mode of excavation (B in Figure 4-16) is also important. C) and D): concave/cuspate craters with intervening promontories roughly 150 km east of Endurance Crater at Meridiani Planum, and which may represent a population of stellar craters that have resisted slumping.

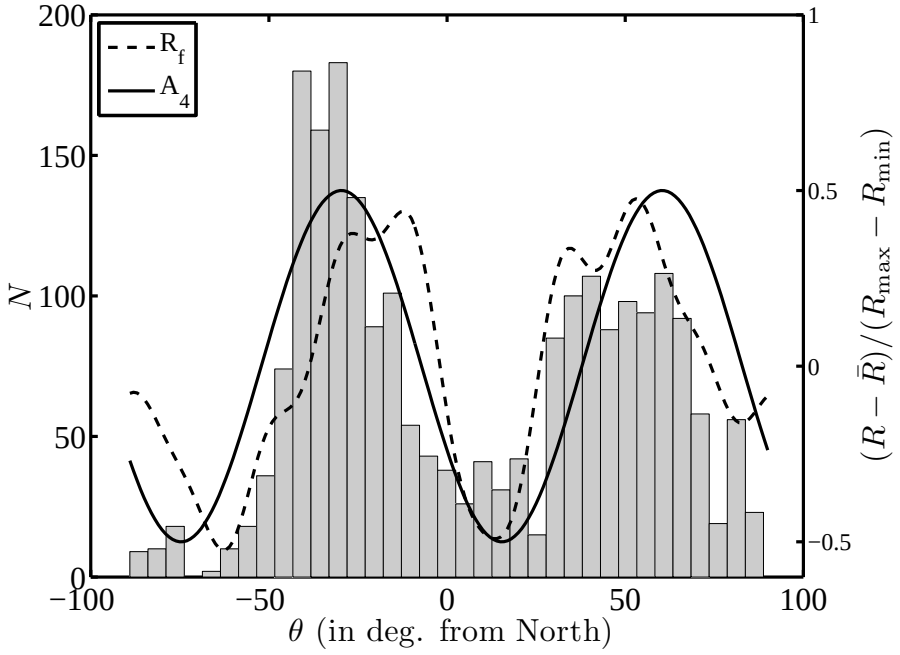

Figure 4-20: Length-weighted histogram of azimuths of fracture-troughs located within 2.5 radii of Endurance Crater as well as the folded radius (R_f: amplitude indicated on right-hand axis) and fourth harmonic (A_4: orientation only) of the Endurance planform. The distribution of fracture azimuths is aligned to within 5° of the diagonals of the crater's planimetric quadrature.

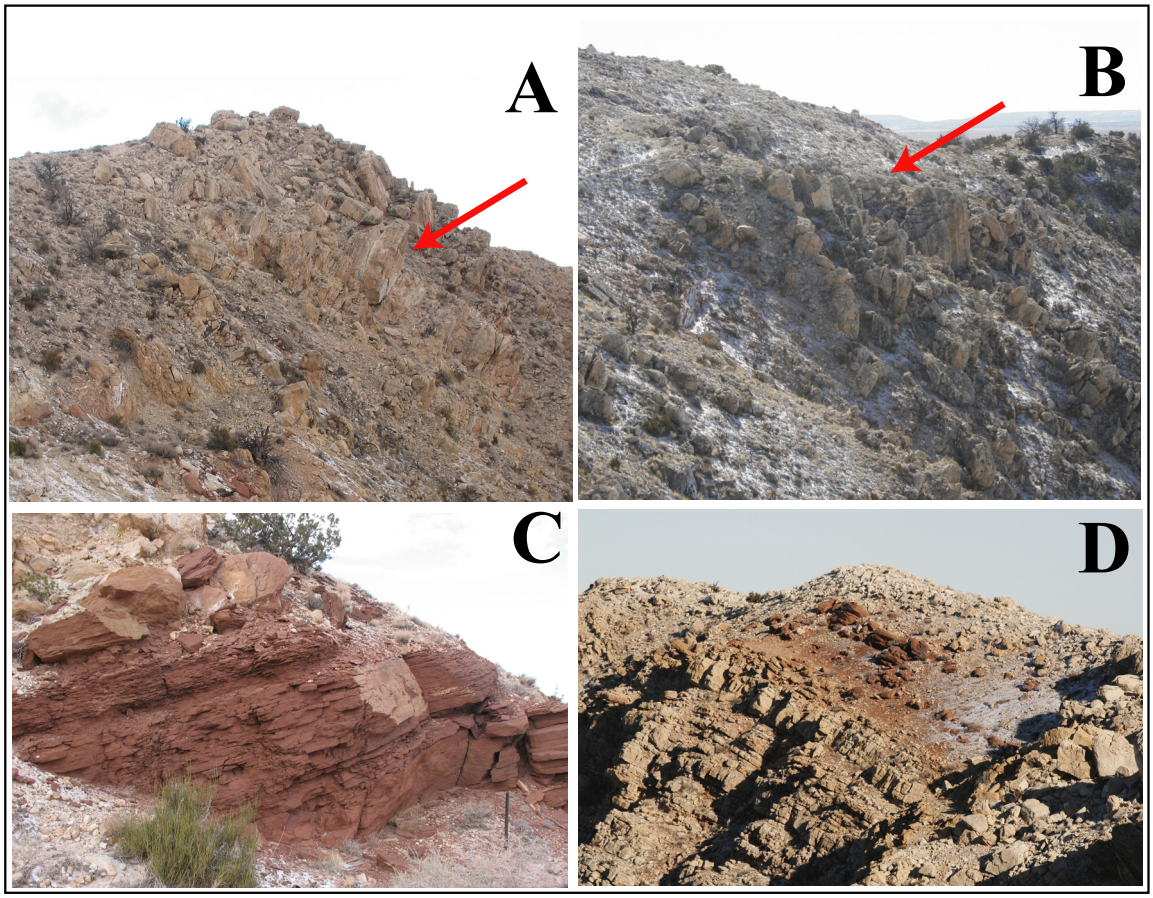

Figure 4-21: Expression of bedding in the walls of Meteor Crater, Arizona, at the positions marked in Figure 4-22. That vertical and overturned beds (Kaibab) occur exclusively near the corners of Meteor Crater (A and B) and that radially-outward dipping beds of the Moenkopi occur exclusively between corners (C and D) strongly suggests a polygonal or stellar mode of excavation for Meteor Crater.

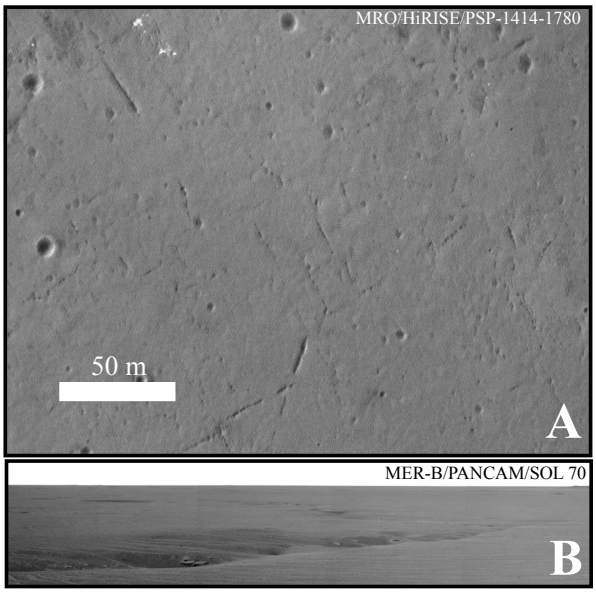

Figure 4-19: Troughs formed by sands draining into fractures in underlying sedimentary rocks at Meridiani Planum as seen in A) MRO/HiRISE and B) MER-B/PANCAM images. Modes in the distribution of trough/fracture orientations align with peaks in the folded radius and 4th harmonic amplitude of the Endurance rim trace, as shown in Figure 4-20.

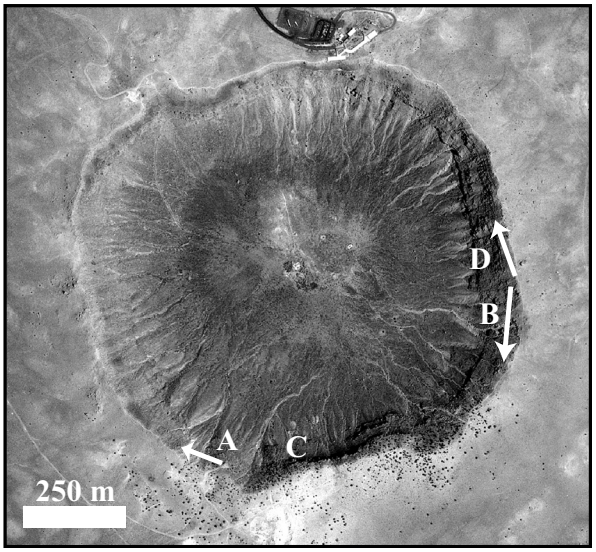

Figure 4-22: Arrows extend from the positions from which images in Figure 4-21 were acquired and toward the features depicted. (Except in the case of C, taken at short range.)

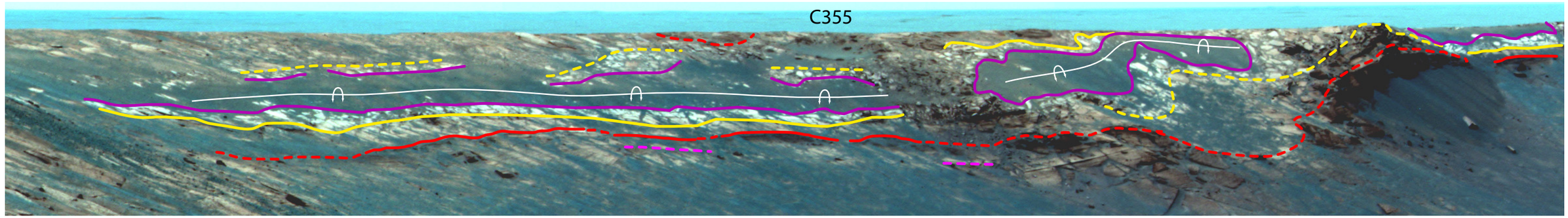

Plate A

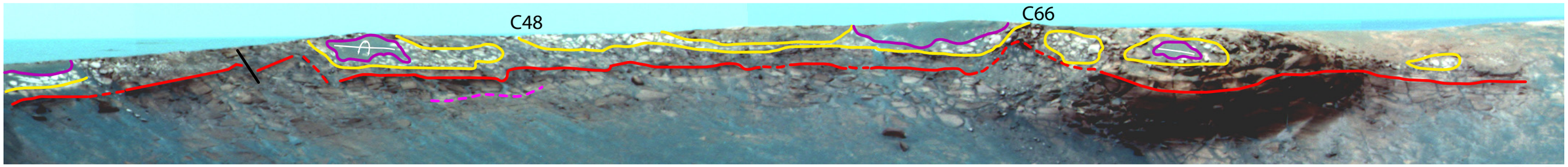

Plate B

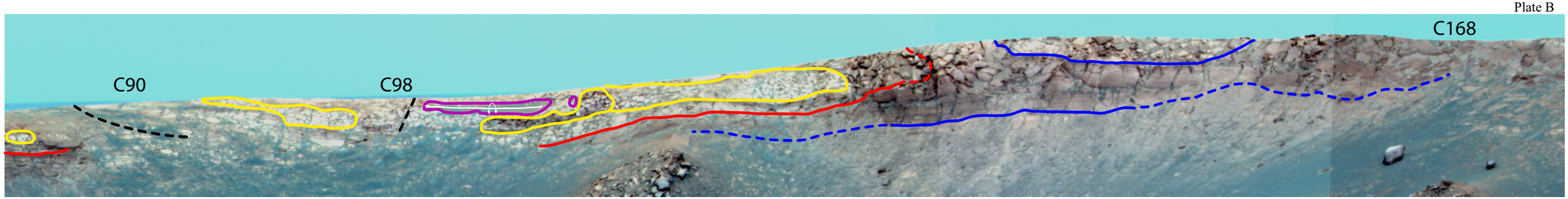

Plate C

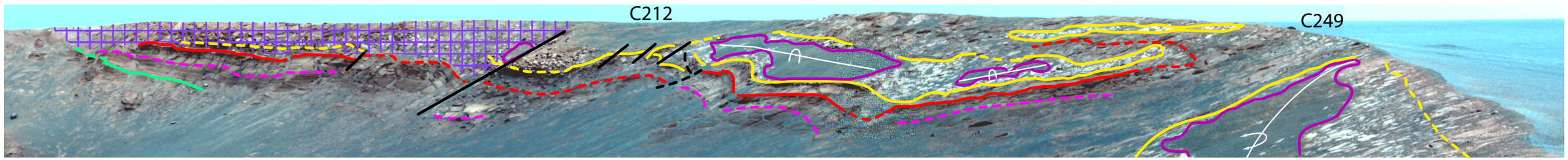

Plate D

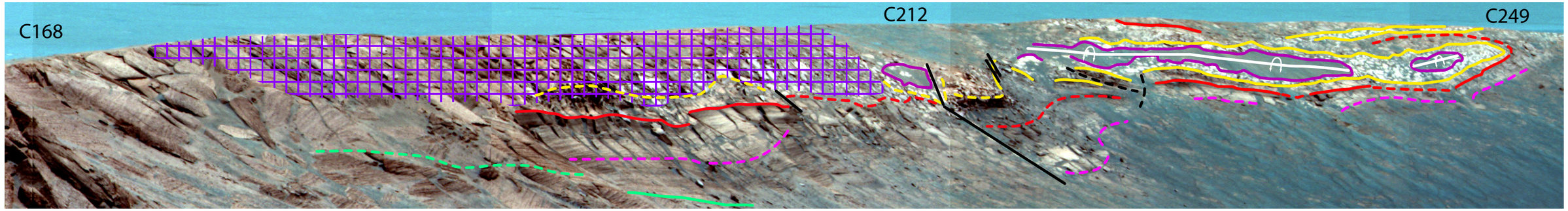

Plate E

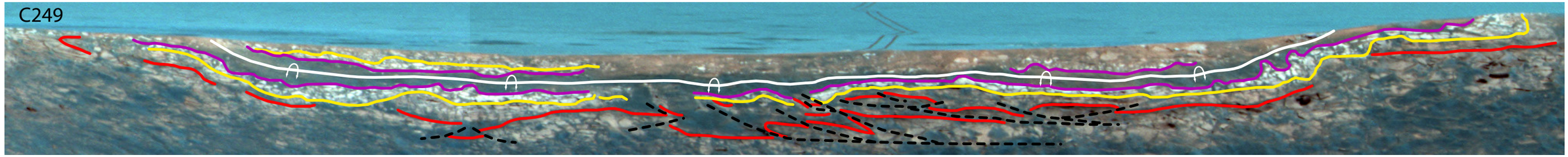

Plate F

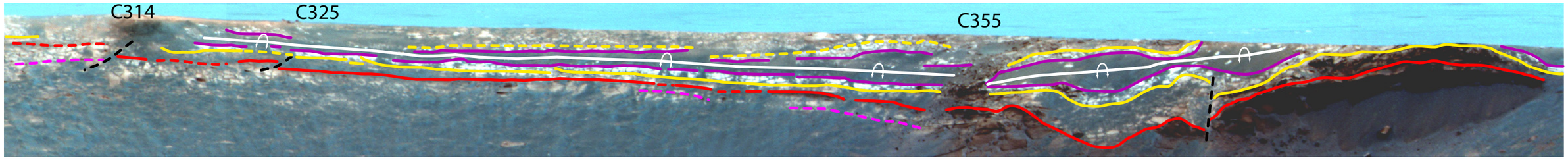

Plate G

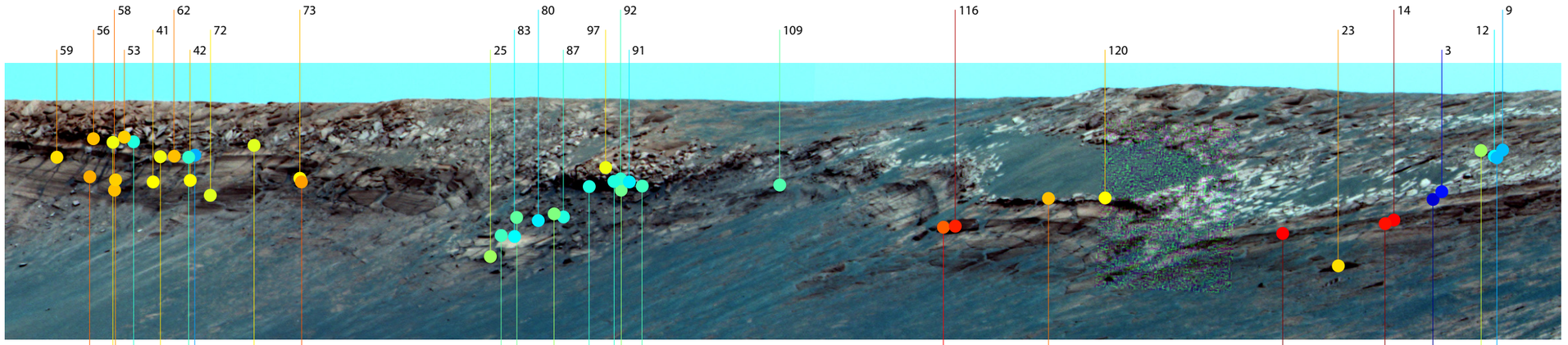

Plate H

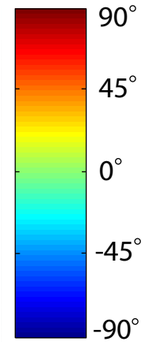

Dip angle
(towards
crater wall)

Collapsed rim wall
(stratigraphy not coherent)

Black only: estimated fault trace

Uncertain inferred fault trace

Stratigraphic layer boundary (e.g., C/D)

Inferred stratigraphic
layer boundary (e.g., C/D)

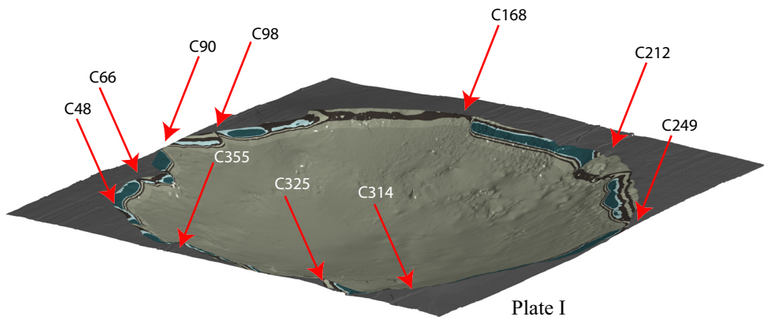

Plate I

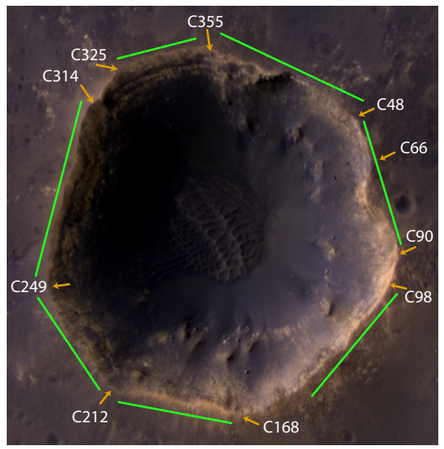

Plate J

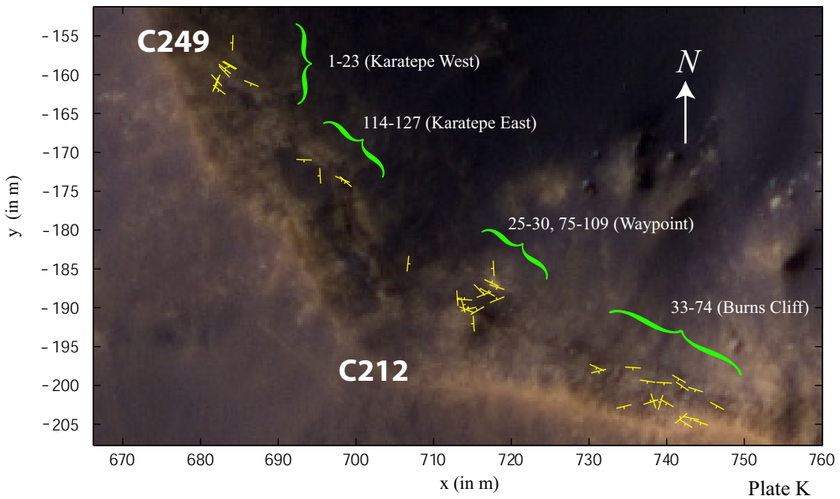

Plate K

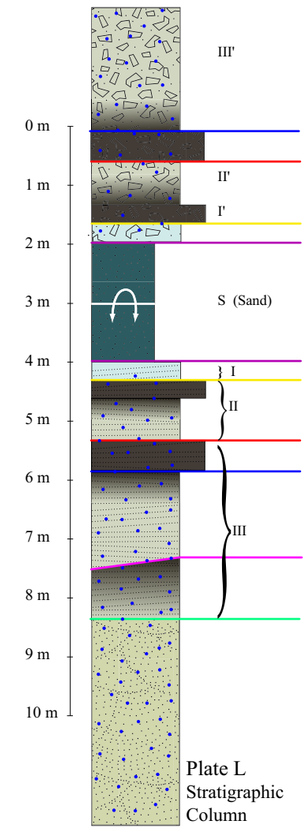

Plate L
Stratigraphic
Column

Chapter 5

Fourier analysis of impact crater morphology: relating target properties and planimetric shape

Abstract: Our aim in this chapter is to illuminate the dependence of planimetric crater shape on the properties of geological targets, as well as modification state. Target properties have been characterized in two ways: (a) by querying global geological maps at crater positions and (b) by noting salient features of target materials in high-resolution context imagery. We have measured the rim trace of 110 comparatively fresh impact craters in HiRISE images (i.e., craters with preserved ejecta), as well as 840 fresh craters in MOC images. From the planimetric shape (i.e., the rim trace) we compute a suite of morphometric quantities, including Fourier harmonic amplitudes and phase angles, as well as measures of deviation from radial symmetry and convexity. We compare the distributions of these quantities for craters that formed in targets exhibiting a range of properties, noting all statistically meaningful differences. We have also measured the departure from radial symmetry of the planimetric shape as a function of crater diameter, which is found to depend on target properties (whether strongly- or weakly-indurated), and which exhibits a clear transition between $D = 150$ and 250 m. Another transition occurs in the range from $D = 330$ m to $D = 650$ m, which marks the onset of significant wall slumping. We also find that the globally-distributed craters in both catalogs exhibit a strong lateral elongation bias (i.e., aligned with the equator). Assuming that elongation azimuth is related to the impact azimuth instead of wind erosion, the distribution of elongation azimuth may be used to make an independent measure of Mars' past obliquity variations.

5.1 MOC Crater-Target Survey

This chapter is devoted to analyses of morphometric quanitites derived from images of simple impact craters on Mars ($D < 5$ km) acquired by orbiting spacecraft, with the aim of recognizing significant relationships between planimetric crater shape and target properties, as well as crater diameter. The results in this chapter are derived from three data sets: (a) MOC Crater-Target Survey (MOC-CTS): a survey of 6,981 MOC narrow-angle images (10% of all narrow-angle MOC images), in which the presence or absence of a small set of crater and target characteristics were noted; (b) MOC Fresh Crater Catalogue (MOC-FCC): 840 fresh impact craters (30 m $\leq D \leq$ 2.8 km) and their morphometric and target attributes, derived from 541 cropped MOC narrow angle images flagged as part of the MOC-CTS (1 to 10 m/pixel). (c) HiRISE Fresh Crater Catalogue (HiRISE-FCC): 110 fresh impact craters (15 m $\leq D \leq$ 4.3 km) and their morphometric and target attributes, derived from 97 high-resolution MRO-HiRISE images (25 or 50

cm/pixel). In this section we are mostly concerned with the MOC-CTS and tallies of qualitative morphometric attributes, used to determine the kinds of target materials in which these occur with the greatest frequency. HiRISE-FCC and MOC-FCC will be described in detail in the following sections, where the results of quantitative morphometric analyses will be compared with the broad conclusions derived from MOC-CTS.

As mentioned, the main goal of this chapter is to relate the properties of target materials to the morphology of impact craters, and to find relationships among morphometric quantities that may reveal new insights into the processes of crater formation and modification. The characterization of target materials has been accomplished in two ways: (a) by querying global geologic maps; (b) by noting structures and patterns that occur in images within the immediate context of an impact crater.

Global geologic maps originally based upon Viking global atlas mosaics (Greeley and Guest [1987], Scott and Tanaka [1986]) were recently vectorized and re-registered in the planetocentric frame (Skinner et al. [2006]), and a more recent northern lowlands map (Tanaka et al. [2005]) based upon THEMIS and MOC imagery and MOLA was originally mapped using vector polygons. Both data sets are formatted as shapefiles, containing the vertices of polygons defining unit boundaries in areocentric coordinates, along with unit symbols and names. We have used these to create high-resolution raster images (100 pixels/degree) in which every geologic unit is assigned a unique color code. These images can be queried to determine the units in which any set of lat-lon positions reside. Because the more recent lowlands map is based upon more complete and higher-resolution imagery, the unit designations made within its domain were given priority (i.e., the Viking-based designations have been ignored in all areas covered by the more recent map).

Each unit has been assigned to a material class on the basis of descriptions published with the aforesaid maps. Our goal has been to distinguish fundamental differences which may account for significant variations in crater formation processes, where the number of possible classes is limited by the often necessarily general character of geological descriptions that are based upon orbiter image data, especially at the low resolutions of Viking-era observations. These broad material classes are listed in Table 5.1 along with with the numeric labels that will be used throughout this chapter and the next one.

It should be noted that some fraction of the planet's surface south of the dichotomy boundary has been misclassified, and that huge variations in geological structure and material properties occur within units assigned to any one of these material groups. For one example, we will discuss later the misclassification of ash deposits on the Tharsis and Elysium rises. The so-called "mantled" class units, which are described as including aeolian sediments and lava flows, is now known to be dominated in many places by sedimentary deposits, such as at Terra Meridiani (Malin and Edgett [2000]). The enormous Vastitas Borealis unit, which dominates the northern lowlands, has been classified as a "sedimentary" unit because of clear evidence for sediments sourced from the highlands and dichotomy boundary, but which has been extensively modified by cryoturbation, desiccation, and thermokarst (Tanaka et al. [2003]). Over large areas, Vastitas Borealis probably overlies extensive flood lavas from the widespread early-Hesparian volcanism that created the ridged plains units covering extensive low-lying portions of the southern plateau (Head et al. [2002]). That is, in addition to local variations in geologic structure and material properties not resolved in global geologic maps, it is important to bear in mind that many geological targets are layered, and that different layers may contain structures and have properties which influence crater formation in different ways. For all of these reasons, it is important also to use context imagery to characterize local target properties to the extent possible – made easier in high-resolution HiRISE images – as well as to compile large numbers of observations in order hopefully to find statistically meaningful relationships that are robust with respect to local deviations from mapped material classifications. In the following

Table 5.1: Target material classes: geological categories to which all map units have been assigned, along with their numeric labels and abbreviations.

No.	Name (abbrev.)	Description
1	Debris (Deb.)	Potentially unconsolidated or weakly-indurated materials from large-scale debris flows and mass-wasting products. Largest concentrations occur along the hemispheric dichotomy boundary.
2	Sediments (Sed.)	Aeolian and alluvial sediments and sedimentary rocks.
3	Debris and sediments (Deb.+Sed.)	Containing examples of material classes 1 and 2
4	Lavas (Lav.)	Lava flows, spanning a broad range of geomorphic expression.
5	Volcanics (Volc.)	Containing examples of material classes 1 and 4; especially including pyroclastic and ash fall deposits, as well as massive volcanic collapse structures.
6	Mantled plains	Lavas or aeolian sediments mantling older rocks.
0	Mixture (Mix)	Containing examples of all material classes, or could not be assigned to any single class or pairwise combination.

sections, and partly because of said difficulties, we have focused upon one of the most basic distinctions: targets dominated by lavas and those dominated by other kinds of materials.

In order to determine whether crater attributes occur more frequently in particular material classes, we first obtain a reference distribution with respect to which deviations can be measured. In Figure 5-1 we have plotted the frequency (as a percentage of total) with which all of the material classes occur in two subsets of the entire image database (MOC-CTS): (a) all images that lie between $\pm 45^\circ$ N, as well as (b) the subset containing fresh impact craters (MOC-FCC). In Figure 5-2 we have plotted the geographical distribution of all the material classes, along with the positions of fresh impact craters in the MOC-FCC and HiRISE-FCC.

The positions of all images evaluated as part of the MOC-CTS have been plotted in Figure 5-3. MOC-CTS consists of all images whose centers lie within one degree of the sequence of latitudes separated in five degree intervals from the South to North Poles (i.e., all images that lie within five degrees of latitudes $\{-85^\circ\text{N}, -80^\circ\text{N}, ..., 80^\circ, 85^\circ\text{N}\}$). All images were evaluated for the presence of the following features: (i) fresh impact craters; (ii) large, highly circular impact craters ($D > 1000$ m); and (iii) numerous ($N > 5$) square-shaped impact craters whose orientations exhibit a consistent relationship with the respect to systematic jointing in the surrounding target materials. In addition, in a large subset of the survey we also noted the presence of (iv) craters with highly concave or cuspate rim wall outlines; and (v) large ($D > 750$ m), markedly quadratic impact craters. The fresh impact crater population catalogued in the survey makes up the MOC-FCC and will be discussed in a later section, along with the criteria used to identify these.

Large circular and square craters ((ii) and (v)) and cuspate/concave craters (iv) were noted in various stages of modification. "Concave/cuspate" refers to the presence of significant concavities in the planimetric crater rim outline (PCRO), or sharp cusps: discontinuities in the otherwise smoothly-varying azimuths of

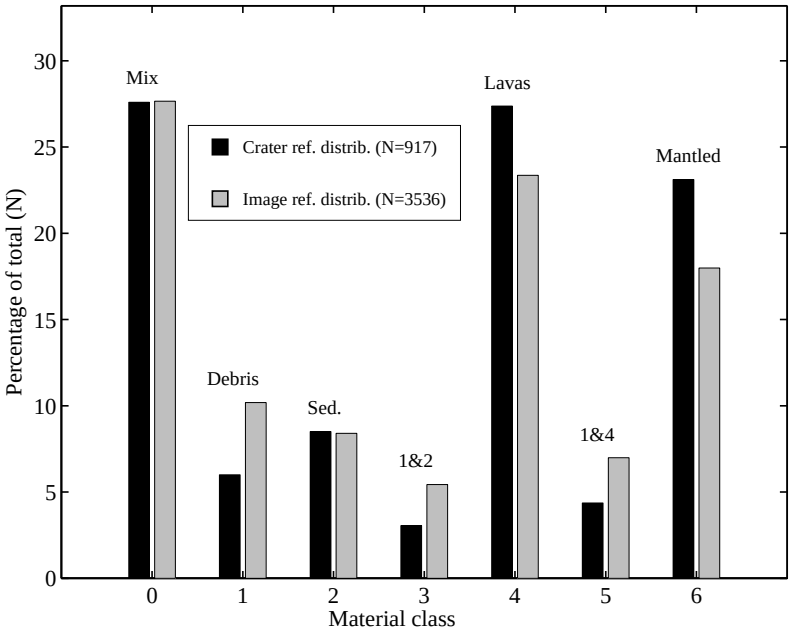

Figure 5-1: Frequency (expressed as a percentage) with which each of the seven material classes described in Table 5.1 occur in two subsets of the MOC-CTS. Gray bars: all images evaluated as part of the MOC-CTS that lie between ±45° N; Black bars: all images containing fresh impact craters.

tangents to the PCRO. Four examples are shown in Figure 5-4. The frequency with which all three of these properties (large-circular, large-square, concave/cuspate) occur in the seven material classes as a percentage of the total number of images in which these shapes were noted, are plotted in Figure 5-5 with respect to the reference distributions shown in Figure 5-1 (i.e., both reference distributions were subtracted from the frequency-of-occurrence (by percentage) of each shape in each class). For example, 18% of all images in the MOC-CTS belong to the "Mantled" material class, but 31% of all observed large square craters occur in this class. The column corresponding to deviations for the "Mantled" class with respect to the image-reference distribution is therefore plotted as $31 - 18 = 13\%$ in Figure 5-5.

In order to determine the statistical significance of deviations from the reference distributions, we have sampled at random 1,000 identically-sized subsets of the reference distributions, to establish what magnitude of deviation may be attributed to chance alone. For example, large circles were observed in 215 images, and we therefore acquired 1000 randomly-sampled subsets from each reference distribution, each containing 215 values (i.e., ranging from 0 to 6). The deviations with respect to reference distributions shown in Figure 5-5 can then be compared with the standard deviation measured for these random samples. We find that all of the following differences exceed the level of three standard deviations: (A) Concave/cuspate craters are more common in sedimentary and mantled units (classes 2 and 6) and less common in volcanics (class 5); and (B) large circles occur more commonly in lavas (class 4). Additionally, the following differences exceed two standard deviations: (C) concave/cuspate craters are more common in debris units (class 1) and less common in lavas (class 4) as well as mixed sediment and debris units (class 3); (D) large circles are more common in sedimentary units (class 2) and less common in debris units (class 1); (E) large squares are more common in mantled units.

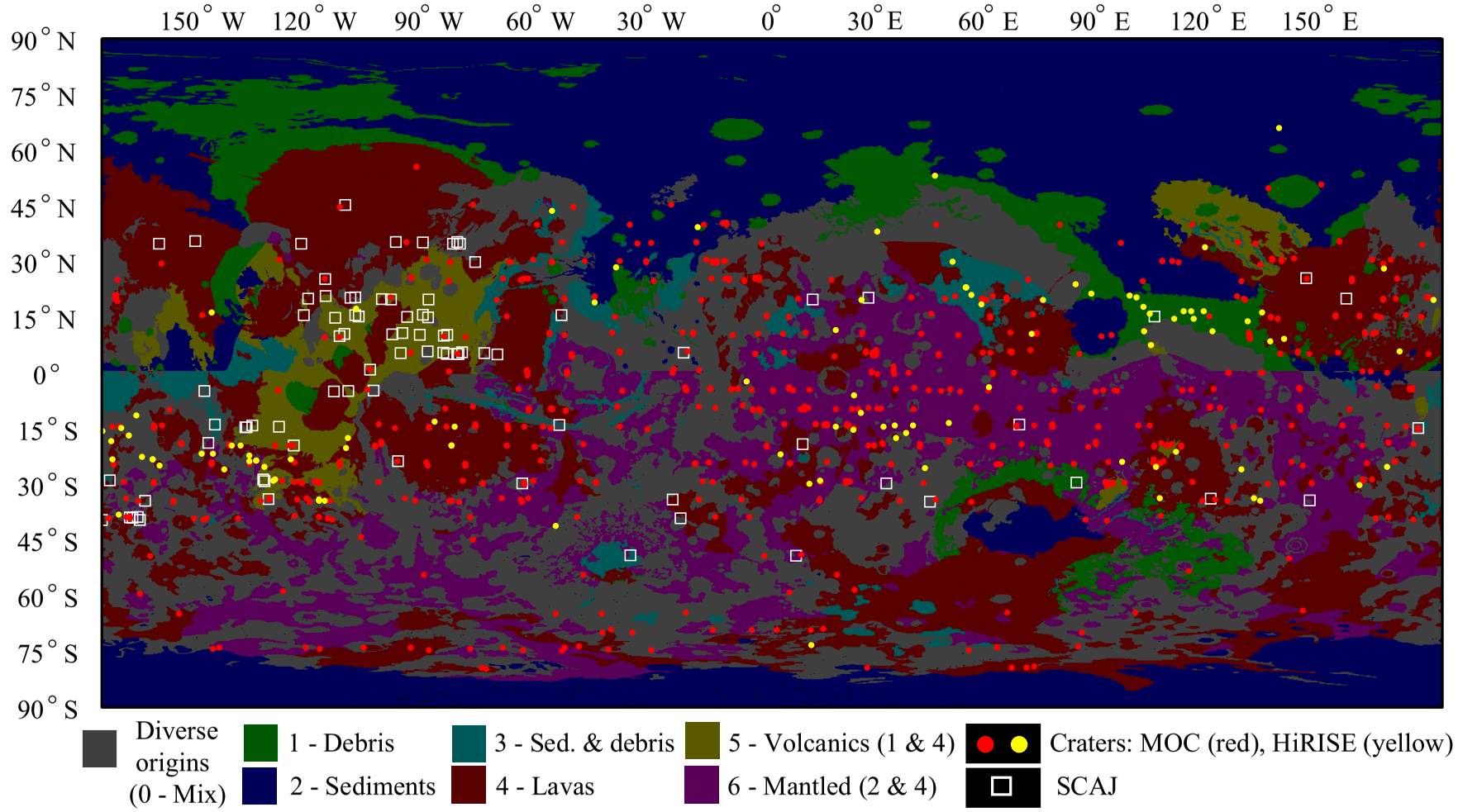

Figure 5-2: Geographical distribution of the seven material classes described in the text. Also plotted are the positions of all fresh impact craters in the MOC (red dots) and HiRISE (yellow dots) Fresh Crater Catalogs, as well as the positions of images containing Square Craters Aligned with Jointing (SCAJ), described in the text and depicted in parts A-C of Figure 5-6.

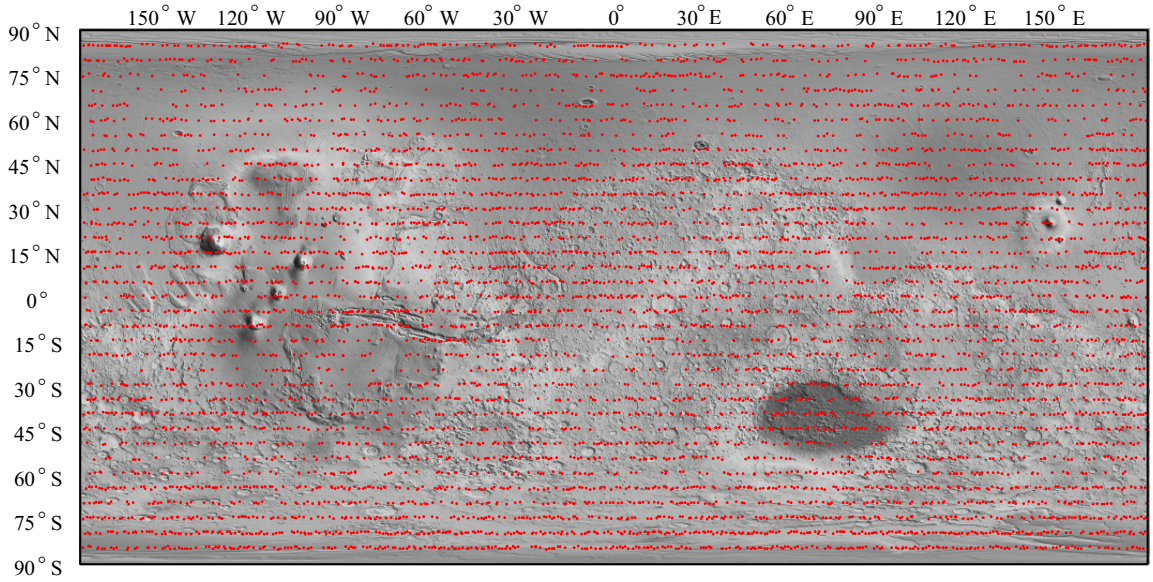

Figure 5-3: The positions of all 6,981 images evaluated as part of the MOC-CTS are plotted in simple cylindrical projection over shaded-relief MOLA topography. Sampled lines of latitude are separated by 5°, and contain all narrow-angle MOC images within 1° of each line. (The much higher density of images at high latitudes is a useful means of compensating for the paucity of impact craters in these regions.)

All three of the morphological properties so far discussed (large-circular, large-square, concave/cuspate) are qualitative designations, recorded in the course of a large image survey for the purpose of drawing preliminary conclusions about the kinds of target materials and geologic environments in which these shapes occur most frequently. Although by themselves less convincing, these results lend support to conclusions derived from studies of fresh crater populations described in later sections, in which quantitative morphological metrics are used as the basis of comparisons.

Aligned square craters

Since the primary aim of this study is to find relationships between target properties and crater shapes, we took special note of all images in which there is a clear relationship between geological structures and crater morphology. Nowhere is this more striking than what occurs in a subset of images where conjugate sets of systematic joints in target rocks clearly align with the walls of mostly square-shaped impact craters. These are overwhelmingly small craters ($D < 500$ m), often with flat bottoms, and may belong to populations of heavily modified craters as well as secondary crater rays and clusters. Two examples are shown in Figure 5-6, where arrows indicate shallow escarpments that are aligned with crater walls. We have plotted the locations of these images in Figure 5-2 (white squares) and tallied their frequency-of-occurrence in the seven material classes, in Figure 5-7. The vast majority occur in volcanic environments, and are probably examples of the horizontally-bedded ash deposits that dominate portions of the Tharsis and Elysium volcanic rises (Carr [2006]): the examples shown in Figure 5-6 are drawn from both locations. Approximately 3% of all images residing in material class 4 (Lavas) exhibit this pattern of aligned square craters and correlated conjugate jointing. That is, at least this fraction of all "lavas" have been misclassified.

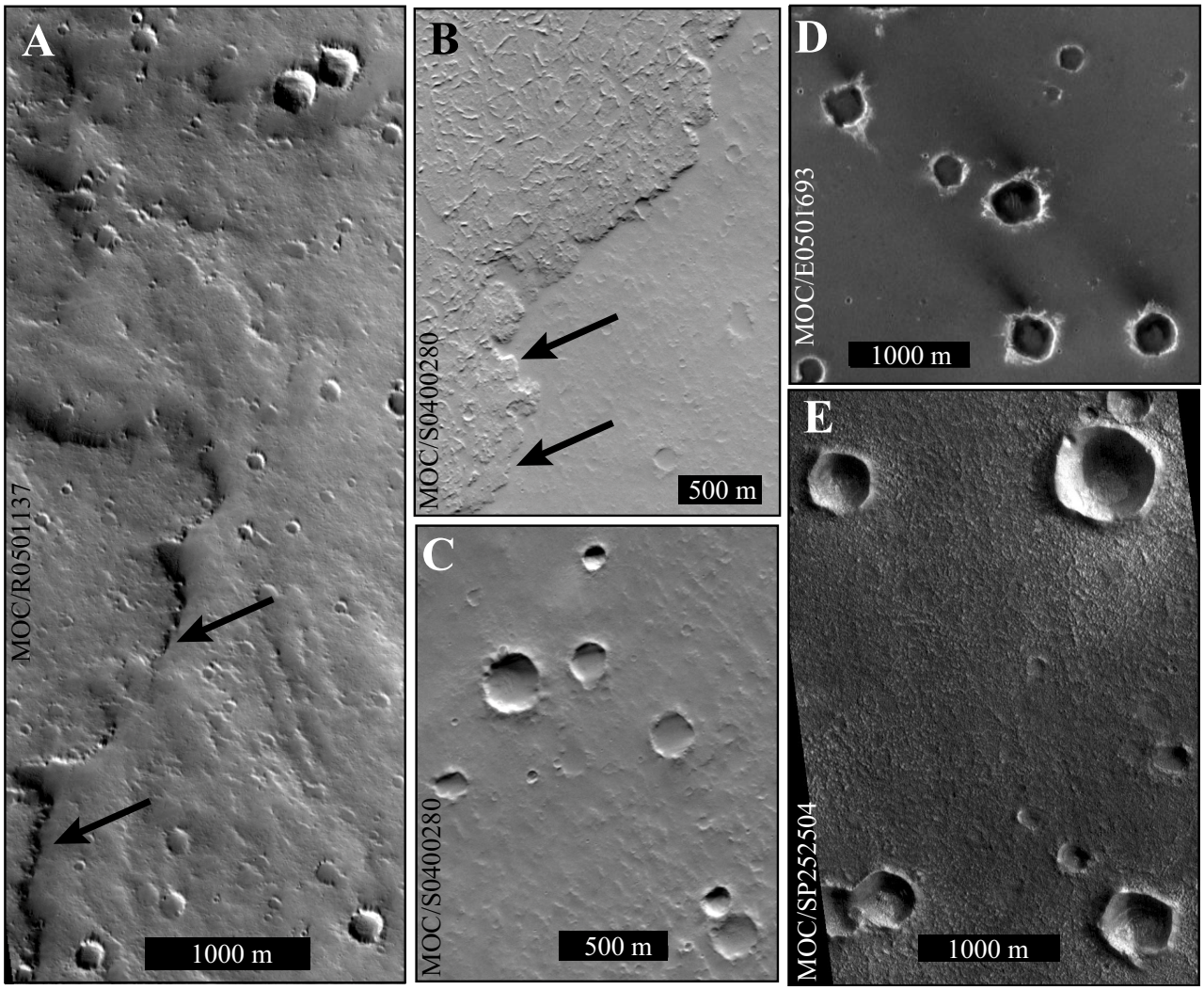

Figure 5-6: A-C) Groups of small, shallow, flat-bottomed, square-shaped and rectangular impact craters aligned with each other as well as conjugate joints in horizontally-bedded indurated ash layers on the Elysium (A) and Tharsis (B-C) volcanic rises. Arrows point to shallow escarpments indicating dominant joint orientations in target rocks. These craters probably belong either to a population of highly modified craters, or else a cluster or ray of secondary craters. D) A dense cluster of probable secondary impact craters 100 km to the southeast of Endurance crater at Meridiani Planum, exhibiting prominent polygonal morphology in the absence of statistically significant alignments. E) An extremely rare group of aligned large, quadratic and bowl-shaped impact craters, located in the Vastitas Borealis Interior unit.

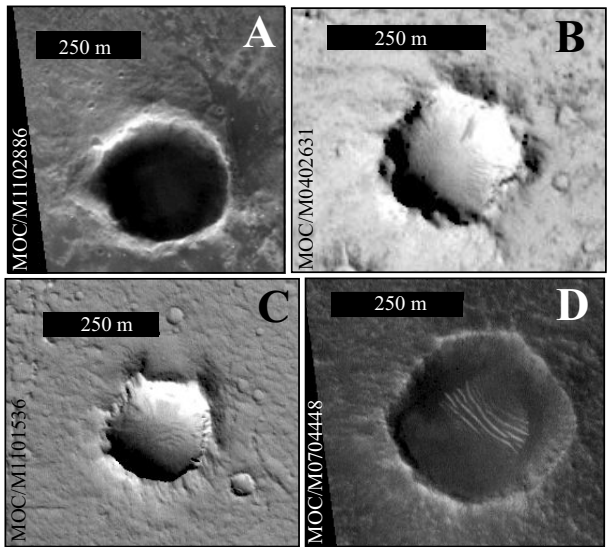

Figure 5-4: Examples of the concave/cuspate morphology, exhibiting marked concavities and or prominent cusps in the planimetric rim outline. A) Unit not identified, (-24.5° N, 97.2° E); B) In lavas on the Elysium rise, (25.5° N, 172.7° E); C) Amazonis Planitia, (20.6° N, 200.2° E); D) Vastitas Borealis interior, (30.5° N, 94.00° E). (All positions expressed in areocentric coordinates.)

In order to search for and demonstrate more rigorously a strong coherence in crater rim strikes, we have developed tools for measuring these orientations in a manual and automated fashion. The most basic manual measurement consists of simply collecting the image pixel positions of endpoints bounding straight segments of the crater rim wall and calculating an orientation angle (azimuth). The main difficulty with this approach is the strong bias that favors recognizing straight features that are oriented vertically, horizontally, and at 45° with respect to an image pixel grid. That is, a straight linear feature whose image representation is spanned by few pixels will only appear perfectly straight at these orientations, and will appear nearly straight in the immediate neighborhood of these orientations. This bias can be erased completely by measuring straight wall segments from nine cropped images of a single impact crater, where

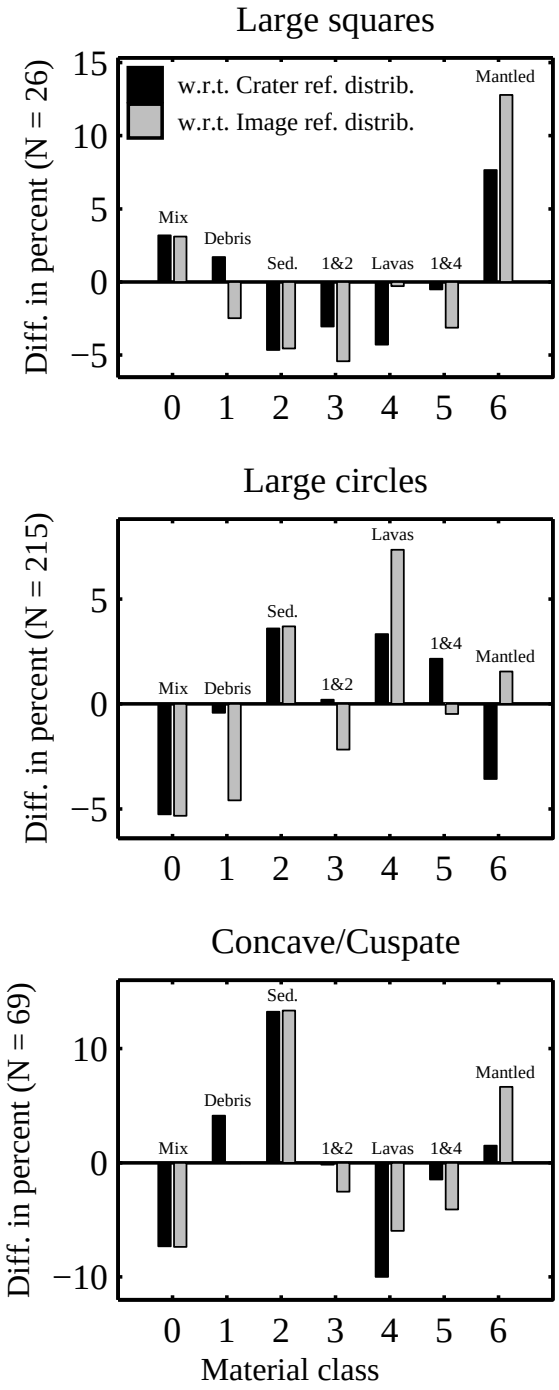

Figure 5-5: Frequency of morphological attributes within each material class, plotted as a deviation with respect to expected values from the reference distributions plotted in Figure 5-1. Bars plotting above zero indicate an increase with respect to reference values, and below zero indicate fewer occurrences than expected.

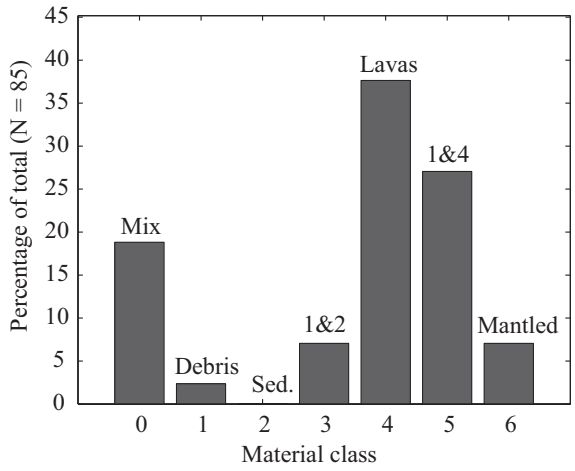

Figure 5-7: Frequency with which groups of aligned square and rectangular impact craters (aligned with conjugate jointing in context materials) occur within each material class, expressed as a percentage of all occurrences. Because the vast majority appear in volcanic environments, target materials in this case are probably horizontally-bedded ash deposits.

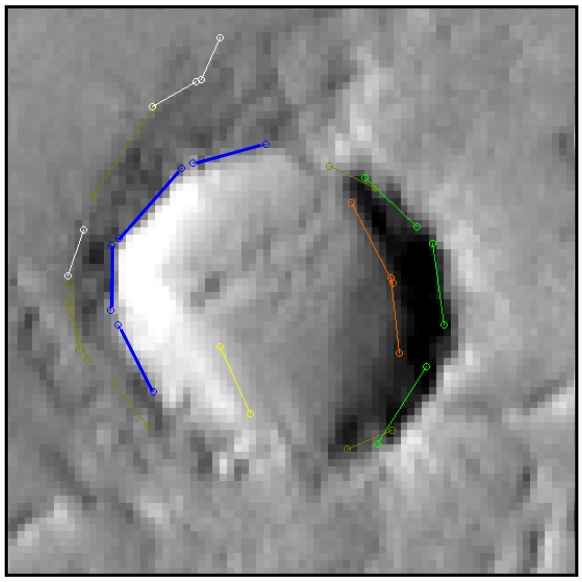

Figure 5-8: Example result of automated detection and classification of straight crater rim segments. Light-green and blue segments were recognized as belonging to rim boundaries, orange and yellow to shadow boundaries, and the remaining to probable ejecta margins. The automated method correctly classifies the majority of straight boundaries once it has been trained with not more than 5 examples.

the nth image has been rotated by $n5°$. (This ensures that all straight segments will have – in at least one case – an orientation that favors detection.)

We have also developed an automated method which relies on Canny edge detection (Canny [1986]) to find and trace boundaries at which grayscale pixel intensity abruptly changes. Because these boundaries can correspond to features other than crater rims, we have trained a decision tree (Breiman et al. [1993]) to distinguish crater rims from shadow boundaries and ejecta margins, on the basis of angular position with respect to the crater center, and the orientation of intensity gradients across detected boundaries. (For this reason, the training must be repeated for each image with a new illumination angle, but requires no more than five examples.) Straight segments of rim outlines were recognized by finding boundary fragments in which the azimuthal orientation of a running linear regression deviated less than a specified amount. An example of the results from this automated detection and classification method is shown in Figure 5-8. Because this automated measurement also suffers from the bias described above, it is repeated for nine rotated images (as before) and the orientations of all detected segments are recorded.

Shown in Figure 5-9 are histograms of rim-strike azimuths measured from craters in MOC image S0400280 (shown in Figure 5-6, parts B and C) using the manual and automated methods. This image was acquired from a location on the eastern flank of the Tharsis rise, near Echus Chasma. The distributions largely concur with each other, and illustrate the dramatic alignment of crater walls (in this case coinciding with the orientations of nearby shallow escarpments). Rim-strike azimuths were also measured in this way for clusters of small impact craters in which no alignments can be discerned by casual inspection. These measurements were car-

ried out for all craters in a ray of probable secondaries at Meridiani Planum (shown in Figure 5-6, part D, $\sim$ 100 km southeast of Endurance crater), and mixed populations of probable primaries and secondaries in northwest Arabia Terra (MOC/R1004721, 30.4° N, 13.8°W, areographic), and Lunae Planum (MOC/R1302158: 19.72°N, 68.08° W; and MOC/R1201534: 20.24° N, 67.79°W, areographic). In these cases, the measured rim-strike azimuthal distributions are statistically indistinguishable from a uniform distribution. Aligned square craters that are simultaneously large ($D \geq 500$ m), bowl-shaped (not flat-bottomed) and comparitively deep are extremely uncommon. A rare example is shown in Figure 5-6, part E, which occurs in the lowlands Vastitas Borealis unit, and where potentially correlated target structures are not in evidence.

Preliminary conclusions

Although mostly consisting of qualitative observations, the MOC Crater-Target Survey (MOC-CTS) offers several preliminary conclusions to supplement the quantitative morphometric analyses of the MOC and HiRISE Fresh Crater Catalogs in the following sections:

- Large circular craters ($D > 1,000$ m) in varying stages of modification are more common in lavas and sedimentary units.
- Concave/cuspate craters in varying stages of modification are more common in sedimentary, debris, and mantled units, and less common in lavas.
- Large square craters ($D > 750$ m) occur more commonly in mantled units.
- Groups of large, aligned square craters that are bowl-shaped are extremely rare, occurring in fewer than 0.1% of all images evaluated as part of the MOC-CTS.
- Groups of aligned square and rectangular craters are overwhelmingly small ($D <$ 500 m), shallow and flat-bottomed. Their rim walls usually align with conjugate systematic joints, and occur most commonly in horizontally-bedded ash deposits in the Tharsis and Elysium volcanic provinces. It is not clear from these observations whether the alignment is the consequence of modification processes or an excavation process peculiar to primary or secondary impact craters.

5.2 Crater/Target Attributes: MOC-FCC & HiRISE-FCC

In this section we define the qualitative attributes used to characterize the crater and target materials in the HiRISE Fresh Crater Catalog (HiRISE-FCC) and MOC Fresh Crater Catalog (MOC-FCC), as well as quantities measured and calculated which describe the shape of planimetric crater rim outlines (PCROs) in these data sets. The HiRISE-FCC is made up of 110 fresh impact craters, and the MOC-FCC is made up of 840 fresh craters. We start by defining what counts as a "fresh" crater, based on the appearance of ejecta. Later, when discussing quantifiable properties, we define the depth-diameter ratio and "fill-ratio," which are both measures of the modification state of an impact crater. For now, we define only the *qualitative* attributes used to select craters for the catalog, bearing in mind that these ratios are also used at a later stage to select subsets of the catalog for analysis.

Qualitative attributes

Craters in the HiRISE-FCC and MOC-FCC were chosen according to characteristics of their ejecta. The vast majority of impact craters on the surface of Mars have been significantly modified by a wide range of processes, so that barely any evidence remains of their ejecta. We have selected craters whose ejecta are expressed in any one of the ways depicted in Figure 5-10: as boulder fields (part A); as having modified or covered the texture of surrounding terrain (part B); as having modified or covered the texture

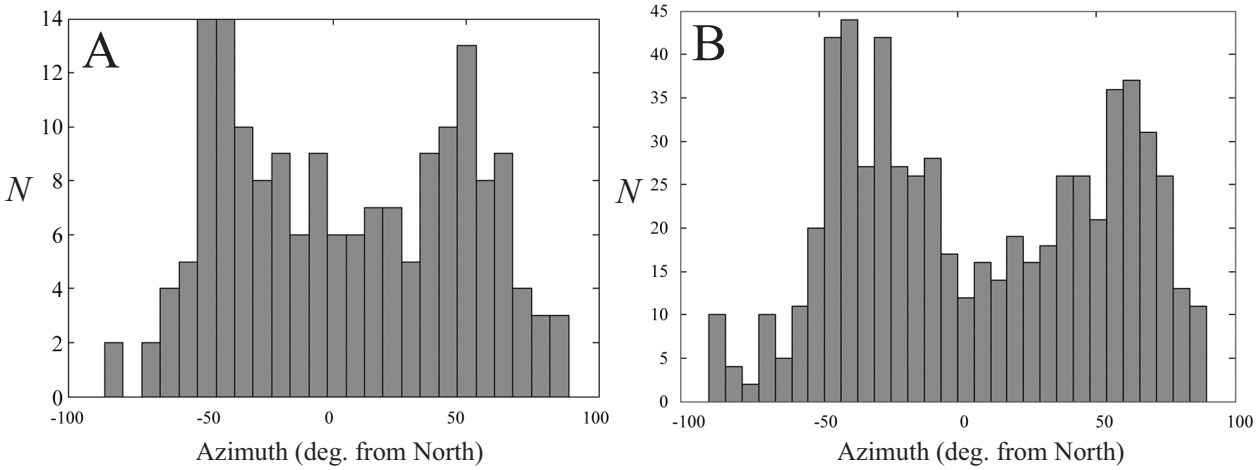

Figure 5-9: Histograms of the azimuths of straight rim walls of craters in MOC/S0400280, shown in Figure 5-6, which formed in horizontally-bedded ash deposits. A) measurements obtained using the automated method described in the text; B) measurements obtained using the manual method, which strongly concur. In this case, peaks in the distribution coincide with the orthogonal orientations of a conjugate set of systematic joints in the target rocks.

of surrounding terrain as well as having a distinct albedo (part D); as having a distinct albedo while merely overprinting features in the surrounding terrain (parts E, F, and G). It is important to acknowledge that ejecta belonging to the latter category may in some cases be a result of aeolian processes transporting material from crater rims and crater interiors onto the surrounding terrain. In practice we find it is very difficult to distinguish objectively between rayed ejecta and long wind streaks.

A number of qualitative attributes relating to the crater rim and walls can be used to characterize modification state as well as properties of the materials in which craters have formed. Major discontinuities in crater rims or "rim breaches" (Figure 5-10, Part C) have been noted and will be used later to help distinguish modified craters. Some of the most important rim and wall attributes are only visible in the higher resolutions at which HiRISE imagery is acquired, where these are illustrated in Figure 5-11: rounded rims (parts A and B; contrast with parts C and D), where the rim crest is significantly broader than 1 m; walls densely covered with rocks and boulders (part B, contrast with D); and slides of scree and other evidence of mass movements on the upper rim wall (part C). For now, our purpose is only to establish the objective criteria according to which these characteristics may be assigned. Later we address what these features mean for the nature of target materials and modification state, and to which macroscopic morphological properties they are strongly correlated.

Also in HiRISE imagery it is often possible to find clues about the nature of target materials by noting features in the immediate context and away from ejecta. The most important of these are shown in Figure 5-12: i.e., the presence of sharp edges (at approximately meter-scale and narrower) bounding escarpments and facets (parts A and B, respectively) as well as troughs and fissures (part C); the presence of significant roughness elements and topographic relief (parts A, B, and D); systematic jointing suggested by aligned fractures and escarpments (part A); the presence of rocks and boulders scattered across the inter-crater terrains and away from ejecta (part A); concentrations of rocks and boulders on topographic (roughness) elements

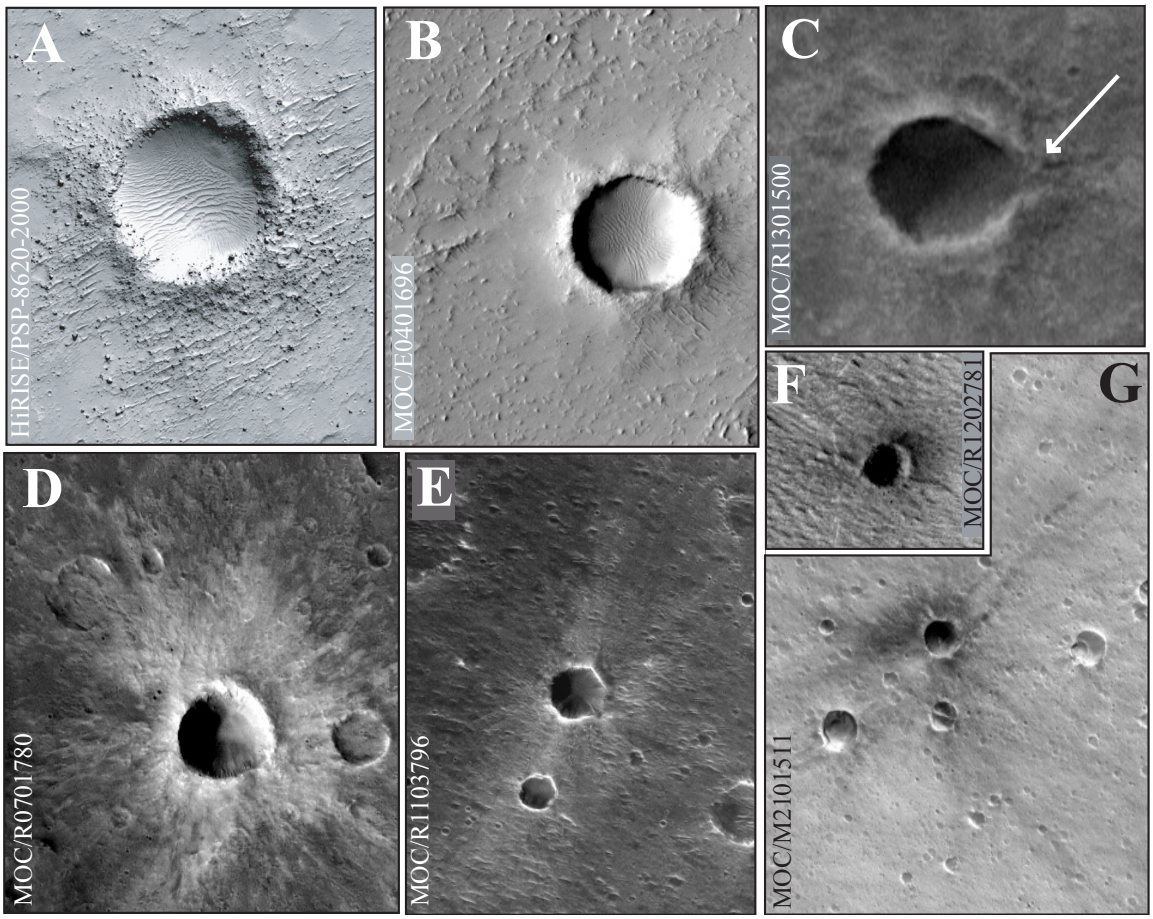

Figure 5-10: Qualitative attributes of crater ejecta and rims used to recognize comparatively fresh impact craters for the MOC-FCC and HiRISE-FCC. Ejecta attributes: A) composed of boulders and rocks; B) modifying or covering surrounding textures, sometimes with D) an albedo contrast; E-G) indicated by anomalous albedo that merely overprints textures. Macroscopic rim attributes: C) rim breach. Crater diameters are supplied for scale: A) 220 m, B) 655 m, C) 215 m, D) 460 m, E) 300 m, F) 380 m, and G) 260 m.

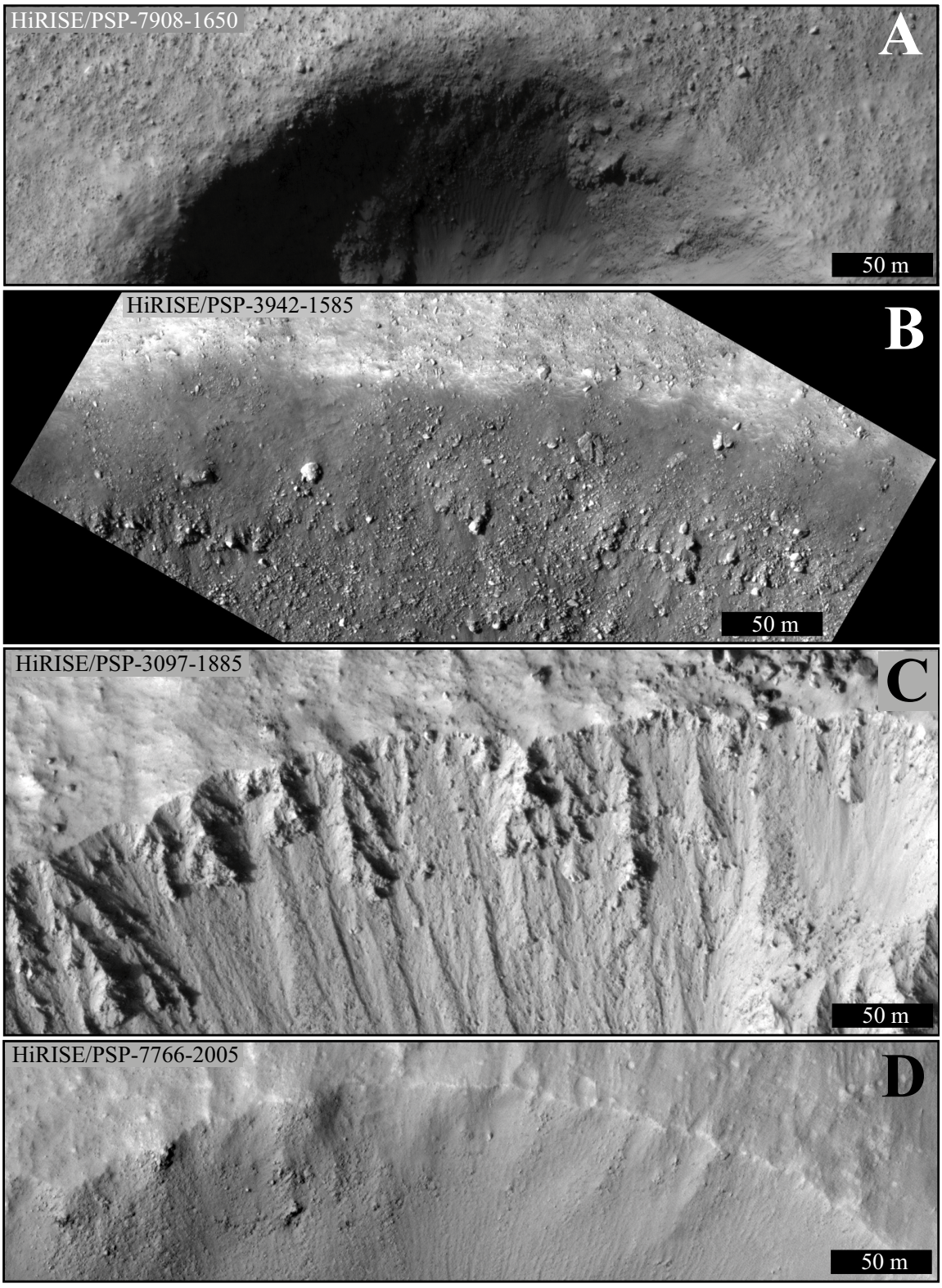

Figure 5-11: Qualitative attributes of crater rims and walls: A-B) The crater has a rounded rim and its walls are densely covered with rocks and boulders; C) the crater has a sharp rim ($\leq$ 1 m) and its walls exhibit slides of scree and other evidence of mass movements, and a paucity of rocks and boulders; C) the crater has a sharp rim and a paucity of rocks and boulders.

(part D). Although many of these "context" attributes are easily recognized on the basis of objective criteria, those which involve recognizing the absence of significant topographic relief are subject to interpretation. Subtle surface roughness is indicated by gradients in grayscale pixel intensity that are consistently aligned, and therefore requires a large solar incidence angle to be seen at all.

Quantifiable attributes

We turn now to defining quantities that can be measured and calculated for characterizing the modification state, cross-sectional and planimetric shapes of impact craters. Among the most important measurable quantities are the basic dimensions shown in Figure 5-13.

1. Apparent crater diameter (D), measured rim-to-rim.

2. Fill diameter (L_F): diameter of the lens of materials filling the bottom of a crater or of its flat bottom, whose extent is indicated by a consistent texture or pixel intensity range, often markedly different from the crater walls. (Clear margins are assumed to indicate a break in slope.) In the absence of topographic information, it is not known whether the filled portion is completely flat or has the shape of a shallow depression, although the shapes of shadows often provide a clue, as discussed below.

3. Shadow length (S_0): measured from the shadow boundary point that lies closest to crater center, to the the same point projected radially onto the crater rim.

4. Shadow margins (S_1, S_2): measured from a shadow boundary point that bounds the shadow's blunted portion (a corner), to the same point projected radially onto the crater rim. These lengths are used estimate L_F in cases where this quantity cannot be measured directly (only in MOC-FCC).

These quantities are in turn used to calculate two ratios which convey information about

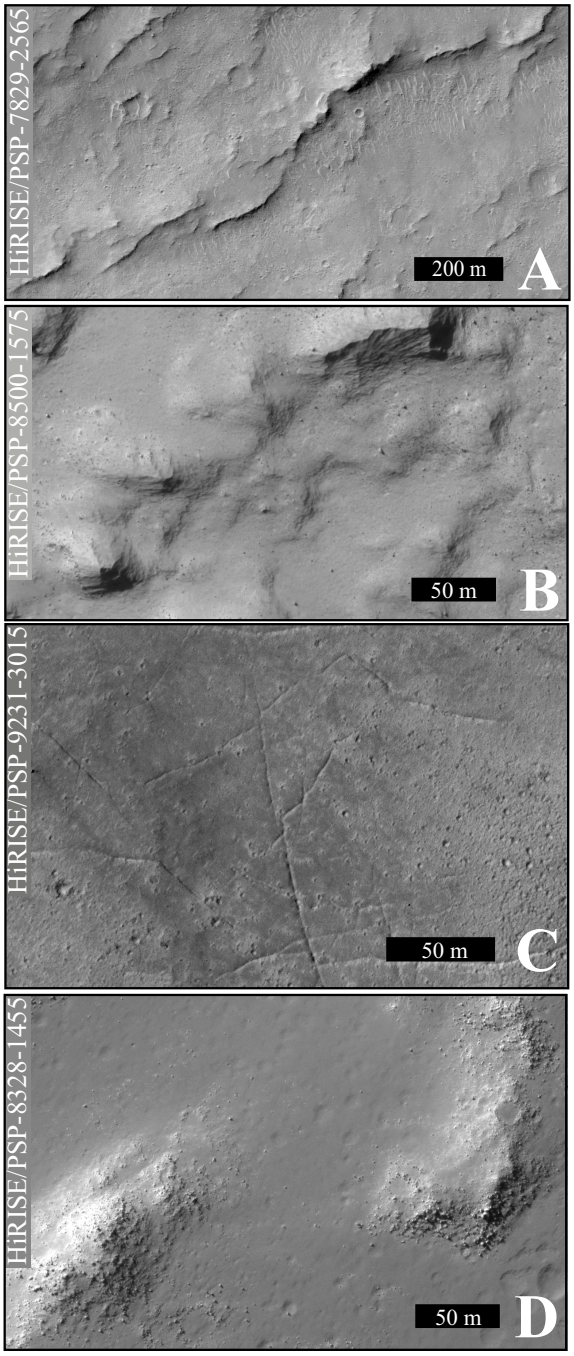

Figure 5-12: Qualitative attributes of context materials. A) Terrain with significant relief, exhibiting sharp edges ($\leq$ 1 m wide) on escarpments whose alignments indicate systematic jointing. B) Terrain with significant relief, with sharp edges bounding faceted roughness elements, and marked by scattered rocks and boulders. C) Terrain with sharp edges bounding fissures and/or fractures in a flat surface. D) Terrain with significant relief, marked by rocks and boulders clustering on roughness elements.

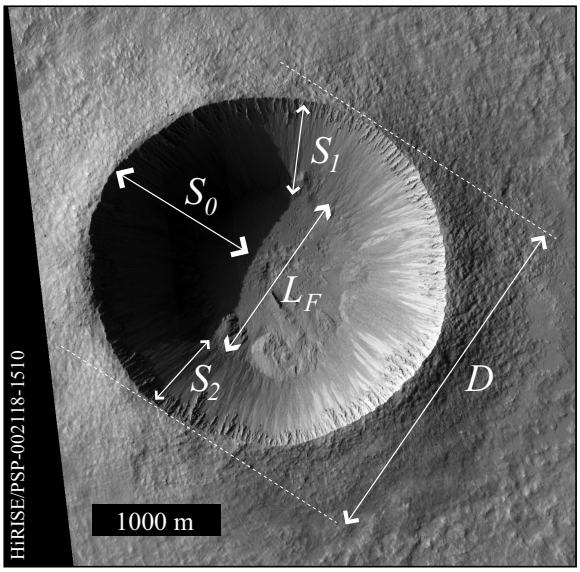

Figure 5-13: Principal crater dimensions: D = rim-to-rim diameter ; L_F = diameter of flat bottom or sediment lens; S_0 = shadow length; (S_1, S_2) = shadow margin length: distance from blunted shadow corners to rim crest.

an impact crater's modification state, as well as whether it was formed in a primary or secondary impact. The first of these is the planimetric fill ratio (hereafter just "fill ratio"), $F = L_F/D$, a measure of the extent to which a crater has been filled by materials sourced from its own walls or transported from outside. Alternatively, if the crater floor is flat and *not* on account of a sediment lens, this ratio indicates how much the cross-section is box-shaped like many secondary impact craters. The fill ratio is automatically set equal to 1 if the crater has a crescent-shaped shadow, which indicates a flat bottom that extends almost to the rim, such as that shown in part B of Figure 5-10. Note that the fill ratio could not be measured in all cases, such as where a shadow occults the crater floor completely, or when the resolution is too small to make a confident estimate.

Second, we also compute the widely-used depth-diameter ratio, d_s/D, for rim-level-to-cavity-depth d_s. The subscript "s" refers to the shape-dependence of this metric. For example, an upper bound on d_s/D is calculated as follows for craters with flat bottoms (Chappelow and Sharpton [2002]):

$$d_{\text{flat}}/D = \frac{S_0}{D\tan(\omega)} \tag{5.1}$$

where ω is the solar incidence angle. An upper bound estimate for crater cavities with a parabolic shape is given by (Chappelow and Sharpton [2002]):

$$d_{\text{par}}/D = \frac{1}{4(1 - S_0/D)\tan(\omega)} \tag{5.2}$$

We have used equation (5.1) for all craters with crescent-shaped shadows (part B of Figure 5-10) and blunted shadows (Figure 5-13), and we have used equation (5.2) for all others. The value of d_s/D could not be estimated in all cases, such as where the shadow boundary was not clearly discernible. Values of d_s/D less than 0.12 are typical of secondary impact craters (Pike and Wilhelms [1978], McEwen et al. [2005]), whereas a value in the range from 0.20 to 0.3 is typical of fresh primary craters. In following sections we will use this quantity to select subsets of both catalogs for morphometric analysis.

Quantities derived from the Planimetric Crater Rim Outline

We turn now to quantities that are calculated from the Planimetric Crater Rim Outline (PCRO) measured from map-projected HiRISE and MOC images. We will examine in detail the three examples shown in Figure 5-14: two craters belonging to the HiRISE-FCC (parts A and B), as well as Barringer/Meteor Crater (part C). We begin by manually tracing the crater rim crest: i.e., acquiring the (x, y) coordinates of pixels along this feature. The rim crest is usually indicated by illumination contrasts and shadows, and sometimes by an albedo or color contrast. Whenever possible, color images were used (HiRISE).

The "deviation centroid" is the point from which distances to all points on the rim trace have the smallest standard deviation.[1] The rim

[1]This is equivalent to the center of a circle that is fitted

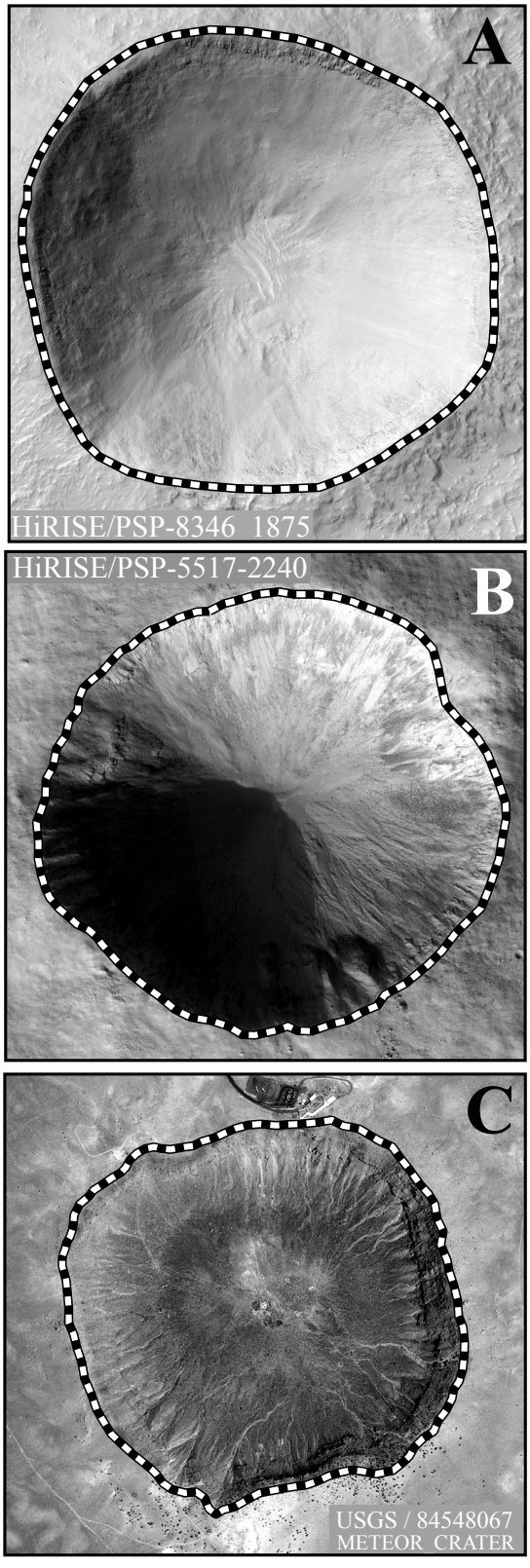

Figure 5-14: Planimetric Crater Rim Outline (PCRO) drawn for three impact craters: A-B) craters in the HiRISE-FCC; C) Barringer/Meteor crater.

trace is then resampled at 360 points in polar coordinates with respect to the deviation centroid. The acronym PCRO refers exclusively to this resampled outline throughout the rest of this chapter, and is also represented by the symbol $R(\theta_i)$. We define the "standard radial deviation" (σ_R) as the standard deviation of radii in the PCRO with respect to the deviation centroid. We define the "radius-normalized" standard radial deviation (σ_R^*) as the standard radial deviation divided by the mean radius $\bar{R}$. That is:

$$\sigma_R \equiv \sqrt{\frac{1}{360}\sum_{i=1}^{360}(R_i - \bar{R})^2}, \quad (5.3)$$

$$\sigma_R^* \equiv \sigma_R/\bar{R}. \quad (5.4)$$

Likewise, we define the "maximum radial deviation" (ΔR) as the difference between the largest and smallest radius in the PCRO, and the "radius-normalized maximum radial deviation" (ΔR^*) as the maximum radial deviation divided by the mean radius:

$$\Delta R \equiv R_{\max} - R_{\min}, \quad (5.5)$$

$$\Delta R^* \equiv \Delta R/\bar{R}. \quad (5.6)$$

A third metric, the "concave fraction" (ν) measures the extent to which any closed shape is significantly concave. We define the concave fraction to be the fraction of points in the PCRO that do not lie on its convex hull.[2]

All three quantities (σ_R, ΔR, ν) are a measure of the extent to which planimetric crater shape deviates from a circle, but none contains information about how this deviation is distributed among different shapes. For that purpose, we also calculate the radial Fourier decomposition of the PCRO using a discrete Fourier transform (Cooley and Tukey [1965]), in the manner described by Eppler et al. [1977] and used in Eppler et al. [1983] to analyze the planimetric shape of lunar complex craters. The amplitudes (A_n) and phase angles (ϕ_n) of terms in the Fourier series

to the rim trace.

[2]In two dimensions, the convex hull of a polygon with n vertices is the minimal subset of those vertices which form a convex polygon that envelops the remaining vertices.

are implicitly defined by:

$$R(\theta_i) = A_0 + \sum_{n=1}^{360} A_n \cos(n\theta_i - n\phi_n) \qquad (5.7)$$

for $\theta_i \in \{1°, 2°, 3°, ..., 360°\}$. "Radius-normalized" harmonic amplitudes are divided by the mean radius, and "Deviation-normalized" harmonic amplitudes are divided by the maximum radial deviation:

$$A_n^* \equiv A_n/\bar{R}, \qquad (5.8)$$
$$A_n' \equiv A_n/\Delta R. \qquad (5.9)$$

For the remainder of this chapter and all of the next one, the terms "first harmonic," "second harmonic," and "third harmonic," etc., will refer to the terms $n = 1$, $n = 2$, $n = 3$, etc., respectively, in equation (5.7). The term "primary harmonic" will refer to the harmonic with the largest amplitude for $n \geq 3$. "Secondary harmonic" and "tertiary harmonic" will refer to the second and third-largest harmonic amplitudes for $n \geq 3$, respectively.

In Figure 5-15 the first 20 harmonic amplitudes (radius-normalized) have been plotted for the three impact craters shown in Figure 5-14, and values of the radial deviations, concave fraction, mean diameter $\bar{D}$, and elongation angle, ϕ_E (defined below), are also reported. Figures 5-16 and 5-17 show the first nine Fourier components for the craters depicted in parts A and C of Figure 5-14. For example, the Fourier amplitude spectrum in part A of Figure 5-15 for the crater shown in part A of Figure 5-14 shows that its primary harmonic is $n = 3$: i.e., it is triangular. Its conspicuously hexagonal shape is reflected in the large amplitude for $n = 6$.

The phase angles indicate the orientations of each harmonic component. For example, the orientation of the strong third and sixth harmonics in Figure 5-16 accord well with the orientation gleaned from the image in part A of Figure 5-14, and likewise for the fourth harmonic in Figure 5-17 and the orientation of Meteor Crater's square frame in part C of Figure 5-14. As can be seen from the spectrum in part C of Figure 5-15, most of Meteor Crater's noncircular amplitude

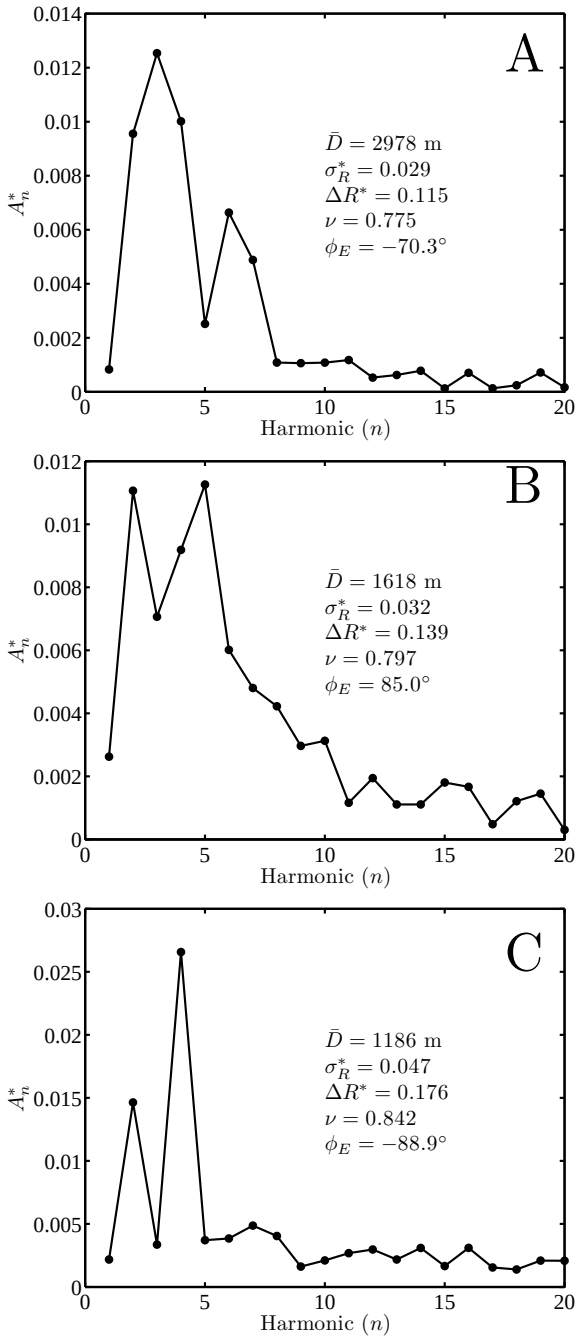

Figure 5-15: Fourier shape spectrum of the PCRO for craters A, B, and C in Figure 5-14. Plotted are the first 20 radius-normalized harmonic amplitudes. Also shown are the mean diameter ($\bar{D}$), radius-normalized standard radial deviation (σ_R^*), radius-normalized maximum radial deviation (ΔR^*), concave fraction (ν) and elongation angle (ϕ_E). The primary harmonics in each case are: A) 3, B) 5, C) 4.

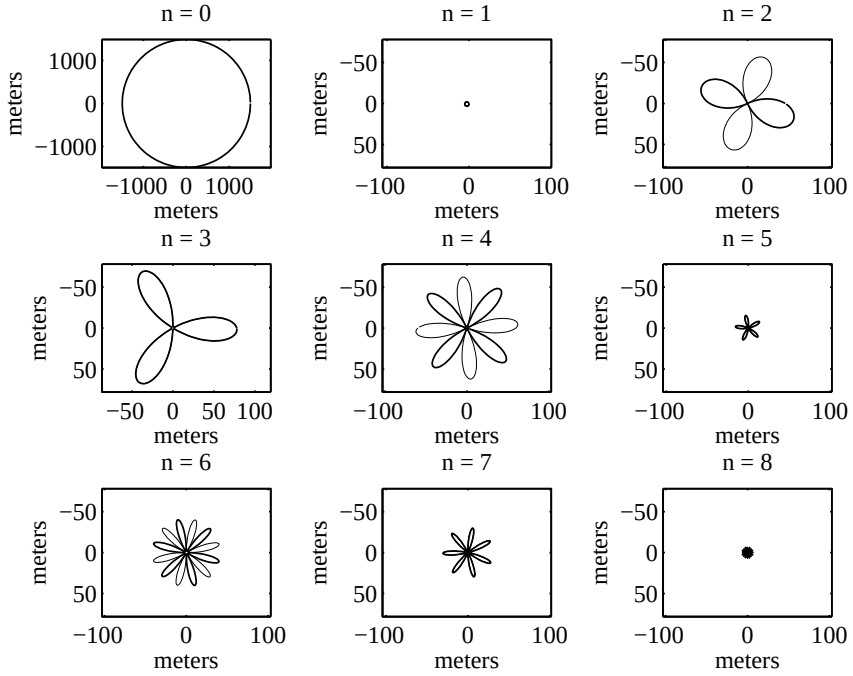

Figure 5-16: First nine components of the Fourier series of the PCRO for the crater shown in part A of Figure 5-14. Thin lines indicate negative values.

Figure 5-17: First nine components of the Fourier series of the PCRO for the crater shown in part C of Figure 5-14 (i.e., Barringer/Meteor Crater). Thin lines indicate negative values.

is concentrated in its primary harmonic, $n = 4$. This exceptionally pure expression of a single low-order harmonic accounts for the higher radial deviations and concave fraction measured for this crater.

The second harmonic is a measure of elongation, and the second harmonic phase angle (ϕ_2) is a measure of its orientation. We define the "elongation angle" (ϕ_E) as the azimuth of the major axis of elongation (i.e., $\phi_2 + 90°$) measured with respect to North (i.e., collapsed onto the domain $(-90°, 90°]$). It is well-known that highly oblique impacts produce elongated craters (Gault and Wedekind [1978]). In the next section we present evidence that the second harmonic phase angle may preserve the horizontal impact angle of most simple impact craters, so that even subtle elongations are possibly caused by this effect. Meteor Crater's elongation has the most probable orientation, at roughly 90° from North.[3]

It is important to bear in mind that the manually-traced PCRO is an approximate measurement based upon an interpretation. That is, the PCRO is an approximate measure of the topographic rim crest, and is based upon an interpretation of three-dimensional features in two-dimensional images. Moreover, in some cases it is difficult or impossible to trace the entire crater rim. This may occur where there are breaches of the rim or alternate paths that the topographic rim may follow. Where the rim is indicated entirely by shadows and pixel intensity gradients (instead of albedo or color), it can be lost altogether where it parallels the sub-solar azimuth (i.e., the direction to the sub-solar point, parallel to the sun's rays in plan view).

In order to address this problem, we have calculated the values of all morphometric quantities for multiple alternate outlines in the case of craters having locally ambiguous rims. First, where there are multiple alternate paths that have been manually selected in one or multiple locations, we assemble every combination of the PCRO with these alternate paths substituted. Second, wherever the rim cannot be traced because it disappears or becomes highly diffuse, three paths are alternately constructed and substituted: (a) the best-estimate that can be traced manually; (b) a straight line connecting the endpoints; (c) a linear interpolation in radius from one endpoint to the other. After computing and tabulating morphometric quantities for every one of the alternate PCROs, we record the maximum and minimum value of each quantity for the entire set. For the remainder of this chapter, the term "mid-range values" (MRV) indicates that values of morphometric quantities have been set equal to the midpoint of their range among alternate outlines. The term "single-estimate values" (SEV) indicates that morphometric quantities have been set equal to values obtained for the best manual estimate of the crater rim trace.

[3] i.e., Averaging over all obliquities and all times of the year, this is the most probable horizontal impact angle for a projectile whose orbit lies in the ecliptic plane.

5.3 HiRISE Fresh Crater Catalog: Analyses

In this section we will use the qualitative attributes defined in previous sections to divide the HiRISE-FCC into subsets according to target properties. We then measure the distributions of morphometric quantities defined above for the craters in each subset, and then compare the results, being careful to note only differences that are statistically significant. We begin by plotting values of the depth-diameter (d_s/D) and fill ratios (F), which indicate something about the origins (primary versus secondary impact) and modification state of the impact craters in our data set. A histogram of the shape-dependent depth-diameter ratio has been plotted in Figure 5-18 for all craters in which it could be measured, and shows that only a small fraction occur below 0.12, the range typical of secondaries. The fill ratio is plotted in Figure 5-19 (also not measurable in all cases). A significant fraction of the data set has $F = 0$, meaning that a relatively flat bottom was not noted, or that a center-crossing shadow was not truncated (e.g., see part B of Figure 5-14). Except in cases where we examine the dependence of morphometric quantities upon modification state, we admit for analysis only those

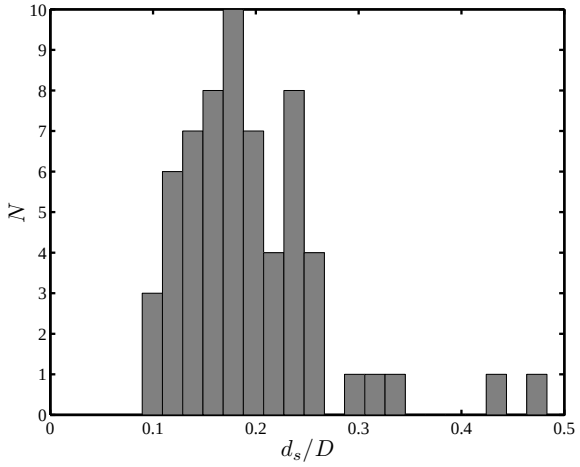

Figure 5-18: Depth-diameter ratio (d_s/D) of all impact craters in the HiRISE-FCC for which this quantity could be measured. (D ranges from 15 m to 4.3 km.)

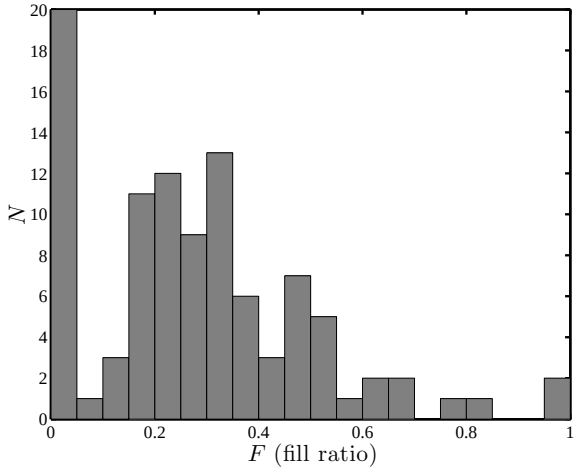

Figure 5-19: Fill ratio (F) of all impact craters in the HiRISE-FCC for which this quantity could be measured.

craters for which $d_s/D \geq 0.12$ and $F \leq 0.75$. The remainder are likely to be secondaries (shallow, flat-bottomed) or at least heavily modified. This condition discards slightly more than 7% of the data set. We will refer to this condition as the Cavity Shape Criterion (CSC) for the remainder of this chapter.[4]

Global analyses (all craters)

We turn now to the dependence of radial deviation upon crater diameter. We have plotted in log-log space the radius-normalized maximum and standard radial deviations (i.e., ΔR^* and σ_R^*) in Figure 5-21 and Figure 5-20, respectively, and the concave fraction (ν) in Figure 5-22, where craters failing the CSC are highlighted. Two prominent features are noted at once: (a) an obvious transition occurs at approximately $D \approx 100$ m, and (b) all three metrics have an approximately power-law dependence on diameter for $D > 100$ m. Possible explanations for (b) will be examined in the next chapter. It is natural to suggest that the transition at $D \approx 100$ m may correspond the boundary of the strength-gravity regime.

It is well-known that crater excavation is limited and halted either mainly by the material strength of target materials or else by gravity, depending which is greater. A simple dimensional analysis may be used to estimate the diameter at which this transition occurs (Melosh [1989]):

$$q_{\rm SG} = \frac{\rho g D}{Y} \tag{5.10}$$

where ρ is the target material density, g is gravitational acceleration, and Y is the target yield stress. Assuming $Y = 2$ MPa (i.e., the observed yield stress at the start of crater collapse in fractured rock surrounding a freshly-formed impact crater (Melosh [1989])), and assuming $\rho = 3.0$ kg/m^3 (dense rock: e.g., basalt), and $g = 3.69$ m/s^2, then the boundary ($q_{\rm SG} = 1$) is estimated to occur at transition diameter $D_{\rm SG} \approx 180$ m on Mars. For terrestrial gravity this estimate is $D_{\rm SG} \approx 70$ m, and using $g = 1.62$ m/s^2 we find $D_{\rm SG} \approx 400$ m on the Moon. The boundary shifts to higher diameters for target rocks of lower density and greater material strength, lower diameters for higher densities and lower strength. Our data set indicates that a transition occurs anywhere in the range from $D = 100$

[4]N.B. In table- and figure captions, "CSC on" means that the CSC has been enforced, while "CSC off" means it has not been enforced. Also, "all D" means only that no lower bound was imposed on crater diameter.

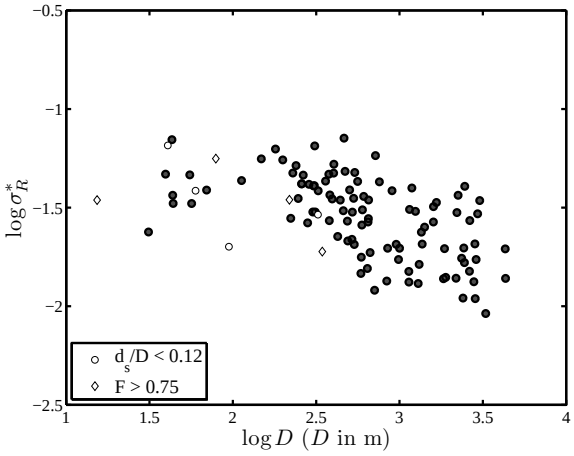

Figure 5-20: Radius-normalized standard radial deviation σ_R^* for all impact craters in the HiRISE-FCC, where craters violating the CSC (Cavity Shape Criterion) are marked with open symbols (i.e., having large fill ratio F and small depth-diameter ratio d_s/D). [SEV; CSC off; all D]

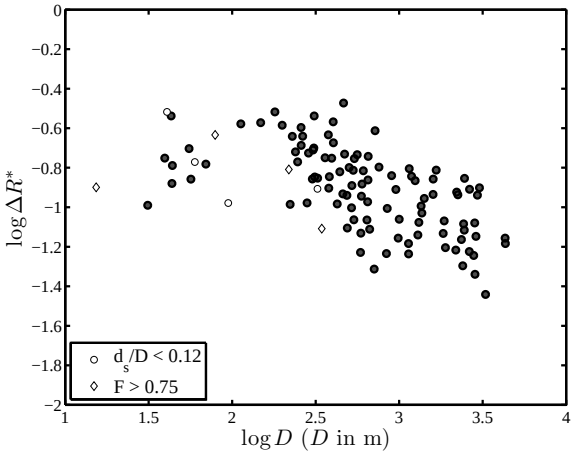

Figure 5-21: Radius-normalized maximum radial deviation ΔR^* for all impact craters in the HiRISE-FCC, where craters violating the CSC (Cavity Shape Criterion) are marked with open symbols (i.e., having large fill ratio F and small depth-diameter ratio d_s/D). [SEV; CSC off; all D]

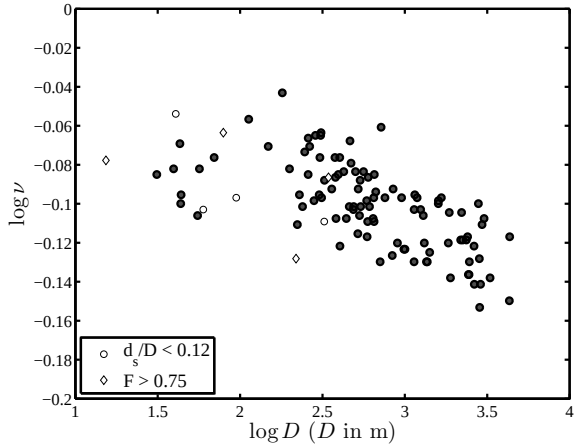

Figure 5-22: Concave fraction ν for all impact craters in the HiRISE-FCC, where craters violating the CSC (Cavity Shape Criterion) are marked with open symbols (i.e., having large fill ratio F and small depth-diameter ratio d_s/D). [SEV; CSC off; all D]

m to $D = 200$ m, consistent with the estimate for Mars. It should be emphasized that the estimate based on equation (5.10) is highly approximate – an order-of-magnitude estimate at best – so that agreement may well be coincidence.

An alternative explanation is that the excavation of craters exceeding a transition diameter is affected by a deep layer with different strength properties. In this case, the transition reflects the difference between, for example, crater excavation in regolith and competent rock. We do not favor this idea on the grounds that our catalog of Martian craters (unlike Lunar craters in the same size range) samples a wide variety of targets having layers with ranging thicknesses, compositions, and tectonic structures. Moreover, only a few craters in the catalog exhibit prominent benches and flat-bottoms of the kind associated with craters forming in targets having weak-on-strong layering (Quaide and Oberbeck [1968], Senft and Stewart [2007]). From Figures 5-21 and 5-20 it is clear *that* a transition occurs between $D = 100$ m and $D = 200$ m, and in the absence of another explanation we suggest that this may correspond to the strength-gravity transition since the process of crater excavation is fundamentally different for these regimes and

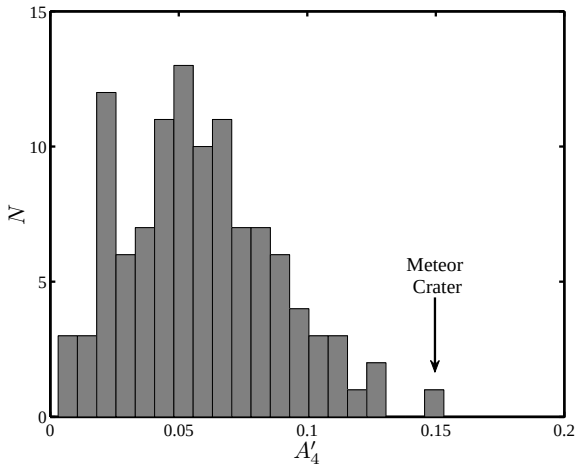

Figure 5-23: Distribution of the deviation-normalized fourth harmonic amplitude for all impact craters in the HiRISE-FCC. The value of A_4' calculated for Meteor Crater is marked with an arrow (see Part C of Figure 5-15).[SEV; CSC off; all D]

may produce markedly different morphologies. It is moreover reasonable (based on the estimate above) to expect the transition diameter to fall in the vicinity of this range. Later in this section, we will perform statistical analyses including as well as excluding craters with $D < 100$ m.

Throughout the remainder of this section, we will report on many features of the distributions of harmonic amplitudes, in the course of drawing comparisons between subsets of the HiRISE-FCC. For now, we will just note an interesting implication of the histogram of deviation-normalized fourth harmonic amplitudes (for the entire data set), shown in Figure 5-23. We have marked in this plot the value calculated for Meteor Crater (part C of Figure 5-15). From this it is clear that Meteor's shape is extremely uncommon, at least among fresh impact craters on the surface of Mars. Only one crater in our data set has a comparable shape, and its diameter is 1.5 orders of magnitude *smaller* than that of Meteor Crater (and does not satisfy the CSC). We'll return to this observation in the next section and in some detail in the following chapter.

Subsets of HiRISE-FCC

We turn now to dividing the catalog into subsets that exhibit different geological properties for the purpose of finding related morphological differences. The HiRISE-FCC has been subdivided into 13 subsets and their complements (26 altogether), where these are defined in Table 5.2 on the basis of properties defined in previous sections. The subsets are designated $L_1, L_2, ..., L_{13}$, and implicitly define the complement sets[5] $L_1^C, L_2^C, ..., L_{13}^C$. These have been defined in terms of the material classes described in Section 5.1, as well as binary attributes such as the presence or absence of systematic jointing in context imagery (L_4), or the presence or absence of scattered boulders and rocks (L_{11}). In order to draw a comparison between craters in different stages of modification, we shall compare the contents of L_7 and L_8, among which the range in fill ratio, F, has been evenly divided. The overlap of subsets in Table 5.2 is plotted in Figure 5-24 for every combination addressed in our analysis. Defining $n(L_x)$ to be the size of set L_x, the overlap $\Lambda(L_x, L_y)$ of the sets L_x and L_y is the number of craters in the intersection of L_x and L_y divided by the number comprising the union of L_x and L_y:

$$\Lambda(L_x, L_y) \equiv \frac{n(L_x \cap L_y)}{n(L_x \cup L_y)} \qquad (5.11)$$

The first three subsets (L_1, L_2, L_3) are defined on the basis of material classifications derived from global geologic maps (see Section 5.1). The main contrast we wish to draw is between post-Noachain lavas (comparitively unbattered by the Late Heavy-Bombardment) and material classes that do not contain lavas ("Not lavas"). This dichotomy is motivated partly by the observations of Chapter 4, where evidence from Endurance and Meteor Craters appears to suggest that the arrangement of fractures plays a role in determining planimetric crater shape. Lavas are well-known to have disordered fracture networks that

[5] If U is the set of all craters in the catalog, then the compliment L_n^C of L_n is the set of all craters in U but not in L_n.

result from volumetric contraction during a slow cooling process. By contrast, unconsolidated debris and sediments will have no fractures, while indurated debris and sediments may have systematic joints with significant alignments spanning broad distances. The other reason for this comparison is practical in nature: lavas are ubiquitous, and neither of the "sediments" or "mantled" classes have enough representation in the catalog to enable a statistically meaningful comparison by themselves. Material class 2 (sediments) comprises just 11% of L_1, so that this subset is dominated by classes 1 ("debris") and 3 ("sediment + debris"). On the assumption that class 6 ("mantled") is dominated by sediments in sedimentary rocks, this has been added to L_1 to make L_2.

D-dependence of radial deviation

We have calculated linear regressions for the radius-normalized maximum and standard radial deviations (ΔR^* and σ_R^*, respectively) in log-log space above the strength-gravity transition ($D > 100$ m), and these are listed in Table 5.3 for single-estimate values[6], along with Pearson correlation coefficients (r_P). The data set as a whole has a slope -0.38 for ΔR^* and -0.34 for σ_R^*. We find that subsets with the strongest correlations between radial deviation and diameter ($|r_p| \geq 0.75$) have slopes ranging from -0.44 to -0.54 for ΔR^* and -0.45 to -0.47 for σ_R^* (and larger, if mid-range values are assumed; see Table B.1). That is, the strongest correlations indicate the following relationship between radius-normalized radial deviations and diameter:

$$\{\Delta R^*, \sigma_R^*\} \propto D^{-1/2}. \tag{5.12}$$

With respect to radial deviation, among the most interesting comparisons are the four plotted in Figure 5-25 (where the CSC is enforced). The endpoints of error bars in these plots indicate the upper and lower bounds of σ_R^* calculated for the set of alternate outlines, in cases where the PCRO was locally ambiguous.[7] We can see at once that the comparison between "lavas" and both sets of "not-lavas" shows that craters in non-lava targets exhibit a similar slope but consistently higher radial deviation, in support of the qualitative tallies in Section 5.1 where lavas were found to host a larger number of large circular craters. Later, we shall address the potential significance of this difference in some detail.

Also shown is a comparison between craters exhibiting significant mass-movements on their upper rim walls (L_9,"slides") and those which do not (L_9^C). Casual inspection and the linear regressions reveal that craters in L_9 (having slides) have generally higher radial devia-

Table 5.3: For 21 subsets of the **HiRISE-FCC**: slope m and intercept b obtained from a linear regression for $\log \sigma_R^* = m \log D + b$ and $\log \Delta R^* = m \log D + b$, along with the Pearson correlation coefficient r_P computed for both relations. **Single-estimate** values were assumed in this case and the fit was computed for $D \geq 100$ m. [CSC on, except for L_7 and L_8]

Set	$m_{\Delta R}$	$b_{\Delta R}$	r_P	m_{σ_R}	b_{σ_R}	r_P
L_1	-0.51	0.56	-0.78	-0.49	-0.13	-0.71
L_2	-0.51	0.56	-0.79	-0.45	-0.24	-0.72
L_3	-0.44	0.26	-0.76	-0.44	-0.38	-0.77
L_4	-0.46	0.42	-0.78	-0.39	-0.44	-0.70
L_4^C	-0.35	0.08	-0.63	-0.32	-0.64	-0.59
L_5	-0.30	-0.04	-0.57	-0.25	-0.82	-0.49
L_5^C	-0.44	0.36	-0.74	-0.40	-0.43	-0.69
L_6	-0.34	0.07	-0.62	-0.26	-0.78	-0.52
L_6^C	-0.42	0.28	-0.73	-0.41	-0.40	-0.72
L_7	-0.35	0.08	-0.67	-0.32	-0.62	-0.65
L_8	-0.41	0.25	-0.64	-0.37	-0.52	-0.59
L_9	-0.40	0.26	-0.63	-0.37	-0.47	-0.58
L_9^C	-0.54	0.54	-0.81	-0.47	-0.28	-0.78
L_{10}	-0.29	-0.02	-0.59	-0.23	-0.83	-0.50
L_{10}^C	-0.40	0.20	-0.70	-0.36	-0.56	-0.66
L_{11}	-0.36	0.14	-0.62	-0.31	-0.66	-0.54
L_{11}^C	-0.40	0.21	-0.74	-0.36	-0.54	-0.70
L_{12}	-0.36	0.14	-0.66	-0.32	-0.63	-0.60
L_{12}^C	-0.44	0.34	-0.74	-0.40	-0.45	-0.70
L_{13}	-0.42	0.23	-0.62	-0.36	-0.56	-0.57
L_{13}^C	-0.41	0.30	-0.73	-0.37	-0.49	-0.66

[6](See the end of Section 5.2 for a definition of "single-estimate values". Linear regressions for mid-range values produce similar results, and can be found in Table B.1

[7]See the end of Section 5.2 for an explanation.

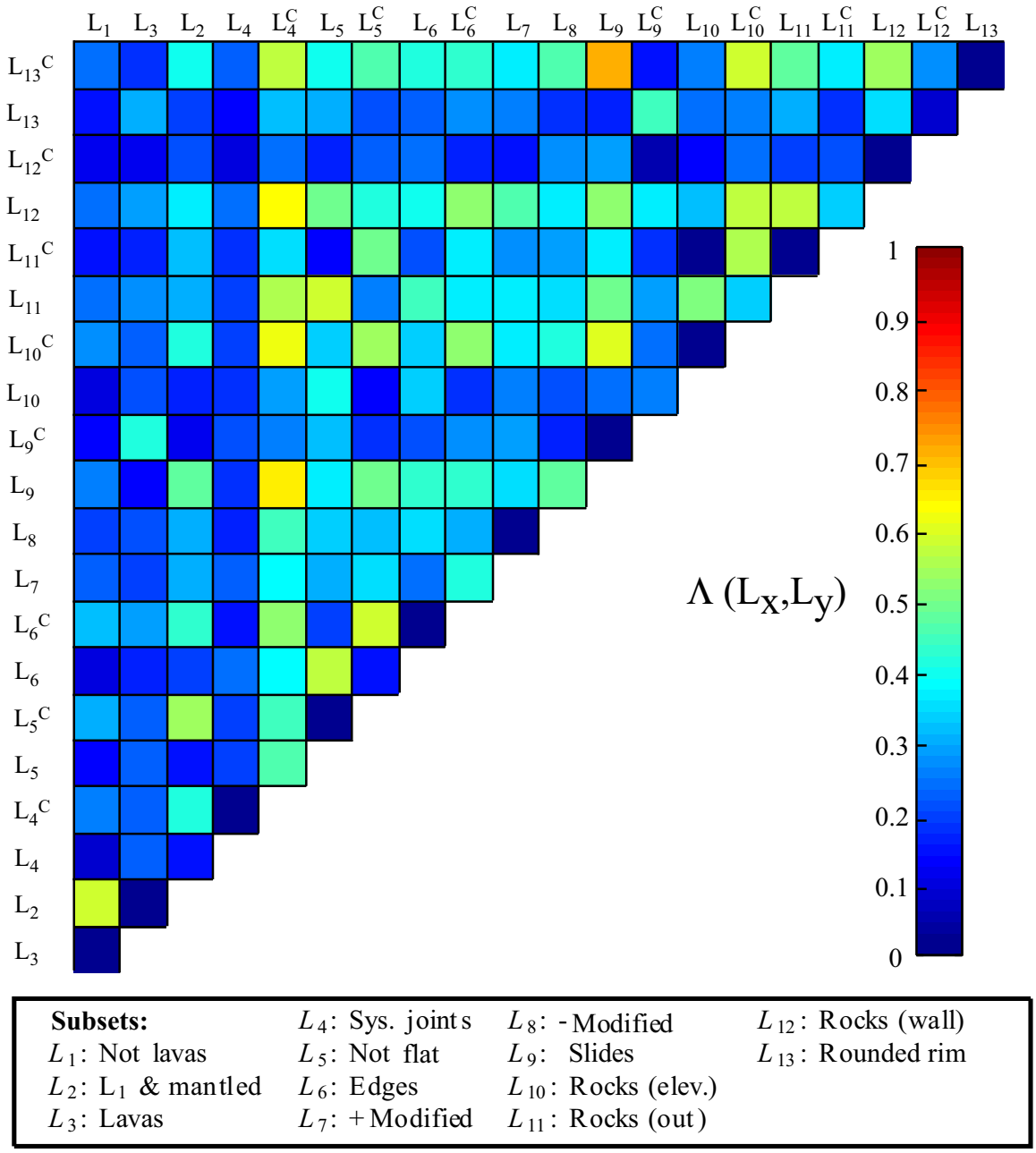

Subsets:	L_4: Sys. joints	L_8: -Modified	L_{12}: Rocks (wall)
L_1: Not lavas	L_5: Not flat	L_9: Slides	L_{13}: Rounded rim
L_2: L_1 & mantled	L_6: Edges	L_{10}: Rocks (elev.)	
L_3: Lavas	L_7: +Modified	L_{11}: Rocks (out)	

Figure 5-24: Overlap between subsets defined in Table 5.2, where the overlap Λ is defined in equation (5.11). [CSC on; $D \geq 100$ m]

Table 5.2: Subsets of the HiRISE-FCC and their defining properties.

Set sym.	Abbreviation	Property of	Description
L_1	Not Lavas	Context	Resides in geological units assigned to material classes 1 (debris) or 2 (sedimentary).
L_2	L_1 + Mantled	Context	Resides in geological units assigned to material classes 1 (debris) or 2 (sedimentary), or 6 (aeolian/lava-mantled).
L_3	Lavas	Context	Resides in geological units assigned to material class 4 (lavas) and which are post-Noachian.
L_4	Sys. joints	Context	Systematic jointing clearly expressed, in the form of fractures, fissures, or escarpments with a consistent orientation.
L_5	Not flat	Context	Significant topographic relief, indicated by shadows and intensity gradients with a consistent orientation.
L_6	Edges	Context	Sharp edges bounding surfaces, spanned by at most ~ 1 m.
L_7	+Modified	Crater	More modified, as indicated by fill ratio $F > 0.26$ (i.e., 50% of craters for which F could be measured).
L_8	–Modified	Crater	Less modified, as indicated by fill ratio $F \leq 0.26$.
L_9	Slides (rim)	Crater	Talus/debris slides visible on upper rim wall.
L_{10}	Rocks (elev.)	Context	Rocks and boulders clustered on elevated surfaces and topographic elements.
L_{11}	Rocks (out)	Context	Rocks and boulders scattered between craters, outside of ejecta.
L_{12}	Rocks (wall)	Crater	Crater walls densely covered with rocks and boulders.
L_{13}	Rounded rim	Crater	Rim crest is in all places wider than ~ 2 m.

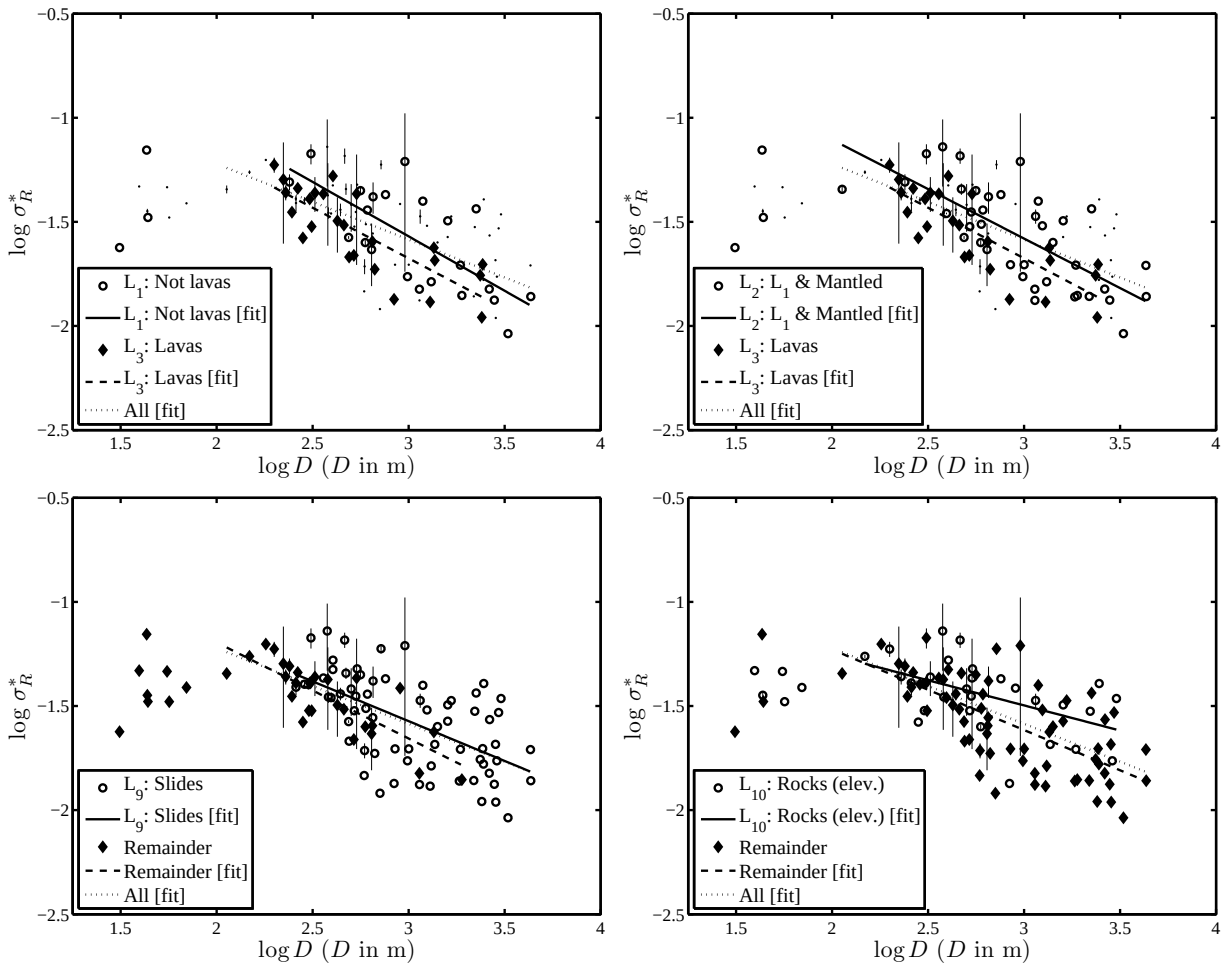

Figure 5-25: Radius-normalized standard radial deviation (σ_R^*) for impact craters in the HiRISE-FCC which satisfy the Cavity Shape Criterion (CSC), and where craters belonging to 7 subsets in 4 subset comparisons are marked with contrasting symbols. ("Remainder" here refers to the compliment set: i.e., L_x^C.) Error bars span the entire range of values for alternate outlines, and points correspond to mid-range values (MRV). Craters with all diameters are shown, but linear regressions are fitted only for $D > 100$ m.

tions than members of L_9^C (no slides), where direct comparison is possible in the small diameters where these two groups overlap. That is, the mass movements appear to push planimetric shape away from circular. In addition, the population having no slides (L_9^C) exhibits the strongest correlation between D and ΔR^* (i.e., r_P = -0.81), and the steepest power law ($m = -0.54$). That is, these data may point the presence of two genetically distinct crater populations: one in which an early-stage slumping has occurred (L_9), and another that is comparatively pristine (L_9^C). The pristine population exhibits a steep and strong deviation-diameter correlation, while the collapsed population is pushed to higher deviations by wall slumping and rim collapse.

The final comparison in Figure 5-25 contrasts the diameter dependence of standard radial deviation in the presence and absence of elevated surfaces and roughness elements where rocks and boulders are clustered in the surrounding terrain (L_{10} and L_{10}^C, respectively). Significantly, we find for L_{10} one of the weakest correlations between σ_R^* and D (i.e., $r_P = -0.5$), and the shallowest power law ($m = -0.23$). We can plausibly interpret L_{10} as the set of craters formed in targets made up of unconsolidated or weakly-indurated debris or rubble, covered by a thin sedimentary mantle. The sets L_{11} (rocks and boulders scattered between craters) and L_{12} (rocks and boulders densely covering crater walls) cannot be easily assigned the same interpretation because the rocks in L_{11} may be transported by far-flung crater excavations (ejecta), and the wall-covering rocks in L_{12} may be the result of shock-related fragmentation processes. That some targets in the set L_{10} are at least weakly indurated is suggested by its 35% overlap with the set L_6 ("sharp edges"; see Figure 5-24). All told, however, the set L_{10} at least superficially resembles a regolith-layer target, where the thickness of this layer and materials that it covers are of course not known and likely variable. The dependence of radial deviations upon diameter appear to indicate a fundamentally different behavior for this target population. A plausible interpretation of these results is that equation (5.12) applies to strongly-indurated targets, while craters in weakly-indurated or unconsolidated materials exhibit no such relation (i.e., as indicated by the low correlation coefficient), or else the weaker dependence is described by a shallower power law:

$$\{\Delta R^*, \sigma_R^*\} \propto D^{-1/4} \quad \text{(debris)} \tag{5.13}$$

The dependence of radial deviation upon diameter creates many difficulties for comparing the distribution of morphometric quantities in one subset to those of another. In cases where the distribution in diameters are exactly alike, it is perfectly sensible to compare these distributions directly. In cases where this is not true (almost all cases), it is important to understand how the difference in sampled diameters can affect the outcome of the comparison before judging differences to be significant. When comparing the distribution of concave fraction or radial deviation itself, there is a very simple solution that does not require a separate evaluation of the sampled diameters: that is simply to compare *detrended* values of ΔR^*, σ_R^*, and ν. First, for the entire HiRISE-FCC where $D \geq 100$ m we compute a linear regression in log-log space with slope $m = m_1$ and intercept $b = b_1$ for ΔR^*, $(m, b) = (m_2, b_2)$ for σ_R^* and $(m, b) = (m_3, b_3)$ for ν. We define the "detrended" maximum and standard radial deviations and concave fraction as follows:

$$\Delta R' \equiv \Delta R^* D^{-m_1} \tag{5.14}$$

$$\sigma_R' \equiv \sigma_R^* D^{-m_2} \tag{5.15}$$

$$\nu' \equiv \nu D^{-m_3} \tag{5.16}$$

In this way, the diameter dependence is eliminated and the distributions of all three quantities can be compared between subsets.

There is unfortunately no similarly trivial solution for comparing harmonic amplitudes. The sum of radius-normalized harmonic amplitudes is directly proportional to the the maximum radial deviation. In order to greatly reduce the dependence of harmonic amplitudes upon diameter, we have normalized the amplitudes instead by ΔR (i.e., these are the deviation-normalized

amplitudes, A'_n, defined in the last section). The deviation-normalized amplitudes are a measure of how deviation from circularity is distributed among multiple harmonics. For example, the *radius-normalized* third harmonic amplitude (A^*_3) of a small crater (large radial deviation) is likely to be much larger than the same value measured for a large crater (smaller radial deviation). Therefore, the comparison between subsets involving the whole range of diameters will be very sensitive to differences in the distribution of diameters in each set. On the other hand, if the third harmonic dominates the spectrum of a small and large crater (i.e., if the primary harmonic of each one is 3), then their deviation-normalized amplitudes (A'_3) will have comparable magnitudes, and can be meaningfully compared.

A significant problem remains. Since radial deviation diminishes with diameter, the amplitude spectrum shifts toward larger harmonics at larger diameters. To see this, consider a crater whose PCRO is a regular octagon. The maximum radial deviation of a regular octagon is significantly smaller than that of an equilateral triangle. That is, owing to the dependence of radial deviation upon diameter, while it is possible for the eighth harmonic to dominate the amplitude spectrum of a large crater, this is far less likely to happen in the case of small-crater populations dominated by high radial deviations. Therefore, we must interpret the results of comparisons in light of this understanding: that subsets having larger diameters should exhibit larger amplitudes at high harmonics and lower amplitudes at low harmonics. Comparisons which indicate a statistically significant difference that contradicts this trend should be regarded with particular interest.

In order to see that normalizing by deviation mostly eliminates the diameter-dependence of low-order harmonic amplitudes, we have plotted A'_n versus D for $n = \{3, 6, 7\}$ in Figure 5-26 (where the CSC is enforced). We see that diameter-dependence is erased for $n = 3$ and $n = 7$. (This is typical of the other low-order amplitudes; i.e., for $n \leq 8$.) We have plotted the results for $n = 6$ in order to highlight a peculiar feature of hexagonal amplitudes. As we will see later in this section, the distribution of A'_6 is the most sensitive to differences between subsets of the HiRISE-FCC. We note from Figure 5-26 that A'_6, unlike the other deviation-normalized amplitudes, appears to exhibit some dependence upon diameter: it is markedly lower for $D < 100$ m, and there is a slight but detectable downward trend for $D \geq 100$ m. This is especially remarkable because the earlier-mentioned geometrical considerations suggest the opposite trend is expected for this harmonic: A'_6 should be larger, on average, at larger diameters (smaller radial deviation). The origin of this behavior is unknown. This observation alongside later analyses, and the sheer number of impact craters with a markedly hexagonal aspect (e.g., part A of Figure 5-14) suggest that an as-yet unrecognized process possibly accounts for the special properties of this harmonic.

We have tabulated the mean and standard deviation of deviation-normalized harmonics A'_2 through A'_8 (for all subsets) in Table 5.4 (single-estimate values for all D) and Appendix Tables B.5 (mid-range values, for all D), B.6 (single-estimate values, $D \geq 100$ m), and B.7 (mid-range values, $D \geq 100$ m). We have also tabulated the number of craters in each subset with a primary harmonic of $n = 3$ through $n = 6$, as well as the mean and standard deviation of detrended radial deviations and concave fraction (for all subsets) in Table 5.5 (single-estimate values for all D) and Appendix Tables B.2 (mid-range values, for all D), B.3 (single-estimate values, $D \geq 100$ m), and B.4 (mid-range values, $D \geq 100$ m).

Difference metrics for comparing distributions of morphometric quantities

We turn now to constructing a method for measuring the difference between the distributions of morphometric quantities and determining what amount of difference is statistically significant. We will use the term "difference metric" to mean a calculation that measures the difference between two distributions of the same quantity. A subset of these difference metrics will rely

Table 5.4: Global properties of shape distributions for 21 subsets of the **HiRISE-FCC**, using **single-estimate** values and **including** craters with $D < 100$ m. Listed are the mean ± standard deviation of deviation-normalized harmonic amplitudes A'_2 through A'_8. [CSC on, except for L_7 and L_8]

Set	N	A'_2	A'_3	A'_4	A'_5	A'_6	A'_7	A'_8
L_1	25	0.097 ± 0.044	0.059 ± 0.026	0.058 ± 0.027	0.048 ± 0.024	0.033 ± 0.016	0.025 ± 0.012	0.020 ± 0.010
L_2	42	0.091 ± 0.041	0.062 ± 0.029	0.060 ± 0.025	0.042 ± 0.022	0.033 ± 0.019	0.024 ± 0.014	0.021 ± 0.010
L_3	25	0.096 ± 0.037	0.066 ± 0.035	0.057 ± 0.032	0.038 ± 0.023	0.037 ± 0.017	0.027 ± 0.012	0.023 ± 0.013
L_4	23	0.105 ± 0.038	0.056 ± 0.024	0.062 ± 0.034	0.036 ± 0.024	0.033 ± 0.018	0.024 ± 0.013	0.020 ± 0.011
L_4^C	79	0.096 ± 0.041	0.067 ± 0.031	0.055 ± 0.026	0.040 ± 0.023	0.035 ± 0.019	0.024 ± 0.015	0.020 ± 0.011
L_5	55	0.101 ± 0.041	0.064 ± 0.030	0.060 ± 0.030	0.037 ± 0.022	0.034 ± 0.017	0.024 ± 0.014	0.018 ± 0.009
L_5^C	47	0.093 ± 0.039	0.064 ± 0.031	0.052 ± 0.025	0.041 ± 0.025	0.034 ± 0.021	0.024 ± 0.015	0.022 ± 0.012
L_6	47	0.100 ± 0.044	0.066 ± 0.031	0.056 ± 0.027	0.040 ± 0.022	0.034 ± 0.016	0.024 ± 0.014	0.019 ± 0.010
L_6^C	55	0.095 ± 0.038	0.063 ± 0.029	0.056 ± 0.029	0.038 ± 0.025	0.034 ± 0.021	0.025 ± 0.014	0.021 ± 0.011
L_7	49	0.103 ± 0.037	0.065 ± 0.029	0.059 ± 0.030	0.041 ± 0.028	0.031 ± 0.016	0.022 ± 0.013	0.021 ± 0.010
L_8	48	0.093 ± 0.042	0.063 ± 0.027	0.056 ± 0.028	0.038 ± 0.019	0.038 ± 0.019	0.024 ± 0.016	0.017 ± 0.009
L_9	66	0.099 ± 0.041	0.066 ± 0.030	0.053 ± 0.026	0.041 ± 0.023	0.034 ± 0.021	0.023 ± 0.015	0.019 ± 0.011
L_9^C	36	0.095 ± 0.040	0.060 ± 0.030	0.062 ± 0.031	0.035 ± 0.024	0.035 ± 0.015	0.027 ± 0.012	0.020 ± 0.010
L_{10}	34	0.108 ± 0.048	0.066 ± 0.030	0.054 ± 0.032	0.035 ± 0.022	0.029 ± 0.014	0.022 ± 0.011	0.019 ± 0.009
L_{10}^C	68	0.092 ± 0.035	0.063 ± 0.030	0.057 ± 0.026	0.041 ± 0.024	0.037 ± 0.020	0.025 ± 0.015	0.020 ± 0.011
L_{11}	64	0.105 ± 0.043	0.061 ± 0.028	0.057 ± 0.030	0.037 ± 0.022	0.032 ± 0.015	0.023 ± 0.012	0.020 ± 0.011
L_{11}^C	38	0.086 ± 0.032	0.070 ± 0.032	0.055 ± 0.025	0.042 ± 0.026	0.038 ± 0.023	0.027 ± 0.017	0.020 ± 0.010
L_{12}	80	0.098 ± 0.042	0.064 ± 0.031	0.057 ± 0.029	0.040 ± 0.025	0.034 ± 0.018	0.025 ± 0.015	0.020 ± 0.011
L_{12}^C	22	0.095 ± 0.033	0.066 ± 0.028	0.052 ± 0.026	0.037 ± 0.018	0.035 ± 0.022	0.023 ± 0.012	0.018 ± 0.010
L_{13}	29	0.090 ± 0.043	0.062 ± 0.030	0.069 ± 0.032	0.038 ± 0.026	0.038 ± 0.021	0.027 ± 0.015	0.022 ± 0.008
L_{13}^C	73	0.100 ± 0.039	0.065 ± 0.030	0.051 ± 0.025	0.040 ± 0.022	0.033 ± 0.017	0.023 ± 0.014	0.019 ± 0.011

Table 5.5: Global properties of shape distributions for 21 subsets of the **HiRISE-FCC**, using **single-estimate** values and **including** craters with $D < 100$ m. Listed are the number of triangles (N_3), squares (N_4), pentagons (N_5), and hexagons (N_6) in each subset, along with mean ± standard deviation of detrended maximum and standard radial deviations ($\Delta R'$ and σ'_R, respectively) and concave fraction (ν'). [CSC on, except for L_7 and L_8]

Set	N	N_3	N_4	N_5	N_6	σ'_R	$\Delta R'$	ν'
L_1	25	7	11	7	0	0.26 ± 0.12	1.49 ± 0.57	1.047 ± 0.046
L_2	42	15	18	8	1	0.27 ± 0.11	1.59 ± 0.59	1.054 ± 0.040
L_3	25	13	7	4	1	0.24 ± 0.07	1.33 ± 0.39	1.039 ± 0.031
L_4	23	10	10	2	1	0.27 ± 0.14	1.53 ± 0.73	1.039 ± 0.050
L_4^C	79	38	26	13	2	0.27 ± 0.10	1.56 ± 0.56	1.049 ± 0.041
L_5	55	26	24	4	1	0.27 ± 0.11	1.54 ± 0.61	1.040 ± 0.047
L_5^C	47	22	12	11	2	0.27 ± 0.10	1.58 ± 0.60	1.055 ± 0.037
L_6	47	21	20	5	1	0.29 ± 0.12	1.65 ± 0.67	1.048 ± 0.043
L_6^C	55	27	16	10	2	0.25 ± 0.09	1.48 ± 0.54	1.046 ± 0.043
L_7	49	24	17	8	0	0.25 ± 0.11	1.40 ± 0.62	1.021 ± 0.043
L_8	48	22	16	8	2	0.24 ± 0.10	1.38 ± 0.52	1.034 ± 0.044
L_9	66	30	23	11	2	0.30 ± 0.12	1.70 ± 0.62	1.058 ± 0.037
L_9^C	36	18	13	4	1	0.23 ± 0.07	1.29 ± 0.47	1.026 ± 0.046
L_{10}	34	21	10	3	0	0.30 ± 0.12	1.67 ± 0.68	1.038 ± 0.046
L_{10}^C	68	27	26	12	3	0.26 ± 0.10	1.50 ± 0.56	1.051 ± 0.041
L_{11}	64	30	26	8	0	0.28 ± 0.11	1.57 ± 0.62	1.047 ± 0.041
L_{11}^C	38	18	10	7	3	0.26 ± 0.10	1.52 ± 0.58	1.047 ± 0.047
L_{12}	80	38	27	13	2	0.28 ± 0.11	1.58 ± 0.63	1.045 ± 0.043
L_{12}^C	22	10	9	2	1	0.25 ± 0.08	1.47 ± 0.48	1.052 ± 0.044
L_{13}	29	12	13	3	1	0.26 ± 0.10	1.45 ± 0.58	1.042 ± 0.035
L_{13}^C	73	36	23	12	2	0.28 ± 0.11	1.60 ± 0.61	1.049 ± 0.046

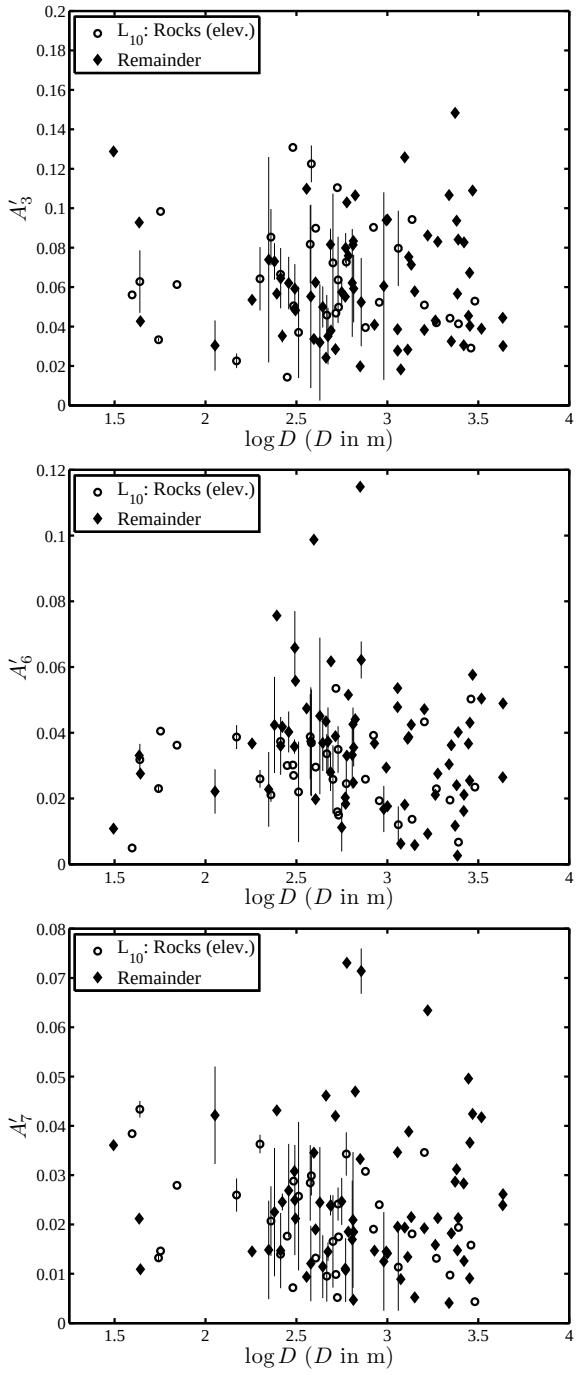

Figure 5-26: Deviation-normalized harmonic amplitudes versus diameter (for $n = 3, 6, 7$). The third and seventh harmonics exhibit no obvious diameter dependence, while $n = 6$ plots at low values for $D < 100$m, and a faintly decreasing mean value for $D \geq 100$ m. Members of the sets L_{10} and L_{10}^C are marked because this comparison exhibits a significant difference in the distribution of A'_6, as we shall see later. [SEV; CSC on; all D]

upon two well-known *distance* metrics commonly used to compare radiance spectra in hyperspectral analyses (Keshava [2004]). For two vectors $\mathbf{x}$ and $\mathbf{y} \in \Re^n$ (i.e., for two ordered sets of n values), the Euclidean distance metric is defined as:

$$d_\Delta(\mathbf{x}, \mathbf{y}) \equiv ||\mathbf{x} - \mathbf{y}|| = \sqrt{\sum_{i=1}^{n} (x_i - y_i)^2}. \quad (5.17)$$

The *angular* distance metric is defined in terms of the dot product $\mathbf{x} \cdot \mathbf{y}$:

$$d_\theta(\mathbf{x}, \mathbf{y}) \equiv \arccos\left(\frac{\mathbf{x} \cdot \mathbf{y}}{||\mathbf{x}||||\mathbf{y}||}\right) \quad (5.18)$$

In order to construct the *difference* metrics, we further require operations that create two kinds of distributions from an ordered set of values. For example, suppose a subset L_x of the HiRISE-FCC has $N = 40$ craters and therefore 40 values of A'_4 stored in a vector $\mathbf{u}$, so that the subset L_x^C therefore has 110-40 = 60 values of A'_4 stored in a vector $\mathbf{v}$. We define an operation $\Xi_H^{(n)}(\mathbf{u}, \mathbf{v})$ which creates a histogram with n bins of the values in $\mathbf{u}$ spanning the whole range of values in $\mathbf{u}$ and $\mathbf{v}$. That is,

$$\Xi_H^{(n)} : (\mathbf{u}, \mathbf{v}) \mapsto \mathbf{H}, \quad (5.19)$$

where $\mathbf{H}$ is an histogram of $\mathbf{u}$ with bins of equal size centered on the values $\mathbf{x} = (x_1, x_2, ..., x_n)$, spanning the range of $\mathbf{u}$ and $\mathbf{v}$ (i.e., from the smallest value in $\mathbf{u}$ or $\mathbf{v}$ to the largest value in $\mathbf{u}$ or $\mathbf{v}$; if this range is denoted by W, the bin size is W/n). Next, we define an operation which creates a *cumulative* distribution of the values in $\mathbf{u}$ on the range spanned by $\mathbf{u}$ and $\mathbf{v}$. That is,

$$\Xi_P^{(n)} : (\mathbf{u}, \mathbf{v}) \mapsto \mathbf{P}, \quad (5.20)$$

where $\mathbf{P}$ is a discrete, monotonically decreasing cumulative distribution of the elements of $\mathbf{u}$ at the ordinate values $\mathbf{x} = (x_1, x_2, ..., x_n)$, where these are evenly spaced and span the range of $\mathbf{u}$ and $\mathbf{v}$. That is, $P(x_i)$ is the fraction of values in $\mathbf{u}$ greater than or equal to x_i. Throughout this chapter and the next one, we will sometimes represent the decreasing-cumulative distribution us-

ing the notation $P(X \geq x)$ (i.e., a notation used for the analogous cumulative probability function: the probability $P(X \geq x)$ that a random variable X will take a value greater than or equal to x).

Finally, we define $\sigma_{\mathbf{u}}$ to be the standard deviation of the elements of $\mathbf{u}$ and $\min(a, b)$ to be the minimum of scalers a and b. We now have all the definitions required to construct nine metrics used to measure the difference between distributions of morphometric quantities, where these are defined in Table 5.6. The first eight of these are absolute measures (always positive), and the last of these (Δ_9) is a relative measure.

In order to determine the statistical significance of differences measured by the metrics in Table 5.6, we have calculated the distribution of *differences* (i.e., of difference-metric calculations) for 10,000 pairings of subsets randomly-sampled from a reference distribution. This exercise is repeated for three reference distributions with markedly different shapes: (a) uniform (flat), (b) Gaussian (peaked, symmetrical), and the Weibull distribution with scale parameter $\lambda = 3/2$ and shape parameter $k = 1/3$ (peaked, asymmetrical). Then we measure the size of differences exceeding 95%, 97.5%, and 99% of all differences between randomly-sampled subsets of the reference distribution. All of these calculations must be repeated for every pairing of subsets of the HiRISE-FCC, since each subset has a different size.

For example, suppose that $\mathbf{u}_1$ contains the values of A'_4 for all $N = 40$ craters in the subset L_x, and $\mathbf{u}_2$ contains the values of A'_4 for all $N = 50$ craters in L_y. Suppose now we calculate the value of the difference metric $\Delta_7(\mathbf{u}_1, \mathbf{u}_2)$. In order to determine the statistical significance of this difference, we calculate the *distribution* of $\Delta_7(\mathbf{v}_1, \mathbf{v}_2)$ for 10,000 sets $\mathbf{v}_1$ of size $N = 40$ and 10,000 sets $\mathbf{v}_2$ of size $N = 50$ randomly-sampled from a Gaussian distribution. If the value of $\Delta_7(\mathbf{u}_1, \mathbf{u}_2)$ exceeds 95% of the 10,000 values of $\Delta_7(\mathbf{v}_1, \mathbf{v}_2)$ (i.e., one for each instance of $\mathbf{v}_1$ and $\mathbf{v}_2$), then we say that the distribution of A'_4 in L_x and L_y are different at the 95% level with respect to a Gaussian reference distribution: i.e., there is only a 5% chance that both are sampled from the same Gaussian distribution. This exercise is repeated for the first eight difference metrics in Table 5.6, and then for the uniform and Weibull reference distributions.

In Figure 5-27 we have plotted the number of difference metrics from among the first eight defined in Table 5.6 for which a difference was measured above the 95% level with respect to a Gaussian distribution, in 11 comparisons of subsets of the HiRISE-FCC, for the first eight deviation-normalized harmonic amplitudes as well as the detrended radial deviations and the concave fraction. The tally was computed for each of four data sets (represented by different quadrants of each grid element): (a) single-estimate values (all D), (b) single-estimates values ($D \geq 100$ m), (c) mid-range values (all D), and (d) mid-range values ($D \geq 100$ m). Also shown are tallies for linear combinations of the deviation-normalized harmonics, where:

$$Q^{abc}_{lmn} \equiv (A'_a + A'_b + A'_c) - (A'_l + A'_m + A'_n), \quad (5.21)$$

and $\{a, b, c, l, m, n\}$ are integers indicating the harmonics included in the sum. (We report these results because although some harmonic amplitudes do not exhibit significant differences by themselves, they sometimes show marked differences in combination.) In Figure 5-28 this exercise is repeated only for the first eight harmonic amplitudes and radial deviations, with respect to the uniform and Weibull reference distributions.

The cumulative distributions for important quantities in the comparison (L_7, L_8) are plotted in Figure 5-29, for (L_9, L_9^C) in Figure 5-30, for (L_{10}, L_{10}^C) in Figure 5-31, and σ'_R and ν' for the comparison (L_2, L_3^C) in Figure 5-33. We have also tabulated in Tables 5.7 and 5.8 for each quantity the difference metrics indicating differences exceeding the 95%, 97.5% and 99% levels with respect to a Gaussian reference distribution (single-estimate values, for all D). The same information is tabulated in Appendix Tables B.8 and B.9 for mid-range values (all D), in Tables B.10 and B.11 for single-estimate values and $D \geq 100$ m, and in Tables B.12 and B.13 for mid-range values and $D \geq 100$ m. Before we discuss the most significant differences

Table 5.6: Difference metrics for the distributions of values in vectors $\mathbf{u}$ and $\mathbf{v}$.

Symbol	Definition	Description
$\Delta_1(\mathbf{u},\mathbf{v}) \equiv$	$d_\Delta\left(\Xi_H^{(n)}(\mathbf{u},\mathbf{v}), \Xi_H^{(n)}(\mathbf{v},\mathbf{u})\right)$	Euclidean distance between histograms; $n = n_L/5$ where n_L is the number of elements in the smallest of $\mathbf{u}$ and $\mathbf{v}$.
$\Delta_2(\mathbf{u},\mathbf{v}) \equiv$	$d_\theta\left(\Xi_H^{(n)}(\mathbf{u},\mathbf{v}), \Xi_H^{(n)}(\mathbf{v},\mathbf{u})\right)$	Angular distance between histograms; $n = n_L/5$.
$\Delta_3(\mathbf{u},\mathbf{v}) \equiv$	$\lvert\bar{\mathbf{u}} - \bar{\mathbf{v}}\rvert / \min(\sigma_\mathbf{u}, \sigma_\mathbf{v})$	Difference of means as a fraction of smallest standard deviation.
$\Delta_4(\mathbf{u},\mathbf{v}) \equiv$	$\lvert\sigma_\mathbf{u} - \sigma_\mathbf{v}\rvert / \min(\sigma_\mathbf{u}, \sigma_\mathbf{v})$	Difference of standard deviations as a fraction of smallest standard deviation.
$\Delta_5(\mathbf{u},\mathbf{v}) \equiv$	$\sum^n \lvert\Xi_P^{(n)}(\mathbf{u},\mathbf{v}) - \Xi_P^{(n)}(\mathbf{v},\mathbf{u})\rvert$	Discrete integral of the absolute difference between decreasing-cumulative distributions; $n = 1000$ $(> n_L)$.
$\Delta_6(\mathbf{u},\mathbf{v}) \equiv$	$\left\lvert\sum^n \left(\Xi_P^{(n)}(\mathbf{u},\mathbf{v}) - \Xi_P^{(n)}(\mathbf{v},\mathbf{u})\right)\right\rvert$	Absolute value of the discrete integral of the difference between decreasing-cumulative distributions; $n = 1000$ $(> n_L)$.
$\Delta_7(\mathbf{u},\mathbf{v}) \equiv$	$d_\Delta\left(\Xi_P^{(n)}(\mathbf{u},\mathbf{v}), \Xi_P^{(n)}(\mathbf{v},\mathbf{u})\right)$	Euclidean distance between decreasing-cumulative distributions; $n = 1000$ $(> n_L)$.
$\Delta_8(\mathbf{u},\mathbf{v}) \equiv$	$d_\theta\left(\Xi_P^{(n)}(\mathbf{u},\mathbf{v}), \Xi_P^{(n)}(\mathbf{v},\mathbf{u})\right)$	Angular distance between decreasing-cumulative distributions; $n = 1000$ $(> n_L)$.
$\Delta_9(\mathbf{u},\mathbf{v}) \equiv$	$\sum^n \left(\Xi_P^{(n)}(\mathbf{u},\mathbf{v}) - \Xi_P^{(n)}(\mathbf{v},\mathbf{u})\right) = (\bar{\mathbf{u}} - \bar{\mathbf{v}})/\text{range}(\mathbf{u},\mathbf{v})$	Discrete integral of the difference between decreasing-cumulative distributions; equivalent to the difference of means as a fraction of the range spanning $\mathbf{u}$ and $\mathbf{v}$. $(n = 1000$ $(> n_L))$

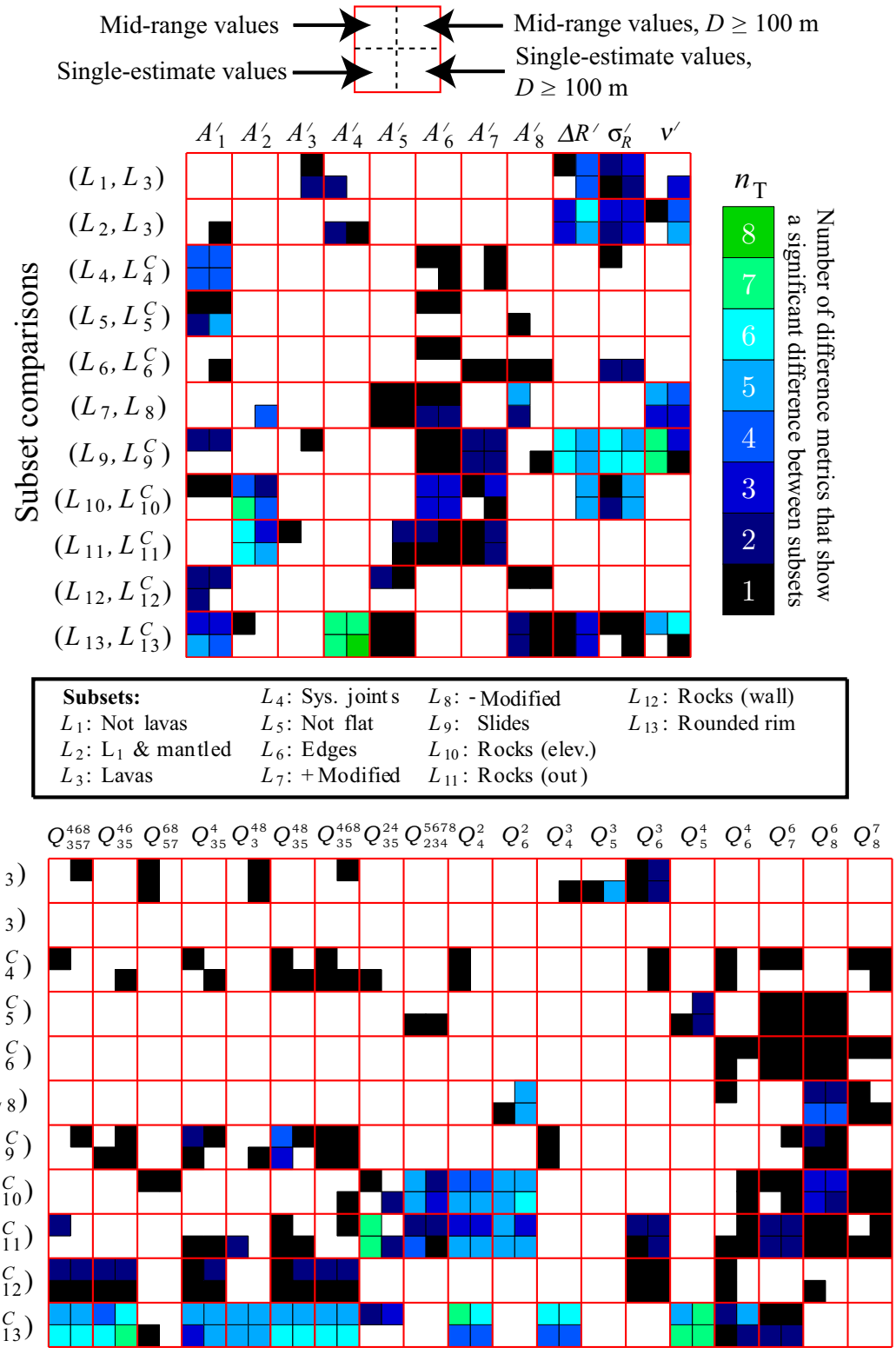

Figure 5-27: The number of absolute difference metrics (Δ_1 through Δ_8, defined in Table 5.6) measuring a statistically significant difference between compared subsets of the HiRISE-FCC at the 95% level with respect to a Gaussian reference distribution, for the first eight deviation-normalized harmonic amplitudes (upper grid) and linear combinations of these (lower grid), as well as detrended radial deviations and concave fraction. [CSC on, except for (L_7, L_8)] (N.B. $Q^{abc}_{lmn} \equiv (A'_a + A'_b + A'_c) - (A'_l + A'_m + A'_n)$)

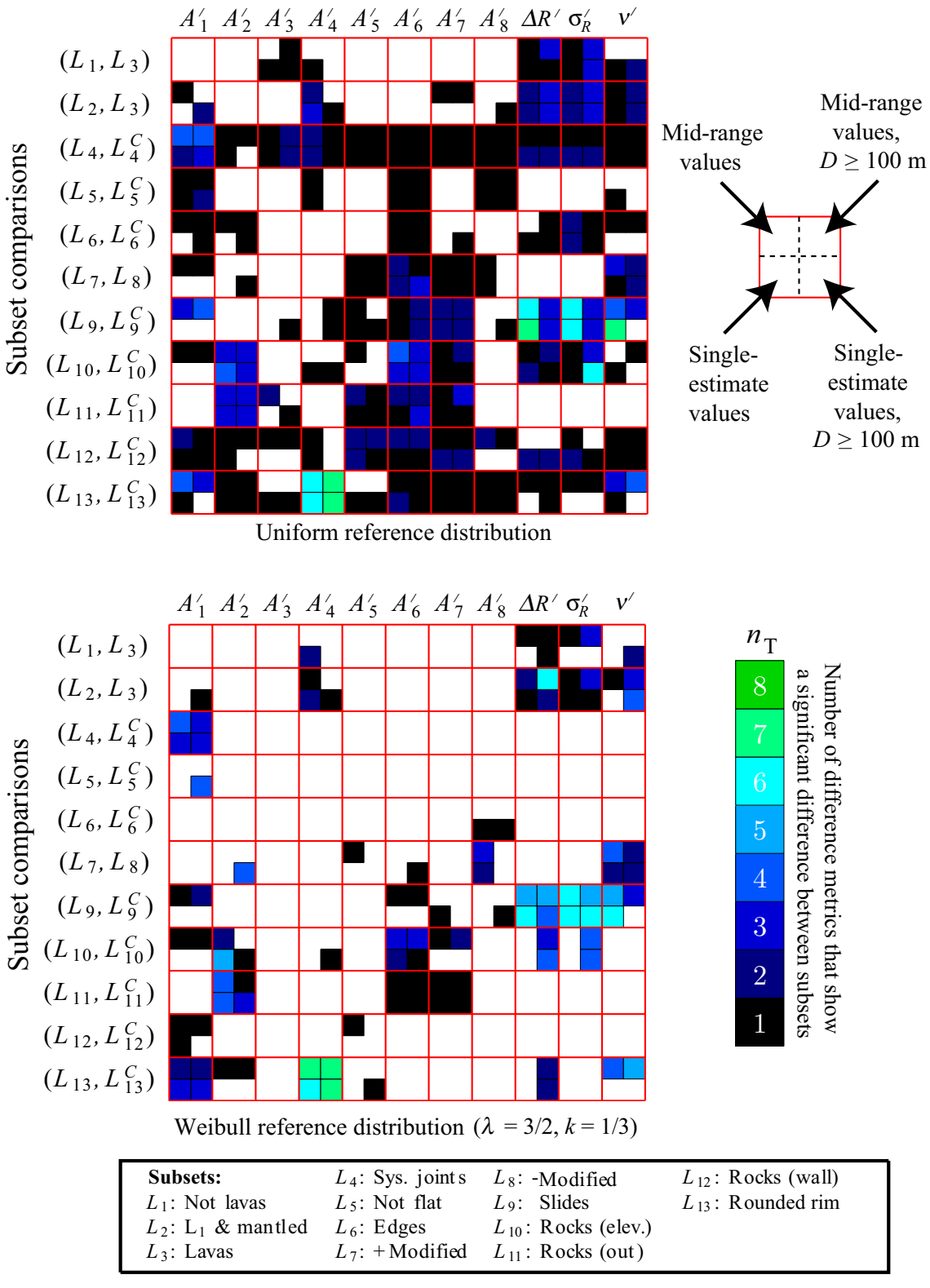

Figure 5-28: The number of absolute difference metrics (Δ_1 through Δ_8, defined in Table 5.6) measuring a statistically significant difference between compared subsets of the HiRISE-FCC at the 95% level with respect to a uniform reference distribution (upper grid) and a Weibull reference distribution ($\lambda = 3/2$ and $k = 1/3$, lower grid), for the first eight deviation-normalized harmonic amplitudes and the detrended radial deviations and concave fraction. [CSC on, except for (L_7, L_8)].

revealed by these comparisons, we complete this analysis by examining differences in the distribution of dominant harmonics: i.e., the percentage of triangular-, square-, and pentagonal craters (etc.) that make up each subset.

Dominant harmonics

Another important measure of the distribution of shapes in a population of impact craters is the relative frequency-of-occurrence of primary and secondary harmonics. Recall from Section 5.2 that the "primary harmonic" of a given PCRO is the largest harmonic amplitude for $n > 2$ ("secondary harmonic" is the second-largest). Figure 5-34 shows a two-dimensional histogram of the number of impact craters in the HiRISE-FCC with every possible pairing of primary and secondary harmonics. We can see at once that the most common combination of (primary, secondary) harmonics is (3,4), followed by (4,3) and then (3,5). Figure 5-35 shows one-dimensional histograms of the frequency with which low-order harmonics occur as primary, secondary and tertiary harmonics, indicating that the most common primary harmonic is $n = 3$, the most common secondary harmonic is $n = 4$, and the most common tertiary harmonic is $n = 6$. In drawing comparisons between subsets of the HiRISE-FCC, we have found significant departures from the overall distribution shown in these figures.

Having tallied the dominant harmonics in each subset, we can compare the frequency-of-occurrence of a single harmonic as a percentage of all primary harmonics. In Figure 5-36 we have plotted the fraction of all craters with primary harmonic $n = 3$ (i.e., N_3/N) in one subset versus the corresponding fraction in another subset. For example, the number of triangular craters in L_{10} comprise roughly 60% of this subset, while only 40% of L_{10}^C are triangular (i.e., $A_3 > A_n$ for all $n > 2$). Points that lie on the line $y = x$ (dashed) indicate no difference between subsets, and points plotting far away from this line indicate a significant difference. The mean value in this case is $N_3/N \approx 0.48$, with only several subsets expressing significant departures. This exer-

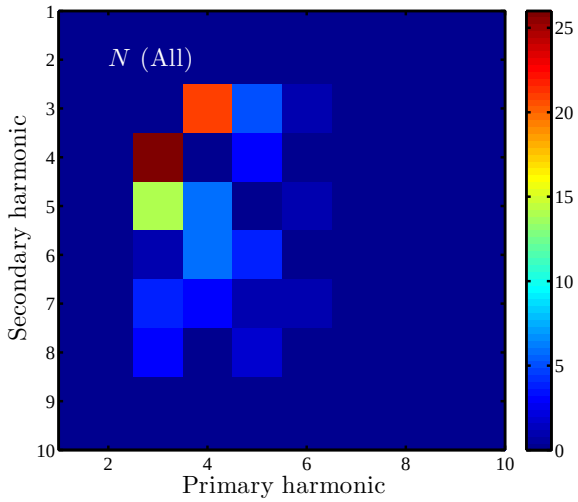

Figure 5-34: Two-dimensional histogram of primary and secondary harmonics for the HiRISE-FCC. [SEV; CSC on; all D]

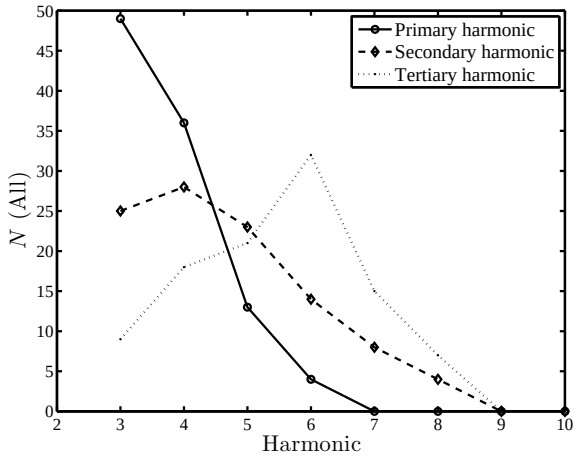

Figure 5-35: Histograms of primary, secondary, tertiary harmonics for the HiRISE-FCC. [SEV; CSC on; all D]

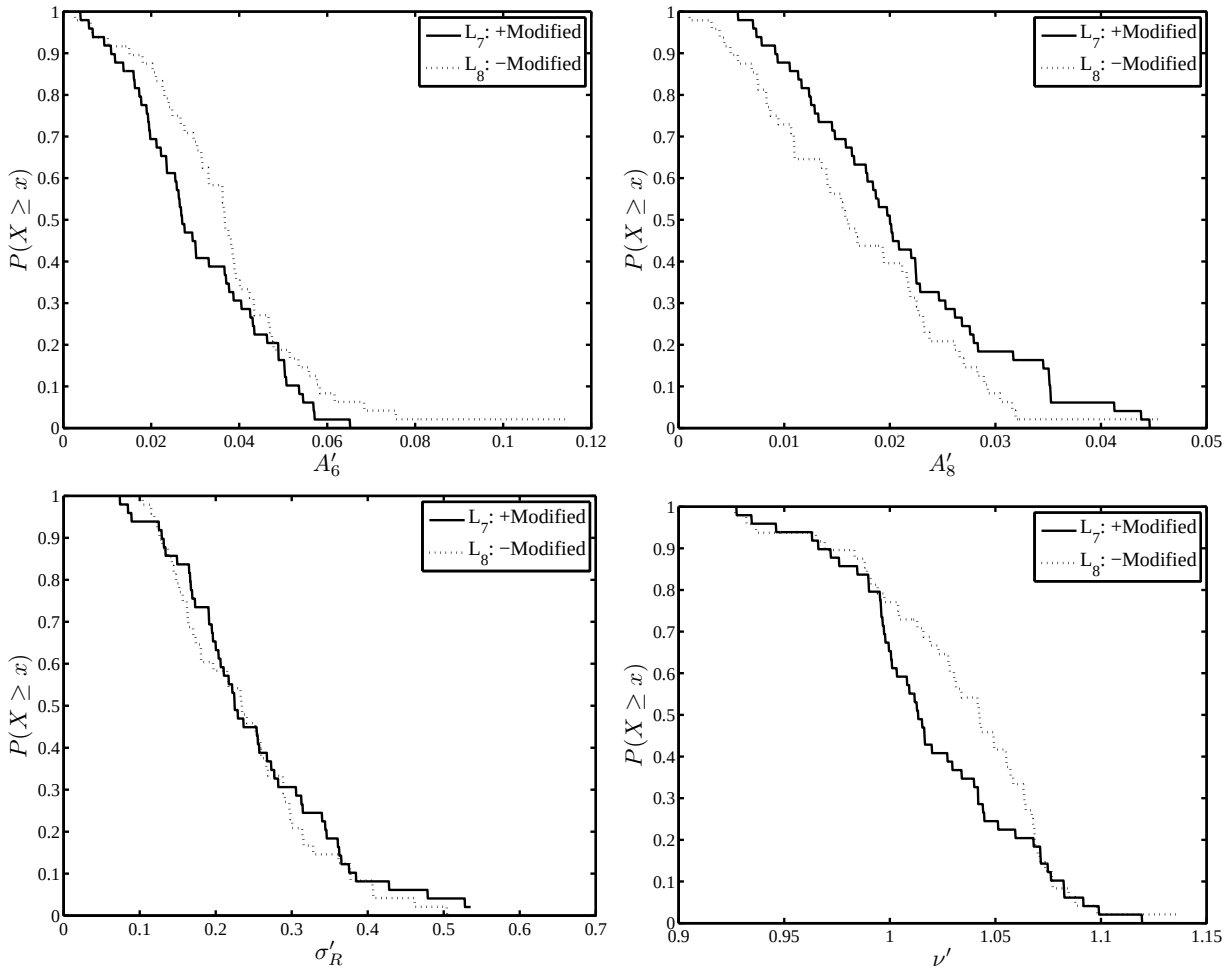

Figure 5-29: Cumulative distributions of important quantities for the comparison of subsets L_7 and L_8. See text for discussion. [SEV; CSC off; all D]

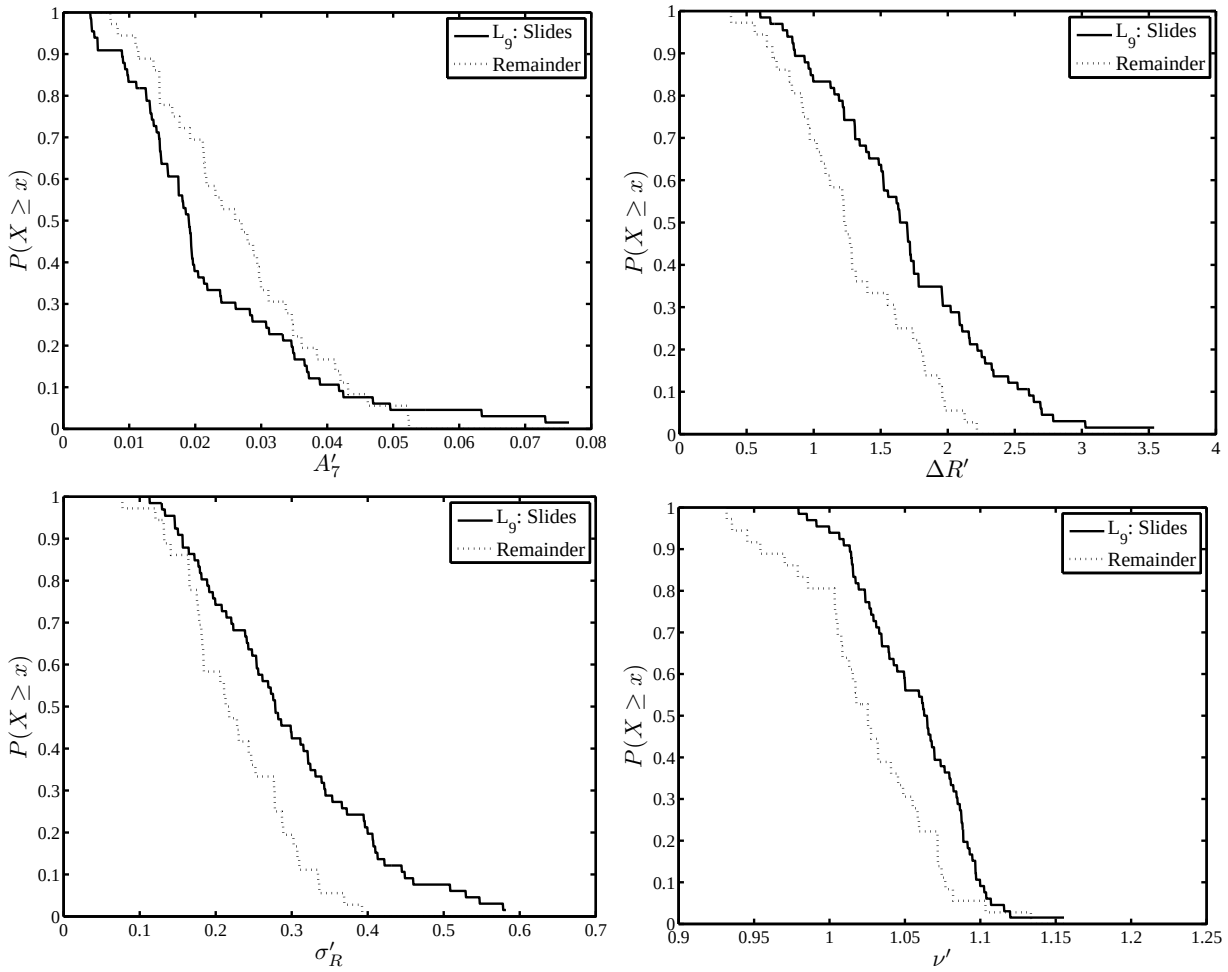

Figure 5-30: Cumulative distributions of important quantities for the comparison of subsets L_9 and L_9^C. See text for discussion. [SEV; CSC on; all D]

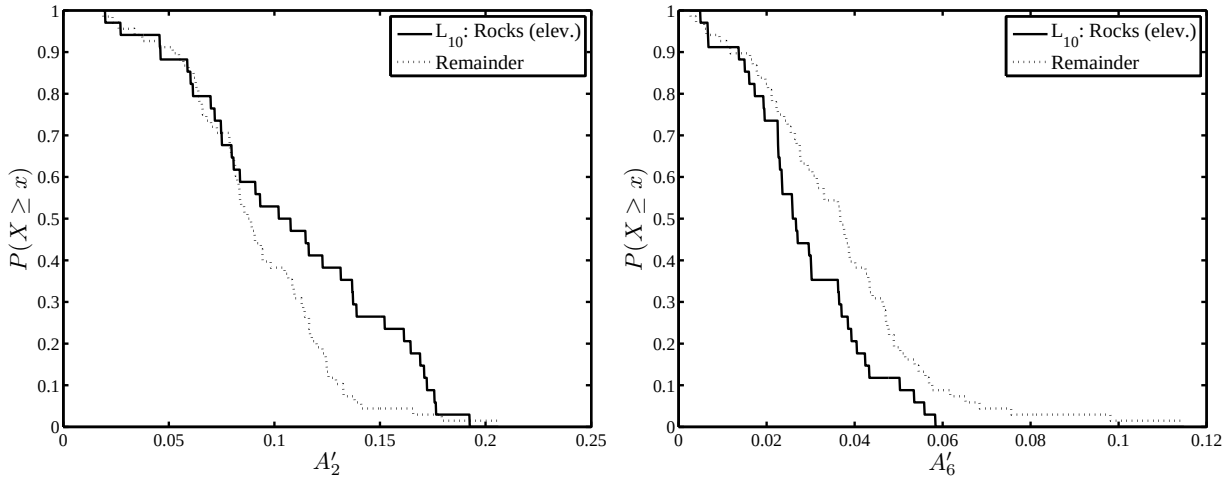

Figure 5-31: Cumulative distributions of important quantities for the comparison of subsets L_{10} and L_{10}^{C}. See text for discussion. [SEV; CSC on; all D]

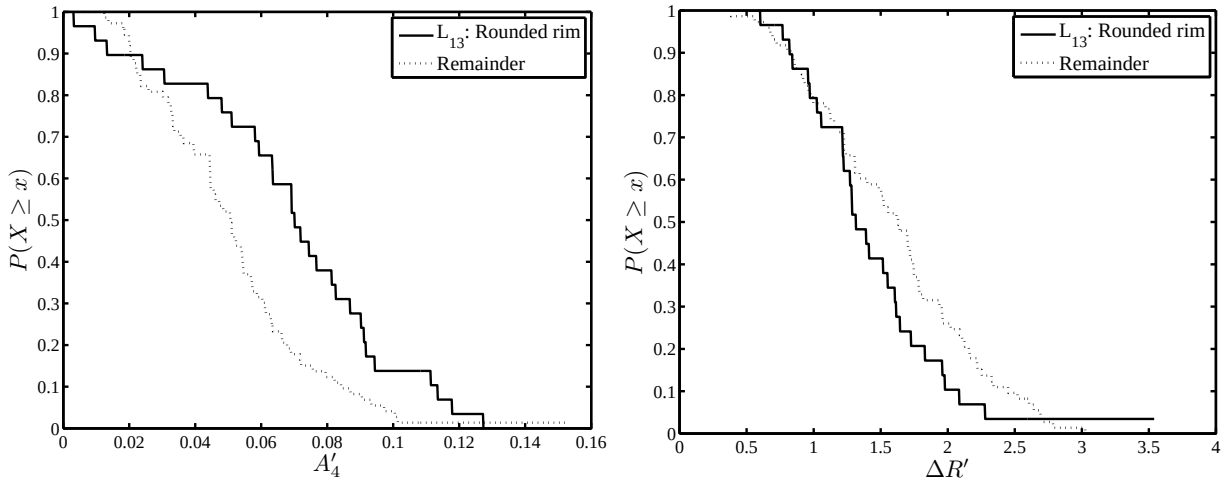

Figure 5-32: Cumulative distributions of important quantities for the comparison of subsets L_{13} and L_{13}^{C}. See text for discussion. [SEV; CSC on; all D]

Table 5.7: Quantities and difference metrics (Δ_n: for $n = 1, 2, ...$ defined in Table 5.6) that indicate a statistically significant difference for 13 pairings of 21 subsets of the **HiRISE-FCC**, with respect to differences computed for 10,000 pairings of randomly-sampled subsets of a **Gaussian** reference distribution on the same domain. Listed are metrics reporting differences that exceed the percentage $p_{\rm lim}$ of differences computed from paired subsets of the reference distribution. **Single-estimate** values were used and craters with $D < 100$ m were **included**. [CSC on, except for L_7 and L_8]

Set	$p_{\rm lim}$	Quantities whose distributions differ at the level $p_{\rm lim}$
(L_1,L_3)	95%	A'_4 (Δ_n:1,2), σ'_R (Δ_n:4), Q^{68}_{57} (Δ_n:8), Q^3_5 (Δ_n:2), Q^3_6 (Δ_n:8)
	97.5%	A'_4 (Δ_n:2), σ'_R (Δ_n:4)
(L_2,L_3)	95%	A'_4 (Δ_n:1,2), $\Delta R'$ (Δ_n:3,4,8), σ'_R (Δ_n:4,8), Q^1_8 (Δ_n:4), Q^3_8 (Δ_n:1,2)
	97.5%	A'_4 (Δ_n:2), $\Delta R'$ (Δ_n:3), σ'_R (Δ_n:4), Q^3_8 (Δ_n:1,2)
(L_4,L^C_4)	95%	A'_1 (Δ_n:2,4,5,7), Q^{48}_{35} (Δ_n:1), Q^{468}_{35} (Δ_n:1), Q^{24}_{35} (Δ_n:3), Q^1_3 (Δ_n:3,4), Q^1_7 (Δ_n:1), Q^2_3 (Δ_n:4), Q^2_4 (Δ_n:2), Q^4_6 (Δ_n:1)
	97.5%	Q^1_7 (Δ_n:1), Q^4_6 (Δ_n:1)
	99%	Q^4_6 (Δ_n:1)
(L_5,L^C_5)	95%	A'_1 (Δ_n:5,8), A'_8 (Δ_n:6), Q^{5678}_{234} (Δ_n:8), Q^2_3 (Δ_n:2), Q^3_7 (Δ_n:2), Q^4_5 (Δ_n:1), Q^6_7 (Δ_n:4), Q^6_8 (Δ_n:4)
	97.5%	A'_1 (Δ_n:8), Q^{5678}_{234} (Δ_n:8), Q^6_7 (Δ_n:4), Q^6_8 (Δ_n:4)
	99%	Q^6_7 (Δ_n:4)
(L_6,L^C_6)	95%	A'_7 (Δ_n:8), A'_8 (Δ_n:2), σ'_R (Δ_n:4,8), Q^4_6 (Δ_n:4), Q^6_7 (Δ_n:4), Q^6_8 (Δ_n:4)
	97.5%	σ'_R (Δ_n:4), Q^4_6 (Δ_n:4), Q^6_7 (Δ_n:4)
(L_7,L_8)	95%	A'_5 (Δ_n:4), A'_6 (Δ_n:3,8), A'_8 (Δ_n:5,6), ν (Δ_n:1,2,8), Q^1_5 (Δ_n:4), Q^1_6 (Δ_n:3), Q^1_7 (Δ_n:4), Q^2_6 (Δ_n:7), Q^5_8 (Δ_n:4), Q^6_8 (Δ_n:3,6,7,8), Q^7_8 (Δ_n:3)
	97.5%	A'_5 (Δ_n:4), Q^6_8 (Δ_n:3,8)
	99%	Q^6_8 (Δ_n:3)
(L_9,L^C_9)	95%	A'_6 (Δ_n:4), A'_7 (Δ_n:1,8), $\Delta R'$ (Δ_n:2,3,5,6,7,8), σ'_R (Δ_n:3,4,5,6,7,8), ν (Δ_n:1,2,3,5,6,7,8), Q^{46}_{35} (Δ_n:3), Q^4_{35} (Δ_n:3), Q^{48}_{35} (Δ_n:1,2,3), Q^{468}_{35} (Δ_n:3), Q^1_5 (Δ_n:1,2), Q^1_6 (Δ_n:4), Q^1_7 (Δ_n:1), Q^3_4 (Δ_n:2), Q^5_7 (Δ_n:1), Q^5_8 (Δ_n:1), Q^6_8 (Δ_n:4)
	97.5%	A'_6 (Δ_n:4), A'_7 (Δ_n:8), $\Delta R'$ (Δ_n:3,5,6,7,8), σ'_R (Δ_n:3,4,5,6,7,8), ν (Δ_n:1,3,5,6,7,8), Q^{48}_{35} (Δ_n:1), Q^1_5 (Δ_n:1,2), Q^1_7 (Δ_n:1), Q^5_7 (Δ_n:1), Q^5_8 (Δ_n:1)
	99%	$\Delta R'$ (Δ_n:3,5,6,7,8), σ'_R (Δ_n:3,4,5,6,7,8), ν (Δ_n:3,5,6,7,8), Q^{48}_{35} (Δ_n:1), Q^1_5 (Δ_n:1)
(L_{10},L^C_{10})	95%	A'_2 (Δ_n:1,3,4,5,6,7,8), A'_6 (Δ_n:3,4,8), σ'_R (Δ_n:6,8), Q^{5678}_{234} (Δ_n:3,5,6,7,8), Q^{468}_0 (Δ_n:2), Q^1_2 (Δ_n:1,3,5,6,7), Q^1_6 (Δ_n:3,4), Q^2_3 (Δ_n:1,2,4,5,7,8), Q^2_4 (Δ_n:1,4,5,7,8), Q^2_5 (Δ_n:1,3,4,5,6,7,8), Q^2_6 (Δ_n:3,5,6,7,8), Q^2_7 (Δ_n:1,3,5,7,8), Q^2_8 (Δ_n:5,6,7,8), Q^6_8 (Δ_n:3,4,8), Q^7_8 (Δ_n:4)
	97.5%	A'_2 (Δ_n:1,7,8), A'_6 (Δ_n:3,4,8), Q^{5678}_{234} (Δ_n:3,5,6,8), Q^1_2 (Δ_n:7), Q^1_6 (Δ_n:4), Q^2_3 (Δ_n:1,2,8), Q^2_4 (Δ_n:4,8), Q^2_5 (Δ_n:3,5,6,7,8), Q^2_6 (Δ_n:3,5,6,7,8), Q^2_7 (Δ_n:1,8), Q^2_8 (Δ_n:8), Q^6_8 (Δ_n:4), Q^7_8 (Δ_n:4)
	99%	A'_2 (Δ_n:8), A'_6 (Δ_n:8), Q^{5678}_{234} (Δ_n:6), Q^2_3 (Δ_n:1,8), Q^2_5 (Δ_n:8), Q^2_6 (Δ_n:8), Q^2_8 (Δ_n:8), Q^6_8 (Δ_n:4)

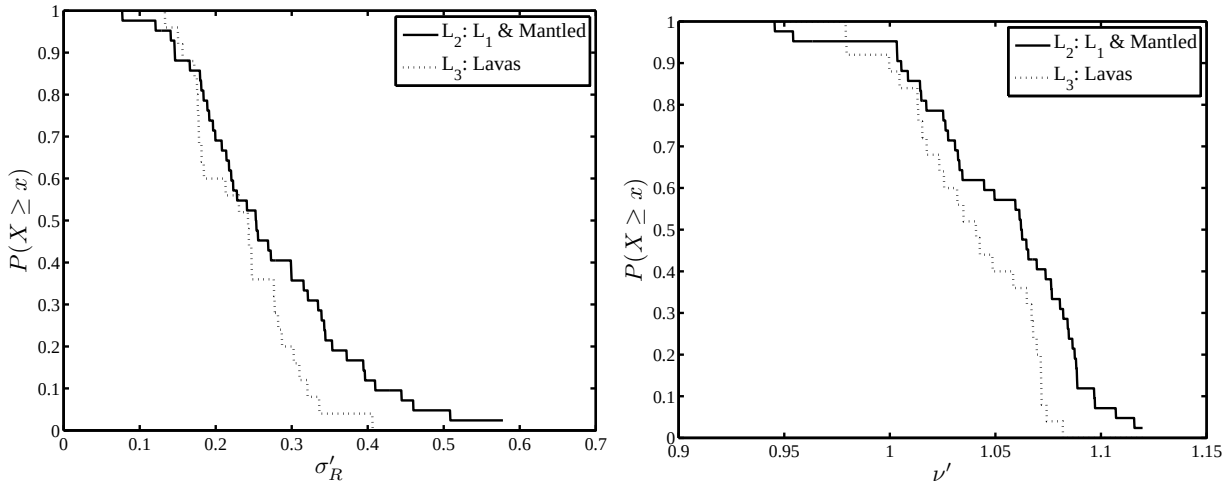

Figure 5-33: Cumulative distributions of important quantities for the comparison of subsets L_2 and L_3. See text for discussion. [SEV; CSC on; all D]

Table 5.8: Continuation of table 5.7.

Set	$p_{\lim}$	Quantities whose distributions differ at the level $p_{\lim}$
(L_{11},L_{11}^C)	95%	A_2' (Δ_n:3,4,5,6,7,8), A_6' (Δ_n:4), A_7' (Δ_n:4), Q_{35}^4 (Δ_n:1), Q_3^{48} (Δ_n:1,2), Q_{35}^{48} (Δ_n:1), Q_{35}^{24} (Δ_n:1,2,3,5,6,7,8), Q_{234}^{5678} (Δ_n:3,5,6,8), Q_2^1 (Δ_n:3,4,5,6,7), Q_4^1 (Δ_n:2), Q_6^1 (Δ_n:4), Q_7^1 (Δ_n:4), Q_3^2 (Δ_n:3,5,6,7,8), Q_4^2 (Δ_n:2,4,5,7,8), Q_5^2 (Δ_n:3,5,6,7,8), Q_6^2 (Δ_n:3,5,6,7,8), Q_7^2 (Δ_n:3,5,6,7,8), Q_8^2 (Δ_n:3,4,5,6,7,8), Q_6^3 (Δ_n:4), Q_6^4 (Δ_n:1), Q_7^5 (Δ_n:4), Q_7^6 (Δ_n:1,4), Q_8^6 (Δ_n:4), Q_8^7 (Δ_n:4)
	97.5%	A_2' (Δ_n:3,5,6,7,8), A_6' (Δ_n:4), A_7' (Δ_n:4), Q_{35}^4 (Δ_n:1), Q_3^{48} (Δ_n:1), Q_{35}^{48} (Δ_n:1), Q_{35}^{24} (Δ_n:2,3,5,6,7,8), Q_2^1 (Δ_n:3,5,6,7), Q_6^1 (Δ_n:4), Q_7^1 (Δ_n:4), Q_3^2 (Δ_n:3,5,6,7,8), Q_4^2 (Δ_n:2,4,8), Q_5^2 (Δ_n:3,5,6,7,8), Q_6^2 (Δ_n:3,5,6,7,8), Q_7^2 (Δ_n:3,5,6), Q_8^2 (Δ_n:3,6,8), Q_6^3 (Δ_n:4), Q_7^6 (Δ_n:1,4), Q_8^6 (Δ_n:4)
	99%	A_2' (Δ_n:3,8), A_6' (Δ_n:4), Q_{35}^{24} (Δ_n:3,7), Q_2^1 (Δ_n:3), Q_6^1 (Δ_n:4), Q_3^2 (Δ_n:3,8), Q_4^2 (Δ_n:8), Q_5^2 (Δ_n:3,6,8), Q_6^2 (Δ_n:3,5,6,8), Q_7^6 (Δ_n:4), Q_8^6 (Δ_n:4)
(L_{12},L_{12}^C)	95%	A_1' (Δ_n:5,6), Q_{357}^{468} (Δ_n:1), Q_{35}^{46} (Δ_n:1), Q_{35}^4 (Δ_n:1), Q_{35}^{48} (Δ_n:1), Q_{35}^{468} (Δ_n:1), Q_8^1 (Δ_n:6), Q_6^3 (Δ_n:1), Q_6^4 (Δ_n:1), Q_8^6 (Δ_n:1)
	97.5%	Q_{35}^{46} (Δ_n:1), Q_{35}^4 (Δ_n:1), Q_{35}^{48} (Δ_n:1), Q_{35}^{468} (Δ_n:1)
(L_{13},L_{13}^C)	95%	A_1' (Δ_n:3,5,6,7,8), A_4' (Δ_n:1,2,3,5,6,7,8), A_5' (Δ_n:8), A_8' (Δ_n:4,7), $\Delta R'$ (Δ_n:8), Q_{357}^{468} (Δ_n:1,2,3,5,7,8), Q_{35}^{46} (Δ_n:1,2,3,5,7,8), Q_{57}^{68} (Δ_n:4), Q_{35}^4 (Δ_n:3,7,8), Q_3^{48} (Δ_n:3,5,6,7,8), Q_{35}^{48} (Δ_n:1,3,5,6,7,8), Q_{35}^{468} (Δ_n:1,3,5,6,7,8), Q_0^{468} (Δ_n:1,2,3,5,6,7,8), Q_0^{48} (Δ_n:1,2,3,5,6,7,8), Q_0^{46} (Δ_n:3,5,6,7,8), Q_4^1 (Δ_n:1,2,3,5,6,7,8), Q_7^1 (Δ_n:1), Q_8^1 (Δ_n:3,5,6,7,8), Q_4^2 (Δ_n:3,5,6,7), Q_4^3 (Δ_n:1,3,5,6), Q_5^4 (Δ_n:1,2,3,5,6,7,8), Q_6^4 (Δ_n:1), Q_7^4 (Δ_n:5,6,7,8), Q_8^4 (Δ_n:3,8), Q_6^5 (Δ_n:1), Q_7^5 (Δ_n:1), Q_7^6 (Δ_n:1,4)
	97.5%	A_1' (Δ_n:6), A_4' (Δ_n:1,3,5,6,7,8), Q_{357}^{468} (Δ_n:1,3), Q_{35}^{46} (Δ_n:1,3,7), Q_3^{48} (Δ_n:3,5,6), Q_{35}^{48} (Δ_n:3,7,8), Q_{35}^{468} (Δ_n:3,5,7,8), Q_0^{468} (Δ_n:1,2,3,5,6,7,8), Q_0^{48} (Δ_n:1,2,3,5,6,7,8), Q_0^{46} (Δ_n:3,5,6,7,8), Q_4^1 (Δ_n:1,2,3,5,6,7,8), Q_8^1 (Δ_n:3,5,6,7,8), Q_4^2 (Δ_n:6,7), Q_5^4 (Δ_n:1,2,5,7,8), Q_6^4 (Δ_n:1), Q_7^4 (Δ_n:5,7,8), Q_6^5 (Δ_n:1), Q_7^5 (Δ_n:1), Q_7^6 (Δ_n:1)
	99%	A_4' (Δ_n:3,5,6,7,8), Q_{357}^{468} (Δ_n:1), Q_{35}^{46} (Δ_n:1), Q_0^{468} (Δ_n:1,2,3,5,6,7,8), Q_0^{48} (Δ_n:1,2,3,5,6,7,8), Q_0^{46} (Δ_n:3,5,6,7,8), Q_4^1 (Δ_n:1,3,5,6,7,8), Q_5^4 (Δ_n:1,2,7,8), Q_6^4 (Δ_n:1), Q_7^4 (Δ_n:8), Q_6^5 (Δ_n:1), Q_7^6 (Δ_n:1)

cise has been repeated for N_4/N, N_5/N, N_6/N, in Figures 5-37, 5-38, and 5-39, respectively.

D-dependence of harmonic amplitudes

As discussed earlier, comparisons of the detrended radial deviations and concave fraction are insensitive to the distribution of diameters sampled by each of the subsets being compared. However, sampled diameters are an important consideration when comparing harmonic amplitudes and the distributions of dominant harmonics. In Figure 5-40 we have plotted cumulative distributions of diameter ($D \geq 100$ m) for each of the subsets compared in this section, as well as the value of Δ_9, a relative difference metric defined in Table 5.6. As discussed earlier, a subset populated by craters with larger diameters is expected to exhibit larger values for high-order deviation-normalized harmonic amplitudes and smaller values for low-order deviation-normalized harmonic amplitudes, on average. Likewise, a population with larger diameters is expected to have a larger percentage of primary harmonics among higher orders. The statistically-significant differences measured for subset comparisons in the foregoing analysis must therefore be evaluated in light of this expectation, in order to note those cases in which the aforesaid geometrical effect may contribute to the differences measured. In Figure 5-41 we have plotted[8] Δ_9 for the difference between the distributions of deviation-normalized harmonic amplitudes for all of the first eight harmonics, repeating this for every subset comparison in Figure 5-27. (For example, a value occurring above zero at $n = 5$ indicates that, in the comparison (L_x, L_y), L_x has larger values of A'_5 than L_y, on average.) The trend just described should be expressed as a transition from positive to negative values or vice versa, for harmonic amplitudes $n \geq 2$. This is observed only in the case of (L_6, L_6^C) and (L_{10}, L_{10}^C). From Figure 5-40 we can see that the diameters sampled in L_6 and L_6^C are nearly identical. The diameter distributions in (L_{10}, L_{10}^C) exhibit a difference that is consistent with the trend shown in Figure 5-41 for this comparison, however, this difference is less than the average of $|\Delta_9|$ for the entire set of diameter-distribution comparisons and is significantly less than some comparisons which do not exhibit this trend (e.g., (L_{13}, L_{13}^C) and (L_9, L_9^C)). By additionally noting no obvious dependence of deviation-normalized harmonic amplitudes upon diameter except in the case of $n = 6$ (Figure 5-26), we conclude that the effect of differences in sampled diameters is less important than other factors.

[8] Error bars indicate the range for first-estimate and mid-range values, for all D as well as $D \geq 100$ m.

Discussion

Before addressing results for particular metrics and subset comparisons, we begin this discussion of results by noting a significant global feature of Figures 5-27 and 5-28. That is, the low-order harmonics ($n = 2$ through $n = 4$) are the least sensitive to differences between subsets, while $n = 7$ and especially $n = 6$ are the most sensitive. That $n = 8$ is not similarly important indicates that there is more to this pattern than a simple contrast between low- and high-order harmonics. This once again suggests that $n = 6$ is special in important respects although for unknown reasons. For example, there does not appear to be an obvious explanation on the basis of purely geometrical considerations for this exception, which may suggest that an unidentified physical process is behind the pattern.

Quadrature: Figure 5-37 shows that square-shaped impact craters are more common in targets in which systematic jointing is clearly expressed. This is also true of targets that are not flat, that are not lavas (L_1 and L_2), that are marked by sharp edges (i.e., which may indicate induration), and that are strewn with rocks and boulders (but where these are not clustered on elevated surfaces (L_{10}), which we have interpreted as debris or regolith). Moreover, impact craters whose rims are rounded (for their entire circumference) are also more commonly square-shaped. Squares outnumber triangles in the non-lava targets (L_1 and L_2), among craters with rounded rims (L_{13}), in targets with systematic jointing

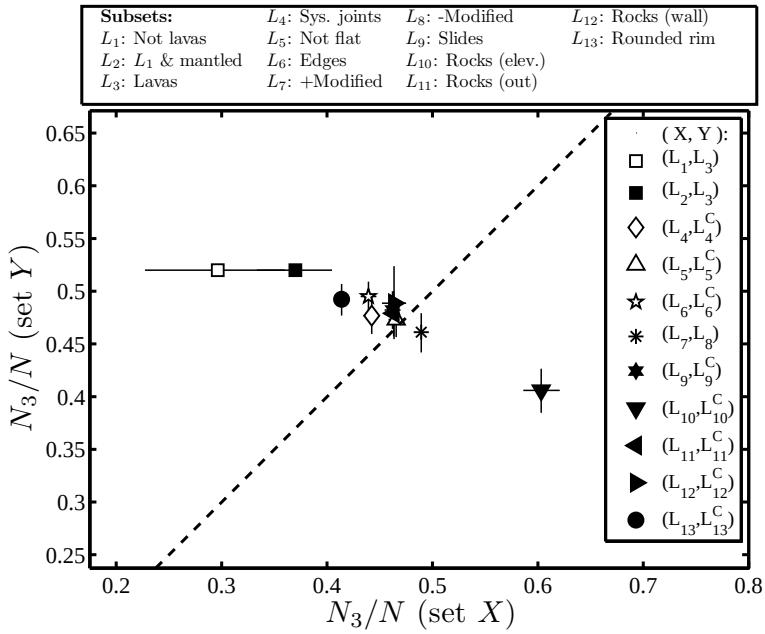

Figure 5-36: For each of 11 subset comparisons (X, Y), the fraction of impact craters with primary harmonic $n = 3$ in Y is plotted versus the same fraction computed for X. Points on the dashed line $y = x$ indicate parity. [CSC on, except for (L_7, L_8); Error bars span the entire range of values computed for (a) SEV for all D, (b) SEV for $D \geq 100$ m, (c) MRV for all D, and (d) MRV for $D \geq 100$ m.]

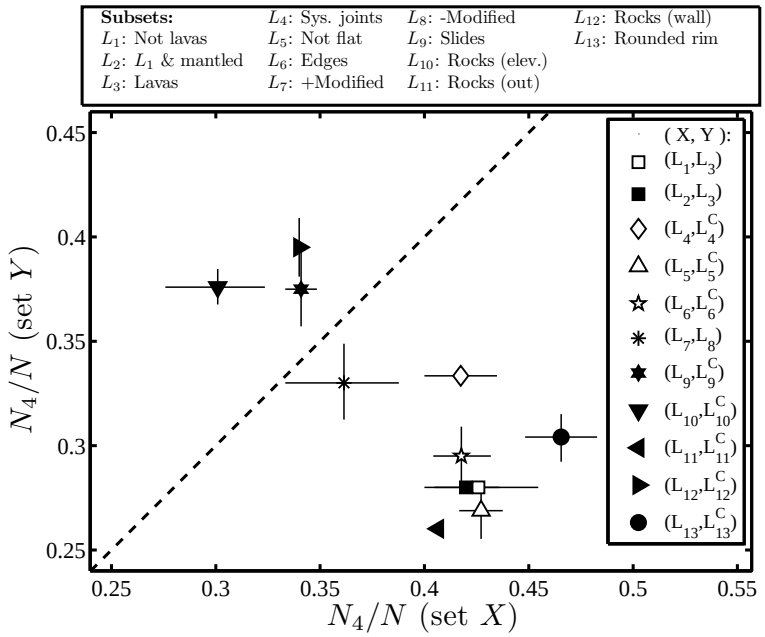

Figure 5-37: For each of 11 subset comparisons (X, Y), the fraction of impact craters with primary harmonic $n = 4$ in Y is plotted versus the same fraction computed for X. (See caption of Figure 5-36.) [CSC on, except for (L_7, L_8)]

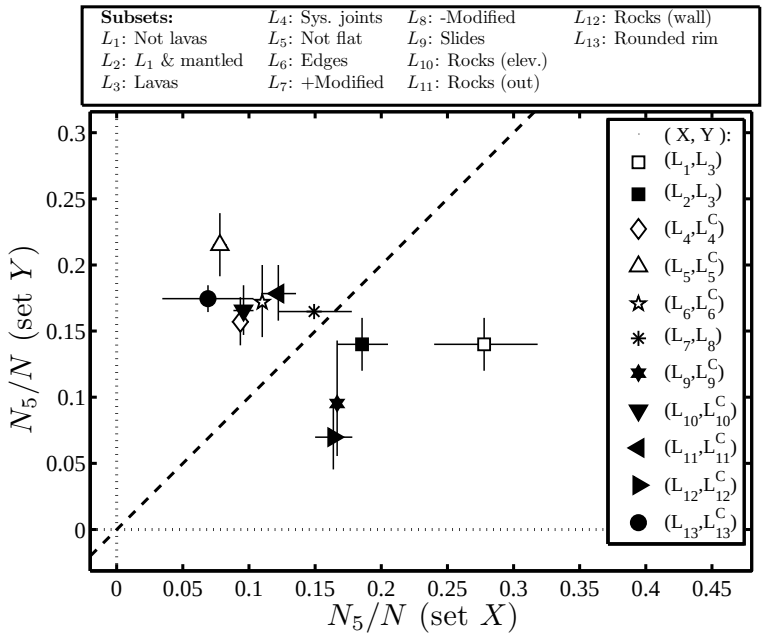

Figure 5-38: For each of 11 subset comparisons (X, Y), the fraction of impact craters with primary harmonic $n = 5$ in Y is plotted versus the same fraction computed for X. (See caption of Figure 5-36.) [CSC on, except for (L_7, L_8)]

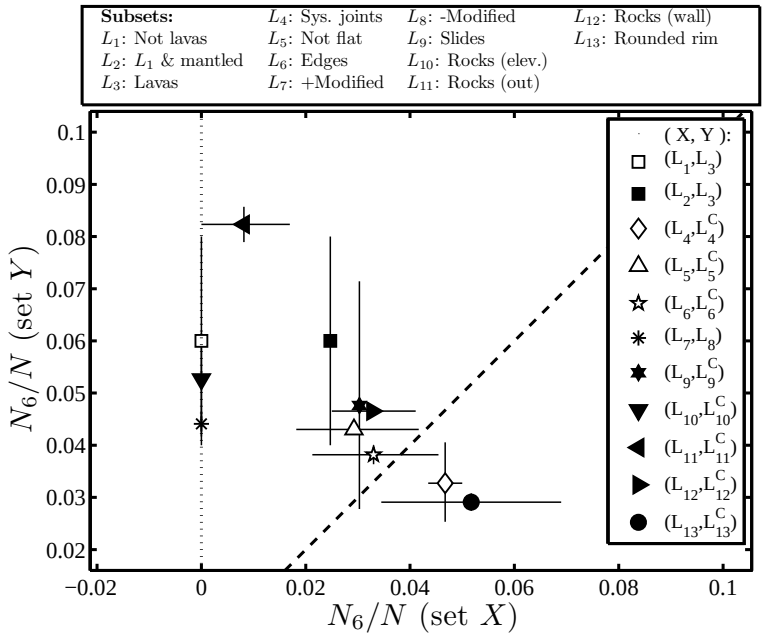

Figure 5-39: For each of 11 subset comparisons (X, Y), the fraction of impact craters with primary harmonic $n = 6$ in Y is plotted versus the same fraction computed for X. (See caption of Figure 5-36.) [CSC on, except for (L_7, L_8)]

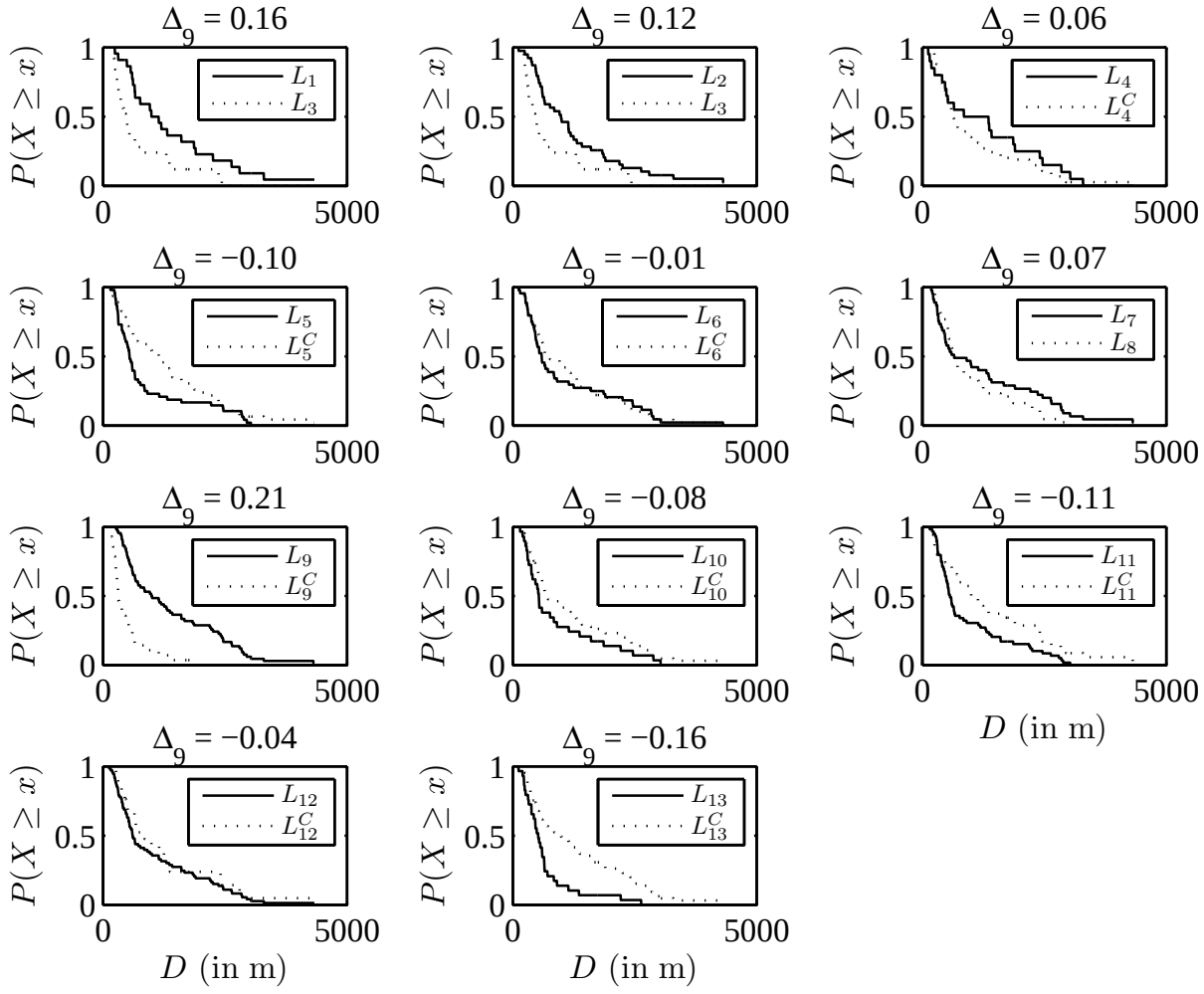

Figure 5-40: Cumulative distribution of diameter for each subset in 11 comparisons, and the difference between these measured by the relative difference metric Δ_9. (i.e., "Δ_9" for the comparison (L_x, L_y) is equal to $\Delta_9(\mathbf{D}_x, \mathbf{D}_y)$ where $\mathbf{D}_x$ are the diameters of craters in L_x and $\mathbf{D}_y$ are the diameters of craters in L_y. A positive value means that craters in L_x are on average larger than craters in L_y.) [SEV; CSC on; $D \geq 100$ m]

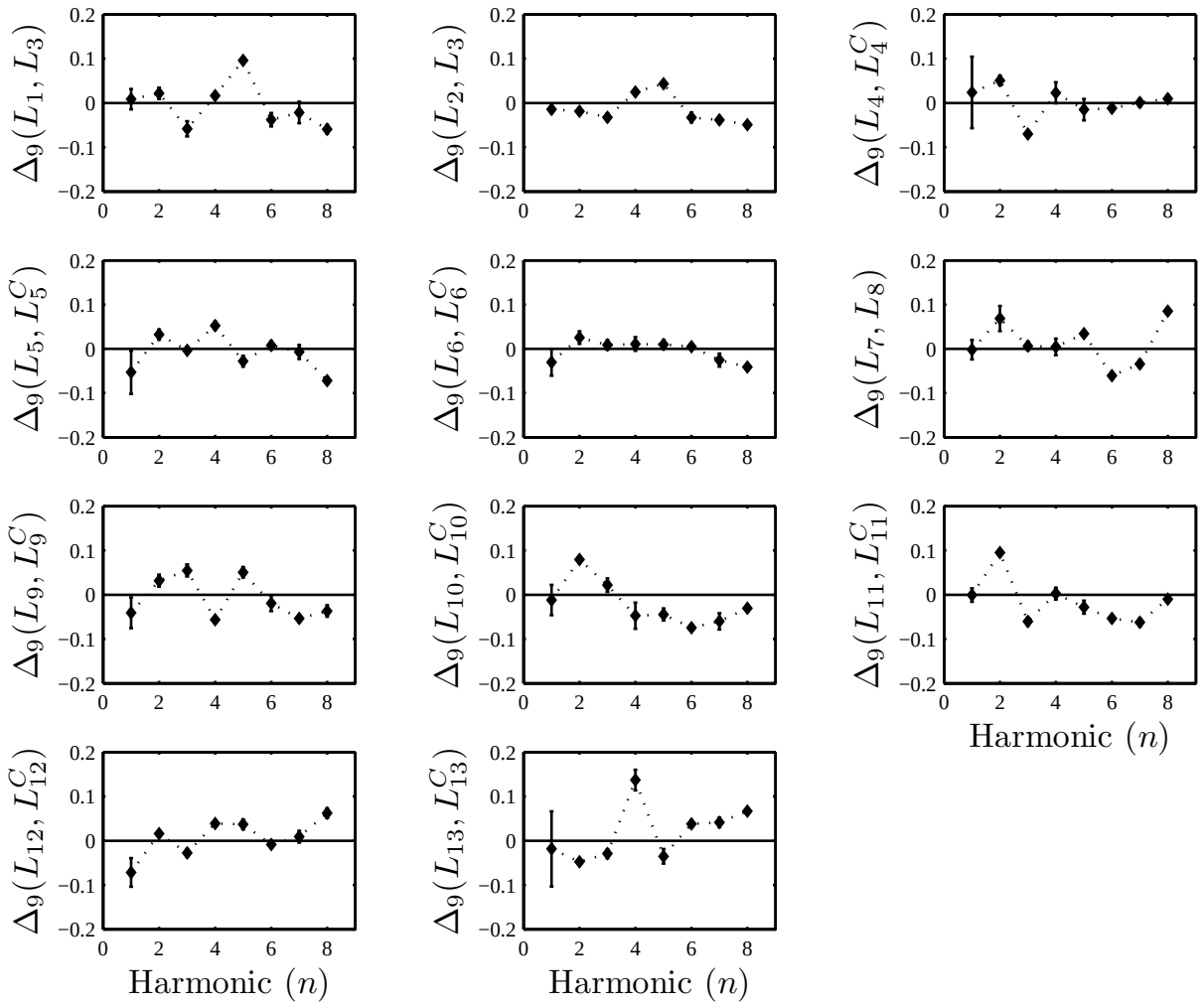

Figure 5-41: Value of the relative difference metric Δ_9 (see Table 5.6) measured for the comparison between distributions of deviation-normalized harmonic amplitudes, for harmonics $n = 1, 2, 3, ..., 8$ and all subset comparisons. A value of Δ_9 for the comparison (L_x, L_y) above zero for harmonic n means that values of A'_n for craters in L_x are larger on average than those in L_y. [CSC on, except for (L_7, L_8); Error bars span the entire range of values computed for (a) SEV for all D, (b) SEV for $D \geq 100$ m, (c) MRV for all D, and (d) MRV for $D \geq 100$ m.]

(for all D only), and targets with sharp edges (for $D \geq 100$, single-estimate values only). In addition, there is a marked difference in the distribution of harmonic amplitudes between populations with rounded rims and [at least partially] sharp rims (see Figures 5-27 and 5-32), where this is significant for five of eight metrics at the 99% level with respect to a Gaussian reference distribution (see Table 5.8).

Lopsidedness: We have said little so far regarding the significance of the first-order harmonic amplitude, A_1. This harmonic is a measure of the extent to which the origin is displaced from the center of the PCRO defined in polar coordinates. Since we have chosen the deviation-centroid as the origin, A_1 is usually very small, and measures the "lopsidedness" of a crater's planimetric shape. The cause of significant symmetry-breaking is unknown, but may arise as a consequence of material heterogeneities in the target or a highly oblique vertical incidence angle. This quantity is the most sensitive to slight changes in the PCRO, as can be seen from the large error bars for $n = 1$ in Figure 5-41, and it is largely for this reason we have not assigned great importance to it. For completeness, however, we report all statistically significant differences for the 11 comparisons. In particular, all of the following subsets contain crater populations that are more lopsided on average (see Figure 5-27): (a) craters with [at least partially] sharp rims (L_{13}^C), (b) craters formed in targets with systematic joints clearly expressed (L_4), craters formed in flat targets (L_5^C), and (d) craters having a paucity of rocks and boulders covering their walls (L_{12}^C).

Modification: There are at least two subset comparisons which carry information about the processes of crater modification: (a) the presence or absence of slides, and (b) large and small fill ratios (F). Earlier we noted in Figure 5-25 that craters with recognizable scree slides on their upper rim slopes and evidence of other mass movements (L_9) are less circular on average than craters not belonging to this group (L_9^C). Figure 5-27 shows that this difference in the distribution of detrended radial deviations (Figure 5-30) is statistically significant. Also noteworthy is that craters having slides (L_9) are significantly more concave (Figure 5-30). By contrast, the comparison between large fill ratios (L_7) and small fill ratios (L_8) produces no statistically significant difference in radial deviations (Figures 5-29 and 5-27), however, craters with large fill ratios are significantly less concave (Figure 5-29).

These results would seem to be at odds with each other unless we consider that processes producing these features may operate on different time-scales. For example, it is well-known that the most significant mass movements and slumps occur in the earliest stage of modification, immediately following excavation (Melosh [1989]). Recall that the population represented by L_9^C (absence of "slides") exhibits the strongest correlations between radial deviation and crater diameter, and among the steepest power-laws connecting these. The set L_9^C may represent an "uncollapsed" population, comparatively unaffected by major slumping in early-stage modification. In cases where this early slumping occurs, this tends to promote departure from circularity and to create concavities. By contrast, if increasing fill ratio F represents the infilling of craters by sediment transport and gradual back-wasting of crater walls, our analysis indicates this does not make craters more or less circular, but tends to smooth-out concavities created by excavation and early-stage slumping.

Neither process appears to significantly affect low-order harmonics: amplitude distributions for $n = 2$ through $n = 4$ are mostly untouched for these comparisons (see Figure 5-27), and the principal harmonic fractions (N_n/N) for $n = 3$ through $n = 5$ are among the closest to parity (see Figures 5-36 through 5-38). Both processes do appear to affect the distribution of *higher*-order harmonics, in agreement with the results of Eppler et al. [1983] for lunar complex craters. Craters with large fill ratios are significantly more octagonal and less hexagonal than craters with small fill ratios. The absence of slides correlates with a significantly larger seventh harmonic amplitude (see Figure 5-30). These obser-

vations would tend to suggest that excavation is more important for determining the low-order harmonic components, while modification tends to affect mostly high-order components.

The largest overlap (73%) calculated for any combination of subsets occurs for L_{13}^C and L_9 (see Figure 5-24). That is, a majority of craters having slides and slumps also have sharp rims along a portion of their circumference. This strongly supports the notion that sharp crater rims are formed by wall slumping. Another observation linking these two groups is found in the comparison of sampled diameters. The number of craters in L_{13} (rounded rims) and L_9^C (no slides) drops off rapidly for $D > 650$ m (see Figure 5-42), where a significant drop occurs in L_9^C also at $D = 330$ m. This is consistent with the view that mass-movements associated with L_9 are an early-stage phenomenon: i.e., transient craters above a critical size D_{slmp} (where 330 m $< D_{\text{slmp}} <$ 650 m) are gravitationally unstable and experience significant slumping. Lending further support to the association between L_9 and L_{13}^C is that members of L_{13}^C (sharp rims) are on average significantly more concave and circular than L_{13} (rounded rims): i.e., recall that L_9^C (no slides) is significantly more concave and circular than L_9 (slides)). These comparisons point to the existence of a "transition population" of small impact craters in the range 100 m $< D <$ 650 m (i.e., above the strength-gravity transition) without wall slumps and sharpened rims – that have not undergone significant early-stage slumping – and whose shapes are therefore primarily determined by excavation. This implies that excavation is responsible for the extraordinarily high fourth-harmonic amplitudes in the L_{13} subset.

Debris targets: Earlier we noted in Figure 5-25 that craters formed in targets marked by rocks and boulders clustering on elevated surfaces (L_{10}) exhibit a very weak relationship between radial deviation and diameter (i.e., a shallow power law indicated by a weak correlation). Figure 5-27 shows that this difference in the distribution of detrended radial deviations is statistically significant. We can moreover see in Figure

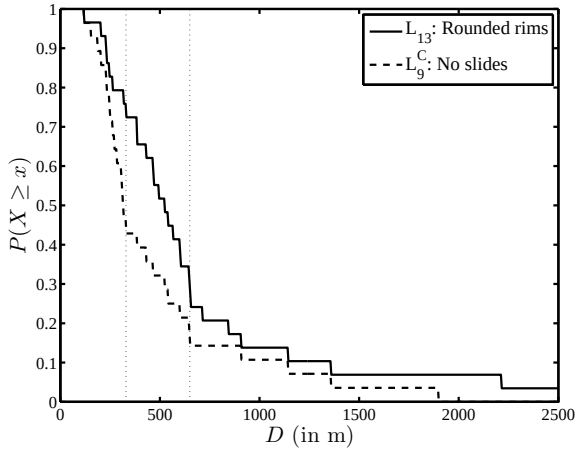

Figure 5-42: Cumulative distributions of diameter for L_{13} (rounded rims) and L_9^C (no slides). The density of sampled diameters drops abruptly at $D \approx 330$ m for L_9^C, and 80% of both sets occur below $D \approx 650$ m, where an inflection marks both curves. $D \approx 650$ m marks the onset diameter for significant rim collapse and slumping. [SEV; CSC on; $D \geq 100$ m]

5-31 that elongations in this subset are significantly larger on average than what is measured for craters not belonging to this group. The distribution of primary harmonics for this group is the steepest of any subset, shown in Figure 5-43. This is expressed in the exceptionally high proportion of triangles occurring in this group (see Figure 5-36) and the exceptionally low proportion of hexagons (see Figure 5-39). In Figure 5-41 we can see that harmonic amplitudes A_2' and A_3' are larger on average for L_{10} with respect to L_{10}^C, and that harmonic amplitudes $n > 3$ are smaller on average. That is, most of the difference in radial deviation is concentrated in the lowest harmonics, and mostly in A_2' (N.B. this is also true for L_{11}: scattered rocks and boulders). This suggests that the radial deviation of craters formed in regolith or debris targets is mostly determined by elongation and hence [possibly] by the vertical impact angle. Craters forming in these targets assume a comparitively oval shape, while craters forming in indurated targets assume a comparatively polygonal shape, where this latter observation is consistent with the experimental results of Fulmer and Roberts [1963].

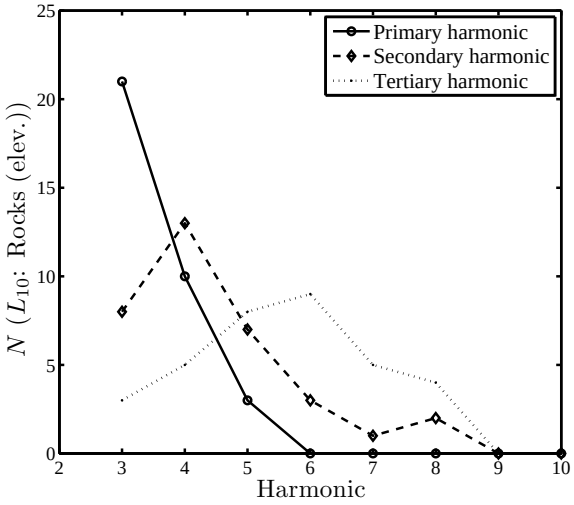

Figure 5-43: Histograms of primary, secondary, tertiary harmonics for subset L_{10}. This subset has the steepest primary harmonic histogram of any considered in this analysis. [SEV; CSC on; all D]

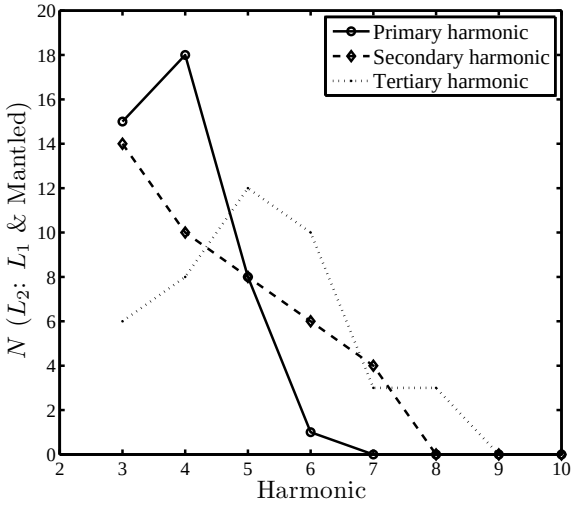

Figure 5-44: Histograms of primary, secondary, tertiary harmonics for subset L_2. [SEV; CSC on; all D]

If the departure from circularity is mostly determined by vertical incidence angle (i.e., highly oblique impacts are more elongated), this may account for the very weak relationship between radial deviation and crater diameter measured for this group. If wind erosion is the primary cause of elongations, then the marked elongation of craters in this group may be the consequence of forming in easily-erodable materials.

Lavas vs. Not-Lavas: It was noted earlier that craters which formed in both kinds of non-lava (L_1 and L_2) are less circular (have larger radial deviations) than craters formed in lavas, and we have since confirmed that this difference, supported by the results from MOC-CTS, is statistically significant (see Figures 5-5, 5-27, 5-33). Also noteworthy is that non-lavas (L_2) are significantly more concave than lavas on average, also in support of conclusions from the MOC-CTS in Section 5.1. That square craters are more numerous in L_2 than lavas is also consistent with results from the previous section.

We note moreover that the fourth and fifth harmonic amplitudes are on average larger in both non-lava subsets (L_1 and L_2) when compared with lavas (L_3), and that all other harmonic amplitudes are smaller for $n > 2$. We shall return to this observation in the next chapter when considering the reasons why radial deviation could be concentrated in these two harmonics. A related result is shown in Figure 5-46, where we have plotted the fraction of primary harmonics that are $n = 3$, $n = 4$, and $n > 4$, for the set of craters formed in lavas and both non-lava groups (I: L_2, II: L_3), for single-estimate values and for all D. (The CSC is not imposed for this analysis because the comparison (L_7, L_8) and others in MOC-FCC (later sections) indicate that low-order shape fractions are unchanged by modification; the result is unchanged if the CSC is imposed.) We find that triangles are far more numerous in lavas, and all higher principal harmonics are less numerous. As we will see in the next section, this result is supported by the analyses of MOC-FCC, and will be addressed in some detail in the following chapter. (This is also apparent in Figure 5-36, where the lava/non-lava comparison plots away from the cluster where most pairings reside. (See also Figures 5-44 and 5-45 for the histograms of primary, secondary, and tertiary harmonics of L_2 and L_3.)

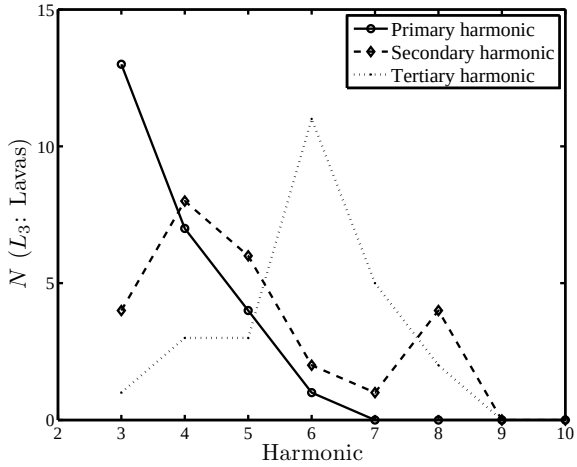

Figure 5-45: Histograms of primary, secondary, tertiary harmonics for subset L_3. [SEV; CSC on; all D]

5.4 Harmonic phase angles and the obliquity of Mars

In this section we transition from completing the analysis of HiRISE-FCC to beginning the analysis of the MOC Fresh Crater Catalog (MOC-FCC). We will do this in the context of discussing distributions of harmonic phase angles, ϕ_n, and how these and other morphometric quantities can be affected by pixelation effects in the comparatively low resolutions at which MOC imagery is captured. Through the course of this analysis, we will find a significant lateral (east-west) bias in the elongation angle (ϕ_E) which may tell us something about the past obliquity of Mars.

Whereas HiRISE images are captured at 25 cm/pixel or 50 cm/pixel resolution, MOC Narrow-Angle images in the MOC-FCC were captured at a range of resolutions, from approximately 1.5 m/pixel to as much as 10 m/pixel. Of the 840 impact craters in the MOC-FCC, 26% are spanned by 20 pixels or fewer, and fully 65% are spanned by 50 pixels or fewer. For the remainder of this chapter, we define the "pixelated diameter,"[9] $D_{\rm pix}$, as the approximate number of pixels spanning the diameter of an im-

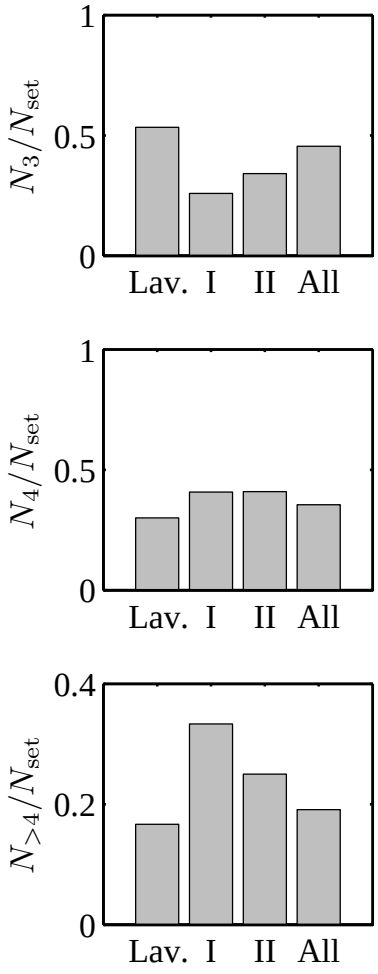

Figure 5-46: Fraction of impact craters in each of four sets with primary harmonic n (i.e., $N_n/N_{\rm set}$) for $n = 3$, $n = 4$, and $n > 4$: Lav. = "Lavas" (i.e., material class 4), I = "Not Lavas I,"(i.e., L_1: material classes 1, 2 and 3), and II = "Not Lavas II" (i.e., L_2: material classes 1,2,3, and 6), and All = the entire HiRISE-FCC. Lavas have more triangles than do the other sets, and fewer higher-order shapes. [SEV; CSC off; all D]

[9] To avoid the confusion caused by "pixel diameter".

pact crater. In the HiRISE-FCC, all craters have $D_{\rm pix} > 50$, and less than 2% have $D_{\rm pix} < 150$. In order to assess the consequences of pixelation effects that become important at low resolutions (MOC-FCC), we have downsampled (using bicubic interpolation) all 110 impact craters in the HiRISE-FCC to $D_{\rm pix} = 20$ and $D_{\rm pix} = 50$, and obtained their PCROs as well as the values of all morphometric quantities.[10]

An example of this downsampling experiment is shown in Figure 5-47 for a comparatively circular impact crater ($D_{\rm pix} = 20$). One of the interesting consequences that we can notice at once is related to the low-resolution effects discussed at the end of Section 5.1: that edges occurring at vertical and horizontal orientations as well as $\pm 45°$ are accentuated. The result in this case is to transform a nearly circular shape into an apparently octagonal one. We can notice this effect when probing consequences for the eighth harmonic, where the distribution of the eighth harmonic phase angles (ϕ_8) is shown in Figure 5-48. Both low-resolution estimates indicate a very strong bias and departure from uniformity, which is absent from the full-resolution estimate. No very obvious differences are evident from comparing the distributions of ϕ_4 (Figure 5-49).

A very marked change also occurs in the distribution of ϕ_2 shown in Figure(5-50), where we can see a strong peak centered at $\phi_2 = 0$ emerge as the resolution improves. For the remainder of this section, we will refer to this as the "lateral elogation bias" (LEB), where this indicates the tendency for elongation angle ϕ_E to align with the east-west direction. (Recall from Section 5.2 that the "elongation angle" (ϕ_E) is the azimuth of the major axis of elongation (i.e., $\phi_2 + 90°$) measured with respect to North (i.e., collapsed onto the domain $(-90°, 90°]$).) The peak corresponding to this tendency is evident at both smaller solutions, but does not begin to dominate until at least $D_{\rm pix} = 50$. The correlation between the absolute elongation angle ($|\phi_E|$) measured from the full-resolution images and

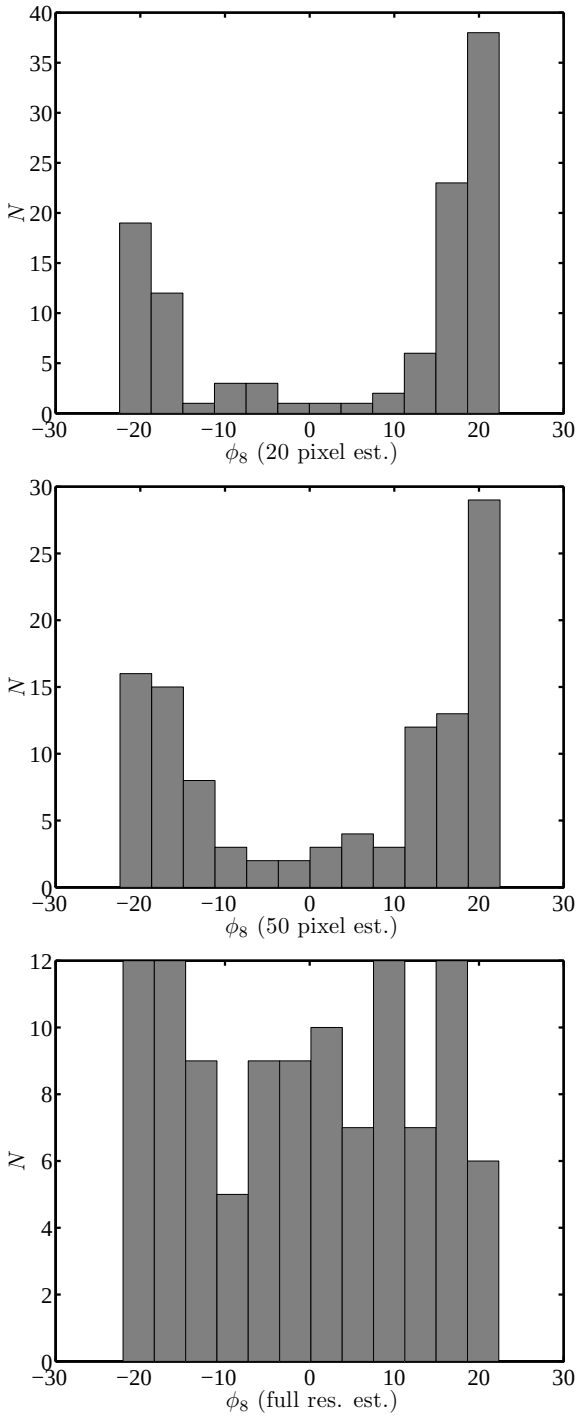

Figure 5-48: TOP: Histogram of eighth harmonic phase angle (ϕ_8) for the 20-pixel diameter estimate, showing the clear bias introduced by the pixel grid, which tends to mold circular craters into an octagonal shape. MIDDLE: Histogram of ϕ_8 for the 50-pixel diameter estimate. BOTTOM: Histogram of ϕ_8 for the full-resolution estimate, where this bias is not evident.

[10]Rim traces from low-resolution images were obtained in the absence of knowledge about the appearance of the full-resolution image, which might otherwise have influenced the interpretation.

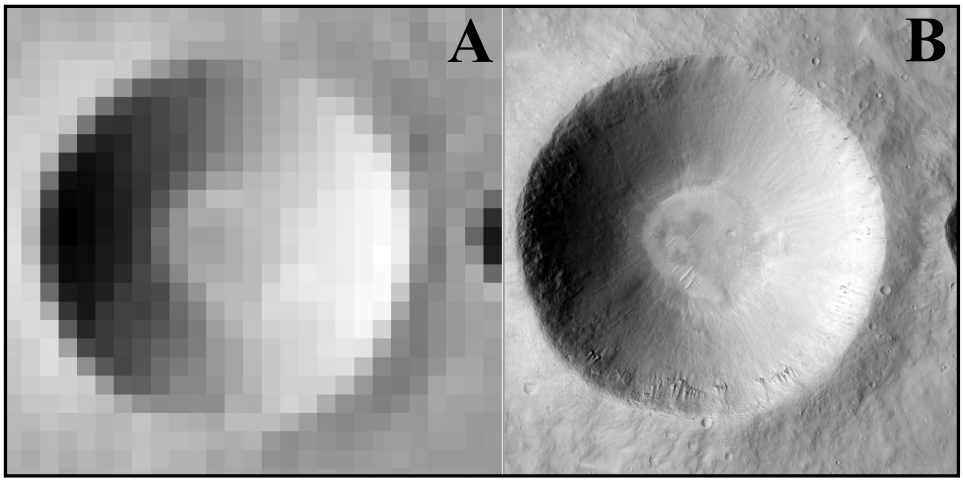

Figure 5-47: Example of downsampling by means of bicubic interpolation (A) of the comparatively circular impact crater shown at the right in (B). We can see readily the effect of pixelation, which transforms a circular crater into a comparatively octagonal shape. This effect is clearly visible in the distribution of eighth-harmonic phase angles (ϕ_8).

at low-resolutions ($D_{\rm pix} = 20$ and $D_{\rm pix} = 50$) are shown in Figure 5-51, where we can see that, while positive, the correlation is poor for $D_{\rm pix} = 20$ ($r_P \approx 0.5$) and somewhat improved for $D_{\rm pix} = 50$ ($r_P \approx 0.7$).

We must bear in mind that the Fourier shape harmonics are not completely independent of one another, and so it is important to search for the influence of the LEB on the other harmonics. In Figure 5-52 we have plotted histograms of the phase angles for all full-resolution estimates in the HiRISE-FCC for harmonics $n = 2, 3, 4, 5, 6,$ and 8. Also reported is the quantity Δ_U, the Euclidean distance of each histogram from an exactly uniform distribution (EUD) – i.e., having the same number of counts in each bin – with respect to the mean of Euclidean distances from the EUD measured for 10,000 histograms (with identical binning) sampled from a uniform distribution, and expressed as a fraction of the standard deviation σ of these distances. For example, $\Delta_U = 3\sigma$ indicates that the histogram in question exhibits a difference with respect to the EUD (a perfectly flat histogram) that is extremely unlikely to occur by chance alone if the measured quantity is uniformly distributed. We find differences exceeding the 2σ level only in the case of $n = 2$ (the lateral elongation bias (LEB)), and $n = 4$, which is therefore possibly also influenced by the LEB.

In Figure 5-53 we have repeated the same plots as shown in Figure 5-52 for all impact craters in the MOC-FCC captured at low resolution (i.e., for which $D_{\rm pix} \leq 50$). Here, ϕ_n is plotted in units of degrees with respect to "Up": the direction to the top of each image, which in the vast majority of cases deviates from North by $\pm 5°$. (While the HiRISE-FCC PCROs were measured from map-projected images aligned with North, MOC-FCC images are map-projected but not north-aligned; for now, we are mainly interested to note effects that occur within the image frame (consequences of pixelation), and so this correction has not been applied.) We can see from these histograms that the expected pattern in ϕ_8 shown in Figure 5-48 is clearly evident. Significant deviations from a uniform distribution also occur for $n = 4$ and $n = 2$. The asymmetry in ϕ_4 is not understood, but disappears for higher resolutions as we will see shortly. While the pattern in ϕ_8 accords with expectations, that the LEB is clearly expressed at low-resolutions in the MOC-FCC and that ϕ_4 does not exhibit the same pattern observed in Figure 5-49 are signs that downsam-

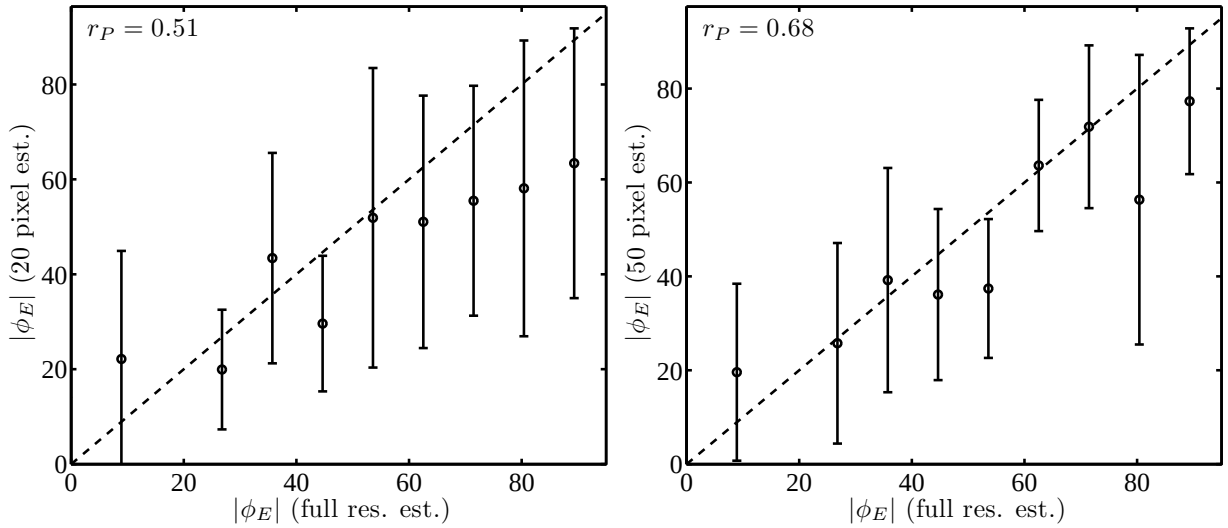

Figure 5-51: Correlation between [binned, averaged] estimates of $|\phi_E|$ based on downsampled images (LEFT: 20-pixel diameter; RIGHT: 50-pixel diameter) and full-resolution images (x-axis). Errorbars span one standard deviation, and r_P is the Pearson correlation coefficient for this comparison.

pling with bicubic interpolation does not mimic perfectly the distortions (to PCROs and derived morphometric parameters) that derive from low-resolution MOC narrow-angle images. That is, these results appear to show that measurements derived from the MOC-FCC are somewhat better than what our comparisons between low- and high-resolution HiRISE-FCC estimates indicate.

In Figure 5-54 we have produced the same histograms for all impact craters in the MOC-FCC captured at comparitively high resolution (i.e., for which $D_{\text{pix}} > 50$). Of the significant departures ($> 3\sigma$) from a uniform distribution seen in Figure 5-54, only $n = 2$ remains pronounced and its width has narrowed (N.B. a $> 2\sigma$ deviation occurs in $n = 5$ but this is localized in few bins and does not correlate to a larger pattern). Significantly, the marked pattern in $n = 8$ has vanished, along with the left-right asymmetry for $n = 4$. It should be noted that peaks in the vicinity of $\pm 45°$ for ϕ_4 were also observed[11] in the case of HiRISE-FCC, and may here also reflect contamination by the LEB. In addition to constraining the resolutions at which significant distortions occur, these analyses have shown that the LEB occurs in the full-resolution estimates of ϕ_2 and potentially ϕ_4 in HiRISE-FCC as well as low-resolution estimates of MOC-FCC (ϕ_2) and high-resolution estimates (ϕ_2 and possibly ϕ_4). A question remains, therefore, about what is causing the anomalous distribution in ϕ_2.

Since the measurement of PCROs in both data sets frequently relies upon the interpretation of gradients and sharp edges in surface radiance, we must consider the possibility that the east-west Lateral Elongation Bias is caused by illumination effects. In order to check for this possibility we can compare the distribution of subsolar azimuths (θ_{sun}) in all of the images from which PCROs were measured, to the computed elongation angle of impact craters in those images. (N.B. The subsolar azimuth is the direction to the subsolar point: the point on the planet's surface directly "beneath" the sun, and is parallel to the sun's rays in projection.) These comparisons are made in Figure 5-55 for all craters in HiRISE-FCC, in Figure 5-56 for all craters in MOC-FCC, and in Figure 5-57 for all craters in MOC-FCC for which $D_{\text{pix}} > 75$ (i.e., well outside the range of resolutions expected to introduce signficant distortions). In all cases, the subsolar azimuth

[11] N.B. This pattern corresponds to the walls of a square tending to align with north-south or east-west: i.e., with lines of latitude or longitude.

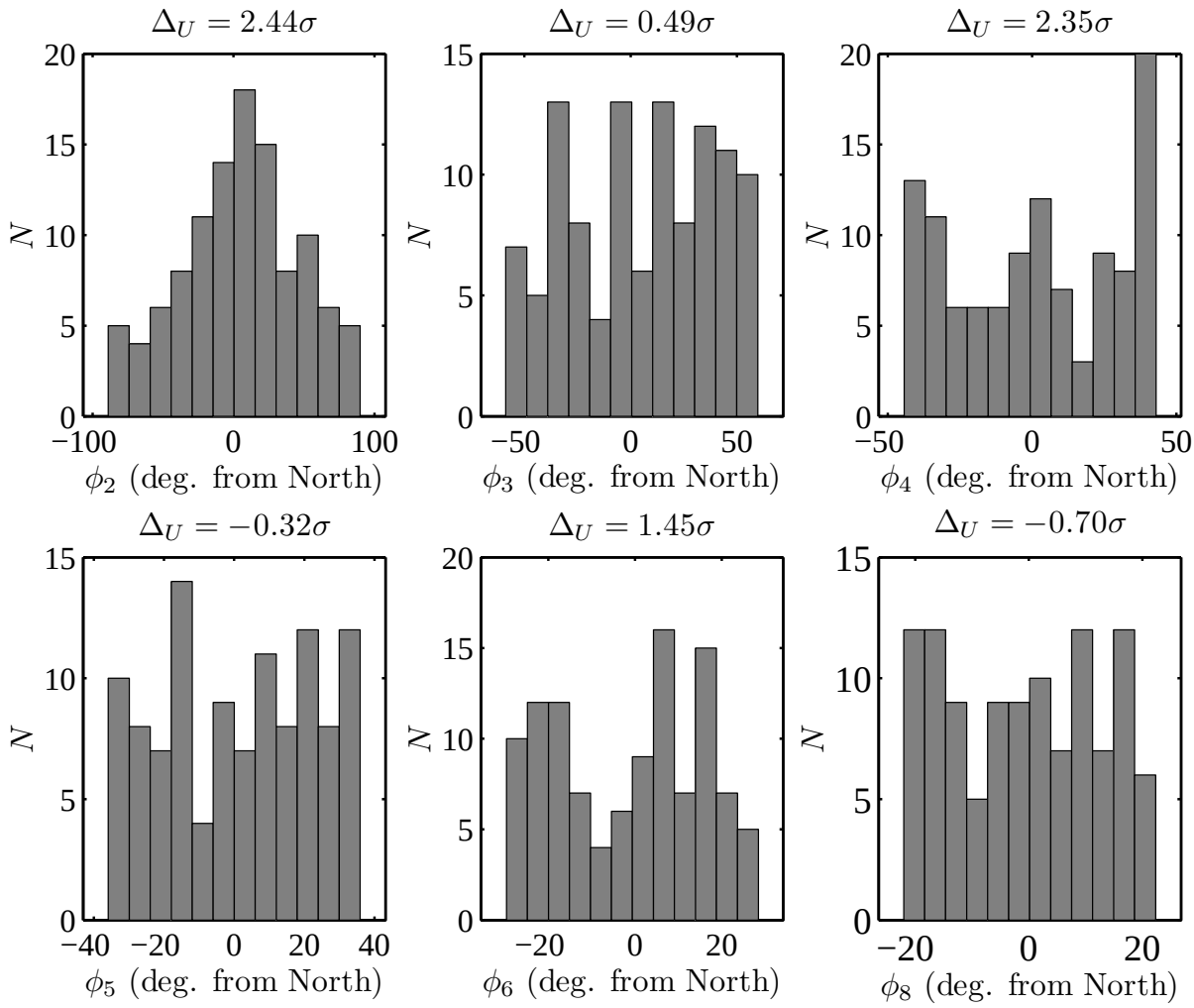

Figure 5-52: Histograms of phase angles for harmonics $n = 2, 3, 4, 5, 6$, and 8, for all craters in the HiRISE-FCC. The quantity Δ_U is a measure of the Euclidean distance of each histogram from an exactly uniform distribution (EUD) – i.e., having the same number of counts in each bin – with respect to the mean of the Euclidean distances from the EUD measured for 10,000 histograms (with identical binning) sampled from a uniform distribution, and expressed as a fraction of the standard deviation σ of these distances. Only harmonics $n = 2$ and $n = 4$ are significantly different from uniform, suggesting that both are influenced by the LEB.

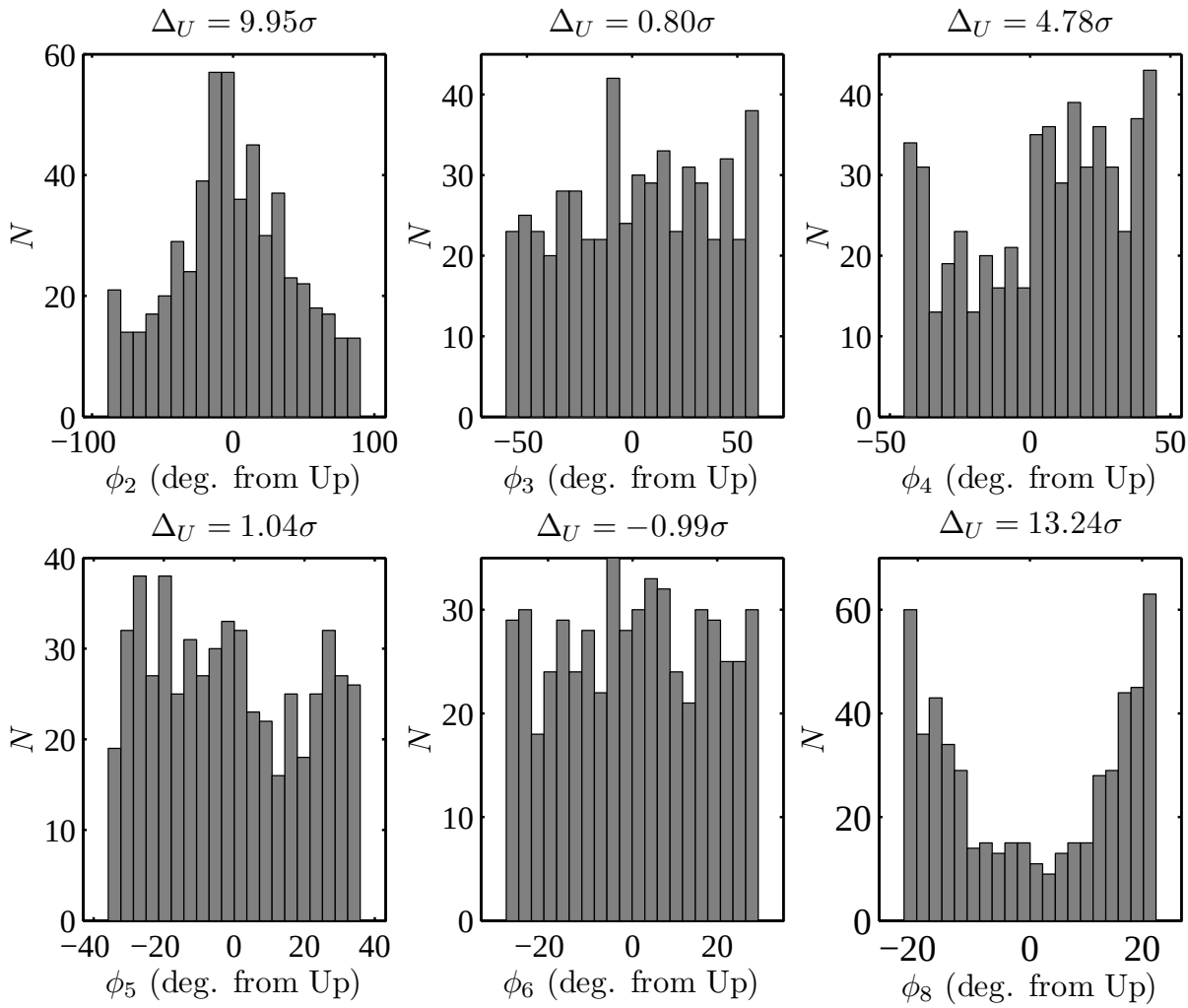

Figure 5-53: Histograms of phase angles for harmonics $n = 2, 3, 4, 5, 6$, and 8, for all craters in the MOC-FCC with $D_{\rm pix} \leq 50$. The 2nd, 4th and 8th harmonics are signficantly different from uniform, where the 8th indicates the strong influence of pixelation effects. (See text and the caption of Figure 5-52 for a definition of Δ_U.) N.B. Units are degrees w.r.t. the up direction in the image frame, which is displaced from North by $\approx 5^\circ$ degrees in the vast majority of cases.

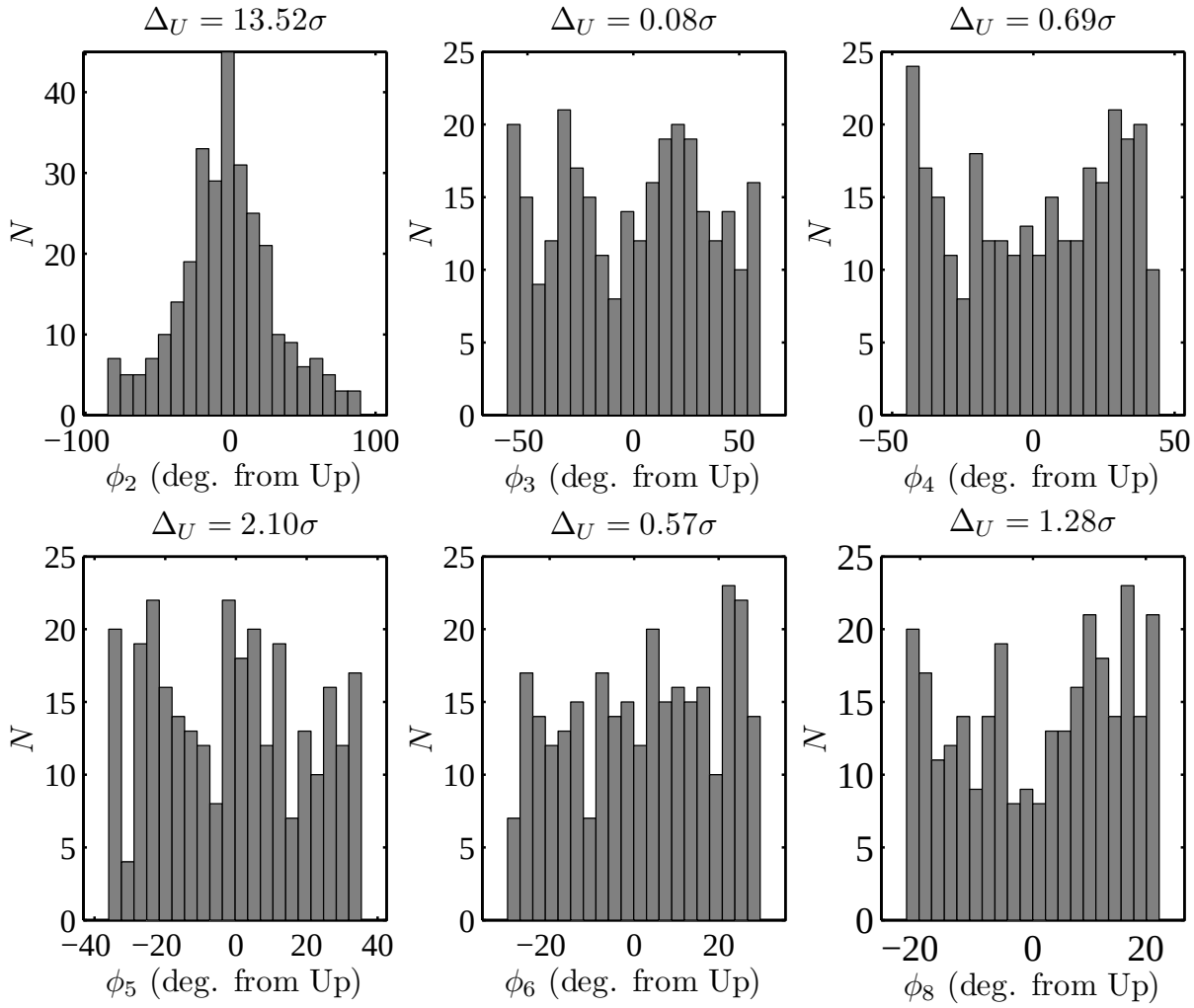

Figure 5-54: Histograms of phase angles for harmonics $n = 2, 3, 4, 5, 6$, and 8, for all craters in the MOC-FCC with $D_{\text{pix}} > 50$. The 2nd harmonic is farthest from being uniformly distributed, although the 5th indicates a $> 2\sigma$ departure. The fourth harmonic exhibits peaks near $\pm 45°$ that may reflect the LEB, as in HiRISE-FCC. (See text and the caption of Figure 5-52 for a definition of Δ_U.) N.B. Units are degrees w.r.t. the up direction in the image frame, which is displaced from North by ≈ 5 degrees in the vast majority of cases.

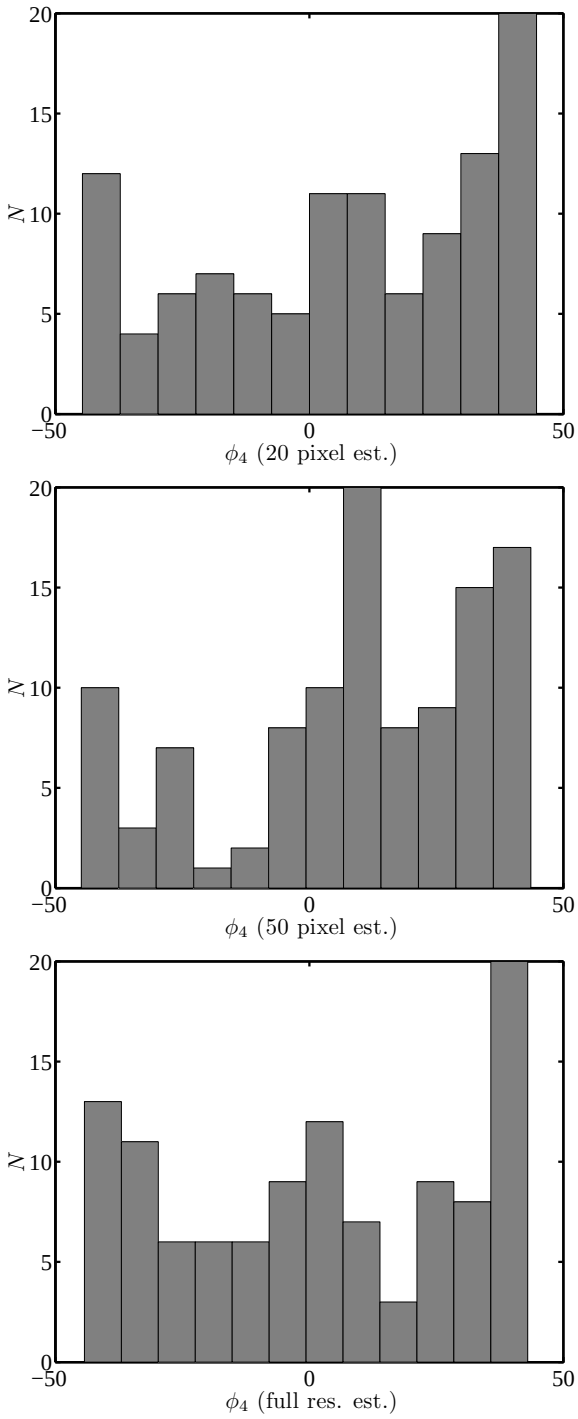

Figure 5-49: TOP: Histogram of fourth harmonic phase angle (ϕ_4) for the 20-pixel diameter estimate. MIDDLE: Histogram of ϕ_4 for the 50-pixel diameter estimate. BOTTOM: Histogram of ϕ_4 for the full-resolution estimate.

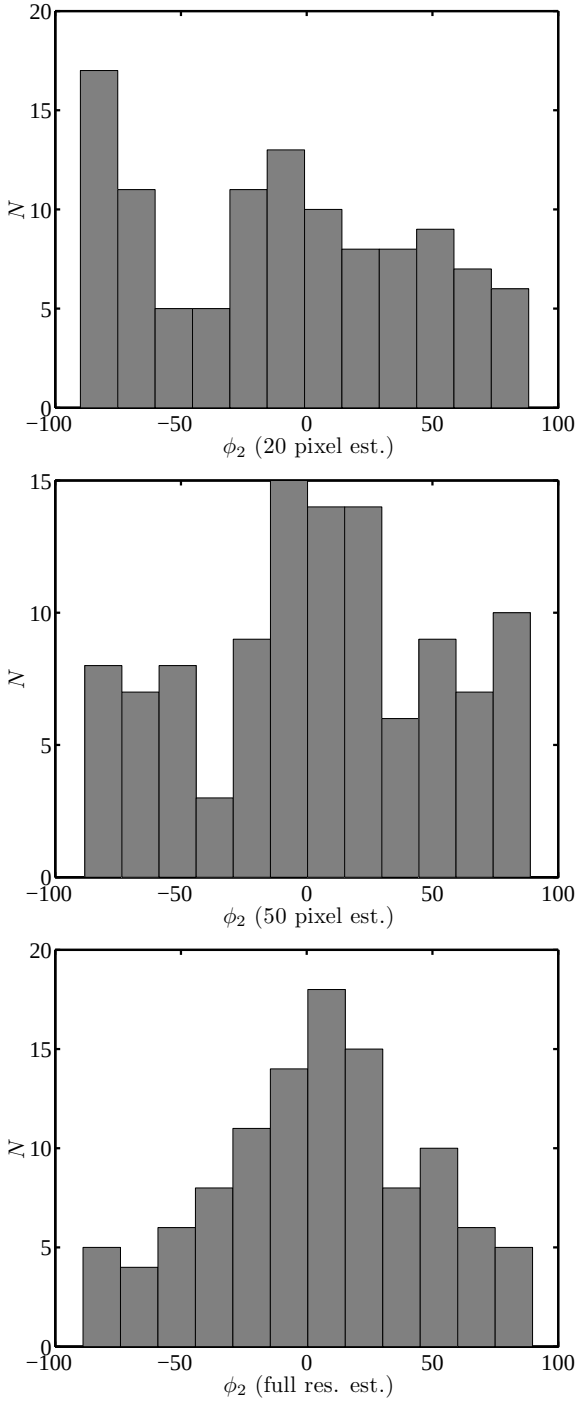

Figure 5-50: TOP: Histogram of second harmonic phase angle (ϕ_2) for the 20-pixel diameter estimate, indicating a clear bias toward small values. MIDDLE: Histogram of ϕ_2 for the 50-pixel diameter estimate. BOTTOM: Histogram of ϕ_2 for the full-resolution estimate.

has been mapped into the domain $(-180°, 180°]$ (degrees from North), and then *folded* into the domain $(-90°, 90°]$ so that it can be compared with the elongation angle (N.B. the "folded" subsolar azimuth is $\phi'_{\rm sun}$). That is, if the subsolar point is located in a direction 150° from North, this has been mapped to $150° - 180° = -30°$ from North: the orientation of any bias in elongation caused by illumination. That none of these histograms resemble one another closely is a strong indication that the LEB is not the consequence of this effect.

If resolution and illumination effects are not the source of the LEB, then it is likely this observation indicates a true bias in the orientation of major-axis elongation (ϕ_E). An intriguing and plausible explanation is that ϕ_E is a reflection of horizontal impact angle for the vast majority of impact craters, rather than just the much smaller population of highly elliptical craters. It has long been known that highly oblique impacts produce elongated craters (Gault and Wedekind [1978]), and recent experiments have shown that an incidence angle[12] of only 10° can produce a measurable asymmetry in laboratory-scale strength-dominated hypervelocity impacts (Wallis et al. [2005]). Because there is no reason to expect horizontal impact angle to exhibit an asymmetry with respect to east-west, we have plotted the *absolute* elongation angle with narrower binning (in absolute degrees from North). Figure 5-58 shows a histogram of the absolute elongation angle, $|\phi_E|$ for all craters in the HiRISE-FCC, and Figures 5-59 we show the same plot for all craters in the MOC-FCC as well as only those having $D_{\rm pix} > 75$. We find similar results when comparing the whole of MOC-FCC to the whole of HiRISE-FCC (a broad distribution), and isolated peaks or steps emerging for the larger-diameter population of MOC-FCC with $D_{\rm pix} > 75$. These occur at $|\phi_E| \approx 28°$, 53°, 68°, and 86°. Although more ambiguous, tall columns occur in the HiRISE-FCC distribution at $|\phi_E| \approx 29°$, 45°, 71°, and 87°.

We saw earlier that the distribution of ϕ_2 is broader for the low-resolution estimates, which

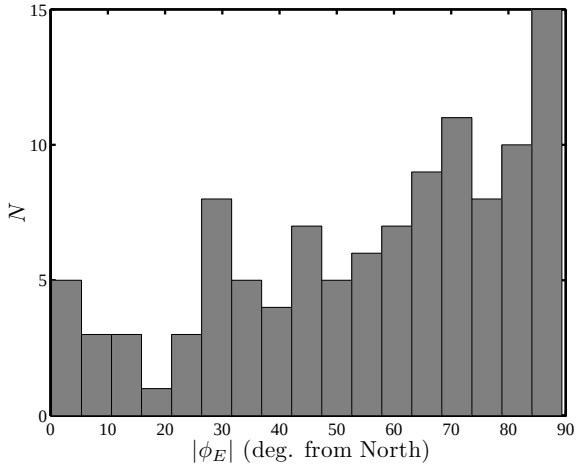

Figure 5-58: Histogram of absolute elongation angle ($|\phi_E|$) for all craters in the HiRISE-FCC.

corresponds to a population of smaller impact craters. The distribution of $|\phi_E|$ for the whole of HiRISE-FCC is also broader than what is shown in Figure 5-59 for the large-diameter (and higher-resolution) population ($D_{\rm pix} > 75$). This latter result suggests that the spreading of the distribution is not merely a consequence of resolution effects. Rather, this suggests that small craters may be somewhat less prone to preserve evidence of horizontal impact direction than larger craters. A horizontal impact angle of 90° from North is the most probable value of the horizontal impact angle assuming that a projectile's orbit lies in the ecliptic plane, while also averaging over all spin-axis obliquities and times of the year. Apart from this, it is reasonable to expect that peaks in the distribution of major axis elongation should correspond to obliquities that have occurred with uncommon frequency over the time that this crater population formed. These most-common or "modal" obliquities do not necessarily correspond to the quasi-stable mean values about which obliquity oscillates, but instead to the bounds of these oscillations.[13] Numerical integrations of Mars' orbital parameters for the last 10 million years indicate that obliq-

[12] i.e., with respect to a surface normal.

[13] To see this, note that the most-common values in a histogram of $\sin(x)$ for $x \in [0, 2\pi]$ occur in the vicinity of ± 1.

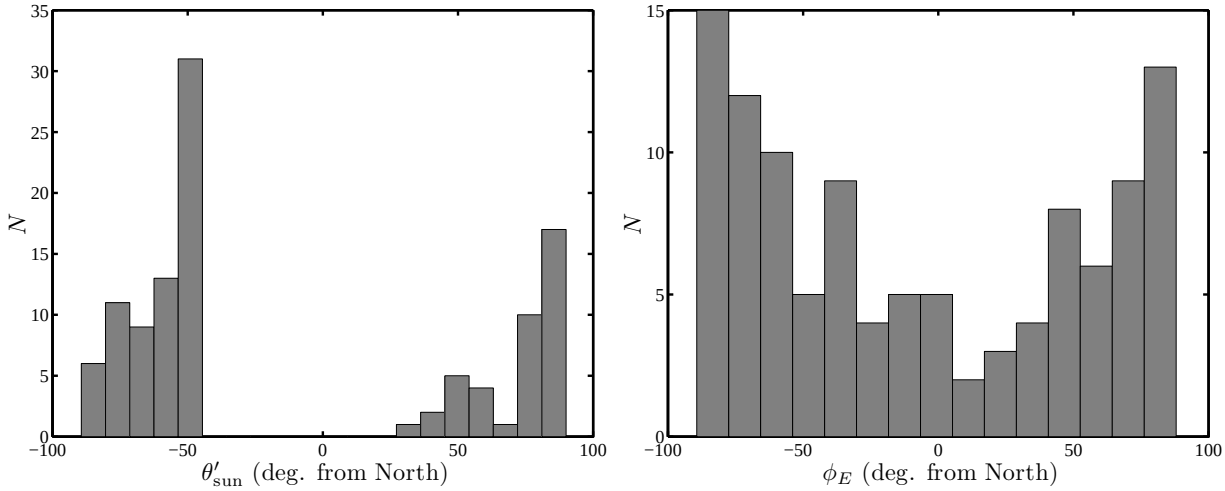

Figure 5-55: LEFT: Histogram of θ'_{sun}, the folded sub-solar azimuth, for all craters in the HiRISE-FCC. Subsolar azimuth is the direction to the subsolar point, and the folded subsolar aziumth is mapped onto the domain $(-90°, 90°]$, measured in degrees from North, so that it may be compared with the elongation angle ϕ_E (RIGHT). The absence of a strong semblance confirms that measured elongations are not due to shadow and illumination effects.

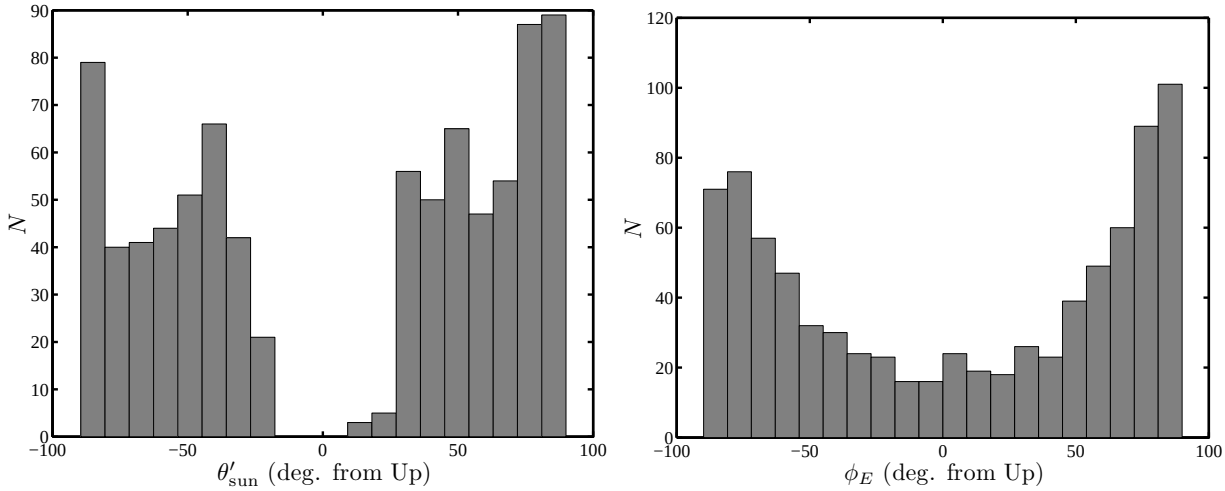

Figure 5-56: LEFT: Histogram of θ'_{sun}, the folded sub-solar azimuth, for all craters in the MOC-FCC. Subsolar azimuth is the direction to the subsolar point, and the folded subsolar aziumth is mapped onto the domain $(-90°, 90°]$, measured in degrees from Up (direction to the top of images), so that it may be compared with the elongation angle ϕ_E (RIGHT). The absence of a strong semblance confirms that measured elongations are not due to shadow and illumination effects.

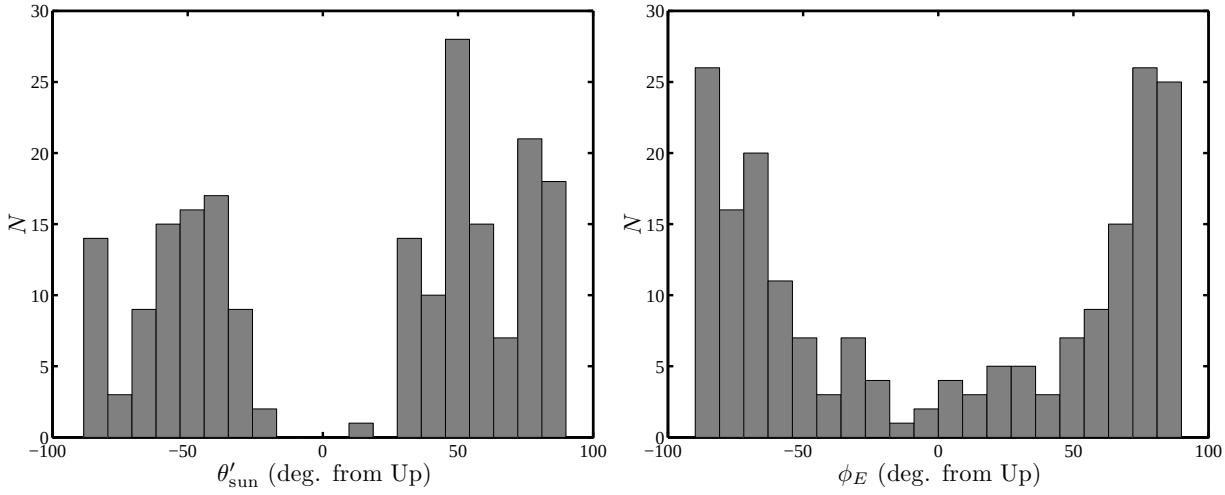

Figure 5-57: LEFT: Histogram of $\theta'_{\rm sun}$, the folded sub-solar azimuth, for all craters in the MOC-FCC with $D_{\rm pix} > 75$. Subsolar azimuth is the direction to the subsolar point, and the folded sub-solar aziumth is mapped onto the domain $(-90°, 90°]$, measured in degrees from Up (direction to the top of images), so that it may be compared with the elongation angle ϕ_E (RIGHT). The absence of a strong semblance confirms that measured elongations are not due to shadow and illumination effects.

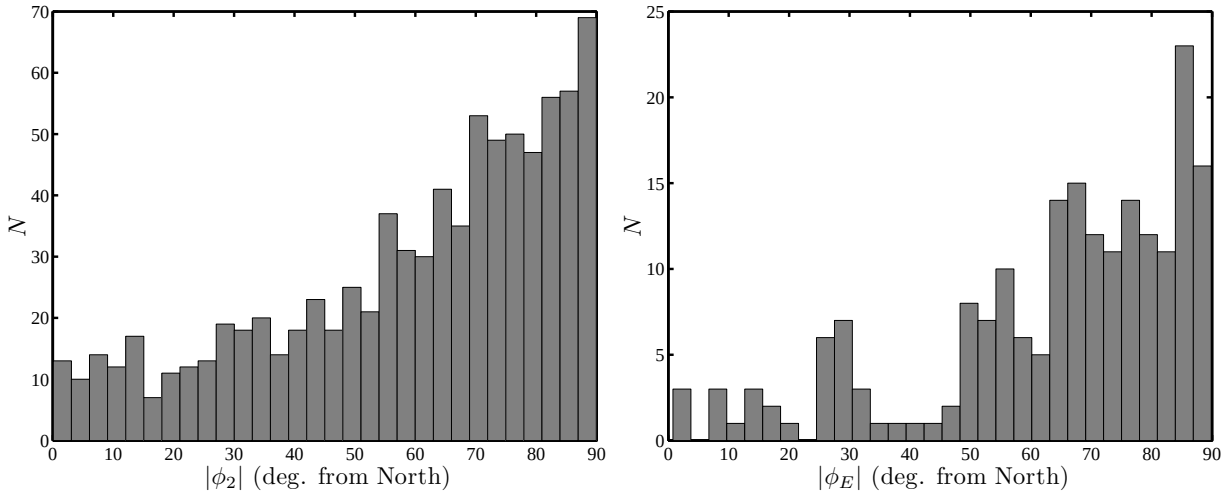

Figure 5-59: LEFT: Histogram of absolute elongation angle ($|\phi_E|$) for all craters in the MOC-FCC; RIGHT: Histogram of $|\phi_E|$ for $D_{\rm pix} > 75$, revealing significant peaks which may correspond to comparitively frequent spin-axis obliquities. [CSC off; all D]

uity occurs in the range from $\approx 10^\circ$ to $\approx 49^\circ$ (Touma and Wisdom [1993]), while other work suggests that the maximum is 60° on larger timescales(Lasker and Robutel [1993]). In all plots of $|\phi_E|$ we find a peak near 90° as expected. The peaks in Figure 5-59 correspond to obliquities of: 62°, 37°, and 22°, which accord with the range of theoretical estimates.

It should be mentioned that polar wander must also be considered as a mechanism that may affect the global distribution of horizontal impact azimuths. However, most workers agree that polar wander is unlikely to have produced major shifts in pole position since the formation of Tharsis and the crustal dichotomy early in Mars' history (Melosh [1980], Willemann [1984], Grimm and Solomon [1986], Zuber and Smith [1997], Roberts and Zhong [2007]). The fresh craters in HiRISE-FCC and MOC-FCC are of course highly unlikely to have formed in that era.

Finally, it should be mentioned that the LEB may be the result of wind-erosion, expected to operate in a predominantly east-west direction. This is likely to be more important for heavily modified crater populations, and especialy those nearest to the equator. That our catalogs are comprised of fresh craters with a global distribution suggests that this is not likely to be the only source of the elongations in our sample. This hypothesis might be tested by measuring the elongations of highly modified populations to determine whether the LEB vanishes or becomes more pronounced. For the moment, it must be acknowledged that an aeolian origin for the LEB is a plausible alternative explanation.

5.5 MOC Fresh Crater Catalog: Analyses

Before reporting results for the MOC-FCC in full, we first complete the downsampling experiment to estimate the effects of measuring PCROs and derived morphometric parameters from low-resolution images. In the last section we explored the consequences for harmonic phase angles, concluding that at least the second, fourth, and eighth harmonics were dramatically affected by the pixel grid. We turn now briefly to estimating the effects upon harmonic amplitudes as well as radial deviation.

The correlation between the radius-normalized standard radial deviations measured from the full resolution images and at low-resolutions ($D_{\rm pix} = 20$ and $D_{\rm pix} = 50$) are shown in Figure 5-60, where a strong correlation ($r_P = 0.85$) is measured for $D_{\rm pix} = 50$, and a weaker correlation for $D_{\rm pix} = 20$ ($r_P = 0.67$). The dashed line in these figures corresponds to equality between estimates ($y = x$). It is worth noting that the low-resolution estimates tend to underestimate radial deviations, and by a greater amount at lower resolutions. Without measuring this relationship for many $D_{\rm pix}$ (a temporally-expensive chore), it is unfortunately impossible to derive a relationship for estimating true radial deviations from estimates at a range of resolutions, in terms of a systematic offset. We have repeated this exercise for the radius-normalized maximum radial deviation (ΔR^*) in Figure 5-61, which indicates a somewhat less-dramatic improvement at higher resolution. Histograms of the difference between estimates of σ_R^* are also shown in Figure 5-62 for both resolutions.

We have computed correlations for estimates of the first six deviation-normalized harmonic amplitudes in Figure 5-63 for $D_{\rm pix} = 20$ and in Figure 5-64 for $D_{\rm pix} = 50$. The lower-resolution result ($D_{\rm pix} = 20$) exhibits a very weak correlation to full-resolution estimates, where this improves dramatically at large values of σ_R^* (also shown). Higher-resolution estimates ($D_{\rm pix} = 50$) are substantially better, although still unremarkable except at large σ_R^*. It is important to bear in mind that although the correlation is dismal for A_2' at $D_{\rm pix} = 20$ and unimpressive at $D_{\rm pix} = 50$ (in keeping with the profound distortion of this harmonic noted earlier in histograms of ϕ_2) we did not witness a significant deterioration in the LEB at low-resolution estimates of ϕ_2 in MOC-FCC results, indicating that our bicubic downsampling experiment introduces distortions that do not occur (or which are not as severe) at low resolution in the MOC-FCC images. The mean and standard deviation of differences between full- and low-resolution esti-

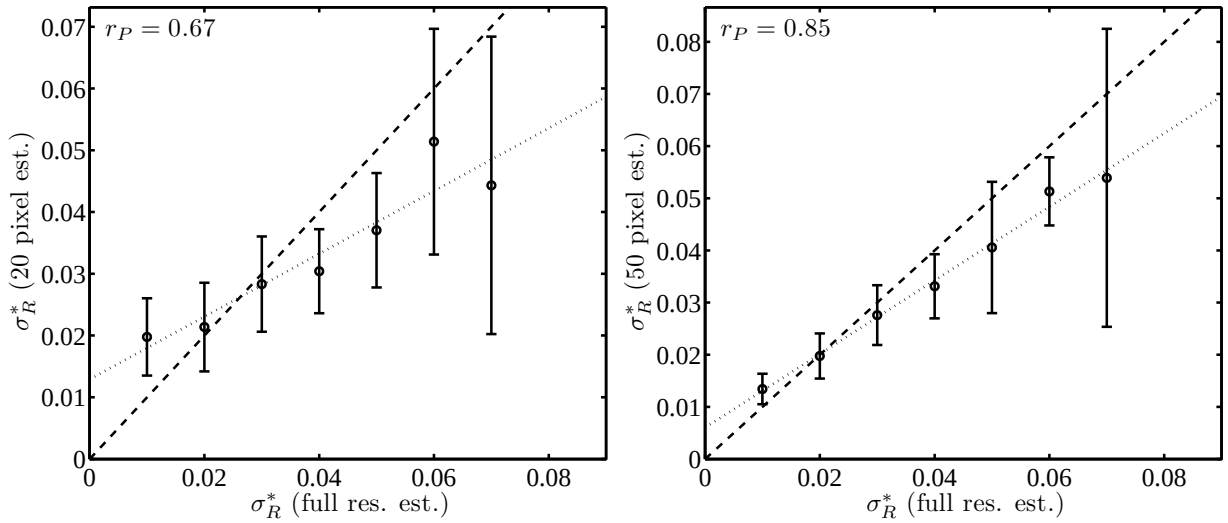

Figure 5-60: Correlation between [binned, averaged] estimates of σ_R^* based on downsampled images (LEFT: 20-pixel diameter; RIGHT: 50-pixel diameter) and full-resolution images (x-axis). Errorbars span one standard deviation, and r_P is the Pearson correlation coefficient for this comparison. The dashed line corresponds to equality of estimates.

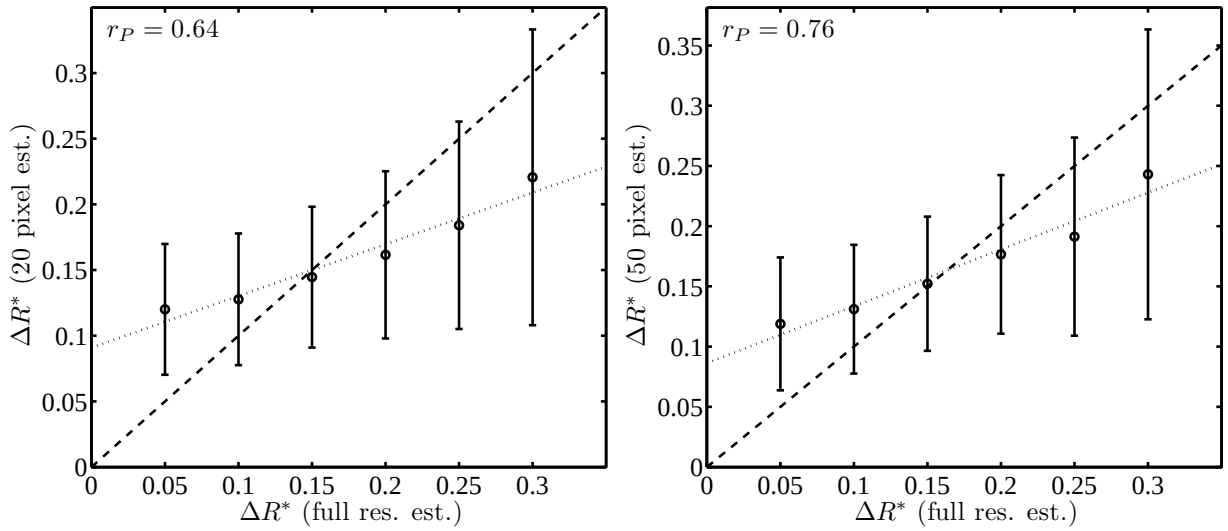

Figure 5-61: Correlation between [binned, averaged] estimates of ΔR^* based on downsampled images (LEFT: 20-pixel diameter; RIGHT: 50-pixel diameter) and full-resolution images (x-axis). Errorbars span one standard deviation, and r_P is the Pearson correlation coefficient for this comparison. The dashed line corresponds to equality of estimates.

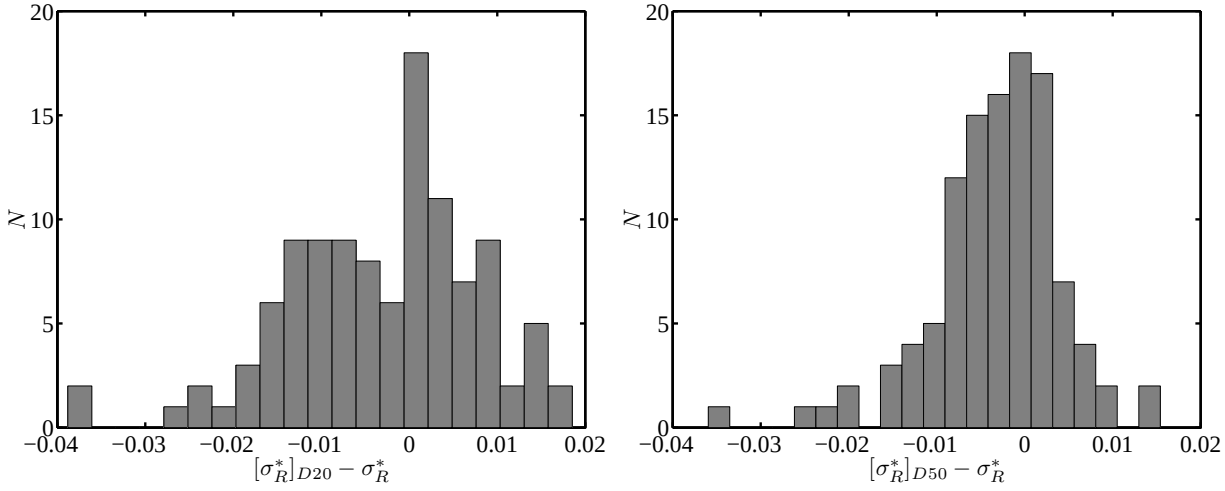

Figure 5-62: Histogram of difference between estimates of σ_R^* based on downsampled images (LEFT: 20-pixel diameter; RIGHT: 50-pixel diameter) and full-resolution images.

mates of radius-normalized radial deviations and deviation-normalized harmonic amplitudes are reported in Appendix Tables C.5 for $D_{\rm pix} = 20$ and C.6 for $D_{\rm pix} = 50$.

Finally, in Figure 5-65 we have plotted the percentage agreement between estimates of principal, secondary, and tertiary harmonics derived from low- and full-resolution images, as a function of the lower bound on σ_R^*. Agreement is $\approx 50\%$ for $D_{\rm pix} = 20$ and all values of σ_R^*, rising to $\approx 60\%$ for $\sigma_R^* > 0.04$. Matters are significantly improved for $D_{\rm pix} = 50$, where agreement is $\approx 57\%$ for all values of σ_R^*, rising to $\approx 75\%$ for $\sigma_R^* > 0.04$. Large radial deviation is clearly connected to higher accuracy in the estimation of morphometric parameters, because the effects of downsampling are less likely to erase or distort very large deviations from circularity. The increase in agreement between estimates of dominant harmonics at large radial deviations is also a consequence of diminishing the number of possibilities, since only very low harmonics can dominate at large radial deviations. In our analysis of MOC-FCC, we will sometimes report results for multiple bounds upon $D_{\rm pix}$ and σ_R^*, using $D_{\rm pix} = 20$, $D_{\rm pix} = 50$ and $\sigma_R^* = 0.04$ in particular.

We turn now to the remaining analyses of morphometric properties derived from impact craters in the MOC-FCC. We refer to the reader to Sections 5.2 and 5.3 for detailed explanations of how the analyses are carried out. In this section, we reproduce the same plots and tables for MOC-FCC craters, and will focus our discussion upon outcomes that strongly accord or differ from those previously obtained for HiRISE-FCC.

A histogram of the depth-diameter ratio d_s/D is shown in Figure 5-66, indicating that d_s/D, an upper bound of the true value, is significantly overestimated in most cases. There may be several reasons for this: (a) lower resolution makes difficult the interpretation of shadow shapes and locating their boundaries, as well as (b) the interpretation of crater cavity shape. Also, (c) some dark albedo features are mistaken for shadows. The fill ratio F is plotted in Figure 5-67. As before, the Cavity Shape Criterion (CSC: i.e., $d_s/D \geq 0.12$ and $F > 0.75$) will be enforced in most analyses. By itself, the CSC excludes 33% of the MOC-FCC. Imposing the additional condition that $D_{\rm pix} \geq 20$ leaves only 45% of the data set for analysis. Unlike the HiRISE-FCC, a significant number of impact craters exhibit a very large range in the value of morphometric quantities because of large portions of the PCRO in which the rim could not be reliably traced. Therefore, wherever the CSC is enforced, we also eliminate all craters for which the range

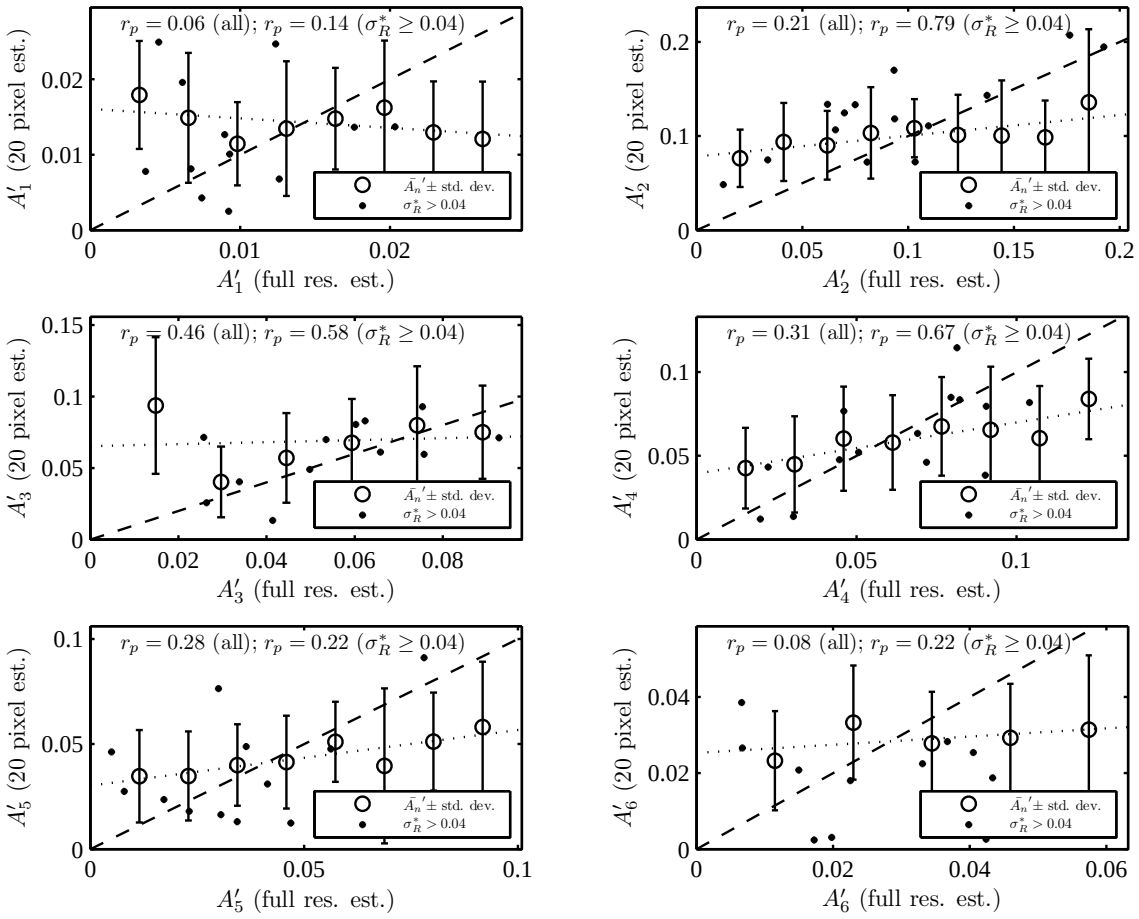

Figure 5-63: Correlation between [binned, averaged] estimates of deviation-normalized harmonic amplitudes (A_n') based on images downsampled for 20-pixel diameters and full-resolution images (x-axis). Errorbars span one standard deviation, and r_P is the Pearson correlation coefficient for this comparison. The dashed line corresponds to equality of estimates. Dark circles correspond to all estimates of A_n' for craters with $\sigma_R^* \geq 0.04$.

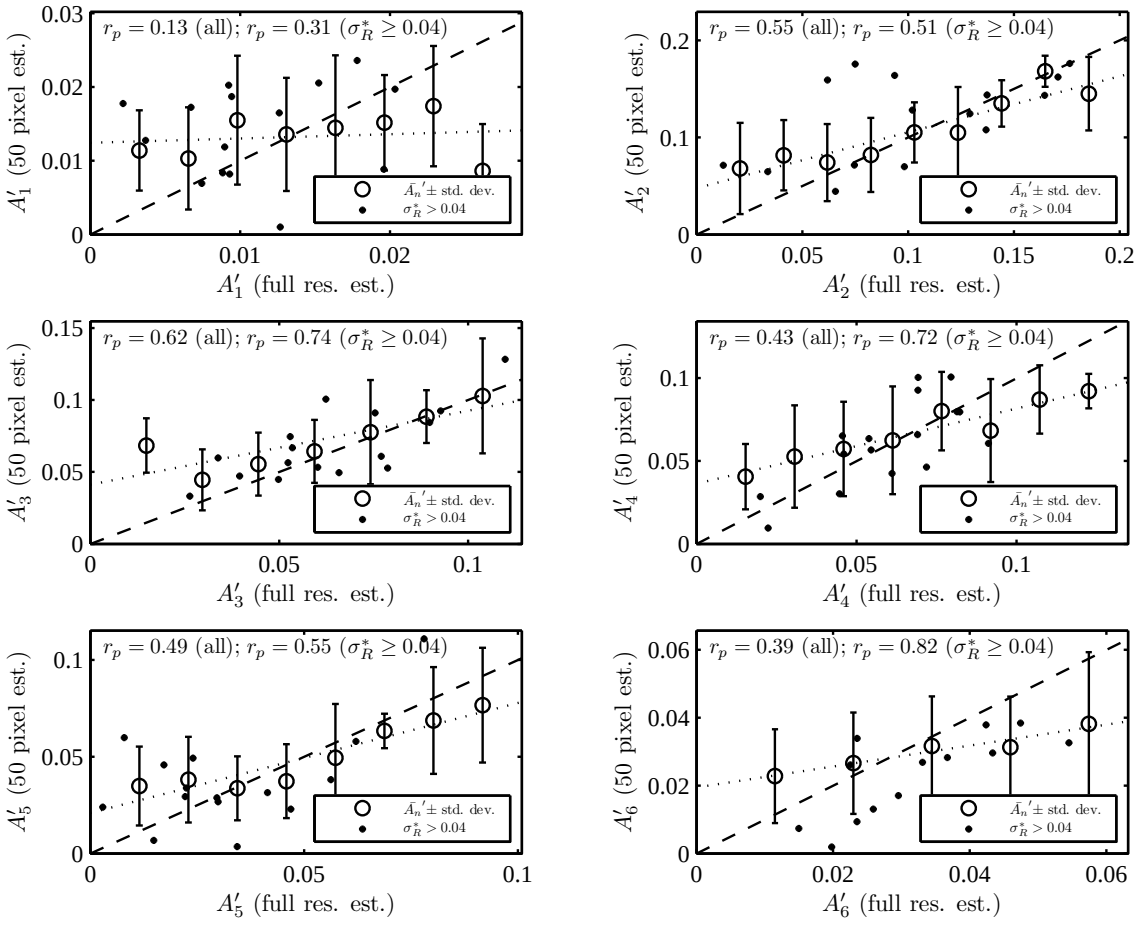

Figure 5-64: Correlation between [binned, averaged] estimates of deviation-normalized harmonic amplitudes (A_n') based on images downsampled for 50-pixel diameters and full-resolution images (x-axis). Errorbars span one standard deviation, and r_P is the Pearson correlation coefficient for this comparison. The dashed line corresponds to equality of estimates. Dark circles correspond to all estimates of A_n' for craters with $\sigma_R^* \geq 0.04$.

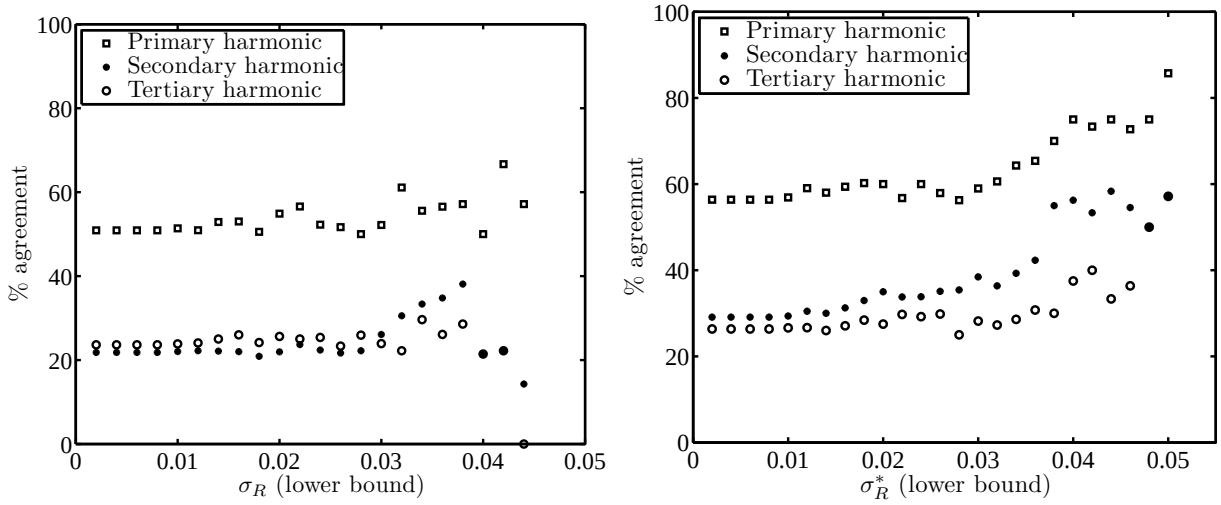

Figure 5-65: Percentage agreement between estimates of principal, secondary, and tertiary harmonics based upon downsampled images (LEFT: 20-pixel diameter; RIGHT: 50-pixel diameter) and full-resolution images (x-axis), versus the lower bound imposed upon σ_R^*. Agreement is $\approx 57\%$ for $D_{\rm pix} = 50$ and all values of σ_R^*, rising to $\approx 75\%$ for $\sigma_R^* > 0.04$.

in ΔR^* exceeds 50% of its single-estimate value (66 craters in all). All told, between this condition, the CSC, and the condition $D_{\rm pix} \geq 20$, 58% of the dataset is removed from consideration. In portions of this analysis, we shall winnow the MOC-FCC still further by imposing bounds on σ_R^* and higher bounds on $D_{\rm pix}$.

As before, we begin with results for the entire data set, from which no craters have been excluded. In Figures 5-68, 5-69, and 5-70 we have plotted ΔR^*, σ_R^*, and ν (respectively) as a function of diameter D in log-log space. Craters for which $D_{\rm pix} < 20$ are highlighted with open diamonds. The features noted earlier in the corresponding plots for HiRISE-FCC are evident here as well: (a) a clear transition in the vicinity of $D = 100$ m as well as (b) a roughly power-law decay for $D > 100$ m. It is difficult, however, to make the claim for morphometric expression of the strength-gravity transition on the basis of these results because of the comparatively poor estimates of σ_R^* that are possible at resolutions indicated by $D_{\rm pix} < 20$ (see Figure 5-60).

In Figure 5-71 we have plotted a histogram of A_4', which peaks at roughly the same value observed for HiRISE-FCC (i.e., 0.05), and again

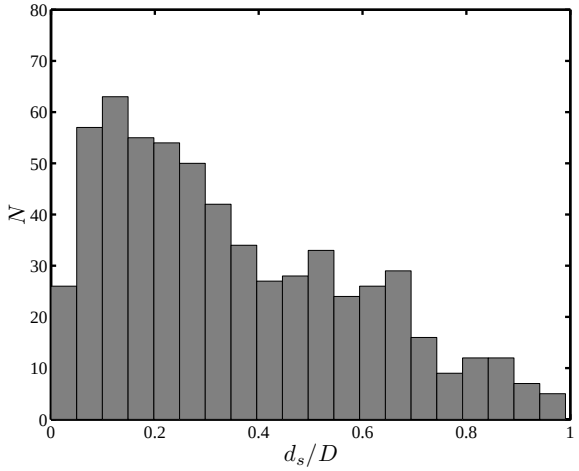

Figure 5-66: Depth-diameter ratio (d_s/D) of all impact craters in the MOC-FCC for which this quantity could be measured. The significant proportion of unrealistically large values ($d_s/D > 0.35$) indicates that this quantity is over-estimated in the majority of cases. (D ranges from 30 m to 3 km.)

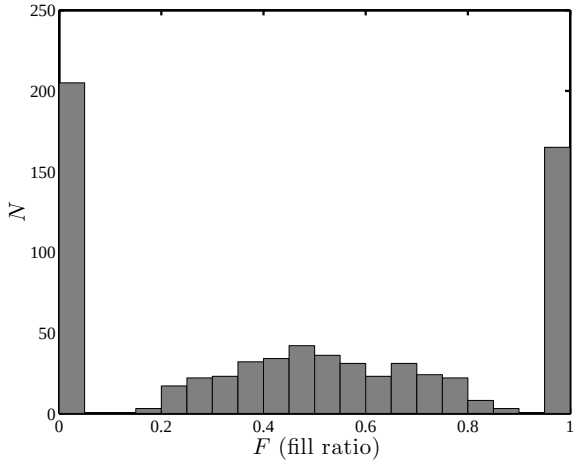

Figure 5-67: Fill ratio (F) of all impact craters in the MOC-FCC for which this quantity could be measured.

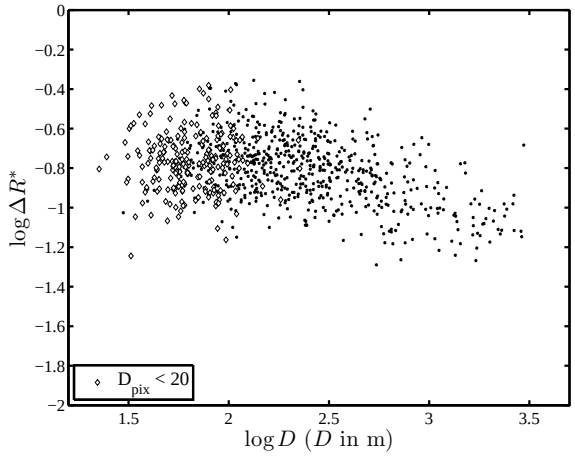

Figure 5-68: Radius-normalized maximum radial deviation ΔR^* for all impact craters in the MOC-FCC, where craters spanned by less than 20 pixels ($D_{\rm pix} < 20$) are marked with open diamonds. [SEV; CSC off; all D; all $D_{\rm pix}$]

indicating that Meteor Crater has an extremely uncommon shape – an observation that will be revisited in the next chapter.

The low resolution of MOC narrow-angle imagery does not enable the sort of detailed target characterization that was possible for HiRISE-FCC. Therefore, the number of subsets that may form the basis of comparisons is comparatively limited, and these are defined in Table 5.9. The first three subsets (L_1 through L_3) have the same definitions as before, and are based upon the material classifications defined in the first section of this chapter. As before, L_4 is a binary attribute signaling the presence or absence of clearly-expressed systematic jointing. In the MOC-FCC, L_5 and L_6 correspond to L_7 and L_8 of the HiRISE-FCC, and divide the range in fill ratio between them. We have added one comparison, that between L_7 and L_7^C (defined in Table 5.9), which contrasts craters failing the CSC and having breached rims (L_7) with those which pass the CSC and have continuous rims (L_7^C).

We begin by replicating the comparison between "lavas" and "not-lavas" in the distribution of σ_R^* as a function of diameter in log-log space (Figure 5-72). As before in HiRISE-FCC, we can see that these groups exhibit a similar dependence upon D, while the craters in non-lava targets are on average less circular. We have

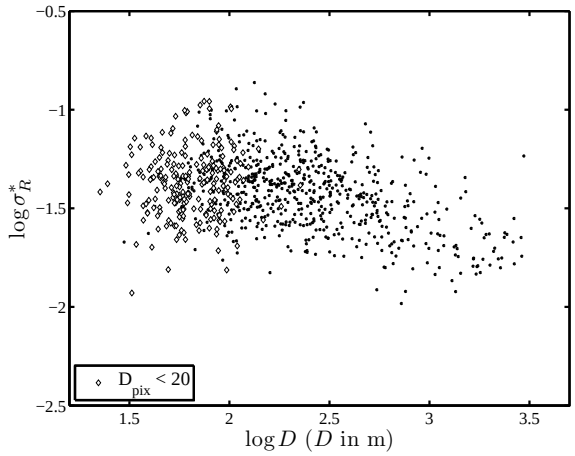

Figure 5-69: Radius-normalized standard radial deviation σ_R^* for all impact craters in the MOC-FCC, where craters spanned by less than 20 pixels ($D_{\rm pix} < 20$) are marked with open diamonds. [SEV; CSC off; all D; all $D_{\rm pix}$]

Table 5.9: Subsets of the MOC-FCC and their defining properties.

Set sym.	Abbreviation	Property of	Description
L_1	Not Lavas	Context	Resides in geological units assigned to material classes 1 (debris) or 2 (sedimentary).
L_2	L_1 + Mantled	Context	Resides in geological units assigned to material classes 1 (debris) or 2 (sedimentary), or 6 (aeolian/lava-mantled).
L_3	Lavas	Context	Resides in geological units assigned to material class 4 (lavas).
L_4	Sys. joints	Context	Systematic jointing clearly expressed, in the form of fractures, fissures, or escarpments with a consistent orientation.
L_5	+Modif. (F)	Crater	More modified, as indicated by fill ratio $F > 0.5$ (i.e., 50% of craters for which F could be measured).
L_6	–Modif. (F)	Crater	Less modified, as indicated by fill ratio $F \leq 0.5$.
L_7	+Modif. (F, d_s/D)	Crater	More modified, as indicated by $F > 0.75$ or $d_s/D < 0.12$, or a breached rim.

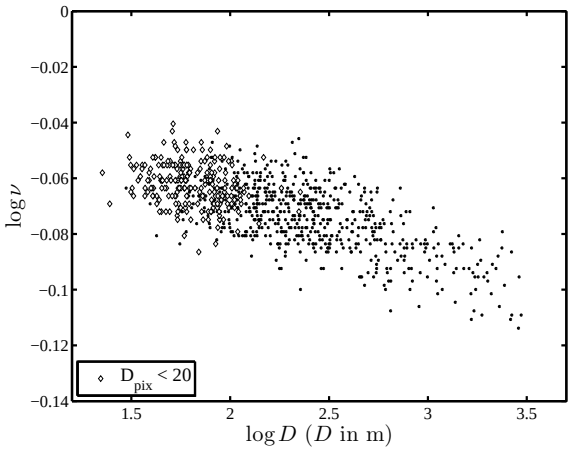

Figure 5-70: Concave fraction ν for all impact craters in the MOC-FCC, where craters spanned by less than 20 pixels ($D_{\text{pix}} < 20$) are marked with open diamonds. [SEV; CSC off; all D; all D_{pix}]

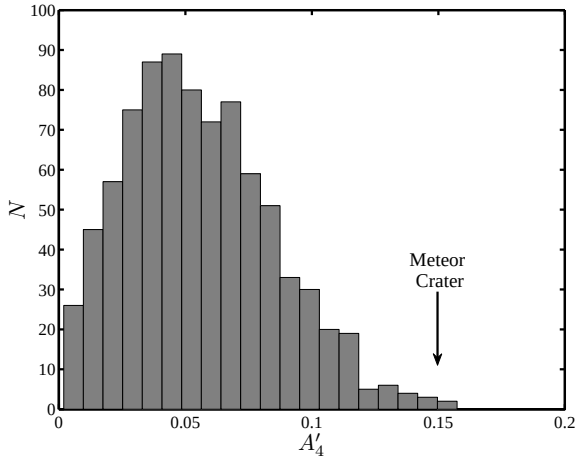

Figure 5-71: Histogram of the deviation-normalized fourth harmonic amplitude for all impact craters in the MOC-FCC. The value of A_4' calculated for Meteor Crater is marked with an arrow (see Part C of Figure 5-15).[SEV; CSC off; all D; all D_{pix}]

Table 5.10: For 9 subsets of the **MOC-FCC**: slope m and intercept b obtained from a linear regression for $\log \sigma_R^* = m \log D + b$ and $\log \Delta R^* = m \log D + b$, along with the Pearson correlation coefficient r_P computed for both relations. **Single-estimate** values were assumed in this case and the fit was computed for $D \geq 100$ m. [CSC on, except for L_5, L_6, L_7, and L_7^C; $D_{\rm pix} \geq 20$]

Set	$m_{\Delta R}$	$b_{\Delta R}$	r_P	m_{σ_R}	b_{σ_R}	r_P
L_1	-0.25	-0.17	-0.59	-0.26	-0.75	-0.57
L_2	-0.23	-0.24	-0.54	-0.26	-0.78	-0.55
L_3	-0.25	-0.21	-0.56	-0.28	-0.76	-0.56
L_4	-0.25	-0.19	-0.49	-0.27	-0.76	-0.49
L_4^C	-0.27	-0.18	-0.58	-0.30	-0.71	-0.59
L_5	-0.24	-0.25	-0.45	-0.26	-0.80	-0.46
L_6	-0.26	-0.18	-0.58	-0.28	-0.75	-0.57
L_7	-0.24	-0.23	-0.48	-0.26	-0.80	-0.47
L_7^C	-0.26	-0.19	-0.57	-0.30	-0.72	-0.58

again computed linear regressions for all subsets over the domain $D \geq 100$ m, were these results are reported in Table 5.10 for single-estimate values and Appendix Table C.1 for mid-range values. The comparatively shallow slopes are consistent with the result in Figure 5-60, which indicates that σ_R^* is under-estimated at low resolutions (corresponding to small diameters). Principal harmonics and the mean values and standard deviations of morphometric quantities are summarized in Tables 5.11 and 5.12 (SEV, all D) and Appendix Tables C.3 and C.2 (MRV, all D). Unlike HiRISE-FCC, we have not reproduced the entire set of tables for the case $D \geq 100$ m because only 1 crater (out of 840) passes the CSC and has $D_{\rm pix} \geq 20$ with $D \geq 100$ m.

We have reproduced in Figure 5-73 the subset comparisons of Figure 5-27, showing the number of difference metrics defined in Table 5.6 that measure a statistically significant contrast. (We have reported only A_2' through A_4' with the expectation, based on the downsampling analysis related earlier, that higher harmonic amplitudes are poorly estimated at low resolutions.) These results are reported in greater detail in Table 5.13 (SEV, all D) and Appendix Table C.4 (MRV, all D). We can see at once that the larger radial deviations noted for non-lavas in Figure 5-72 are not a very significant difference (at the 95% level with respect to the three reference distributions). The most robust contrast measured for any of the subset comparisons occurs in concave fraction for (L_1, L_3). All told, the detrended radial deviations and concave fraction are on average larger for non-lavas, as shown in Figure 5-74 and Figure 5-75, in agreement with the results from HiRISE-FCC as well as the qualitative tallies of Section 5.1 made as part of the MOC-CTS. Another important result from Figure 5-73 is that contrasting large and small fill ratios (L_5, L_6) reveals no significant differences in the examined quantities. We have plotted a comparison of the [almost identical] cumulative distributions of σ_R^* for (L_5, L_6) in Figure 5-76. The marked difference in concave fraction noted in HiRISE-FCC for this comparison is not apparent here, but we must bear in mind that the two comparisons are not the same. The value that evenly divides the range in fill ratio is much larger for MOC-FCC ($F = 0.5$) because of the larger proportion of craters with large F.

One- and two-dimensional histograms of primary, secondary, and tertiary harmonics are plotted in Figures 5-77 and 5-78. We find once again that the most common combination of (primary, secondary) harmonics is (3,4), closely followed by (4,3) and (3,5). Unlike the HiRISE-FCC, the tertiary harmonic histogram peaks at $n = 5$ instead of $n = 6$, possibly owing to the greater importance of $n = 4$ in HiRISE-FCC and its relationship to $n = 6$. The fraction of craters with primary harmonic $n = 4$ is plotted for each subset comparison in Figure 5-79, where we can see that non-lavas and targets with systematic jointing have a slightly larger proportion of squares than their counterparts. Also significant is that the comparisons (L_5, L_6) and (L_6, L_6^C) (which reflect modification state and primary/secondary impact status) are both close to parity, suggesting that what distinguishes these sets has little effect on the fourth harmonic (at least at high amplitudes). In Figure 5-80 we have again plotted the shape fractions N_3/N, N_4/N, $N_{>4}/N$ for the entire

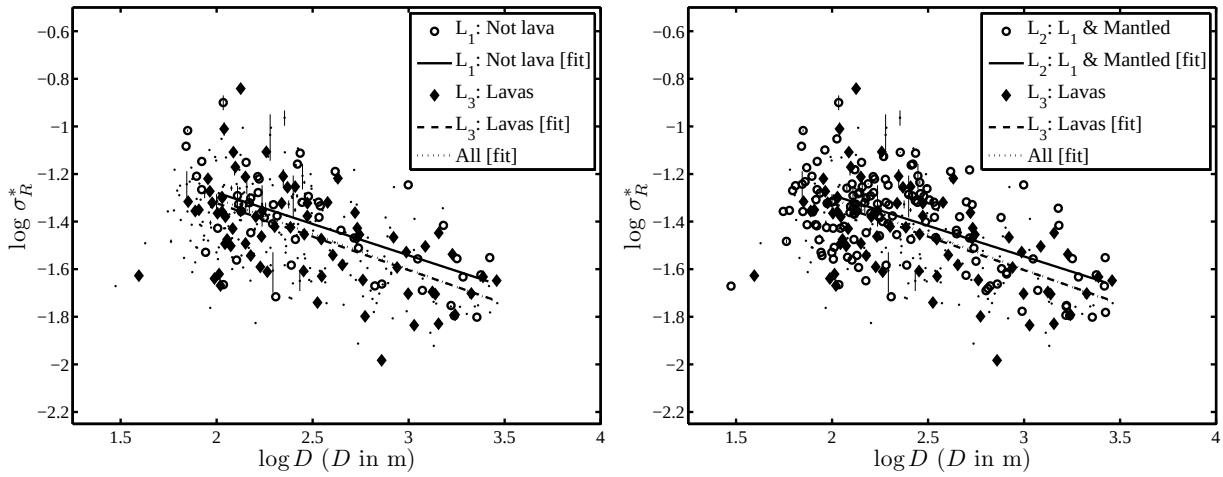

Figure 5-72: Radius-normalized standard radial deviation (σ_R^*) for impact craters in the MOC-FCC which satisfy the Cavity Shape Criterion (CSC), and where craters belonging to material class "Lavas" and two subsets of "Not-Lavas" are plotted with contrasting symbols. Error bars span the entire range of values for alternate outlines, and points correspond to mid-range values (MRV). Linear regressions are fitted only for $D \geq 100$ m. [MRV; CSC on; all D; $D_{\rm pix} \geq 20$]

Table 5.11: Global properties of shape distributions for 9 subsets of the **MOC-FCC**, using **single-estimate** values and **including** craters with $D < 100$ m. Listed are the mean ± standard deviation of deviation-normalized harmonic amplitudes A'_2 through A'_5.[CSC on, except for L_5, L_6, L_7, and L_7^C; $D_{\rm pix} \geq 20$]

Set	N	A'_2	A'_3	A'_4	A'_5
L_1	51	0.120 ± 0.049	0.070 ± 0.036	0.052 ± 0.032	0.038 ± 0.019
L_3	72	0.110 ± 0.049	0.069 ± 0.033	0.051 ± 0.029	0.037 ± 0.023
L_2	141	0.125 ± 0.044	0.064 ± 0.035	0.055 ± 0.031	0.037 ± 0.019
L_3	72	0.110 ± 0.049	0.069 ± 0.033	0.051 ± 0.029	0.037 ± 0.023
L_4	105	0.111 ± 0.043	0.068 ± 0.036	0.054 ± 0.028	0.038 ± 0.020
L_4^C	245	0.117 ± 0.046	0.067 ± 0.035	0.055 ± 0.030	0.039 ± 0.022
L_5	263	0.115 ± 0.045	0.068 ± 0.034	0.055 ± 0.029	0.039 ± 0.021
L_6	261	0.114 ± 0.045	0.067 ± 0.033	0.055 ± 0.027	0.038 ± 0.021
L_7	317	0.115 ± 0.044	0.068 ± 0.034	0.054 ± 0.027	0.039 ± 0.020
L_7^C	252	0.116 ± 0.045	0.068 ± 0.034	0.055 ± 0.029	0.038 ± 0.022

Table 5.12: Global properties of shape distributions for 9 subsets of the **MOC-FCC**, using **single-estimate** values and **including** craters with $D < 100$ m. Listed are the number of triangles (N_3), squares (N_4), pentagons (N_5), and hexagons (N_6) in each subset, along with mean ± standard deviation of detrended maximum and standard radial deviations ($\Delta R'$ and σ'_R, respectively) and concave fraction (ν').[CSC on, except for L_5, L_6, L_7, and L_7^C; $D_{\rm pix} \geq 20$]

Set	N	N_3	N_4	N_5	N_6	σ'_R	$\Delta R'$	ν'
L_1	51	32	14	2	2	0.23 ± 0.09	0.77 ± 0.26	0.953 ± 0.017
L_2	141	75	46	13	3	0.21 ± 0.08	0.72 ± 0.24	0.946 ± 0.019
L_3	72	43	19	8	1	0.20 ± 0.08	0.69 ± 0.26	0.943 ± 0.019
L_4	105	52	36	13	2	0.20 ± 0.08	0.71 ± 0.26	0.945 ± 0.019
L_4^C	245	135	75	25	6	0.20 ± 0.08	0.68 ± 0.24	0.944 ± 0.019
L_5	263	144	78	27	11	0.18 ± 0.07	0.65 ± 0.22	0.950 ± 0.020
L_6	261	146	80	28	3	0.19 ± 0.07	0.66 ± 0.22	0.950 ± 0.019
L_7	317	173	95	37	8	0.19 ± 0.07	0.67 ± 0.22	0.952 ± 0.020
L_7^C	252	140	77	24	7	0.18 ± 0.07	0.63 ± 0.22	0.948 ± 0.019

Table 5.13: Quantities and difference metrics (Δ_n: for $n = 1, 2, ...$; defined in Table 5.6) that indicate a statistically significant difference for 5 pairings of 9 subsets of the **MOC-FCC**, with respect to differences computed for 10,000 pairings of randomly-sampled subsets of a **Gaussian** reference distribution on the same domain. Listed are metrics reporting differences that exceed the percentage $p_{\rm lim}$ of differences computed from paired subsets of the reference distribution. **Single-estimate** values were used and craters with $D < 100$ m were **included**. [CSC on, except for (L_5, L_6) and (L_7, L_7^C); $D_{\rm pix} \geq 20$]

Set	$p_{\rm lim}$	Quantities whose distributions differ at the level $p_{\rm lim}$
(L_1,L_3)	95%	A'_2 (Δ_n:2), σ'_R (Δ_n:8), ν (Δ_n:3,5,6,7,8), Q^{468}_{357} (Δ_n:4), Q^{48}_{3} (Δ_n:1,2), Q^{5678}_{234} (Δ_n:8), Q^{48}_{0} (Δ_n:2), Q^{3}_{4} (Δ_n:1), Q^{5}_{6} (Δ_n:4)
	97.5%	A'_2 (Δ_n:2), ν (Δ_n:3,5,6,7), Q^{48}_{3} (Δ_n:1,2)
	99%	A'_2 (Δ_n:2), ν (Δ_n:3,5,6,7), Q^{48}_{3} (Δ_n:1,2)
(L_2,L_3)	95%	A'_2 (Δ_n:2,3,5,6,7), A'_5 (Δ_n:1), ν (Δ_n:1,2), Q^{48}_{3} (Δ_n:8), Q^{24}_{35} (Δ_n:3,5,6,7,8), Q^{5678}_{234} (Δ_n:3,4,5,6,8), Q^{1}_{2} (Δ_n:3,5,6,7,8), Q^{2}_{3} (Δ_n:5,6,7), Q^{2}_{5} (Δ_n:5,6,7), Q^{2}_{6} (Δ_n:3,5,6,7), Q^{2}_{7} (Δ_n:3,5,6,7), Q^{2}_{8} (Δ_n:3,5,6,7), Q^{5}_{6} (Δ_n:1), Q^{7}_{8} (Δ_n:1)
	97.5%	A'_2 (Δ_n:2,5,6,7), Q^{24}_{35} (Δ_n:5,6,7), Q^{5678}_{234} (Δ_n:8), Q^{1}_{2} (Δ_n:6,8), Q^{2}_{5} (Δ_n:5), Q^{2}_{6} (Δ_n:5,6), Q^{2}_{7} (Δ_n:5,6,7), Q^{2}_{8} (Δ_n:5,6,7), Q^{5}_{6} (Δ_n:1)
	99%	Q^{5}_{6} (Δ_n:1)
(L_4,L_4^C)	95%	A'_6 (Δ_n:8), $\Delta R'$ (Δ_n:1), σ'_R (Δ_n:1,2), Q^{1}_{8} (Δ_n:1)
	97.5%	σ'_R (Δ_n:1,2), Q^{1}_{8} (Δ_n:1)
	99%	σ'_R (Δ_n:1)
(L_5,L_6)	95%	Q^{6}_{7} (Δ_n:1), Q^{7}_{8} (Δ_n:1)
	97.5%	Q^{6}_{7} (Δ_n:1)
(L_7,L_7^C)	95%	A'_3 (Δ_n:2), A'_6 (Δ_n:2,3,5,6,7,8), A'_7 (Δ_n:5,7,8), $\Delta R'$ (Δ_n:8), ν (Δ_n:3,6), Q^{468}_{357} (Δ_n:1), Q^{48}_{3} (Δ_n:4), Q^{468}_{35} (Δ_n:1), Q^{24}_{35} (Δ_n:2), Q^{5678}_{234} (Δ_n:1,8), Q^{1}_{6} (Δ_n:2,3,5,6,7,8), Q^{1}_{7} (Δ_n:5,6,7,8), Q^{6}_{8} (Δ_n:7,8)
	97.5%	A'_6 (Δ_n:5,6,7,8), A'_7 (Δ_n:7,8), Q^{468}_{357} (Δ_n:1), Q^{468}_{35} (Δ_n:1), Q^{1}_{6} (Δ_n:3,5,6,7,8), Q^{1}_{7} (Δ_n:7), Q^{6}_{8} (Δ_n:8)
	99%	A'_6 (Δ_n:8), A'_7 (Δ_n:8), Q^{1}_{6} (Δ_n:7,8)

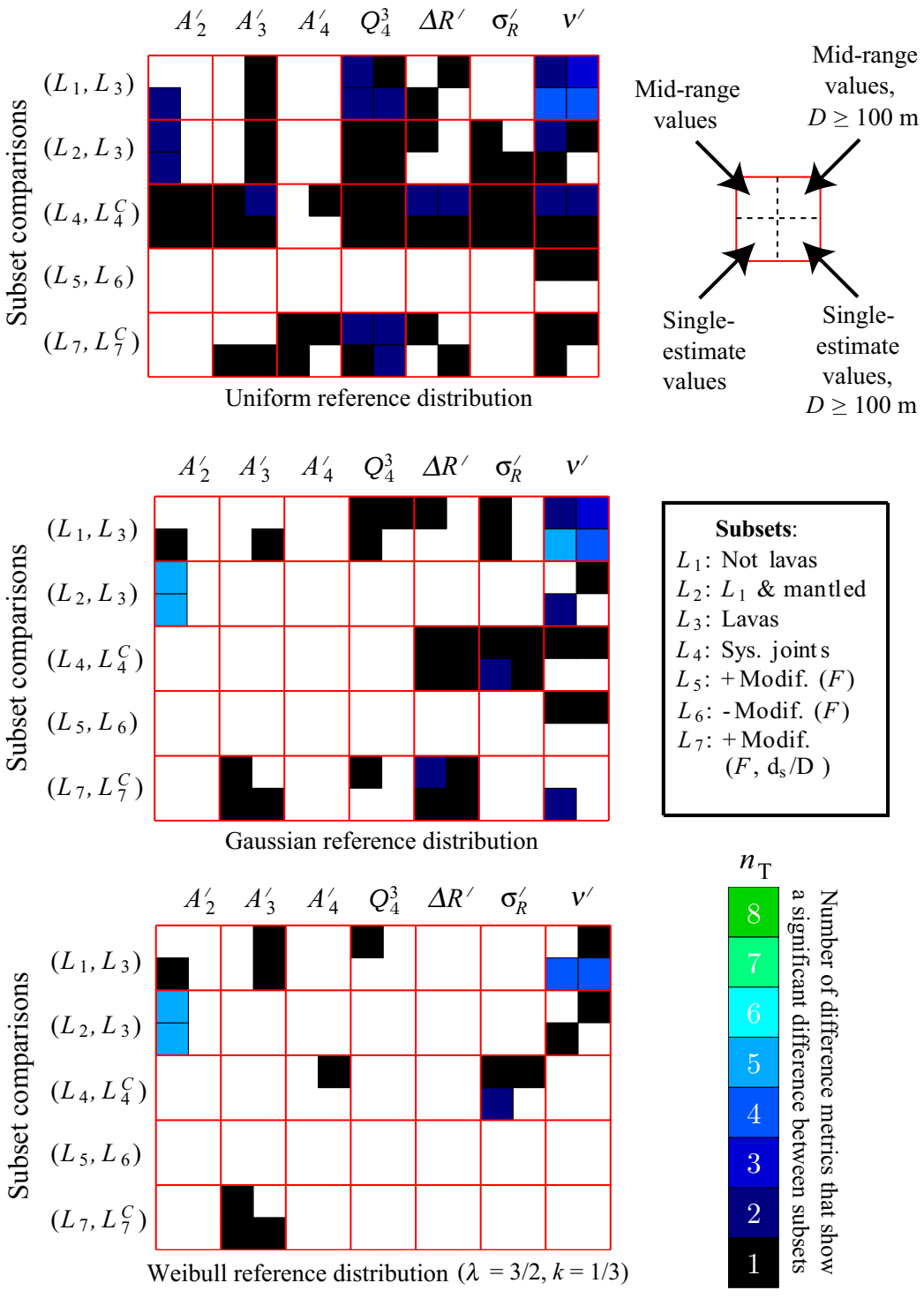

Figure 5-73: The number of absolute difference metrics (Δ_1 through Δ_8, defined in Table 5.6) measuring a statistically significant difference between compared subsets of the MOC-FCC at the 95% level with respect to uniform (TOP), Gaussian (MIDDLE), and Weibull (BOTTOM) reference distributions, for the first several deviation-normalized harmonic amplitudes, as well as detrended radial deviations and concave fraction. [CSC on, except for (L_5, L_6) and (L_7, L_7^C); $D_{\text{pix}} \geq 20$]

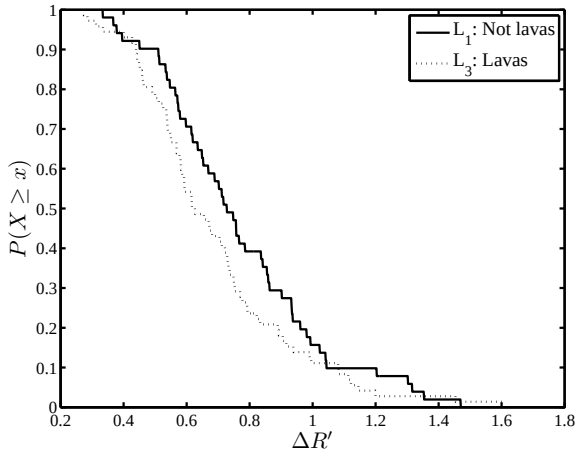

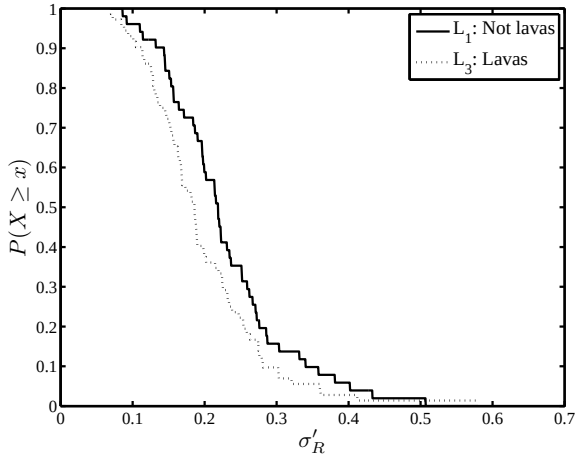

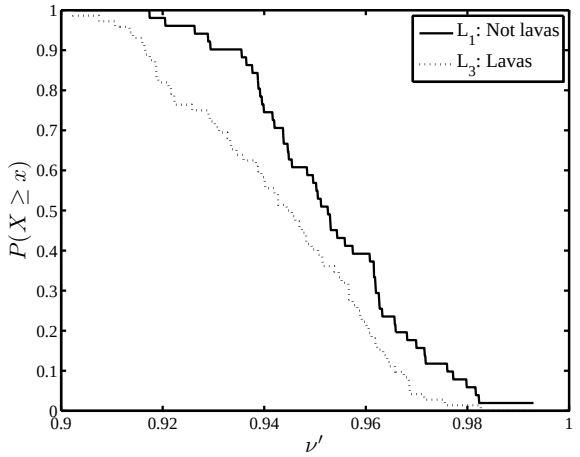

Figure 5-74: Cumulative distributions of important quantities for the comparison of subsets L_1 and L_3 of the MOC-FCC, confirming that σ'_R, $\Delta R'$, and ν' are greater on average for non-lavas. [SEV; CSC on; all D; $D_{\text{pix}} \geq 20$]

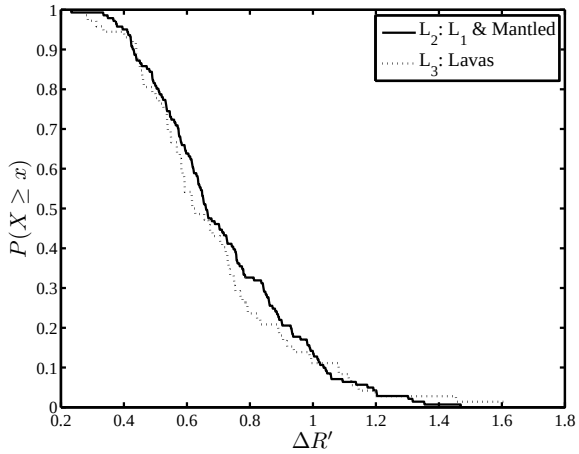

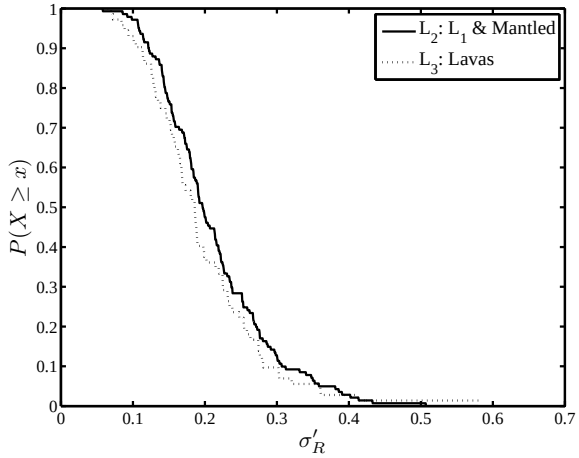

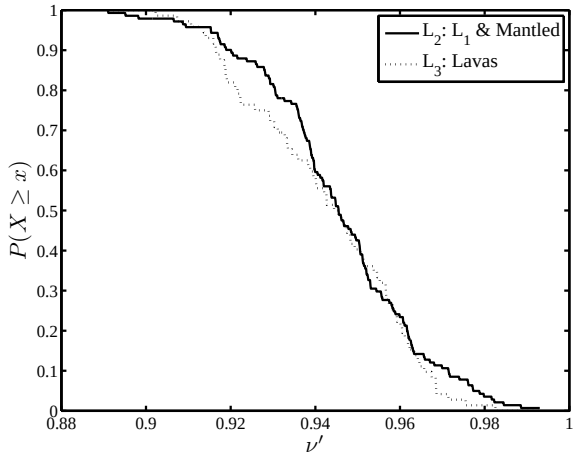

Figure 5-75: Cumulative distributions of important quantities for the comparison of subsets L_2 and L_3 of the MOC-FCC, confirming that σ'_R, $\Delta R'$, and ν' are greater on average for non-lavas. [SEV; CSC on; all D; $D_{\text{pix}} \geq 20$]

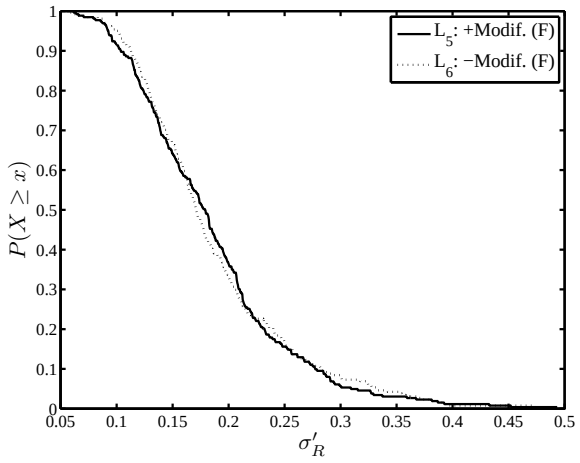

Figure 5-76: Cumulative distribution of detrended standard radial deviation (σ'_R) for subsets L_5 (large fill ratio) and L_6 (low fill ratio), which are effectively identical. [SEV; CSC off; all D; $D_{\text{pix}} \geq 20$]

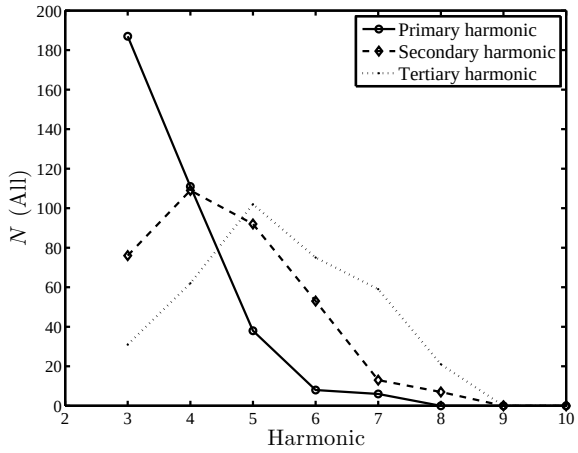

Figure 5-77: Histograms of primary, secondary, tertiary harmonics for the MOC-FCC. [SEV; CSC on; all D; $D_{\text{pix}} \geq 20$]

dataset,[14] for lavas and both non-lava categories, once again finding a larger proportion of triangles in lavas, as well as a lower proportion of all higher dominant harmonics in this target group. Finally, we have plotted Δ_9 for A'_n of harmonics $n = 1$ through $n = 8$ for each comparison, in Appendix Figure C-1, and compared these with the diameter distributions (for all comparisons) in Appendix Figure C-2, finding that none of the trends in the former can be explained soley in terms of differences detected in the latter. That is, the expected dependence of deviation-normalized harmonic amplitudes that derives solely from differences in sampled diameters is not consistent with the observed patterns in A'_n, and we discount this once again as a signficant source of systematic error.[15]

We close this chapter by repeating some of the foregoing analyses for $\sigma^*_R \geq 0.04$, because of the marked improvement in accuracy noted for large radial deviations earlier in this section.

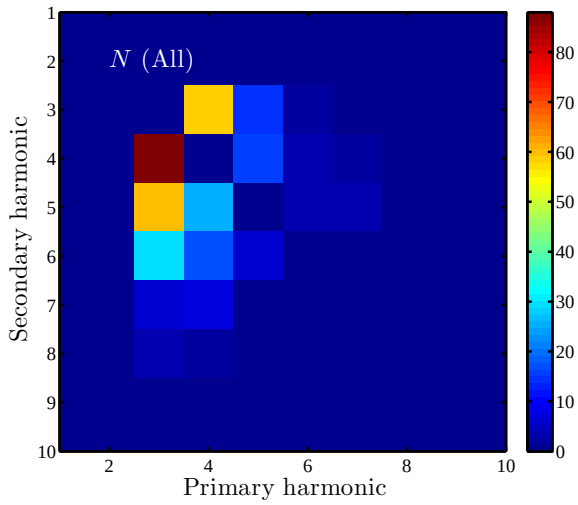

Figure 5-78: Two-dimensional histogram of primary and secondary harmonics for the MOC-FCC. [SEV; CSC on; all D; $D_{\text{pix}} \geq 20$]

[14]The CSC is turned off for this analysis because, as we have seen, the comparisons in (L_5, L_6) and (L_6, L_6^C) (and (L_7, L_8) in HiRISE-FCC) appear to have little or no effect on these fractions

[15]This assessment relies on measures of harmonic amplitudes for $n > 4$, which are not expected to be reliable at low resolutions.

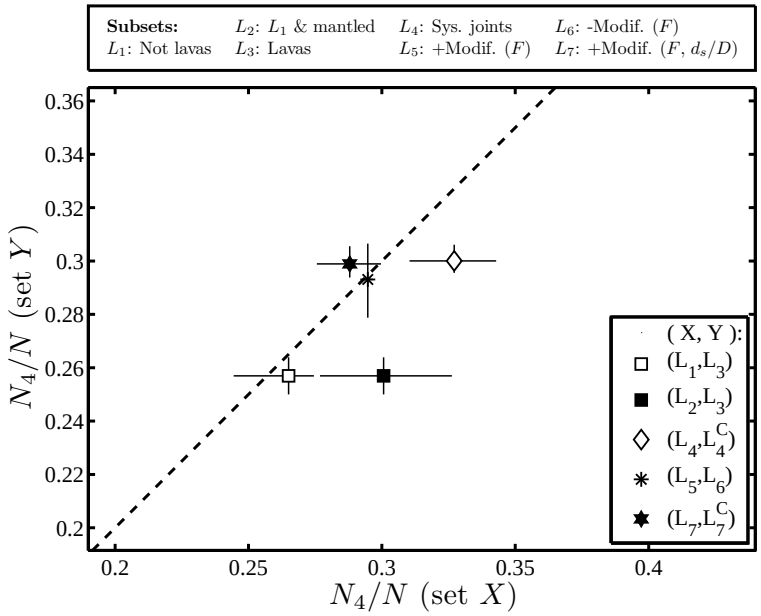

Figure 5-79: For each of 5 subset comparisons (X, Y), the fraction of impact craters with primary harmonic $n = 3$ in Y is plotted versus the same fraction computed for X. Points on the dashed line $y = x$ indicate parity. [CSC on except for (L_5, L_6) and (L_7, L_7^C); $D_{\rm pix} \geq 20$; Error bars span the entire range of values computed for (a) SEV for all D, (b) SEV for $D \geq 100$ m, (c) MRV for all D, and (d) MRV for $D \geq 100$ m.]

Imposing a lower bound on σ_R^* causes numerous problems that make the results difficult to interpret and to compare with the other analyses for HiRISE-FCC and MOC-FCC: (a) excluding craters with small σ_R^* also tends to eliminate craters in which higher-order harmonics are strong, and (b) this tends to shorten dramatically the range of diameters considered, which renders highly suspect the linear regression used to obtain detrended values of the concave fraction and of radial deviations (i.e., the correlation between radial deviation and diameter becomes very weak). Bearing this in mind, we will not attempt a detailed comparison between these results and former results, and we include them mainly for the sake of completeness. Figure 5-81 shows the by-now familiar estimates of statistically significant differences between subsets. The most interesting of these are plotted in Figures 5-82 (confirming the larger concave fraction of non-lavas in L_1) and Figure 5-83. The latter indicates that targets without a clear expression of systematic joints have larger elongations. While a statistically significant difference was not detected either for HiRISE-FCC or MOC-FCC (for all σ_R^*) in this subset comparison, the result is consistent with earlier suggestions (HiRISE-FCC) that weaker induration may be connected with larger elongations. The quadratic fraction (N_4/N) is plotted for all comparisons in Figure 5-84, in which non-lavas are once again host to a larger number of squares. Targets with systematic jointing in this case appear to have fewer squares (contradicting former results), while the comparisons relating to modification state and cavity shape (i.e., (L_5, L_6) and (L_7, L_7^C)) once again plot very close to parity. In Figure 5-85 we have again plotted the shape fractions N_3/N, N_4/N, $N_{>4}/N$ for the entire dataset (CSC off, but $\sigma_R^* \geq 0.04$), for lavas and both non-lava categories, once again finding a larger proportion of triangles in lavas, as well as a lower proportion of all higher dominant harmonics in this target group. This apparently very robust observation (MOC-CTS, HiRISE-FCC, MOC-FCC for all σ_R^* and now for $\sigma_R^* \geq 0.04$) will be addressed in

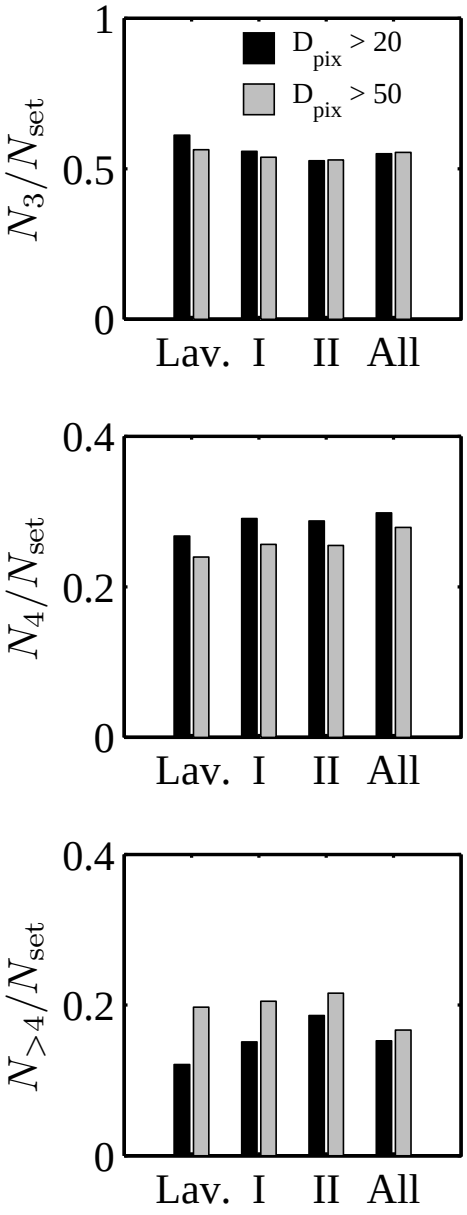

Figure 5-80: Fraction of impact craters in each of four subsets of the MOC-FCC with primary harmonic n (i.e., $N_n/N_{\rm set}$) for $n = 3$, $n = 4$, and $n > 4$: Lav. = "Lavas" (i.e., material class 4), I = "Not Lavas I,"(i.e., L_1: material classes 1, 2 and 3), and II = "Not Lavas II" (i.e., L_2: material classes 1,2,3, and 6), and All = the entire MOC-FCC. Lavas have more triangles than do the other sets, and fewer higher-order shapes. [SEV; CSC off; all D; Gray and black bars indicate different bounds on $D_{\rm pix}$]

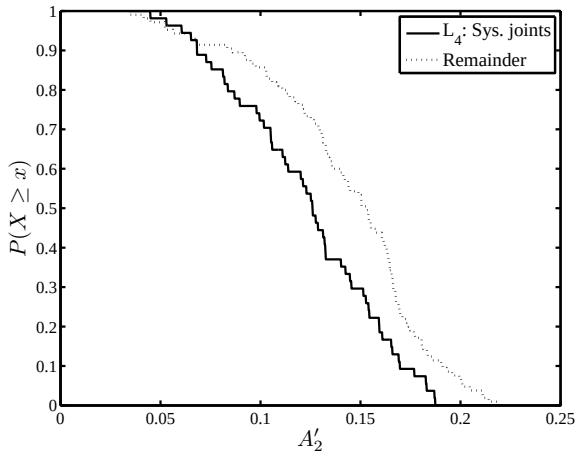

Figure 5-83: For craters having $\sigma_R^* \geq 0.04$: Cumulative distribution of the deviation-normalized second harmonic amplitude for the subset comparison (L_4, L_4^C) indicating larger elongations (on average) in targets that do not clearly exhibit systematic jointing. [SEV; CSC on; all D; $D_{\rm pix} \geq 20$; $\sigma_R^* \geq 0.04$]

more detail in the next chapter. Last but not least, we have plotted Δ_9 for A_n' of harmonics $n = 1$ through $n = 8$ for each comparison, in Appendix Figure C-3, and compared these with the diameter distributions (for all comparisons) in Appendix Figure C-4, finding that none of the trends in the former can be explained soley with respect to differences detected in the latter.

5.6 Conclusions

The most significant conclusions of the present chapter are summarized in Table 5.14, where the supporting data sets for each case (i.e., MOC-CTS, MOC-FCC, and HiRISE-FCC) are also indicated.

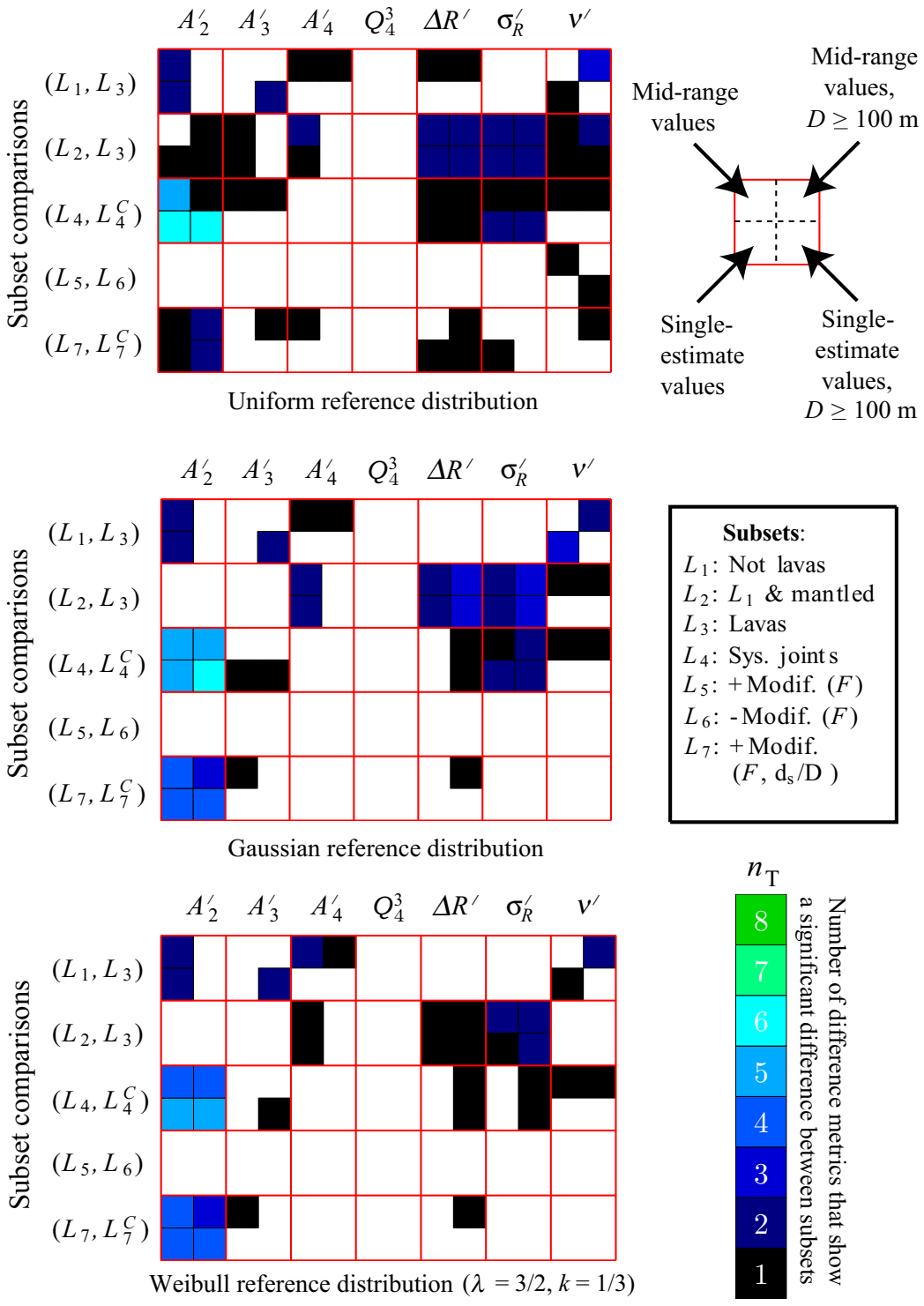

Figure 5-81: For craters having $\sigma_R^* \geq 0.04$ in the MOC-FCC: the number of absolute difference metrics (Δ_1 through Δ_8, defined in Table 5.6) measuring a statistically significant difference between compared subsets of the MOC-FCC at the 95% level with respect to a uniform (TOP), Gaussian (MIDDLE), and Weibull (BOTTOM) reference distribution, for the first several deviation-normalized harmonic amplitudes, as well as detrended radial deviations and concave fraction. [CSC on except for (L_5, L_6) and (L_7, L_7^C); $D_{\text{pix}} \geq 20$; $\sigma_R^* \geq 0.04$]

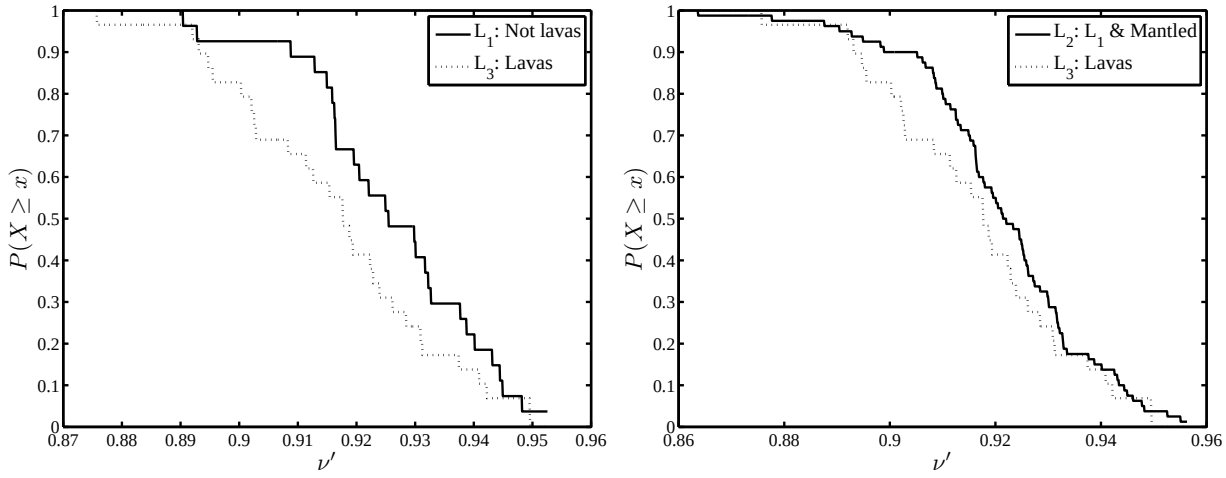

Figure 5-82: For craters having $\sigma_R^* \geq 0.04$ in the MOC-FCC: Cumulative distribution of detrended concave fraction (ν') for subset comparisons (L_1, L_2) and (L_1, L_3), confirming the relationship observed in for all values of σ_R^* in the MOC-FCC, as well as the HiRISE-FCC and MOC-CTS. [SEV; CSC on; all D; $D_{\text{pix}} \geq 20$; $\sigma_R^* \geq 0.04$]

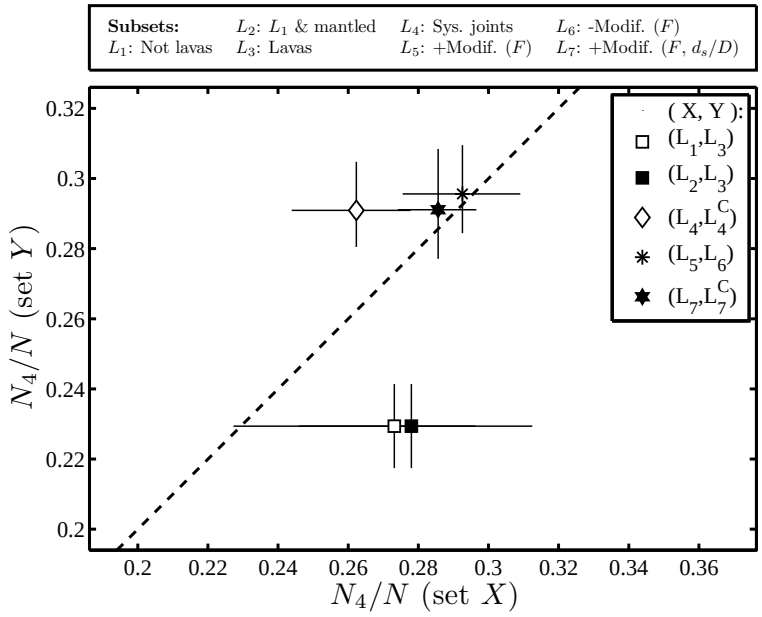

Figure 5-84: For craters having $\sigma_R^* \geq 0.04$ in the MOC-FCC: For each of 5 subset comparisons (X, Y), the fraction of impact craters with primary harmonic $n = 3$ in Y is plotted versus the same fraction computed for X. Points on the dashed line $y = x$ indicate parity. [CSC on, except for (L_5, L_6) and (L_7, L_7^C); $D_{\text{pix}} \geq 20$; $\sigma_R^* \geq 0.04$; Error bars span the entire range of values computed for (a) SEV for all D, (b) SEV for $D \geq 100$ m, (c) MRV for all D, and (d) MRV for $D \geq 100$ m.]

Table 5.14: Significant conclusions of the present chapter and supporting results derived from analyses of the MOC-CTS (MOC Crater-Target Survey), MOC-FCC (MOC Fresh Crater Catalog), and HiRISE-FCC (HiRISE Fresh Crater Catalog). "Y" indicates that the conclusion is supported, "?" indicates an inconclusive result (i.e., neither confirmed or contradicted), "N" indicates the conclusion is not supported, and "N/A" means that the conclusion cannot be evaluated using the data in question.

Conclusion	MOC-CTS	MOC-FCC	HiRISE-FCC
a. Populations of craters forming in lavas have a larger number of triangular planforms (i.e., the fourier spectrum is dominated by harmonic $n = 3$) and a smaller number of higher-order shapes than craters forming in non-lavas.	N/A	Y	Y
b. Craters forming in lavas are on average more circular than craters forming in non-lavas.	Y	Y	Y
c. Craters forming in lavas exhibit fewer planform concavities on average than craters forming in non-lavas.	Y	Y	Y
d. Radial deviation of the rim trace is independent of diameter or increases with diameter up to a transitional value between $D = 150$ m and $D = 250$ m, and follows a power-law decay in D for $D > 250$ m. We suggest this may correspond to the transition between cratering regimes dominated by strength (small diameters) and gravity (large diameters).	N/A	?	Y
e. Fresh impact craters with the very large quadrature of Meteor Crater are extremely rare on Mars (less than 1%).	N/A	Y	Y
f. In globally-distributed crater popluations, the azimuth of the major axis elongation (ϕ_E) of the crater planform tends to align with the equator. If related to impact azimuth instead of wind erosion, the distribution of ϕ_E may yield a measure of Mars' past obliquity variations.	N/A	Y	Y
g. Planimetric concavity is larger on average in craters with clear evidence of mass movements on their upper rim walls, and smaller in craters with a large amount of sedimentary infill.	N/A	N/A,N	Y
h. Square craters (i.e., craters whose planform fourier spectrum is dominated by the fourth harmonic amplitude) occur more commonly in targets that exhibit systematic joints.	Y	?	Y
i. Square craters are more common in populations forming in targets that are clearly indurated (exhibiting facets and sharp edges) or which have rounded rims (rim width > 1 m), or which exhibit significant topography.	N/A	N/A	Y
j. The sixth harmonic is the most sensitive (of all harmonics) to changes between crater populations forming in different kinds of geologic targets. Sixth harmonic amplitude decreases slightly with increasing diameter above $D \approx 150$ m.	N/A	N/A	Y
k. Significant slumping of crater walls is extremely uncommon for craters with $D < 330$ m and is widespread for craters with $D \geq 650$ m.	N/A	N/A	Y
l. Radial deviation of the rim trace is larger for craters with clear evidence of mass movements on their upper rim walls.	N/A	N/A	Y
m. $\{\Delta R^*, \sigma_R^*\} \propto D^{-1/2}$ where $\log \Delta R^*$ and $\log \sigma_R^*$ are strongly correlated with $\log D$, for craters formed in lavas or having uncollapsed rim walls.	N/A	N/A	Y
n. $\{\Delta R^*, \sigma_R^*\} \propto D^{-1/4}$ where $\log \Delta R^*$ and $\log \sigma_R^*$ are weakly correlated with $\log D$, for craters formed in debris or weakly-indurated target materials.	N/A	N/A	Y
o. Craters forming in unconsolidated or weakly-indurated target materials exhibit much larger elongations on average and lower-order principal harmonics than craters formed in other targets.	N/A	N/A	Y

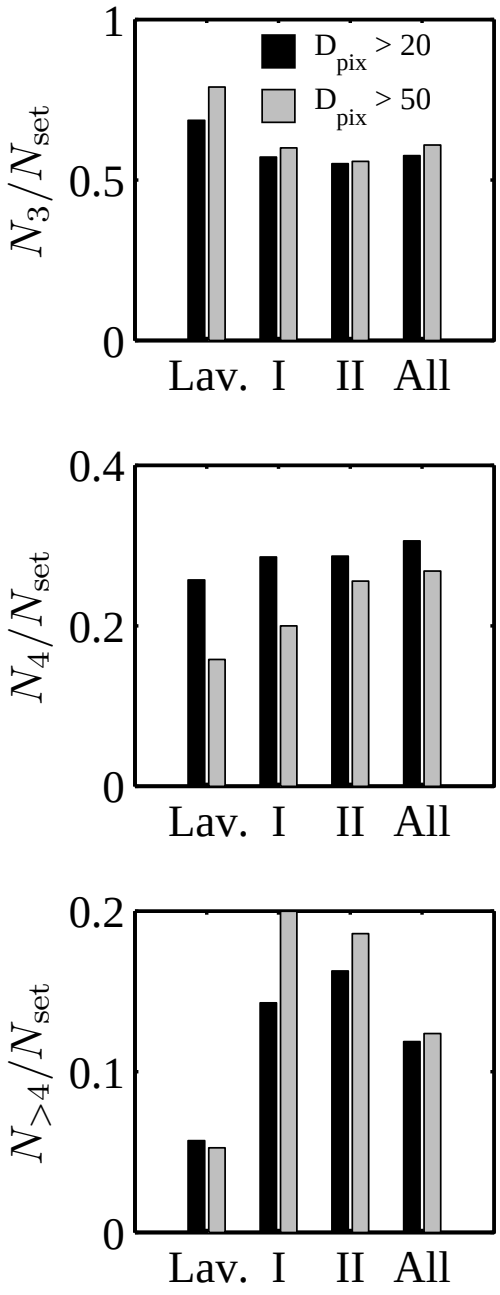

Figure 5-85: For craters having $\sigma_R^* \geq 0.04$ in the MOC-FCC: fraction of impact craters in each of four subsets with primary harmonic n (i.e., $N_n/N_{\rm set}$) for $n = 3$, $n = 4$, and $n > 4$: Lav. = "Lavas" (i.e., material class 4), I = "Not Lavas I,"(i.e., L_1: material classes 1, 2 and 3), and II = "Not Lavas II" (i.e., L_2: material classes 1,2,3, and 6), and All = the entire MOC-FCC. Lavas have more triangles than do the other sets, and fewer higher-order shapes. [SEV; CSC off; all D; Gray and black bars indicate different bounds on $D_{\rm pix}$; $\sigma_R^* \geq 0.04$]

Table 5.15: Symbols and acronyms

Symbol	Definition
D	Crater rim crest diameter (in m)
$D_{\rm pix}$	Number of pixels spanning crater diameter
F	Fill ratio
d_s/D	Shape-dependent depth-diameter ratio
ΔR	Maximum radial deviation
ΔR^*	Radius-normalized maximum radial deviation
$\Delta R'$	Detrended maximum radial deviation
σ_R	Standard radial deviation
σ_R^*	Radius-normalized standard radial deviation
σ_R'	Detrended standard radial deviation
ν	Concave fraction
ν'	Detrended concave fraction
A_n	Amplitude of nth harmonic
A_n'	Deviation-normalized amplitude of nth harmonic
A_n^*	Radius-normalized amplitude of nth harmonic
Q_{lmn}^{abc}	$(A_a' + A_b' + A_c') - (A_l' + A_m' + A_n')$
N_n	Number of craters with primary harmonic n.
n	(usu.) Harmonic order
"all D"	No lower bound imposed on diameter
SEV	Single-estimate values (see end Sec.5.2)
MRV	Mid-range values (see end Sec.5.2)
CSC	Cavity Shape Criterion ($F \leq 0.75$, $d_s/D \geq 0.12$)
EUD	Exactly Uniform Distribution
LEB	Lateral Elongation Bias

Chapter 6

Stochastic-kinematic model of crater excavation in fractured targets

Abstract: In this chapter we describe a two-dimensional kinematic-stochastic model of crater excavation (in planform) in which the excavation front is accelerated by a constant factor where crossing fractures in the target, represented by linear elements. This class of model has no precedent among previous modeling studies, which make use of hydrocodes (e.g., Pierazzo et al. [1997]) or variants of the kinematic Z-model (e.g., Maxwell [1977], Grieve and Garvin [1984]). The model presented here is able to reproduce several of the observations described in Chapter 5, including the power-law decay of radial deviation with crater diameter as well as the observed distribution of primary harmonics: i.e., the relative frequency with which each harmonic dominates the fourier decomposition of the crater rim trace or planimetric outline. Model results are computed for two fracture azimuth distributions – uniform and conjugate-orthogonal – where the relationship between modal azimuths of the conjugate-orthogonal fracture distribution and peaks of the fourth harmonic amplitude of the crater rim trace is consistent with that observed at Endurance Crater and Meteor Crater, as described in Chapter 4.

6.1 Model requirements

In this chapter we construct a simple two-dimensional Monte Carlo model of crater excavation in fractured targets which is able to reproduce many of the observations described in Chapter 5. As in Chapter 5, we are concerned only with simple craters, whose final shape is determined by excavation and minor slumping of rim walls, rather than a total collapse and flattening of the transient cavity that marks complex craters. The Stochastic-Kinematic Excavation Model (SKEM) relies upon "quantifying" a very old intuition. It was originally proposed by Shoemaker [1960] that the excavation flow may exploit planes-of-weakness in the target, and that crater excavation is more efficient in the horizontal component of the along-plane direction of faults and fractures (i.e., along strike). This idea is supported by a laboratory experiment (Gault et al. [1968]) as well as the evidence presented in Chapter 4 for the case of Endurance Crater, where surface fractures align with the peaks of the fourth harmonic amplitude of that crater's planimetric shape. Without providing a physical theory for how this occurs, we propose a simple rule which the complex physics of crater excavation are assumed to follow. That is, we will assume that the physics of a very complex process operates on a particular structure (a fracture network) in a particular way, and then explore the consequences of this assumption. Our motivation is to see to what extent this assumption can help us to explain many of the observations that we have so far compiled. In particular, a successful model of crater formation must be able to account for at least the following observations:

1. The planimetric shape is mostly determined

by the excavation process (rather than modification), in keeping with strong evidence presented for Endurance Crater and Meteor Crater in Chapter 4.

2. For small craters like Endurance ($D \approx 150$ m), the modes of fracture-azimuth distributions in targets marked by conjugate sets of orthogonal joints should align with maxima of the fourth harmonic amplitude of the crater's planimetric shape. (i.e., fractures align with the square-crater diagonals.)

3. For large craters like Meteor Crater ($D = 1.2$ km), it may occur instead that the modes of fracture-azimuth distributions (of orthogonal joints) align with the *troughs* of the fourth harmonic amplitude of the crater's planimetric shape. (i.e., fractures align with the square-crater walls.)

4. Craters with the extremely large quadrature of Meteor Crater (large A_4') must occur, even if rarely.

5. The modeled distribution of primary harmonics should resemble what is found for the HiRISE-FCC: i.e., the model should replicate the observed distribution of shapes.

6. The modeled dependence of radial deviation upon diameter should also resemble what is observed for the HiRISE-FCC – a power law decay with exponent $\approx -1/2$.

6.2 Model description

When a projectile collides at speeds exceeding the speed of sound in the target (hypervelocity impacts), the target is first compressed by the ensuing shock wave, and is then rapidly unloaded by a decompression wave. The initial kinetic energy of the projectile is partitioned into the internal- and kinetic energy of the projectile and target. The residual velocity of target materials following decompression is responsible for excavating the crater (Melosh [1989]). The crater grows radially away from the site of impact: i.e., an "excavation front" advances from the center toward the final margins of the transient cavity.

Crater excavation is an inherently three-dimensional process, but our concern in this chapter is only to understand the processes which break the *planimetric* radial symmetry that would otherwise produce a circular shape. The model that we propose here is defined in terms of the horizontal dimensions only (i.e., it is two-dimensional, ignoring depth), and these are described using polar coordinates where the origin corresponds to the site of impact. Planes-of-weakness such as fractures and faults are represented as lines (aligned with strike), assumed to span the effective local depth of excavation.

The Stochastic-Kinematic Excavation Model (SKEM) that we propose here relies upon an *ansatz* about the interaction of the excavation flow with fractures in the target. This *ansatz* is just that the velocity of an idealized excavation front (the outermost margin of the expanding cavity in plan view) is increased by some factor when crossing fractures in the target.

The basic model geometry is illustrated in Figure 6-1. Fractures in the target are represented by "fracture elements": lines of constant length λ. A "ray" is a triangular wedge bounded by two straight lines extending from the origin to the circular margin of the model domain, and has length R_0. The widest point along each ray is therefore also the farthest from the origin, and is spanned by one cell width (i.e., one fracture length, λ). Adding narrower rays is not necessary, because the computation (which measures the radially-projected fracture length in each ray) would produce identical or very similar results for all the rays sudividing the same cell at a distance R_0. In this sense, λ serves as a natural fundamental length-scale for the model. The model's radial domain is divided into concentric "rungs," which are the radial positions that fracture elements can occupy. Since all rays have length R_0, there are $N_r \equiv R_0/\lambda$ rungs, and $N_\varphi \approx 2\pi N_r$ rays (i.e., rounded to the nearest integer). The circumference of each rung is close-packed with cells, as shown in Figure 6-1, so that

the number of cells spanning the circumference of a rung increases with rung radius.

As mentioned, we will assume that the excavation front advances at a faster speed while crossing fractures. This is illustrated in Figure 6-2, where the front advances at a speed v_0 along distances not crossing fractures, and $G(\psi)v_0$ where crossing fractures. The quantity ψ is the angle between the direction of excavation (radial direction) and the orientation of a fracture element. We will focus on the case where $G(\psi)$ is constant for all ψ, but we will also briefly consider the effects of a functional dependence on this quantity in Section 6.7. In reality, v_0 is a function of distance from the site of impact; to assume it is constant would appear to be a significant assumption. In fact, adding a radial dependence for v_0 is expected to have almost no consequence for the outcome since we assume that $G(\psi)$ has no radial dependence. That is, all that matters for determining in what directions (in what rays) the excavation front advances farthest is the distance spent crossing fractures, since this is always traversed by a factor $G(\psi)$ faster.

We turn now to computing the radially-projected length of all fracture elements in each ray, in order to know over what distance the excavation front crosses fractures. We first calculate the width of each ray at the position of each rung. This is used at each step of the calculation to find the radially-projected length of each fracture element residing entirely within a given ray. In what follows, we will use the index j to refer to rays, and i to refer to rungs. The coupled subscript i, j is used to refer to a quantity measured at the position of ray j and rung i.

The calculation advances by addressing one ray at a time, moving in a clockwise direction. Rather than calculate the positions of all fracture elements in all rungs over the entire domain at the start, we simplify the computation by keeping track only of fracture elements overlapping the current ray. Moving clockwise, for each ray and at each rung we record: (a) the orientation $\theta_{i,j}$ of the fracture element whose domain overlaps the current ray and (b) the number of rays $p_{i,j}$ that it spans in the clockwise direction, as well as (c) the number of rays $q_{i,j}$ spanned by its *domain*, in the clockwise direction (i.e., this latter quantity is just λ divided by the width of rays at the radial position of a rung; the "domain" of a fracture element is the "cell domain" labeled in Figures 6-2 and 6-1). Also, we record (d) the radially-projected fracture length $x_{i,j}$ in the ray j at each rung i, as well as (e) the angle $\psi_{i,j}$, defined as the difference between the fracture element orientation $\theta_{i,j}$ and the excavation direction φ_j (i.e., the ray's orientation).

The calculation begins with choosing the orientations of fracture elements at each rung of the first ray ($\theta_{i,1}$), sampling from a specified fracture-azimuth distribution (see below), and then computing $p_{i,j}$ and $q_{i,j}$. As the calculation proceeds from one ray to the next (clockwise), $p_{i,j} = p_{i,j-1} - 1$ and $q_{i,j} = q_{i,j-1} - 1$. Where $p_{i,j}$ reaches zero, the radially-projected fracture length within the current ray j at rung i is set to zero (i.e., $x_{i,j} = 0$). Where $q_{i,j}$ reaches zero, a new fracture element orientation θ is selected from the fracture-azimuth distribution, and a new value of $p_{i,j}$ is calculated based on this orientation as well as the width of rays at the rung's position and the constant fracture length λ (N.B. $q_{i,j}$ is also reset). This is repeated 50 times before processing the whole model domain, to prevent the highly unusual "initial" condition (in which all orientations are reset) from influencing outcomes. (Note that results for each ray are correlated to those of its neighbor because only the farthest cell domain does not overlap both of them.) The calculation proceeds through the total number of N_φ rays spanning the entire circumference of the model domain. The products of this calculation are the arrays $x_{i,j}$ and $\psi_{i,j}$.

New values of $\theta_{i,j}$ are sampled from either one of two distributions. For the case of randomly-oriented fractures, this value is just sampled from a uniform distribution. To simulate the case of orthogonal conjugate fracture sets, we sample θ_i from a distribution similar to that measured at Meridiani Planum for the fractures surrounding Endurance Crater. The full width at half maximum (FWHM) measured of azimuthal orientations for those fractures is $\approx 25°$. This corresponds to a standard deviation for the azimuthal joint orientations of $\sigma_J = \text{FWHM}/(2\sqrt{2\ln 2}) \approx$

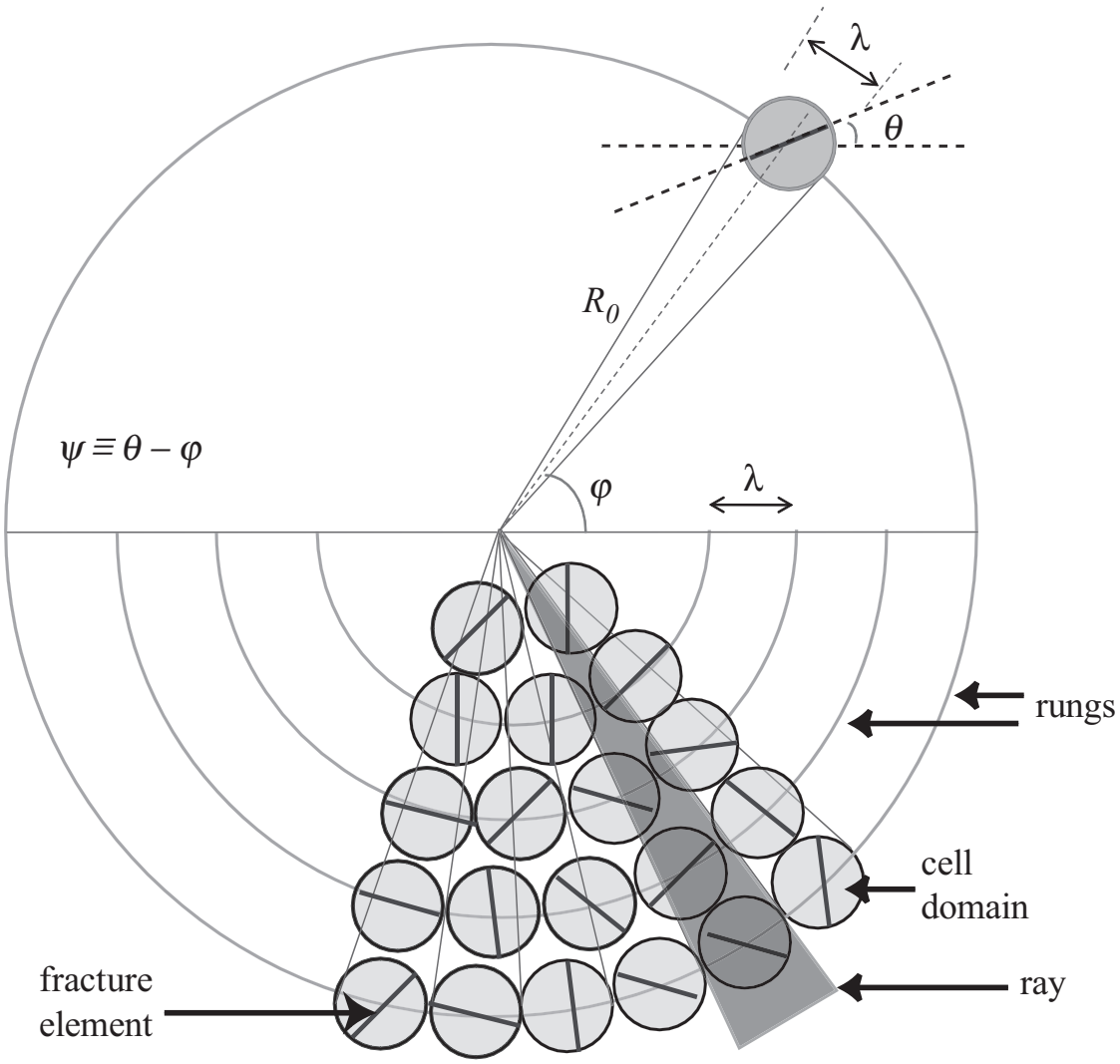

Figure 6-1: Diagram defining important SKEM model quantities and computational elements. Each cell contains a fracture element of length λ, centered upon a "rung" at distance $n\lambda$ from the origin (for integer n). The angle ϕ is the measure of angular position (also the direction of excavation), and θ is the orientation of the fracture element of a given cell. The angle ψ is the difference between the excavation direction and fracture orientation. See text for discussion.

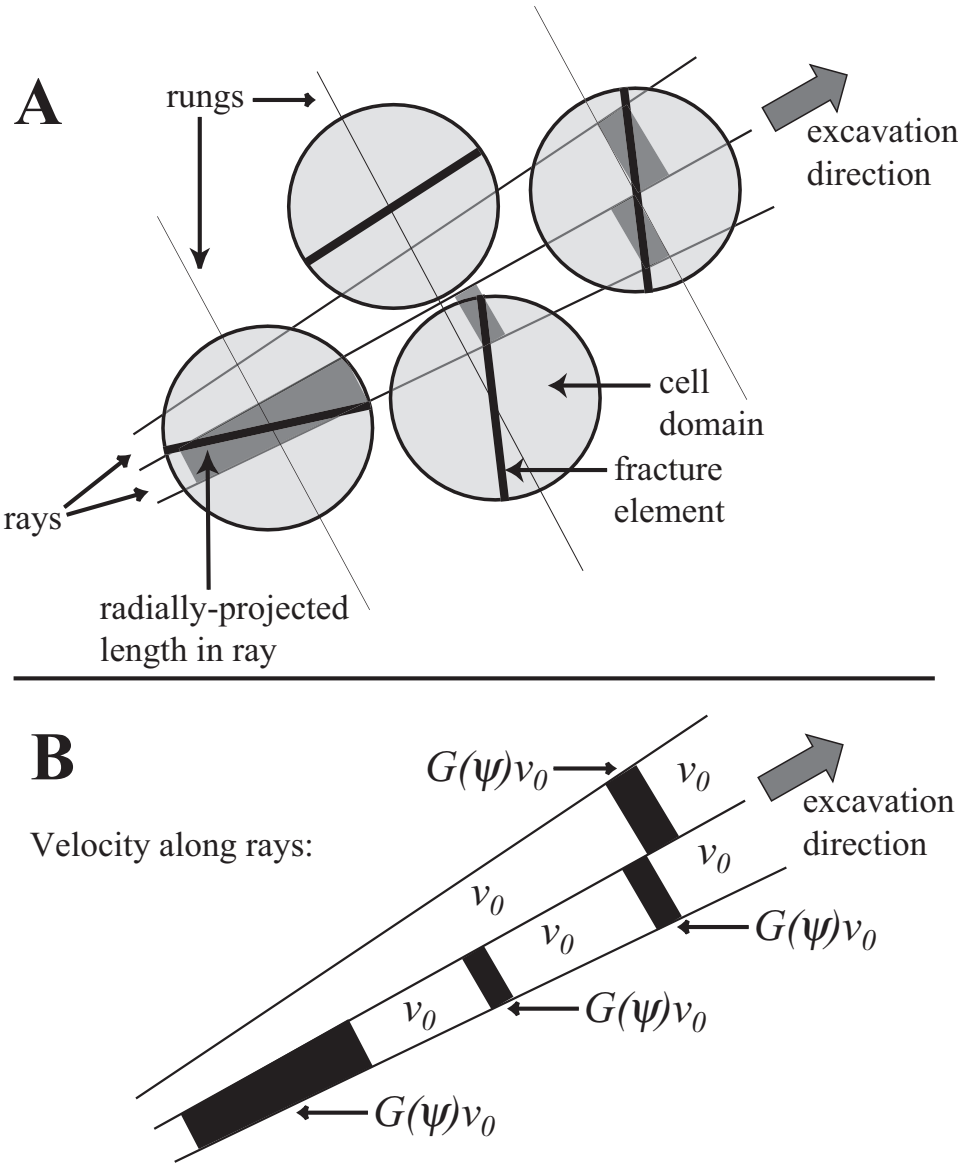

Figure 6-2: Diagrams illustrating the calculation of fracture length projected radially in two rays overlapping four cells. The velocity in the absence of fractures is v_0, whereas the velocity crossing radially-projected fracture lengths is $G(\psi)v_0$.

$\pi/16$. We locate the peaks of the distrubtion at $\pm\pi/4$. Using von-Neumann rejection, we sample the double-Gaussian distribution $P_J(\theta)$ to simulate an orthogonal joint set:

$$P_J(\theta) = \frac{1}{2\sigma_J\sqrt{2\pi}} \sum_{k=1}^{2} \exp\left[\frac{-(\theta - (-1)^k\pi/4)^2}{2\sigma_J^2}\right] \tag{6.1}$$

We turn now to the calculation of R_j, the estimated excavation radius in the ray j that occurs in a time $\tau_{\rm ex}$, using the arrays $x_{i,j}$ and $\psi_{i,j}$, and assuming that the front advances at a speed $G(\psi)v_0$ when crossing fractures and v_0 when not crossing fractures. In overview, we first calculate the amount of time Δt_j required for the excavation front to reach a distance R_0 within each ray. The mean value of this timescale determines the excavation time $\tau_{\rm ex}$ required to excavate a crater of mean radius R_0. The total excavation distance in each ray is then estimated by $R_j = R_0(\tau_{\rm ex}/\Delta t_j)$. As we'll discuss later, the final planimetric shape is the convex hull of the curve traced by (R_j, φ_j) in polar coordinates: i.e., the global excavation front is determined by rays in which the excavation has advanced the farthest.

In what follows, an over-bar (such as $\bar\beta$) represents the mean value of a quantity computed for all rays. Recall that R_0 is the total length of each ray, where all rays have N_r rungs, so that $R_0 = N_r\lambda$. The time Δt_j required for the excavation front to reach R_0 within ray j is therefore given by:

$$\Delta t_j = \sum_{i}^{N_r} \left(\frac{\lambda - x_{i,j}}{v_0} + \frac{x_{i,j}}{G(\psi_{i,j})v_0}\right). \tag{6.2}$$

where $x_{i,j}$ is the radially-projected fracture element length at rung i residing within the ray j (i.e., in the direction φ_j), and where v_0 is the radial front velocity in the absence of fractures. To simplify the notation in what follows, we introduce the following definitions:

$$\gamma_j \equiv \frac{1}{R_0}\sum_{i}^{n} x_{i,j}, \tag{6.3}$$

$$\beta_j \equiv \sum_{i}^{n} \frac{x_{i,j}}{G(\psi_{i,j})}. \tag{6.4}$$

Note that γ_j is the fraction of R_0 spanned by projected fracture lengths within the jth ray. Equation (6.2) can be re-written as:

$$\Delta t_j = \frac{1}{v_0}((1-\gamma_j)R_0 + \beta_j). \tag{6.5}$$

The average excavation time τ_{ex} for all rays is then:

$$\tau_{\rm ex} \equiv \Delta\bar t = \frac{1}{v_0}((1-\bar\gamma)R_0 + \bar\beta). \tag{6.6}$$

We now use the mean and individual calculations of the excavation time within rays to estimate an excavation radius R_j for each ray assuming the crater's mean radius is R_0: i.e., assuming crater excavation occurs over the time $\tau_{\rm ex}$ in all rays:

$$R_j = (R_0/\Delta t_j)\tau_{\rm ex} = R_0\frac{(1-\bar\gamma)R_0 + \bar\beta}{(1-\gamma_j)R_0 + \beta_j} \tag{6.7}$$

The function $G(\psi)$ has the general form:

$$G(\psi) = 1 + (G_0 - 1)g(\psi) \tag{6.8}$$

where $g(\psi)$ ranges from 0 to 1 and G_0 is the largest factor by which v_0 is multiplied. When $G_0 = 1$, then $G(\psi) = 1$ for all ψ. If $g(\psi) = 1$ for all ψ, then $G(\psi) = G_0$ for all ψ. In that case, equation (6.7) simplifies to:

$$R_j(G(\psi) = G_0) = R_0\frac{(1-\bar\gamma)G_0 + \bar\gamma}{(1-\gamma_j)G_0 + \gamma_j} \tag{6.9}$$

In the limit of large G_0, this becomes:

$$\lim_{G_0\to\infty} R_j(G(\psi) = G_0) = \frac{1-\bar\gamma}{1-\gamma_j}R_0 \tag{6.10}$$

We will assume that $G(\psi) = G_0$ and adopt the limit in equation (6.10) by using large values of G_0 (i.e., $G_0 = 1000$) except in Section 6.7, where we explore possible consequences of a ψ dependence. As a result, the model has only one parameter: the dimensionless radius $R^* \equiv R_0/\lambda$. For the remainder of this chapter, we define D^* to be the dimensionless simulated crater diame-

ter, where $D^* = 2R_0/\lambda$. Later, λ will be used to fit model results to observations (i.e., where λ is the fundamental length-scale: a measure of both the uniform fracture length and spacing between fracture elements).

As mentioned earlier, the final planimetric shape is the convex hull of $R_j(\varphi_j)$. That is, the global shape is just determined by those rays in which the excavation front has traveled farthest (N.B. this recalls the "stellar" mode of crater formation, shown in Figure 4-16). Six examples are shown in Figure 6-3: three for the case of randomly-oriented fractures, and three for the case of orthogonal conjugate fractures. We can see at once that conjugate fractures tend to produce square-shaped craters at small and large diameters.

6.3 SKEM Simulated Crater Catalogue (SKEM-SCC)

In this section we use the same tools developed and used in Chapter 5 to analyze the planimetric shape of impact craters in the HiRISE-FCC and MOC-FCC, to compute the same quantities for a population of simulated craters.[1] This simulated population is called the SKEM Simulated Crater Catalogue or SKEM-SCC. Fifty percent of the craters in the SKEM-SCC were generated using the conjugate fracture azimuth distribution in equation (6.1), and the remaining were generated with the assumption that fracture azimuths are uniformly distributed. We begin with a result for simulated craters in orthogonal-conjugate fractured targets. Figure 6-4 shows a bin-averaged plot of the dependence of $|\phi_4|$ with respect to D^*. We find at once that peaks in the fourth harmonic amplitude for small craters ($D^* < 500$) tend to align with peak fracture orientations ($\pm 45°$), whereas for large craters ($D^* > 1500$), the opposite is true (i.e., the walls of a large

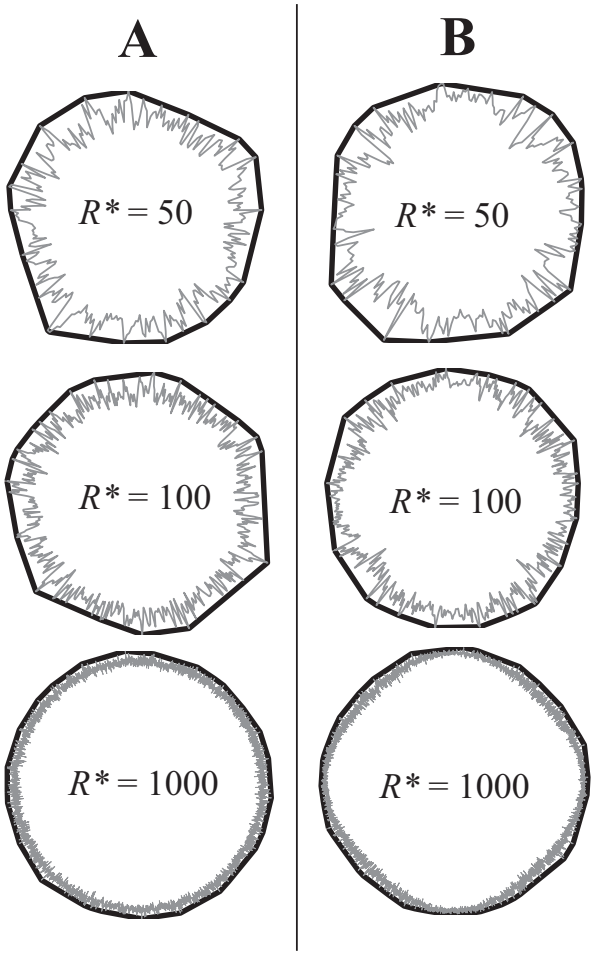

Figure 6-3: Example planimetric crater outlines generated by SKEM for three dimensionless radii and A) randomly-oriented fractures as well as B) orthogonal conjugate fractures. The former case tends to produce a wide range of shapes at small radii, and highly circular craters at large radii. The latter tends to produce a larger fraction of square craters at small radii (where many other shapes occur as well) and large radii (where squares dominate). The gray lines are a plot of $R_j(\phi_j)$, whereas the black solid lines are the convex hull of $R_j(\phi_j)$.

[1] Not reported here are the distributions of harmonic phase angles. These are uniformly distributed for simulated craters in L_2 (randomly-oriented fractures). That the LEB is not observed in the SKEM-SCC distribution of ϕ_2 confirms that the calculations used to estimate this quantity in MOC-FCC and HiRISE-FCC were not themselves the source of the LEB.

square crater align with fractures). That is, we immediately find the relationship between fracture azimuths and crater walls that are opposite for Endurance Crater (small) and Meteor Crater (large).[2] This was already apparent in Figure 6-3, where the large crater exhibits an orientation that differs by 45° with respect to the small crater in the right-hand column. The transition between these two regimes occurs in the diameter range between $D^* = 500$ and $D^* = 1500$. We use these bounds to divide the SKEM-SCC into eight subsets, defined in Table 6.1. The subset L_1 contains all craters in the conjugate-fracture group, while L_2 contains all craters in the "random" fracture group. The remaining groups divide the domain in D^* according to the bounds just obtained from Figure 6-4.

Table 6.1: Subsets of the SKEM-SCC and their defining properties.

Set sym.	Description
L_1	Orthogonal conjugate set of fractures, all D^*
L_2	Randomly-orientated fractures, all D^*
L_3	Conjugate fractures, $D^* < 500$
L_4	Random fractures, $D^* < 500$
L_5	Conjugate fractures, $500 \leq D^* \leq 1500$
L_6	Random fractures, $500 \leq D^* \leq 1500$
L_7	Conjugate fractures, $D^* > 1500$
L_8	Random fractures, all $D^* > 1500$

In Figure 6-5 we have plotted histograms of A_4' for sets L_1 (right) and L_2 (left), along with the value measured for Meteor crater. We find that these distributions roughly accord with what was measured in Chapter 5 for HiRISE-FCC and MOC-FCC, except that L_2 ("random") contains no craters exhibiting the very large quadrature measured for Meteor Crater, whereas a fraction of craters in L_1 match and even surpass this value. With this result, we have so far answered four of the six requirements that a successful model should satisfy, listed at the beginning of this chapter. We turn now to examine the dependence of radial deviation upon diameter, as well as the distribution of other shapes in the simulated population.

[2] i.e., Assuming that fracture length and spacing is approximately the same at both sites (meter-scale), then D^* for Meteor is almost ten times larger than Endurance.

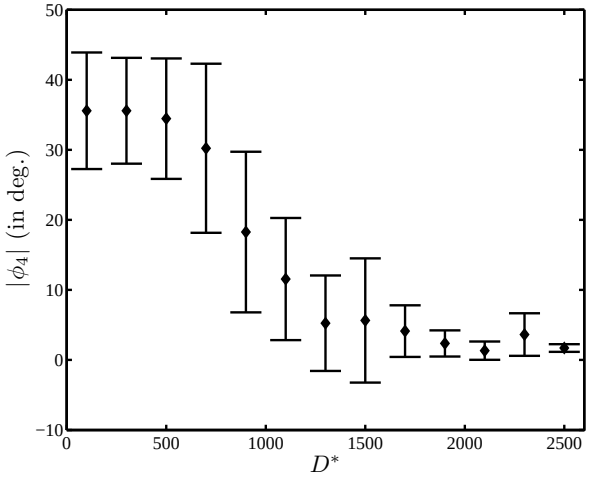

Figure 6-4: Bin-averaged plot of absolute value of the fourth harmonic phase angle ($|\phi_4|$) as a function of dimensionless diameter D^* for craters in the subset L_1 of the SKEM-SCC (i.e., orthogonal conjugate fractures). Error bars correspond to one standard deviation about the mean in each bin. For small D^* (i.e., $D^* < 500$), the peaks of the fourth harmonic are aligned with the modes of the fracture azimuth distribution. For large D^* (i.e., $D^* > 1500$), the troughs of the fourth harmonic are aligned with the modes of the fracture azimuth distribution. That is, the diagonals of a square crater are aligned with fractures for small diameters, and the walls are aligned with fractures for large diameters.

6.4 D^*-dependence of radial deviation

In Figures 6-6 and 6-7 we have plotted the radius-normalized maximum and standard radial deviations versus D^*, respectively, in log-log space. The members of L_1 and L_2 are indicated with contrasting symbols. We notice at once an approximate power-law decay resembling those observed for HiRISE-FCC and MOC-FCC above $D > 100$ m. (The abrupt departure of L_1 craters

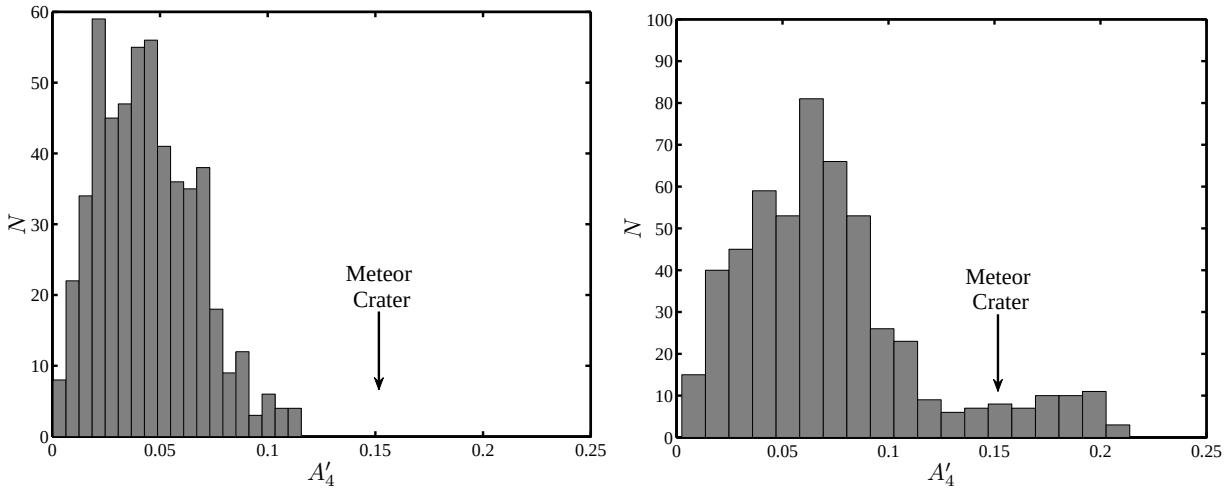

Figure 6-5: Histograms of the deviation-normalized fourth harmonic amplitude for subsets L_2 (randomly-oriented fractures, LEFT) and L_1 (orthogonal conjugate fractures, RIGHT). The value of A'_4 calculated for Meteor Crater is marked with an arrow (see Part C of Figure 5-15). Planimetric shapes with the enormous quadrature measured for Meteor crater do not occur in L_2, but are readily produced in the L_1 population at large D^*.

from this trend at $D^* \approx 1500$ corresponds to the transition in $|\phi_4|$ noted above, and will be addressed later.) As before, we have fitted linear regressions to obtain the dependence of radius-normalized radial deviation for each subset of the SKEM-SCC, and these results are listed in Table 6.2. In subsets of L_2 (random) we find decay law exponents ranging from -0.52 to -0.69 for σ_R^* and -0.50 to -0.64 for ΔR^*. In order to make a direct comparison with the exponents measured for HiRISE-FCC, we have obtained linear regressions for subsets of L_2 in SKEM-SCC having the same range in σ_R^* and ΔR^* as the compared subsets of HiRISE-FCC. In Table 6.3 this comparison is made for HiRISE-FCC subsets L_3 ("Lavas") and L_9^C ("No slides") which exhibit the strongest correlations between radial deviation and crater diameter. Listed in this table are the values of fit parameters m and b (where the latter is expressed in log(meters) for HiRISE-FCC and units of λ for SKEM-SCC: i.e., it is only meaningful to compare the decay-law exponents, m). The best agreement occurs for L_9^C, where exponents differ by as little as 0.02 and as much as 0.05.

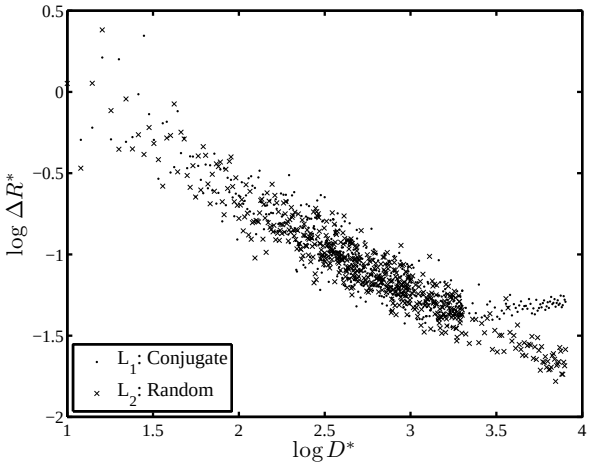

Figure 6-6: Radius-normalized maximum radial deviation (ΔR^*) for impact craters in the SKEM-SCC, as a function of dimensionless diameter D^* in log-log space, where craters belonging to subsets L_1 (conjugate fractures) and L_2 (randomly-oriented fractures) are plotted with contrasting symbols.

Setting the decay laws obtained in Table

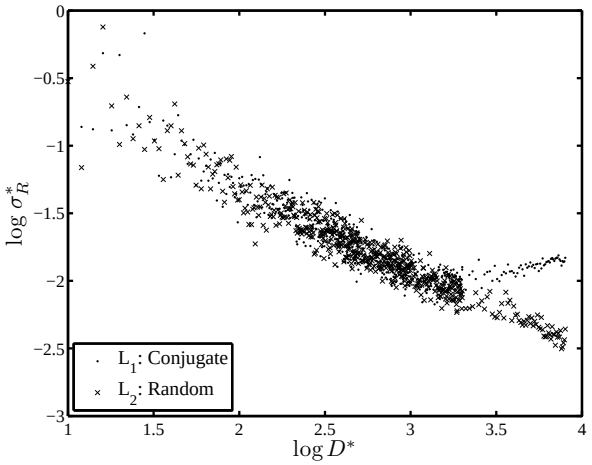

Figure 6-7: Radius-normalized standard radial deviation (σ_R^*) for impact craters in the SKEM-SCC, as a function of dimensionless diameter D^* in log-log space, where craters belonging to subsets L_1 (conjugate fractures) and L_2 (randomly-oriented fractures) are plotted with contrasting symbols.

Table 6.2: For 8 subsets of the **SKEM-SCC**: slope m and intercept b obtained from a linear regression for $\log \sigma_R^* = m \log D + b$ and $\log \Delta R^* = m \log D + b$, along with the Pearson correlation coefficient r_P computed for both relations.

Set	$m_{\Delta R}$	$b_{\Delta R}$	r_P	m_{σ_R}	b_{σ_R}	r_P
L_1	-0.49	0.30	-0.89	-0.47	-0.42	-0.85
L_2	-0.56	0.47	-0.95	-0.61	-0.09	-0.96
L_3	-0.65	0.69	-0.88	-0.71	0.15	-0.90
L_4	-0.64	0.63	-0.90	-0.69	0.08	-0.91
L_5	-0.51	0.29	-0.57	-0.54	-0.32	-0.66
L_6	-0.52	0.34	-0.61	-0.58	-0.20	-0.70
L_7	0.01	-1.34	0.03	0.24	-2.77	0.80
L_8	-0.50	0.27	-0.85	-0.52	-0.39	-0.90

Table 6.3: Linear regressions for maximum and standard radial deviations (ΔR^* and σ_R^*, respectively) in the HiRISE-FCC and SKEM-SCC, as well as the estimated cell size λ (i.e., $\lambda = D/D^*$). Linear fits to modeled data were computed over the domain (in model diameter, D^*) that corresponds to the observed range in radial deviations for the indicated subset of HiRISE-FCC (L_3: Lavas, and L_9^C: absence of talus slides on walls). "Alt." (alternate outlines) is "se" for single-estimate values and "mr" for mid-range values (HiRISE-FCC). See text for discussion.

		HiRISE-FCC	SKEM-SCC	
Set	Alt.	$(m_{\Delta R}, b_{\Delta R})$	$(m_{\Delta R}, b_{\Delta R})$	λ
L_3	se	(-0.44,0.26)	(-0.56,-0.23)	2.64m
L_3	mr	(-0.49,0.22)	(-0.56,-0.23)	2.69m
L_9^C	se	(-0.54,0.54)	(-0.51,-0.35)	2.41m
L_9^C	mr	(-0.53,0.56)	(-0.51,-0.35)	2.89m
Set	Est.	$(m_{\sigma_R}, b_{\sigma_R})$	$(m_{\sigma_R}, b_{\sigma_R})$	λ
L_3	se	(-0.44,-0.38)	(-0.59,0.51)	2.22m
L_3	mr	(-0.49,-0.22)	(-0.59,0.51)	1.03m
L_9^C	se	(-0.47,-0.28)	(-0.51,0.32)	1.79m
L_9^C	mr	(-0.46,-0.27)	(-0.51,0.32)	2.25m

6.3 (for compared subsets of SKEM-SCC and HiRISE-SCC) equal to each other at the center of the HiRISE-FCC diameter range (to ensure maximum overlap), we can solve for the value of λ in order to estimate the size (in real units) of model fracture size and spacing. The results are also listed in Table6.3, where this value ranges from approximately 1 to 3 meters in these comparisons. We will revist this observation in a later section. For now we take a brief excursus in order to illuminate the origin of the approximate $D^{-1/2}$ dependence of radius-normalized radial deviation observed for HiRISE-FCC and now also for SKEM-SCC. For this purpose, suppose that we have a collection of n random variables, where the ith variable is uniformly-distributed between $\pm b_i$. For large n the probability density $p(y)$ of the sum y of these n variables is a Gaussian (Mitra [1971]):

$$p(y) \approx \left[\frac{3}{2\pi \sum_i^n b_i^2}\right]^{1/2} \exp\left[-\frac{3y^2}{2\sum_i^n b_i^2}\right] \quad (6.11)$$

If $b_i = \lambda/2$ (for all i) then the standard deviation σ_y of y scales as $\sigma_y \sim \sqrt{n\lambda^2}$. Since $\bar{y} \approx n\lambda$, the mean-normalized standard deviation scales as $\sigma_y^* \equiv \sigma_y/\bar{y} \sim \sqrt{\lambda/\bar{y}}$. First, this indicates that larger λ pushes the decay-curve to higher values in log-log space. Second, we have uncovered the source of the approximate $D^{-1/2}$ dependence of radius-normalized radial deviation in our model (i.e., $\sigma_y^* \sim \bar{y}^{-1/2}$). The SKEM-SCC exhibits a somewhat steeper slope, however, and this is likely due to the aforesaid correlation between rays (owing to fractures crossing multiple rays), and that the value of $x_{i,j}$ (the radially-projected fracture length at rung i in ray j, analogous to the random variables summed above) is not uniformly distributed. To see this, just consider that projected fracture length within a slender ray varies enormously for values of ψ near 0, and very little for values of ψ near $\pi/2$.

We close this section by observing that the dependence of radial deviation upon diameter is very different for a model in which λ prescribes the length of the straight sides of a regular polygon. If R is the maximum radius of a regular polygon with sides of length λ, then it is easy to show that the dependence of radius-normalized maximum radial deviation is: $\Delta R^* \sim R^{-2}$. i.e.,

$$\Delta R^* = 1 - \sqrt{1 - \left(\frac{\lambda}{2R}\right)^2} \approx \frac{\lambda^2}{8} R^{-2} \quad \left(\text{for } \frac{\lambda}{2R} < 1\right) \quad (6.12)$$

6.5 Distributions of morphometric quantites

We turn now to comparing the distributions of morphometric quantities in subsets of the SKEM-SCC defined in Table 6.1. As before, we have tabulated the tallies of primary harmonics (N_n) and the means and standard deviations of morphometric quantities in Tables 6.4 and 6.5. The number of difference metrics (Table 5.6) measuring statistically significant differences between subsets of the SKEM-SCC are displayed in Figure 6-8 and a detailed compilation of these results is supplied in Table 6.6 for a Gaussian reference distribution. Cumulative distributions of important harmonic amplitudes and radial deviations are shown in Figure 6-9 for the comparison (L_3, L_4), 6-10 for the comparison (L_5, L_6), and 6-11 for the comparison (L_7, L_8).

We find for small craters ($D^* < 500$) that the most affected quantities are the low-order harmonic amplitudes A_3' through A_5', with on-average larger values of A_4' (higher quadrature) occurring in conjugate fractures. (The amplitudes A_3' and A_5' are comparatively small for this group.) Detrended radial deviations are also larger on average for simulated craters forming amid conjugate fractures. The pattern of larger A_4', σ_R^* (and ΔR^*), and smaller A_3 accords with the comparisons of non-lavas (some conjugate fractures) and lavas (randomly-oriented fractures) in the HiRISE-FCC. The same pattern holds for large craters, where all but A_8' are markedly different. We shall discuss this comparison (i.e., (L_7, L_8)) in more detail in a later section. For now, we should also remark that the highest-order harmonic shown here, A_8', exhibits almost no contrast between compared subsets in any diameter range, consistent with the rel-

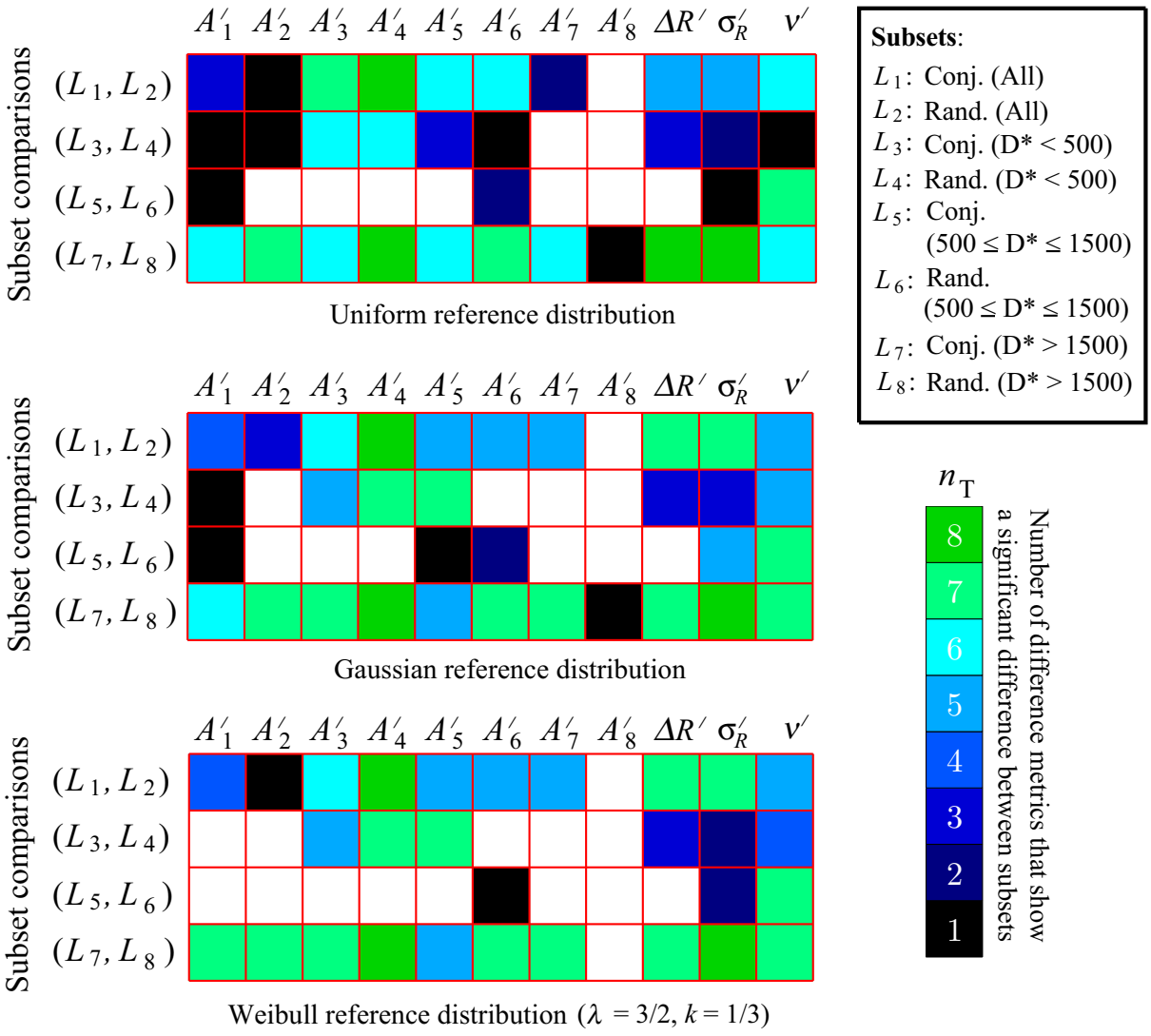

Figure 6-8: The number of absolute difference metrics (Δ_1 through Δ_8, defined in Table 5.6) measuring a statistically significant difference between compared subsets of the SKEM-SCC at the 95% level with respect to a uniform (TOP), Gaussian (MIDDLE), and Weibull (BOTTOM) reference distribution, for the first eight deviation-normalized harmonic amplitudes, as well as detrended radial deviations and concave fraction.

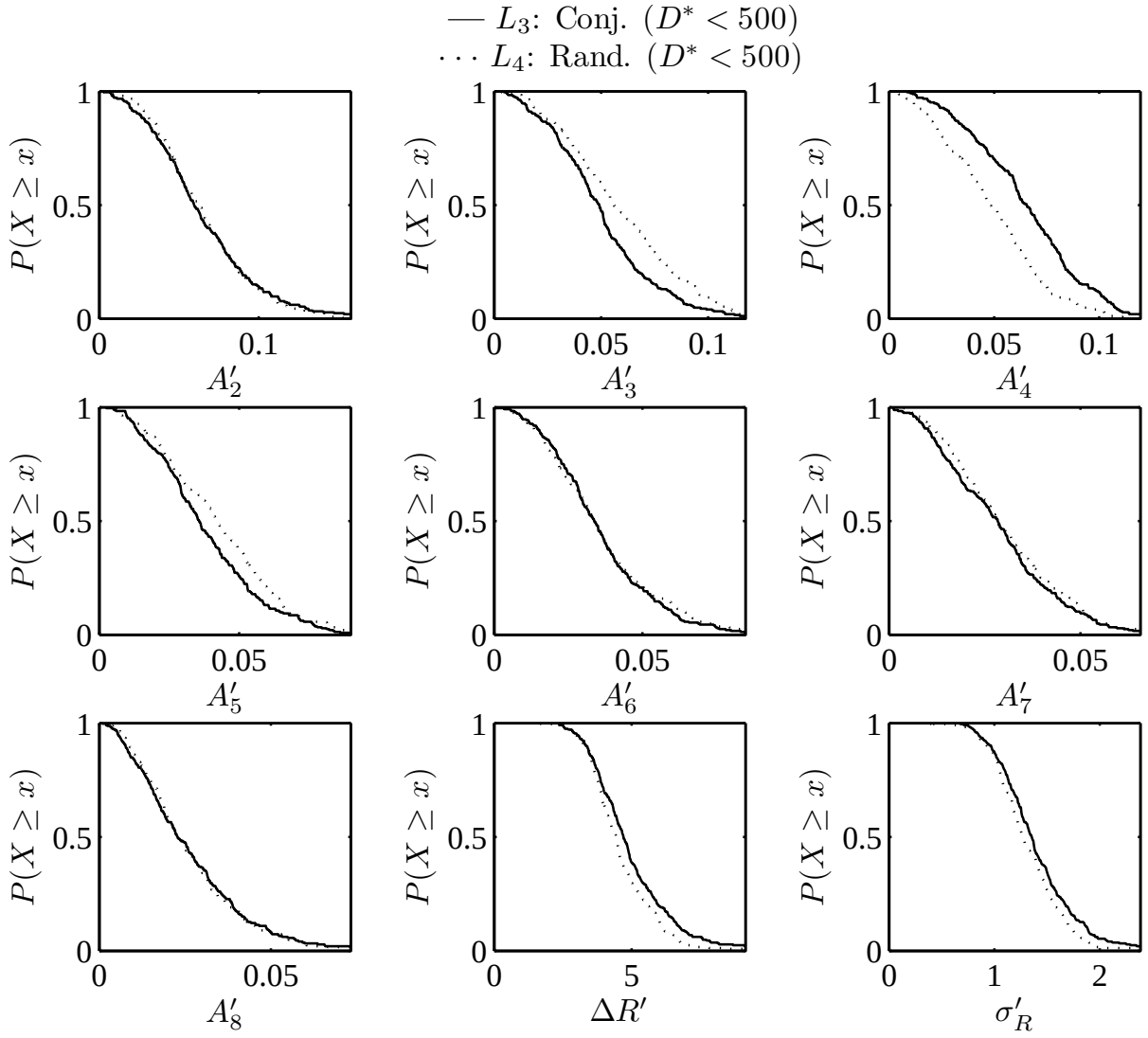

Figure 6-9: Cumulative distributions of deviation-normalized harmonic amplitudes A'_2 through A'_8 as well as detrended radial deviations, for the comparison of subsets L_3 and L_4. See text for discussion.

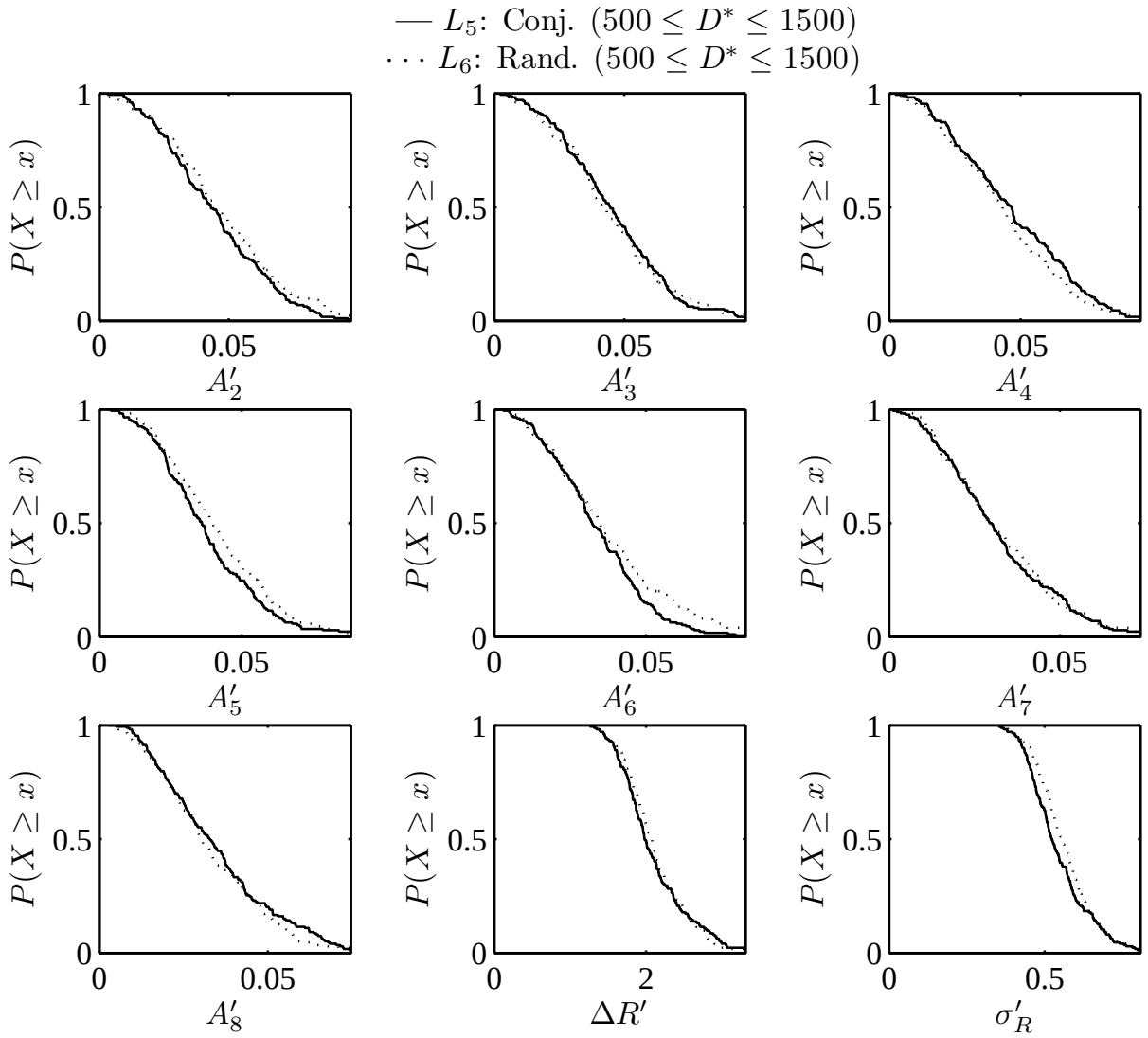

Figure 6-10: Cumulative distributions of deviation-normalized harmonic amplitudes A'_2 through A'_8 as well as detrended radial deviations, for the comparison of subsets L_5 and L_6. Curiously, for intermediate diameters, A'_6 exhibits the most significant difference. See text for discussion.

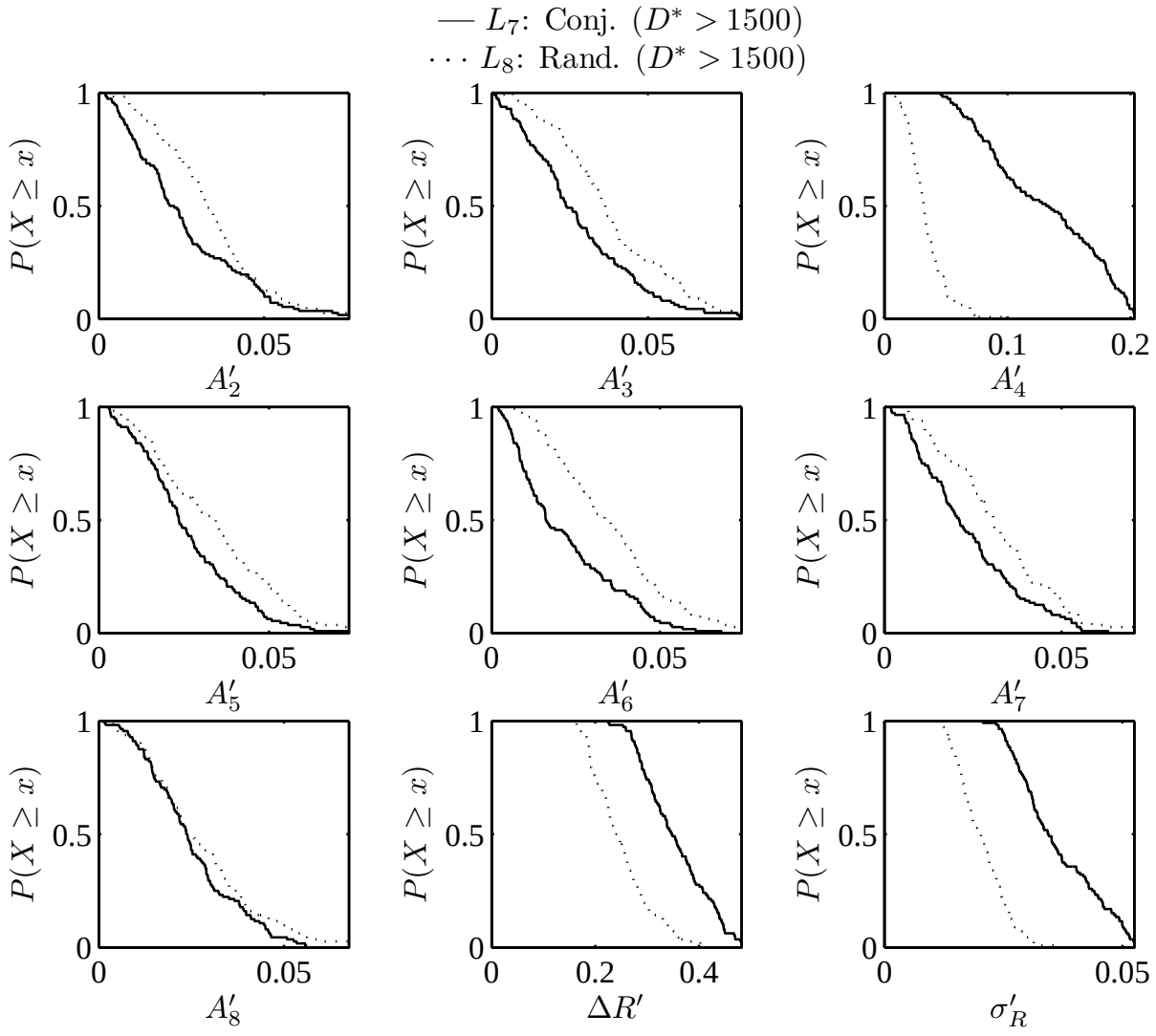

Figure 6-11: Cumulative distributions of deviation-normalized harmonic amplitudes A'_2 through A'_8 as well as detrended radial deviations, for the comparison of subsets L_7 and L_8. See text for discussion.

Table 6.4: Global properties of shape distributions for 8 subsets of the **SKEM-SCC**. Listed are the number of triangles (N_3), squares (N_4), pentagons (N_5), and hexagons (N_6) in each subset, along with mean ± standard deviation of detrended maximum and standard radial deviations ($\Delta R'$ and σ'_R, respectively) and concave fraction (ν').

Set	N	N_3	N_4	N_5	N_6	σ'_R	$\Delta R'$	ν'
L_1	532	103	292	52	37	0.65 ± 0.35	2.68 ± 1.03	1.201 ± 0.036
L_2	532	181	123	93	65	0.54 ± 0.19	2.36 ± 0.67	1.213 ± 0.034
L_3	246	54	134	29	17	1.42 ± 0.53	4.97 ± 1.68	1.053 ± 0.018
L_4	246	102	62	41	23	1.33 ± 0.41	4.61 ± 1.31	1.056 ± 0.016
L_5	174	48	51	21	20	0.54 ± 0.10	2.10 ± 0.48	1.323 ± 0.029
L_6	174	46	45	32	27	0.56 ± 0.10	2.13 ± 0.44	1.342 ± 0.026
L_7	112	1	107	2	0	0.04 ± 0.01	0.36 ± 0.07	1.657 ± 0.045
L_8	112	33	16	20	15	0.02 ± 0.01	0.25 ± 0.06	1.690 ± 0.040

ative paucity of changes to this harmonic noted in subset comparisons of the HiRISE-FCC. Intriguingly, the sixth harmonic exhibits the most significant change between conjugate and random fractures for craters in the transitional diameter range (i.e., for $500 \leq D^* \leq 1500$, compared in (L_5, L_6)). That is, although the conjugate fractures exhibit symmetries consistent with $n = 4$ and $n = 8$, craters forming amid "random" fractures have on-average significantly larger A'_6 in the high-amplitude range. It is not known whether this or a related effect may account for the marked sensitivity of $n = 6$ noted earlier for the HiRISE-FCC, but there is currently no compelling reason to draw this connection. Most of the comparisons in which $n = 6$ is strongly affected (in HiRISE-FCC) were not related to an expected contrast between joint-patterns in the target.

6.6 Dominant harmonics

We turn now to comparisons of distributions of dominant harmonics, between subsets of the SKEM-SCC, and between observations and simulated results. Histograms of the primary, secondary, and tertiary harmonics for L_4 (randomly-oriented fractures and small craters) are shown in Figure 6-12. Like the results for HiRISE-FCC, we find that $n = 3$ is the most common primary harmonic, $n = 4$ the most-common secondary harmonic, and $n = 6$ the most-common tertiary harmonic. We have plotted the two-dimensional histogram of primary and secondary harmonics in Figure 6-13 for $L_3, L_4, ..., L_8$ (i.e., for each of the diameter regimes). We can see that $n = 4$ is the primary harmonic for conjugate-fracture targets at small and large diameters, but not for intermediate diameters.

The noticeably larger range in dominant harmonics (when compared with HiRISE-FCC) occurs because of the larger diameters represented in the SKEM-SCC. (i.e., the largest diameter in the HiRISE-FCC is ≈ 4 km, whereas the largest diameter in the SKEM-SCC is $10^4\lambda \approx 30$ km.) Over this range, the effect of differences in sampled diameters discussed in Chapter 5 is clearly important: i.e., at large diameters, radial deviation is small enough that many higher-order harmonics can dominate the amplitude spectrum. In order to make a direct comparison between model results and observations, we must sample the model over a similar range in diameters, or preferrably at identical diameters. We have therefore sampled SKEM using the diameter distribution in HiRISE-FCC as a whole, for three values of λ used to normalize model diameters (i.e., $D = \lambda D^*$, for $\lambda = 2.0$ m, 3.5 m, and 5.0 m). The primary harmonic fractions (i.e., N_n/N, the fraction of craters with primary harmonic n) for HiRISE-FCC as a whole and the "lava" subset are compared with SKEM-SCC results (assuming the aforesaid values of λ)

Table 6.5: Global properties of shape distributions for 8 subsets of the **SKEM-SCC**. Listed are the mean ± standard deviation of deviation-normalized harmonic amplitudes A'_2 through A'_8.

Set	N	A'_2	A'_3	A'_4	A'_5	A'_6	A'_7	A'_8
L_1	532	0.050 ± 0.031	0.044 ± 0.024	0.073 ± 0.044	0.036 ± 0.019	0.032 ± 0.018	0.029 ± 0.016	0.029 ± 0.017
L_2	532	0.053 ± 0.028	0.050 ± 0.026	0.044 ± 0.023	0.040 ± 0.020	0.036 ± 0.019	0.031 ± 0.016	0.029 ± 0.016
L_3	246	0.065 ± 0.034	0.050 ± 0.025	0.065 ± 0.027	0.038 ± 0.020	0.036 ± 0.018	0.029 ± 0.016	0.026 ± 0.017
L_4	246	0.065 ± 0.030	0.059 ± 0.028	0.049 ± 0.025	0.043 ± 0.021	0.036 ± 0.019	0.030 ± 0.015	0.026 ± 0.016
L_5	174	0.045 ± 0.021	0.045 ± 0.021	0.047 ± 0.023	0.038 ± 0.018	0.034 ± 0.016	0.032 ± 0.018	0.035 ± 0.018
L_6	174	0.047 ± 0.023	0.045 ± 0.022	0.044 ± 0.022	0.042 ± 0.019	0.037 ± 0.020	0.033 ± 0.018	0.033 ± 0.016
L_7	112	0.026 ± 0.018	0.028 ± 0.018	0.130 ± 0.049	0.026 ± 0.015	0.022 ± 0.016	0.024 ± 0.015	0.025 ± 0.013
L_8	112	0.034 ± 0.016	0.038 ± 0.018	0.034 ± 0.016	0.034 ± 0.018	0.035 ± 0.017	0.032 ± 0.015	0.028 ± 0.015

Table 6.6: Quantities and difference metrics (Δ_n : for $n = 1, 2, ...$; defined in Table 5.6) that indicate a statistically significant difference for 4 pairings of 8 subsets of the SKEM-SCC, with respect to differences computed for 10,000 pairings of randomly-sampled subsets of a **Gaussian** reference distribution on the same domain. Listed are metrics reporting differences that exceed the percentage p_{lim} of differences computed from paired subsets of the reference distribution. Not listed are results for linear combinations of the deviation-normalized harmonics (i.e., the quantities Q_n^m).

Set	p_{lim}	Quantities whose distributions differ at the level p_{lim}
(L_1,L_2)	95%	A'_1 (Δ_n : 3,4,7,8), A'_2 (Δ_n : 4,7,8), A'_3 (Δ_n : 2,3,5,6,7,8), A'_4 (Δ_n : 1,2,3,4,5,6,7,8), A'_5 (Δ_n : 3,5,6,7,8), A'_6 (Δ_n : 3,5,6,7,8), A'_7 (Δ_n : 3,5,6,7,8), $\Delta R'$ (Δ_n : 1,3,4,5,6,7,8), σ'_R (Δ_n : 1,3,4,5,6,7,8), ν (Δ_n : 3,5,6,7,8)
	97.5%	A'_1 (Δ_n : 3,4,8), A'_3 (Δ_n : 3,5,6,7,8), A'_4 (Δ_n : 1,2,3,4,5,6,7,8), A'_5 (Δ_n : 3,5,6,7,8), A'_6 (Δ_n : 3,5,6,7,8), A'_7 (Δ_n : 3,5,6,7,8), $\Delta R'$ (Δ_n : 1,3,4,5,6,7,8), σ'_R (Δ_n : 1,3,4,5,6,7,8), ν (Δ_n : 3,5,6,7,8)
	99%	A'_1 (Δ_n : 3,4,8), A'_3 (Δ_n : 3,5,6,7,8), A'_4 (Δ_n : 1,2,3,4,5,6,7,8), A'_5 (Δ_n : 3,5,6,7,8), A'_6 (Δ_n : 3,5,6,7,8), A'_7 (Δ_n : 3,5,6,7,8), $\Delta R'$ (Δ_n : 1,3,4,5,6,7,8), σ'_R (Δ_n : 1,3,4,5,6,7,8), ν (Δ_n : 3,5,6,7,8)
(L_3,L_4)	95%	A'_1 (Δ_n : 8), A'_3 (Δ_n : 3,5,6,7,8), A'_4 (Δ_n : 1,2,3,5,6,7,8), A'_5 (Δ_n : 1,2,3,5,6,7,8), $\Delta R'$ (Δ_n : 3,4,8), σ'_R (Δ_n : 3,4,8), ν (Δ_n : 3,5,6,7,8)
	97.5%	A'_3 (Δ_n : 3,5,6,7,8), A'_4 (Δ_n : 1,2,3,5,6,7,8), A'_5 (Δ_n : 1,3,5,6,7,8), $\Delta R'$ (Δ_n : 3,4,8), σ'_R (Δ_n : 3,4,8), ν (Δ_n : 5,6,7,8)
	99%	A'_3 (Δ_n : 3,5,6,7,8), A'_4 (Δ_n : 1,2,3,5,6,7,8), A'_5 (Δ_n : 7,8), $\Delta R'$ (Δ_n : 3,4,8), σ'_R (Δ_n : 4), ν (Δ_n : 7)
(L_5,L_6)	95%	A'_1 (Δ_n : 8), A'_5 (Δ_n : 8), A'_6 (Δ_n : 4,8), σ'_R (Δ_n : 3,5,6,7,8), ν (Δ_n : 1,2,3,5,6,7,8)
	97.5%	A'_1 (Δ_n : 8), A'_6 (Δ_n : 4,8), σ'_R (Δ_n : 7,8), ν (Δ_n : 1,2,3,5,6,7,8)
	99%	A'_6 (Δ_n : 4,8), ν (Δ_n : 1,3,5,6,7,8)
(L_7,L_8)	95%	A'_1 (Δ_n : 3,4,5,6,7,8), A'_2 (Δ_n : 1,2,3,5,6,7,8), A'_3 (Δ_n : 1,2,3,5,6,7,8), A'_4 (Δ_n : 1,2,3,4,5,6,7,8), A'_5 (Δ_n : 3,5,6,7,8), A'_6 (Δ_n : 1,2,3,5,6,7,8), A'_7 (Δ_n : 1,2,3,5,6,7,8), A'_8 (Δ_n : 4), $\Delta R'$ (Δ_n : 1,2,3,5,6,7,8), σ'_R (Δ_n : 1,2,3,4,5,6,7,8), ν (Δ_n : 1,2,3,5,6,7,8)
	97.5%	A'_1 (Δ_n : 3,4,5,6,7,8), A'_2 (Δ_n : 1,2,3,5,6,7,8), A'_3 (Δ_n : 2,3,5,6,7,8), A'_4 (Δ_n : 1,2,3,4,5,6,7,8), A'_5 (Δ_n : 3,5,6,7,8), A'_6 (Δ_n : 1,2,3,5,6,7,8), A'_7 (Δ_n : 1,2,3,5,6,7,8), A'_8 (Δ_n : 4), $\Delta R'$ (Δ_n : 1,2,3,5,6,7,8), σ'_R (Δ_n : 1,2,3,4,5,6,7,8), ν (Δ_n : 1,2,3,5,6,7,8)
	99%	A'_1 (Δ_n : 3,4,5,6,7,8), A'_2 (Δ_n : 1,2,3,5,6,7,8), A'_3 (Δ_n : 2,3,5,6,7,8), A'_4 (Δ_n : 1,2,3,4,5,6,7,8), A'_5 (Δ_n : 3,5,6,7,8), A'_6 (Δ_n : 1,2,3,5,6,7,8), A'_7 (Δ_n : 2,3,5,6,7,8), $\Delta R'$ (Δ_n : 1,2,3,5,6,7,8), σ'_R (Δ_n : 1,2,3,4,5,6,7,8), ν (Δ_n : 1,2,3,5,6,7,8)

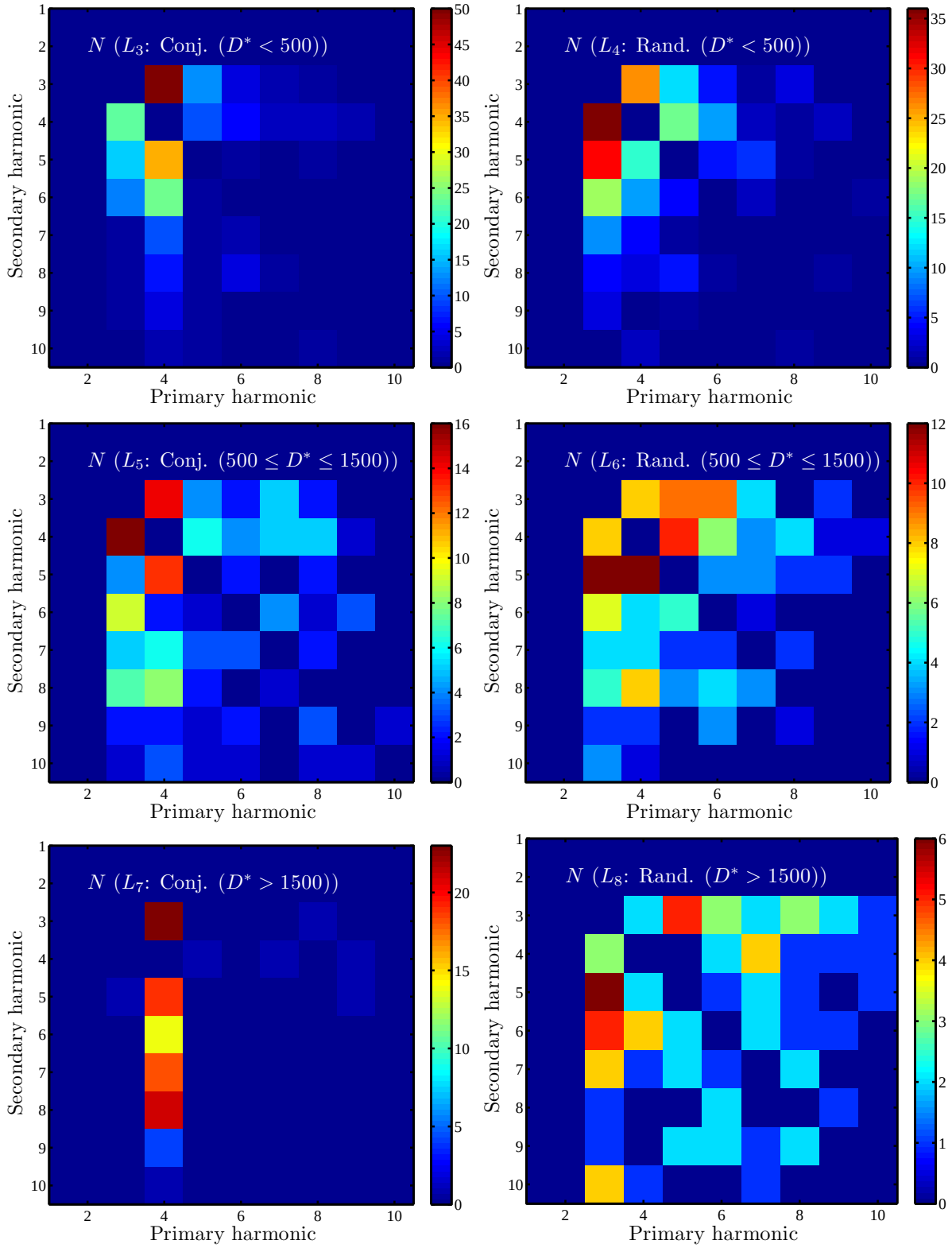

Figure 6-13: Two-dimensional histograms of primary and secondary harmonics for six subsets of the SKEM-SCC. The 3rd harmonic dominates for all randomly-oriented fracture targets and for conjugate fractures in the range of intermediate diameters. The fourth harmonic dominates orthogonal-conjugate fracture subsets at small and large diameters.

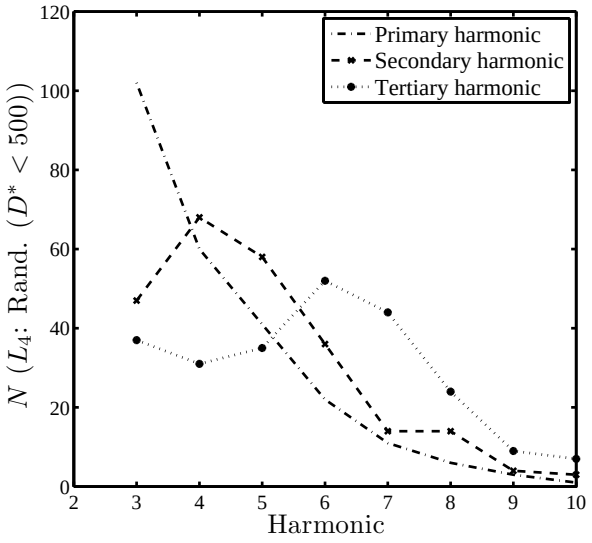

Figure 6-12: Histograms of primary, secondary, and tertiary harmonics for subset L_4 of the SKEM-SCC (i.e., randomly-oriented fractures at small diameters). Of all subsets, the histogram of dominant-harmonics for L_4 most closely resembles corresponding results for HiRISE-FCC and MOC-FCC.

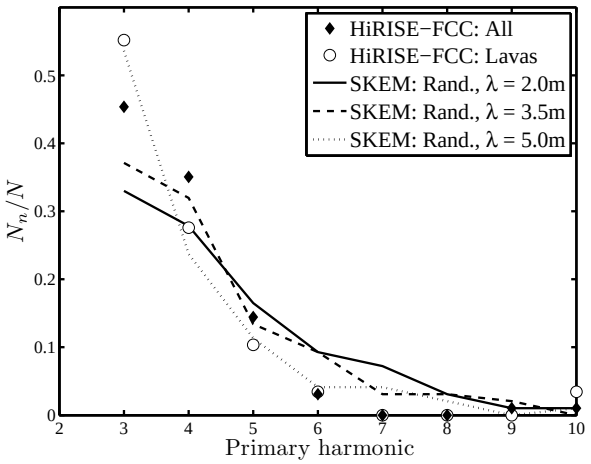

Figure 6-14: Principal harmonic fractions (N_n/N) for harmonics $n = 3$ through $n = 10$ from simulated (SKEM) and HiRISE-FCC crater populations. (e.g., N_3/N is the fraction of craters in the set whose primary harmonic is $n = 3$.) To generate the SKEM distribution, we have sampled the model with a diameter distribution identical to that of the entire HiRISE-FCC, assuming three values of the fracture element length, λ (used to dimensionalize D^*). In this case, we assumed randomly-oriented fractures to generate the SKEM results. Principal harmonic fractions for two subsets of the HiRISE-FCC are plotted: the entire data set, as well as all those craters formed in targets with material class 4 (i.e., "lavas"). (N.B. the CSC has not been enforced.)

for randomly-oriented fractures in Figure 6-14. In Figure 6-15 this exercise is repeated for the "not-lava" subsets of HiRISE-FCC and conjugate fractures in SKEM-SCC. Squares are seen to outnumber triangles by roughly the amount expected. In both figures, agreement is good in the range from $\lambda = 3.5$ m to $\lambda = 5.0$ m. That is, we find that SKEM is able to approximately reproduce the distribution of crater shapes observed in the HiRISE-FCC as a whole as well as in subsets expected to favor certain kinds of fracture-networks. With this latest finding, the model has met all of the requirements stipulated at the beginning of the chapter.

6.7 Acceleration function $G(\psi)$

We briefly consider the consequences if the acceleration factor (G) has a functional dependence on ψ, the angle between the direction of excavation and the orientation of fractures. A reasonable candidate function for $g(\psi)$ in equation (6.8) (where $G(\psi)$ is defined) will have a maximum in the vicinity of $\psi = 0$ (i.e., excavation is made easier along planes of weakness), where this peak may have variable widths, and where the acceleration factor away from this peak is zero or else a nonzero constant. A candidate function that satisfies these requirements is described by the following equation, also plotted in Figure 6-16 for several values of Q_0 and σ_ψ:

$$g(\psi) = (1 - Q_0) + Q_0 \exp\left[\frac{-\psi^2}{(2\sigma_\psi^2)}\right] \qquad (6.13)$$

In Figure 6-17 we have plotted the SKEM-computed and bin-averaged σ_R^* versus D^* for several values of Q_0, σ_ψ, and G_0, finding that the diameter marking the departure from power-

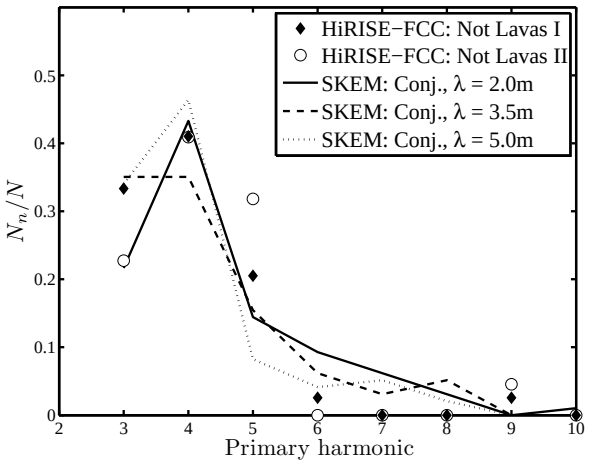

Figure 6-15: Principal harmonic fractions (N_n/N) for harmonics $n = 3$ through $n = 10$ from simulated (SKEM) and HiRISE-FCC non-lava crater populations. (See caption to Figure 6-14.) In this case, we assumed orthogonal conjugate fractures to generate the SKEM results. Principal harmonic fractions for two subsets of the HiRISE-FCC are plotted: "Not Lavas I": craters formed in targets with material classes 1,2, and 3, and "Not Lavas II": craters formed in targets with material classes 1, 2, 3, and 6. (N.B. the CSC has not been enforced.)

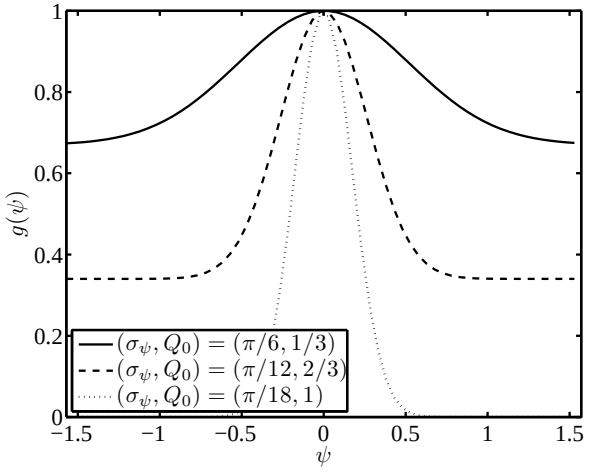

Figure 6-16: The acceleration function $g(\psi)$ as defined in equation (6.13) for example values of the parameters σ_ψ and Q_0.

law decay (earlier noted in Figure 6-7) is shifted. The magnitude of this shift is the only significant difference observed for a wide range of parameter values to the candidate function $g(\psi)$. We will touch on the importance of this departure from power-law decay in the next section.

6.8 Outstanding questions

We turn now to the discussion of some remaining questions. In the SKEM-SCC analysis we have found two explanations for the larger radial deviations measured for craters formed in "non-lava" targets with respect to craters formed in "lava" targets: (a) for the small diameter range ($D^* < 500$) this is observed for the comparison between "random" and "conjugate" fractures in SKEM-SCC (see Figure 6-9). (b) The departure from power-law decay of radial deviation at large diameters of craters formed in conjugate-fracture targets (SKEM-SCC) may contribute to this difference as well. That is, sets of coherent fractures in the target, for sufficiently large diameters, may result in very significant departures from circularity that cannot occur in targets with randomly-oriented fractures (e.g., lavas), and this may account for why large craters in lavas tend to be more circular on average. In reality, systematic fracture sets that are coherent (aligned) over large distances may occur in multiple orientations (i.e., other configurations are possible apart from the two sets of orthogonal fractures explored here). For small numbers of fracture sets and modal fracture azimuths, this will tend to produce shapes that are dominated by the lower harmonics, especially in $n = 4$, $n = 5$, and $n = 6$. It is important to bear in mind that principal orientations in the fracture-azimuth distribution may also change or vanish over the region in which a crater forms, making possible a wide range of shapes at larger diameters that are influenced by this effect.

We have obtained the value of λ by comparing SKEM-SCC results to observations in two ways: i.e., by comparing the distribution of σ_R^* as a function of D^* as well as by comparing the distribution of primary harmonic fractions (N_n/N). In the former case we found that λ

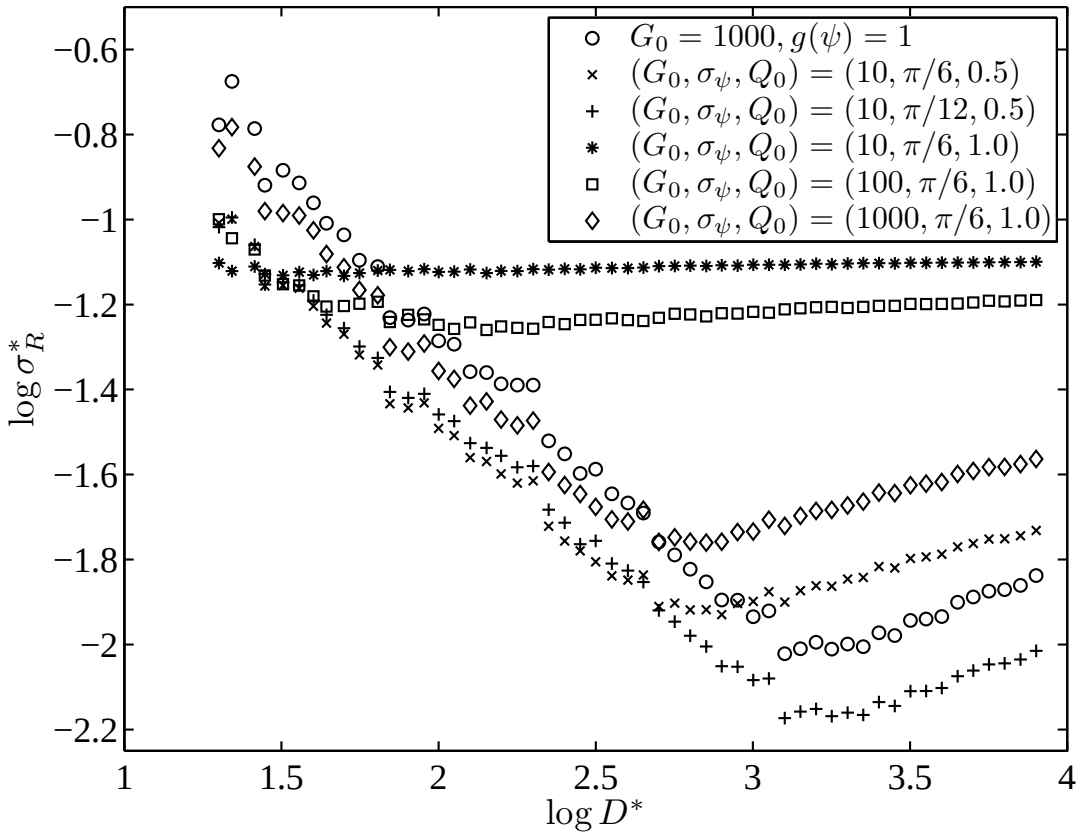

Figure 6-17: Radius-normalized standard radial deviation (σ_R^*) versus dimensionless diameter (D^*) in log-log space for multiple values of the acceleration factor G_0 and parameters σ_ψ and Q_0 of $g(\psi)$ (see equation (6.13)). The critical diameter for departing from power-law behavior depends on all three parameters. For a broad space of parameter values, the overall pattern of the D^*-dependence of radial deviation is the same: i.e., a power law decay and abrupt departure at some D^*.

ranges from 1 to 3 m, and in the later case we found that λ ranges from 3.5 to 5 m. The source of this discrepancy may lie with the former result, since choosing to equate the linear regressions for modeled and observed data at the middle-range of HiRISE-FCC diameters is somewhat arbitrary (see Section 6.4). In either case, we might suppose that $\lambda \approx 3.25$ m, at the middle of this range of estimates. In reality, the separation of fractures in lavas ranges from 0.25 to 2.0 m (Grossenbacher and McDuffie [1995]), so that λ seems somewhat too large. It should be noted first that fractures in our model are not close-packed like those in columnar jointing, so that a direct comparison is not necessarily possible. Second, λ is effectively a measure of the length-scale separating fractures as well as the distance over which *fracture orientations are consistent*. That is, although columnar joints may exhibit separations as small as 0.25 m, they can exhibit significant alignments spanning several meters (beyond which this coherence is erased).

In Chapter 5 we found evidence that the horizontal impact angle may often determine the orientation of the second harmonic, and may significantly influence the fourth harmonic as well. In SKEM, this effect is not taken into consideration, and the second harmonic is entirely determined by the distribution of fractures. This must undoubtedly affect the comparison between model and observed distributions (and hence the value of λ), but it is not immediately obvious how this difference should be taken into account. Moreover, a significant prediction of the model is that craters forming in targets with fractures exhibiting a single orientation should be significantly elongated in one direction. Although we have observed rare populations of small craters demonstrating significant elongations, we cannot rule-out that this was caused by the LEB described in Chapter 5. That such populations are rare may pose a problem for the model, or else indicates that fracture sets marked by a single orientation are extremely rare on the surface of Mars.

Finally, although SKEM suggests that the power-law decay of radial deviation as a function of diameter is an outcome of increasing crater size with respect to the size and spacing of fracture elements, it should be noted that this effect may have other sources. For example, the increasing impact energy that produces larger craters may also destroy target structures and strength heterogeneities that can influence the excavation flow (and which introduce asymmetries), such as by comminution and acoustic fluidization.

Appendix A

Auxiliary Material for Chapter 3

A.1 Spreading time-scale relation: estimated parameter values

Estimates of the spreading time-scale, t_s, have the following dependence on the dimensionless perturbation parameters $\Theta \equiv \Delta T_p / \Delta T_c$, $\Lambda \equiv \lambda_p / \lambda_m$, and the Rayleigh number:

$$t_s = K_0 \Theta^{\alpha} \Lambda^{\beta} Ra_{(H)}^{\gamma} \tag{A.1}$$

The values of the exponents α, β, and γ were estimated by means of a simple parameter search, minimizing the residuals of a least-squares linear regression to plots of t_{s1} versus $\Theta^{\alpha} \Lambda^{\beta} Ra_{(H)}^{\gamma}$ in log-log space. In particular, the values of β and γ were determined by the parameter search directly, and the values of α and K_0 were then fixed by the slope and intercept of the fitted line. In the main body of the text we reported the estimates obtained from the inversion conducted in exactly this way.

In Tables A.1 and A.2 of this appendix we report the results of the inversion conducted for each Rayleigh number separately. It is worth noting that the value of α is significantly larger for the lowest Rayleigh number in set A. A trend toward increasing α with decreasing Rayleigh number is however not observed in the other sets.

In these tables we also report the crossover limit explicitly: i.e., the combination of values of Θ and Λ where a transition occurs to power-law behavior at low perturbation magnitudes. We have reported the estimated values of α and β for each Rayleigh number, where the inversion was performed with and also without the results for perturbations below this limit.

A.2 Type I perturbations and global stagnation

In Section 3.6 of the main text we related perturbations of type I to perturbations of type II and the critical impact magnitude for global stagnation, assuming a convective driving temperature ΔT_c and the high Rayleigh numbers appropriate for the early solar system. In Figures A-1 and A-2 of this appendix we supply the same diagrams for the Earth and Mars, respectively, although assuming a modern and intermediate value of ΔT_c (parts (a) and (b)). See Section 3.6 of the main text for the values of other parameters (such as mantle thickness and mean mantle density) assumed for this calculation.

Table A.1: Estimated parameter values for $t_{s1} = K_0 \Theta^{\alpha} \Lambda^{\beta} Ra_{(H)}^{\gamma}$, obtained by means of a simple parameter search, minimizing the norm of residuals from a least-squares linear regression in log-log space. Also reported are the 95.4% confidence limits from a bootstrap analysis ($N = 1000$ random samplings with replacement), where: $Ra_{(H)}$ = Rayleigh number (internal heating Rayleigh number if $H > 0$); H = dimensionless internal heating; BC = upper boundary condition (where "f" = stress-free and "r" = rigid (i.e., no-slip)); "IC" = initial condition (where "t.i." = time-independent and "t.d." = time-dependent); n = number of separate calculation outcomes used in the inversion; a = exponent of Θ in crossover condition, where Ω_{crit} is the crossover abscissa value (i.e., the crossover condition is given by: $\Theta^a \Lambda > \Omega_{crit}$), and where both are assigned "N/A" in the case where all values are used. The inversion was performed separately for each subset (each Rayleigh number), and then for calculations derived from the set as a whole, where these latter estimates are listed below the single-line divisions (i.e., where γ is estimated).

$Ra_{(H)}/10^5$	H	BC	IC	n	a	Ω_{crit}	$\log K_0$	α	β	γ
Set A: Free upper boundary condition, with 100% bottom heating and time-independent I.C.s										
10.0	0.00	f	t.i.	212	N/A	N/A	2.863	0.25 ± 0.03	0.94 ± 0.03	N/A
10.0	0.00	f	t.i.	161	0.25	-0.80	2.869	0.24 ± 0.02	0.98 ± 0.02	N/A
7.50	0.00	f	t.i.	178	N/A	N/A	2.925	0.25 ± 0.03	1.01 ± 0.05	N/A
7.50	0.00	f	t.i.	125	0.25	-0.80	2.926	0.24 ± 0.02	1.03 ± 0.03	N/A
2.50	0.00	f	t.i.	179	N/A	N/A	3.122	0.28 ± 0.05	0.89 ± 0.04	N/A
2.50	0.00	f	t.i.	132	0.25	-0.80	3.137	0.21 ± 0.03	1.00 ± 0.02	N/A
0.75	0.00	f	t.i.	198	N/A	N/A	3.433	0.39 ± 0.04	0.86 ± 0.04	N/A
0.75	0.00	f	t.i.	134	0.25	-0.80	3.592	0.46 ± 0.03	1.15 ± 0.05	N/A
-	-	f	t.i.	767	N/A	N/A	5.843	0.30 ± 0.03	0.92 ± 0.02	-0.50 ± 0.01
-	-	f	t.i.	552	0.25	-0.80	5.843	0.29 ± 0.02	1.01 ± 0.02	-0.49 ± 0.01
Set B: Rigid (no-slip) upper boundary condition, with 100% bottom heating and time-independent I.C.s										
2.50	0.00	r	t.i.	53	N/A	N/A	3.305	0.44 ± 0.09	1.07 ± 0.05	N/A
2.50	0.00	r	t.i.	45	0.25	-0.68	3.255	0.34 ± 0.06	1.07 ± 0.08	N/A
0.75	0.00	r	t.i.	132	N/A	N/A	3.453	0.15 ± 0.13	1.04 ± 0.10	N/A
0.75	0.00	r	t.i.	74	0.25	-0.68	3.462	0.23 ± 0.14	0.98 ± 0.07	N/A
-	-	r	t.i.	185	N/A	N/A	5.993	0.42 ± 0.09	1.07 ± 0.04	-0.50 ± 0.03
-	-	r	t.i.	119	0.25	-0.68	6.085	0.33 ± 0.06	1.03 ± 0.06	-0.53 ± 0.02

Table A.2: Estimated parameter values for the spreading timescale $t_{s2} = K_0 \Theta^{\alpha} \Lambda^{\beta} Ra_{(H)}^{\gamma}$ and 95.4% confidence limits obtained from a bootstrap ($N = 1000$ random samplings with replacement). For details see the caption of Table A.1.

$Ra_{(H)}/10^5$	H	BC	IC	n	a	Ω_{crit}	$\log K_0$	α	β	γ
Set A: Free upper boundary condition, with 100% bottom heating and time-independent I.C.s										
10.0	0.00	f	t.i.	219	N/A	N/A	2.900	0.36 ± 0.03	1.04 ± 0.07	N/A
10.0	0.00	f	t.i.	178	0.33	-0.87	2.875	0.36 ± 0.02	0.93 ± 0.05	N/A
7.50	0.00	f	t.i.	179	N/A	N/A	3.075	0.51 ± 0.06	1.05 ± 0.08	N/A
7.50	0.00	f	t.i.	136	0.33	-0.87	3.071	0.54 ± 0.04	0.99 ± 0.08	N/A
2.50	0.00	f	t.i.	303	N/A	N/A	3.193	0.29 ± 0.06	1.12 ± 0.08	N/A
2.50	0.00	f	t.i.	241	0.33	-0.87	3.200	0.38 ± 0.03	0.97 ± 0.03	N/A
0.75	0.00	f	t.i.	210	N/A	N/A	3.524	0.39 ± 0.07	1.06 ± 0.05	N/A
0.75	0.00	f	t.i.	192	0.33	-0.87	3.520	0.43 ± 0.06	0.98 ± 0.05	N/A
-	-	f	t.i.	911	N/A	N/A	6.017	0.37 ± 0.02	1.07 ± 0.05	-0.51 ± 0.02
-	-	f	t.i.	747	0.33	-0.87	6.013	0.40 ± 0.03	0.96 ± 0.03	-0.52 ± 0.01
Set B: Rigid (no-slip) upper boundary condition, with 100% bottom heating and time-independent I.C.s										
7.50	0.00	r	t.i.	50	N/A	N/A	3.192	0.57 ± 0.17	1.01 ± 0.05	N/A
7.50	0.00	r	t.i.	50	0.50	-0.75	3.198	0.58 ± 0.17	1.02 ± 0.06	N/A
2.50	0.00	r	t.i.	90	N/A	N/A	3.455	0.67 ± 0.08	0.84 ± 0.06	N/A
2.50	0.00	r	t.i.	90	0.50	-0.75	3.456	0.67 ± 0.08	0.84 ± 0.06	N/A
0.75	0.00	r	t.i.	278	N/A	N/A	3.738	0.64 ± 0.06	1.08 ± 0.06	N/A
0.75	0.00	r	t.i.	242	0.50	-0.75	3.705	0.60 ± 0.04	0.98 ± 0.04	N/A
-	-	r	t.i.	418	N/A	N/A	6.097	0.65 ± 0.06	1.05 ± 0.05	-0.48 ± 0.02
-	-	r	t.i.	381	0.50	-0.75	6.158	0.62 ± 0.05	0.96 ± 0.04	-0.50 ± 0.02
Set C: Free upper boundary condition, with 100% volumetric heating and time-dependent I.C.s										
533	21.30	f	t.d.	146	N/A	N/A	3.360	0.32 ± 0.03	1.03 ± 0.07	N/A
154	15.42	f	t.d.	41	N/A	N/A	3.392	0.35 ± 0.17	1.01 ± 0.03	N/A
104	13.93	f	t.d.	122	N/A	N/A	3.396	0.30 ± 0.06	1.02 ± 0.07	N/A
-	-	f	t.d.	309	N/A	N/A	4.167	0.30 ± 0.03	1.03 ± 0.04	-0.13 ± 0.04

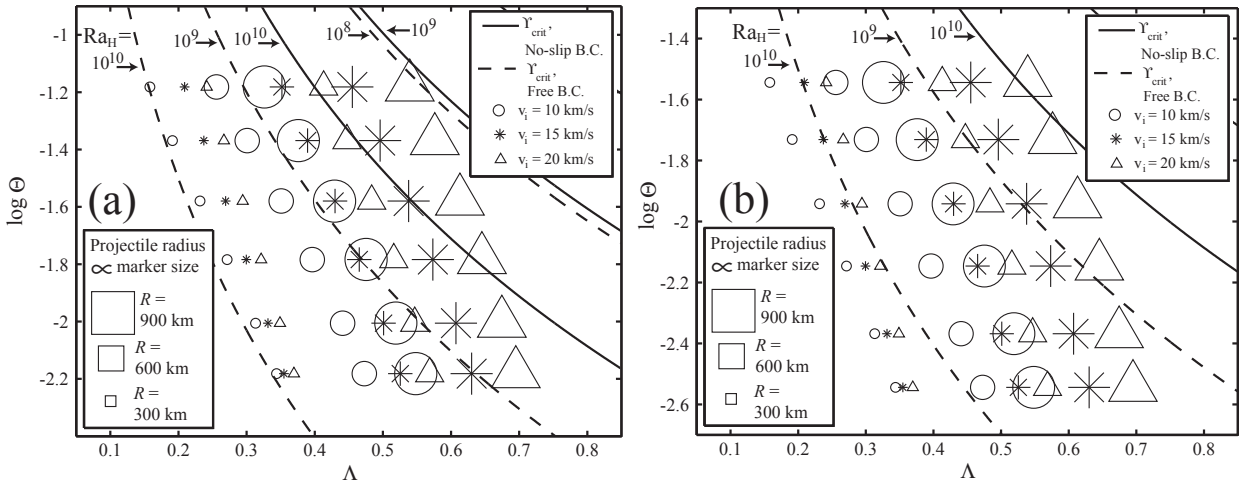

Figure A-1: Diagrams relating perturbations of type I to perturbations of type II and the global stagnation criterion, $\Upsilon \equiv \Theta\Lambda^3 > \Upsilon_{\rm crit}$ for internal-heating Rayleigh numbers $10^8, 10^9$ and 10^{10} in the case of a rigid- (solid lines) and stress-free upper boundary (dashed lines) for a model mantle with terrestrial dimensions and material properties (i.e., used to calculate shock-heating). In each case we have chosen a different effective driving temperature ΔT_c: (a) $\Delta T_c = 1.52 \times 10^4$ K; (b) $\Delta T_c = 3.5 \times 10^4$ K. The former is a modern value, and the latter is intermediate with respect to the early solar system value assumed in Section 3.6 of the main text. Each point represents a projectile radius, R, and incident velocity, v_i, which can be related to the dimensionless perturbation temperature and size, Θ and Λ, respectively (where the peak shock pressure decays with exponent $n = n_0$ and the "climbing-shock" method was used to calculate the amount of heating). Points that lie above a given solid or dashed curve satisfy the global stagnation criterion for the corresponding Rayleigh number and upper boundary condition, and therefore will depress the globally-averaged mantle flow velocity to 3σ below its temporal mean value prior to anomaly insertion. The perturbation temperature, which respresents the separation between geotherm and solidus is, from top to bottom, $\Delta T_p = \{1000, 650, 400, 250, 150, 100\}$ K (where $\Theta = \Delta T_p / \Delta T_c$). Note that Λ corresponds to the dimensionless mantle depth at which the shock-heating curve crosses the solidus. See the main text for details.

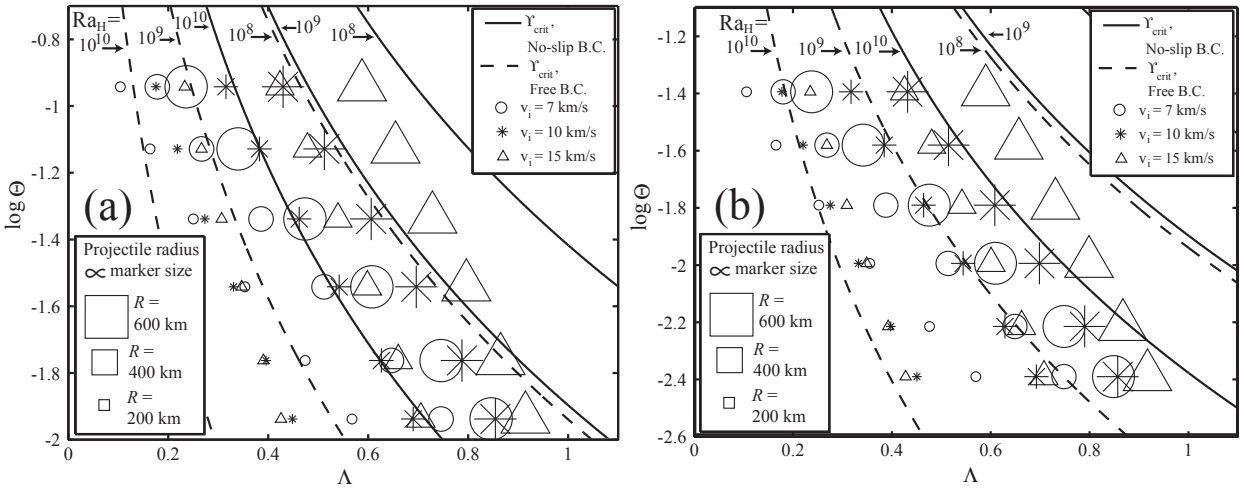

Figure A-2: Diagrams relating perturbations of type I to perturbations of type II and the global stagnation criterion, $\Upsilon \equiv \Theta\Lambda^3 > \Upsilon_{\rm crit}$ for internal-heating Rayleigh numbers $10^8, 10^9$ and 10^{10} in the case of a rigid- (solid lines) and stress-free upper boundary (dashed lines) for a model mantle with martian dimensions and material properties (i.e., used to calculate shock-heating). In each case we have chosen a different effective driving temperature ΔT_c: (a) $\Delta T_c = 7.5{\times}10^3$ K; (b) $\Delta T_c = 2.5{\times}10^4$ K. The former is a modern value, and the latter is intermediate with respect to the early-solar-system value assumed in Section 3.6 of the main text. Each point represents a projectile radius, R, and incident velocity, v_i, which can be related to the dimensionless perturbation temperature and size, Θ and Λ, respectively (where the peak shock pressure decays with exponent $n = n_0$ and the "climbing-shock" method was used to calculate the amount of heating). Points that lie above a given solid or dashed curve satisfy the global stagnation criterion for the corresponding Rayleigh number and upper boundary condition, and therefore will depress the globally-averaged mantle flow velocity to 3σ below its temporal mean value prior to anomaly insertion. The perturbation temperature, which respresents the separation between geotherm and solidus is, from top to bottom, $\Delta T_p = \{1000, 650, 400, 250, 150, 100\}$ K (where $\Theta = \Delta T_p / \Delta T_c$). Note that Λ corresponds to the dimensionless mantle depth at which the shock-heating curve crosses the solidus. See the main text for details.

Appendix B

Auxiliary Material for Chapter 5: HiRISE-FCC

This Appendix contains additional tables and figures pertaining to the analysis of morphometric quantities derived from craters in the HiRISE Fresh Crater Catalog (HiRISE-FCC). Please see the text of Chapter 5 for detailed explanations of their contents. We begin with a list of the geological unit symbols mapped in Greeley and Guest [1987], Scott and Tanaka [1986] and Tanaka et al. [2005], as well as their durations and the material classes to which they have been assigned. The format is: `unit_symbol, starting_epoch, ending_epoch, material_class`, where epochs are indicated by: 1 = early Noachian, 2 = middle Noachian, 3 = late Noachian, 4 = early Hesperian, 5 = middle Hesperian, 6 = late Hesperian, 7 = early Amazonian, 8 = middle Amazonian, 9 = late Amazonian; and where material classes are: 0 = mix (of all), 1 = debris, 2 = sediments, 3 = sediments + debris, 4 = lavas, 5 = lavas + debris, 6 = mantled terranes (i.e., lavas + sediments).

Globally-distributed units mapped in Greeley and Guest [1987] and Scott and Tanaka [1986]:

```
AHa,5,7,1; AHat,6,7,1; AHcf,5,7,2;
AHh,5,7,1; AHpe,5,8,4; AHt,5,7,1;
AHt3,6,7,2; Aa1,7,7,2; Aa2,7,8,2;
Aa3,8,8,2; Aa4,9,9,2; Aa5,9,9,2;
Aam,7,7,2; Aau,7,7,2; Ach,9,9,4;
Achu,9,9,4; Achp,9,9,4; Ad,9,9,4;
Adc,9,9,4; Adl,9,9,4; Ae,9,9,4;
Ael1,7,7,1; Ael2,7,7,2; Ael3,7,7,1;
Ael4,7,7,3; Ah4,7,7,0; Ah5,7,7,6;
Ah6,8,8,0; Ah7,8,8,0; Ah8,8,8,0;
Am,9,9,4; Aml,7,8,0; Amm,8,8,5;
Amu,9,9,5; Aoa1,7,7,1; Aoa2,7,7,1;
Aoa3,7,7,1; Aoa4,7,8,1; Aop,9,9,2;
Aos,9,9,2; Api,9,9,4; Apk,7,8,0;
Apl,9,9,4; Aps,7,9,0; As,9,9,3;
At4,7,7,1; At5,8,8,1; At6,9,9,2;
Avf,7,8,5; HNu,1,5,0; Had,4,4,2;
Hal,4,6,2; Hap,4,5,2; Hch,5,6,5;
Hchp,5,6,5; Hcht,5,6,0; Hdl,5,5,6;
Hdu,5,5,2; Hf,4,5,0; Hh2,4,5,2;
Hh3,5,6,4; Hhet,5,6,1; Hpl3,4,5,6;
Hplm,4,5,6; Hr,4,4,2; Hs,4,5,2;
Hsl,4,5,2; Hsu,5,5,2; Ht1,4,4,1;
Ht2,5,5,1; Htl,3,4,2; Htm,4,4,2;
Htu,4,5,2; Hvg,5,5,6; Hvk,4,4,0;
Hvl,5,5,6; Hvm,5,5,6; Hvr,5,5,6;
Nb,1,1,0; Nf,1,3,0; Nh1,1,1,3;
Nm,1,1,0; Npl1,2,2,0; Npl2,2,3,6;
Npld,2,3,6; Nple,2,3,5; Nplh,1,1,0;
Nplr,2,2,2; b,0,0,0; cb,0,0,0;
cs,0,0,0; d,0,0,0; m,0,0,0; s,0,0,0;
v,0,0,1;
```

Northern lowlands units mapped in Tanaka et al. [2005]:

```
HTa,6,6,2; HCa,6,6,0; HCs,6,6,0;
HNn,1,4,3; HAa,4,6,0; AEta,7,7,1;
ABd2,8,9,3; AHAa1s,6,7,1; AEtb,7,7,5;
ABb1,9,9,4; ATl,8,8,3; ABb2,9,9,4;
AAa2n,8,9,2; AHEe,6,7,2; AEc1,7,8,3;
ABvi,7,7,4; AAa1n,7,8,2; AEc2,8,9,2;
AHc,4,7,3; AEc3,9,9,2; AAm,7,9,4;
ABo,9,9,4; ABvm,7,7,4; AAa2s,8,9,2;
AHcf,4,7,4; HNCc1,3,4,5; HIa,4,4,1;
```

Table B.1: For 21 subsets of the **HiRISE-FCC**: slope m and intercept b obtained from a linear regression for $\log \sigma_R^* = m \log D + b$ and $\log \Delta R^* = m \log D + b$, along with the Pearson correlation coefficient r_P computed for both relations. **Mid-range** values were assumed in this case and the fit was computed for $D \geq 100$ m. [CSC on, except for L_7 and L_8]

Set	$m_{\Delta R}$	$b_{\Delta R}$	r_P	m_{σ_R}	b_{σ_R}	r_P
L_1	-0.54	0.67	-0.77	-0.52	-0.00	-0.72
L_2	-0.52	0.62	-0.79	-0.48	-0.16	-0.71
L_3	-0.49	0.42	-0.82	-0.49	-0.22	-0.81
L_4	-0.46	0.41	-0.78	-0.39	-0.44	-0.71
L_4^C	-0.38	0.19	-0.67	-0.35	-0.53	-0.62
L_5	-0.31	-0.00	-0.59	-0.26	-0.79	-0.51
L_5^C	-0.48	0.49	-0.77	-0.44	-0.27	-0.72
L_6	-0.35	0.13	-0.65	-0.28	-0.72	-0.54
L_6^C	-0.45	0.39	-0.76	-0.44	-0.29	-0.73
L_7	-0.38	0.20	-0.72	-0.36	-0.50	-0.70
L_8	-0.42	0.30	-0.64	-0.38	-0.46	-0.57
L_9	-0.42	0.31	-0.63	-0.38	-0.43	-0.58
L_9^C	-0.53	0.56	-0.86	-0.46	-0.27	-0.81
L_{10}	-0.31	0.04	-0.63	-0.24	-0.77	-0.52
L_{10}^C	-0.42	0.29	-0.72	-0.39	-0.46	-0.68
L_{11}	-0.39	0.22	-0.65	-0.33	-0.57	-0.58
L_{11}^C	-0.42	0.29	-0.75	-0.38	-0.46	-0.70
L_{12}	-0.39	0.22	-0.69	-0.34	-0.55	-0.63
L_{12}^C	-0.46	0.41	-0.75	-0.42	-0.36	-0.71
L_{13}	-0.46	0.38	-0.70	-0.41	-0.41	-0.65
L_{13}^C	-0.42	0.33	-0.72	-0.37	-0.46	-0.65

```
HBu1,4,4,3; HBd1,4,4,3; ABa,9,9,3;
HIs,4,6,2; HBu2,6,6,3; AIi,7,7,4;
ABs,7,7,3; Nl,1,2,0; HNTl,2,4,2;
HCc2,4,6,5; Nn,2,3,0; HCc3,6,6,4;
HCc4,6,6,3;
```

Table B.2: Global properties of shape distributions for 21 subsets of the **HiRISE-FCC**, using **mid-range** values and **including** craters with $D < 100$ m. Listed are the number of triangles (N_3), squares (N_4), pentagons (N_5), and hexagons (N_6) in each subset, along with mean ± standard deviation of detrended maximum and standard radial deviations ($\Delta R'$ and σ'_R, respectively) and concave fraction (ν'). [CSC on, except for L_7 and L_8]

Set	N	N_3	N_4	N_5	N_6	σ'_R	$\Delta R'$	ν'
L_1	25	9	10	6	0	0.33 ± 0.16	1.84 ± 0.78	0.954 ± 0.039
L_2	42	17	17	7	1	0.34 ± 0.15	1.93 ± 0.76	0.961 ± 0.036
L_3	25	13	7	3	2	0.29 ± 0.08	1.63 ± 0.42	0.935 ± 0.045
L_4	23	10	10	2	1	0.31 ± 0.15	1.77 ± 0.83	0.951 ± 0.044
L_4^C	79	39	26	11	3	0.33 ± 0.13	1.90 ± 0.70	0.950 ± 0.044
L_5	55	26	23	4	2	0.32 ± 0.13	1.82 ± 0.73	0.947 ± 0.042
L_5^C	47	23	13	9	2	0.33 ± 0.14	1.92 ± 0.73	0.954 ± 0.046
L_6	47	21	19	5	2	0.35 ± 0.15	1.97 ± 0.79	0.952 ± 0.039
L_6^C	55	28	17	8	2	0.31 ± 0.12	1.78 ± 0.66	0.948 ± 0.048
L_7	49	24	19	6	0	0.30 ± 0.12	1.68 ± 0.71	0.923 ± 0.049
L_8	48	23	15	8	2	0.30 ± 0.14	1.70 ± 0.68	0.943 ± 0.036
L_9	66	31	22	11	2	0.36 ± 0.15	2.04 ± 0.76	0.959 ± 0.036
L_9^C	36	18	14	2	2	0.28 ± 0.09	1.55 ± 0.53	0.933 ± 0.051
L_{10}	34	20	11	3	0	0.36 ± 0.15	1.99 ± 0.80	0.947 ± 0.040
L_{10}^C	68	29	25	10	4	0.31 ± 0.13	1.81 ± 0.68	0.951 ± 0.046
L_{11}	64	30	26	7	1	0.34 ± 0.13	1.89 ± 0.73	0.950 ± 0.043
L_{11}^C	38	19	10	6	3	0.32 ± 0.14	1.83 ± 0.72	0.950 ± 0.046
L_{12}	80	38	27	12	3	0.34 ± 0.14	1.89 ± 0.75	0.949 ± 0.044
L_{12}^C	22	11	9	1	1	0.30 ± 0.11	1.78 ± 0.63	0.953 ± 0.042
L_{13}	29	12	14	1	2	0.32 ± 0.10	1.77 ± 0.59	0.930 ± 0.049
L_{13}^C	73	37	22	12	2	0.33 ± 0.15	1.91 ± 0.77	0.958 ± 0.039

Table B.3: Global properties of shape distributions for 21 subsets of the **HiRISE-FCC**, using **single-estimate** values and **excluding** craters with $D < 100$ m. Listed are the number of triangles (N_3), squares (N_4), pentagons (N_5), and hexagons (N_6) in each subset, along with mean ± standard deviation of detrended maximum and standard radial deviations ($\Delta R'$ and σ'_R, respectively) and concave fraction (ν'). [CSC on, except for L_7 and L_8]

Set	N	N_3	N_4	N_5	N_6	σ'_R	$\Delta R'$	ν'
L_1	22	5	10	7	0	0.28 ± 0.11	1.59 ± 0.52	1.058 ± 0.036
L_2	39	13	17	8	1	0.28 ± 0.11	1.65 ± 0.56	1.060 ± 0.032
L_3	25	13	7	4	1	0.24 ± 0.07	1.33 ± 0.39	1.039 ± 0.031
L_4	20	9	8	2	1	0.29 ± 0.14	1.65 ± 0.72	1.050 ± 0.043
L_4^C	74	34	25	13	2	0.28 ± 0.10	1.62 ± 0.53	1.055 ± 0.035
L_5	48	22	21	4	1	0.29 ± 0.11	1.65 ± 0.56	1.051 ± 0.038
L_5^C	46	21	12	11	2	0.27 ± 0.10	1.60 ± 0.60	1.056 ± 0.036
L_6	44	19	19	5	1	0.30 ± 0.12	1.71 ± 0.64	1.053 ± 0.038
L_6^C	50	24	14	10	2	0.26 ± 0.09	1.55 ± 0.50	1.054 ± 0.036
L_7	45	22	15	8	0	0.27 ± 0.10	1.48 ± 0.57	1.026 ± 0.039
L_8	43	19	15	7	2	0.25 ± 0.10	1.45 ± 0.50	1.043 ± 0.036
L_9	66	30	23	11	2	0.30 ± 0.12	1.70 ± 0.62	1.058 ± 0.037
L_9^C	28	13	10	4	1	0.25 ± 0.07	1.44 ± 0.40	1.043 ± 0.035
L_{10}	29	18	8	3	0	0.33 ± 0.11	1.83 ± 0.60	1.050 ± 0.035
L_{10}^C	65	25	25	12	3	0.26 ± 0.10	1.53 ± 0.54	1.055 ± 0.038
L_{11}	59	27	24	8	0	0.29 ± 0.11	1.65 ± 0.59	1.053 ± 0.034
L_{11}^C	35	16	9	7	3	0.27 ± 0.10	1.59 ± 0.55	1.054 ± 0.041
L_{12}	73	33	25	13	2	0.29 ± 0.11	1.66 ± 0.60	1.053 ± 0.036
L_{12}^C	21	10	8	2	1	0.26 ± 0.08	1.51 ± 0.45	1.057 ± 0.038
L_{13}	29	12	13	3	1	0.26 ± 0.10	1.45 ± 0.58	1.042 ± 0.035
L_{13}^C	65	31	20	12	2	0.29 ± 0.11	1.70 ± 0.56	1.059 ± 0.037

Table B.4: Global properties of shape distributions for 21 subsets of the **HiRISE-FCC**, using **mid-range** values and **excluding** craters with $D < 100$ m. Listed are the number of triangles (N_3), squares (N_4), pentagons (N_5), and hexagons (N_6) in each subset, along with mean ± standard deviation of detrended maximum and standard radial deviations ($\Delta R'$ and σ'_R, respectively) and concave fraction (ν'). [CSC on, except for L_7 and L_8]

Set	N	N_3	N_4	N_5	N_6	σ'_R	$\Delta R'$	ν'
L_1	22	7	9	6	0	0.36 ± 0.15	1.97 ± 0.71	0.958 ± 0.039
L_2	39	15	16	7	1	0.35 ± 0.14	2.01 ± 0.71	0.964 ± 0.036
L_3	25	13	7	3	2	0.29 ± 0.08	1.63 ± 0.42	0.935 ± 0.045
L_4	20	9	8	2	1	0.33 ± 0.16	1.91 ± 0.80	0.957 ± 0.042
L_4^C	74	35	25	11	3	0.35 ± 0.12	1.97 ± 0.65	0.952 ± 0.044
L_5	48	22	20	4	2	0.35 ± 0.13	1.97 ± 0.66	0.952 ± 0.041
L_5^C	46	22	13	9	2	0.34 ± 0.14	1.95 ± 0.71	0.954 ± 0.046
L_6	44	19	18	5	2	0.36 ± 0.14	2.05 ± 0.75	0.954 ± 0.039
L_6^C	50	25	15	8	2	0.33 ± 0.12	1.88 ± 0.61	0.952 ± 0.048
L_7	45	22	17	6	0	0.32 ± 0.11	1.79 ± 0.65	0.925 ± 0.050
L_8	43	20	14	7	2	0.32 ± 0.13	1.79 ± 0.65	0.947 ± 0.035
L_9	66	31	22	11	2	0.36 ± 0.15	2.04 ± 0.76	0.959 ± 0.036
L_9^C	28	13	11	2	2	0.31 ± 0.07	1.76 ± 0.38	0.938 ± 0.056
L_{10}	29	17	9	3	0	0.39 ± 0.13	2.19 ± 0.68	0.953 ± 0.039
L_{10}^C	65	27	24	10	4	0.32 ± 0.12	1.85 ± 0.66	0.953 ± 0.046
L_{11}	59	27	24	7	1	0.35 ± 0.13	1.98 ± 0.69	0.953 ± 0.042
L_{11}^C	35	17	9	6	3	0.33 ± 0.13	1.92 ± 0.68	0.953 ± 0.047
L_{12}	73	33	25	12	3	0.35 ± 0.14	2.00 ± 0.70	0.952 ± 0.045
L_{12}^C	21	11	8	1	1	0.31 ± 0.11	1.83 ± 0.60	0.955 ± 0.041
L_{13}	29	12	14	1	2	0.32 ± 0.10	1.77 ± 0.59	0.930 ± 0.049
L_{13}^C	65	32	19	12	2	0.35 ± 0.14	2.04 ± 0.71	0.963 ± 0.037

Table B.5: Global properties of shape distributions for 21 subsets of the **HiRISE-FCC**, using **mid-range** values and **including** craters with $D < 100$ m. Listed are the mean ± standard deviation of deviation-normalized harmonic amplitudes A'_2 through A'_8. [CSC on, except for L_7 and L_8]

Set	N	A'_2	A'_3	A'_4	A'_5	A'_6	A'_7	A'_8
L_1	25	0.102 ± 0.041	0.059 ± 0.025	0.057 ± 0.026	0.046 ± 0.023	0.032 ± 0.014	0.025 ± 0.010	0.020 ± 0.010
L_2	42	0.094 ± 0.038	0.062 ± 0.028	0.058 ± 0.025	0.041 ± 0.021	0.033 ± 0.017	0.023 ± 0.014	0.020 ± 0.010
L_3	25	0.097 ± 0.035	0.065 ± 0.033	0.055 ± 0.032	0.037 ± 0.020	0.035 ± 0.016	0.025 ± 0.011	0.023 ± 0.013
L_4	23	0.104 ± 0.037	0.056 ± 0.023	0.061 ± 0.034	0.037 ± 0.023	0.032 ± 0.017	0.023 ± 0.012	0.020 ± 0.011
L_4^C	79	0.097 ± 0.039	0.065 ± 0.029	0.054 ± 0.026	0.039 ± 0.021	0.034 ± 0.018	0.024 ± 0.014	0.020 ± 0.010
L_5	55	0.101 ± 0.041	0.062 ± 0.026	0.059 ± 0.030	0.037 ± 0.021	0.034 ± 0.015	0.023 ± 0.013	0.018 ± 0.009
L_5^C	47	0.096 ± 0.036	0.063 ± 0.031	0.052 ± 0.025	0.039 ± 0.023	0.033 ± 0.021	0.024 ± 0.014	0.021 ± 0.011
L_6	47	0.100 ± 0.044	0.064 ± 0.028	0.055 ± 0.026	0.039 ± 0.021	0.034 ± 0.015	0.022 ± 0.013	0.019 ± 0.010
L_6^C	55	0.098 ± 0.034	0.062 ± 0.028	0.056 ± 0.029	0.037 ± 0.022	0.033 ± 0.020	0.025 ± 0.014	0.020 ± 0.011
L_7	49	0.103 ± 0.036	0.064 ± 0.029	0.058 ± 0.028	0.041 ± 0.026	0.030 ± 0.014	0.022 ± 0.012	0.021 ± 0.009
L_8	48	0.096 ± 0.038	0.062 ± 0.026	0.056 ± 0.028	0.037 ± 0.018	0.036 ± 0.019	0.023 ± 0.015	0.017 ± 0.009
L_9	66	0.100 ± 0.040	0.065 ± 0.029	0.053 ± 0.026	0.041 ± 0.023	0.033 ± 0.020	0.022 ± 0.015	0.019 ± 0.011
L_9^C	36	0.097 ± 0.037	0.059 ± 0.027	0.062 ± 0.031	0.034 ± 0.019	0.034 ± 0.013	0.026 ± 0.010	0.020 ± 0.010
L_{10}	34	0.108 ± 0.046	0.063 ± 0.028	0.053 ± 0.030	0.034 ± 0.019	0.028 ± 0.011	0.021 ± 0.010	0.018 ± 0.009
L_{10}^C	68	0.094 ± 0.034	0.062 ± 0.029	0.057 ± 0.026	0.040 ± 0.022	0.036 ± 0.020	0.025 ± 0.015	0.020 ± 0.011
L_{11}	64	0.105 ± 0.042	0.059 ± 0.026	0.056 ± 0.029	0.037 ± 0.019	0.032 ± 0.014	0.022 ± 0.011	0.019 ± 0.010
L_{11}^C	38	0.088 ± 0.031	0.069 ± 0.032	0.055 ± 0.025	0.040 ± 0.025	0.037 ± 0.023	0.026 ± 0.016	0.020 ± 0.011
L_{12}	80	0.099 ± 0.041	0.062 ± 0.029	0.057 ± 0.028	0.039 ± 0.023	0.033 ± 0.017	0.024 ± 0.014	0.020 ± 0.011
L_{12}^C	22	0.096 ± 0.030	0.065 ± 0.027	0.051 ± 0.025	0.035 ± 0.015	0.035 ± 0.021	0.023 ± 0.011	0.017 ± 0.010
L_{13}	29	0.093 ± 0.041	0.059 ± 0.024	0.068 ± 0.031	0.035 ± 0.020	0.037 ± 0.020	0.025 ± 0.014	0.022 ± 0.008
L_{13}^C	73	0.101 ± 0.038	0.064 ± 0.030	0.051 ± 0.025	0.039 ± 0.022	0.032 ± 0.017	0.023 ± 0.013	0.019 ± 0.011

Table B.6: Global properties of shape distributions for 21 subsets of the **HiRISE-FCC**, using **single-estimate** values and **excluding** craters with $D < 100$ m. Listed are the mean ± standard deviation of deviation-normalized harmonic amplitudes A'_2 through A'_8. [CSC on, except for L_7 and L_8]

Set	N	A'_2	A'_3	A'_4	A'_5	A'_6	A'_7	A'_8
L_1	22	0.098 ± 0.046	0.055 ± 0.021	0.060 ± 0.028	0.049 ± 0.025	0.035 ± 0.016	0.025 ± 0.012	0.020 ± 0.010
L_2	39	0.091 ± 0.042	0.060 ± 0.027	0.061 ± 0.025	0.043 ± 0.023	0.034 ± 0.019	0.024 ± 0.015	0.021 ± 0.010
L_3	25	0.096 ± 0.037	0.066 ± 0.035	0.057 ± 0.032	0.038 ± 0.023	0.037 ± 0.017	0.027 ± 0.012	0.023 ± 0.013
L_4	20	0.106 ± 0.039	0.055 ± 0.023	0.055 ± 0.028	0.039 ± 0.024	0.034 ± 0.018	0.025 ± 0.013	0.021 ± 0.011
L_4^C	74	0.094 ± 0.041	0.066 ± 0.031	0.055 ± 0.027	0.040 ± 0.024	0.035 ± 0.019	0.024 ± 0.015	0.020 ± 0.011
L_5	48	0.100 ± 0.042	0.064 ± 0.029	0.059 ± 0.029	0.038 ± 0.023	0.036 ± 0.017	0.024 ± 0.014	0.018 ± 0.009
L_5^C	46	0.093 ± 0.040	0.063 ± 0.031	0.051 ± 0.025	0.042 ± 0.024	0.034 ± 0.021	0.024 ± 0.015	0.022 ± 0.012
L_6	44	0.101 ± 0.045	0.064 ± 0.030	0.057 ± 0.028	0.040 ± 0.023	0.035 ± 0.016	0.024 ± 0.015	0.019 ± 0.010
L_6^C	50	0.093 ± 0.037	0.063 ± 0.030	0.054 ± 0.027	0.040 ± 0.025	0.035 ± 0.021	0.024 ± 0.014	0.021 ± 0.011
L_7	45	0.106 ± 0.036	0.064 ± 0.028	0.057 ± 0.028	0.042 ± 0.028	0.031 ± 0.016	0.021 ± 0.012	0.021 ± 0.010
L_8	43	0.089 ± 0.041	0.064 ± 0.028	0.058 ± 0.028	0.038 ± 0.020	0.039 ± 0.020	0.024 ± 0.017	0.018 ± 0.010
L_9	66	0.099 ± 0.041	0.066 ± 0.030	0.053 ± 0.026	0.041 ± 0.023	0.034 ± 0.021	0.023 ± 0.015	0.019 ± 0.011
L_9^C	28	0.091 ± 0.040	0.057 ± 0.028	0.061 ± 0.029	0.037 ± 0.025	0.038 ± 0.014	0.027 ± 0.012	0.021 ± 0.010
L_{10}	29	0.107 ± 0.049	0.067 ± 0.031	0.050 ± 0.028	0.038 ± 0.021	0.029 ± 0.014	0.021 ± 0.011	0.019 ± 0.010
L_{10}^C	65	0.092 ± 0.036	0.062 ± 0.029	0.058 ± 0.027	0.041 ± 0.025	0.038 ± 0.020	0.025 ± 0.016	0.020 ± 0.011
L_{11}	59	0.104 ± 0.044	0.061 ± 0.029	0.055 ± 0.028	0.039 ± 0.021	0.033 ± 0.015	0.022 ± 0.012	0.020 ± 0.011
L_{11}^C	35	0.085 ± 0.033	0.068 ± 0.031	0.055 ± 0.026	0.042 ± 0.027	0.039 ± 0.024	0.027 ± 0.018	0.020 ± 0.010
L_{12}	73	0.097 ± 0.043	0.063 ± 0.030	0.056 ± 0.027	0.041 ± 0.025	0.035 ± 0.018	0.024 ± 0.015	0.021 ± 0.011
L_{12}^C	21	0.095 ± 0.034	0.067 ± 0.028	0.052 ± 0.027	0.037 ± 0.019	0.036 ± 0.023	0.024 ± 0.012	0.018 ± 0.010
L_{13}	29	0.090 ± 0.043	0.062 ± 0.030	0.069 ± 0.032	0.038 ± 0.026	0.038 ± 0.021	0.027 ± 0.015	0.022 ± 0.008
L_{13}^C	65	0.100 ± 0.040	0.065 ± 0.030	0.049 ± 0.023	0.041 ± 0.022	0.034 ± 0.018	0.023 ± 0.014	0.019 ± 0.012

Table B.7: Global properties of shape distributions for 21 subsets of the **HiRISE-FCC**, using **mid-range** values and **excluding** craters with $D < 100$ m. Listed are the mean ± standard deviation of deviation-normalized harmonic amplitudes A'_2 through A'_8. [CSC on, except for L_7 and L_8]

Set	N	A'_2	A'_3	A'_4	A'_5	A'_6	A'_7	A'_8
L_1	22	0.103 ± 0.043	0.055 ± 0.020	0.058 ± 0.028	0.046 ± 0.024	0.034 ± 0.015	0.025 ± 0.010	0.020 ± 0.010
L_2	39	0.095 ± 0.039	0.060 ± 0.026	0.059 ± 0.025	0.041 ± 0.022	0.033 ± 0.018	0.023 ± 0.014	0.021 ± 0.010
L_3	25	0.097 ± 0.035	0.065 ± 0.033	0.055 ± 0.032	0.037 ± 0.020	0.035 ± 0.016	0.025 ± 0.011	0.023 ± 0.013
L_4	20	0.106 ± 0.038	0.055 ± 0.023	0.055 ± 0.028	0.040 ± 0.023	0.034 ± 0.017	0.023 ± 0.013	0.020 ± 0.011
L_4^C	74	0.096 ± 0.040	0.064 ± 0.029	0.055 ± 0.026	0.039 ± 0.022	0.034 ± 0.018	0.023 ± 0.014	0.020 ± 0.010
L_5	48	0.100 ± 0.042	0.061 ± 0.025	0.058 ± 0.029	0.038 ± 0.021	0.035 ± 0.015	0.022 ± 0.013	0.018 ± 0.009
L_5^C	46	0.096 ± 0.036	0.063 ± 0.031	0.051 ± 0.024	0.040 ± 0.022	0.033 ± 0.021	0.024 ± 0.014	0.021 ± 0.012
L_6	44	0.101 ± 0.045	0.062 ± 0.027	0.056 ± 0.027	0.039 ± 0.022	0.035 ± 0.015	0.022 ± 0.013	0.019 ± 0.010
L_6^C	50	0.096 ± 0.034	0.062 ± 0.029	0.053 ± 0.027	0.039 ± 0.022	0.034 ± 0.021	0.024 ± 0.014	0.021 ± 0.011
L_7	45	0.106 ± 0.036	0.062 ± 0.028	0.055 ± 0.026	0.041 ± 0.026	0.030 ± 0.014	0.021 ± 0.012	0.021 ± 0.010
L_8	43	0.092 ± 0.038	0.062 ± 0.027	0.057 ± 0.028	0.037 ± 0.018	0.037 ± 0.019	0.023 ± 0.015	0.017 ± 0.009
L_9	66	0.100 ± 0.040	0.065 ± 0.029	0.053 ± 0.026	0.041 ± 0.023	0.033 ± 0.020	0.022 ± 0.015	0.019 ± 0.011
L_9^C	28	0.094 ± 0.038	0.056 ± 0.025	0.059 ± 0.029	0.035 ± 0.019	0.036 ± 0.012	0.025 ± 0.010	0.021 ± 0.010
L_{10}	29	0.108 ± 0.048	0.064 ± 0.029	0.048 ± 0.025	0.036 ± 0.019	0.028 ± 0.011	0.019 ± 0.009	0.019 ± 0.009
L_{10}^C	65	0.094 ± 0.035	0.061 ± 0.028	0.058 ± 0.027	0.040 ± 0.023	0.037 ± 0.020	0.025 ± 0.015	0.020 ± 0.011
L_{11}	59	0.104 ± 0.042	0.059 ± 0.026	0.054 ± 0.027	0.038 ± 0.019	0.032 ± 0.014	0.021 ± 0.011	0.020 ± 0.011
L_{11}^C	35	0.088 ± 0.031	0.067 ± 0.031	0.055 ± 0.026	0.040 ± 0.026	0.038 ± 0.023	0.026 ± 0.017	0.020 ± 0.010
L_{12}	73	0.099 ± 0.042	0.061 ± 0.028	0.056 ± 0.027	0.040 ± 0.023	0.034 ± 0.017	0.023 ± 0.014	0.021 ± 0.011
L_{12}^C	21	0.096 ± 0.030	0.066 ± 0.027	0.051 ± 0.026	0.035 ± 0.015	0.035 ± 0.022	0.023 ± 0.011	0.017 ± 0.010
L_{13}	29	0.093 ± 0.041	0.059 ± 0.024	0.068 ± 0.031	0.035 ± 0.020	0.037 ± 0.020	0.025 ± 0.014	0.022 ± 0.008
L_{13}^C	65	0.101 ± 0.038	0.063 ± 0.029	0.048 ± 0.022	0.041 ± 0.022	0.033 ± 0.017	0.022 ± 0.014	0.019 ± 0.011

Table B.8: Quantities and difference metrics (Δ_n: for $n = 1, 2, ...$; defined in Table 5.6) that indicate a statistically significant difference for 13 pairings of 21 subsets of the **HiRISE-FCC**, with respect to differences computed for 10,000 pairings of randomly-sampled subsets of a **Gaussian** reference distribution on the same domain. Listed are metrics reporting differences that exceed the percentage $p_{\rm lim}$ of differences computed from paired subsets of the reference distribution. **Mid-range** values were used and craters with $D < 100$ m were **included**. [CSC on, except for L_7 and L_8]

Set	$p_{\rm lim}$	Quantities whose distributions differ at the level $p_{\rm lim}$
(L_1,L_3)	95%	$\Delta R'$ (Δ_n :4), σ'_R (Δ_n :4,8), Q^{68}_{57} (Δ_n :8), Q^3_6 (Δ_n :8)
	97.5%	$\Delta R'$ (Δ_n :4), σ'_R (Δ_n :4)
	99%	$\Delta R'$ (Δ_n :4), σ'_R (Δ_n :4)
(L_2,L_3)	95%	$\Delta R'$ (Δ_n :3,4,8), σ'_R (Δ_n :3,4,8), ν (Δ_n :3), Q^1_7 (Δ_n :1)
	97.5%	$\Delta R'$ (Δ_n :3,4), σ'_R (Δ_n :4), ν (Δ_n :3), Q^1_7 (Δ_n :1)
	99%	$\Delta R'$ (Δ_n :4), σ'_R (Δ_n :4)
(L_4,L_4^C)	95%	A'_1 (Δ_n :1,3,4,8), A'_6 (Δ_n :1), σ'_R (Δ_n :8), Q^{468}_{357} (Δ_n :1), Q^4_{35} (Δ_n :1), Q^{48}_{35} (Δ_n :1), Q^{468}_{35} (Δ_n :1), Q^1_3 (Δ_n :4), Q^1_5 (Δ_n :4), Q^1_6 (Δ_n :4), Q^1_7 (Δ_n :4), Q^1_8 (Δ_n :3,4,8), Q^2_4 (Δ_n :1), Q^3_8 (Δ_n :2), Q^4_6 (Δ_n :1), Q^5_7 (Δ_n :1), Q^6_7 (Δ_n :1), Q^7_8 (Δ_n :1)
	97.5%	A'_1 (Δ_n :1,3,4,8), A'_6 (Δ_n :1), Q^{468}_{357} (Δ_n :1), Q^4_{35} (Δ_n :1), Q^{48}_{35} (Δ_n :1), Q^{468}_{35} (Δ_n :1), Q^1_3 (Δ_n :4), Q^1_6 (Δ_n :4), Q^1_7 (Δ_n :4), Q^1_8 (Δ_n :3,4), Q^5_7 (Δ_n :1), Q^6_7 (Δ_n :1)
	99%	A'_1 (Δ_n :1,3,4,8), Q^1_6 (Δ_n :4), Q^1_7 (Δ_n :4), Q^1_8 (Δ_n :4), Q^5_7 (Δ_n :1)
(L_5,L_5^C)	95%	A'_1 (Δ_n :8), A'_6 (Δ_n :4), Q^{468}_0 (Δ_n :1), Q^1_6 (Δ_n :4), Q^1_8 (Δ_n :4), Q^2_8 (Δ_n :1,2), Q^6_7 (Δ_n :4), Q^6_8 (Δ_n :4)
	97.5%	A'_6 (Δ_n :4), Q^6_7 (Δ_n :4), Q^6_8 (Δ_n :4)
	99%	Q^6_7 (Δ_n :4), Q^6_8 (Δ_n :4)
(L_6,L_6^C)	95%	A'_6 (Δ_n :4), Q^1_7 (Δ_n :4), Q^4_6 (Δ_n :4), Q^6_7 (Δ_n :4), Q^6_8 (Δ_n :4), Q^7_8 (Δ_n :4)
	97.5%	Q^4_6 (Δ_n :4), Q^6_7 (Δ_n :4), Q^6_8 (Δ_n :4), Q^7_8 (Δ_n :4)
	99%	Q^4_6 (Δ_n :4), Q^6_7 (Δ_n :4), Q^6_8 (Δ_n :4)
(L_7,L_8)	95%	A'_5 (Δ_n :4), A'_6 (Δ_n :4), A'_8 (Δ_n :3,5,6,7,8), ν (Δ_n :1,3,4,5,7), Q^1_6 (Δ_n :4), Q^4_6 (Δ_n :1), Q^5_8 (Δ_n :4), Q^6_8 (Δ_n :3,8), Q^7_8 (Δ_n :3)
	97.5%	A'_5 (Δ_n :4), A'_8 (Δ_n :6), ν (Δ_n :1,3), Q^1_6 (Δ_n :4), Q^5_8 (Δ_n :4), Q^6_8 (Δ_n :3)
	99%	Q^1_6 (Δ_n :4), Q^6_8 (Δ_n :3)
(L_9,L_9^C)	95%	A'_1 (Δ_n :1,8), A'_6 (Δ_n :4), A'_7 (Δ_n :4,8), $\Delta R'$ (Δ_n :3,4,5,6,7,8), σ'_R (Δ_n :3,4,5,6,7,8), ν (Δ_n :1,3,4,5,6,7,8), Q^4_{35} (Δ_n :3,6), Q^{48}_{35} (Δ_n :3,5,6,7), Q^{468}_{35} (Δ_n :3), Q^1_3 (Δ_n :1), Q^1_4 (Δ_n :1), Q^1_5 (Δ_n :1,3,8), Q^1_7 (Δ_n :1), Q^1_8 (Δ_n :1), Q^3_4 (Δ_n :2), Q^5_7 (Δ_n :3), Q^5_8 (Δ_n :1), Q^6_8 (Δ_n :1,4)
	97.5%	A'_1 (Δ_n :1,8), A'_6 (Δ_n :4), A'_7 (Δ_n :4), $\Delta R'$ (Δ_n :3,4,5,6,7,8), σ'_R (Δ_n :3,4,5,6,7,8), ν (Δ_n :1,3,4,5,6,7), Q^1_3 (Δ_n :1), Q^1_5 (Δ_n :1), Q^1_7 (Δ_n :1), Q^5_8 (Δ_n :1)
	99%	A'_1 (Δ_n :1,8), A'_6 (Δ_n :4), $\Delta R'$ (Δ_n :3,5,6,7,8), σ'_R (Δ_n :3,4,5,6,7,8), ν (Δ_n :3,7), Q^1_3 (Δ_n :1), Q^1_7 (Δ_n :1)
(L_{10},L_{10}^C)	95%	A'_1 (Δ_n :1), A'_2 (Δ_n :1,5,7,8), A'_6 (Δ_n :3,4,8), A'_7 (Δ_n :4), σ'_R (Δ_n :8), Q^{68}_{57} (Δ_n :2), Q^{24}_{35} (Δ_n :2), Q^{5678}_{234} (Δ_n :3,5,6,7,8), Q^1_2 (Δ_n :1,5,7), Q^1_4 (Δ_n :1), Q^2_3 (Δ_n :1,2,4,7,8), Q^2_4 (Δ_n :1,4,7,8), Q^2_5 (Δ_n :1,3,5,6,7,8), Q^2_6 (Δ_n :3,5,6,7,8), Q^2_7 (Δ_n :1,8), Q^2_8 (Δ_n :1,2,7,8), Q^6_7 (Δ_n :4), Q^6_8 (Δ_n :3,4,8), Q^7_8 (Δ_n :4)
	97.5%	A'_1 (Δ_n :1), A'_2 (Δ_n :8), A'_6 (Δ_n :3,4,8), A'_7 (Δ_n :4), Q^{5678}_{234} (Δ_n :3,5,6,8), Q^1_2 (Δ_n :1), Q^2_3 (Δ_n :1,8), Q^2_4 (Δ_n :1,8), Q^2_5 (Δ_n :3,5,6,7,8), Q^2_6 (Δ_n :3,5,6,7,8), Q^2_8 (Δ_n :8), Q^6_8 (Δ_n :4)
	99%	A'_1 (Δ_n :1), A'_2 (Δ_n :8), A'_6 (Δ_n :3,4,8), Q^{5678}_{234} (Δ_n :3,8), Q^2_5 (Δ_n :8), Q^6_8 (Δ_n :4)

Table B.9: Continuation of table B.8.

Set	p_{lim}	Quantities whose distributions differ at the level p_{lim}
(L_{11},L_{11}^C)	95%	A_2' (Δ_n :3,4,5,6,7,8), A_3' (Δ_n :8), A_6' (Δ_n :1,4), A_7' (Δ_n :4), Q_{357}^{468} (Δ_n :1,4), Q_{35}^{48} (Δ_n :1), Q_{35}^{24} (Δ_n :1,2,3,5,6,7,8), Q_{234}^{5678} (Δ_n :4,8), Q_2^1 (Δ_n :3,4), Q_3^1 (Δ_n :1,4), Q_4^1 (Δ_n :2), Q_6^1 (Δ_n :4), Q_7^1 (Δ_n :1), Q_3^2 (Δ_n :3,5,6,7,8), Q_4^2 (Δ_n :4,7,8), Q_5^2 (Δ_n :2,3,5,6,7,8), Q_6^2 (Δ_n :3,5,6,7,8), Q_7^2 (Δ_n :3,5,6), Q_8^2 (Δ_n :3,5,6,7,8), Q_6^3 (Δ_n :1,4), Q_8^3 (Δ_n :8), Q_6^5 (Δ_n :1,2,4), Q_7^5 (Δ_n :4), Q_7^6 (Δ_n :1,4), Q_8^6 (Δ_n :4)
	97.5%	A_2' (Δ_n :3,8), A_6' (Δ_n :4), A_7' (Δ_n :4), Q_{357}^{468} (Δ_n :1), Q_{35}^{24} (Δ_n :3,5,6,7), Q_3^1 (Δ_n :1), Q_6^1 (Δ_n :4), Q_7^1 (Δ_n :1), Q_3^2 (Δ_n :3,5,6,7,8), Q_4^2 (Δ_n :8), Q_5^2 (Δ_n :2,3,5,6,8), Q_6^2 (Δ_n :3,5,6), Q_7^2 (Δ_n :3,6), Q_8^2 (Δ_n :3,8), Q_6^3 (Δ_n :1,4), Q_6^5 (Δ_n :1,4), Q_7^5 (Δ_n :4), Q_7^6 (Δ_n :1,4), Q_8^6 (Δ_n :4)
	99%	A_2' (Δ_n :8), A_6' (Δ_n :4), A_7' (Δ_n :4), Q_7^1 (Δ_n :1), Q_3^2 (Δ_n :3,8), Q_6^3 (Δ_n :4), Q_6^5 (Δ_n :1,4), Q_7^6 (Δ_n :4), Q_8^6 (Δ_n :4)
(L_{12},L_{12}^C)	95%	A_1' (Δ_n :1,8), A_5' (Δ_n :4,8), A_8' (Δ_n :8), Q_{357}^{468} (Δ_n :1,2), Q_{35}^{46} (Δ_n :1,2), Q_{35}^{4} (Δ_n :1), Q_{35}^{48} (Δ_n :1), Q_{35}^{468} (Δ_n :1,2), Q_5^1 (Δ_n :4), Q_6^1 (Δ_n :1), Q_7^1 (Δ_n :1), Q_8^1 (Δ_n :1,8), Q_5^2 (Δ_n :4), Q_7^2 (Δ_n :4), Q_6^3 (Δ_n :1), Q_6^4 (Δ_n :1)
	97.5%	A_1' (Δ_n :1,8), A_5' (Δ_n :4), A_8' (Δ_n :8), Q_{357}^{468} (Δ_n :1,2), Q_{35}^{46} (Δ_n :1), Q_{35}^{468} (Δ_n :1,2), Q_5^1 (Δ_n :4), Q_6^1 (Δ_n :1), Q_7^1 (Δ_n :1), Q_8^1 (Δ_n :1,8)
	99%	A_1' (Δ_n :1), A_8' (Δ_n :8), Q_{357}^{468} (Δ_n :1,2), Q_{35}^{46} (Δ_n :1), Q_{35}^{468} (Δ_n :1,2), Q_5^1 (Δ_n :4), Q_6^1 (Δ_n :1), Q_8^1 (Δ_n :1)
(L_{13},L_{13}^C)	95%	A_1' (Δ_n :1,4,8), A_2' (Δ_n :2), A_4' (Δ_n :1,2,3,5,6,7,8), A_5' (Δ_n :8), A_8' (Δ_n :4,7), $\Delta R'$ (Δ_n :8), σ_R' (Δ_n :4), ν (Δ_n :1,3,5,6,7), Q_{357}^{468} (Δ_n :3,5,6,7,8), Q_{35}^{46} (Δ_n :3,5,6,7), Q_{35}^{4} (Δ_n :3,5,6,7,8), Q_3^{48} (Δ_n :3,5,6,7,8), Q_{35}^{48} (Δ_n :3,5,6,7,8), Q_{35}^{468} (Δ_n :3,5,6,7,8), Q_{35}^{24} (Δ_n :2,7), Q_0^{468} (Δ_n :1,2,3,5,6,7,8), Q_0^{48} (Δ_n :1,2,3,5,6,7,8), Q_0^{46} (Δ_n :3,5,6,7,8), Q_4^1 (Δ_n :1,2,4,7), Q_5^1 (Δ_n :1), Q_6^1 (Δ_n :1,4), Q_7^1 (Δ_n :1,4), Q_8^1 (Δ_n :1,4,8), Q_4^2 (Δ_n :1,2,3,5,6,7,8), Q_4^3 (Δ_n :1,3,5,6,7,8), Q_7^3 (Δ_n :2), Q_5^4 (Δ_n :3,5,6,7,8), Q_6^4 (Δ_n :1,8), Q_7^4 (Δ_n :3,5,6,7,8), Q_8^4 (Δ_n :3), Q_6^5 (Δ_n :1,2), Q_7^6 (Δ_n :1)
	97.5%	A_1' (Δ_n :1,4,8), A_4' (Δ_n :1,3,5,6,7,8), $\Delta R'$ (Δ_n :8), ν (Δ_n :3,6,7), Q_{357}^{468} (Δ_n :3,5,6,7), Q_{35}^{46} (Δ_n :3,5,6,7), Q_{35}^{4} (Δ_n :3,5,6,7), Q_3^{48} (Δ_n :3,5,6,7), Q_{35}^{48} (Δ_n :3,5,6,7,8), Q_{35}^{468} (Δ_n :3,5,6,7), Q_0^{468} (Δ_n :1,2,3,5,6,7,8), Q_0^{48} (Δ_n :1,2,3,5,6,7,8), Q_0^{46} (Δ_n :3,5,6,7,8), Q_4^1 (Δ_n :1,2,4), Q_5^1 (Δ_n :1), Q_6^1 (Δ_n :1), Q_7^1 (Δ_n :1), Q_8^1 (Δ_n :1), Q_4^2 (Δ_n :1,3,6,7), Q_4^3 (Δ_n :3,5,6,7), Q_7^3 (Δ_n :2), Q_5^4 (Δ_n :3,5,6,7,8), Q_6^4 (Δ_n :1), Q_7^4 (Δ_n :3,5,6,7,8), Q_6^5 (Δ_n :1), Q_7^6 (Δ_n :1)
	99%	A_1' (Δ_n :1,8), A_4' (Δ_n :1,3,5,6,7,8), ν (Δ_n :3), Q_{357}^{468} (Δ_n :3), Q_{35}^{46} (Δ_n :3), Q_{35}^{4} (Δ_n :3), Q_3^{48} (Δ_n :3,5,6), Q_{35}^{48} (Δ_n :3,5,6,7), Q_{35}^{468} (Δ_n :3,5,6), Q_0^{468} (Δ_n :1,2,3,5,6,7,8), Q_0^{48} (Δ_n :1,2,3,5,6,7,8), Q_0^{46} (Δ_n :3,5,6,7,8), Q_4^1 (Δ_n :1,2), Q_5^1 (Δ_n :1), Q_6^1 (Δ_n :1), Q_8^1 (Δ_n :1), Q_4^2 (Δ_n :1), Q_5^4 (Δ_n :7,8), Q_6^4 (Δ_n :1), Q_7^4 (Δ_n :5,7,8), Q_6^5 (Δ_n :1), Q_7^6 (Δ_n :1)

Table B.10: Quantities and difference metrics (Δ_n :1,2,...; defined in Table 5.6) that indicate a statistically significant difference for 13 pairings of 21 subsets of the **HiRISE-FCC**, with respect to differences computed for 10,000 pairings of randomly-sampled subsets of a **Gaussian** reference distribution on the same domain. Listed are metrics reporting differences that exceed the percentage $p_{\rm lim}$ of differences computed from paired subsets of the reference distribution. **Single-estimate** values were used and craters with $D < 100$ m were **excluded**. [CSC on, except for L_7 and L_8]

Set	$p_{\rm lim}$	Quantities whose distributions differ at the level $p_{\rm lim}$
(L_1,L_3)	95%	A'_3 (Δ_n :4,8), $\Delta R'$ (Δ_n :3,5,6,8), σ'_R (Δ_n :4,8), ν (Δ_n :1,2,6), Q_3^{48} (Δ_n :4), Q_3^1 (Δ_n :4), Q_4^3 (Δ_n :4), Q_5^3 (Δ_n :2,5,6,7,8), Q_6^3 (Δ_n :4,8), Q_8^3 (Δ_n :4), Q_8^5 (Δ_n :6)
	97.5%	A'_3 (Δ_n :4), σ'_R (Δ_n :8), ν (Δ_n :1,2), Q_3^1 (Δ_n :4), Q_6^3 (Δ_n :4,8)
	99%	σ'_R (Δ_n :8), Q_6^3 (Δ_n :8)
(L_2,L_3)	95%	A'_1 (Δ_n :2), A'_4 (Δ_n :2), $\Delta R'$ (Δ_n :3,5,6,7,8), σ'_R (Δ_n :3,4,8), ν (Δ_n :3,5,6,7,8), Q_8^1 (Δ_n :4), Q_8^3 (Δ_n :1,2)
	97.5%	A'_1 (Δ_n :2), $\Delta R'$ (Δ_n :3,8), σ'_R (Δ_n :3,4,8), ν (Δ_n :3,5,6,7), Q_8^3 (Δ_n :1,2)
	99%	$\Delta R'$ (Δ_n :3), σ'_R (Δ_n :8), ν (Δ_n :5,6)
(L_4,L_4^C)	95%	A'_1 (Δ_n :2,5,6,7), A'_6 (Δ_n :1), A'_7 (Δ_n :1), Q_{35}^{46} (Δ_n :1), Q_{35}^4 (Δ_n :1), Q_{35}^{48} (Δ_n :1), Q_{35}^{468} (Δ_n :1), Q_3^1 (Δ_n :3,4), Q_3^2 (Δ_n :2,3,4,7), Q_6^3 (Δ_n :1), Q_8^7 (Δ_n :1)
	97.5%	A'_1 (Δ_n :5,7), Q_{35}^4 (Δ_n :1), Q_{35}^{48} (Δ_n :1), Q_{35}^{468} (Δ_n :1)
	99%	Q_{35}^4 (Δ_n :1), Q_{35}^{48} (Δ_n :1)
(L_5,L_5^C)	95%	A'_1 (Δ_n :3,5,6,7,8), Q_{234}^{5678} (Δ_n :8), Q_0^{46} (Δ_n :8), Q_5^4 (Δ_n :1,2), Q_8^4 (Δ_n :6), Q_7^6 (Δ_n :4), Q_8^6 (Δ_n :4)
	97.5%	A'_1 (Δ_n :5,6,8), Q_7^6 (Δ_n :4), Q_8^6 (Δ_n :4)
	99%	Q_7^6 (Δ_n :4)
(L_6,L_6^C)	95%	A'_1 (Δ_n :8), A'_7 (Δ_n :1), A'_8 (Δ_n :2), σ'_R (Δ_n :4,8), Q_7^6 (Δ_n :4), Q_8^6 (Δ_n :4)
	97.5%	Q_7^6 (Δ_n :4), Q_8^6 (Δ_n :4)
	99%	Q_7^6 (Δ_n :4)
(L_7,L_8)	95%	A'_2 (Δ_n :3,5,6,7), A'_5 (Δ_n :4), A'_6 (Δ_n :3,8), ν (Δ_n :3,7,8), Q_0^{48} (Δ_n :1,2), Q_2^1 (Δ_n :3,5,6,7), Q_5^1 (Δ_n :4), Q_6^1 (Δ_n :3), Q_6^2 (Δ_n :3,5,6,7,8), Q_7^2 (Δ_n :3,5,6,7), Q_8^5 (Δ_n :4), Q_8^6 (Δ_n :3,6,7,8), Q_8^7 (Δ_n :3)
	97.5%	A'_2 (Δ_n :5), Q_0^{48} (Δ_n :1,2), Q_2^1 (Δ_n :5), Q_6^2 (Δ_n :3,5,6,7,8), Q_7^2 (Δ_n :3), Q_8^6 (Δ_n :3,8)
	99%	Q_0^{48} (Δ_n :2), Q_6^2 (Δ_n :3,5,6,7), Q_8^6 (Δ_n :3)
(L_9,L_9^C)	95%	A'_6 (Δ_n :4), A'_7 (Δ_n :1,8), A'_8 (Δ_n :2), $\Delta R'$ (Δ_n :3,4,5,7,8), σ'_R (Δ_n :3,4,5,6,7,8), ν (Δ_n :8), Q_{35}^{46} (Δ_n :3), Q_3^{48} (Δ_n :2), Q_{35}^{468} (Δ_n :3), Q_0^{48} (Δ_n :8), Q_6^1 (Δ_n :4), Q_7^1 (Δ_n :1), Q_6^5 (Δ_n :1), Q_7^5 (Δ_n :1), Q_8^5 (Δ_n :1), Q_8^6 (Δ_n :4)
	97.5%	A'_7 (Δ_n :8), $\Delta R'$ (Δ_n :3,4,8), σ'_R (Δ_n :3,4,5,6,8), ν (Δ_n :8), Q_3^{48} (Δ_n :2), Q_6^1 (Δ_n :4), Q_7^5 (Δ_n :1)
	99%	$\Delta R'$ (Δ_n :4,8), σ'_R (Δ_n :3,4,8), Q_7^5 (Δ_n :1)
(L_{10},L_{10}^C)	95%	A'_2 (Δ_n :1,4,7,8), A'_6 (Δ_n :3,4,8), A'_7 (Δ_n :4), $\Delta R'$ (Δ_n :3,5,6,7,8), σ'_R (Δ_n :3,5,6,7,8), Q_{35}^{468} (Δ_n :1), Q_{35}^{24} (Δ_n :1,2), Q_{234}^{5678} (Δ_n :3,6,8), Q_0^{468} (Δ_n :2,3,5,6,7), Q_0^{46} (Δ_n :2,3,5,6,7), Q_2^1 (Δ_n :1,7), Q_4^1 (Δ_n :2), Q_6^1 (Δ_n :4), Q_3^2 (Δ_n :1,4,5,8), Q_4^2 (Δ_n :1,2,4,7,8), Q_5^2 (Δ_n :1,2,5,7,8), Q_6^2 (Δ_n :1,3,5,6,7,8), Q_7^2 (Δ_n :1,7,8), Q_8^2 (Δ_n :8), Q_6^4 (Δ_n :4), Q_7^6 (Δ_n :4), Q_8^6 (Δ_n :3,4), Q_8^7 (Δ_n :4)
	97.5%	A'_2 (Δ_n :8), A'_6 (Δ_n :3,4,8), $\Delta R'$ (Δ_n :8), σ'_R (Δ_n :3,5,6,7,8), Q_{35}^{24} (Δ_n :1,2), Q_0^{468} (Δ_n :2,7), Q_3^2 (Δ_n :4,8), Q_4^2 (Δ_n :1,2,8), Q_5^2 (Δ_n :2,8), Q_6^2 (Δ_n :1,6,8), Q_7^2 (Δ_n :1,8), Q_8^2 (Δ_n :8), Q_6^4 (Δ_n :4), Q_7^6 (Δ_n :4), Q_8^6 (Δ_n :4), Q_8^7 (Δ_n :4)
	99%	A'_2 (Δ_n :8), A'_6 (Δ_n :8), σ'_R (Δ_n :5,6,7,8), Q_{35}^{24} (Δ_n :2), Q_4^2 (Δ_n :1), Q_8^6 (Δ_n :4), Q_8^7 (Δ_n :4)

Table B.11: Continuation of table B.10.

Set	p_{lim}	Quantities whose distributions differ at the level p_{lim}
(L_{11},L_{11}^C)	95%	A_2' (Δ_n :3,5,6,7,8), A_5' (Δ_n :8), A_6' (Δ_n :4), A_7' (Δ_n :4,8), Q_{35}^4 (Δ_n :1), Q_{35}^{48} (Δ_n :1), Q_{35}^{24} (Δ_n :3,7), Q_{234}^{5678} (Δ_n :8), Q_2^1 (Δ_n :3,4,5,6,7), Q_6^1 (Δ_n :4), Q_7^1 (Δ_n :4), Q_3^2 (Δ_n :3,4,5,6,7,8), Q_4^2 (Δ_n :1,2,5,7,8), Q_5^2 (Δ_n :3,5,6,7,8), Q_6^2 (Δ_n :3,5,6,7,8), Q_7^2 (Δ_n :3,5,6), Q_8^2 (Δ_n :3,5,6,8), Q_6^3 (Δ_n :1,4), Q_6^4 (Δ_n :4), Q_7^5 (Δ_n :1,4), Q_7^6 (Δ_n :1,4), Q_8^6 (Δ_n :4), Q_8^7 (Δ_n :4)
	97.5%	A_2' (Δ_n :3,8), A_6' (Δ_n :4), A_7' (Δ_n :4), Q_{35}^4 (Δ_n :1), Q_2^1 (Δ_n :3,6), Q_6^1 (Δ_n :4), Q_7^1 (Δ_n :4), Q_3^2 (Δ_n :3,8), Q_4^2 (Δ_n :1,2,8), Q_5^2 (Δ_n :8), Q_6^2 (Δ_n :3,5,6,8), Q_7^2 (Δ_n :3,6), Q_8^2 (Δ_n :8), Q_6^3 (Δ_n :1), Q_7^6 (Δ_n :1,4), Q_8^6 (Δ_n :4)
	99%	A_6' (Δ_n :4), Q_6^1 (Δ_n :4), Q_3^2 (Δ_n :8), Q_4^2 (Δ_n :1,2), Q_6^2 (Δ_n :6), Q_7^6 (Δ_n :4), Q_8^6 (Δ_n :4)
(L_{12},L_{12}^C)	95%	Q_{357}^{468} (Δ_n :1), Q_{35}^{46} (Δ_n :1), Q_{35}^4 (Δ_n :1), Q_{35}^{48} (Δ_n :1), Q_{35}^{468} (Δ_n :1), Q_6^3 (Δ_n :1)
	97.5%	Q_{357}^{468} (Δ_n :1), Q_{35}^{46} (Δ_n :1), Q_{35}^4 (Δ_n :1), Q_{35}^{48} (Δ_n :1), Q_{35}^{468} (Δ_n :1)
	99%	Q_{35}^4 (Δ_n :1), Q_{35}^{48} (Δ_n :1)
(L_{13},L_{13}^C)	95%	A_1' (Δ_n :5,6,7,8), A_4' (Δ_n :1,2,3,4,5,6,7,8), A_5' (Δ_n :8), A_8' (Δ_n :4), $\Delta R'$ (Δ_n :5,7,8), σ_R' (Δ_n :8), ν (Δ_n :6), Q_{357}^{468} (Δ_n :1,2,3,5,7,8), Q_{35}^{46} (Δ_n :1,2,3,5,6,7,8), Q_{35}^4 (Δ_n :1,3,5,7,8), Q_3^{48} (Δ_n :3,5,6,7,8), Q_{35}^{48} (Δ_n :1,3,5,6,7,8), Q_{35}^{468} (Δ_n :1,3,5,6,7,8), Q_0^{468} (Δ_n :1,2,3,4,5,6,7,8), Q_0^{48} (Δ_n :1,2,3,4,5,6,7,8), Q_0^{46} (Δ_n :3,5,6,7,8), Q_4^1 (Δ_n :1,2,3,4,5,6,7,8), Q_7^1 (Δ_n :1,2), Q_8^1 (Δ_n :3,5,6,7,8), Q_4^2 (Δ_n :3,5,6,7), Q_4^3 (Δ_n :3,5,6,7), Q_5^4 (Δ_n :1,2,3,5,6,7,8), Q_6^4 (Δ_n :3,7), Q_7^4 (Δ_n :2,3,5,6,7,8), Q_8^4 (Δ_n :3,5,6,7,8), Q_6^5 (Δ_n :1), Q_7^5 (Δ_n :1), Q_7^6 (Δ_n :1,4)
	97.5%	A_1' (Δ_n :5,6), A_4' (Δ_n :1,2,3,5,6,7,8), $\Delta R'$ (Δ_n :8), Q_{357}^{468} (Δ_n :1,3,7), Q_{35}^{46} (Δ_n :1,3,7,8), Q_{35}^4 (Δ_n :1,3,7,8), Q_3^{48} (Δ_n :3,5,6,7), Q_{35}^{48} (Δ_n :1,3,5,7,8), Q_{35}^{468} (Δ_n :1,3,5,7,8), Q_0^{468} (Δ_n :1,2,3,5,6,7,8), Q_0^{48} (Δ_n :1,2,3,4,5,6,7,8), Q_0^{46} (Δ_n :3,5,6,7,8), Q_4^1 (Δ_n :1,2,3,4,5,6,7,8), Q_7^1 (Δ_n :1,2), Q_8^1 (Δ_n :5,8), Q_4^2 (Δ_n :3,5,6,7), Q_5^4 (Δ_n :1,2,3,5,6,7,8), Q_7^4 (Δ_n :2,3,5,6,7,8), Q_8^4 (Δ_n :3,5,6,7,8), Q_6^5 (Δ_n :1), Q_7^5 (Δ_n :1), Q_7^6 (Δ_n :1,4)
	99%	A_4' (Δ_n :3,5,6,7,8), $\Delta R'$ (Δ_n :8), Q_{357}^{468} (Δ_n :1), Q_{35}^{46} (Δ_n :1), Q_{35}^{468} (Δ_n :3), Q_0^{468} (Δ_n :2,3,5,6,7,8), Q_0^{48} (Δ_n :1,2,3,5,6,7,8), Q_0^{46} (Δ_n :3,5,6,7,8), Q_4^1 (Δ_n :1,2,3,5,6,7,8), Q_7^1 (Δ_n :1,2), Q_5^4 (Δ_n :2,3,5,6,7,8), Q_7^4 (Δ_n :2,5,6,7,8), Q_8^4 (Δ_n :6), Q_6^5 (Δ_n :1), Q_7^6 (Δ_n :1)

Table B.12: Quantities and difference metrics (Δ_n :1,2,...; defined in Table 5.6) that indicate a statistically significant difference for 13 pairings of 21 subsets of the **HiRISE-FCC**, with respect to differences computed for 10,000 pairings of randomly-sampled subsets of a **Gaussian** reference distribution on the same domain. Listed are metrics reporting differences that exceed the percentage $p_{\rm lim}$ of differences computed from paired subsets of the reference distribution. **Mid-range** values were used and craters with $D < 100$ m were **excluded**. [CSC on, except for L_7 and L_8]

Set	$p_{\rm lim}$	Quantities whose distributions differ at the level $p_{\rm lim}$
(L_1,L_3)	95%	A'_3 (Δ_n :4), $\Delta R'$ (Δ_n :3,4,6,8), σ'_R (Δ_n :3,4,8), Q^{468}_{357} (Δ_n :4), Q^{48}_{3} (Δ_n :4), Q^{468}_{35} (Δ_n :4), Q^{48}_{0} (Δ_n :1,2), Q^{3}_{6} (Δ_n :4,8), Q^{3}_{8} (Δ_n :4)
	97.5%	$\Delta R'$ (Δ_n :3,4,8), σ'_R (Δ_n :3,4,8), Q^{3}_{6} (Δ_n :4,8)
	99%	$\Delta R'$ (Δ_n :8), σ'_R (Δ_n :4,8)
(L_2,L_3)	95%	$\Delta R'$ (Δ_n :3,4,5,6,7,8), σ'_R (Δ_n :3,4,8), ν (Δ_n :3,5,6,7), Q^{1}_{7} (Δ_n :1)
	97.5%	$\Delta R'$ (Δ_n :3,4,5,6,8), σ'_R (Δ_n :3,4,8), ν (Δ_n :3)
	99%	$\Delta R'$ (Δ_n :3,4,8), σ'_R (Δ_n :4,8), ν (Δ_n :3)
(L_4,L^C_4)	95%	A'_1 (Δ_n :1,3,4,8), A'_6 (Δ_n :1), A'_7 (Δ_n :1), Q^{1}_{3} (Δ_n :4), Q^{1}_{5} (Δ_n :4), Q^{1}_{6} (Δ_n :1,4), Q^{1}_{7} (Δ_n :4), Q^{1}_{8} (Δ_n :3,4,8), Q^{3}_{6} (Δ_n :1), Q^{5}_{7} (Δ_n :1), Q^{6}_{7} (Δ_n :1), Q^{7}_{8} (Δ_n :1)
	97.5%	A'_1 (Δ_n :1,3,4,8), Q^{1}_{3} (Δ_n :4), Q^{1}_{6} (Δ_n :1,4), Q^{1}_{7} (Δ_n :4), Q^{1}_{8} (Δ_n :4), Q^{7}_{8} (Δ_n :1)
	99%	A'_1 (Δ_n :1,3,4,8), Q^{1}_{6} (Δ_n :4), Q^{1}_{7} (Δ_n :4), Q^{1}_{8} (Δ_n :4), Q^{7}_{8} (Δ_n :1)
(L_5,L^C_5)	95%	A'_1 (Δ_n :8), A'_6 (Δ_n :4), Q^{2}_{8} (Δ_n :1,2), Q^{4}_{5} (Δ_n :1,2), Q^{6}_{7} (Δ_n :4), Q^{6}_{8} (Δ_n :4)
	97.5%	Q^{2}_{8} (Δ_n :1,2), Q^{6}_{7} (Δ_n :4), Q^{6}_{8} (Δ_n :4)
	99%	Q^{2}_{8} (Δ_n :1), Q^{6}_{7} (Δ_n :4), Q^{6}_{8} (Δ_n :4)
(L_6,L^C_6)	95%	A'_6 (Δ_n :4), Q^{1}_{6} (Δ_n :4), Q^{1}_{7} (Δ_n :4), Q^{2}_{8} (Δ_n :1), Q^{4}_{6} (Δ_n :4), Q^{6}_{7} (Δ_n :4), Q^{6}_{8} (Δ_n :4), Q^{7}_{8} (Δ_n :4)
	97.5%	A'_6 (Δ_n :4), Q^{1}_{7} (Δ_n :4), Q^{6}_{7} (Δ_n :4), Q^{6}_{8} (Δ_n :4), Q^{7}_{8} (Δ_n :4)
	99%	Q^{6}_{7} (Δ_n :4), Q^{6}_{8} (Δ_n :4)
(L_7,L_8)	95%	A'_5 (Δ_n :4), A'_6 (Δ_n :4), ν (Δ_n :3,4,5,7), Q^{1}_{3} (Δ_n :1), Q^{1}_{4} (Δ_n :4), Q^{1}_{6} (Δ_n :4), Q^{2}_{6} (Δ_n :3,5,6,7,8), Q^{5}_{8} (Δ_n :4), Q^{6}_{8} (Δ_n :3,8)
	97.5%	A'_5 (Δ_n :4), ν (Δ_n :3,4), Q^{1}_{6} (Δ_n :4), Q^{2}_{6} (Δ_n :7), Q^{6}_{8} (Δ_n :3)
	99%	ν (Δ_n :3), Q^{1}_{6} (Δ_n :4), Q^{6}_{8} (Δ_n :3)
(L_9,L^C_9)	95%	A'_1 (Δ_n :1,8), A'_3 (Δ_n :8), A'_6 (Δ_n :4), A'_7 (Δ_n :4,8), $\Delta R'$ (Δ_n :3,4,5,7,8), σ'_R (Δ_n :3,4,5,7,8), ν (Δ_n :1,3,4), Q^{468}_{357} (Δ_n :3), Q^{46}_{35} (Δ_n :3), Q^{4}_{35} (Δ_n :3), Q^{48}_{35} (Δ_n :3), Q^{468}_{35} (Δ_n :3), Q^{1}_{3} (Δ_n :1,3,6,7), Q^{1}_{5} (Δ_n :1,3), Q^{1}_{6} (Δ_n :1), Q^{1}_{7} (Δ_n :1), Q^{1}_{8} (Δ_n :1,8), Q^{6}_{7} (Δ_n :4), Q^{6}_{8} (Δ_n :4)
	97.5%	A'_1 (Δ_n :1,8), A'_6 (Δ_n :4), A'_7 (Δ_n :4), $\Delta R'$ (Δ_n :3,4,5,7,8), σ'_R (Δ_n :3,4,8), ν (Δ_n :1,3,4), Q^{1}_{3} (Δ_n :1), Q^{1}_{5} (Δ_n :1), Q^{1}_{6} (Δ_n :1), Q^{1}_{7} (Δ_n :1), Q^{1}_{8} (Δ_n :1), Q^{6}_{7} (Δ_n :4)
	99%	A'_1 (Δ_n :1,8), A'_6 (Δ_n :4), $\Delta R'$ (Δ_n :3,4,8), σ'_R (Δ_n :3,4,8), Q^{1}_{5} (Δ_n :1), Q^{1}_{6} (Δ_n :1), Q^{1}_{7} (Δ_n :1), Q^{1}_{8} (Δ_n :1)
(L_{10},L^C_{10})	95%	A'_1 (Δ_n :1), A'_2 (Δ_n :4,8), A'_6 (Δ_n :3,4,8), A'_7 (Δ_n :3,4,8), $\Delta R'$ (Δ_n :3,5,6,7,8), σ'_R (Δ_n :3,5,6,7,8), Q^{68}_{57} (Δ_n :4), Q^{5678}_{234} (Δ_n :3,8), Q^{468}_{0} (Δ_n :3,5,6,7), Q^{46}_{0} (Δ_n :3,5,6,7), Q^{1}_{2} (Δ_n :1,4), Q^{1}_{5} (Δ_n :1), Q^{1}_{6} (Δ_n :1), Q^{2}_{3} (Δ_n :1,2,4,8), Q^{2}_{4} (Δ_n :1,3,7,8), Q^{2}_{5} (Δ_n :1,2,5,7,8), Q^{2}_{6} (Δ_n :3,5,6,7,8), Q^{2}_{7} (Δ_n :8), Q^{2}_{8} (Δ_n :8), Q^{4}_{6} (Δ_n :4), Q^{6}_{7} (Δ_n :4), Q^{6}_{8} (Δ_n :3,4,8), Q^{7}_{8} (Δ_n :4)
	97.5%	A'_1 (Δ_n :1), A'_2 (Δ_n :8), A'_6 (Δ_n :3,4,8), A'_7 (Δ_n :3,4,8), $\Delta R'$ (Δ_n :5,6,7,8), σ'_R (Δ_n :3,5,6,7,8), Q^{5678}_{234} (Δ_n :8), Q^{468}_{0} (Δ_n :3,5,6,7), Q^{46}_{0} (Δ_n :5,6), Q^{1}_{6} (Δ_n :1), Q^{2}_{3} (Δ_n :1,2,4,8), Q^{2}_{4} (Δ_n :1), Q^{2}_{5} (Δ_n :8), Q^{2}_{6} (Δ_n :8), Q^{2}_{8} (Δ_n :8), Q^{4}_{6} (Δ_n :4), Q^{6}_{7} (Δ_n :4), Q^{6}_{8} (Δ_n :3,4,8), Q^{7}_{8} (Δ_n :4)
	99%	A'_1 (Δ_n :1), A'_2 (Δ_n :8), A'_6 (Δ_n :3,4,8), A'_7 (Δ_n :4), σ'_R (Δ_n :8), Q^{4}_{6} (Δ_n :4), Q^{6}_{7} (Δ_n :4), Q^{6}_{8} (Δ_n :4), Q^{7}_{8} (Δ_n :4)

Table B.13: Continuation of table B.12.

Set	p_{lim}	Quantities whose distributions differ at the level p_{lim}
(L_{11},L_{11}^C)	95%	A_2' (Δ_n :3,6,8), A_5' (Δ_n :4,8), A_6' (Δ_n :4), A_7' (Δ_n :4,8), Q_{35}^{468} (Δ_n :1), Q_{234}^{5678} (Δ_n :4,8), Q_2^1 (Δ_n :4), Q_4^1 (Δ_n :2), Q_6^1 (Δ_n :4), Q_3^2 (Δ_n :3,4,5,6,7,8), Q_4^2 (Δ_n :1,2,8), Q_5^2 (Δ_n :8), Q_6^2 (Δ_n :3,5,6), Q_7^2 (Δ_n :3,5,6), Q_8^2 (Δ_n :3,8), Q_6^3 (Δ_n :1,4), Q_6^4 (Δ_n :4), Q_6^5 (Δ_n :4), Q_7^5 (Δ_n :1,4), Q_7^6 (Δ_n :1,4), Q_8^6 (Δ_n :4), Q_8^7 (Δ_n :4)
	97.5%	A_2' (Δ_n :8), A_6' (Δ_n :4), A_7' (Δ_n :4), Q_6^1 (Δ_n :4), Q_3^2 (Δ_n :3,8), Q_4^2 (Δ_n :2), Q_6^2 (Δ_n :3,6), Q_6^3 (Δ_n :1,4), Q_6^4 (Δ_n :4), Q_6^5 (Δ_n :4), Q_7^5 (Δ_n :4), Q_7^6 (Δ_n :4), Q_8^6 (Δ_n :4)
	99%	A_6' (Δ_n :4), A_7' (Δ_n :4), Q_3^2 (Δ_n :8), Q_4^2 (Δ_n :2), Q_6^3 (Δ_n :4), Q_6^5 (Δ_n :4), Q_7^5 (Δ_n :4), Q_7^6 (Δ_n :4), Q_8^6 (Δ_n :4)
(L_{12},L_{12}^C)	95%	A_1' (Δ_n :1,8), A_5' (Δ_n :4), A_8' (Δ_n :8), Q_{357}^{468} (Δ_n :1,2), Q_{35}^{46} (Δ_n :1,2), Q_{35}^{4} (Δ_n :1,2), Q_{35}^{48} (Δ_n :1,2), Q_{35}^{468} (Δ_n :1,2), Q_5^1 (Δ_n :4), Q_6^1 (Δ_n :1), Q_7^1 (Δ_n :1), Q_8^1 (Δ_n :1,8), Q_6^3 (Δ_n :1)
	97.5%	A_1' (Δ_n :1), A_5' (Δ_n :4), A_8' (Δ_n :8), Q_{357}^{468} (Δ_n :1,2), Q_{35}^{46} (Δ_n :1,2), Q_{35}^{4} (Δ_n :1), Q_{35}^{468} (Δ_n :1,2), Q_5^1 (Δ_n :4), Q_6^1 (Δ_n :1), Q_7^1 (Δ_n :1), Q_8^1 (Δ_n :1)
	99%	A_1' (Δ_n :1), Q_{357}^{468} (Δ_n :1,2), Q_{35}^{46} (Δ_n :1), Q_{35}^{468} (Δ_n :1,2), Q_5^1 (Δ_n :4), Q_6^1 (Δ_n :1), Q_8^1 (Δ_n :1)
(L_{13},L_{13}^C)	95%	A_1' (Δ_n :1,4,8), A_4' (Δ_n :1,3,4,5,6,7,8), A_5' (Δ_n :8), A_8' (Δ_n :4), $\Delta R'$ (Δ_n :5,7,8), σ_R' (Δ_n :8), ν (Δ_n :1,3,5,6,7,8), Q_{357}^{468} (Δ_n :3,5,6,7,8), Q_{35}^{46} (Δ_n :1,3,5,6,7,8), Q_{35}^{4} (Δ_n :3,5,6,7,8), Q_3^{48} (Δ_n :3,5,6,7,8), Q_{35}^{48} (Δ_n :3,5,6,7,8), Q_{35}^{468} (Δ_n :3,5,6,7,8), Q_{35}^{24} (Δ_n :2,5,7), Q_0^{468} (Δ_n :1,2,3,5,6,7,8), Q_0^{48} (Δ_n :1,2,3,4,5,6,7,8), Q_0^{46} (Δ_n :3,5,6,7,8), Q_4^1 (Δ_n :1,2,4,5,7), Q_5^1 (Δ_n :1,8), Q_6^1 (Δ_n :1), Q_7^1 (Δ_n :1,4), Q_8^1 (Δ_n :1,8), Q_4^2 (Δ_n :1,2,3,5,6,7), Q_4^3 (Δ_n :1,3,5,6,7,8), Q_7^3 (Δ_n :2), Q_5^4 (Δ_n :1,2,3,5,6,7,8), Q_6^4 (Δ_n :1,3,5,7,8), Q_7^4 (Δ_n :2,3,5,6,7,8), Q_8^4 (Δ_n :3,5,6,7,8), Q_6^5 (Δ_n :1), Q_8^5 (Δ_n :8), Q_7^6 (Δ_n :1)
	97.5%	A_1' (Δ_n :1,8), A_4' (Δ_n :1,3,5,6,7,8), $\Delta R'$ (Δ_n :8), ν (Δ_n :1,3,5,6,7), Q_{357}^{468} (Δ_n :3,5,6,7,8), Q_{35}^{46} (Δ_n :3,5,6,7), Q_{35}^{4} (Δ_n :3,5,6,7,8), Q_3^{48} (Δ_n :3,5,6,7), Q_{35}^{48} (Δ_n :3,5,6,7,8), Q_{35}^{468} (Δ_n :3,5,6,7,8), Q_0^{468} (Δ_n :1,2,3,5,6,7,8), Q_0^{48} (Δ_n :1,3,4,5,6,7,8), Q_0^{46} (Δ_n :3,5,6,7,8), Q_4^1 (Δ_n :1,4), Q_5^1 (Δ_n :1), Q_6^1 (Δ_n :1), Q_8^1 (Δ_n :1), Q_4^2 (Δ_n :1,3,5,6,7), Q_4^3 (Δ_n :3,5,6,7), Q_7^3 (Δ_n :2), Q_5^4 (Δ_n :1,2,3,5,6,7,8), Q_6^4 (Δ_n :3,7,8), Q_7^4 (Δ_n :2,3,5,6,7,8), Q_8^4 (Δ_n :3,5,6,7), Q_6^5 (Δ_n :1), Q_7^6 (Δ_n :1)
	99%	A_1' (Δ_n :1,8), A_4' (Δ_n :3,5,6,7,8), $\Delta R'$ (Δ_n :8), ν (Δ_n :1,3,6,7), Q_{357}^{468} (Δ_n :3,7), Q_{35}^{46} (Δ_n :3), Q_{35}^{4} (Δ_n :3,7), Q_3^{48} (Δ_n :3,5,6), Q_{35}^{48} (Δ_n :3,5,6,7), Q_{35}^{468} (Δ_n :3,6,7), Q_0^{468} (Δ_n :2,3,5,6,7,8), Q_0^{48} (Δ_n :3,5,6,7,8), Q_0^{46} (Δ_n :3,5,6,7,8), Q_4^1 (Δ_n :1,4), Q_6^1 (Δ_n :1), Q_4^2 (Δ_n :1), Q_5^4 (Δ_n :2,3,5,6,7,8), Q_7^4 (Δ_n :3,5,6,7,8), Q_8^4 (Δ_n :5,6), Q_7^6 (Δ_n :1)

Appendix C

Auxiliary Material for Chapter 5: MOC-FCC

This Appendix contains additional tables and figures pertaining to the analysis of morphometric quantities derived from craters in the MOC Fresh Crater Catalog (MOC-FCC). Please see the text of Chapter 5 for detailed explanations of their contents.

Table C.1: For 9 subsets of the **MOC-FCC**: slope m and intercept b obtained from a linear regression for $\log \sigma_R^* = m \log D + b$ and $\log \Delta R^* = m \log D + b$, along with the Pearson correlation coefficient r_P computed for both relations. **Mid-range** values were assumed in this case and the fit was computed for $D \geq 100$ m. [CSC on, except for L_5, L_6, L_7, and L_7^C; $D_{\rm pix} \geq 20$]

Set	$m_{\Delta R}$	$b_{\Delta R}$	r_P	m_{σ_R}	b_{σ_R}	r_P
L_1	-0.26	-0.16	-0.60	-0.26	-0.75	-0.58
L_2	-0.23	-0.23	-0.54	-0.26	-0.77	-0.55
L_3	-0.25	-0.21	-0.56	-0.28	-0.76	-0.57
L_4	-0.26	-0.18	-0.49	-0.28	-0.75	-0.49
L_4^C	-0.27	-0.17	-0.59	-0.30	-0.70	-0.59
L_5	-0.24	-0.24	-0.45	-0.26	-0.80	-0.45
L_6	-0.26	-0.17	-0.58	-0.28	-0.74	-0.57
L_7	-0.24	-0.22	-0.48	-0.26	-0.80	-0.47
L_7^C	-0.27	-0.18	-0.58	-0.30	-0.71	-0.58

Table C.2: Global properties of shape distributions for 9 subsets of the **MOC-FCC**, using **mid-range** values and **including** craters with $D < 100$ m. Listed are the number of triangles (N_3), squares (N_4), pentagons (N_5), and hexagons (N_6) in each subset, along with mean ± standard deviation of detrended maximum and standard radial deviations ($\Delta R'$ and σ'_R, respectively) and concave fraction (ν'). [CSC on, except for L_5, L_6, L_7, and L_7^C; $D_{\rm pix} \geq 20$]

Set	N	N_3	N_4	N_5	N_6	σ'_R	$\Delta R'$	ν'
L_1	51	33	14	2	2	0.23 ± 0.09	0.79 ± 0.26	0.917 ± 0.028
L_2	141	79	43	13	3	0.21 ± 0.08	0.73 ± 0.25	0.911 ± 0.028
L_3	72	44	19	7	1	0.20 ± 0.09	0.70 ± 0.27	0.908 ± 0.023
L_4	105	53	35	13	2	0.20 ± 0.08	0.72 ± 0.27	0.911 ± 0.021
L_4^C	245	139	73	24	6	0.20 ± 0.08	0.69 ± 0.24	0.909 ± 0.026
L_5	263	146	78	25	11	0.19 ± 0.07	0.66 ± 0.23	0.908 ± 0.029
L_6	261	150	77	28	3	0.19 ± 0.07	0.67 ± 0.23	0.910 ± 0.025
L_7	317	178	92	35	8	0.19 ± 0.07	0.68 ± 0.23	0.909 ± 0.028
L_7^C	252	144	75	23	7	0.18 ± 0.08	0.65 ± 0.23	0.908 ± 0.026

Table C.3: Global properties of shape distributions for 9 subsets of the **MOC-FCC**, using **mid-range** values and **including** craters with $D < 100$ m. Listed are the mean ± standard deviation of deviation-normalized harmonic amplitudes A'_2 through A'_5.[CSC on, except for L_5, L_6, L_7, and L_7^C; $D_{\rm pix} \geq 20$]

Set	N	A'_2	A'_3	A'_4	A'_5
L_1	51	0.118 ± 0.048	0.071 ± 0.035	0.052 ± 0.032	0.038 ± 0.019
L_2	141	0.124 ± 0.043	0.065 ± 0.034	0.054 ± 0.031	0.037 ± 0.019
L_3	72	0.110 ± 0.048	0.069 ± 0.031	0.052 ± 0.028	0.037 ± 0.023
L_4	105	0.111 ± 0.043	0.068 ± 0.036	0.054 ± 0.028	0.038 ± 0.020
L_4^C	245	0.115 ± 0.045	0.068 ± 0.034	0.056 ± 0.030	0.039 ± 0.022
L_5	263	0.114 ± 0.044	0.068 ± 0.034	0.054 ± 0.028	0.038 ± 0.020
L_6	261	0.113 ± 0.045	0.067 ± 0.033	0.055 ± 0.027	0.038 ± 0.021
L_7	317	0.114 ± 0.044	0.068 ± 0.033	0.053 ± 0.026	0.039 ± 0.020
L_7^C	252	0.114 ± 0.045	0.069 ± 0.034	0.055 ± 0.029	0.038 ± 0.021

Table C.4: Quantities and difference metrics (Δ_n: for $n = 1, 2, ...$; defined in Table 5.6) that indicate a statistically significant difference for 5 pairings of 9 subsets of the **MOC-FCC**, with respect to differences computed for 10,000 pairings of randomly-sampled subsets of a **Gaussian** reference distribution on the same domain. Listed are metrics reporting differences that exceed the percentage $p_{\rm lim}$ of differences computed from paired subsets of the reference distribution. **Mid-range** values were used and craters with $D < 100$ m were **included**.[CSC on, except for L_5, L_6, L_7, and L_7^C; $D_{\rm pix} \geq 20$]

Set	$p_{\rm lim}$	Quantities whose distributions differ at the level $p_{\rm lim}$
(L_1,L_3)	95%	$\Delta R'$ (Δ_n :8), σ'_R (Δ_n :8), ν (Δ_n :3,7), Q^{468}_{357} (Δ_n :4), Q^{46}_{35} (Δ_n :4), Q^{48}_{3} (Δ_n :1,2,4), Q^{468}_{35} (Δ_n :4), Q^{48}_{0} (Δ_n :1,2), Q^{3}_{4} (Δ_n :1), Q^{5}_{6} (Δ_n :4)
	97.5%	Q^{468}_{357} (Δ_n :4), Q^{48}_{3} (Δ_n :1), Q^{468}_{35} (Δ_n :4)
	99%	Q^{468}_{357} (Δ_n :4)
(L_2,L_3)	95%	A'_1 (Δ_n :1), A'_2 (Δ_n :2,3,5,6,7), A'_8 (Δ_n :1), Q^{468}_{357} (Δ_n :4), Q^{48}_{3} (Δ_n :8), Q^{24}_{35} (Δ_n :5,6,7), Q^{5678}_{234} (Δ_n :4,8), Q^{1}_{2} (Δ_n :6), Q^{1}_{6} (Δ_n :1), Q^{2}_{3} (Δ_n :6), Q^{2}_{5} (Δ_n :5,6), Q^{2}_{6} (Δ_n :3,5,6), Q^{2}_{7} (Δ_n :1,2,3,5,6,7), Q^{2}_{8} (Δ_n :3,5,6,7), Q^{5}_{6} (Δ_n :1), Q^{5}_{7} (Δ_n :4), Q^{7}_{8} (Δ_n :1)
	97.5%	A'_1 (Δ_n :1), A'_2 (Δ_n :2,5,6), A'_8 (Δ_n :1), Q^{5678}_{234} (Δ_n :8), Q^{1}_{6} (Δ_n :1), Q^{2}_{6} (Δ_n :6), Q^{2}_{7} (Δ_n :5,6), Q^{7}_{8} (Δ_n :1)
	99%	A'_1 (Δ_n :1), Q^{1}_{6} (Δ_n :1)
(L_4,L_4^C)	95%	A'_1 (Δ_n :1), A'_6 (Δ_n :8), $\Delta R'$ (Δ_n :1), σ'_R (Δ_n :1), ν (Δ_n :4), Q^{68}_{57} (Δ_n :1), Q^{1}_{6} (Δ_n :1), Q^{1}_{7} (Δ_n :1), Q^{1}_{8} (Δ_n :1), Q^{5}_{6} (Δ_n :1), Q^{6}_{8} (Δ_n :1), Q^{7}_{8} (Δ_n :1)
	97.5%	A'_1 (Δ_n :1), A'_6 (Δ_n :8), σ'_R (Δ_n :1), ν (Δ_n :4), Q^{1}_{6} (Δ_n :1), Q^{1}_{7} (Δ_n :1), Q^{1}_{8} (Δ_n :1)
	99%	A'_1 (Δ_n :1), σ'_R (Δ_n :1), Q^{1}_{8} (Δ_n :1)
(L_5,L_6)	95%	ν (Δ_n :4), Q^{3}_{7} (Δ_n :2), Q^{6}_{7} (Δ_n :1), Q^{7}_{8} (Δ_n :1,2)
	97.5%	ν (Δ_n :4), Q^{7}_{8} (Δ_n :1,2)
	99%	Q^{7}_{8} (Δ_n :1)
(L_7,L_7^C)	95%	A'_3 (Δ_n :2), A'_6 (Δ_n :3,5,6,7,8), A'_7 (Δ_n :5,7,8), $\Delta R'$ (Δ_n :3,8), Q^{48}_{3} (Δ_n :4), Q^{468}_{35} (Δ_n :1), Q^{24}_{35} (Δ_n :2), Q^{5678}_{234} (Δ_n :1,7,8), Q^{1}_{6} (Δ_n :7,8), Q^{2}_{3} (Δ_n :2), Q^{2}_{7} (Δ_n :2), Q^{3}_{4} (Δ_n :4), Q^{6}_{8} (Δ_n :7,8)
	97.5%	A'_3 (Δ_n :2), A'_6 (Δ_n :6,7,8), A'_7 (Δ_n :7,8), Q^{5678}_{234} (Δ_n :1), Q^{1}_{6} (Δ_n :8), Q^{6}_{8} (Δ_n :8)
	99%	A'_6 (Δ_n :8), A'_7 (Δ_n :8)

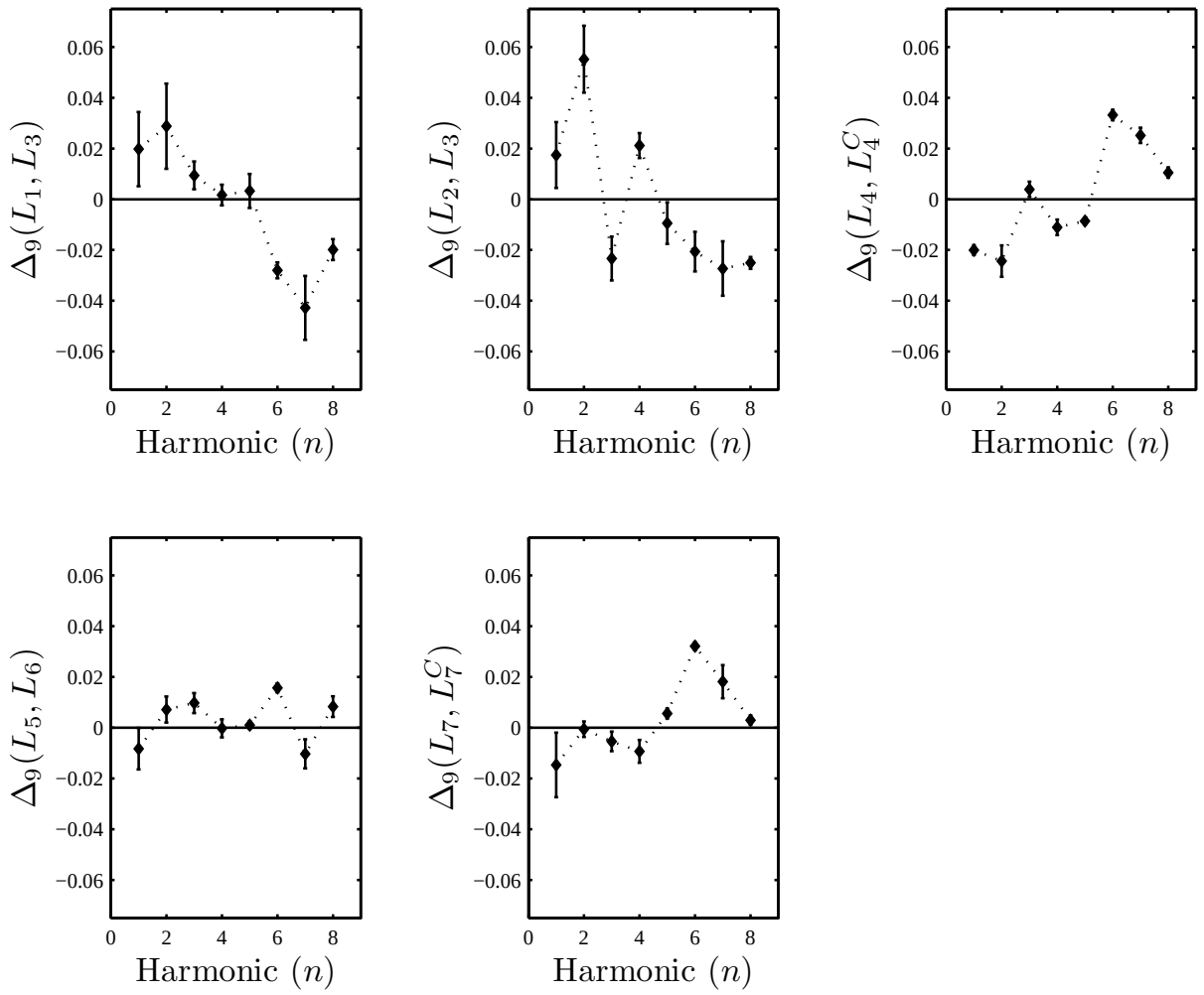

Figure C-1: Value of the relative difference metric Δ_9 (see Table 5.6) measured for the comparison between distributions of deviation-normalized harmonic amplitudes, for harmonics $n = 1, 2, 3, ..., 8$ and all subset comparisons in the MOC-FCC. A value of Δ_9 for the comparison (L_x, L_y) above zero for harmonic n means that values of A'_n for craters in L_x are larger on average than those in L_y. [CSC on, except for (L_7, L_8); Error bars span the entire range of values computed for (a) SEV for all D, (b) SEV for $D \geq 100$ m, (c) MRV for all D, and (d) MRV for $D \geq 100$ m.]

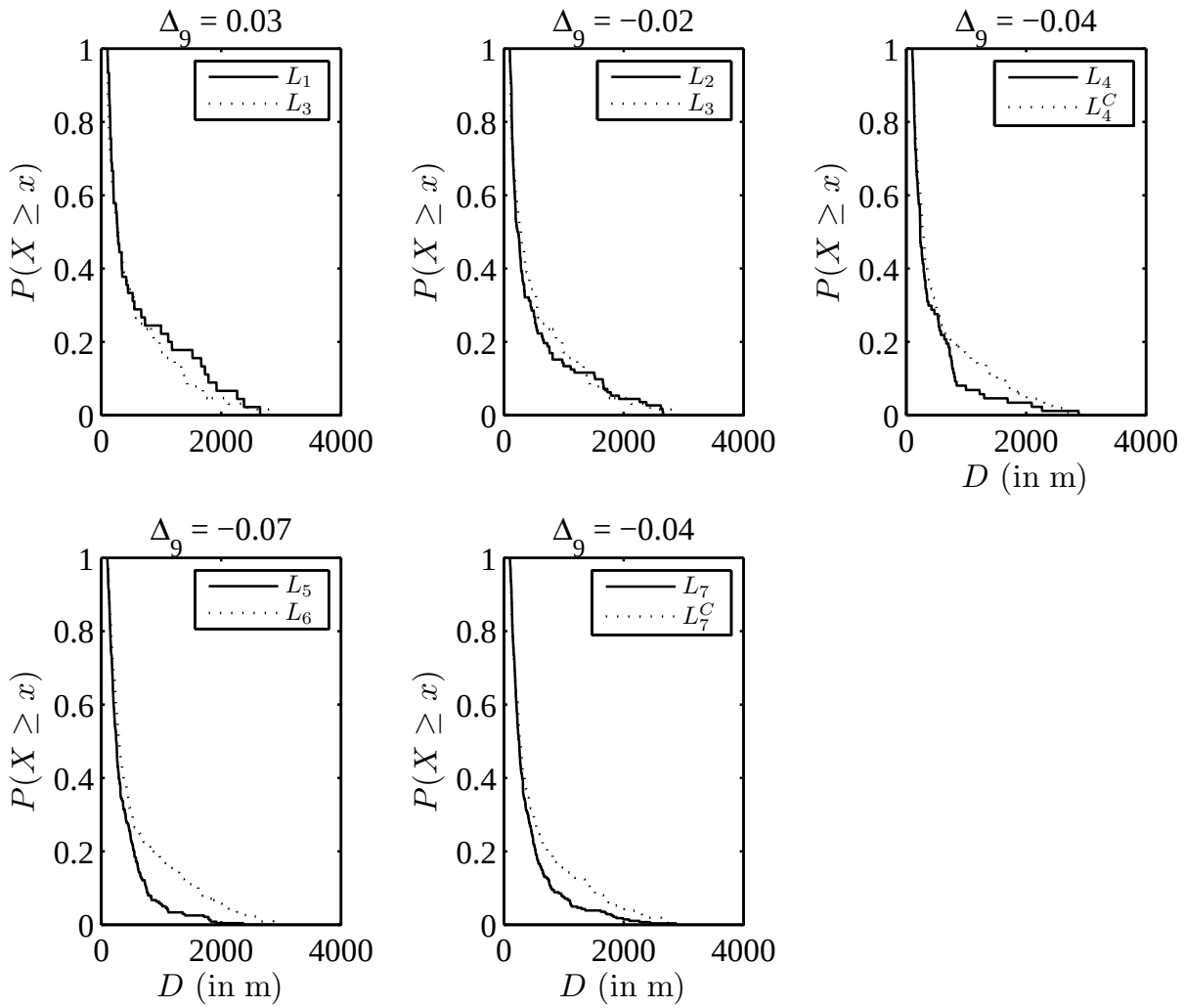

Figure C-2: Cumulative distribution of diameter for each subset in 5 subset comparisons (MOC-FCC) with no bounds imposed on σ_R^*, and the difference between these measured by the relative difference metric Δ_9. (i.e., "Δ_9" for the comparison (L_x, L_y) is equal to $\Delta_9(\mathbf{D}_x, \mathbf{D}_y)$ where $\mathbf{D}_x$ are the diameters of craters in L_x and $\mathbf{D}_y$ are the diameters of craters in L_y. A positive value means that craters in L_x are on average larger than craters in L_y.) [SEV; CSC on; $D \geq 100$ m; $\sigma_R^* \geq 0.04$]

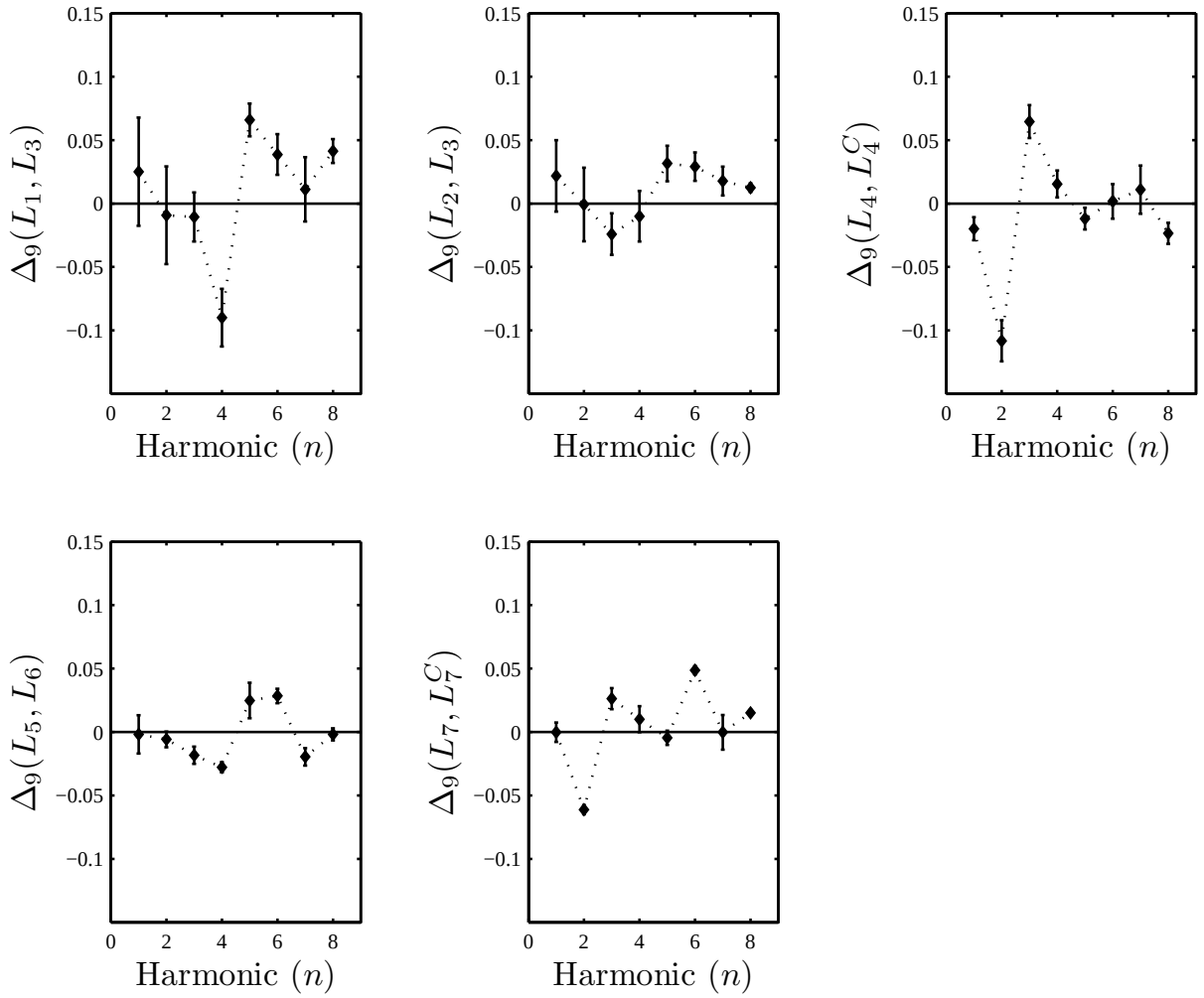

Figure C-3: Value of the relative difference metric Δ_9 (see Table 5.6) measured for the comparison between distributions of deviation-normalized harmonic amplitudes, for harmonics $n = 1, 2, 3, ..., 8$ and all subset comparisons in the MOC-FCC for craters with $\sigma_R^* \geq 0.04$. A value of Δ_9 for the comparison (L_x, L_y) above zero for harmonic n means that values of A'_n for craters in L_x are larger on average than those in L_y. In comparing results for low harmonics with dominant harmonic fractions reported in the main text, note that it is possible for a harmonic n to be smaller, on average, in a subset with a comparitively large fraction of primary harmonics of order n: i.e., it is important to note where in the distribution a difference occurs. [CSC on, except for (L_7, L_8); $\sigma_R^* \geq 0.04$; Error bars span the entire range of values computed for (a) SEV for all D, (b) SEV for $D \geq 100$ m, (c) MRV for all D, and (d) MRV for $D \geq 100$ m.]

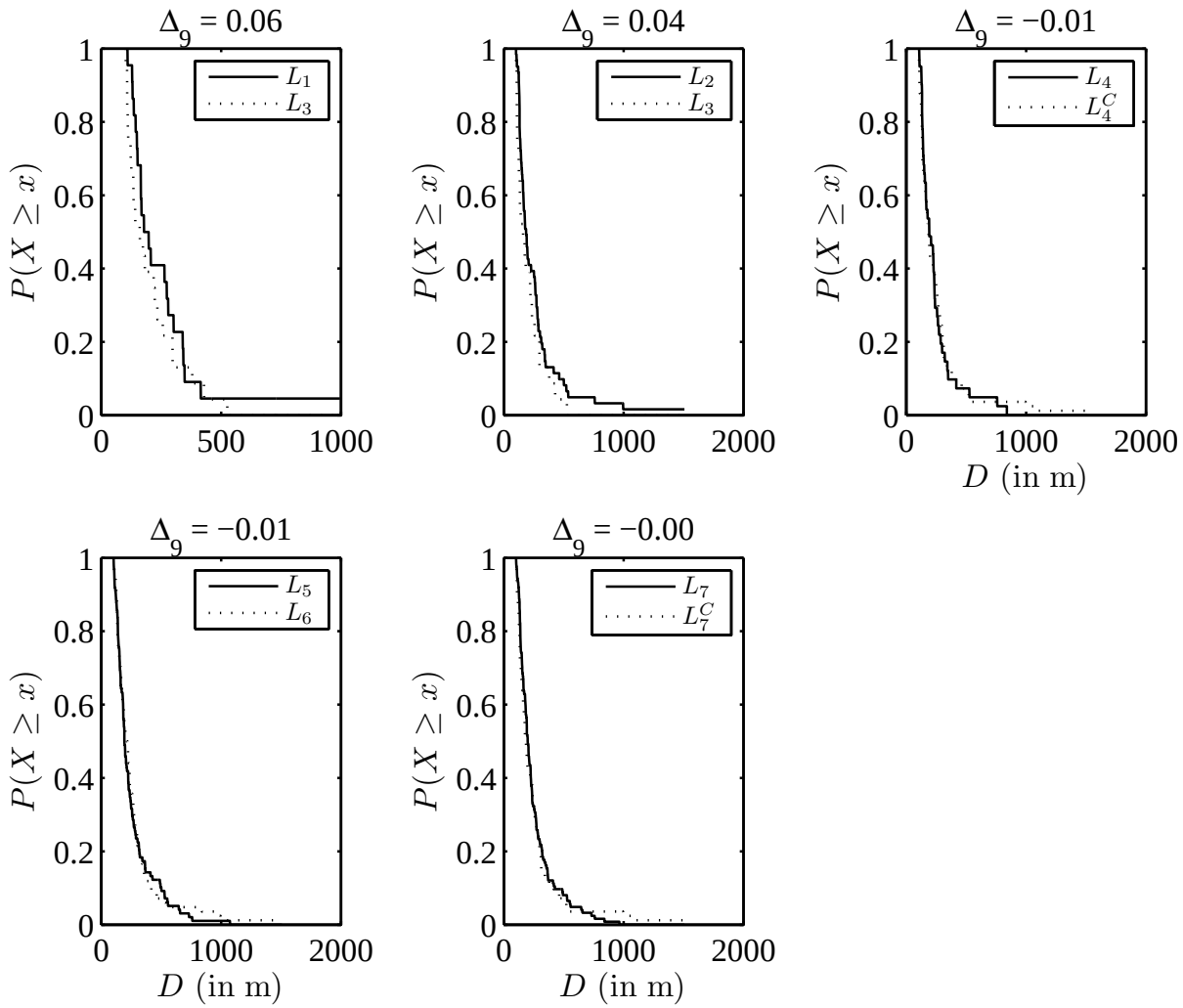

Figure C-4: Cumulative distribution of diameter for each subset in 5 subset comparisons (MOC-FCC) for $\sigma_R^* \geq 0.04$, and the difference between these measured by the relative difference metric Δ_9. (i.e., "Δ_9" for the comparison (L_x, L_y) is equal to $\Delta_9(\mathbf{D}_x, \mathbf{D}_y)$ where $\mathbf{D}_x$ are the diameters of craters in L_x and $\mathbf{D}_y$ are the diameters of craters in L_y. A positive value means that craters in L_x are on average larger than craters in L_y.) [SEV; CSC on; $D \geq 100$ m; $\sigma_R^* \geq 0.04$;]

Table C.5: Comparison of morphometric properties of PCROs from full-resolution HiRISE images and the same images downsampled to $D_{\rm pix} = 20$ (20 pixel diameter). "Std. dev" is the standard deviation of the difference between the high- and low-resolution estimate, "Range" is the range of the full-resolution values (for all craters in the HiRISE-FCC), and r_P is the Pearson correlation coefficient for the entire set of full- versus low-resolution estimates.

	Std. dev.	**Range**	r_P
A'_1	0.0099	0.0305	0.0633
A'_2	0.0530	0.1934	0.2138
A'_3	0.0357	0.1452	0.4612
A'_4	0.0351	0.1501	0.3118
A'_5	0.0279	0.1117	0.2783
A'_6	0.0228	0.1122	0.0832
A'_7	0.0157	0.0726	0.2203
A'_8	0.0165	0.0482	0.2056
ΔR^*	0.0518	0.3007	0.6361
σ^*_R	0.0107	0.0619	0.6729
ν	0.0394	0.2028	0.2891
$\sigma^*_R < 0.025$			
A'_1	0.0100	0.0269	0.0119
A'_2	0.0559	0.1525	0.0388
A'_3	0.0381	0.1340	0.4915
A'_4	0.0396	0.1242	0.1946
A'_5	0.0266	0.1032	0.3244
A'_6	0.0229	0.1122	0.0759
A'_7	0.0178	0.0690	0.1251
A'_8	0.0203	0.0461	0.1237
$\sigma^*_R \geq 0.04$			
A'_1	0.0100	0.0193	0.1415
A'_2	0.0316	0.1798	0.7868
A'_3	0.0221	0.0731	0.5803
A'_4	0.0227	0.0840	0.6743
A'_5	0.0318	0.0970	0.2162
A'_6	0.0223	0.0618	0.2174
A'_7	0.0187	0.0717	0.1210
A'_8	0.0136	0.0372	-0.0488

Table C.6: Identical to table C.5, except that $D_{\rm pix} = 50$ (50 pixel diameter).

	Std. dev.	**Range**	r_P
A'_1	0.0095	0.0305	0.1321
A'_2	0.0411	0.1934	0.5546
A'_3	0.0278	0.1452	0.6174
A'_4	0.0322	0.1501	0.4282
A'_5	0.0239	0.1117	0.4909
A'_6	0.0194	0.1122	0.3891
A'_7	0.0156	0.0726	0.3968
A'_8	0.0142	0.0482	0.2439
ΔR^*	0.0432	0.3007	0.7630
σ^*_R	0.0076	0.0619	0.8484
ν	0.0363	0.2028	0.4595
$\sigma^*_R < 0.025$			
A'_1	0.0095	0.0246	0.0325
A'_2	0.0355	0.1422	0.4605
A'_3	0.0310	0.1452	0.5114
A'_4	0.0333	0.1141	0.3616
A'_5	0.0234	0.1091	0.5879
A'_6	0.0219	0.1122	0.2775
A'_7	0.0185	0.0483	0.2092
A'_8	0.0167	0.0461	0.0506
$\sigma^*_R \geq 0.04$			
A'_1	0.0089	0.0181	0.3096
A'_2	0.0472	0.1638	0.5121
A'_3	0.0172	0.0835	0.7424
A'_4	0.0181	0.0712	0.7223
A'_5	0.0249	0.0990	0.5464
A'_6	0.0096	0.0534	0.8244
A'_7	0.0159	0.0723	0.4942
A'_8	0.0117	0.0390	0.5757

Bibliography

D. Abbott and A. E. Isley. Extraterrestrial influences on mantle plume activity. *Earth and Planet. Sci. Lett.*, 202:551–561, 2002.

M. H. Acuna, J. E. P. Connerney, N. F. Ness, R. P. Lin, D. Mitchell, C. W. Carlson, J. McFadden, K. A. Anderson, H. Rème, C. Mazelle, D. Vignes, P. Wasilewski, and P. Cloutier. Global distribution of crustal magnetization discovered by the Mars Global Surveyor MAG/ER experiment. *Science*, 284: 790–793, 1999.

T. J. Ahrens. Shock wave techniques for geophysics and planetary physics. In *Methods of Experimental Physics*, pages 185–225. Academic Press Inc., 1987.

T. J. Ahrens and M. L. Johnson. Shock wave data for rocks. In *AGU Reference Shelf 3*, pages 35–43. American Geophysical Union, 1995.

T. J. Ahrens and J. D. O'Keefe. Equations of state and impact-induced shock-wave attenuation on the moon. In D. J. Roddy, R. O. Pepin, and R. B. Merrill, editors, *Impact and Explosion Cratering*, pages 639–656. Pergamon Press, Elmsford, NY, 1977.

R. C. Anderson, J. M. Dohm, M. P. Golombek, A. F. C. Haldemann, B. J. Franklin, K. L. Tanaka, J. Lias, and B. Peer. Primary centers and secondary concentrations of tectonic activity through time in the western hemisphere of Mars. *Journal Geophys. Res.*, 106:20563–20585, 2001.

J. C. Andrews-Hanna, M. T. Zuber, and W. B. Banerdt. The borealis basin and the origin of the Martian crustal dichotomy. *Nature*, 453: 1212–1215, 2008.

J. Arkani-Hamed and A. Pentecost. On the source region of the lunar mare basalt. *Journal Geophys. Res.*, 106:14691–14700, 2001.

R. E. Arvidson, R. C. Anderson, P. Bartlett, J. F. B. III, P. R. Christensen, P. Chu, K. Davis, B. L. Ehlmann, M. P. Golombek, S. Gorevan, E. A. Guinness, A. F. C. Haldemann, K. E. Herkenhoff, G. Landis, R. Li, R. Lindemann, D. W. Ming, T. Myrick, T. Parker, L. Richter, F. P. Seelos, L. A. Soderblom, S. W. Squyres, R. J. Sullivan, and J. Wilson. Localization and physical property experiments conducted by Opportunity at Meridiani Planum. *Science*, 306:1730–1733, 2004.

W. B. Banerdt and M. P. Golombek. Tectonics of the Tharsis region of Mars: insights from MGS topography and gravity. *Lunar Planet Sci. Conf. XXXI*, page Abstr. 2039, 2000.

N. G. Barlow and T. L. Bradley. Martian impact craters: Correlations of the ejecta and interior morphologies with diameter, altitude, and terrain. *Icarus*, 87:156–179, 1990.

D. M. Barringer. Coon mountain and its crater. *Proc. Acad. Nat. Sci of Philadelphia*, 57:861–886, 1905.

D. Bercovici and A. Kelly. The non-linear initiation of diapirs and plume heads. *Phys. Earth Planet. Int.*, 101:119–130, 1997.

C. M. Bertka and Y. Fei. Density profile of an SNC model Martian interior and the moment-of-inertia factor of Mars. *Earth and Planet. Sci. Lett.*, 157, 1998.

D. Boutin and J. Arkani-Hamed. Elliptical craters on Mars: Evidence for polar wander of Mars. *Lunar Plant. Sci Conf.*, 38:1249, 2007.

J. M. Boyce, P. Mouginis-Mark, and L. L. Tornabene. Deep impact craters in the Isidis and southwestern Utopia Planitia regions of Mars: High target material strength as a possible cause. *Geophys. Res. Lett.*, 33: doi:10.1029/2005GL024462, 2006.

L. Breiman, J. Friedma, C. J. Stone, and R. A. Olshen. *Classification and Regression Trees*. Chapman and Hall, Boca Raton, Belmont,Ca, 1993.

D. Breuer, D. A. Yuen, T. Spohn, and S. Zhang. Three dimensional models of Martian mantle convection with phase transitions. *Geophys. Res. Lett.*, 25(3):229–232, 1998.

J. Canny. A computational approach to edge detection. *IEEE Transactions on Pattern Analysis and Machine Intelligence*, PAMI-8:679–698, 1986.

M. Carr. *The Surface of Mars*. Cambridge Univ. Press, Cambridge, UK, 1st edition, 2006.

J. E. Chappelow and V. L. Sharpton. An improved shadow measurement technique for constraining the morphometry of simple impact craters. *Meteoritics and Planetary Science*, 37:479–486, 2002.

M. J. Cintala and P. J. Mouginis-Mark. Martian fresh crater depths: more evidence for subsurface volatiles? *Geophys. Res. Lett.*, 7:329–332, 1980.

J. W. Cooley and J. W. Tukey. An algorithm for the machine computation of the complex fourier series. *Mathematics of Computation*, 19:297–301, 1965.

S. K. Croft. Cratering flow fields: Implications for the excavation and transient expansion stages of crater formation. *Proc. Lunar Planet. Sci. Conf.*, 11:2347–2378, 1980.

M. R. Dence. Shock zoning at Canadian craters: Petrography and structural implications. *Shock metamorphism of natural materials*, 1:169–184, 1968.

A. M. Dziewonski and D. L. Anderson. Preliminary reference Earth model. *Phys. Earth Planet. Int.*, 25:297–356, 1981.

L. Elkins-Tanton and B. H. Hager. Giant meteoroid impacts can cause volcanism. *Earth and Planet Sci. Lett.*, 3-4:219–232, 2005.

D. T. Eppler, D. Nummedal, and R. Ehrlech. Fourier analysis of lunar crater shape – possible guide to impact history and lunar geology. In D. Roddy, R. Pepin, and R. Merrill, editors, *Impact and explosion cratering*, pages 511–526. Pergamon Press, New York, New York, 1977.

D. T. Eppler, R. Ehrlich, D. Nummedal, and P. H. Schultz. Source of shape variation in lunar impact craters: Fourier shape analysis. *GSA Bull.*, 94:274–291, 1983.

G. L. Evans. Investigations at the Odessa meteor craters. *Proceedings of the Geophysical Laboratory – Lawrence Radiation Cratering Symposium*, 1:D1–D11, 1961.

H. Fechtig, D. E. Gault, G. Neukum, and E. Schneider. Laboratory simulation of lunar craters. *Die Naturwissenschaften*, 59:151–157, 1972.

W. M. Folkner, C. F. Yoder, D. N. Yuan, E. M. Standish, and R. A. Preston. Interior structure and seasonal mass redistribution of Mars from radio tracking of Mars Pathfinder. *Science*, 1997.

H. V. Frey, J. H. Roark, K. M. Shockey, E. L. Frey, and S. E. H. Sakimoto. Ancient lowlands on Mars. *Geophys. Res. Lett.*, 29:1384, 2002. doi: 10.1029/2001GL013832.

C. V. Fulmer and W. A. Roberts. Rock induration and crater shape. *Icarus*, 2:452–465, 1963.

J. B. Garvin and J. J. Frawley. Geometric properties of martian impact craters: Preliminary results from the Mars Orbiter Laser Altimeter. *Geophys. Res. Lett.*, 25:4405–4408, 1998.

J. B. Garvin, S. E. H. Sakimoto, J. J. Frawley, and C. Schnetzler. North polar region crater-forms on Mars: Geometric characteristics from the Mars Orbiter Laser Altimeter. *Icarus*, 144: 329–352, 2000.

D. E. Gault and E. D. Heitowit. The partition of energy for hypervelocity impact craters formed in rock. *Proceedings of the 6th Hypervelocity Impact Symposium*, 2:419–456, 1963.

D. E. Gault and J. A. Wedekind. Experimental studies of oblique impact. *Lunar Planet. Sci*, 9:3843–3875, 1978.

D. E. Gault, W. L. Quaide, and V. R. Oberbeck. Impact cratering mechanics and structures. In B. French and N. Short, editors, *Shock Metamorphism of Natural Materials*, pages 87–99. Mono Book Corp, Baltimore, Maryland, 1968.

A. Ghods and J. Arkani-Hamed. Impact-induced convection as the main mechanism for formation of lunar mare basalts. *Journal Geophys. Res.*, 112:E03005, 2007. doi: 10.1029/2006JE002709.

J. A. Grant, R. E. Arvidson, L. S. Crumpler, M. P. Golombek, B. Hahn, A. F. C. Haldemann, R. Li, L. A. Soderblom, S. W. Squyres, S. P. Wright, and W. A. Watters. Crater gradation in Gusev crater and Meridiani Planum, Mars. *Journal of Geophysical Research - Planets*, 111, 2006.

R. Greeley and J. E. Guest. Geologic map of the eastern equatorial region of Mars, scale 1:15,000,000. *U.S. Geol. Survey Map*, I-1802-B, 1987.

D. H. Green. Archaean greenstone belts may include terrestrial equivalents of lunar maria? *Nature*, 15:263–270, 1972.

R. A. F. Grieve and J. B. Garvin. A geometric model for excavation and modification at terrestrial simple impact craters. *J. Geophys. Res.*, 89:11,561–11,572, 1984.

R. E. Grimm and S. C. Solomon. Tectonic tests of proposed polar wander paths for Mars and the moon. *Icarus*, 65:110–121, 1986.

K. A. Grossenbacher and S. M. McDuffie. Conductive cooling of lava: columnar joint diameter and stria width as functions of cooling rate and thermal gradient. *Journal of Volcanology and Geothermal Research*, 69:95–103, 1995.

J. P. Grotzinger, R. E. Arvidson, J. F. Bell, W. Calvin, B. C. Clark, D. A. Fike, M. Golombek, R. Greeley, A. Haldemann, K. E. Herkenhoff, B. L. Jolliff, A. H. Knoll, M. Malin, S. M. McLennan, T. Parker, L. Soderblom, J. N. Sohl-Dickstein, S. W. Squyres, N. J. Tosca, and W. A. Watters. Stratigraphy and sedimentology of a dry to wet eolian depositional system, Burns formation, Meridiani Planum, Mars. *Earth and Planet. Sci. Lett.*, 240:11–72, 2005.

H. Harder and U. R. Christensen. A one-plume model of Martian mantle convection. *Nature*, 380:507–509, 1996.

W. K. Hartmann and G. Neukum. Cratering chronology and the evolution of Mars. *Space Science Reviews*, 96:164–194, 2001.

J. W. Head, M. A. Kreslavsky, and S. Pratt. Northern lowlands of Mars: Evidence for widespread volcanic flooding and tectonic deformation in the Hesperian period. *Journal Geophys. Res.*, 107:E15003, 2002. doi: 10.1029/2000JE001445.

L. N. Howard. Convection at high Rayleigh number. In H. Gortler, editor, *Proc. 11th Intl. Cong. Appl. Mech.*, pages 1109–15. Springer-Verlag, Berlin, 1966.

H. E. Huppert. The propagation of two-dimensional and axisymmetric viscous gravity currents over a rigid horizontal surface. *J. Fluid Mech.*, 121:43–58, 1982.

B. A. Ivanov and H. J. Melosh. Impacts do not initiate volcanic eruptions: Eruptions close to the crater. *Geology*, 31(10):869–872, 2003.

A. P. Jones, G. D. Price, N. J. Price, P. S. DeCarli, and R. A. Clegg. Impact induced melting and the development of large igneous

provinces. *Earth and Planet. Sci. Lett.*, 202: 551–561, 2002.

N. Keshava. Distance metrics and band selection in hyperspectral processing with applications to material identification and spectral libraries. *IEEE Transactions on Geoscience and Remote Sensing*, 42:1552–1565, 2004.

W. S. Kiefer. Melting in the Martian mantle: Shergottite formation and implications for present-day mantle convection on Mars. *Meteoritics and Planetary Science*, 39:1815–1832, 2003.

S. D. King, A. Raefsky, and B. H. Hager. Conman: Vectorizing a finite element code for incompressible two-dimensional convection in the Earth's mantle. *Phys. Earth Planet. Int.*, 59:195–207, 1990.

D. A. Kring. *Guidebook to the Geology of Barringer Meteorite Crater, Arizona*. Lunar and Planetary Institute, Houston, Texas, 1st edition, 2007.

P. S. Kumar. Structural effects of meteorite impact on basalt: Evidence from Lonar crater, India. *J. Geophys. Res.*, doi:10.1029/2005JB003662, 2005.

P. S. Kumar and D. Kring. Impact fracturing and structural modification of sedimentary rocks at Meteor Crater, Arizona. *J. Geophys. Res.*, In Press, 2008.

J. Lasker and P. Robutel. The chaotic obliquity of the planets. *Nature*, 361:608–612, 1993.

R. Li, R. E. Arvidson, M. G. K. Di, J. Guinn, A. Johnson, M. Maimone, L. H. Matthies, M. Malin, T. Parker, S. W. Squyres, and W. A. Watters. Opportunity rover localization and topographic mapping at the landing site of Meridiani Planum, Mars,. *J. Geophys. Res. Planet.*, 112, 2007.

J. Lister and R. Kerr. The propagation of two-dimensional and axisymmetric viscous gravity currents at a fluid interface. *J. Fluid Mech.*, 203:215–249, 1989.

D. E. Loper. Mantle plumes. *Tectonophysics*, 187:373–384, 1991.

M. C. Malin and K. S. Edgett. Sedimentary rocks of early Mars. *Science*, 290:1927–1937, 2000.

A. C. Maloof, S. T. Stewart, S. A. S. B. P. Weiss, N. L. Swanson-Hysell, K. Louzada, I. Garrick-Bethell, and P. M. Poussart. Geology of Lonar crater, India. *GSA Bull.*, Submitted, 2007.

M. Manga and J. Arkani-Hamed. Remelting mechanisms for shallow source regions of mare basalts. *Physics of Earth and Planetary Interiors*, 68:9–31, 1991.

M. M. Marinova, O. Aharonson, and E. Asphaug. Mega-impact formation of the Mars hemispheric dichotomy. *Nature*, 453:1216–1219, 2008.

D. E. Maxwell. Simple z model of cratering, ejection, and the overturned flap. In D. Roddy, R. Pepin, and R. Merrill, editors, *Impact and explosion cratering*, pages 983–1022. Pergamon Press, New York, New York, 1977.

A. S. McEwen, B. S. Preblich, E. P. Turtle, N. A. Artemieva, and M. P. Golombek. The rayed crater Zunil and interpretations of small impact craters on Mars. *Icarus*, 176:351–381, 2005.

T. R. McGetchin, M. Settle, and J. W. Head. Radial thickness variation in impact crater ejecta: implications for lunar basin deposits. *Earth Planet. Sci. Lett.*, 20:226–236, 1973.

J. M. McGlaun, S. L. Thompson, and M. G. Elrick. A three-dimensional shock wave physics code. *J. Impact Eng.*, 10:351–360, 1990.

S. M. McLennan, J. F. B. III, W. M. Calvin, P. R. Christensen, B. C. Clark, P. A. de Souza, J. Farmer, W. H. Farrand, D. A. Fike, R. Gellert, A. Ghosh, T. D. Glotch, J. P. Grotzinger, B. Hahn, K. E. Herkenhoff, J. A. Hurowitz, J. R. Johnson, S. S. Johnson, B. Jolliff, G. Klingelhofer, A. H. Knoll, Z. Learner, M. C. Malin, H. Y. McSween, J. Pocock, S. W. Ruff, L. A. Soderblom, S. W. Squyres, N. J.

Tosca, W. A. Watters, M. B. Wyatt, and A. Yenp. Provenance and diagenesis of the evaporite-bearing Burns formation, Meridiani Planum, Mars. *Earth and Planet. Sci. Lett.*, 240:95–121, 2005.

R. G. McQueen. Hugoniot equation of state of twelve rocks. *Journal Geophys. Res.*, 72(20): 373–384, 1967.

R. G. McQueen. Shock waves in condensed media: their properties and the equation of state of materials derived from them. In S. Eliezer and R. Ricci, editors, *Equazioni di stato ad alta pressione: teoria e applicazioni*, Scuola Internazionale di Fisica Enrico Fermi, pages 101–313. Società Italiana di Fisica, Bologna, Italy, 1991.

R. G. McQueen, S. P. Marsh, and J. N. Fritz. Hugoniot equation of state of twelve rocks. *Journal Geophys. Res.*, 72(20):4999–5036, 1967.

H. J. Melosh. Tectonic patterns on a reoriented planet–Mars. *Icarus*, 44:745–751, 1980.

M. J. Melosh. *Impact Cratering: A Geological Process*. Oxford Univ. Press, New York, 1st edition, 1989.

M. A. Meyers. *The Dynamic Behavior of Materials*. Wiley, New York, 1st edition, 1994.

D. J. Milton. Structural geology of the Henbury meteorite craters, Northern Territory, Australia. *Geological Survey Professional Papers*, 599-C:C1–C17, 1968.

D. J. Milton and F. C. Michel. Structure of a ray crater at Henbury, Northern Territory, Australia. *Geological Survey Professional Papers*, 525-C:C5–C11, 1965.

S. K. Mitra. On the probability distribution of the sum of uniformly distributed random variables. *SIAM J. Appl. Math.*, 20:195–198, 1971.

J. Monteux, N. Coltice, F. Dubuffet, and Y. Ricard. Thermo-mechanical adjustment after impacts during planetary growth. *Geophys. Res. Lett.*, 34:L24201, 2007. doi: 10.1029/2007GL031635.

P. J. Mouginis-Mark. Morphology of martian rampart cratres. *Nature*, 272:691–694, 1978.

R. A. Muller. Avalanches at the core-mantle boundary. *Geophys. Res. Lett.*, 29:41,1–4, 2002. doi: 10.1029/2002GL015938.

J. B. Murray and J. E. Guest. Circulaity of craters and related structures on the earth and moon. *Modern Geology*, 1:149–159, 1970.

V. K. Nayak. Glassy objects (impactite glasses?) a possible new evidence for meteoritic origin of the Lonar crater, Maharashtra State, India. *Earth and Planet. Sci. Lett*, 14:1–6, 1972.

F. Nimmo, S. D. Hart, D. G. Korycansky, and C. B. Agnor. Implications of an impact origin for the Martian hemispheric dichotomy. *Nature*, 453:1220–1223, 2008.

T. Ohman, M. Aittola, V. Kostama, and J. Raitala. The preliminary analysis of polygonal impact craters within greater Hellas region, Mars. In C. Koeberl and H. Henkel, editors, *Impact Tectonics*, pages 131–143. Springer, Berlin, 2005.

P. Olson, G. Schubert, and C. Anderson. Plume formation in the D"-layer and the roughness of the core-mantle boundary. *Nature*, 327:409–413, 1987.

W. R. Perret and R. C. Bass. Free-field ground motion induced by underground explosions. *Sandia report*, SAND74-0252, 1975.

R. J. Phillips, M. T. Zuber, S. C. Solomon, M. P. Golombek, B. M. Jakosky, W. B. Banerdt, D. E. Smith, R. M. E. Williams, B. M. Hynek, O. Aharonson, and S. A. Hauck. Ancient geodynamics and global-scale hydrology on Mars. *Science*, 291:2587–2591, 2001.

A. J. Piekutowski. Cratering mechanisms observed in laboratory-scale high-explosive experiments. In D. Roddy, R. Pepin, and R. Merrill, editors, *Impact and explosion cratering*,

pages 67–102. Pergamon Press, New York, New York, 1977.

E. Pierazzo, A. M. Vickery, and H. J. Melosh. A reevaluation of impact melt production. *Icarus*, 127:408–423, 1997.

R. J. Pike. Size-dependence in the shape of fresh impact craters on the moon. In D. Roddy, R. Pepin, and R. Merrill, editors, *Impact and explosion cratering*, pages 489–509. Pergamon Press, New York, New York, 1977.

R. J. Pike and D. E. Wilhelms. Secondary-impact craters on the moon: topographic form and geologic process. *Lunar Planet Sci.*, 9: 907–909, 1978.

J. A. Pilon, R. A. F. Grieve, and V. L. Sharpton. The subsurface character of Meteor Crater, Arizona, as determined by ground-probing radar. *J. Geophys. Res.*, 96:15563–15576, 1991.

W. H. Press, S. A. Teukolsky, W. T. Vetterling, and B. P. Flannery. *Numerical Recipes in C*. Cambridge Univ. Press, Cambridge, UK, 2nd edition, 1988.

W. L. Quaide and V. R. Oberbeck. Thickness determinations of the lunar surface layer from lunar impact craters. *J. Geophys. Res.*, 73: 5247–5270, 1968.

C. C. Reese and V. S. Solomatov. Fluid dynamics of local Martian magma oceans. *Icarus*, 184:102–120, 2006.

C. C. Reese and V. S. Solomatov. Non-newtonian stagnant lid convection and magmatic resurfacing of Venus. *Icarus*, 139:67–80, 1999.

C. C. Reese, V. S. Solomatov, J. R. Baumgardner, D. R. Stegman, and A. V. Vezolainen. Magmatic evolution of impact-induced Martian mantle plumes and the origin of Tharsis. *Journal Geophys. Res.*, 109:E08009, 2004. doi: 10.1029/2003JE002222.

F. M. Richter. Convection and the large-scale circulation of the mantle. *J. Geophys. Res.*, 78:8735–8745, 1973.

J. H. Roberts and S. Zhong. The cause for the north-south orientation of the crustal dichotomy and the equatorial location of Tharsis on Mars. *Icarus*, 190:24–31, 2007.

D. J. Roddy. Pre-impact geologic conditions, physical properties, energy calculations, meteorite and initial crater dimensions and orientations of joints, faults and walls at Meteor Crater, Arizona. *Lunar Planet. Sci. Conf 9th*, pages 3891–3930, 1978.

D. J. Roddy, J. M. Boyce, G. W. Colton, and A. L. Dial. Meteor Crater, Arizona, rim drilling with thickness, structural uplift, diameter, depth, volume, and mass-balance calculations. *Proc. Lunar Sci. Conf. 6th*, pages 2621–2644, 1975.

L. B. Ronca and J. W. Salisbury. Lunar history as suggested by the circularity index of lunar craters. *Icarus*, 5:130–138, 1966.

C. Schmerr, Y. Fei, and C. Bertka. Extending the solidus for a model iron-rich Martian mantle composition to 25 GPa. *Lunar and Planetary Science XXXII*, (1157), 2001.

G. Schubert and T. Spohn. Thermal history of Mars and the sulfer content of its core. *J. Geophys. Res.*, 95:14095–104, 1990.

G. Schubert, D. Turcott, and P. Olson. *Mantle Convection in the Earth and Planets*. Cambridge Univ. Press, Cambridge, UK, 1st edition, 2001.

P. Schultz and A. Lutz-Garihan. Grazing impacts on Mars: A record of lost satellites. *LPSC 13, J. Geophys. Res. Supp.*, 87:A84–96, 1982.

P. H. Schultz. *Moon Morphology*. University of Texas Press, Austin, Texas, 1976.

P. H. Schultz and D. E. Gault. Seismic effects of major basin formation on the moon and mercury. *The Moon*, pages 159–177, 1975.

D. H. Scott and K. L. Tanaka. Geological map of the western equatorial region of Mars, scale 1:15,000,000. *U.S. Geol. Survey Map*, I-1802-A, 1986.

D. H. Scott and J. A. Watkins. Lunar farside tectonics and volcanism. *Lunar Plant. Sci Conf.*, 8:1119–1130, 1997.

L. E. Senft and S. T. Stewart. Modeling impact cratering in layered surfaces. *J. Geophys. Res.*, doi:10.1029/2007JE002894:E11002, 2007.

E. M. Shoemaker. Penetration mechanics of high velocity meteorites, illustrated by Meteor Crater, Arizona. *International Geological Congress*, 21, 1960.

E. M. Shoemaker and R. E. Eggleton. Terrestrial features of impact origin. *Proceedings of the Geophysical Laboratory – Lawrence Radiation Cratering Symposium*, 1:A1–A27, 1961.

J. A. Skinner, T. M. Hare, and K. L. Tanaka. Digital renovation of the atlas of Mars 1:15,000,000-scale global geologic series maps. *Lunar and Planetary Science XXXVII*, (2331), 2006.

V. S. Solomatov. Scaling of temperature- and stress-dependent viscosity convection. *Physics of Fluids*, 7:266–274, 1995.

T. Spohn, F. Sohl, and D. Breuer. Mars. *Astron. Astrophys. Rev.*, 8:181–286, 1998.

T. Spohn, M. H. A. na, D. Breuer, M. Golombek, R. Greeley, A. Halliday, E. Hauber, R. Jaumann, and F. Sohl. Geophysical constraints on the evolution of Mars. *Space Science Reviews*, 96:231–262, 2001.

F. D. Stacey. *Physics of the Earth.* Brookfield Press, Queensland, Australia, 3rd edition, 1992.

D. Stevenson, T. Spohn, and G. Schubert. Magnetism and thermal evolution of the terrestrial planets. *Icarus*, 54:466–489, 1983.

D. J. Stevenson. Mars' core and magnetism. *Nature*, 412:214–219, 2001.

S. T. Stewart and G. J. Valiant. Martian subsurface properties and crater formation processes inferred from fresh impact crater geometries. *Meteor. and Planet. Sci*, 41:1509–1537, 2006.

S. Stewart-Mukhopadhyay. Personal communication. *Deep Impact Mission, EGG Tutorial STSM*, 2002.

D. Stoeffler, D. E. Gault, J. Wedekind, and G. Polkowski. Experimental hypervelocity impact into quartz sand: Distribution and shock metamorphism of ejecta. *J. Geophys. Res.*, 80: 4062–4077, 1975.

R. Sullivan, D. Banfield, J. F. Bell, W. Calvin, D. Fike, M. Golombek, R. Greeley, J. Grotzinger, K. Herkenhoff, D. Jerolmack, M. Malin, D. Ming, L. A. Soderblom, S. W. Squyres, S. Thompson, W. A. Watters, C. M. Weitz, and A. Yen. Aeolian processes at the Mars Exploration Rover Meridiani Planum landing site. *Nature*, 436:58–61, 2005.

K. L. Tanaka, J. A. Skinner, T. M. Hare, T. Joyal, and A. Wenker. Resurfacing history of the northern plains of Mars based on geologic mapping of Mars Global Surveyor data. *Journal Geophys. Res.*, art. E48043, 2003. doi: 10.1029/2002JE001908.

K. L. Tanaka, J. J. A. Skinner, and T. M. Hare. Geologic map of the northern plains of Mars. *U. S. Geol. Survey Map*, SIM-2888, 2005.

S. L. Thompson. *CSQ III: An Eulerian Finite Difference Program for Two-Dimensional Material Response: Users Manual.* Sandia Natl. Lab, Albuguerque, NM, 1988.

W. B. Tonks and H. J. Melosh. Magma ocean formation due to giant impacts. *Journal Geophys. Res.*, 98:5319–5333, 1993.

J. T. Touma and J. Wisdom. The chaotic obliquity of Mars. *Science*, 259:1294–1297, 1993.

L. J. Vortman. Ten years of high explosive cratering research at Sandia Laboratory. *Nuc. App. and Tech.*, 7:269–304, 1969.

D. Wallis and N. McBride. Planetary impact crater analysis with eigenfunction expansion. *Mon. Not. Roy. Ast. Soc.*, 330:458–472, 2002.

D. Wallis, M. J. Burchell, A. C. Cook, C. J. Solomon, and N. McBride. Azimuthal impact directions from oblique impact crater morphology. *Monthly Notices of the Royal Astronomical Society*, 359:1137–1149, 2005.

G. W. Wetherill. Formation of the Earth. *Ann. Rev. Earth Planet Sci.*, 18:205–256, 1990.

J. A. Whitehead. Dynamics of laboratory diapir and plume models. *Journal Geophys. Res.*, 80: 705–717, 1975.

R. J. Willemann. Reorientation of planets with elastic lithospheres. *Icarus*, 60:701–709, 1984.

D. A. Williams and R. Greeley. Assessment of antipodal-impact terrains on Mars. *Icarus*, 110:196–202, 1994.

C. F. Yoder, A. S. Konopliv, D. N. Yuan, E. M. Standish, and W. M. Folkner. Fluid core size of Mars from detection of the solar tide. *Science*, 300:299–303, 2003.

A. Zerr, A. Diegeler, and R. Boehler. Solidus of Earth's deep mantle. *Science*, 281, 1998.

M. T. Zuber and D. E. Smith. Mars without Tharsis. *J. Geophys. Res.*, 102:28673–28686, 1997.

M. T. Zuber, S. C. Solomon, R. J. Phillips, D. E. Smith, G. L. Tyler, O. Aharonson, G. Balmino, W. B. Banerdt, J. W. Head, C. L. Johnson, F. H. Lemoine, P. J. McGovern, G. A. Neumann, D. D. Rowlands, and S. Zhong. Internal structure and early thermal evolution of Mars from Mars Global Surveyor topography and gravity. *Science*, 287: 1788–1793, 2000.